Dissertations, Theses, and Masters Projects   Theses, Dissertations, & Master Projects

2000

Theoretical and experimental study of generation mechanisms for laser ultrasound in woven graphite /epoxy composites with translaminar stitching

Adam D. Friedman

College of William & Mary - Arts & Sciences

Follow this and additional works at: https://scholarworks.wm.edu/etd

Part of the Acoustics, Dynamics, and Controls Commons, Materials Science and Engineering Commons, and the Optics Commons

Recommended Citation

INFORMATION TO USERS

This manuscript has been reproduced from the microfilm master. UMI films the text directly from the original or copy submitted. Thus, some thesis and dissertation copies are in typewriter face, while others may be from any type of computer printer.

The quality of this reproduction is dependent upon the quality of the copy submitted. Broken or indistinct print, colored or poor quality illustrations and photographs, print bleedthrough, substandard margins, and improper alignment can adversely affect reproduction.

In the unlikely event that the author did not send UMI a complete manuscript and there are missing pages, these will be noted. Also, if unauthorized copyright material had to be removed, a note will indicate the deletion.

Oversize materials (e.g., maps, drawings, charts) are reproduced by sectioning the original, beginning at the upper left-hand corner and continuing from left to right in equal sections with small overlaps.

Photographs included in the original manuscript have been reproduced xerographically in this copy. Higher quality 6" x 9" black and white photographic prints are available for any photographs or illustrations appearing in this copy for an additional charge. Contact UMI directly to order.

Theoretical and Experimental Study of Generation Mechanisms for Laser Ultrasound in Woven Graphite/Epoxy Composites with Translaminar Stitching

---

A Dissertation

Presented to The Faculty of the Department of Applied Science

The College of William and Mary

In Partial Fulfillment

Of the Requirements for the Degree of

Doctor of Philosophy

By

Adam D. Friedman

May 2000

UMI Number: 9989344

Copyright 2000 by
Friedman, Adam Daniel

All rights reserved.

UMI®
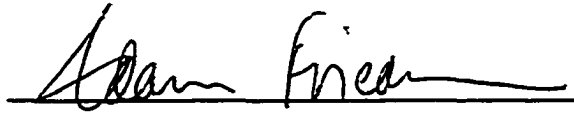
Copyright

by

Adam D. Friedman

2000

APPROVAL SHEET

This dissertation is submitted in partial fulfillment
of the requirements for the degree of

Doctor of Philosophy.

Adam D. Friedman

Approved, May 2000

Mark Hinders
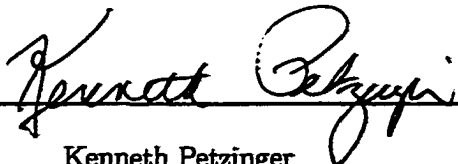
Eric Madaras

Dennis Manos

Brian Holloway

Kenneth Petzinger

This thesis is dedicated to my parents for all of their love and support.

Contents

List of Tables

List of Figures

x

xi

xii

xiii

Acknowledgments

I would like to express my thanks to my advisors Dr. Mark Hinders and Dr. Eric Madaras for their assistance and direction throughout the course of this work. Also, I want to thank Dr. Dennis Manos fo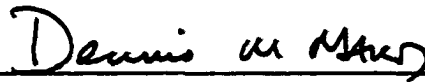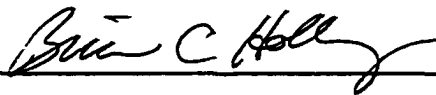r bringing me into the department and his commitment to building a strong program here at William and Mary. I wish to thank my other committee members for their critical reading of my dissertation.

Thanks also goes to Kathee Card for her sincere efforts to take care of the students and to keep the department functional.

I would like to acknowledge Dr. Meng Chou Wu for his help when I first started my research at NASA. I would also like to acknowledge my friends, Jesse Diggs, Eric Allman, Mark Wensell for their help with all types of problems.

Finally, I would like to thank my parents for all of their support and patience thoughout this long process.

Abstract

The aerospace industry is beginning to use advanced composite materials for primary load bearing structures and their failure mechanisms must be better understood to predict their behavior in service. The Combined Loads Tests (COLTS) facility is being constructed at the NASA Langley Research Center to characterize these failure mechanisms. Laser based ultrasonic NDE can monitor the samples *during* dynamic loading without interfering with the structural tests. However, the constraints of implementing laser ultrasound in a structures laboratory reduces the efficiency of the technique. The system has to be "eye-safe" because many people will be present during the structural tests. Consequently, laser light has to be delivered through fiber optics and a significant amount of light is lost. Also, the nature of the composite materials makes laser ultrasonic inspection difficult. The composites of interest are formed from woven layers that are stitched through the laminate thickness and bound in a resin matrix. These materials attenuate ultrasound strongly and exhibit a high degree of scattering.

Generation mechanisms in laser based ultrasound must be better understood to improve generation efficiency and consequently improve the signal-to-noise ratio. Although some experimental and theoretical studies have been conducted to characterize generation mechanisms, more extensive work is needed for composite materials. Specifically, we are concerned with generation mechanisms in thick, stitched composite structures. We describe a theoretical and experimental investigation of laser generated ultrasound in complex composite materials. We first develop a mathematical model describing the thermoelastic generation of ultrasound in a general anisotropic material. We then present a wide range of experimental data investigating the effects of laser and material parameters on the generated ultrasound. We specifically consider the relationship between laser pulse width, laser wavelength, and material composition. Finally, we compare this data to our mathematical model.

Theoretical and Experimental Study of Generation Mechanisms for

Laser Ultrasound in Woven Graphite/Epoxy Composites with

Translaminar Stitching

Chapter 1

Introduction

1.1 Laser Based Ultrasonic Nondestructive Evaluation

Nondestructive evaluation (NDE) for investigating material integrity and for process control has become increasingly important. For example, nondestructive testing of our nation's aircraft has become critical as the aircraft continue to age. At the same time companies, have begun to realize the economic benefit of real-time process monitoring during "high-value-added processing". There are strong incentives to develop techniques that allow rapid and accurate inspection of materials without interfering with the function or operation of the product. Laser based ultrasonic NDE is one of the techniques that has many attractive characteristics for NDE and process control because it is completely remote and therefore can be used to monitor moving parts and complex geometries. Although laser based ultrasonics is relatively new, it is now being studied extensively by many groups. In this chapter, we will describe laser based ultrasonic NDE, discuss its advantages and disadvantages compared to conventional techniques, and present the motivation for further

2

research.

For an excellent comprehensive review of laser based ultrasonics, the reader is referred to *Laser Ultrasonics: Techniques and Applications*, by C. B. Scruby and L. E. Drain [1] Here, we will summarize some of the important features.

Several different physical processes may occur when laser light is applied to a solid surface. In the thermoelastic regime, where incident power densities are below the damage threshold of the sample, these processes include sample heating, generation of thermal waves, and the generation of elastic waves (ultrasound). This last effect is the basis for laser ultrasonic NDE. In this process, the incident laser causes a localized heating and volume expansion in the sample which generates thermoelastic strain fields that act as an elastodynamic source for ultrasonic waves. These waves can then be utilized to characterize the sample as in conventional ultrasonic NDE.

At power densities that exceed the damage threshold of the material, the ablative regime, other processes may occur. The surface of the sample can be ablated and the sample may melt, plastically deform, and exhibit crack formation. In general, the processes in the thermoelastic regime are more appropriate for nondestructive evaluation since the sample is not damaged. In some cases, however, surface ablation may be acceptable and even desirable since larger amplitude waveforms can be generated. For example, in the inspection of concrete structures, a small amount of surface damage may be permissible. Also, special coatings can be applied to some samples so that only the coating is damaged and the sample is unharmed. For our purposes, we would prefer not to alter the sample and will restrict further discussion to only the thermoelastic regime.

Laser based ultrasonic NDE uses lasers to generate and detect elastic waves in a sample. Typically, one laser is used to generate ultrasonic waves while a second laser is used with an optical technique like interferometry to measure the surface displacements.

3

The two lasers can be applied on the same surface of the sample or they can be arranged on opposite sides of the sample in either a pulse-echo or pitch-catch configuration. These two modes of operation are illustrated in Figure 1.1. Laser based ultrasonic NDE offers significant advantages over conventional ultrasonic NDE methods because it is a completely *non-contact* technique and does not require close proximity to the sample. Laser based ultrasound can remotely measure samples in environments that are inaccessible to contact techniques because physical couplants are undesirable or impossible. For example, samples can be examined in environments at elevated temperature (> 500 degrees Celsius), where there is no suitable fluid couplant. Similarly, samples in high vacuum systems can be monitored, possibly even during aggressive chemical or plasma processing. Also, since no couplant is required, signal variability due to bonding quality is eliminated.

Furthermore, laser based ultrasound can be used to remotely examine structures in hostile environments that are hazardous to human operators and equipment. For example, measurements can be made on samples in radioactive or chemically corrosive environments. Similarly, laser based ultrasound can be used during experiments where other methods might interfere with the experiment. For example, samples can be monitored in wind tunnels without affecting aerodynamic tests.

Laser based ultrasound can evaluate small and very thin samples that would be difficult to investigate with conventional contact techniques. Ultrasonic waves can be excited and received on small samples because the diameter of the laser beams can be made very small. Contact transducers tend to have a dead zone just below the surface so that they cannot measure defects immediately below the surface. The small probe area of laser based ultrasonics leads to a much smaller dead zone so that this is not a problem.

Samples with complex geometries or confined spaces can be inspected more easily with laser based ultrasound. The laser beams do not have to be normally incident to the

4
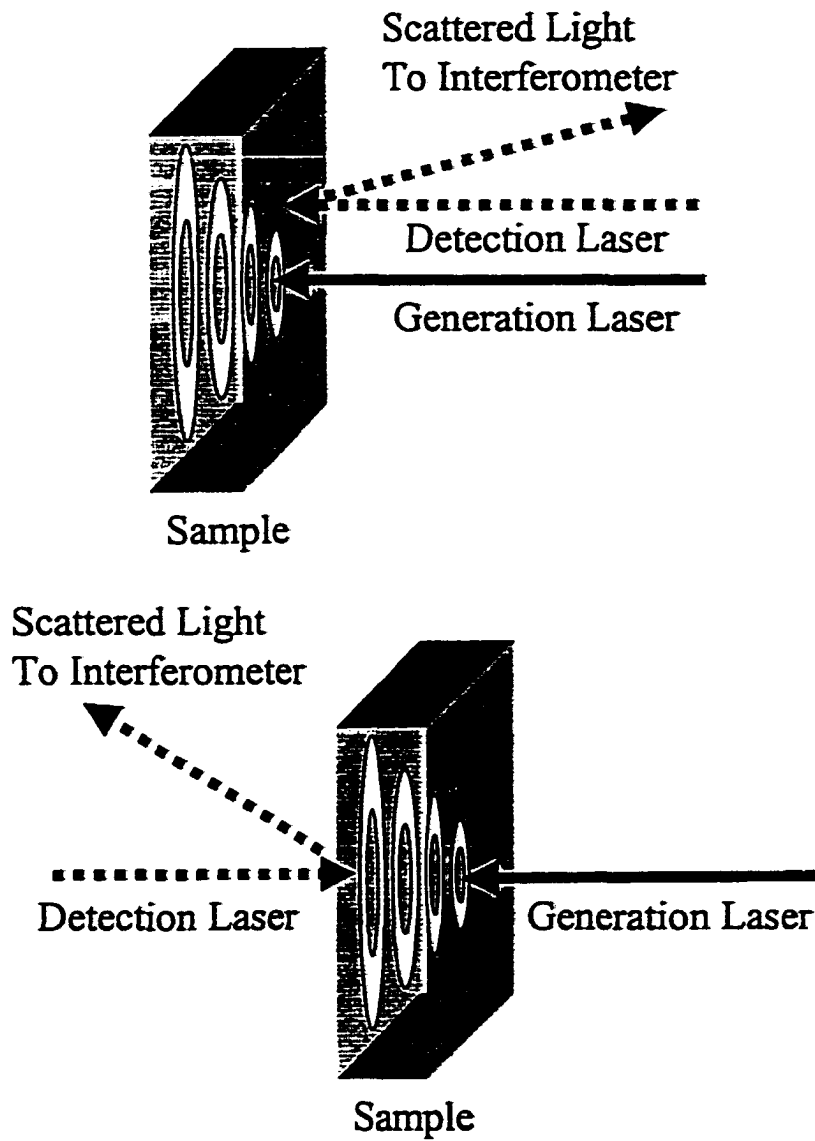
Figure 1.1: Illustration of the two modes of laser based ultrasonic NDE. Top: Detection and generation on the same side. Bottom: Generation and detection on opposite sides.

sample surface so that both the detection and generation lasers can be delivered by mirrors or fiber optics around awkward geometries or into regions that would be inaccessible to large contact probes. Similarly, delicate samples can be investigated since no physical contact is required. Laser ultrasound can inspect samples with sensitive surfaces or surfaces that must be kept clean and free of scratches.

Laser ultrasound can also be used for area inspections at speeds that cannot be obtained by mechanical techniques. Since the lasers can be rapidly rastered, large areas can be quickly scanned. Also, quickly moving parts can be investigated. For example parts on an assembly line can be scanned or the rotor blades of a helicopter can be examined *while the rotors are spinning.*

The directivity of laser generated ultrasound can be modified by optically changing the laser source. In contrast a conventional contact probe has a fixed directivity. Also, the bandwidth of laser generated ultrasound is larger than for contact probes. The bandwidth of laser generated ultrasound can also be modified by adjusting the laser source to better match attenuation characteristics of the test material. Furthermore, any type of ultrasonic wave can be generated with a laser source.

Finally, laser based ultrasound solves difficulties encountered by other non-contact ultrasound techniques. Electromagnetic acoustic transducers (EMATS) require conducting specimens. Similarly, magnetostrictive devices require ferromagnetic materials. Capacitance transducers require locally polished parallel surfaces, close proximity, and precise handling. In contrast, laser based ultrasound does not require close proximity to the sample and is not restricted to specific materials or very careful sample preparation [1].

6

1.2 Motivation

1.2.1 General Considerations

Contact techniques have some advantages over laser based ultrasound. Contact techniques are considerably less expensive than laser based ultrasonics. Also, special safety precautions like eye protection are not required for contact techniques but are required to use laser based ultrasonics.

Perhaps most significantly, contact ultrasound techniques currently provide a superior signal-to-noise ratio than laser based ultrasound. Peak displacements of laser generated ultrasound are estimated to be about 12 db less than those of a resonant piezoelectric transducers but of the same order of magnitude as short-pulse (i.e. damped) piezoelectric probes. This leads only to a slight loss in sensitivity. However, the sensitivity of laser detection of ultrasound is significantly lower than contact techniques. Consequently, the overall sensitivity of contact techniques is several orders of magnitude better than laser based ultrasound [1].

To be competitive with contact techniques and to fully realize its potential, laser based ultrasonics must be better understood. Considerable work has been done to improve the sensitivity of laser detection of ultrasound but less attention has been devoted to optimizing the laser ultrasound source. In most cases, ultrasound is generated by whatever laser is available, with minimal consideration of matching laser and material parameters so that the ultrasonic source is maximized. This research is an effort to more fully understand generation mechanisms so that ultrasonic generation can be optimized for a given laser/sample system.

7

1.2.2 Specific Considerations

The aerospace industry is beginning to use advanced composite materials for primary load bearing structures and the failure mechanisms of these materials must be better understood to predict their behavior in service. The Combined Loads Tests (COLTS) facility is being constructed at the NASA Langley Research Center to characterize these failure mechanisms. Illustrated in Figure 1.2, the COLTS facility is designed to test large structures like an aircraft fuselage up to 13.716 meters (45 feet) long and 4.572 meters (15 feet) in diameter. It will be a large open area with multiple testing bays and many experiments occurring simultaneously. To illustrate the scale of the COLTS facility, Figure 1.3 shows a composite wing box structure that was tested in a similar facility. Laser based ultrasonic NDE is desirable because it can monitor the samples *during* dynamic loading without interfering with the structural tests.

However, implementing laser ultrasound in a structures laboratory further reduces the efficiency of the technique. In general, there will always be design constraints when trying to implement laser based ultrasound outside of a laser laboratory. For example, the COLTS system has to be "eye-safe" because many people will be present during the structural tests. Therefore, laser light will be delivered through fiber optics and a significant amount of the initially available light is lost. A description of the laser based ultrasonic NDE system developed for the COLTS facility along with some preliminary results is presented in the appendix. A much more powerful detection laser could be integrated into the system but this is generally not a financially feasible solution. Instead, it is preferable to maximize the *available* technology.

Furthermore, the nature of the composite materials makes laser ultrasonic inspection difficult. The composites of interest at COLTS are formed from woven layers that are stitched through the laminate thickness and bound in a resin matrix. Figure 1.4 shows

8
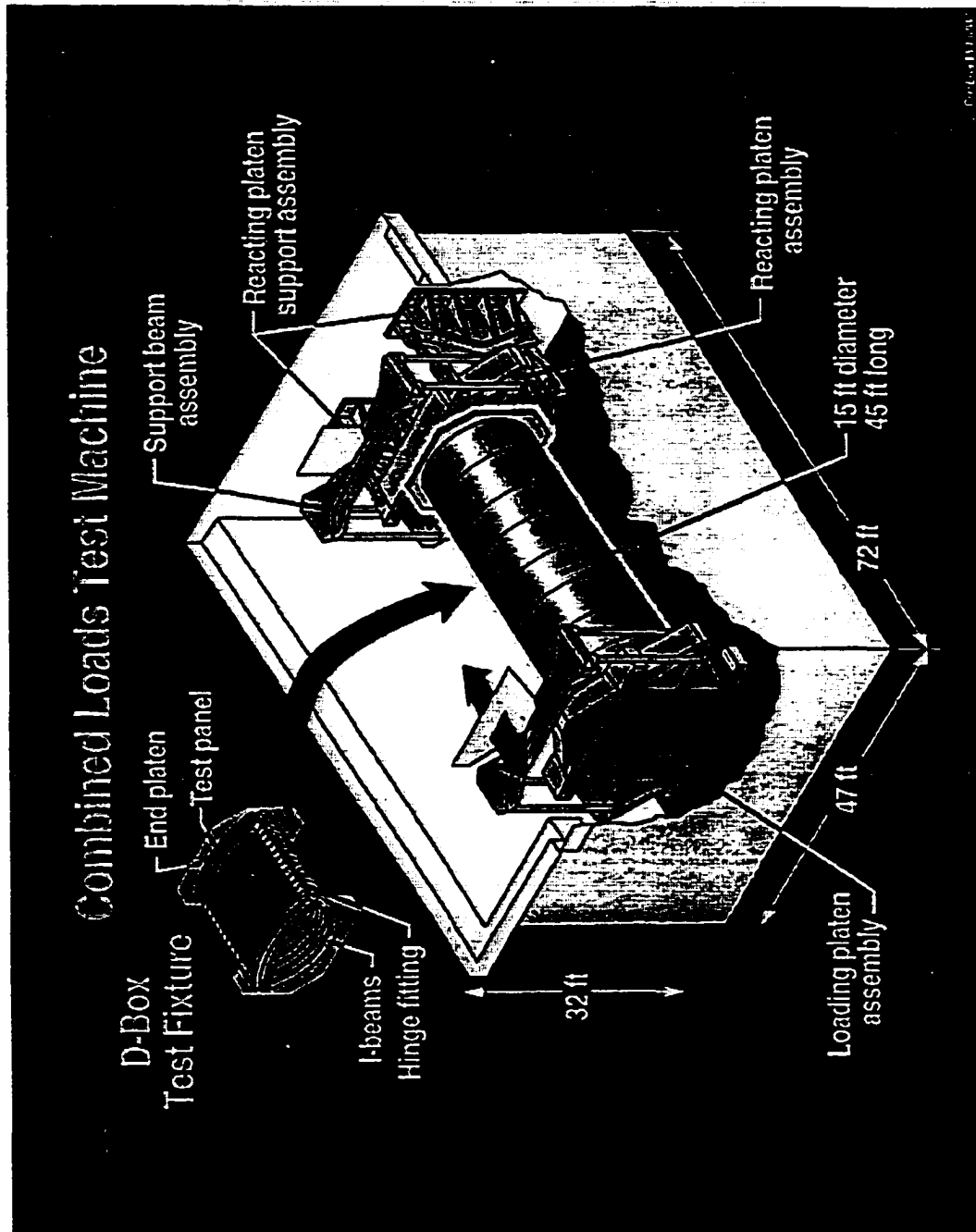
Figure 1.2: Schematic illustration of the COLTS facility. (From the NASA/Langley Web Site.)

9

Figure 1.3: Facility similar to the COLTS facility where a composite wing is being tested.

10

photographs of composite pieces from the wing box in Figure 1.3 after it had been stressed to failure. The sample in the bottom of Figure 1.4 is a piece of the wing box skin and the rows of translaminar stitches are clearly visible. The skin is approximately five inches square and consists of ten stacks of [45/-45/0$_2$/90/0$_2$/-45/45] AS-4-3501-6 graphite epoxy material stitched together, resulting in a 0.58 inch total thickness. The stitched reinforcements of Kevlar are in rows spaced 0.2 to 0.5 inches apart with a stitch spacing of approximately 0.1 inches. The structure on the top is a seven inch square piece of the wing box skin that has been bidirectionally T-stiffened. These materials strongly attenuate ultrasound and exhibit a high degree of scattering. They are difficult to inspect with conventional contact or immersion techniques.

Although some experimental [2], [3] and theoretical studies (e.g. [3] - [7]) have been conducted to characterize laser ultrasonic generation mechanisms, more extensive work is needed for composite materials. Specifically, more effort is required to understand generation mechanism in the anisotropic composites that will be studied at COLTS. The purpose of this research is to better understand the generation mechanisms in these complex composite materials. Consequently, we hope to maximize the laser ultrasonic source so that generation efficiency and therefore signal-to-noise ratio is improved.

1.3 Summary

Laser based ultrasonics offers significant advantages over conventional ultrasonic methods because it is a non-contact and remote technique. However, it is more expensive than conventional techniques, requires safety precautions, and is currently not as sensitive as contact techniques. In order for laser based ultrasonics to be competitive with conventional contact techniques, its signal-to-noise ratio must be improved. Generation mechanisms must be better understood to optimize the laser ultrasonic source for a given laser/sample system.

11
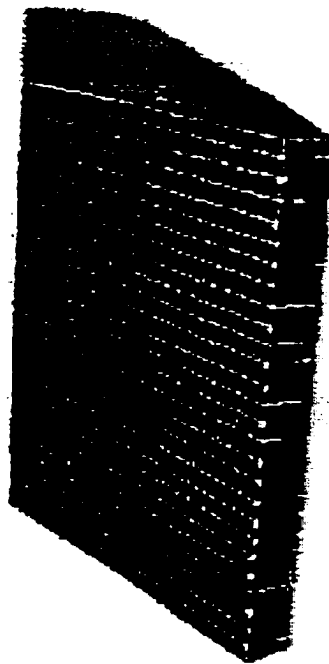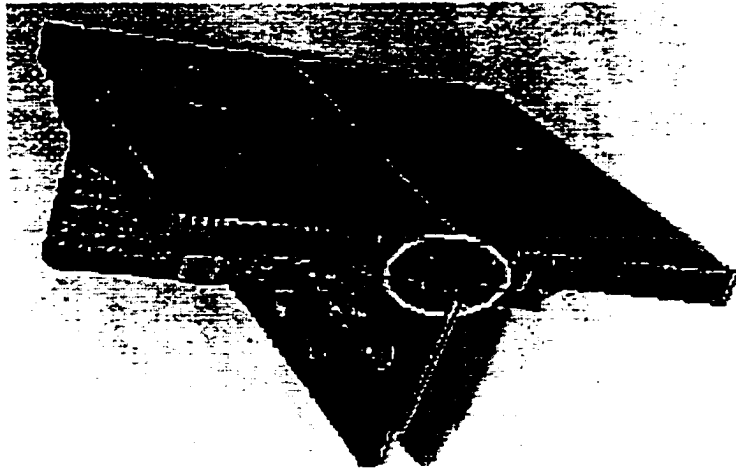
Figure 1.4: Composite samples from the ACT wingbox after being dynamically tested to failure. Top: Bidirectionally stiffened skin sample with interlaminar failure. Bottom: Skin sample with impact damage.

12

The purpose of this work is to characterize generation mechanisms as a function of laser and material parameters through a theoretical and experimental investigation. Specifically, we are concerned with generation mechanism in anisotropic composite structures.

1.4 Overview of the Present Work

In this chapter, a brief introduction to laser based ultrasonic NDE was presented and the motivation for our work was explained. Chapter 2 will provide a comprehensive literature review as background for our work and chapters 3 and 4 will develop a theoretical model for laser generated ultrasound in isotropic and anisotropic materials. Chapter 5 will present an experimental investigation of laser generated ultrasound as a function of laser and material parameters. These theoretical and experimental results will be analyzed and compared in chapter 6 and conclusions will be made. Chapter 7 will summarize the work and suggest directions for future efforts. An appendix will include computer code used in the theoretical modeling and a discussion of a field-deployable, laser based ultrasonic system developed during the course of this work.

13

Chapter 2

Literature Review

For many practical cases in laser based ultrasonics, the laser source can be approximated as a point source or line source in a plate or half-space. The problem of determining the elastic response of a half-space (or plate) due to an applied point or line load belongs to a class of problems referred to collectively as "Lamb's problem." Furthermore, the solution to Lamb's problem for an impulse point source is by definition, the Green's function for the problem and may be used to construct more complicated sources.

Lamb's problem has been studied extensively, and the first part of this review summarizes some notable and recent contributions. A comprehensive list of references is also provided for the reader's benefit. Following this, some of the major theoretical and experimental studies of laser generated ultrasound in solids are reviewed in detail. A separate section reviews efforts to apply laser based ultrasound to nondestructive evaluation. A final section summarizes other contributions to the field of laser based ultrasonics.

14

2.1 Lamb's Problem

In 1904, H. Lamb [8] presented the classical analysis of the elastic response of a half-space due to line and point loads applied at the surface and below the surface. Harmonic loads were initially considered and then superposition techniques were used to analyze pulse loads.

A thorough review of Lamb's analysis can be found in Ewing *et al.* [9] and more recently, in Miklowitz [10]. Reviews of some of results can also be found in chapters six and seven of Graff [11] and Achenbach [12], respectively.

In 1957, Pekeris and Lifson [13] presented an exact solution describing the surface motion of a uniform elastic half-space produced by a vertical point force buried beneath the surface. Both vertical and horizontal displacement components were represented in terms of complex integrals which were numerically evaluated. From this analysis, plots of surface displacement as a function of distance from epicenter were presented for both components.

Kraut [14] was the first to use the Cagniard de Hoop [15], [12] method to study Lamb's problem with a line source in 1963.

Pardee [16] presented a mathematically rigorous derivation of the frequency domain Green's function for an infinite isotropic media and an isotropic plate in 1977. The details of this derivation are complicated and we only summarize some of the main results; an expression in the form of an integral equation was generated for a *stress* Green's function for the infinite isotropic media. This stress Green's function was constructed to include stress free boundary conditions for the case of a *finite* solid. An expression was presented from this result for the usual *displacement* Green's function. It was claimed that the integral equation for the stress Green's function could be analytically integrated but that it was only necessary to partially integrate it for the plate problem. Subsequently, the infinite space stress Green's function was used to construct the stress Green's function for the isotropic

15

slab which was also in the form of an integral equation. It was noted that the displacement and stress Green's function tensors for the case of body forces could be derived from this expression by suitable differentiation.

In 1979, Pao et al. [17] used generalized ray theory to model acoustic waves generated in infinite isotropic plates. Three buried point sources were considered; a single force, a double force, and a center of dilatation. Additionally, a fourth source considered was a single force on the surface of the plate. The radial and normal surface displacements generated by these forces were calculated with a generalized ray integral technique described by Pao and Gajewski. [18] Plots were presented of both displacement components for the various sources. It was demonstrated that a single vertical force buried in the midplane of the plate generated antisymmetric plate motion about the midplane, producing a fundamental flexural mode of the plate. It was also found that it was difficult to distinguish between a surface source and an interior source from the displacements on the opposite surface of the surface force. However, there were differences between surface sources and buried source when displacements were observed on the same surface as the surface source. Specifically, displacements on the same side as the surface source were characterized by an abrupt change caused by the arrival of the Rayleigh wave. This change was absent on the opposite side of the plate. In the case of the buried double force, symmetric motion about the plate midplane was generated. It was observed that the plate response to the double force and buried center of dilatation were similar, but completely different from the response due to a single force. The double force and center of dilatation produced nearly periodic waveforms while the single force generated a steadily increasing wave. Finally, it was found that the epicentral response of a concentrated force (nonequilibrium force) was characterized by a steadily increasing in intensity while a double force or center of dilation (self-equilibrium force) was nearly periodic. At off center observation points, the nonequilibrium force exhibited a slow

16

rise in intensity while the self-equilibrium force showed a strong initial signal.

Also in 1979, Sinclair [19] presented a derivation of the Green's function for an isotropic half-space. It was noted that expressions had previously been given for the elastic Green's function of a half-space [13], [20], [21] but that these solutions were in the form of a single integral that was generally not expressible in closed analytic form. In contrast, Sinclair derived a closed analytic expression for the Green's function of an isotropic half-space with source and receiver on epicenter. We summarize the main features here. In Sinclair's notation, $G_{ij}(t;\bar{x};\bar{x}')$ is the Green's function giving the ith component of the displacement at position $\bar{x}$ and time t due to an impulse point source in the x_i direction applied at point $\bar{x}'$ at time $t = 0$. Then, the displacement field due to a multipole source can be obtained from appropriate spatial derivatives of the Green's function. For example, the vertical displacement due to a horizontal force dipole is given by $G_{31,1'}$. It was noted that the reciprocal relation for Green's functions given by Burridge and Knopoff [22] gives

$$G_{ij,k'l'...}(t;0;\bar{x}') = G_{ji,kl...}(t;\bar{x}';0)$$

so that the response due to a buried multipole source could be determined from a point force applied to the surface. Following the formulation by Willis [20], the equivalent surface force was specified and used to determine spatial derivatives of the Green's function for an isotropic half-space with source and receiver on epicenter. It was noted that the final form could be expressed analytically because of the restriction to an isotropic solid with epicentral source and receiver position. Once the Green's function was obtained, displacements were calculated and plotted for a variety of buried multipole sources including: a tangential (i.e. parallel to the surface) single force, a vertical single force, an infinitesimal horizontal edge dislocation loop source (equivalent to three orthogonal force dipoles), and a force quadrupole source.

In 1983, Scruby et al. [23] examined the elastic response of half-space to defect

17

sources. The defects were represented as distributions of force dipoles and a Green's function analysis was applied to obtain resultant displacement. Nearly identical work applied directly to laser ultrasound is reviewed in more detail in the next section.

In 1984, Yeatts [24] determined a Green's function for an unbounded anisotropic elastic medium. In this work, the equations of motion were Fourier transformed in time and then the Radon transform was applied to obtain an ordinary matrix differential (wave) equation in transform space. Tensor algebra was used to solve this equation and the solution was implemented in the inverse Radon and Fourier transforms. The final result for the displacement was written explicitly as a summation of a surface integral over a function containing the forcing function and the elastic constants. For numerical implementation, integration was taken over a unit sphere. Subsequently, an approximate expression was obtained for the displacement field at points sufficiently far from the source. The integral was taken over a slowness surface and differential geometry was used to transform this integral to an integral over the "spherical image" of the slowness surface. Then, successive integration by parts was performed to generate a series in powers of $1/r$, where r was the distance from the source. The lead terms varying as $1/r$ were taken as the asymptotic approximation. The Hilbert transform was used to write the final solution for the complex displacement field. This solution was used to compute group velocity and displacement amplitude in transversely isotropic media, specifically, Apatite and Cobalt.

Work by Chang and Sachse [25] in 1985 considered the forward and inverse problems of extended finite line sources in thick elastic plates. Line sources were mathematically described as the superposition of time dependent point sources. These point sources were expressed as integrals over a Green's function that had previously been determined by Pao et al. [17], [26]. The expression for the normal displacement component were discretized and presented in matrix form. Numerical calculations were presented for various distributions

18

of line sources (*i.e.* the forward problem). Following this, it was demonstrated that both the source spatial distribution and time-dependence could be determined from the normal surface displacements (*i.e.* the inverse problem). Two cases were considered; if the time-dependence was known, the Green's function matrix was convolved with the source-time function, the product matrix was inverted, and then the inverted matrix was multiplied with the normal displacement to obtain the source distribution. If the time-dependence was not known, an initial guess of the distribution was made and the time-dependence was computed. Then, new values of the source distribution were generated by the above procedure and the process was iteratively repeated until a desired accuracy was obtained. The displacements computed in the forward problem were analyzed by this method and the source spatial and temporal dependence were accurately recovered for all cases considered.

Tverdokhlebov and Rose [27], [28] discussed Green's functions for elastic waves in anisotropic media in 1988 and 1989. A weak anisotropy was assumed and approximate plane wave solutions were obtained for transversely isotropic materials. Subsequently, the exact frequency domain Green's function determined by Radon's method was written in terms of these approximate plane-wave solutions. It had been noted that a generalized Helmholtz decomposition could be used to separate the Green's function into three terms corresponding to wave propagation of a quasilongitudinal and two quasitransverse plane-wave modes. The weak anisotropy condition allowed an analytic expression for each of these components. The main restrictions of this formalism was it was limited to weakly anisotropic materials that had no cusps in the energy velocity profiles. In the later work, a scaling transform was proposed so that this technique would not be restricted to weakly anisotropic materials.

Wu *et al.* [29] derived expressions for the far field radiation in a semi-infinite elastic anisotropic solid due to a point source acting on the surface. In this work, first an incident

19

plane wave originating *within* the half-space and incident on the free surface was considered. Reflection coefficients were calculated for the three wave modes (quasilongitudinal and two quasishear) reflected at the boundary. Then, the reciprocity theorem [30], [31] was employed to write the displacement field in the solid due to a point source on the free surface. These expressions were in terms of the reflection coefficients determined above and the undetermined amplitudes of the reflected waves. Then, the Green's function analysis by Tverdokhlebov and Rose along with Lamb's approach were used to calculate the wave amplitudes. Directivity patterns generated from these solutions were presented for aluminum and nickel crystal and isotropic aluminum.

In 1992, Tewary and Fortunko [32] presented an exact solution of the Christoffel equation [33] for wave propagation in anisotropic elastic solids that was designed for numerical computational efficiency. This representation was used to derive Green's functions for an infinite anisotropic solid and an anisotropic half-space. Subsequently, the elastic response of a cubic solid was determined separately for a point source with a delta function time dependence and a step function time dependence. It was noted that traditional methods based on Fourier or Laplace transforms (see for example, references [12] and [34]) were computationally difficult. The Fourier transform method required a four-dimensional integration over space and time. For anisotropic solids, this integration had to be performed numerically, except possibly over one coordinate, leaving three numerical integrations. In contrast, the method described in [32] involved only three-dimensional integrals, one of which could in general be determined analytically. Consequently, only a two-dimensional numerical integration was necessary. Furthermore, it was argued that the basis functions used provided better convergence than the oscillatory functions used in Fourier techniques..

In 1994, Every and Kim [35] obtained the displacement response function tensor for an infinite elastic anisotropic solid subjected to a point source with Heaviside step

20

function time dependence. Here, a quadruple space-time Fourier transform was applied to the Christoffel equation to obtain the time-domain Green's function for the Heaviside step function source. The resulting expression involved three integrals that had to be solved numerically. It was noted that the time derivative of this solution would generate the Green's function for the Dirac delta function source. Following this, wave arrival singularities were discussed in detail for various slowness surfaces. Numerical examples of waveforms were presented for zinc, diamond, and silicon.

Also in 1994, Spies [36] examined elastic waves in layered transversely isotropic materials. Plane wave solutions of the equations of motion were derived for transversely isotropic materials using a coordinate-free representation. With this formulation, reflection and transmission coefficients were calculated for plane waves at the interface between two arbitrarily oriented transversely isotropic media. This work was continued by the same author [37], [38] to determine the elastodynamic dyadic and triadic Green's functions for transversely isotropic materials. It was assumed that the displacements could be represented as plane waves discussed previously. Then, the equations of motion were Fourier transformed in space and the resulting system was solved for the transformed Green's function with tensor algebra. However, the transformed solution could not be completely inverted because of its complexity. Instead, only one of the transformed dimensions was inverted to obtain a two-dimensional Fourier transformed version of the Green's function, called a "space-time spectral representation" (STSR). A similar procedure was used to compute a two-dimensional STSR of Green's triadic function. Subsequently, Huygen's principle was used to develop an algorithm to back propagate the entire displacement field from measured surface displacements. This was referred to as elastodynamic holography.

In 1995, Mourad and Deschamps [39] used the Cagniard de Hoop method to solve Lamb's problem for an anisotropic half-space with orthorhombic symmetry. It was argued

21

that the Cagniard de Hoop method was more appropriate than previously employed methods [40], [32], [41], [42] because it included diffraction effects in a simple way, was suited for numerical implementation, and was analytically rigorous. Drawing on early results [43], the Laplace transform of the Green's tensor for a line source was given without derivation. Then, it was argued that the case of a point source could be obtained by considering a large number of line sources scanning a limited area of the free surface. Subsequently, the transformed Green's tensor for the point source case was expressed in terms of an integral over the transformed line source Green's function. This expression was inverted by the Cagniard de Hoop method to obtain the real space Green's function for the point source. This result was in the form of an integral that was numerically calculated for zinc (hexagonal symmetry) and silicon (cubic symmetry). The computed displacements were compared to experimental results presented by Kim and Sachse [44] and showed good agreement. Furthermore, it was indicated that this method had more accurately modelled the experimental data than an earlier model by Every and Kim [35].

Also in 1995, Nayfeh [45] studied Lamb's problem and wave propagation in layered anisotropic media. Specifically, Nayfeh considered a line load in a material with monoclinic symmetry oriented so that displacement was independent of one of the coordinates. He considered a hypothetical interface containing the applied line load and enforced continuity boundary conditions across this interface. Consequently, the line load was essentially converted into an equivalent set of boundary conditions. The homogeneous field equations and artificial boundary conditions were Laplace transformed in time and Fourier transformed in space and the algebraic system was solved for the transformed displacements. The transformed displacements were inverted using the Caignaird de Hoop technique. Although this technique was able to model wave propagation due to the transient line source, it was very difficult for problems that did not exhibit the symmetry of this example.

In 1996 and 1997, Spies [46], [47] presented a solution to Lamb's problem for a point source in an anisotropic material. Following an identical analysis to earlier work [37], the full-space, two-dimensional, space-time spectral representation of the Green's dyadic and triadic functions were considered. From these solutions, the half-space Green's functions in the transform domain were determined. An ansatz composed of the sum of the Green's function for the homogeneous and inhomogeneous problem was postulated and traction free boundary conditions were enforced at the surface. From this analysis, a complete solution of Lamb's problem in the transform domain for any anisotropic half-space was obtained. Results were specifically calculated for a generally transversely isotropic medium from this representation.

In 1998, Bescond and Deschamps [48] used the Cagnaird de Hoop technique again and presented another solution for the surface response of an anisotropic half-space to an impulsive point source or line source on the free surface. The applied point force was specified as a pure normal force so that it was suggested that loading was consistent with laser generation in the ablation regime. Following work by Van der Hijden [49], the Laplace transform in time and a double Fourier transform over space was applied to the equations of motion and boundary conditions. An expression for the Laplace transform of the normal displacement was obtained. The Cagniard de Hoop technique was used to analytically invert this transform. The solution was still in terms of an integral that was evaluated numerically. A similar analysis was performed for a line source. Also, a detailed discussion of the propagation of the generated Rayleigh waves was presented. Finally, numerical results for copper crystal were computed and agreed very well with experimental results.

2.2   Laser Generated Ultrasound in Solids

White [89] is generally cited as the first to investigate laser generated ultrasound. In his 1963 letter, he considered several one-dimensional problems of ultrasonic generation in an isotropic elastic solid including: uniform heating of a semi-infinite body, uniform heating of the end of a thin rod, nonuniform heating of a semi-infinite body, and nonuniform heating of a thin lamina. White noted that it is difficult to obtain formal solutions to the equations of motion for many temperature distributions of interest. Consequently, it was argued that the principal effects could be most easily described by solving the equations of motion for a harmonically varying power density applied at the surface. We can summarize the formulation for the case of a semi-infinite body as follows. It was assumed that the surface ($x = 0$) uniformly absorbed a harmonically varying power density given by the real part of

$$P_0(t) = P_0 \exp[i(\omega t + \epsilon_0 + \pi/4)] \tag{2.1}$$

so that the harmonic temperature rise in the solid was given by [90]

$$\theta_{harmonic}(x,t) = (\frac{P_0}{J})(\frac{\kappa}{\omega})^{1/2} K^{-1} \exp[i(\omega t + \epsilon_0)] \times \exp[-x(\frac{\omega}{2\kappa})^{1/2}(1+i)] \tag{2.2}$$

where J is the mechanical equivalent of heat (4.185 J/cal), K is the thermal conductivity, κ is the thermal diffusivity ($\kappa = \frac{K}{\rho C}$, C is the specific heat, ρ is the density). Then, it was assumed that the displacement, $u(x)$ had a harmonic time dependence, and the one-dimensional equation of motion for an isotropic body with a heat source [91]

$$\rho \frac{\partial^2 u}{\partial t^2} = (\lambda + 2\mu)\frac{\partial^2 u}{\partial x^2} - B\alpha \frac{\partial \theta}{\partial x} \tag{2.3}$$

was solved with θ determined from equation (2.2). Here, λ and μ are the Lamé parameters, α is the linear thermal expansion coefficient, and B is the bulk modulus. Solutions were obtained for the two separate cases of a stress free surface and a constrained surface. From

24

these solutions, it was found that the generation of elastic waves depended on the frequency of the applied harmonic power density and the material properties of the sample. Also, it was found that the functional dependence of the stress wave amplitude was governed by the boundary conditions applied to the heated surface, specifically that the stress wave amplitude for a constrained surface was much larger than for a free surface.

This early work provided some insight about the laser acoustic source, but had some significant limitations. It could not predict the generation of shear waves because it only considered one-dimensional motions. Also, it was restricted to isotropic materials and it ignored thermal diffusion and the finite extent of the laser source.

It was not until work appearing in 1980 by Scruby et al. [3] that the theoretical modeling of laser generated ultrasound in solids was explored more extensively. A simple three-dimensional model was developed to describe laser generated ultrasound in aluminum. The model treated the thermal expansion due to the laser pulse as the instantaneous addition of a small volume at the sample's surface. It was assumed that the laser pulse was instantaneously and uniformly absorbed at the surface throughout a cylindrical volume element with the same radius as the laser beam and a depth equal to the electromagnetic skin depth. The consequent temperature rise and bulk strain were calculated and this strain was approximated by a distribution of dislocation loops [19]. Then, a Green's function analysis was used to calculate epicentral displacements.

The computed epicentral displacements matched the features of experimentally observed waveforms. Specifically, the computed waveforms correctly predicted an overall depression of the back surface of the sample (i.e. towards the acoustic source) and matched the overall shape of the experimental waveforms. The model also predicted that the longitudinal wave would have an amplitude four times greater than the shear wave amplitude. This ratio was measured as 3.8. The model was also used to determine the source func-

25

tion (*i.e.* time evolution of the expanding volume) from experimentally measured surface displacements. An analysis of this source function predicted that approximately 9% of the incident radiation was absorbed and converted into elastic waves. This value was also in good agreement with experimentally determined data.

However, this model could not predict the detailed time dependence of the longitudinal and shear wave arrivals. In particular, it did not predict a small "precursor" positive pulse which represented an initial expansion at the back surface of the sample that appeared at the beginning of the arrival of the longitudinal wave. The authors suggested that this failure was because the model neglected thermal diffusion and the finite dimensions of the laser source. This was later confirmed in the work by Doyle [5] and described below.

In the same paper, Scruby *et al.* included an experimental study of laser generated ultrasound. Laser parameters were varied to characterize their effects on laser generated ultrasound. First, ultrasonic displacements generated with a multimode and a TEM$_{00}$ mode laser, were compared. Observations suggested that the displacements were independent of laser mode at constant energy. Laser pulse area was also varied and it was determined that the amplitudes of the longitudinal and shear waves were proportional to the total energy of the pulse. Laser power density was also varied, from which it was concluded that the amplitudes of the longitudinal and shear waves were proportional to the laser pulse energy and consequently, the optical power density. The final comments were that variations in laser energy and area of irradiation were of secondary importance in determining the shape of the epicentral acoustic waveforms in the thermoelastic regime.

In 1982, Dewhurst *et al.* [92] extended the experimental and theoretical work by Scruby [3] to investigate the effects of higher incident power densities and surface modification of metal samples. From experimental results in the thermoelastic regime, they observed that changes in laser power density at the surface did not significantly affect the acoustic

26

amplitude. However, when the plasma generation threshold was exceeded, they found that both the shape and amplitude of the epicentral waveforms changed as a function of incident laser energy and power density. In the presence of a plasma, the incident optical power density determined the shape of the acoustic waveform, while the amplitude was proportional to the absolute laser energy. When the surface was constrained, both the amplitude and the shape of the longitudinal waveform was changed while the shear wave amplitude remained relatively unaffected. The amplitude of the longitudinal wave increased and changed from a step-like depression to a pulse like elevation at the free surface.

Using similar analysis techniques as in Scruby et al. [3] the authors presented theoretical waveforms for the epicentral acoustic displacement. They showed preliminary work which suggested that diffusion and the finite dimensions of the source generated the precursor positive longitudinal pulse that was not predicted by previous models. They also extended the model to the ablative regime by including an additional force acting normal to the surface. This force modeled the momentum transfer that occurs when material ablates away from the free surface. The theoretical waveforms could only capture general trends of the observed waveforms but seemed to confirm that lateral forces dominate in the thermoelastic regime while normal forces dominate in the ablative regime.

Although they did not extend the model to account for a constrained surface, the authors discussed effects of surface modification. They suggested possible effects that a transparent constraining layer on a surface could have on the acoustic source. First, the coating could increase the amount of absorbed energy. This would increase the generation efficiency and consequently increase the amplitude of the acoustic waveform but not affect the shape of the waveform. Second, the coating could generate forces normal to the surface during evaporation or ablation. Consequently, the waveform would show characteristics of the ablative source. Third, the constraining layer could undergo thermal expansion and

27

act as an additional thermoelastic source. Consequently, the acoustic source could exhibit characteristics associated with a buried source in addition to a surface source. Finally, the coating would change the boundary conditions by constraining the surface. This would also act to generate additional normal forces. Since all of these mechanisms were expected to produce forces normal to the surface, the authors argued that the longitudinal mode should be enhanced. This was confirmed experimentally in waveforms generated when a layer of oil was applied to the surface of metal samples and when a glass plate was bonded to the surface of the samples.

In the same year, Wetsel [93] may have been the first to discuss laser generated ultrasound in a composite material. He developed a simple one-dimensional model for a sample consisting of a backing material, an absorbing bulk or surface film and a sample. Harmonic heating and displacement functions were assumed and implemented in the equations of motion. The resulting equations were solved numerically for the elastic wave amplitude in each of the three regions and the computed values were in good agreement with experimental values. The variation of elastic wave amplitude with the optical-absorption coefficient and the film thickness were computed for a sapphire-molybdenum-quartz sample. It was found that the elastic wave amplitude increased with increasing optical absorption and with increasing film thickness. The effects of thermoelastic parameters on the amplitude of the elastic waves were also examined. A parameter dependent upon the material density, thermal conductivity, and specific heat was identified as an indicator of generation efficiency.

In 1984, Rose [4] developed a more rigorous point-source model of laser generated ultrasound in an isotropic solid from first principles. We summarize the main features of this work here. Following work by Aki and Richards [72], the components u_n ($n = 1, 2, 3$) of the elastic displacement in Cartesian coordinates were represented by

$$u_n(\bar{x}, t) = \int_V C_{ijkl}\, \epsilon_{kl}^T(\bar{\xi}, t) * \frac{\partial}{\partial \xi_j} G_{ni}(\bar{x}, \bar{\xi}; t) \, dV(\bar{\xi}) \tag{2.4}$$

28

where C_{ijkl} are the elastic stiffness constants and $\epsilon_{kl}^T(\bar{\xi}, t)$ is the unconstrained (or stress free) transformation strain specifying the source. $G_{ni}(\bar{x}; \bar{\xi}; t)$ is the Green's function giving the n th component of the displacement at position $\bar{x}$ and time t due to an impulse point source parallel to the x_i axis applied at point $\bar{\xi}$ at time $t = 0$. By considering a point source for the isotropic case, equation (2.4) was reduced to

$$\bar{u}(\bar{x}, t) = \Gamma \bar{g}^H(\bar{x}; 0; t) \tag{2.5}$$

where $\bar{g}^H(\bar{x}; 0; t)$ was the appropriate Green's function and the scalar parameter Γ depended upon the total heat input and the thermoelastic properties of the sample.

Subsequently, the Green's function for the displacement field due to a surface point loading on a semi-infinite isotropic half-space was determined. Axial symmetry was assumed and a Helmholtz decomposition was used to represent the Green's function in terms of two scalar potentials fields. The Green's function was applied to the equations of motion with a buried impulse source function. Stress free boundary conditions were assumed at the surface so that four coupled partial differential equations were obtained. Hankel and Laplace transform techniques were used to solve these coupled differential equations. Subsequently, the buried source was replaced with a surface source by a limiting process. Therefore, the thermoelastic source was considered only at the surface of the half-space and was described as a surface center of expansion or "SCOE." Then, the Caignard-de Hoop [15], [94] method was used to analytically invert the transformed solutions and wave-front expansions were used to approximate the Green's function. Axial displacements produced by the SCOE along the axis normal to the half-space were calculated and plotted using equation (2.5). An expression for the surface displacements was also derived from this relation. A similar formulation was applied to laser generated ultrasound in an isotropic plate and for the case of surface modification by a transparent overlay. In each analysis, the axial displacement at the back face of the plate was computed and plotted.

29

Predictions from these models were in good agreement with the waveforms computed in earlier theoretical work by Scruby *et al.* and also agreed with the experimental data. However, this model was still a point-source model and neglected the finite extent of the laser source and the thermal diffusion into the sample. Consequently, it could not predict the precursor pulse observed in the experimental waveforms.

In 1986, Doyle [5] included the finite extent of the laser source and thermal diffusion in his model and showed that this generated the precursor pulse not accounted for in previous theories. Work by Bachus and Mulcahy [95] was followed to represent the displacement field due to the extended source as the convolution of a *stress glut* and an appropriate Green's function. The stress glut was a function of the thermoelastic material parameters and the temperature rise induced by the laser pulse. The temperature rise, in turn, was modeled by an equation determined by Ready [96]. Generalized ray theory detailed by Ceranoglu and Pao [26] was considered to develop the appropriate Green's function. The resultant displacement field was in the form of a triple integral and was numerically evaluated for a 25 mm thick aluminum block. The computed epicentral displacement exhibited the initial positive pulse that had been experimentally observed in earlier work. One limitation of this work was that only two "generalized rays" were used in this derivation; the direct longitudinal wave and the longitudinal wave reflected from the front surface. Consequently, the model was only valid up until the arrival of the first shear wave.

In 1989, Bresse and Hutchins [97], [98], [99] investigated elastic waves generated by a disk shaped thermoelastic source on the surface of a solid. It was assumed that a laser beam with a finite radius and with an optical power density that was a function of radius, was incident on the surface of a semi-infinite solid. The Green's function for a point source in a semi-infinite solid (obtained by Laplace and Hankel transform techniques [12], [34]) was convolved with the spatial power density function to obtain the normal and radial

30

displacements (in transform space) due to the extended source. Several source power density distributions were examined and Cagniard's technique was used to invert the transforms and obtain displacements in real space. These computed displacements were in good agreement with experimental data.

A comprehensive general model for laser generated ultrasound was outlined by Schleichert et al. also in 1989 [100]. First, the intensity of a monomode laser pulse was determined in terms of the laser parameters including optical energy, mode indices, frequency, pulse duration, beam waist, and spot radius. Then, the electromagnetic interaction of the laser with the sample was considered to obtain the thermal power density generated in an isotropic solid. A Green's function analysis was outlined to solve the heat equation and determine the generated thermal field. Subsequently, a second Green's function analysis was described to determine elastic displacement from this thermal field. This second analysis involved a four-dimensional integral (integration over three-dimensional space and time) including off-epicenter Green's functions which was solved numerically. The calculated waveforms were presented as a function of observation angle and compared to experimentally obtained waveforms. The computed waves agreed very well with the experimental data, even predicting the precursor pulse. The maximum amplitude difference between the experimental and theoretical waveforms was less than thirty percent.

Also in 1989, McDonald [101] presented a model for laser generated ultrasound in an isotropic material based on generalized thermoelasticity. The models described above were similar in that the elastic and thermal problems were solved separately: first, a thermal field was determined and then techniques of elasticity were used to determine ultrasonic displacement. In contrast, this work modeled the laser source by solving the coupled thermoelastic equations. A hyperbolic form of the heat diffusion equation developed by Green and Lindsay [102] was employed to avoid an infinite thermal propagation velocity. The

31

particle displacement was Helmholtz decomposed in terms of scalar potentials and applied in the equations of motion with a thermal source. Laplace and Hankel transforms were performed on the differential equations for the potentials and the hyperbolic heat diffusion equation. Then, thermal and elastic boundary conditions were imposed to solve for the transformed displacement potentials. These transformed solutions were then inverted numerically. Results were presented for the displacement along the z-axis in an infinite medium caused by a unit instantaneous point and ring heat source in the plane $z = 0$. Subsequently, heat sources in a semi-infinite solid were considered. Displacements were determined for a buried unit impulse point source and then for an instantaneous Gaussian surface source. During this work, it was also found that the thermal mode terms did not appreciably affect the final results. Consequently, it was concluded that the *a priori* neglect of thermal conduction in previous models was justified.

In 1990, Telschow and Conant [6] reconsidered the precursor pulse and showed that it's shape depended upon the optical penetration and thermal diffusion into the material. Initially, a one-dimensional model was formulated describing the elastic response of a half-space to a suddenly applied temperature rise occurring in a thin layer at a depth h below the surface. Subsequently, a one-dimensional model was described to account for optical penetration of a laser source without thermal diffusion. It was assumed that the laser heat source was axi-symmetric, exhibited a delta function time dependence, and decayed exponentially into the bulk of the material according to the optical absorption coefficient. This heat source was applied in the heat equation to obtain the resulting temperature distribution which was in turn applied in the equations of motion to obtain displacements. The resulting waveforms contained the precursor pulse. Furthermore, it was found that the magnitude of the precursor pulse depended upon the optical absorption coefficient. A similar analysis was carried out for the case of thermal diffusion without optical penetration.

The computed waveforms again showed the precursor pulse and it was concluded that the precursor pulse results from the penetration of heat into the material. A two-dimensional analysis accounting for optical penetration was also formulated for a plate geometry and the computed waveforms compared well with experimental data.

In his 1991 Ph.D. thesis, Spicer [7] continued McDonald's work[101] and modeled laser generated ultrasound by considering the coupled thermoelastic equations. Spicer argued that the coupled equations of thermoelasticity should be solved to obtain an accurate representation of the laser ultrasonic source. Initially, Spicer described the mathematical formalism for treating the interaction of electromagnetic fields with a general anisotropic sample. However, when calculating the functional form of the laser heating source, he assumed that the sample exhibited either isotropic or cubic crystal symmetry since electromagnetic waves propagate the same in either medium. Consequently, the rest of his discussion was restricted to these two simple crystal symmetries. Spicer then presented a first principles derivation of the classical differential equations of thermoelasticity and for "temperature rate dependent thermoelasticity," which incorporated the hyperbolic heat diffusion equation derived by Green and Lindsay. [102] These equations differed from the classical equations in that a modified Fourier law that limited the rate of heat flux was used in their derivation. This modification had no physical basis except that it resulted in a finite speed of heat propagation.

Subsequently, Spicer solved both the fully coupled classical and temperature rate dependent thermoelasticity equations for the case of an isotropic, cylindrically symmetric system. A point impulse heating source in an infinite space was considered. A Helmholtz decomposition was applied to the displacement which was in turn applied in the thermoelastic equations. Integral transform techniques were employed to solve the resulting equations for the potential fields. A perturbation method was used to evaluate the strength and

33

significance of the coupling of the differential equations. It was concluded that the classical equations led to the unphysical result of a finite amount of energy travelling at speeds approaching infinity. Also, it was determined that the coupling between the thermoelastic equations was small so that "partially-coupled" equations of thermoelasticity could be employed. As a result, a "thermal stress" approximation was proposed that eliminated the coupling between the elastic field to the governing thermal differential equation.

After an analysis of appropriate boundary conditions, laser heating of an isotropic half space was considered, with the laser heat source computed from the earlier work. Integral transform techniques were used to solve the partially-coupled differential equations of thermoelasticity along with appropriate boundary conditions. Several approximations were made to simplify the resulting transformed solutions which were finally numerically inverted to obtain displacements. It was suggested that an equivalent elastic boundary source could be specified in place of the laser source for observations outside of the heated volume. These equivalent sources were then presented.

Laser heating in an isotropic plate geometry was also considered. However, in this analysis, it was argued that for practical plate thicknesses, the laser source could be accurately modeled by the equivalent elastic source previously described. A similar analysis was applied to laser heating of a semi-infinite half-space exhibiting cubic symmetry.

Experimental waveforms generated in thermally thick, isotropic plates were compared with the theoretically computed waveforms. Epicentral waveforms showed very good agreement when both the thickness of the plate and radius of the laser spot was varied. Experimental surface waves were also compared to theoretical waveforms with good agreement. It was observed that surface wave amplitude dramatically decreased with increasing source size. A final comparison was made between experimentally observed "Lamb" waves with theoretical predictions, again showing good agreement.

Work by McKie and Addison in 1994 [2] was an initial effort to characterize the laser acoustic source as a function of laser and material parameters. The acoustic sources generated by a Nd:YAG laser and a CO_2 laser in coated and uncoated graphite/epoxy composite materials were compared. The lasers were adjusted so that energy within each pulse was equal. By examining the spectral components of the laser pulses, it was determined that the Nd:YAG laser pulse could efficiently generate ultrasound within a frequency range of DC to > 20 MHz while the longer pulse CO_2 laser was efficient from DC to ~ 10 MHz. It was noted that composite materials attenuate ultrasound strongly and that this attenuation increases with frequency. Consequently, without any other factors, it was expected that the CO_2 laser would be a more efficient generation source in composites since its energy is concentrated at the lower frequencies.

However, it was found that the wavelength of the lasers had a significant effect on the generation sources. Cured Hercules 3501-5A resin, typically used as the binder in composites was analyzed with a spectrometer. It was found that the resin transmits 92.8% of the Nd:YAG wavelength (1.06 μm) but only 2.7% of the CO_2 wavelength (10.6 μm). Consequently, it was expected that during irradiation of a graphite/epoxy composite with a similar resin, the Nd:YAG wavelength would transmit through the resin and be absorbed mostly by the first layer of graphite fibers, resulting in a buried source. Conversely, the CO_2 wavelength would be exponentially absorbed within the resin layer and produce a volume ultrasonic source. Both a buried source and volume source were expected to be more efficient acoustic sources than surface sources (i.e. as occurs in irradiation of a metal sample). However, the relative generation efficiencies of a buried source versus a volume source were not known.

Subsequently, the relative generation efficiency of the two different laser sources was experimentally determined. It was found that the Nd:YAG laser had a higher ultrasonic

35

generation efficiency than the CO_2 laser when applied to an uncoated graphite/epoxy sample. Furthermore, it was found that the ultrasonic pulse amplitude increased approximately linearly with pulse energy of the Nd:YAG laser until the damage threshold was exceeded. After this point, no further increase in ultrasonic amplitude was observed. The damage threshold was never exceeded with the CO_2 laser because of the longer pulse length.

However, it was noted that in practice, samples will often be coated and this affects the acoustic source. A thin coating, like paint, modifies the surface boundary conditions and affects the absorption of laser radiation and consequently changes the acoustic source. Therefore, two different coatings were applied to the composite and the generation sources were again compared. It was found that a white polyurethane paint increased the generation efficiency of both wavelengths, and actually caused the CO_2 laser to be more efficient at all measured power levels. Furthermore, at higher powers, the Nd:YAG laser exceeded the damage threshold and the ultrasonic amplitudes could not be increased. In contrast, the CO_2 never exceeded the damage threshold because of its longer pulse length. Consequently, significantly greater ultrasonic displacements could be generated than with the Nd:YAG laser since more power could be delivered to the sample. Similar results were obtained with a coating of grey paint, except that the CO_2 laser was only more efficient at higher energy levels.

Several conclusions were made from this research. First, the ultrasonic generation efficiency of the Nd:YAG laser was higher than that of the CO_2 laser in an uncoated graphite/epoxy, but the power density at which damage occurred was lower. Second, for *rapid* inspection of uncoated graphite/epoxy composites, the CO_2 laser may be better suited because at a sufficient pulse repetition frequency, the Nd:YAG would cause damage.[1] Third, the CO_2 laser could generate significantly larger ultrasonic amplitudes than the Nd:YAG

---

[1] It was noted for this application, an ideal laser might be a Nd:YAG with a longer pulse width.

36

with the application of an appropriate constraining layer.[2]

Also in 1994, Dubois *et al.* [42] modeled thermoelastic generation of ultrasound in a medium with orthotropic symmetry. In contrast to previous work (see for example, ref. [39]), it was argued that Green's function techniques or Laplace and Hankel transform techniques (*i.e.* Cagnaird de Hoop) were not appropriate to investigate the thermoelastic source in anisotropic media. Instead, the coupled equations of motion and hyperbolic heat equation were solved with Fourier and Laplace transform techniques. A Laplace transform in time and a double Fourier transform in space were applied and the resulting partial differential equations were solved. Although part of this derivation could be performed analytically, some portions had to be derived numerically. Also, the Laplace transform was inverted numerically. Waveforms generated from this model agreed well with experimental values measured with an aluminum sample and a graphite/epoxy plate.

In 1995, Sanderson *et al.* [103] investigated the effects of using hyperbolic heat equations instead of classical equations in laser generated ultrasound models. In addition to the classical thermoelastic equations, two alternative formulations were considered; the Lord-Schulman [104] equations and the Green-Lindsay [102] equations. A simple one-dimensional model of a uniformly irradiated half-space was used to illustrate the differences in the generated temperature fields and mechanical displacements. It was concluded that the benefit of using the hyperbolic equations was that numerical inversions of Laplace transforms could be simplified for large time scales. However, on smaller time scales that were not determined, the hyperbolic equations could require more computational effort.

---

[2]It was also noted that this could be a retroreflective coating to enhance the detection of ultrasound.

2.3 Applications to NDE

A considerable amount of work has been done to apply laser ultrasonics to nonde-
structive evaluation [2] - [201] and interest in this technique continues to grow. We briefly
summarize some examples and provide references to other efforts. For a more comprehen-
sive review, the reader is again referred to Scruby and Drain [1] who present a thorough
discussion of laser based ultrasonic NDE.

In 1977, von Gutfeld and Melcher [114] presented one of the earliest examples of laser
ultrasonic nondestructive evaluation. In this work, they investigated using a constraining
boundary to enhance laser generated ultrasound. A 40 dB increase in signal was observed
when compared to generation in a free surface. In a specific example of flaw detection, they
bonded a thin glass layer to an aluminum sample and were able to identify 0.04 cm diameter
holes, 0.04 cm deep at the aluminum/glass interface.

Wickramasinghe *et al.* [115] applied laser ultrasonics in a modified transmission
acoustic microscope in 1978. A laser was used as the generation source instead of a piezo-
electric transducer. Ultrasonic waves were generated with frequency as high as 1.05 GHz
but experiments were performed at 840 MHz. Images from this microscope compared well
with images from both optical transmission and reflection microscopes.

In 1982, Wadley *et al.* [108] measured the speed of extensional propagation in
metallic glass ribbon with laser based ultrasound. Consequently, they could extrapolate
the degree of crystallization as a function of isothermal annealing. Later in 1984, Tam[118]
used laser generated ultrasound to investigate thin films. A laser with a 0.5 ns pulse width
was used to generated ultrashort acoustic pulses. Using the laser as the generation source
and a specialized transducer in a pitch-catch configuration, the thickness of stainless steel
films as thin as 12 μm was measured with 1% accuracy. Also, the ultrasonic wave speed
and attenuation were measured. These quantities are highly correlated with film properties

38

like porosity, strain, grain size, and microstructure.

In 1986, Monchalin and Heon [123] described a fully laser based ultrasonic system intended as a tool for nondestructive evaluation. This system consisted of a Nd:YAG laser as the generation source and a colinear HeNe laser used with a confocal Fabry-Perot interferometer to detect surface displacements. Experimental waveforms were presented from inspection of a half-inch thick plate of steel and a 3 mm thick plate of aluminum. However, both of these were two sided measurements where the generation laser and detection lasers were on opposite sides (i.e. transmission mode). Furthermore, a water film was applied to the steel plate to enhance the ultrasonic generation. Only one waveform was presented for the steel plate where both lasers were incident on the same side but this signal was produced in the ablative regime. Operated in this manner, the system clearly wasn't suitable for nondestructive evaluation. The authors indicated that the system was limited by the low power of the detection laser and expected that a better detection laser would make the system useful for nondestructive inspection. Nevertheless, the system demonstrated the feasibility of using lasers to remotely generate and detect ultrasound in a solid sample.

Work in 1987 by Dewhurst et al. [125] demonstrated the ability of laser generated Lamb waves to determine the thickness of thin metal sheet. A Q-switched Nd:YAG laser was used in the thermoelastic regime with a cylindrical lens to produce line sources on the surface of aluminum plates. This generated Lamb waves with a preferential propagation direction perpendicular to the line source. Both antisymmetric and symmetric modes were generated simultaneously. Consequently, the plate thickness could be estimated without any prior knowledge of the elastic properties by measuring the sheet velocity and the frequency dispersion of the long wavelength antisymmetric modes. Using this method, an accuracy better than 2% for a 30 μm thick aluminum sheet was obtained.

In 1988, Bresse et al. [129] [130] reported on a technique to determine elastic con-

stants from experimental waveforms generated with laser based ultrasonics. A Q-switched ruby laser was used to generate acoustic waves in an aluminum plate. Simultaneously, a Michelson interferometer was used with a HeNe laser to detect the resultant surface displacements. A simple theoretical model was described to predict the normal component of displacement. Then, a least-squares fit to of this theoretical model to experimental waveforms was used to extract the longitudinal and shear wave velocities which in turn provided the Lamé parameters.

Also in 1988, Telschow [131] discussed microstructure characterization of metal and ceramic materials with laser based ultrasound. Here, microstructural scattering was calculated by measuring ultrasonic attenuation. To measure the small grain sizes, high frequency ultrasound was required and it was noted that lasers could generate high frequency ultrasound more easily than piezoelectric transducers. In fact, it was found that at these high frequencies, the laser produced larger amplitude ultrasound than could be obtained with the piezoelectric transducer. Measurements were made on three Inconel samples that were 0.25 inches thick. The nominal grain size in each sample was 22 μm, 76 μm, and 106 μm, respectively. The laser based measurements of these grain sizes agreed well with measurements made with the contact transducer.

In 1989, laser generated Lamb waves were studied by Hutchins et al. [133]. Here, Lamb waves were used to interrogate household aluminum foil and metallic glass with a mechanically measured thickness of 15 and 22 μm, respectively. A technique was developed to fit the theoretical dispersion relationship to dispersion curves obtained via a fast Fourier transform of experimental waveforms. With this technique, both the thickness and the elastic constants of the sample could be determined. The estimated error in the laser based measurements was between 3 and 11 percent.

Aussel and Monchalin [134] studied laser generated surface acoustic waves (SAW) in

40

thick and thin metallic substrates. In this work, SAW waves were generated by a ring source and the amplitude was detected in the center of the ring. The SAW waves from the ring source converged at the center to produce larger amplitudes. Also, a time-domain signal processing technique was used to measure both phase and group velocity as a function of frequency. It was suggested that this technique could be used on-line to measure the thickness of a zinc layer deposited by a hot-dip galvanization line.

Bresse et al. [135] used laser ultrasound to inspect composite panels constructed by attaching a thin layer of aluminum to a rigid foam substrate with an epoxy resin. Laser generated Lamb waves were used to detect delamination at the aluminum/epoxy interface. Bulk waves resonating in the epoxy were used to determine material properties of the epoxy layer.

In 1989 and 1990, Tittmann et al. [136], [137], [138] used laser based ultrasound to investigate graphite/epoxy composites. An acoustic-optic modulator was used to modulate a CW laser at a frequency of several MHz. Consequently, the generated ultrasound was confined to a narrow band around 2.25 MHz. It was found that this was a less efficient generation source than a Q-switched laser. However, it was argued that with a better laser, this technique should be more efficient than using a Q-switched laser. The effect of surface reflectance was also studied. A simulated delamination was detected in a graphite/epoxy plate and a C-scan image identifying the flaw was presented.

In 1990, Ringermacher et al. [139] discussed laser ultrasonic evaluation of bonding integrity. C-scan images were presented of various thin films and substrate combinations. Disbonds and defects at the bonding interface were detected. Also in this year, Every and Sachse [140] used laser based ultrasound to determine elastic constants of anisotropic solids. Specifically, materials with cubic symmetry were considered and elastic constants were measured for silicon.

41

In 1991, Addison et al. [142] applied laser-based ultrasound to investigate large area graphite/epoxy composites. Angular diffraction effects were measured for aluminum and graphite/epoxy samples. Also, angular diffraction was compared for free and constrained surfaces. A synthetic aperture technique was used with an array laser source to produce sector scans in both the graphite and aluminum samples. In the same year, Davies et al. [143] investigated the phase change of laser generated ultrasound after interaction with either a hole or slot defect.

In 1992, Tas et al. [145] used femtosecond laser pulses to detect ultrathin interfacial layers of fluorocarbon (CF_x) at the interface of aluminum films on silicon substrates. An ultrafast dye laser with a pulse width of 200 fs was used to generate ultrasound at a frequency of 210 GHz in 150 Å thick aluminum films. It was reported that a 5 Å interfacial layer of CF_x was easily detectable.

Scala and Doyle [146] presented a method to measure seven of the nine elastic constants needed to characterize interfacial waves in unidirectional orthotropic composites. Specifically, elastic constants for unidirectional boron-epoxy composites were measured with laser-based ultrasound. Subsequently, these constants were used to determine if leaky interface waves were supported when the composite was bonded to various metals.

McKie and Addison [151] discussed using laser based ultrasound to inspect complex geometries. In this work, they studied the effect of the angle of incidence of the detection laser with a variety of surfaces. For example, a 20 dB reduction in the ultrasonic signal-to-noise ratio was observed when the probe laser beam angle of incidence was varied from 0 to ± 45° on surfaces coated with a white polyurethane paint. Also in this work, the laser-based system was successfully used to scan a contoured part that required angles of incidence of 0 to ± 45°.

Later in 1993 and 1994, McKie and Addison [152], [2] described a laser based ultra-

42

sonic system for inspecting composite materials without surface damage. Here an argon-ion laser was used with a confocal Fabry-Perot interferometer to detect ultrasonic displacement. Both a CO_2 and Nd:Yag laser were separately used as generation sources (see above, p. 2.2). An impact damaged graphite/epoxy plate was imaged and compared to a transducer immersion tank C-scan. The laser based scan agreed well with the immersion scan and took only 5 minutes to acquire. The immersion scan required 2.5 hours, a scanning time about a factor of *30* larger.

A graphite/epoxy "hat section" was also inspected with both the laser and immersion tank systems. The hat section exhibited a complex geometry that made the immersion tank inspection difficult because the system was not equipped with contour-following capabilities. Consequently, manual reorientation of the sample was required to inspect the diagonal planes, resulting in five separate C-scans. Conversely, the ability of the laser system to conform to the part geometry, even without mechanical contour-following, allowed the part to be inspected with only one scan.

In 1993, Edwards *et al.* [154] used laser generated Lamb waves to measure the sheet thickness of thin sheets. In particular, measurements were made of plastic film while it was being extruded. The film thickness ranged from 10 to 150 μm and was measured with an accuracy of ± 0.1 μm with signal averaging. Similarly, Ringermacher *et al.* [155] used laser generated Lamb waves to measure the thickness of silicon nitride coatings on carbon/carbon surfaces at 1200 °C. The calculated thickness was within 5% of the actual values. This work represented a preliminary effort to implement laser-based ultrasound in a Chemical Vapor Deposition (CVD) reactor environment for on-line process monitoring. Costley and Berthelot [159] also studied laser generated Lamb and Rayleigh waves. A Fresnel lens was used to produce curved line sources to generate the guided wave modes. A two-dimensional Fast Fourier Transform method was applied to the data to determine

43

dispersion curves and the propagating modes. Huang et al. [149] used a cylindrical lens and a holographic diffraction grating to generate narrow-band surface acoustic waves with a laser. This acoustic source was applied with a dual probe interferometer [202] to detect artificial cracks (EDM notches) emanating from rivet holes in a simulated fuselage panel.

Still in 1993, Monchalin [163] reported on two laser based ultrasonic NDE systems that had been successfully used for two separate applications. The first system was used for on-line thickness gauging of seamless steel tubes with wall temperatures of $\sim 1000°C$. A KrF excimer laser was used in the ablative regime as the generation source. A long pulse Nd:YAG laser was used with a confocal Fabry-Perot interferometer as the detection system. Wall thickness was calculated from the time-of-flight measurements and thickness profiles were generated. The laser based ultrasonic profiles agreed very well with profiles generated from a hand held ultrasonic thickness-gauge. It was found that the thickness variation along the tube had two spatial frequencies associated with the initial piercing process and to the stretching/rolling operation.

The second system was used to inspect large area polymer matrix composite parts. This system was identical to the first, except that a TEA CO_2 was used as the generation source. The distance between the surface of the sample and the optical scanner was approximately 1.5 m and a scan area of 1.8 m x 1.8 m was possible. Results from a composite panel representative of an actual aircraft wing part were presented. The panel was curved, had stiffeners on its back surface, and had a complicated thickness profile. A laser-ultrasonic time-of-flight C-scan image clearly indicated the stiffeners, thickness variation, and implanted flaws. A laser-ultrasonic B-scan resolved the individual fiber layers.

In 1994, Chai and Wu [167] detailed a method to determine anisotropic elastic constants using laser generated surface waves. Specifically, surface waves in a single-crystal silicon with orientation [111] were studied. Schindel et al. [168] also studied laser generated

44

surface acoustic waves. Measurements of surface wave velocity were made on polycrystalline aluminum and single-crystal silicon both at room temperature and at 800°C. The uncertainty in the measurements was quoted as 0.5% at room temperature and neglibly different up to 500°C. In that year, Huang et al. [169] continued earlier work to use laser ultrasound to detect cracks around rivets with a fiberized dual-probe interferometer.

Also in 1994, Lu et al. [170] discussed a possible laser ultrasound technique to measure substrate temperature during wafer processing by molecular beam epitaxy. As proof of principle, laser generated Lamb waves were used to measure temperature in 0.6 mm thick Si substrates that were radiatively heated from room temperature to 310 °C. From the results of these experiments, it was estimated that a 5 °C and 3 °C precision in temperature measurement could be achieved at 0.5 MHz and 1 MHz, respectively.

In 1995, Weiss and Sigrist [174] described a technique to use laser generated acoustic waves to perform coating adhesion measurements. In this work, the laser generated ultrasound was used to spallate the coating (i.e. separate the coating from the substrate). By measuring the resultant surface displacement with an interferometer, adhesion strength could be quantitatively determined in the range of 0.2-2 Gpa.

Karabutov and Podymova [176] used laser-based ultrasonics to characterize damage in glass-fiber-reinforced plastics used in helicopter rotor blades. Both freshly prepared samples and samples that had been subjected to cyclic loading were investigated. Ultrasonic attenuation was measured and damage mechanisms responsible for observed differences between the loaded and unloaded samples were suggested.

In 1996, Abbate et al. [181] showed that laser generated dispersive surface waves could be used to characterize chromium coatings that were electro-deposited on copper and steel substrates. Here, dispersion curves were generated by a time-frequency wavelet decomposition of the measured waveforms. The surface wave group velocity was computed

45

from this dispersion curve and the Knoop hardness was extrapolated. Values obtained with the laser based system agreed very well with the values determined by conventional ultrasonics.

Walter and Telschow [182] described a laser ultrasonic system to detect the solidification front during casting of tin and a tin-lead alloy. A Nd:YAG laser was used as the generation source and an argon laser was used with a Fabry-Perot interferometer for detection. Simultaneous measurements were made with a contact technique for comparison. Both techniques were used to determine the position of the solidification front which was systematically altered by changing the thermal gradient in the metal. The laser based method accurately reproduced the positions determined by the contact technique. Laser based measurements were also made on a moving solidification front.

Also in 1996, Dunning et al. [184] described a laser based ultrasonic system to inspect weld joints for high volume industrial applications. The system included two Nd:YAG lasers for the generation source and detection beam. Displacement was measured with a double phase conjugate mirror and balanced optical heterodyne detector described in their work. The fusion weld width was measured for two parts of approximately 2 and 3 mm thick 1010 steel that were lap-welded together by a 5kW CO_2 laser. A neural network was developed to classify the fusion weld width from the laser based measurements. This system was tested on actual automotive transmission production parts and correctly distinguished between two different weld widths with a 91% recognition rate.

Laser based ultrasonic inspection of concrete was described by Jacobs and Whitcomb in 1997 [191]. Four different concrete mixtures with different coarse aggregates were examined. All other ingredients were the same for each mixture. A pulsed ruby laser was used as the generation source. An argon laser was used with a heterodyne interferometer to measure displacements. A small amount of reflective tape was applied at the observation

point on the concrete to increase the amount of reflected detection light. Also, an oil film covered by a glass slide was applied to the generation side to enhance acoustic generation in the thermoelastic regime. It was observed that the frequency content of the generated ultrasound had little dependence on the coarse aggregate size. It was noted that the high frequency of the laser generated ultrasonic waves made the technique more suitable than conventional techniques to measure smaller defects.

Also in 1997, Audoin and Bescond [195] presented laser ultrasonic measurements of stiffness coefficients of an anisotropic sample at elevated temperatures. An Nd:YAG laser was used as the generation source and a Mach-Zehnder heterodyne interferometer was used to measure displacements. Elastic constants were obtained by measuring phase velocities and employing Christoffel's equation [33].

In 1998, Coulette et al. [196] demonstrated a laser based ultrasonic technique to optimize coatings on substrates. An analytical description of laser generated ultrasound in two-layered materials was presented by applying Hankel and Laplace transforms to the equations of motion for dynamic thermoelasticity. Waveforms from the model were compared with experimental data taken from both a carbon/epoxy plate covered with a resin layer and an aluminum plate with a paint coating. Both sets of computed waveforms agreed very well with the corresponding experiment. From this analysis, it was suggested that the model could be used with experiments to characterize the mechanical and physical properties of the coating. Furthermore, the model could be used to optimize the thickness of a coating used to enhance laser generated ultrasonic signals.

2.4   Other Contributions

There have been many other contributions to the field of laser ultrasonics.[203]- [254] We briefly review some of these efforts here and provide references to others.

47

In 1965, Ready [205] addressed the thermal interaction of lasers with solids. One-dimensional models were presented for the temperature rise in metals due to irradiation by realistic laser pulses. This work was later summarized in a more comprehensive discussion of laser interaction with solids in 1971 [96].

Many others have investigated various problems in the field of laser generated ultrasonics. In 1964 and 1966, Carome *et al.* [203], [204] discussed laser generated acoustic signals in liquids and showed good agreement between theoretical and experimental results. Also in 1966, Gournay [206] developed a one-dimensional mathematical analysis of laser generated elastic waves in liquids that showed excellent agreement with experimental results. Penner and Sharma [207] developed a one-dimensional model for the laser generated temperature and stress fields produced during material ablation. In 1967, Brienza and Demaria [208] generated microwave frequency (2 GHz) ultrasonic waves in a metal film with a mode-locked laser.

Later work by White and Lee in 1968 [209], examined laser generation of surface elastic waves. It was argued it would be possible to maximize the elastic wave output at any desired frequency by temporally modulating the laser. Furthermore, it was suggested that one could increase the efficiency of generating a surface wave of a given frequency by producing an array of sources having a period equal to the surface elastic wavelength.

In 1971, Cachier [210] also reported the generation of microwave frequency ultrasound in dielectric crystal and a metal film deposited on dielectric crystal. In 1975, Kohanzadeh *et al.* [211] developed a rigorous mathematical model for laser generated ultrasound in fluids contained within a ceramic cylindrical cavity. In their work, this cavity was in fact the transducer that measured the ultrasonic signals. To develop this model, a Helmholtz decomposition was used to represent the ceramic cavity displacement. An harmonic time dependence was assumed for both the potentials and the generating source. These poten-

48

tials were applied in the equations of motion and the resulting differential equation were solved numerically to model the stress fields.

In 1979, Ledbetter and Moulder [212] observed laser generated Rayleigh waves in aluminum. However, this was accomplished with powers in the ablative regime. Later in 1981, Aindow *et al.* [213] experimentally investigated laser generated ultrasound and found that longitudinal, shear, and Rayleigh wave modes were generated simultaneously in the thermoelastic regime. Furthermore, they found that the time duration of the Rayleigh wave was dependent on the effective width of the irradiated area. Specifically, it was observed that increasing the irradiated area broadened the Rayleigh wave pulse. This work also studied the dependence of acoustic amplitude on laser energy. Experiments again confirmed that the acoustic amplitude was proportional to the applied laser energy. It was noted that operating in the ablation regime enhanced the longitudinal mode amplitude but not the shear wave amplitude.

Theoretical work by Berthelot and Busch-Vishniac [216] in 1985 demonstrated that modulating a laser source at a specific frequency should increase the amplitude of that frequency component in the generated ultrasonic displacement. A narrow bandwidth source was desirable because the sensitivity of a detection system is often inversely proportional to the bandwidth and an unmodified laser source is a broadband source.

Several general reviews of processes related to laser generated ultrasound were presented in 1986. McDonald [218] discussed the broad topics of photoacoustic and photothermal techniques. Tam [219] provided a detailed review of many photoacoustic sensing techniques and theories. Hutchins [220] presented a review of the mechanisms for laser generated ultrasound. He noted that the form of the acoustic source depends upon the optical-absorption characteristics of the sample. For a high absorption coefficient, as in metals, the absorbed energy is localized near the surface of the sample. Consequently, the

49

thermoelastic source can be modeled as a thin disc. If the absorption coefficient is low and the laser can penetrate into the bulk of the sample, the thermoelastic source is modeled as a cylinder and the optical absorption coefficient determines the characteristic length of the cylinder. Hutchins also presented directivity measurements of the thermoelastic source in aluminum. It was found that the combination of using high frequency components and a wide source diameter enhanced the directivity in the normal direction for both the shear and longitudinal modes. Hutchins later summarized this and other work in a comprehensive review of laser ultrasound generation mechanisms presented in 1988. [255]

In 1988, Addison et al. [223], discussed using an array of laser sources to generate a tone burst of ultrasound in solids. In the course of this work, it was estimated that in the frequency range of 1 to 10 MHz, the amplitude of laser generated ultrasound in a constrained surface would be four times greater than the amplitude in a free surface. In 1988 and 1989, narrow band laser generated ultrasound was produced in the ablative regime by repetitively Q-switching a pulsed laser in work by Wagner et al. [224], [225].

In 1989, Dewhurst and Al'Rubai [228] used a laser with a 30 ps pulse width to generate ultrasound in thin structures. The pulse width was small enough so that high frequency longitudinal waves were generated and waveforms could be obtained in materials less than 120 μm thick. In this work, the laser source was in the ablative regime. Jarynski and Berthelot [229] investigated using fiber optics to deliver the laser source. It was suggested that fiber optics were a convenient way to spatially and temporally control multiple laser sources if an array of sources was desired. It was demonstrated that the signal-to-noise ratio could be improved by properly adjusting the relative phase of laser sources from two optic fibers.

In 1990, Wagner et al. [230] investigated using spatial and temporal modulation of the laser source to control the directivity of the generated ultrasound. By carefully arranging

50

an array of line or point-sources [222], it was found that the ultrasound amplitude for a given frequency could be increased in a desired direction. It was shown that ultrasound generated in aluminum had significant energy in a narrow frequency band centered around the pulse repetition frequency. Berthelot and Jarzynski [232] continued work with arrays of optical fibers for directional generation and detection of ultrasound. A method was described to use fiber optics to generate narrow band directional ultrasound. Furthermore, a method was described to use an array of fibers as a detection system to increase the signal-to-noise ratio.

In 1990 and 1991, Deaton *et al* [233], [234] continued work to generate narrow-band ultrasound. In this work, a long-cavity mode-locked laser with a pulse repetition frequency of 13.4 MHz was used. This was compared to the 50 KHz repetition rate obtained previously with the Q-switched laser [225]. Similarly, in 1992, Huang *et al* [237] studied narrow-band laser generated surface waves using an array of line sources. It was observed that the characteristics of the generated ultrasound could be adjusted by varying the number of line sources, the width of each line, and the separation distance. Optimum generation conditions were experimentally determined and it was found that the amplitude could be increase by a factor of N, the effective number of array elements. By bandpass filtering the detected ultrasound to match the narrow band generation frequency, a significant improvement in the signal-to-noise ratio was obtained. In the same year, Deaton *et al* [238] also explored improving signal-to-noise ratio by digitally filtering narrowband ultrasound obtained with a long-cavity mode-locked laser. In 1993, Noroy *et al* [240] measured directivity patterns of ultrasound generated by a phased array and compared the results to theoretical modeling based on Rose's work [4]. The theoretical predictions closely matched experimental values obtained with duraluminum and steel samples. It was found that the phase array increased the ultrasonic amplitude by a factor of 15 in the duraluminum sample.

51

In 1994, Murray and Wagner [243] reviewed techniques to produce arrays of laser sources to improve laser generated ultrasound. They described a laser that used an extra cavity White cell delay that produced an array source from a single laser and provided both temporal and spatial control of the array elements. Surface and longitudinal waveforms generated with this system were presented and demonstrated significant improvement over a single laser source.

In 1995, Lee and Burger [245] presented a finite element analysis of laser generated lamb waves. In 1996, Caron and Steiner [250] investigated the transition between the thermolelastic and ablative regimes in laser generated ultrasound in graphite/polymer composites. Hector and Hetnarski [251] modeled the thermal stresses in an elastic half-space due to a laser pulse. In this work, it was assumed that the spatial distribution was a superposition of the two lowest order modes from a cylindrical laser resonator and that the energy was absorbed at the material surface. Khan and Diebold [252] modeled laser generated ultrasound in an isotropic cylinder surrounded by a fluid medium. Also in this year, Duffer and Burger [249] examined generating narrow band ultrasound with lasers.

In 1996, Murray et al. [253] studied an array of laser sources to enhance laser generated ultrasonic waves. In this work, two methods of applying the array were described. First, the array was used to create a spatially and temporally modulated source where incident laser pulses were carefully separated in time and space so that the wavefronts from each pulse arrived at the observation point simultaneously. The superposition of the pulses resulted in a larger ultrasonic displacement. It was theoretically demonstrated that the increase in surface displacement was on the order of the number of elements in the array. This was confirmed with experiments on aluminum. The authors noted a disadvantage of this technique was that spatial resolution might be lost because a larger volume of the sample was being interrogated. For this reason, small defects near the source might be

52

missed. A further disadvantage cited was that the source-to-detector distance and the acoustic velocity must be know to calculate the appropriate spacing parameters. However, in practical applications, these values may not be known *a priori.*

In the second method, the incident pulses were separated in time or space so that there was a fixed temporal spacing (Δt) between wavefronts at the point of observation. This resulted in a narrow-band tone burst with the acoustic energy centered around the fundamental frequency, $1/\Delta t$. The bandwidth of the optical detection system was then matched to this frequency resulting in an increased sensitivity. It was theoretically shown that the increase in sensitivity was on the order of the square-root of the number of pulses divided by the number of harmonics filtered (used) by the detection system. This was also experimentally verified with an aluminum specimen. The authors noted that in. contrast to the first technique, material parameters are not required. However, it was also noted that care was required when matching the bandwidth of the detector to the signal to maintain the integrity of the signal.

In 1997, Sanderson *et al.* [254] presented a thermoelastic analysis of the laser source for ultra-short laser pulses in isotropic materials. Here, the authors motivated the study by noting that current lasers with very short pulses (ps rise times) were being used to generate ultrasound for inspection of very small dimensions. (See for example, Morath *et al.* [194] and the included references) Also, fiber optics with small diameter cores were being used to deliver the lasers so that the laser source was beginning to approach the spatial and temporal impulse functions used in point source models. Consequently, the authors argued that it was important to determine the time scale and spot size limits for which the point source models were still valid. In addition, this work was a continuation of their previous effort to determine the minimum time scale for which hyperbolic heat equations could be accurately used. [103] In this work, a parameter was determined that defined the

53

largest Gaussian rise times and highest modulation frequencies for which hyperbolic heat conduction effects were negligible. Also, results indicated that metals respond much faster thermally than mechanically. Consequently, it was asserted that the temporal point source limit is a mechanical rather than thermal limit. It was also found that approximately a 1 ns rise time in temporally Gaussian pulses was the point source limit for a SCOE in aluminum or steel. Finally, the temperature field due to a Gaussian laser pulse was used to estimate the shape of the laser generated acoustic source. It was found that the radial dimension of the acoustic source would not exceed 1.65 times the Gaussian radius in metals.

54

Chapter 3

Modeling the Thermal Response: The Temperature Field in an Isotropic Half-Space due to a Q-Switched Laser Pulse

In this section, we model the thermoelastic generation of ultrasound in isotropic and anisotropic half-spaces. For a general anisotropic body, the governing field equations of thermoelasticity are given by [91]

$$C_{ijkl} u_{k,lj} + \rho f_i + \beta_{ij}\theta,_j = \rho \ddot{u}_i \tag{3.1}$$

$$(k_{ij}\theta,_j),_i - cp\dot{\theta} + \rho h + T_0\beta_{ij}\dot{u}_{i,j} = 0 \tag{3.2}$$

The first expression represents the elastodynamic equations of motion with a thermal forcing function and the second equation is the classical equation of heat conduction. The parameters are the stiffness tensor, C_{ijkl}, the material density, ρ, the thermal moduli tensor, β_{ij}.

55

the thermal conductivity tensor, k_{ij}, and the specific heat at constant strain, c. The field variables are the body force per unit mass, f_i, the heat produced by internal sources per unit time and unit mass, h, the displacement, u_i and the change in temperature, θ defined by

$$\theta \equiv T - T_0$$

where T is the absolute temperature above the reference temperature, T_0. In both equations, the summation convention is used for repeated indices, the subscripted comma denotes differentiation with respect to the following index space variables, and the superscipted dot represents differentiation with respect to time. The system of differential equations defined by (3.1) and (3.2) are coupled and consequently must be solved simultaneously for an exact solution. Although this approach has been used to describe laser generated ultrasound for a few specific cases [7], the complexity of these equations makes their general solution prohibitively difficult. Instead, we partially decouple the thermoelastic equations by suppressing the term $T_0\beta_{ij}\dot{u}_{i,j}$ in equation (3.2). This is equivalent to assuming that the elastic fields do not affect the temperature fields. This approximation is reasonable for describing laser generated ultrasound because this term is very small when compared to the other terms in equation (3.2). This approximation has been verified in earlier work [7].

We summarize our solution technique for modeling laser generated ultrasound in an anisotropic material in the following steps. First, we assume that heat diffusion in the material behaves as if the material were isotropic. This approximation can be adjusted later if we find that more complexity is required to accurately model the thermoelastic process. Next, we suppress the term $T_0\beta_{ij}\dot{u}_{i,j}$ in equation (3.2) and use the point source solution of the resulting differential equation to develop analytical equations describing the thermal fields generated by a Q-switched laser pulse. We numerically solve these equations to obtain the generated thermal fields and the resulting thermal forcing function. Subsequently, we

56

consider the elastodynamic equations of motion in an anisotropic material. We replace the thermal forcing function in equations (3.1) with an impulse forcing function. We Laplace transform these equations in time and Fourier transform in space, and then solve the resulting algebraic system for the transformed displacements. We numerically invert these transformed displacements to obtain the Green's function solution. Finally, we convolve this Green's function with the thermal forcing function to compute the elastic fields generated by the laser pulse.

3.1 Instantaneous Surface Source

Following the work by Ready [96] we derive here the temperature field in an isotropic semi-infinite half-space due to an incident Q-switched laser pulse. We use point heat sources to construct ring sources. We then use these ring sources to construct a surface disc source with a Gaussian radial intensity dependence.

If we assume that there are no internal heat sources and that the material is isotropic, equation (3.2) reduces to the classical homogenous differential equation for heat conduction

$$\nabla^2 T(x,y,z,t) = \frac{1}{\kappa}\frac{\partial}{\partial t}T(x,y,z,t) \tag{3.3}$$

where κ is the thermal diffusivity and where we have set $T_0 = 0$ so that $\theta(x,y,z,t) = T(x,y,z,t)$ is the temperature rise of the sample. From Carslaw and Jaeger [90], the temperature field due to an instantaneous point source of strength $q[m^3 \cdot {}^\circ C]$ at (x',y',z') at $t=0$ is given by

$$T(x,y,z,t) = \frac{q}{8(\pi\kappa t)^{\frac{3}{2}}}e^{-[(x-x')^2+(y-y')^2+(z-z')^2]/4\kappa t} \tag{3.4}$$

For a semi-infinite solid that does not radiate into its surroundings the corresponding tem-

57
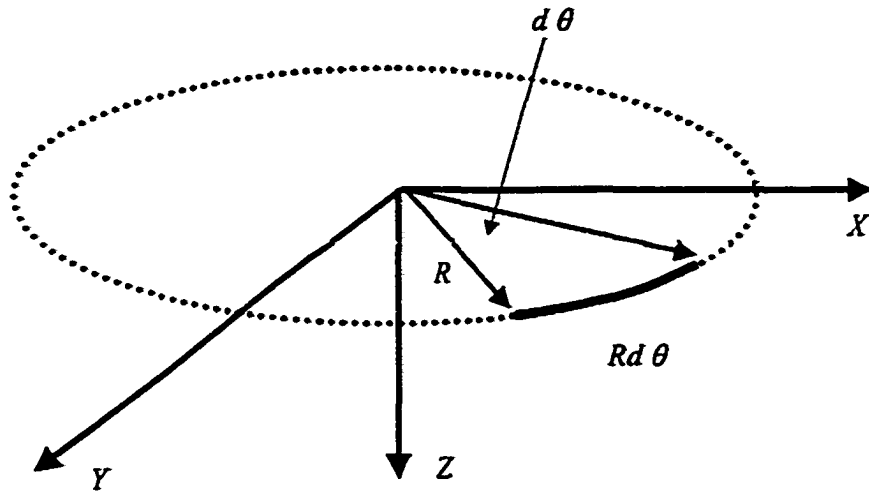
Figure 3.1: Defining a ring source as a collection of point sources.

perature field will be twice as large or

$$T(x,y,z,t) = \frac{q}{4(\pi\kappa t)^{\frac{3}{2}}}e^{-[(x-x')^2+(y-y')^2+(z-z')^2]/4\kappa t} \tag{3.5}$$

We use this solution to construct the temperature field due to an instantaneous ring source of strength Q' and radius R in the plane $z' = 0$. We rewrite equation (3.5) in cylindrical coordinates as

$$T(r,\theta,z,t) = \frac{q}{4(\pi\kappa t)^{\frac{3}{2}}}e^{-[(z-z')^2+r^2+r'^2-2rr'\cos(\theta-\theta')]/4\kappa t} \tag{3.6}$$

where $r' \equiv \sqrt{x'^2 + y'^2}$. We distribute point sources along a ring with radius R as illustrated in Figure 3.1.We set the strength of each point source to $QRd\theta'$ where $Q[\frac{\text{J} \cdot ^\circ C}{\text{m}}]$ is the heat source strength per unit length and $Rd\theta'$ is an infinitesimal length along the circumference of the ring. We integrate these point sources over θ:

$$\underset{\substack{\text{Instantaneous} \\ \text{surface ring}}}{T(r,\theta,z,t)} = \int_0^{2\pi} \frac{Q}{4(\pi\kappa t)^{\frac{3}{2}}}e^{-[(z-z')^2+r^2+r'^2-2rr'\cos(\theta-\theta')]/4\kappa t}Rd\theta' \tag{3.7}$$

58

Along the ring, $r' = R$ and $z' = 0$ so that we have

$$T(r,\theta,z,t)\underset{\substack{\text{Instantaneous}\\\text{surface ring}}}{=} \frac{QR}{4(\pi\kappa t)^{\frac{3}{2}}}\int_0^{2\pi} e^{-[z^2+r^2+R^2-2rR\cos(\theta-\theta')]/4\kappa t}\,d\theta' \tag{3.8}$$

which we can rewrite as

$$T(r,\theta,z,t)\underset{\substack{\text{Instantaneous}\\\text{surface ring}}}{=} \frac{QR}{4(\pi\kappa t)^{\frac{3}{2}}}\exp\left(-\frac{r^2+R^2+z^2}{4\kappa t}\right)\int_0^{2\pi} e^{rR\cos(\theta-\theta')]/2\kappa t}\,d\theta' \tag{3.9}$$

Evaluating the integral we obtain

$$T(r,\theta,z,t)\underset{\substack{\text{Instantaneous}\\\text{surface ring}}}{=} \frac{2\pi QR}{4(\pi\kappa t)^{\frac{3}{2}}}\exp\left(-\frac{r^2+R^2+z^2}{4\kappa t}\right)I_0\left(\frac{rR}{2\kappa t}\right) \tag{3.10}$$

where I_0 is the zeroth-order modified Bessel function. This can also be written as

$$T(r,\theta,z,t)\underset{\substack{\text{Instantaneous}\\\text{surface ring}}}{=} \frac{Q'}{4(\pi\kappa t)^{\frac{3}{2}}}\exp\left(-\frac{r^2+R^2+z^2}{4\kappa t}\right)I_0\left(\frac{rR}{2\kappa t}\right) \tag{3.11}$$

where $Q' = 2\pi RQ$. Then, the total quantity of heat absorbed is $q' = \rho C Q'$ and we can write

$$T(r,\theta,z,t)\underset{\substack{\text{Instantaneous}\\\text{surface ring}}}{=} \frac{q'}{4\rho C(\pi\kappa t)^{\frac{3}{2}}}\exp\left(-\frac{r^2+R^2+z^2}{4\kappa t}\right)I_0\left(\frac{rR}{2\kappa t}\right) \tag{3.12}$$

Here, ρ [$\frac{kg}{m^3}$] is the mass density, C [$\frac{W\cdot s}{kg\cdot{}^{\circ}C}$] is the specific heat, the units of Q' are [$m^3\cdot{}^{\circ}C$], and the units of q' are [W·s]. Now, we express the area of the ring source as the circumference multiplied by a thickness, dR and we write q' in terms of the instantaneous heat flux, $f(r)$ [$\frac{W\cdot s}{m^2}$] as

$$q' = f(R) \times 2\pi R dR \tag{3.13}$$

We assume a Gaussian distribution for $f(R)$ of the form

$$f(R) = f_0\exp\left(-\frac{R^2}{d^2}\right) \tag{3.14}$$

59

where f_0 is the maximum flux density at the center of the Gaussian spot and d is the Gaussian spot radius. This describes the intensity profile of a pure TEM$_{00}$ mode laser. In practice, the generation laser may not be a pure TEM$_{00}$ but this is typically the dominant mode. Then, we can rewrite equation (3.12) as

$$T(r,\theta,z,t) = \frac{2\pi RdR f_0}{4\rho C(\pi\kappa t)^{\frac{3}{2}}} \exp\left(-\frac{R^2}{d^2}\right) \exp\left(-\frac{r^2 + R^2 + z^2}{4\kappa t}\right) I_0\left(\frac{rR}{2\kappa t}\right) \qquad (3.15)$$

Instantaneous surface ring

To obtain the temperature distribution for an instantaneous surface source with a Gaussian radial dependence, we integrate equation (3.15) with respect to R. This is graphically illustrated in Figure 3.2 and we obtain

$$T(r,\theta,z,t) = \int_0^\infty \frac{2\pi RdR f_0}{4\rho C(\pi\kappa t)^{\frac{3}{2}}} \exp\left(-\frac{R^2}{d^2}\right) \exp\left(-\frac{r^2 + R^2 + z^2}{4\kappa t}\right) I_0\left(\frac{rR}{2\kappa t}\right) \qquad (3.16)$$

Instantaneous surface gaussian

We rewrite this equation in the form

$$T(r,\theta,z,t) = \frac{f_0}{2\rho C(\pi\kappa^3 t^3)^{\frac{1}{2}}} \exp\left(-\frac{r^2 + z^2}{4\kappa t}\right) \times$$

Instantaneous surface gaussian

$$\int_0^\infty \exp\left[-R^2\left(\frac{1}{d^2} + \frac{1}{4\kappa t}\right)\right] I_0\left(\frac{rR}{2\kappa t}\right) RdR \qquad (3.17)$$

To evaluate the integral in equation (3.17) we set $x = R^2$ so that $dx/2 = RdR$ and rewrite it as

$$\int_0^\infty \frac{1}{2} \exp\left[-ax\right] J_0\left(b\sqrt{x}\right) dx \qquad (3.18)$$

where $J_n(x)$ denotes the Bessel function of order n , we define a and b as

$$a = \frac{1}{d^2} + \frac{1}{4\kappa t}$$

$$b = i\frac{r}{2\kappa t}$$

and we have used

$$I_n = i^{-n} J_n(ix) \qquad (3.19)$$

60

Gaussian
Radial Intensity
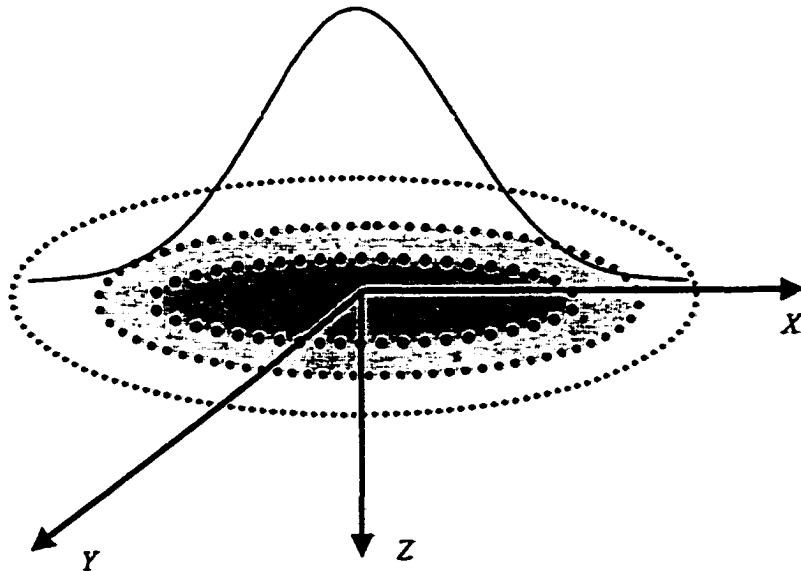
Figure 3.2: Describing a surface disc source with Gaussian radial dependence as a collection of ring sources.

From integral tables [256] we find that the solution to equation (3.18) is

$$\frac{1}{2a} \exp\left(-\frac{b^2}{4a}\right)$$

so that equation (3.17) gives

$$
\begin{aligned}
T(r,\theta,z,t) &= \frac{f_0}{2\rho C(\pi\kappa^3 t^3)^{\frac{1}{2}}} \exp\left(-\frac{r^2+z^2}{4\kappa t}\right) \frac{1}{2a} \exp\left(-\frac{b^2}{4a}\right) \\[2mm]
&= \frac{f_0}{4\rho C(\pi\kappa^3 t^3)^{\frac{1}{2}}} \exp\left(-\frac{r^2+z^2}{4\kappa t}\right) \times \\[2mm]
&\quad \frac{4\kappa t d^2}{4\kappa t + d^2} \exp\left[\frac{1}{4}\left(\frac{r}{2\kappa t}\right)^2 \frac{4\kappa t d^2}{4\kappa t + d^2}\right]
\end{aligned}
$$

(3.20)

61

which can be simplified to

$$T(r,\theta,z,t)_{\substack{\text{Instantaneous} \\ \text{surface gaussian}}} = \frac{f_0 d^2}{\rho C(\pi\kappa t)^{\frac{1}{2}}(4\kappa t + d^2)} \exp\left(-\frac{r^2}{4\kappa t + d^2} - \frac{z^2}{4\kappa t}\right) \qquad (3.21)$$

Using the relationship between the thermal diffusivity $\kappa[\frac{m^2}{s}]$, and the thermal conductivity, $K[\frac{W}{m^J.^\circ C}]$

$$\kappa = \frac{K}{\rho C} \qquad (3.22)$$

we can write equation (3.21) as

$$T(r,\theta,z,t)_{\substack{\text{Instantaneous} \\ \text{surface gaussian}}} = \frac{f_0 d^2}{K(4\kappa t + d^2)}\left(\frac{\kappa}{\pi t}\right)^{\frac{1}{2}} \exp\left(-\frac{r^2}{4\kappa t + d^2} - \frac{z^2}{4\kappa t}\right) \qquad (3.23)$$

Now, from the units of $f(r)$ we see that it is the energy per unit area incident on the half space. The total instantaneous incident energy (i.e. the laser pulse energy) is then given by

$$E = \int_0^{2\pi}\int_0^\infty f_0 \exp\left(-\frac{r^2}{d^2}\right) r\, dr\, d\theta = \pi d^2 f_0 \qquad (3.24)$$

so that we can write

$$T(r,\theta,z,t)_{\substack{\text{Instantaneous} \\ \text{surface gaussian}}} = \frac{E}{K}\left(\frac{\kappa}{\pi^3}\right)^{1/2}\frac{1}{t^{\frac{1}{2}}(4\kappa t + d^2)} \exp\left(-\frac{r^2}{4\kappa t + d^2} - \frac{z^2}{4\kappa t}\right) \qquad (3.25)$$

3.2   Instantaneous Buried Source

The previous expression is valid if the laser energy is absorbed entirely at the surface and agrees with the expression given by Ready [96]. If the laser light penetrates into the bulk of the sample, then the radiant flux density or irradiance, F [$\frac{W}{m^2}$] varies with depth according to [257]

$$f(z) = f_0 e^{-\chi z} \qquad (3.26)$$

where χ is the absorption coefficient. To include this effect, we use a distribution of point sources to construct a buried ring source of strength Q' and radius R. We set the strength

62

of each point source to $Q(z')Rd\theta'$ where $Q(z')[\frac{m^3 \cdot {}^\circ C}{m}]$ is the heat source strength per unit length. Then, for a ring at depth z' we have

$$\underset{\substack{\text{Instantaneous}\\\text{buried ring}}}{T(r,\theta,z,t)} = \int_0^{2\pi} \frac{Q(z')}{4(\pi\kappa t)^{\frac{3}{2}}} e^{-[(z-z')^2+r^2+r'^2-2rr'\cos(\theta-\theta')]/4\kappa t} Rd\theta' \qquad (3.27)$$

Along the ring, $r' = R$ so that we have

$$\underset{\substack{\text{Instantaneous}\\\text{buried ring}}}{T(r,\theta,z,t)} = \frac{RQ(z')}{4(\pi\kappa t)^{\frac{3}{2}}} \exp\left(-\frac{(z-z')^2+r^2+R^2}{4\kappa t}\right) \times$$
$$\int_0^{2\pi} \exp\left(\frac{rR\cos(\theta-\theta')}{2\kappa t}\right) d\theta' \qquad (3.28)$$

Evaluating the integral, we obtain

$$\underset{\substack{\text{Instantaneous}\\\text{buried ring}}}{T(r,\theta,z,t)} = \frac{2\pi RQ(z')}{4(\pi\kappa t)^{\frac{3}{2}}} \exp\left(-\frac{(z-z')^2+r^2+R^2}{4\kappa t}\right) I_0\left(\frac{rR}{2\kappa t}\right) \qquad (3.29)$$

or

$$\underset{\substack{\text{Instantaneous}\\\text{buried ring}}}{T(r,\theta,z,t)} = \frac{q'(z')}{4\rho C(\pi\kappa t)^{\frac{3}{2}}} \exp\left(-\frac{(z-z')^2+r^2+R^2}{4\kappa t}\right) I_0\left(\frac{rR}{2\kappa t}\right) \qquad (3.30)$$

where $Q'(z)[m^3 \cdot {}^\circ C] = 2\pi RQ(z')$ and the heat absorbed is $q'(z')[\text{W·s}] = \rho C Q'(z)$. We write the liberated heat source in terms of the instantaneous flux as

$$q'(z') = f(R,z') \times 2\pi R\, dR \qquad (3.31)$$

where now $f(R,z')$ has the form

$$f(R,z') = f_0 \exp\left(-\frac{R^2}{d^2} - \chi z'\right) \qquad (3.32)$$

so that the flux has a Gaussian radial distribution and is exponentially absorbed into the bulk and we have

$$q'(z') = 2\pi f_0 \exp\left(-\frac{R^2}{d^2} - \chi z'\right) R\, dR \qquad (3.33)$$

63

Then, we can construct the buried Gaussian disc source from equation (3.30) as

$$
\underset{\substack{\text{Instantaneous} \\ \text{buried Gaussian} \\ \text{disc}}}{T(r,\theta,z,t)} = \frac{1}{4\rho C(\pi\kappa t)^{\frac{3}{2}}} \int_0^\infty f_0 \exp\left(-\frac{R^2}{d^2} - \chi z'\right) \times
$$

$$
\exp\left(-\frac{(z-z')^2 + r^2 + R^{\,2}}{4\kappa t}\right) I_0\left(\frac{rR}{2\kappa t}\right) 2\pi R dR \qquad (3.34)
$$

We rewrite this as

$$
\underset{\substack{\text{Instantaneous} \\ \text{buried Gaussian} \\ \text{disc}}}{T(r,\theta,z,t)} = \frac{f_0}{2\rho C(\pi\kappa^3 t^3)^{\frac{1}{2}}} \exp\left(-\frac{(z-z')^2 + r^2}{4\kappa t} - \chi z'\right) \times
$$

$$
\int_0^\infty \exp\left[-R^2\left(\frac{1}{d^2} + \frac{1}{4\kappa t}\right)\right] I_0\left(\frac{rR}{2\kappa t}\right) R dR \qquad (3.35)
$$

and see that the integration over R in equation (3.35) is identical to that in equation (3.17).

Then, we have

$$
\underset{\substack{\text{Instantaneous} \\ \text{buried Gaussian} \\ \text{disc}}}{T(r,\theta,z,t)} = \frac{f_0}{2\rho C(\pi\kappa^3 t^3)^{\frac{1}{2}}} \frac{2\kappa t d^2}{4\kappa t + d^2} \exp\left(-\frac{r^2}{4\kappa t + d^2}\right) \exp\left(-\frac{(z-z')^2}{4\kappa t} - \chi z'\right)
$$

$$
= \frac{f_0}{\rho C(\pi\kappa t)^{\frac{1}{2}}} \frac{d^2}{4\kappa t + d^2} \exp\left(-\frac{r^2}{4\kappa t + d^2} - \frac{z^2}{4\kappa t}\right) \times
$$

$$
\exp\left(-\frac{z'^{\,2} - (2z - 4\chi\kappa t)\, z'}{4\kappa t}\right) \qquad (3.36)
$$

which we can rewrite as

$$
\underset{\substack{\text{Instantaneous} \\ \text{buried Gaussian} \\ \text{disc}}}{T(r,\theta,z,t)} = \frac{f_0}{K} \frac{d^2}{4\kappa t + d^2} \left(\frac{\kappa}{\pi t}\right)^{\frac{1}{2}} \exp\left(-\frac{r^2}{4\kappa t + d^2} - \frac{z^2}{4\kappa t}\right) \times
$$

$$
\exp\left[-\left(\frac{1}{4\kappa t} z'^{\,2} + \frac{(2\chi\kappa t - z)}{2\kappa t} z'\right)\right] \qquad (3.37)
$$

We note that if $z' = 0$ so that the disc source is at the surface and consequently is not attenuated, we regain the solution for the surface source in equation (3.21). The burried disk is illustrated in Figure 3.3. Now, we construct a buried volume thermal source by stacking the buried discs as in Figure 3.4.

64

Gaussian Radial Intensity

Exponential Absorption
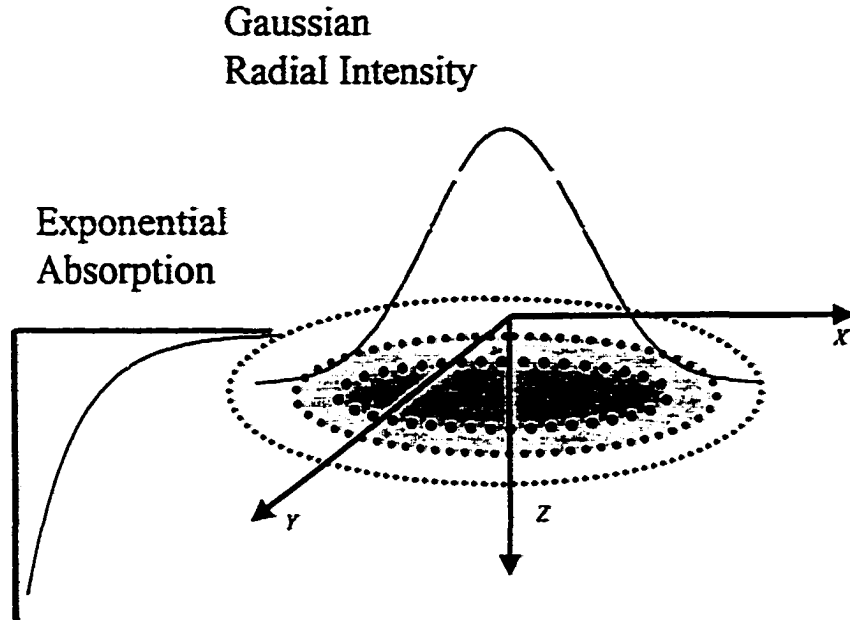
Figure 3.3: Buried disc source with Gaussian radial dependence and exponential absorption with depth.

We start with equation (3.30)

$$T(r,\theta,z,t) = \frac{q'(z')}{4\rho C(\pi\kappa t)^{\frac{3}{2}}} \exp\left(-\frac{(z-z')^2 + r^2 + R^2}{4\kappa t}\right) I_0\left(\frac{rR}{2\kappa t}\right) \qquad (3.38)$$

Instantaneous
buried ring

and write the heat source in terms of the energy density, $n(r,z)[\frac{W \cdot s}{m^3}]$, as

$$q'(z') = 2\pi n(R, z') R dR dz' \qquad (3.39)$$

where

$$n(R, z') = n_0 \exp\left(-\frac{R^2}{d^2} - \chi z'\right) \qquad (3.40)$$

We want to express n_0 in terms of f_0. We found from equation (3.24) that the energy of

65
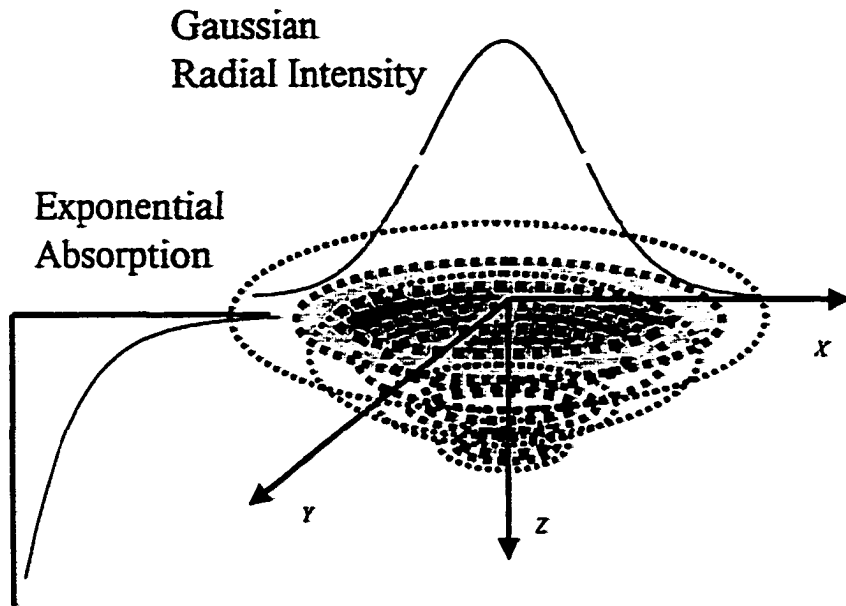
Figure 3.4: Describing a buried disc source with Gaussian radial dependence and exponential decay as a collection of disc sources.

the laser pulse is given by

$$E = \pi d^2 f_0 \qquad (3.41)$$

If we integrate the energy density over the volume in which the pulse is absorbed it must equal this total energy so that we require

$$
\begin{aligned}
\pi d^2 f_0 &= 2\pi \int_0^\infty \int_0^\infty n(R, z') R \, dR \, dz' \\
&= 2\pi n_0 \int_0^\infty \int_0^\infty \exp\left(-\frac{R^2}{d^2} - \chi z\right) R \, dR \, dz = \frac{\pi d^2 n_0}{\chi}
\end{aligned} \qquad (3.42)
$$

Therefore, we must have

$$n_0 = \chi f_0 \qquad (3.43)$$

Then, plugging equations (3.39), (3.40), and (3.43) into equation (3.38) and integrating we

66

obtain

$$
\begin{aligned}
T(r,\theta,z,t) \atop \text{Instantaneous buried Gaussian volume} \quad = \quad & \frac{2\pi\chi f_0}{4\rho C(\pi\kappa t)^{\frac{3}{2}}} \int_0^\infty \int_0^\infty \exp\left(-\frac{R^2}{d^2} - \chi z'\right) \times \\
& \exp\left(-\frac{(z-z')^2 + r^2 + R^2}{4\kappa t}\right) I_0\left(\frac{rR}{2\kappa t}\right) R\,dR\,dz'
\end{aligned}
$$

$$(3.44)$$

Performing the integration over R gives

$$
\begin{aligned}
T(r,\theta,z,t) \atop \text{Instantaneous buried Gaussian volume} \quad = \quad & \frac{\chi f_0}{\rho C(\pi\kappa t)^{\frac{1}{2}}} \frac{d^2}{4\kappa t + d^2} \exp\left(-\frac{r^2}{4\kappa t + d^2}\right) \times \\
& \int_0^\infty \exp\left[-\left(\frac{1}{4\kappa t}z'^2 + \frac{(2\chi\kappa t - z)}{2\kappa t}z' + \frac{z^2}{4\kappa t}\right)\right]dz'
\end{aligned}
$$

$$(3.45)$$

The integral in equation (3.45) is of the form

$$
\int_0^\infty e^{-\left(ax^2 + bx + c\right)}dx
$$

$$(3.46)$$

with

$$
a = \frac{1}{4\kappa t}
$$

$$
b = \frac{1}{2\kappa t}(2\chi\kappa t - z)
$$

$$
c = \frac{z^2}{4\kappa t}
$$

From tables [256] the solution to this integral is

$$
\frac{1}{2}\sqrt{\frac{\pi}{a}}e^{(b^2-4ac)/4a}\,\mathrm{erf}\,c\left(\frac{b}{2\sqrt{a}}\right)
$$

so that the integral evaluates to

$$
\int_0^\infty \{\cdots\}dz' = (\pi\kappa t)^{\frac{1}{2}}\exp\left[\chi\left(\chi\kappa t - z\right)\right]\mathrm{erf}\,c\left(\frac{1}{2}\frac{2\chi\kappa t - z}{(\kappa t)^{\frac{1}{2}}}\right)
$$

$$(3.47)$$

67

Combining equations (3.45) and equation (3.47) gives

$$T(r,\theta,z,t) = \frac{\chi f_0}{\rho C (\pi \kappa t)^{\frac{1}{2}}} \frac{d^2}{4\kappa t + d^2} \exp\left(-\frac{r^2}{4\kappa t + d^2}\right) \times$$
$$\text{Instantaneous buried Gaussian volume}$$

$$(\pi \kappa t)^{\frac{1}{2}} \exp\left[\chi(\chi\kappa t - z)\right] \text{erf c}\left(\frac{1}{2}\frac{2\chi\kappa t - z}{(\kappa t)^{\frac{1}{2}}}\right) \tag{3.48}$$

which we can write as

$$T(r,\theta,z,t) = \frac{\chi f_0}{\rho C}\frac{d^2}{(4\kappa t + d^2)} \exp\left(-\frac{r^2}{4\kappa t + d^2}\right) \times$$
$$\text{Instantaneous buried Gaussian volume}$$

$$\exp\left(\chi^2\kappa t - \chi z\right) \text{erf c}\left(\chi(\kappa t)^{\frac{1}{2}} - \frac{z}{2(\kappa t)^{\frac{1}{2}}}\right) \tag{3.49}$$

or as

$$T(r,\theta,z,t) = \frac{\chi f_0 \kappa}{K}\frac{d^2}{(4\kappa t + d^2)} \exp\left(-\frac{r^2}{4\kappa t + d^2}\right) \times$$
$$\text{Instantaneous buried Gaussian volume}$$

$$\exp\left(\chi^2\kappa t - \chi z\right) \text{erf c}\left(\chi(\kappa t)^{\frac{1}{2}} - \frac{z}{2(\kappa t)^{\frac{1}{2}}}\right) \tag{3.50}$$

3.3 Verification of Instantaneous Buried Source Equation

To verify this result, we take the limit as $\chi \to \infty$ so that the input energy is absorbed entirely at the surface. In this case, we should regain the previous result derived for a surface source in equation (3.23). For large arguments, the complimentary error function can be expanded as [258]

$$\text{erf c}(x) \sim \frac{e^{-x^2}}{x\sqrt{\pi}}\left(1 - \frac{1}{2x^2} + \frac{1\cdot3}{(2x^2)^2} - \frac{1\cdot3\cdot5}{(2x^2)^3}\cdots\right)$$

68

so that in the limit of large χ equation (3.50) can be expanded as

$$T(r,\theta,z,t) =$$
Instantaneous
buried Gaussian
volume

$$\lim_{\chi \to \infty} \left\{ \frac{\chi f_0 \kappa}{K} \frac{d^2 \exp\left(-\frac{r^2}{4\kappa t + d^2}\right) \exp\left(\chi^2 \kappa t - \chi z\right)}{(4\kappa t + d^2)} \times \right.$$

$$\left. \frac{\exp\left[-\Delta^2\right]}{\sqrt{\pi}\Delta} \left(1 - \frac{1}{2\Delta^2} + \frac{1 \cdot 3}{(2\Delta^2)^2} - \frac{1 \cdot 3 \cdot 5}{(2\Delta^2)^3} \cdots \right) \right\} \tag{3.51}$$

with

$$\Delta \equiv \left(\chi (\kappa t)^{\frac{1}{2}} - \frac{z}{2(\kappa t)^{\frac{1}{2}}}\right)$$

As $\chi \to \infty$, the first term in the expansion dominates and we can neglect the other terms and write

$$T(r,\theta,z,t) =$$
Instantaneous
buried Gaussian
volume

$$\lim_{\chi \to \infty} \left\{ \frac{\chi f_0 \kappa}{K} \frac{d^2}{(4\kappa t + d^2)} \exp\left(-\frac{r^2}{4\kappa t + d^2}\right) \frac{\exp\left(\chi^2 \kappa t - \chi z\right) \exp\left(-\chi^2 \kappa t + \chi z - \frac{z^2}{4\kappa t}\right)}{\sqrt{\pi}\left(\chi (\kappa t)^{\frac{1}{2}} - \frac{z}{2(\kappa t)^{\frac{1}{2}}}\right)} \right\} \tag{3.52}$$

After collecting terms and simplifying, we have

$$T(r,\theta,z,t) = \lim_{\chi \to \infty} \left\{ \frac{\chi f_0 \kappa}{K} \frac{d^2}{(4\kappa t + d^2)} \exp\left(-\frac{r^2}{4\kappa t + d^2}\right) \frac{\exp\left(-\frac{z^2}{4\kappa t}\right)}{\sqrt{\pi}\left(\chi (\kappa t)^{\frac{1}{2}} - \frac{z}{2(\kappa t)^{\frac{1}{2}}}\right)} \right\} \tag{3.53}$$
Instantaneous
buried Gaussian
volume

Evaluating the limit, we obtain

$$T(r,\theta,z,t) = \frac{f_0 \kappa}{K} \frac{d^2}{(4\kappa t + d^2)} \exp\left(-\frac{r^2}{4\kappa t + d^2}\right) \frac{\exp\left(-\frac{z^2}{4\kappa t}\right)}{(\pi \kappa t)^{\frac{1}{2}}} \tag{3.54}$$
Instantaneous
buried Gaussian
volume

69

and after simplifying this result, we have

$$T(r,\theta,z,t)_{\substack{\text{Instantaneous}\\\text{buried Gaussian}\\\text{volume}}} = \frac{f_0 d^2}{K(4\kappa t + d^2)} \left(\frac{\kappa}{\pi t}\right)^{\frac{1}{2}} \exp\left(-\frac{r^2}{4\kappa t + d^2} - \frac{z^2}{4\kappa t}\right) \qquad (3.55)$$

which is identical to equation (3.23) as desired.

3.4 Q-Switched Laser: Surface and Buried Sources

Next, we use the instantaneous sources given by equations (3.25) and (3.34) as convolution kernels to construct laser thermal sources with a finite temporal extent. If $P(t)$ represents the normalized time dependence of the power per unit area (flux) of the laser pulse, then a laser thermal source acting at the surface of a half-space can be written as the convolution integral

$$
\begin{aligned}
T(r,\theta,z,t)_{\substack{\text{Surface}\\\text{Gaussian}}} &= T(r,\theta,z,t)_{\substack{\text{Instantaneous}\\\text{surface gaussian}}} * P(t) \\
&= \frac{f_0 d^2}{K}\left(\frac{\kappa}{\pi}\right)^{\frac{1}{2}} \int_{-\infty}^{\infty} \frac{P(t-t')}{t'^{\frac{1}{2}}(4\kappa t' + d^2)} \exp\left(-\frac{r^2}{4\kappa t' + d^2} - \frac{z^2}{4\kappa t'}\right) dt'
\end{aligned}
\qquad (3.56)
$$

Similarly, for a buried laser thermal source we have the convolution integral

$$
\begin{aligned}
T(r,\theta,z,t)_{\substack{\text{Buried}\\\text{Gaussian}\\\text{volume}}} &= T(r,\theta,z,t)_{\substack{\text{Instantaneous}\\\text{buried Gaussian}\\\text{volume}}} * P(t) \\
&\quad \frac{\chi f_0 \kappa}{K} \int_{-\infty}^{\infty} \left\{ \frac{P(t-t')d^2}{(4\kappa t' + d^2)} \exp\left(-\frac{r^2}{4\kappa t' + d^2}\right) \times \right. \\
&\quad \left. \exp\left(\chi^2 \kappa t' - \chi z\right) \operatorname{erfc}\left(\chi(\kappa t')^{\frac{1}{2}} - \frac{z}{2(\kappa t')^{\frac{1}{2}}}\right) \right\} dt'
\end{aligned}
\qquad (3.57)
$$

However, the functions $P(t)$ and $T(r,\theta,z,t)$ are one sided so that

$$T(r,\theta,z,t') = 0, \quad t' < 0$$

$$P(t-t') = 0, \quad t' > t$$

70

Consequently, all of the contributions to the integral come when $0 < t' < t$ and we can rewrite the previous equations as

$$T(r,\theta,z,t)\underset{\substack{\text{Surface}\\\text{Gaussian}}}{=} \frac{f_0 d^2}{K}\left(\frac{\kappa}{\pi}\right)^{\frac{1}{2}}\int_0^t \frac{P(t-t')}{t'^{\frac{1}{2}}(4\kappa t'+d^2)}\exp\left(-\frac{r^2}{4\kappa t'+d^2}-\frac{z^2}{4\kappa t'}\right)dt' \qquad (3.58)$$

and

$$T(r,\theta,z,t)\underset{\substack{\text{Buried}\\\text{Gaussian}\\\text{volume}}}{=} \frac{\chi f_0 \kappa}{K}\int_0^t\left\{\frac{P(t-t')d^2}{(4\kappa t'+d^2)}\exp\left(-\frac{r^2}{4\kappa t'+d^2}\right)\times\right.$$

$$\left.\exp\left(\chi^2\kappa t'-\chi z\right)\operatorname{erfc}\left(\chi(\kappa t')^{\frac{1}{2}}-\frac{z}{2(\kappa t')^{\frac{1}{2}}}\right)\right\}dt' \qquad (3.59)$$

From Rose [4] and Ready [96], the time dependence of a Q-switched laser can be described by

$$p(t)=\frac{t}{\tau^2}\exp\left(-\frac{t}{\tau}\right) \qquad (3.60)$$

where τ represents the rise time of the pulse. Normalizing the amplitude to unity, we have

$$P(t)=\frac{t}{\tau}\exp\left(1-\frac{t}{\tau}\right) \qquad (3.61)$$

Figure 3.5 illustrates the function in equation (3.61) with $\tau = 20\times10^{-9}$s. We see that the intensity of the laser pulse reaches a maximum around 20 ns and then decays exponentially until it is zero around 150 ns. The full width half maximum (FWHM) is approximately 50 ns. Typical Q-switched laser pulses in our experiments exhibited a similar shape with a FWHM between 20 and 200 ns.

With this time dependence, the surface and buried source convolution integrals respectively become

$$T(r,\theta,z,t)\underset{\substack{\text{Surface}\\\text{Gaussian}}}{=} \frac{f_0 d^2}{K}\left(\frac{\kappa}{\pi}\right)^{\frac{1}{2}}\int_0^t\frac{(t-t')}{\tau}\exp\left(1-\frac{(t-t')}{\tau}\right)\frac{1}{t'^{\frac{1}{2}}(4\kappa t'+d^2)}\times$$

$$\exp\left(-\frac{r^2}{4\kappa t'+d^2}-\frac{z^2}{4\kappa t'}\right)dt' \qquad (3.62)$$

71

Figure 3.5: Normalized Q-Switch pulse time dependence

$$T(r,\theta,z,t) = \frac{\chi f_0 \kappa}{K} \int_0^t \left\{ \frac{(t-t')}{\tau} \exp\left(1 - \frac{(t-t')}{\tau}\right) \frac{d^2}{(4\kappa t' + d^2)} \exp\left(-\frac{r^2}{4\kappa t' \div d^2}\right) \times \right.$$

$$\left. \exp\left(\chi^2 \kappa t' - \chi z\right) \operatorname{erfc}\left(\chi (\kappa t')^{\frac{1}{2}} - \frac{z}{2(\kappa t')^{\frac{1}{2}}}\right) \right\} dt' \qquad (3.63)$$

(left margin of equation) Buried Gaussian volume

3.5 Numerical Convolution and Results

These equations were numerically integrated with *Mathematica* which uses an adaptive Gaussian quadrature technique with error estimation based on evaluation at Kronrod points. The resulting solutions agree with the work by Ready [96]. However, this procedure is very slow and there is some concern that the numerical integration is not robust. Consequently, an alternative method of evaluating the convolution integrals was employed using discrete Fourier analysis. According to Fourier analysis theory (for details see [259], [260])

72

the Fourier transform of the convolution of two functions f and g is equal to the product of their individual transforms F and G:

$$\Im[f(t) * g(t)] = F(\omega)G(\omega) \tag{3.64}$$

Consequently, the convolution of f and g can be determined by taking the inverse Fourier transform of the right hand side of equation (3.64)

$$f(t) * g(t) = \Im^{-1}[F(\omega)G(\omega)] \tag{3.65}$$

Weaver [260] describes how to calculate the Fourier transform of a function $f(t)$ from the discrete Fourier transform of the sequence $\{f(k)\}$ obtained from the samples of the original function. We assume that the function $f(t)$ is zero outside of the interval $[0, T]$ and say that $f(t)$ has "bounded support" over the time interval $[0, T]$. We also assume that $f(t)$ is band limited over the frequency domain interval of $[-\Omega, \Omega]$. Then, the function is sampled at the Nyquist rate which is the minimum sampling rate to recover the function without aliasing. This sampling rate is $\Delta t = 1/2\Omega$ and the number of samples is chosen so that

$$N\Delta t \geq 2T$$

The sampling theorem states that we can recover the function $f(t)$ from its sampled sequence $\{f(k)\}$ according to

$$f(t) = \sum_{k=0}^{N-1} f(k)\text{sinc}\,(2\pi\Omega\,(t - k\Delta t)) \tag{3.66}$$

If we Fourier transform both sides of this equation we obtain

$$F(\omega) = \sum_{k=0}^{N-1} f(k)\Im\,[\text{sinc}\,(2\pi\Omega\,(t - k\Delta t))] \tag{3.67}$$

Now, if $f(t)$ and $F(\omega)$ are Fourier transform pairs then

$$\Im\,[f(at)] = \frac{F\left(\frac{\omega}{a}\right)}{|a|} \tag{3.68}$$

73

$$F(\omega - a) = f(t)\exp[2\pi iat] \tag{3.69}$$

so that we may rewrite equation (3.67) as

$$F(\omega) = \frac{1}{2\Omega}\sum_{k=0}^{N-1} f(k)\exp[-2\pi i\omega k\Delta t]\,p_{1/2\Omega}(\omega) \tag{3.70}$$

Here, we have used the fact that

$$\Im[\mathrm{sinc}(t)] = \pi p_{1/2\Omega}(\omega)$$

where $p_{1/2\Omega}(\omega)$ is a sequence of Dirac delta functions defined by

$$p_{1/n}(t) = \begin{cases} n/2, & |t| \leq 1/n, \\ 0, & \text{otherwise} \end{cases}$$

However, we have assumed that $F(\omega)$ is nonzero only in the interval $[-\Omega, \Omega]$ where

$$p_{1/2\Omega}(\omega) = 1$$

so that we have

$$\begin{aligned} F(\omega) &= \frac{1}{2\Omega}\sum_{k=0}^{N-1} f(k)\exp[-2\pi i\omega k\Delta t] \\ &= \frac{1}{2\Omega}\sum_{k=0}^{N-1} f(k)[\cos(2\pi i\omega k\Delta t) - i\sin(2\pi i\omega k\Delta t)] \end{aligned} \tag{3.71}$$

Next, we sample $F(\omega)$ given in equation (3.71) with sampling rate $\Delta\omega = 2\Omega/N$. This sampling rate is adequate to uniquely recover $F(\omega)$ because

$$\Delta\omega = \frac{2\Omega}{N} = \frac{1}{N\Delta t} = \frac{1}{2T}$$

which is equal to the bandwidth of $F(\omega)$. At this sampling rate, equation (3.71) gives

$$F(j) = \frac{1}{2\Omega}\sum_{k=0}^{N-1} f(k)\exp[-2\pi ijk\Delta\omega\Delta t] \tag{3.72}$$

74

and since

$$\Delta\omega\Delta t \;=\; \frac{2\Omega}{N}\frac{1}{2\Omega} = \frac{1}{N}$$
$$\frac{1}{2\Omega} \;=\; \Delta t N\left(\frac{1}{N}\right)$$

we obtain finally

$$F(j) = N\Delta t\left(\frac{1}{N}\right)\sum_{k=0}^{N-1} f(k)\exp\left[\frac{-2\pi i j k}{N}\right] = N\Delta t\,\Im\left[\{f(k)\}\right] \qquad (3.73)$$

Equation (3.73) indicates that the samples $F(j)$ of the Fourier transform $F(\omega)$ (using sampling rate $\Delta\omega = 2\Omega/N$) are equal to the discrete Fourier transform of the sampled sequence $\{f(k)\}$ multiplied by $N\Delta T$. This result is based on the symmetric transform pair defined by

$$\hat{f}(\omega) \;=\; \int_{-\infty}^{\infty} f(t)e^{-2\pi i\omega t}dt$$
$$f(t) \;=\; \int_{-\infty}^{\infty} \hat{f}(\omega)e^{2\pi i\omega t}d\omega$$

so that we can write the inverse relationship

$$f(k) = N\Delta\omega\,\Im^{-1}\left[\{F(j)\}\right] \qquad (3.74)$$

which states that the samples $f(k)$ of the function $f(t)$ (using sampling rate $\Delta t = 2T/N$) are equal to the discrete inverse Fourier transform of the sampled sequence $\{F(j)\}$ multiplied by $N\Delta\omega$.

The entire procedure of computing the Fourier transform of a general signal can be summarized in six steps. Assume that $f(t)$ has bounded support over the interval $[-A,T]$ and is band limited over the frequency domain interval $[-\Omega,\Omega]$.

1. If $A \neq 0$ form the new function $g(t)$ by shifting $f(t)$ to the right by an amount A

$$g(t) = f(t-A)$$

75

2. Sample the function $g(t)$ with sampling rate at least $\Delta t = 1/2\Omega$ and choose the number of samples such that

$$N\Delta T > 2(T + A)$$

3. Calculate the discrete Fourier transform of this sampled sequence and multiply the result by $N\Delta T$ to obtain the sequence $\{G(j\Delta\omega)\}$.

4. Use the fact that for discrete Fourier transform pairs $\{f(k)\}$ and $\{F(j)\}$

$$F(-j) = F(N-j) \tag{3.75}$$

$$f(-k) = f(N-k) \tag{3.76}$$

to obtain transform values for the negative indices j that represent values for the negative frequencies.

5. Recover $G(\omega)$ from $\{G(j\Delta\omega)\}$ from the sampling theorem (equation (3.71)) or by constructing a smooth curve between the sampled values.

6. Recover $F(\omega)$ from $G(\omega)$ from $F(\omega) = G(\omega)\exp[2\pi i A\omega]$.

The discrete Fourier and inverse Fourier transform of an Nth order sequence are both periodic with period N. Therefore, the discrete Fourier transform assumes that the sequence repeats itself periodically outside of the domain of definition. This is equivalent to assuming that the laser pulse has been turning on and off since the beginning of time without any time between each pulse. If we do not account for this, the computed thermal fields will be incorrect at early times because the material has never cooled down to zero temperature. To accurately represent a single laser pulse and reproduce the thermal fields generated immediately after its application, the sequences obtained from equations (3.25) and (3.61) must be padded with zeros on the left-hand side before they are Fourier transformed. The

discrete Fourier transform still assumes that we have a sequence of laser pulses that started from the beginning of time but now there is a long enough time between the laser pulses so that we can compute the reaction of the material to an individual pulse.

The described technique was used with the convolution rule (3.65) to evaluate the integral in equation (3.62) and compute thermal fields generated by a laser incident on an aluminum half-space. The material and laser parameters used to compute the thermal fields are listed in Table 3.1. The discretization values used in the calculations are also listed. Figure 3.6 shows the temperature computed at the x-y origin as a function of time at three different depths: 0, 0.7, and 2.0 μm. These temperature curves agree with curves obtained from numerical integration of equation (3.62) which are represented by the dashed lines. These results are also consistent with similar results published by Ready [96] and Scruby [1]. Figure 3.7 shows a contour plot of the temperature rise on the surface of the aluminum sample (i.e. the x-y plane). Figure 3.8 shows the time evolution of the thermal field in the y-z plane. The horizontal axis (z-axis) represents depth into the aluminum and is measured in microns. The vertical axis (y-axis) is perpendicular to the incident laser pulse and is given in millimeters. Each successive contour plot represents a time step of 16 ns. As expected, we see the heat source start at the surface and decay in strength as it diffuses into the depth of the half-space.

Similarly, thermal fields generated in Pyrex were computed from equation (3.63). Figure 3.9 shows the temperature at the x-y origin at depths of 0.0 and 1.75 and 3.25 mm as a function of time. Again, there is good agreement between the temperatures calculated using the discrete Fourier transform (solid line) and the temperature values obtained by numerical integration (dashed lines). We see that the temperature rise is significantly lower than the temperature rise due to the surface source in aluminum. This is expected because the incident energy is distributed over the entire volume instead of just the surface area.
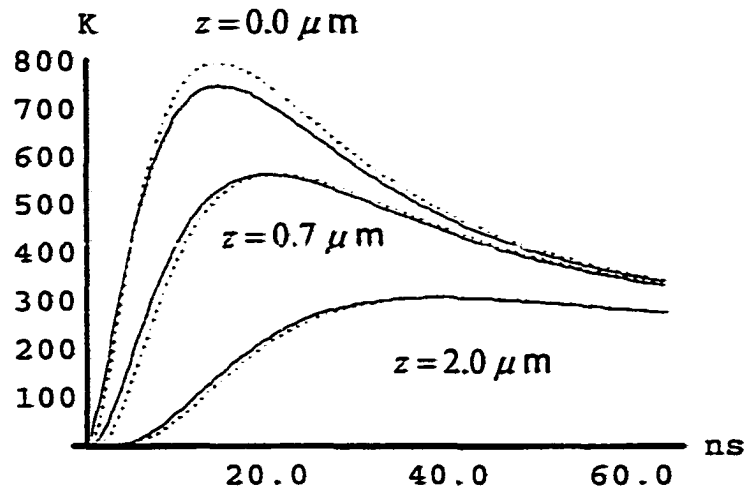
Figure 3.6: Temperature as a function of time due to a Q-switched laser applied to aluminum. Calculated from equation (3.62). Depth as a parameter: 0.0, 0.7, and 2.0 μm. Solid lines represent solutions from discrete Fourier analysis technique. Dashed lines represent solutions from numerical integration.

We also see that the thermal fields do not decay as rapidly as in the aluminum. This is also expected because the thermal diffusivity is between two and three orders of magnitude smaller than in aluminum. Figure 3.10 shows the surface temperature (0.0 mm) found in Figure 3.9 over a much longer time scale. *Mathematica* was used to integrate equation (3.63) to generated this plot. We see that the temperature decays exponentially over a period of over five seconds. The sharp cutoff at 4.5 seconds is a numerical artifact generated when Mathematica attempted to handle numbers that were outside of its precision range.

Figure 3.11 illustrates the time evolution of the thermal field in the y-z plane. The horizontal axis (z-axis) represents depth into the Pyrex and is measured in millimeters. The vertical axis (y-axis) is perpendicular to the incident laser pulse and is also given in millimeters. Each successive contour plot represents a time step of 0.5 ns. Figure 3.12

78
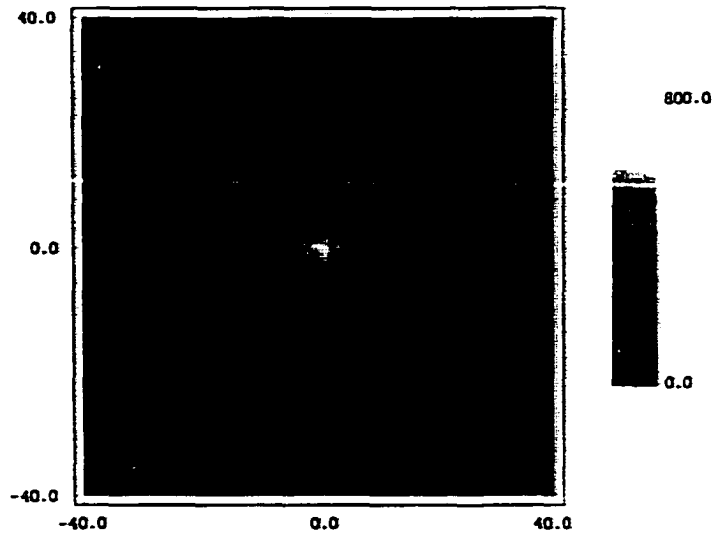
Figure 3.7: Top view of temperature rise in aluminum.

shows the a close up of one of these cross-sections at 25 ns. Here, we see that the generation source is buried beneath the surface and that the heat source diffuses much further into the bulk of the sample.

To further verify our equations describing the buried thermal source, we use the buried source equation (3.63) with the material parameters appropriate for aluminum [1]. We set the absorption coefficient to 1.0×10^8 so that the laser doesn't penetrate into the bulk and we expect that the buried source should reduce to a surface source. We found that it was cumbersome to use the Fourier analysis technique to solve the buried source integral with these parameters. In equation (3.63) the argument of the exponential, $\left(\chi^2 \kappa t' - \chi z\right)$, gets very large as χ gets large. For example, at $z = 1.0 \times 10^{-6}$ m, $t' = 10.0 \times 10^{-9}$ s, and

79
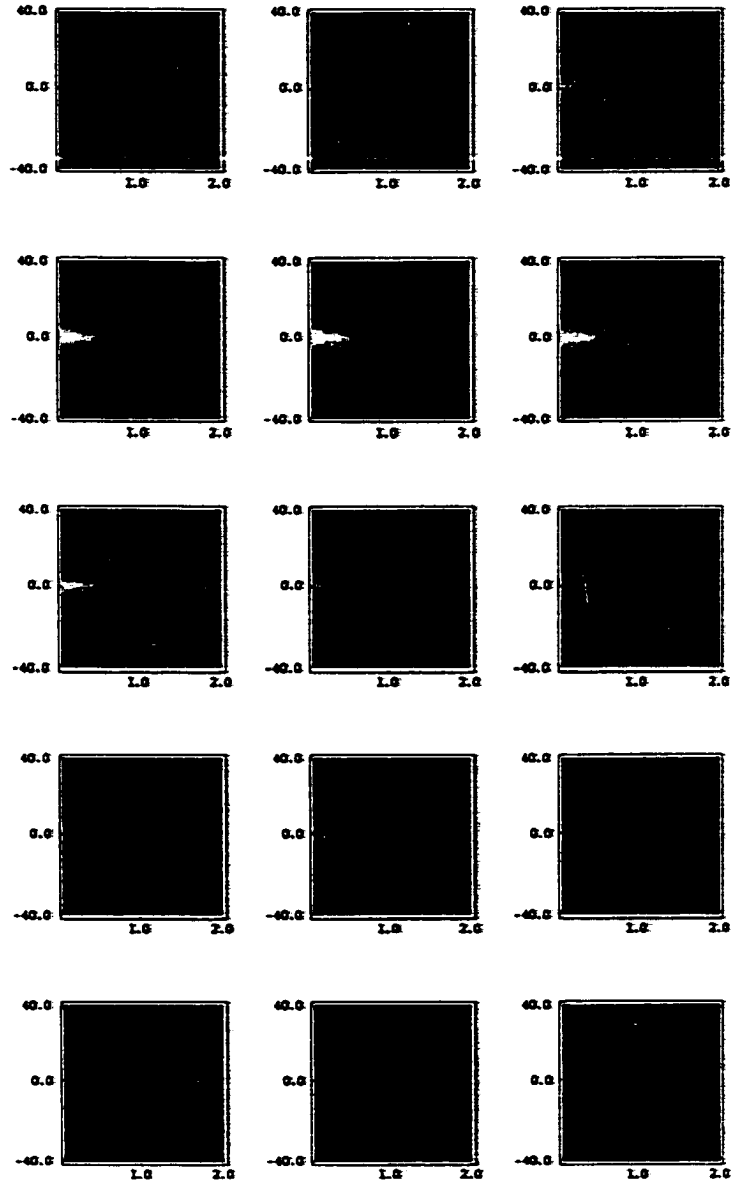
Figure 3.8: Calculated from equation (3.62) with discrete Fourier transform technique. 16 ns time steps. Vertical axis is perpendicular to incident laser pulse and is measured in millimeters. Horizontal represents depth into the sample measured in microns.

80

Parameter	Units	Aluminum	Pyrex
K = Thermal conductivity	$\frac{W}{m\,C^o}$	240.0	1.177
κ = Thermal diffusivity	$\frac{m^2}{s}$	1.0×10^{-4}	5.94×10^{-7}
d = Gaussian spot radius	m	7×10^{-3}	7×10^{-3}
f_0 = Maximum incident flux density	$\frac{MW}{m^2}$	2.0×10^{11}	2.0×10^{11}
τ_r^l = Laser pulse rise time	s	6×10^{-9}	6×10^{-9}
χ = Absorption coefficient	$\frac{1}{m}$	1.0×10^{8}	0.001
n_x = number of steps in x-direction	-	16	16
n_y = number of steps in y-direction	-	16	16
n_z = number of steps in z-direction	-	20	32
n_t = number of time steps	-	128	32
Δx = x-increment	m	0.0025	0.001
Δy = y-increment	m	0.0025	0.001
Δz = z-increment	m	1.0×10^{-7}	0.25×10^{-3}
Δt = t-increment	s	0.5×10^{-9}	1.0×10^{-9}

Table 3.1: Material and laser parameters used to calculate thermal fields
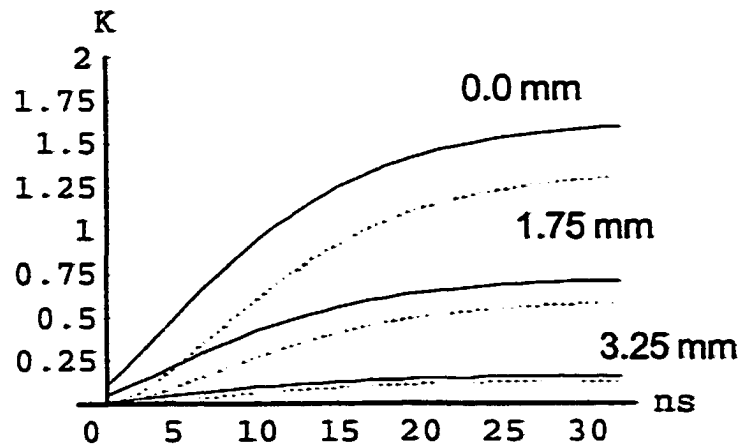
Figure 3.9: Temperature as a function of time due to a Q-switched laser applied to Pyrex. Calculated from equation (3.63). Depth as a parameter: 0.0, 1.75, and 3.25 mm. Solid lines represent solutions from discrete Fourier analysis technique. Dashed lines represent solutions from numerical integration.

81
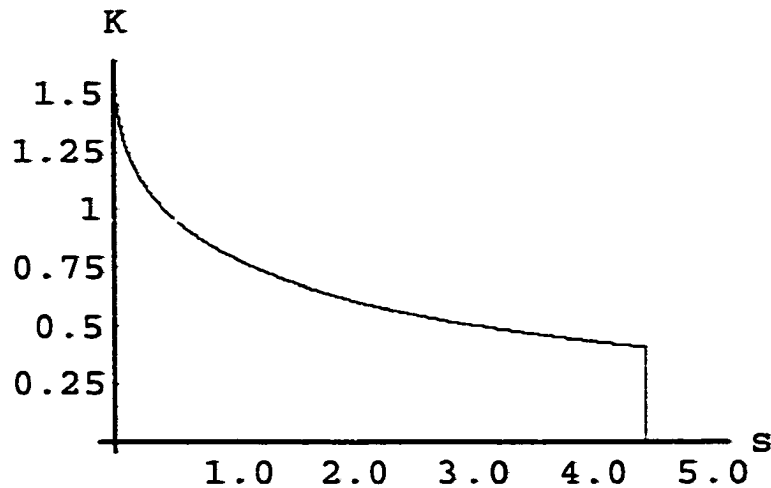
Figure 3.10: Temperature in Pyrex as a function of time at the surface.

$\chi = 1.0 \times 10^8$ m^{-1} we obtain

$$\left(\chi^2 \kappa t' - \chi z\right) = 9900.0$$

The intrinsic routines in Fortran cannot compute the exponential of this argument because the resulting number requires greater precision than the largest available data word length. *Mathematica* employs "multiple precision routines" that allow it to handle this situation. Figure 3.13 shows the resulting temperature computed at the x-y origin as a function of time at the three depths; 0.1, 0.7, and 2.0 μm. The solid lines represent temperature computed by numerically integrating equation (3.63) while the dashed lines were computed by numerical integration of equation (3.62). We see that the two equations produce indistinguishable results with these parameters. Although multiple precision packages exist for Fortran. we chose not to implement them because they require significantly more memory and computational time. We have shown previously that when the absorption coefficient grows large,

82
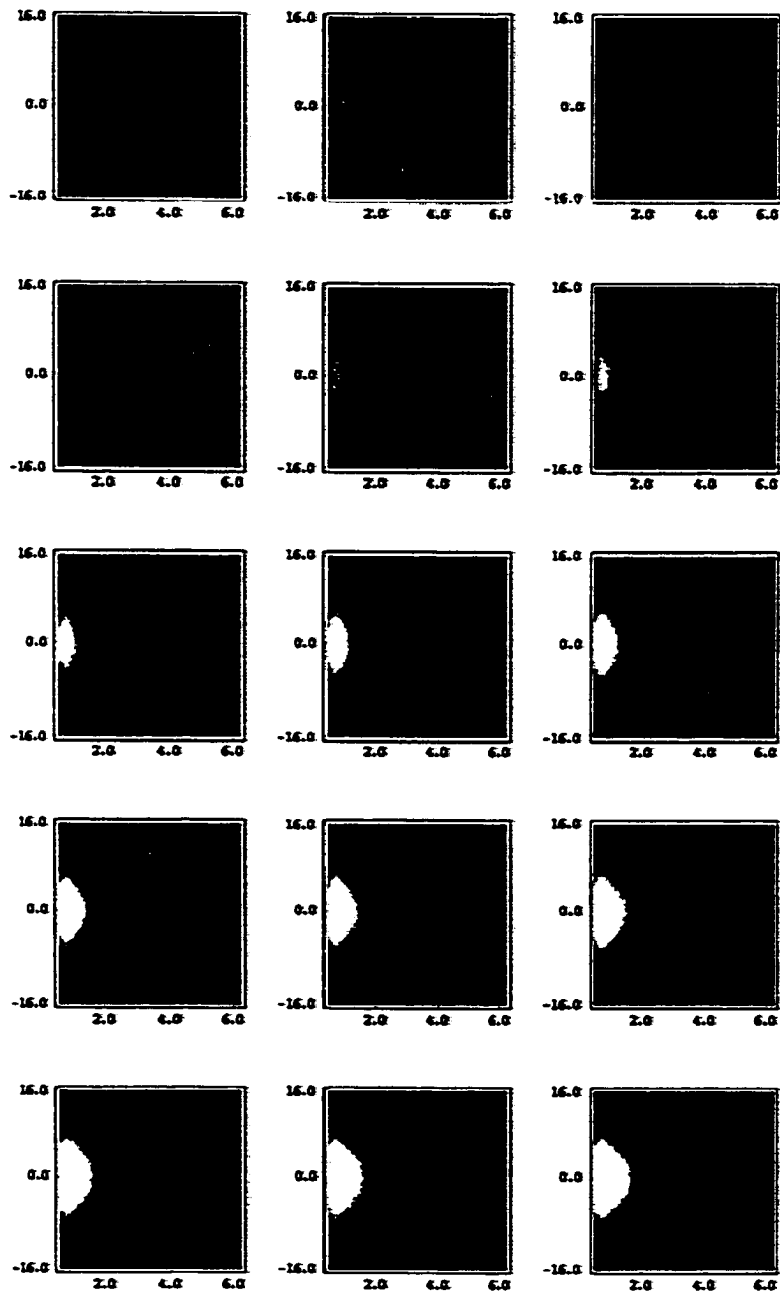
Figure 3.11: Calculated from equation (3.63) with discrete Fourier transform technique.1.0 ns time steps. Vertical axis is perpendicular to incident laser pulse and is measured in millimeters. Horizontal represents depth into the sample measured in millimeters.

83
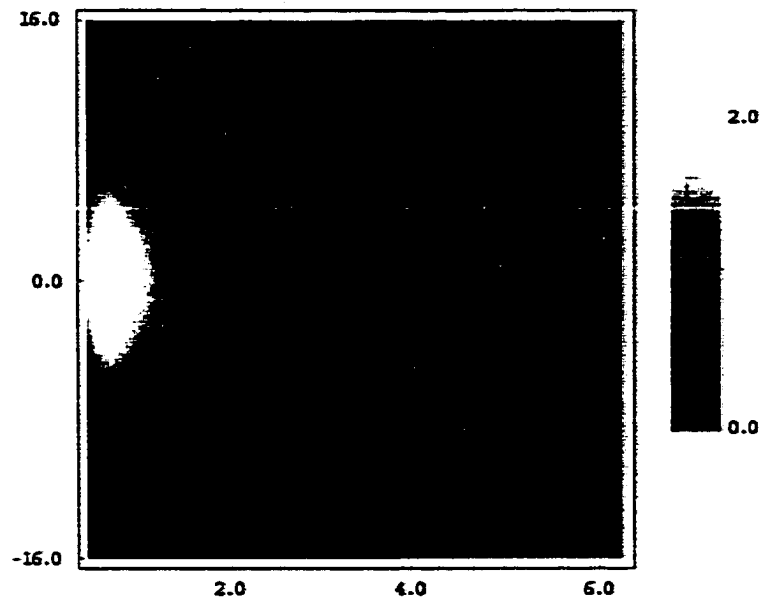
Figure 3.12: Close up of temperature cross section in Pyrex at 25 ns.

the equation describing a buried source (3.63) analytically reduces to the equation for a

surface source $(3.62)^2$.

---

[2]See page, 68
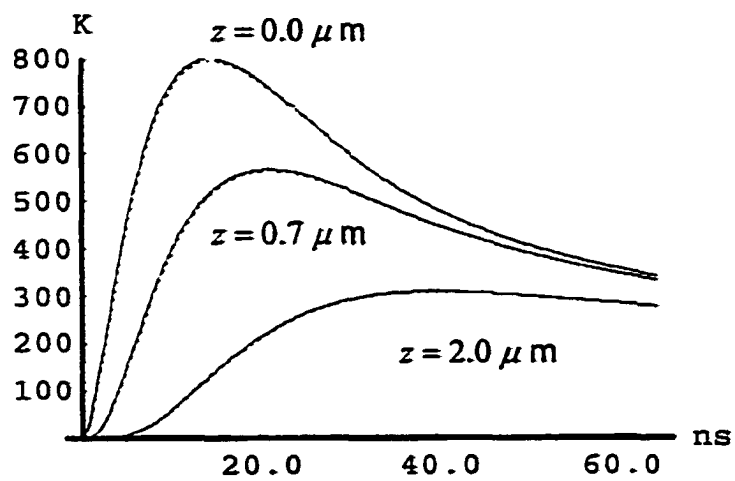
Figure 3.13: Temperature as a function of time in Aluminum with depths as a parameter. The solid lines represent solution from buried source equation and dashed lines represent the solutions from the surface source equation. Curves are identical.

85

Chapter 4

Modeling the Elastodynamic Response

4.1 Green's Function Solution

4.1.1 Governing Equations

We first review the governing elastodynamic equations for a general anisotropic material. In Cartesian coordinates, the equation of motion for a material is given by

$$\nabla \cdot \sigma = \rho \frac{\partial^2 \vec{u}}{\partial t^2} - \rho \vec{f} \tag{4.1}$$

where σ is the stress tensor, $\vec{u}$ is the displacement vector, ρ is the mass density per unit volume, and $\vec{f}$ is the body force per unit mass of material [11]. This may be written more compactly in tensor notation as

$$\sigma_{ij,j} = \rho \ddot{u}_i - \rho f_i \tag{4.2}$$

where the subscripted index after the comma denotes differentiation with respect to the corresponding space variable, and the superscripted dot represents differentiation with re-

86

spect to time. The stress tensor is related to the strain tensor, ϵ_{ij} through the fourth rank stiffness tensor, C_{ijkl} according to the generalized Hooke's law

$$\sigma_{ij} = C_{ijkl}\epsilon_{kl} \tag{4.3}$$

The strain tensor is in turn related to the material displacement through the relationship

$$\epsilon_{kl} = \frac{1}{2}(u_{k,l} + u_{l,k}) \tag{4.4}$$

If equations (4.4) and (4.3) are substituted into equation (4.2), we obtain the equations of motion for the material

$$\frac{1}{2}(C_{ijkl}u_{k,lj} + C_{ijkl}u_{l,kj}) = \rho\ddot{u}_i - \rho f_i \tag{4.5}$$

However, in the absence of couple stresses, the stress and strain tensors are symmetric and this requires that

$$C_{ijkl} = C_{ijlk} = C_{jikl} \tag{4.6}$$

Then, since l and k are dummy variables, the second term in equation (4.5) can be rewritten as

$$C_{ijkl}u_{l,kj} = C_{ijlk}u_{k,lj} \tag{4.7}$$

Now, since

$$C_{ijlk} = C_{ijkl}$$

we have from equation (4.7)

$$C_{ijkl}u_{l,kj} = C_{ijkl}u_{k,lj} \tag{4.8}$$

so that equation (4.5) can be simplified to [261]

$$C_{ijkl}u_{k,lj} = \rho\ddot{u}_i - \rho f_i \tag{4.9}$$

87

We see that this equation is identical to equation (3.1) without the thermal forcing term, $\beta_{ij}\theta_{,j}$. The symmetry of the stiffness tensor allows us to refer to its components with only two subscripts in an abbreviated form according to the convention [33]

$$
\begin{array}{ll}
I & ij \\
1 & 11 \\
2 & 22 \\
3 & 33 \\
4 & 23, 32 \\
5 & 13, 31 \\
6 & 12, 21
\end{array}
\tag{4.10}
$$

Then, the stiffness tensor can be represented as a symmetric 6×6 matrix of the form

$$
C_{ijkl} = C_{IJ} =
\begin{pmatrix}
C_{11} & C_{12} & C_{13} & C_{14} & C_{15} & C_{16} \\
 & C_{22} & C_{23} & C_{24} & C_{25} & C_{26} \\
 & & C_{33} & C_{34} & C_{35} & C_{36} \\
 & & & C_{44} & C_{45} & C_{46} \\
 & & & & C_{55} & C_{56} \\
 & & & & & C_{66}
\end{pmatrix}
\tag{4.11}
$$

88

For completeness, we apply this convention and write out the three coupled equations of

motion in equation 4.9 :

$$C_{11}\frac{\partial^2 u_1}{\partial x_1^2} + C_{66}\frac{\partial^2 u_1}{\partial x_2^2} + C_{55}\frac{\partial^2 u_1}{\partial x_3^2} +$$

$$2C_{16}\frac{\partial^2 u_1}{\partial x_1 \partial x_2} + 2C_{15}\frac{\partial^2 u_1}{\partial x_1 \partial x_3} + 2C_{56}\frac{\partial^2 u_1}{\partial x_2 \partial x_3} +$$

$$C_{16}\frac{\partial^2 u_2}{\partial x_1^2} + C_{26}\frac{\partial^2 u_2}{\partial x_2^2} + C_{45}\frac{\partial^2 u_2}{\partial x_3^2} +$$

$$(C_{12} + C_{66})\frac{\partial^2 u_2}{\partial x_1 \partial x_2} + (C_{14} + C_{56})\frac{\partial^2 u_2}{\partial x_1 \partial x_3} + (C_{46} + C_{25})\frac{\partial^2 u_2}{\partial x_2 \partial x_3} + \qquad (4.12)$$

$$C_{15}\frac{\partial^2 u_3}{\partial x_1^2} + C_{46}\frac{\partial^2 u_3}{\partial x_2^2} + C_{35}\frac{\partial^2 u_3}{\partial x_3^2} +$$

$$(C_{14} + C_{56})\frac{\partial^2 u_3}{\partial x_1 \partial x_2} + (C_{13} + C_{55})\frac{\partial^2 u_3}{\partial x_1 \partial x_3} + (C_{36} + C_{45})\frac{\partial^2 u_3}{\partial x_2 \partial x_3}$$

$$= \rho\frac{\partial^2 u_1}{\partial t^2} - \rho f_1$$

$$C_{16}\frac{\partial^2 u_1}{\partial x_1^2} + C_{26}\frac{\partial^2 u_1}{\partial x_2^2} + C_{45}\frac{\partial^2 u_1}{\partial x_3^2} +$$

$$(C_{12} + C_{66})\frac{\partial^2 u_1}{\partial x_1 \partial x_2} + (C_{14} + C_{56})\frac{\partial^2 u_1}{\partial x_1 \partial x_3} + (C_{46} + C_{25})\frac{\partial^2 u_1}{\partial x_2 \partial x_3} +$$

$$C_{66}\frac{\partial^2 u_2}{\partial x_1^2} + C_{22}\frac{\partial^2 u_2}{\partial x_2^2} + C_{44}\frac{\partial^2 u_2}{\partial x_3^2} +$$

$$2C_{26}\frac{\partial^2 u_2}{\partial x_1 \partial x_2} + 2C_{46}\frac{\partial^2 u_2}{\partial x_1 \partial x_3} + 2C_{24}\frac{\partial^2 u_2}{\partial x_2 \partial x_3} + \qquad (4.13)$$

$$C_{56}\frac{\partial^2 u_3}{\partial x_1^2} + C_{24}\frac{\partial^2 u_3}{\partial x_2^2} + C_{34}\frac{\partial^2 u_3}{\partial x_3^2} +$$

$$(C_{46} + C_{25})\frac{\partial^2 u_3}{\partial x_1 \partial x_2} + (C_{36} + C_{45})\frac{\partial^2 u_3}{\partial x_1 \partial x_3} + (C_{23} + C_{44})\frac{\partial^2 u_3}{\partial x_2 \partial x_3}$$

$$= \rho\frac{\partial^2 u_2}{\partial t^2} - \rho f_2$$

$$C_{15}\frac{\partial^2 u_1}{\partial x_1^2} + C_{46}\frac{\partial^2 u_1}{\partial x_2^2} + C_{35}\frac{\partial^2 u_1}{\partial x_3^2} +$$

$$(C_{14} + C_{56})\frac{\partial^2 u_1}{\partial x_1 \partial x_2} + (C_{13} + C_{55})\frac{\partial^2 u_1}{\partial x_1 \partial x_3} + (C_{36} + C_{45})\frac{\partial^2 u_1}{\partial x_2 \partial x_3} +$$

$$C_{56}\frac{\partial^2 u_2}{\partial x_1^2} + C_{24}\frac{\partial^2 u_2}{\partial x_2^2} + C_{34}\frac{\partial^2 u_2}{\partial x_3^2} +$$

$$(C_{46} + C_{25})\frac{\partial^2 u_2}{\partial x_1 \partial x_2} + (C_{36} + C_{45})\frac{\partial^2 u_2}{\partial x_1 \partial x_3} + (C_{23} + C_{44})\frac{\partial^2 u_2}{\partial x_2 \partial x_3} + \qquad (4.14)$$

$$C_{55}\frac{\partial^2 u_3}{\partial x_1^2} + C_{44}\frac{\partial^2 u_3}{\partial x_2^2} + C_{33}\frac{\partial^2 u_3}{\partial x_3^2} +$$

$$2C_{45}\frac{\partial^2 u_3}{\partial x_1 \partial x_2} + 2C_{35}\frac{\partial^2 u_3}{\partial x_1 \partial x_3} + 2C_{34}\frac{\partial^2 u_3}{\partial x_2 \partial x_3}$$

$$= \rho\frac{\partial^2 u_3}{\partial t^2} - \rho f_3$$

4.1.2 Solution in Transform Domain: Isotropic Case

We now consider the elastic response of an isotropic half-space due to an impulse forcing function. For an isotropic material there are only two independent stiffness constants and the abbreviated stiffness tensor takes the form [33]

$$
\underset{\text{isotropic}}{C_{IJ}} =
\begin{pmatrix}
C_{11} & C_{12} & C_{12} & 0 & 0 & 0 \\
C_{12} & C_{11} & C_{12} & 0 & 0 & 0 \\
C_{12} & C_{12} & C_{11} & 0 & 0 & 0 \\
0 & 0 & 0 & C_{44} & 0 & 0 \\
0 & 0 & 0 & 0 & C_{44} & 0 \\
0 & 0 & 0 & 0 & 0 & C_{44}
\end{pmatrix}
\tag{4.15}
$$

with

$$
C_{12} = C_{11} - 2C_{44}
\tag{4.16}
$$

If we substitute these constants into equations(4.12),(4.13), and (4.14) we obtain

$$
C_{11}\frac{\partial^2 u_1}{\partial x_1^2} + C_{44}\frac{\partial^2 u_1}{\partial x_2^2} + C_{44}\frac{\partial^2 u_1}{\partial x_3^2} +
$$

$$
(C_{12} + C_{44})\frac{\partial^2 u_2}{\partial x_1 \partial x_2} +
$$

$$
(C_{12} + C_{44})\frac{\partial^2 u_3}{\partial x_1 \partial x_3}
$$

$$
= \rho\frac{\partial^2 u_1}{\partial t^2} - \rho f_1
\tag{4.17}
$$

$$
(C_{12} + C_{44})\frac{\partial^2 u_1}{\partial x_1 \partial x_2} +
$$

$$
C_{44}\frac{\partial^2 u_2}{\partial x_1^2} + C_{11}\frac{\partial^2 u_2}{\partial x_2^2} + C_{44}\frac{\partial^2 u_2}{\partial x_3^2} +
$$

$$
(C_{12} + C_{44})\frac{\partial^2 u_3}{\partial x_2 \partial x_3}
$$

$$
= \rho\frac{\partial^2 u_2}{\partial t^2} - \rho f_2
\tag{4.18}
$$

90

$$(C_{12} + C_{44}) \frac{\partial^2 u_1}{\partial x_1 \partial x_3} +$$

$$(C_{12} + C_{44}) \frac{\partial^2 u_2}{\partial x_2 \partial x_3} +$$

$$C_{44} \frac{\partial^2 u_3}{\partial x_1^2} + C_{44} \frac{\partial^2 u_3}{\partial x_2^2} + C_{11} \frac{\partial^2 u_3}{\partial x_3^2}$$

$$= \rho \frac{\partial^2 u_3}{\partial t^2} - \rho f_3 \tag{4.19}$$

These three equations can be written as a single matrix equation

$$
\begin{pmatrix}
C_{11} \frac{\partial^2}{\partial x_1^2} + C_{44} \frac{\partial^2}{\partial x_2^2} + C_{44} \frac{\partial^2}{\partial x_3^2} & (C_{12} + C_{44}) \frac{\partial^2}{\partial x_1 \partial x_2} \\
(C_{12} + C_{44}) \frac{\partial^2}{\partial x_1 \partial x_2} & C_{44} \frac{\partial^2}{\partial x_1^2} + C_{11} \frac{\partial^2}{\partial x_2^2} + C_{44} \frac{\partial^2}{\partial x_3^2} \\
(C_{12} + C_{44}) \frac{\partial^2}{\partial x_1 \partial x_3} & C_{44} \frac{\partial^2}{\partial x_2 \partial x_3}
\end{pmatrix}
$$

$$
\begin{pmatrix}
(C_{12} + C_{44}) \frac{\partial^2}{\partial x_1 \partial x_3} \\
C_{44} \frac{\partial^2}{\partial x_2 \partial x_3} \\
C_{44} \frac{\partial^2}{\partial x_1^2} + C_{44} \frac{\partial^2}{\partial x_2^2} + C_{11} \frac{\partial^2}{\partial x_3^2}
\end{pmatrix}
\begin{pmatrix} u_1 \\ u_2 \\ u_3 \end{pmatrix}
$$

$$= \rho \frac{\partial^2}{\partial t^2} \begin{pmatrix} u_1 \\ u_2 \\ u_3 \end{pmatrix} - \rho \begin{pmatrix} f_1 \\ f_2 \\ f_3 \end{pmatrix} \tag{4.20}$$

The stiffness coefficients are related to the Lamé constants λ and μ by

$$
\begin{aligned}
C_{11} &= \lambda + 2\mu \\
C_{44} &= \mu \\
C_{12} &= \lambda
\end{aligned}
\tag{4.21}
$$

91

and we can rewrite equation (4.20) as

$$
\left(
\begin{array}{cc}
\frac{(\lambda+2\mu)}{\rho}\frac{\partial^2}{\partial x_1^2} + \frac{\mu}{\rho}\left(\frac{\partial^2}{\partial x_2^2} + \frac{\partial^2}{\partial x_3^2}\right) & \frac{(\lambda+\mu)}{\rho}\frac{\partial^2}{\partial x_1 \partial x_2} \\
\frac{(\lambda+\mu)}{\rho}\frac{\partial^2}{\partial x_1 \partial x_2} + & \frac{\mu}{\rho}\left(\frac{\partial^2}{\partial x_1^2} + \frac{\partial^2}{\partial x_3^2}\right) + \frac{(\lambda+2\mu)}{\rho}\frac{\partial^2}{\partial x_2^2} \\
\frac{(\lambda+\mu)}{\rho}\frac{\partial^2}{\partial x_1 \partial x_3} & \frac{(\lambda+\mu)}{\rho}\frac{\partial^2}{\partial x_2 \partial x_3}
\end{array}
\right.
$$

$$
\left.
\begin{array}{c}
\frac{(\lambda+\mu)}{\rho}\frac{\partial^2}{\partial x_1 \partial x_3} \\
\frac{(\lambda+\mu)}{\rho}\frac{\partial^2}{\partial x_2 \partial x_3} \\
\frac{\mu}{\rho}\left(\frac{\partial^2}{\partial x_1^2} + \frac{\partial^2}{\partial x_2^2}\right) + \frac{(\lambda+2\mu)}{\rho}\frac{\partial^2}{\partial x_3^2}
\end{array}
\right)
\left(
\begin{array}{c}
u_1 \\
u_2 \\
u_3
\end{array}
\right)
\qquad (4.22)
$$

$$
= \frac{\partial^2}{\partial t^2}
\left(
\begin{array}{c}
u_1 \\
u_2 \\
u_3
\end{array}
\right)
-
\left(
\begin{array}{c}
f_1 \\
f_2 \\
f_3
\end{array}
\right)
$$

where we have divided through by ρ. The longitudinal and transverse wave speeds in an isotropic solid are given by

$$
c_L = \sqrt{\frac{\lambda + 2\mu}{\rho}}
\qquad (4.23)
$$

$$
c_T = \sqrt{\frac{\mu}{\rho}}
\qquad (4.24)
$$

so that we may write equation (4.22) in terms of the wave speeds as

$$
\left(
\begin{array}{cc}
c_L^2\frac{\partial^2}{\partial x_1^2} + c_T^2\left(\frac{\partial^2}{\partial x_2^2} + \frac{\partial^2}{\partial x_3^2}\right) & (c_L^2 - c_T^2)\frac{\partial^2}{\partial x_1 \partial x_2} \\
(c_L^2 - c_T^2)\frac{\partial^2}{\partial x_1 \partial x_2} & c_T^2\left(\frac{\partial^2}{\partial x_1^2} + \frac{\partial^2}{\partial x_3^2}\right) + c_L^2\frac{\partial^2}{\partial x_2^2} \\
(c_L^2 - c_T^2)\frac{\partial^2}{\partial x_1 \partial x_3} & (c_L^2 - c_T^2)\frac{\partial^2}{\partial x_2 \partial x_3}
\end{array}
\right.
$$

$$
\left.
\begin{array}{c}
(c_L^2 - c_T^2)\frac{\partial^2}{\partial x_1 \partial x_3} \\
(c_L^2 - c_T^2)\frac{\partial^2}{\partial x_2 \partial x_3} \\
c_T^2\left(\frac{\partial^2}{\partial x_1^2} + \frac{\partial^2}{\partial x_2^2}\right) + c_L^2\frac{\partial^2}{\partial x_3^2}
\end{array}
\right)
\left(
\begin{array}{c}
u_1 \\
u_2 \\
u_3
\end{array}
\right)
\qquad (4.25)
$$

$$
= \frac{\partial^2}{\partial t^2}
\left(
\begin{array}{c}
u_1 \\
u_2 \\
u_3
\end{array}
\right)
-
\left(
\begin{array}{c}
f_1 \\
f_2 \\
f_3
\end{array}
\right)
$$

92

If we divide this equation by c_T^2, we obtain

$$
\begin{pmatrix}
R^2 \frac{\partial^2}{\partial x_1^2} + \frac{\partial^2}{\partial x_2^2} + \frac{\partial^2}{\partial x_3^2} & (R^2 - 1) \frac{\partial^2}{\partial x_1 \partial x_2} & (R^2 - 1) \frac{\partial^2}{\partial x_1 \partial x_3} \\
(R^2 - 1) \frac{\partial^2}{\partial x_1 \partial x_2} & \frac{\partial^2}{\partial x_1^2} + \frac{\partial^2}{\partial x_3^2} + R^2 \frac{\partial^2}{\partial x_2^2} & (R^2 - 1) \frac{\partial^2}{\partial x_2 \partial x_3} \\
(R^2 - 1) \frac{\partial^2}{\partial x_1 \partial x_3} & (R^2 - 1) \frac{\partial^2}{\partial x_2 \partial x_3} & \frac{\partial^2}{\partial x_1^2} + \frac{\partial^2}{\partial x_2^2} + R^2 \frac{\partial^2}{\partial x_3^2}
\end{pmatrix}
\begin{pmatrix} u_1 \\ u_2 \\ u_3 \end{pmatrix}
$$

$$
= \frac{1}{c_T^2} \frac{\partial^2}{\partial t^2} \begin{pmatrix} u_1 \\ u_2 \\ u_3 \end{pmatrix} - \frac{1}{c_T^2} \begin{pmatrix} f_1 \\ f_2 \\ f_3 \end{pmatrix}
\tag{4.26}
$$

where R is the ratio of the wave speeds

$$
R \equiv \frac{c_L}{c_T}
$$

We wish to find the solution of this equation in response to an impulse point source forcing function

$$
\bar{f}(x, y, z, t) = \bar{Q}\, \delta(x_1)\, \delta(x_2) \delta(x_3)\, \delta(t)
\tag{4.27}
$$

where $\bar{Q}$ is the points source strength and δ is the Dirac delta function so that equation (4.26) becomes

$$
\begin{pmatrix}
R^2 \frac{\partial^2}{\partial x_1^2} + \frac{\partial^2}{\partial x_2^2} + \frac{\partial^2}{\partial x_3^2} & (R^2 - 1) \frac{\partial^2}{\partial x_1 \partial x_2} & (R^2 - 1) \frac{\partial^2}{\partial x_1 \partial x_3} \\
(R^2 - 1) \frac{\partial^2}{\partial x_1 \partial x_2} & \frac{\partial^2}{\partial x_1^2} + \frac{\partial^2}{\partial x_3^2} + R^2 \frac{\partial^2}{\partial x_2^2} & (R^2 - 1) \frac{\partial^2}{\partial x_2 \partial x_3} \\
(R^2 - 1) \frac{\partial^2}{\partial x_1 \partial x_3} & (R^2 - 1) \frac{\partial^2}{\partial x_2 \partial x_3} & \frac{\partial^2}{\partial x_1^2} + \frac{\partial^2}{\partial x_2^2} + R^2 \frac{\partial^2}{\partial x_3^2}
\end{pmatrix}
\begin{pmatrix} u_1 \\ u_2 \\ u_3 \end{pmatrix}
$$

$$
= \frac{1}{c_T^2} \frac{\partial^2}{\partial t^2} \begin{pmatrix} u_1 \\ u_2 \\ u_3 \end{pmatrix} - \frac{1}{c_T^2} \begin{pmatrix} Q_1 \delta(x_1)\, \delta(x_2) \delta(x_3)\, \delta(t) \\ Q_2 \delta(x_1)\, \delta(x_2) \delta(x_3)\, \delta(t) \\ Q_3 \delta(x_1)\, \delta(x_2) \delta(x_3)\, \delta(t) \end{pmatrix}
\tag{4.28}
$$

To solve this system of coupled partial differential equations, we begin by applying a one-sided Laplace transform in time according to

$$
\mathcal{L}\{f(t)\} \equiv \bar{f}(p) = \int_0^\infty e^{-pt} f(t)\, dt
\tag{4.29}
$$

93

and then a three-dimensional spatial Fourier transform defined by

$$\Im\left\{\bar{f}(x_1,x_2,x_3,p)\right\} \equiv \hat{f}(\xi,\eta,\varsigma,p) = \int_{-\infty}^{\infty}\int_{-\infty}^{\infty}\int_{-\infty}^{\infty} \bar{f}(x_1,x_2,x_3,p)\, e^{-i(\xi x_1+\eta x_2+\varsigma x_3)}dx_1\,dx_2\,dx_3 \qquad (4.30)$$

with the inverse transform given by

$$\Im^{-1}\left\{\hat{f}(\xi,\eta,\varsigma,p)\right\} \equiv \bar{f}(x_1,x_2,x_3,p) = \frac{1}{(2\pi)^3}\int_{-\infty}^{\infty}\int_{-\infty}^{\infty}\int_{-\infty}^{\infty} \hat{f}(\xi,\eta,\varsigma,p)\, e^{i(\xi x_1+\eta x_2+\varsigma x_3)}d\xi\,d\eta\,d\varsigma \qquad (4.31)$$

The Laplace transform of the n th order derivative of a function with respect to its argument is given by [262]

$$\mathcal{L}\left\{\frac{d^n f(t)}{dt}\right\} = p^n\,\bar{f}(p) - p^{n-1}\,\bar{f}(0) - p^{n-2}\,\bar{f}^{(1)}(0) - \cdots - \bar{f}^{(n-1)}(0) \qquad (4.32)$$

Similarly, the Fourier transform of the n th order derivative of a function with respect to its argument is

$$\Im\left\{\frac{d^n \bar{f}(x)}{dx}\right\} = (i\xi)^n\,\hat{f}(\xi) \qquad (4.33)$$

We apply these rules and assume that all functions are zero at time $t=0$. Then, noting that

$$\mathcal{L}\left\{\delta(x_1)\,\delta(x_2)\delta(x_3)\,\delta(t)\right\} = \delta(x_1)\,\delta(x_2)\delta(x_3)$$

and that

$$\Im\left\{\delta(x_1)\,\delta(x_2)\delta(x_3)\,\delta(t)\right\} = 1$$

94

equation (4.28) reduces to an algebraic system of equations in the form

$$
\begin{pmatrix}
-R^2\xi^2 - \eta^2 - \varsigma^2 & (1-R^2)\xi\eta & (1-R^2)\xi\varsigma \\
(1-R^2)\xi\eta & -\xi^2 - \varsigma^2 - R^2\eta^2 & (1-R^2)\eta\varsigma \\
(1-R^2)\xi\varsigma & (1-R^2)\eta\varsigma & -\xi^2 - \eta^2 - R^2\varsigma^2
\end{pmatrix}
\begin{pmatrix}
\hat{u}_1 \\
\hat{u}_2 \\
\hat{u}_3
\end{pmatrix}
$$

$$
= \frac{p^2}{C_T^2}
\begin{pmatrix}
\hat{u}_1 \\
\hat{u}_2 \\
\hat{u}_3
\end{pmatrix}
- \frac{1}{C_T^2}
\begin{pmatrix}
Q_1 \\
Q_2 \\
Q_3
\end{pmatrix}
\tag{4.34}
$$

The first term in the right hand side of equation (4.34) can be combined with the left hand side and we can write

$$
\begin{pmatrix}
-R^2\xi^2 - \eta^2 - \varsigma^2 - \left(\frac{p}{C_T}\right)^2 & (1-R^2)\xi\eta \\
(1-R^2)\xi\eta & -\xi^2 - \varsigma^2 - R^2\eta^2 - \left(\frac{p}{C_T}\right)^2 \\
(1-R^2)\xi\varsigma & (1-R^2)\eta\varsigma
\end{pmatrix}
$$

$$
\begin{pmatrix}
(1-R^2)\xi\varsigma \\
(1-R^2)\eta\varsigma \\
-\xi^2 - \eta^2 - R^2\varsigma^2 - \left(\frac{p}{C_T}\right)^2
\end{pmatrix}
\begin{pmatrix}
\hat{u}_1 \\
\hat{u}_2 \\
\hat{u}_3
\end{pmatrix}
\tag{4.35}
$$

$$
= -\frac{1}{C_T^2}
\begin{pmatrix}
Q_1 \\
Q_2 \\
Q_3
\end{pmatrix}
$$

We solve the matrix equation in (4.35) with *Mathematica* to obtain solutions for the displacement components in the Laplace-Fourier transform domain

$$
\hat{u}_1 = \frac{Q_1 p^2 + C_T^2 \left[(\varsigma^2 + \eta^2) Q_1 R^2 - (Q_3\varsigma + Q_2\eta)(R^2 - 1)\xi + Q_1\xi^2 \right]}{[p^2 + C_T^2(\xi^2 + \eta^2 + \varsigma^2)][p^2 + C_T^2 R^2(\xi^2 + \eta^2 + \varsigma^2)]}
\tag{4.36}
$$

$$
\hat{u}_2 = \frac{Q_2 p^2 + C_T^2 \left[(\varsigma^2 + \xi^2) Q_2 R^2 - (Q_3\varsigma + Q_1\xi)(R^2 - 1)\eta + Q_2\eta^2 \right]}{[p^2 + C_T^2(\xi^2 + \eta^2 + \varsigma^2)][p^2 + C_T^2 R^2(\xi^2 + \eta^2 + \varsigma^2)]}
\tag{4.37}
$$

$$
\hat{u}_3 = \frac{Q_3 p^2 + C_T^2 \left[(\eta^2 + \xi^2) Q_3 R^2 - (Q_2\eta + Q_1\xi)(R^2 - 1)\varsigma + Q_3\varsigma^2 \right]}{[p^2 + C_T^2(\xi^2 + \eta^2 + \varsigma^2)][p^2 + C_T^2 R^2(\xi^2 + \eta^2 + \varsigma^2)]}
\tag{4.38}
$$

In this case, the inverse Laplace transform can be found analytically with *Mathematica* and we have the Fourier transformed displacement components

$$\tilde{u}_1 = \frac{R\left((\varsigma^2 + \eta^2)Q_1 - (\varsigma Q_3 + \eta Q_2)\xi\right)\sin(t\, C_T A) + \xi B \sin(t\, R C_T A)}{C_T\, R\, A^3} \quad (4.39)$$

$$\tilde{u}_2 = \frac{R\left((\xi^2 + \varsigma^2)Q_2 - (\varsigma Q_3 + \xi Q_1)\eta\right)\sin(t\, C_T A) + \eta B \sin(t\, R C_T A)}{C_T\, R A^3} \quad (4.40)$$

$$\tilde{u}_3 = \frac{R\left((\eta^2 + \xi^2)Q_3 - (\eta Q_2 + \xi Q_1)\varsigma\right)\sin(t\, C_T A) + \varsigma B \sin(t\, R C_T A)}{C_T\, R\, A^3} \quad (4.41)$$

with

$$A \equiv \sqrt{\xi^2 + \eta^2 + \varsigma^2}$$

$$B \equiv \eta Q_2 + \varsigma Q_3 + \xi Q_1$$

As expected, each displacement component is composed of one wave propagating at the longitudinal wave speed and another propagating at the transverse wave speed. Unless otherwise noted, we set

$$Q_1 = Q_2 = Q_3 = \frac{1}{\sqrt{3}}$$

so that the impulse forcing function was general and had unity magnitude.

4.1.3 Numerically Inverting the Three-Dimensional Fourier Transform

The three-dimensional Fourier transform defined in equation (4.30) can be inverted with three consecutive one-dimensional inverse transform operations. Therefore, we can invert equations (4.39), (4.40), and (4.41) by inverting each spatial dimension separately with the discrete inverse transform. We use the technique described above with some slight modifications to the definition of the sampling frequencies and to equation (3.74) to account for differences in the definitions of the Fourier transform.

First, the spatial frequencies are obtained by evaluating equations (4.39), (4.40), and

96

(4.41) along the grid points

$$\xi_i = (i - n_x - 1) \times d\xi, \quad i = 1 \ldots 2n_x$$

$$\eta_j = (j - n_y - 1) \times d\eta, \quad j = 1 \ldots 2n_y$$

$$\zeta_k = (k - n_z - 1) \times d\zeta, \quad k = 1 \ldots 2n_z$$

with the sampling frequencies defined by

$$d\xi = \frac{2\pi}{2n_x \Delta x} = \frac{\pi}{n_x \Delta x}$$

$$d\eta = \frac{2\pi}{2n_y \Delta y} = \frac{\pi}{n_y \Delta y} \tag{4.42}$$

$$d\zeta = \frac{2\pi}{2n_y \Delta y} = \frac{\pi}{n_y \Delta y}$$

where $2n_x$, $2n_y$, and $2n_z$ are the desired number of sampling points in real space and Δx, Δy, and Δz are the desired spatial resolutions. Compared to the definitions in our earlier discussion, there is an extra factor of 2π in the numerator of these sampling frequencies because the earlier results were based on the Fourier transform pair defined by

$$\hat{f}(\omega) = \int_{-\infty}^{\infty} f(t)e^{-2\pi i \omega t} dt$$

$$f(t) = \int_{-\infty}^{\infty} \hat{f}(\omega)e^{2\pi i \omega t} d\omega$$

with the extra factor of 2π explicitly appearing in the exponents. Another difference is an extra factor of 2π that appears in equation (3.74) as

$$f(k) = \frac{N\Delta\omega}{2\pi}\Im^{-1}\left[\{F(j)\}\right] \tag{4.43}$$

Next, we inverse transform with respect to the z-dimension. At each (ξ_i, η_j) grid point we have a sequence with length $2n_z$. We rotate the sequence to the left by n_z bins and the discrete inverse Fourier transform is applied to the rotated sequence. Then, equation (4.43) is used to compute the inverse transform in the z-direction and the resulting sequence is

97
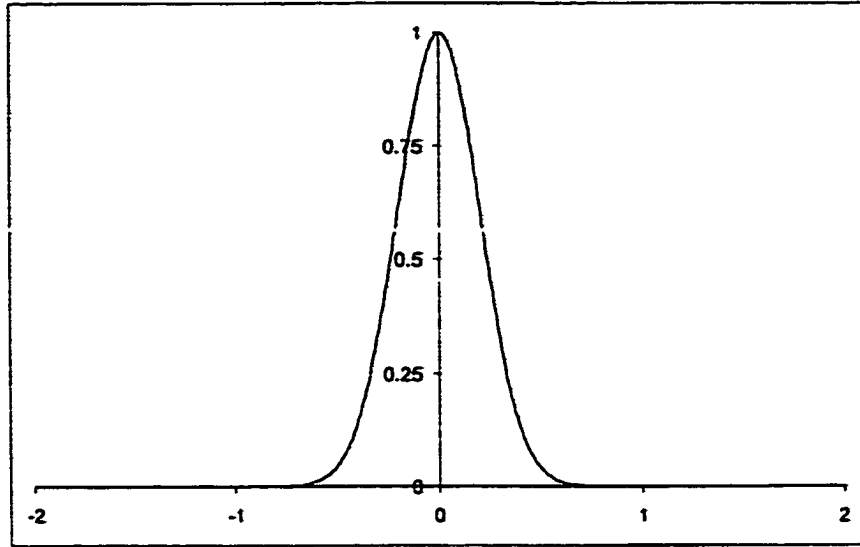
Figure 4.1: One-dimensional Gaussian $\exp\left[\frac{-\pi x^2}{a^2}\right]$ with $a = \frac{1}{2}$.

rotated by $n_z + 1$ bins to the left and reversed. This set of operations is repeated in the y- and x-dimensions. As an example and verification of this procedure, consider the Gaussian function

$$f(x) = \exp\left[\frac{-\pi x^2}{a^2}\right] \tag{4.44}$$

with the Fourier transform given by

$$\hat{f}(\xi) \equiv \int_{-\infty}^{\infty} f(x)e^{-i\xi x}dx = a\exp\left[-\frac{a^2\xi^2}{4\pi}\right] \tag{4.45}$$

These two functions are plotted in figures (4.1) and (4.2)the three-dimensional equivalent is given by

$$f(x) = \exp\left[-\pi\left(\frac{x^2}{a^2} + \frac{y^2}{b^2} + \frac{z^2}{c^2}\right)\right] \tag{4.46}$$

$$\hat{f}(\xi,\eta,\varsigma) = abc\exp\left[-\frac{1}{4\pi}\left(a^2\xi^2 + b^2\eta^2 + c^2\varsigma^2\right)\right] \tag{4.47}$$

98
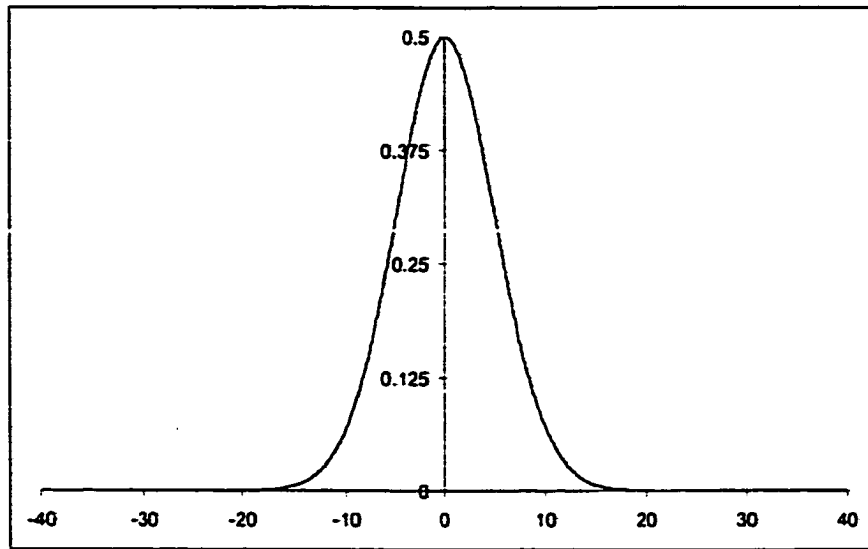
Figure 4.2: Fourier transform of one-dimensional Gaussian.

Our problem is to regain equation (4.46) from equation (4.47) with the discrete inverse Fourier transform. We sample equation (4.47) at the frequencies defined in equations(4.42) with

$$a = b = c \;=\; \frac{1}{2}$$

$$n_x = n_y = n_z \;=\; 32$$

$$\Delta x = \Delta y = \Delta z \;=\; 0.025$$

to obtain

$$F(\xi_i, \eta_j, \varsigma_k) \;=\; \tilde{f}\,((i - n_x - 1)d\xi, (j - n_y - 1)d\eta, (k - n_z - 1)d\varsigma)$$

$$(i, j, k) \;=\; (1 \ldots 2n_x, 1 \ldots 2n_y, 1 \ldots 2n_z) \qquad (4.48)$$

We first invert in the z-dimension at every point (ξ_i, η_j). Figure 4.3 shows the frequency

99
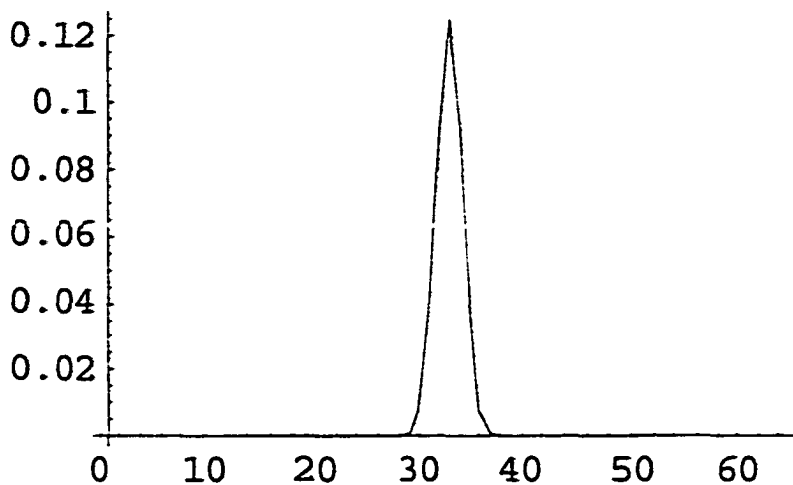
Figure 4.3: Sampled Fourier transform of three-dimensional Gaussian function at the point $x = y = 0$.

sequence at $(\xi_{n_x+1}, \eta_{n_y+1})$ generated from equation (4.48). At each point (ξ_i, η_j) we rotate the sequence by n_z bins to the left. The resulting sequence at $(\xi_{n_x+1}, \eta_{n_y+1})$ is illustrated in Figure 4.4. The inverse Fourier transform is computed from this sequence with equation (4.43) and the discrete inverse transform. At each (ξ_i, η_j) point the sequence is rotated $n_z + 1$ bins to the left and then reversed. The result is shown at $(\xi_{n_x+1}, \eta_{n_y+1})$ in Figure 4.5. Next, we invert in the y-dimension at every point (ξ_i, z_k) and then the procedure is repeated in the x-direction at every point (y_j, z_k).

Figure 4.6 shows a surface plot of the resulting solution at $x = 0$. We have reproduced the original Gaussian function given by equation (4.46) and illustrated in Figure 4.7. The agreement between the numerical technique and the exact solution is seen in Figure 4.8 which shows a plot in the z-direction of the numerically computed result and of equation

100
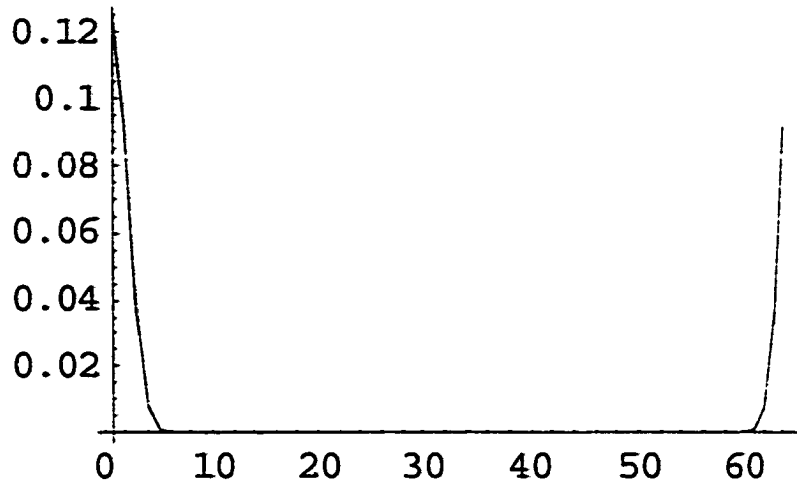
Figure 4.4: Rotated sampled Fourier transform of the three-dimensional Gaussian function.
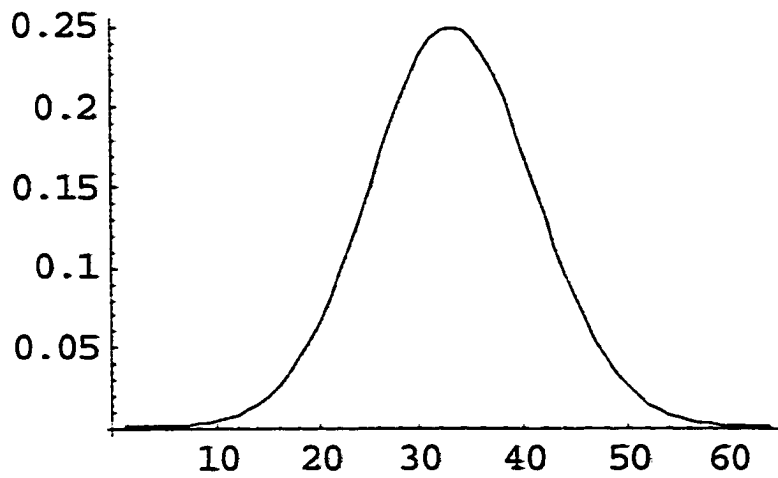
Figure 4.5: Result after inverse tranforming, rotating, and reversing in the z-direction

101
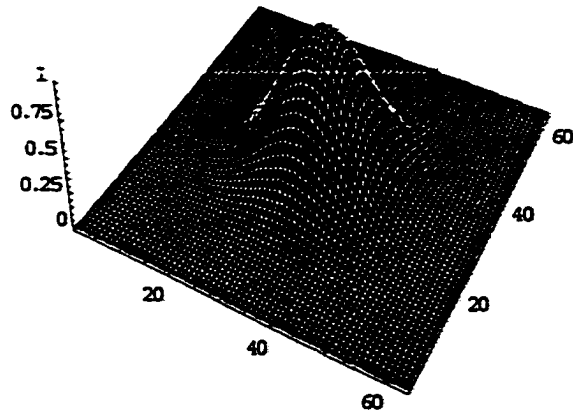
Figure 4.6: Surface plot at $x = 0$ computed by the discrete inverse Fourier transform.
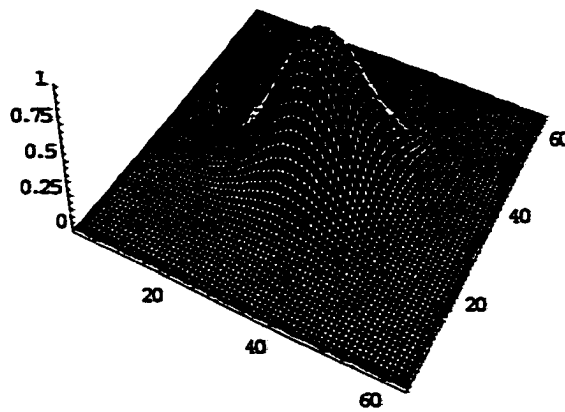
Figure 4.7: Exact solution. Surface plot of equation 4.46 calculated at $x = 0$.

102
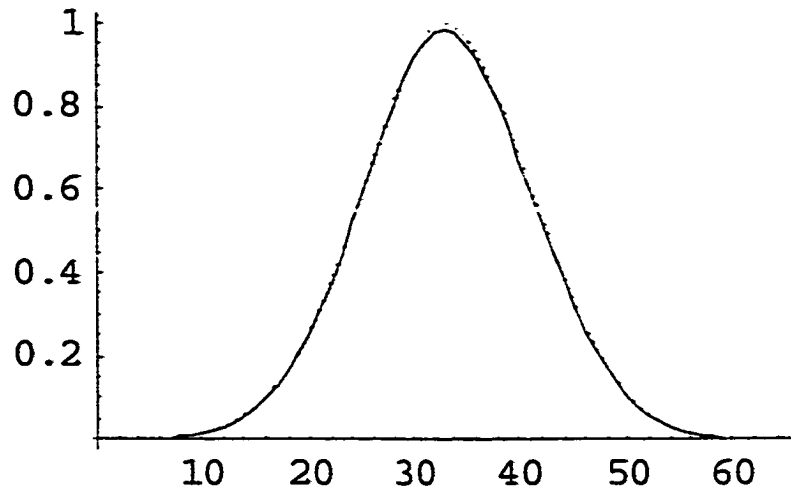
Figure 4.8: Comparison of numerical inverse Fourier transform and analytic solution. Curves are identical.

(4.46) at the point $(x, y) = (0, 0)$. As further examples, consider the functions

$$\hat{f}(\xi, \eta, \varsigma) = \frac{\sin(\pi\xi)\sin(\pi\eta)\sin(\pi\varsigma)}{\pi^2 \xi \eta \varsigma} \tag{4.49}$$

and

$$\hat{f}(\xi, \eta, \varsigma) = \frac{\sin(2\pi s) - 2\pi s \cos(2\pi s)}{2\pi^2 s^3} \tag{4.50}$$

where $s^2 = \xi^2 + \eta^2 + \varsigma^2$. From Bracewell [259], the inverse Fourier transform of these functions are, respectively

$$^3\Pi(x, y, z) \equiv \Pi(x)\Pi(y)\Pi(z) \tag{4.51}$$

and

$$\Pi(\frac{r}{2}) \tag{4.52}$$

where Π is defined by

$$\Pi(x) = \begin{cases} 0, & |x| > \frac{1}{2} \\ 1, & |x| < \frac{1}{2} \end{cases}$$

103
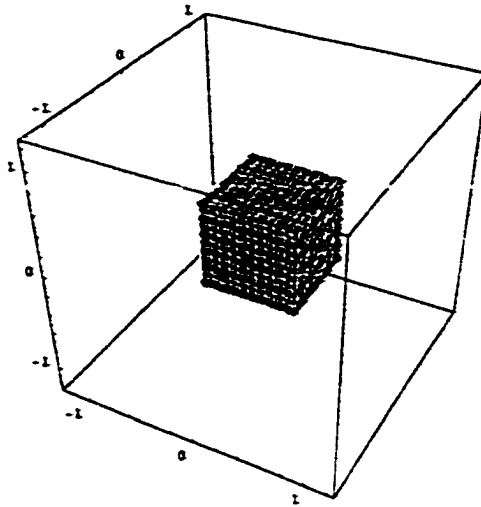
Figure 4.9: Numerically computed inverse transform of equation (4.49).
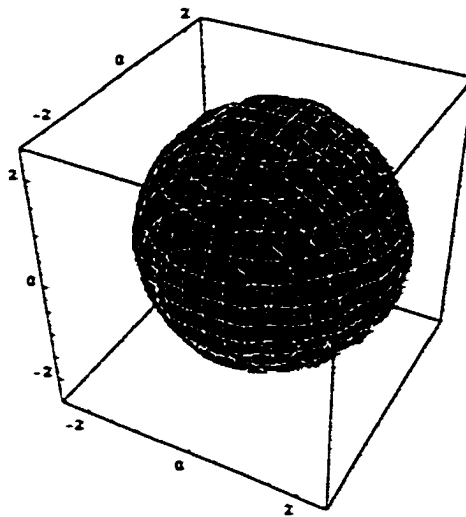
Figure 4.10: Numerically computed inverse transform of equation (4.50).

104

and $r^2 = x^2 + y^2 + z^2$. Equation (4.51) is zero everywhere except within a unit cube where it has a value of one. Similarly, equation (4.52) is zero everywhere except within a unit sphere (*i.e* radius is equal to one) where it has a value of one. The numerically inverted Fourier transforms of equations (4.49) and (4.50) are illustrated in Figures 4.9 and 4.10. These are three-dimensional contour plots showing all contours with a value of one. The functions are zero everywhere else. We see that the results agree with equations (4.51) and (4.52) as desired. We note that these examples have all been even functions. The inversion technique has also been successfully implemented with odd functions and with test functions that do not exhibit any symmetry.

4.1.4 Results: Isotropic Case with Exact Inverse Laplace Transform

We use this numerical inversion technique to obtain the displacements given in equations (4.39), (4.40), and (4.41) for an isotropic aluminum sample. The material parameters for isotropic aluminum are given by [263]

$$C_{11} = 1.075 \times 10^{11} \left[\frac{N}{m^2} \right]$$

$$C_{12} = 5.459 \times 10^{10} \left[\frac{N}{m^2} \right]$$

$$C_{44} = 2.6455 \times 10^{10} \left[\frac{N}{m^2} \right]$$

$$\rho = 2700 \left[\frac{kg}{m^3} \right]$$

From equations (4.23), (4.24) and (4.21) the longitudinal and transverse wave speeds are, respectively

$$c_L = \sqrt{\frac{\lambda + 2\mu}{\rho}} = \sqrt{\frac{C_{11}}{\rho}} = 6301.0 \, \frac{m}{s} \tag{4.53}$$

$$c_T = \sqrt{\frac{\mu}{\rho}} = \sqrt{\frac{C_{44}}{\rho}} = 3130.20 \, \frac{m}{s} \tag{4.54}$$

105

so that,

$$R = \frac{c_L}{c_T} = 2.016$$

We are most interested in the out-of-plane or z-component displacement since this is the quantity measured in our experiments and we first consider equation (4.41). We use the values for c_T and R given above and use discretization values given by

$$n_x = 16$$

$$n_y = 16$$

$$n_z = 32$$

$$n_t = 32$$

$$\Delta x = 0.25 \ [cm]$$

$$\Delta y = 0.25 \ [cm]$$

$$\Delta z = 0.0625 \ [cm]$$

$$\Delta t = 0.4 \ [\mu s]$$

The resulting numerically inverted function is illustrated in Figures 4.11, 4.12, and 4.13. Figures 4.11 and 4.12 show a series of surface plots of the z-component displacement magnitude in the x-y plane ($z = 0$) as a function of time. The plots range from 0 to 12.8 μs with each plot separated by 0.8 μs. The magnitude of the displacement is given in units of meters and the spatial units for the x-y plane are given in centimeters. Figure 4.13 shows the corresponding contour plots in the x-y plane for the first fifteen surface plots. We see that an initial impulse spike decays into a circular wave which propagates out to the end of the computational space and reflects at the boundaries. Since we are considering the z-displacement in the x-y plane, we expect that the wave should correspond to the pure transverse wave mode. To verify that this is the transverse wave we compute the wave speed

106

from Figure 4.13. The wave reaches the edge of the computational space in approximately 32 time steps or 12.8 μs. The distance travelled is

$$(n_x) \Delta x = 4.00 \text{ [cm]}$$

so that the computed wave speed is

$$\frac{4.0 \text{ [cm]}}{12.8 \text{ [}\mu s\text{]}} = 3125.0 \frac{m}{s} \tag{4.55}$$

The percent error between the numerically computed wave speed in equation (4.55) and the exact wave speed given in equation (4.54) is

$$\frac{|3125.0 - 3130.2|}{3130.2} \times 100 = 0.17\%$$

This agreement is very good and the small error is dependent on the determination of the arrival time of the wave from the figures. An even better result could be obtained if the time steps were smaller so that the wave arrival could be determined more accurately.

4.1.5 Numerically Inverting the Laplace Transform

Although we could analytically invert the Laplace transforms in equations (4.36), (4.37), and (4.38), we need a numerical technique for more general problems in the next section. There are several methods for numerically inverting the Laplace transform [264]. For example, the inversion can be computed with polynomial interpolation schemes or by expansions in terms of special functions (e.g. Chebyshev or Legendre polynomials). However, we expect our solutions to consist of propagating waves so that we used a method based on the Fourier transform. We found that this technique was much more efficient than polynomial interpolation for inverting Laplace transformed sinusoidal functions. Furthermore, this method allows us to use the numerical Fourier transform techniques that we have already developed in the previous sections.

107
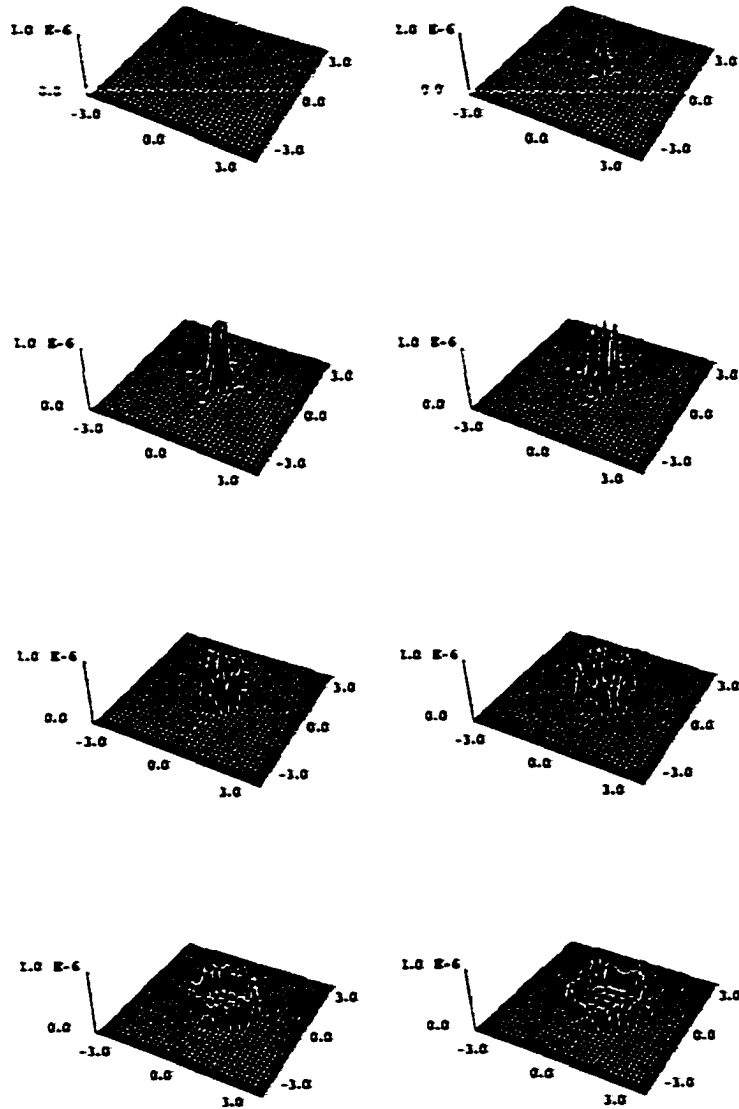
Figure 4.11: Surface plots of z-component displacement in isotropic aluminum numerically computed from exact inverse Laplace transform. 0.0-6.4 μs in steps of 0.8 μs.

108
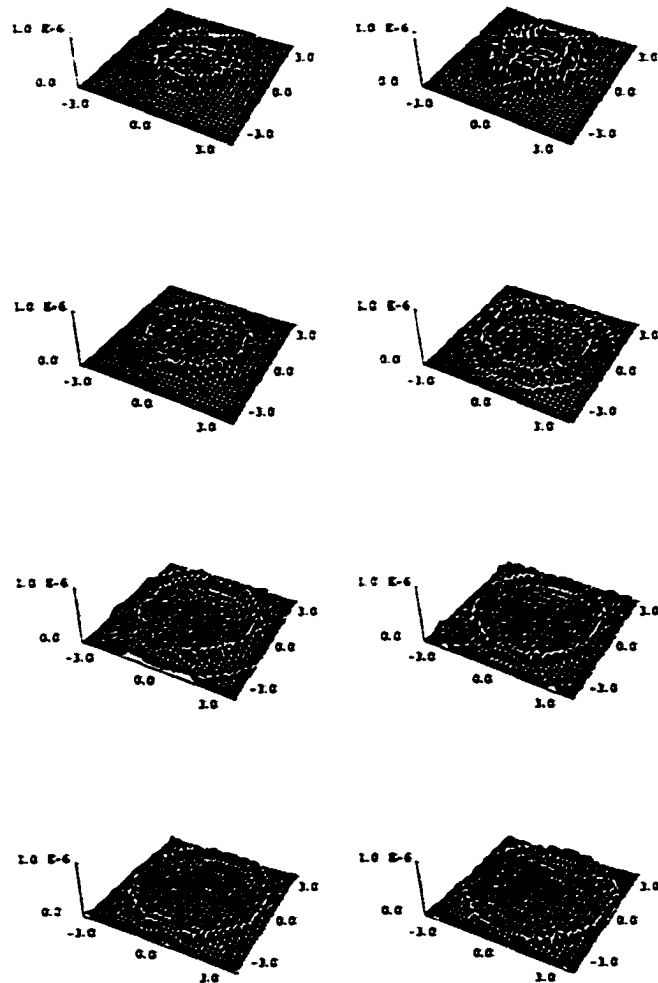
Figure 4.12: Surface plots of z-component displacement in isotropic aluminum numerically computed from exact inverse Laplace transform. 6.8–12.8 μs in steps of 0.8 μs.

109
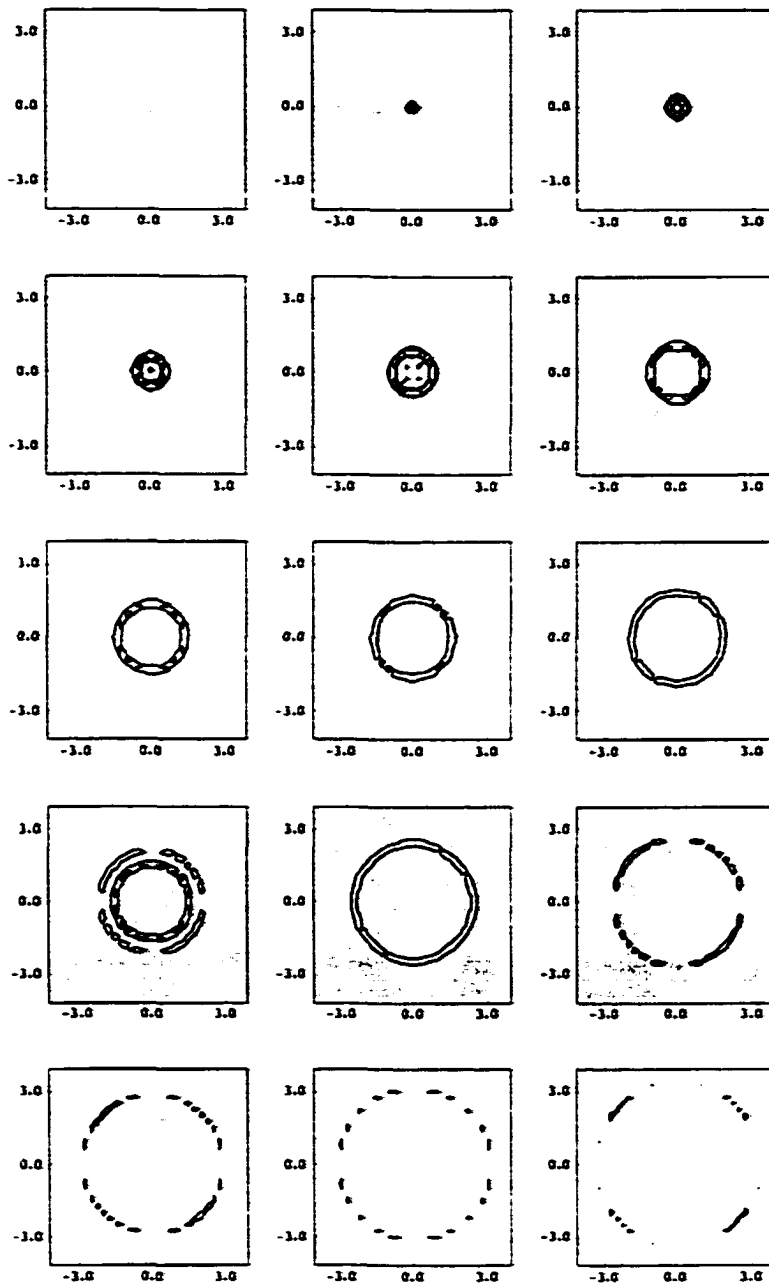
Figure 4.13: Contour plots in the x-y plane of the z-component displacement in isotropic aluminum numerically computed from the exact inverse Laplace transform. 0.0-12.0 μs in steps of 0.8 μs. y-axis is vertical.

110

Following Krylov [264], the Laplace transform is numerically inverted by converting the Bromwich inversion integral to a Fourier transform. The inverse Laplace transform is given by the Bromwich integral

$$f(t) = \frac{1}{2\pi i} \int_{c-i\infty}^{c+i\infty} e^{pt} \bar{f}(p) dp \tag{4.56}$$

We change the variable of integration to σ by setting

$$p = c + i\sigma, \quad -\infty < \sigma < \infty \tag{4.57}$$

Then, equation (4.56) can be written as

$$f(t) = \frac{e^{ct}}{2\pi} \int_{-\infty}^{\infty} e^{i\sigma t} \bar{f}(c + i\sigma) d\sigma \tag{4.58}$$

Next, we introduce the notation

$$g(t) \equiv f(t) e^{-ct} \tag{4.59}$$

$$\bar{g}(\sigma) \equiv \bar{f}(c + i\sigma) \tag{4.60}$$

so that equation (4.58) becomes

$$g(t) = \frac{1}{2\pi} \int_{-\infty}^{\infty} e^{i\sigma t} \bar{g}(\sigma) d\sigma \tag{4.61}$$

With this notation, the forward Laplace transform given in equation (4.29) and rewritten here for clarity

$$\bar{f}(p) = \int_{0}^{\infty} e^{-pt} f(t) dt \tag{4.62}$$

becomes

$$\bar{g}(\sigma) = \int_{0}^{\infty} e^{-i\sigma t} g(t) dt \tag{4.63}$$

111

If we assume that $f(t)$ and therefore $g(t)$ is not identically zero in a finite interval $(0, T)$ but either vanishes or becomes negligibly small outside of this interval, we can write

$$\bar{g}(\sigma) = \int_{-\infty}^{\infty} e^{-i\sigma t} g(t) \, dt \tag{4.64}$$

since there is no contribution to the integral along $(-\infty < t < 0)$. This assumption is satisfied in physical problems like ours where we demand zero response until an impulse generates a wave that decays to zero amplitude in some finite time period. Equations (4.64) and (4.61) are recognized as a Fourier transform pair so that we see that the Laplace transform relating the functions $f(t)$ and $\bar{f}(p)$ is the same as the Fourier transform relating the functions

$$g(t) = f(t)e^{-ct} \text{ and } \bar{g}(\sigma) = \bar{f}(c + i\sigma)$$

Now, we expand $g(t)$, defined in the interval $(0, T)$, in a complex Fourier series

$$g(t) = \sum_{-\infty}^{\infty} c_n e^{in\omega t} \tag{4.65}$$

where

$$\omega = \frac{2\pi}{T} \tag{4.66}$$

and the coefficient c_n are given by

$$c_n = \frac{\omega}{2\pi} \int_0^T g(t)e^{-in\omega t} dt \tag{4.67}$$

Since we have assumed that $g(t)$ is negligible outside of the interval $(0, T)$ we can rewrite this as

$$c_n = \frac{\omega}{2\pi} \int_0^{\infty} g(t)e^{-in\omega t} dt = \frac{\omega}{2\pi} \bar{g}(n\omega) \tag{4.68}$$

where we have used equation (4.63). Then, plugging equation (4.68) into equation (4.65) we can write

$$g(t) = \frac{\omega}{2\pi} \left[\bar{g}(0) + \sum_{k=1}^{\infty} \left(\bar{g}(n\omega)e^{in\omega t} + \bar{g}(-n\omega)e^{-in\omega t} \right) \right] \tag{4.69}$$

112

We separate the function $\bar{g}(n\omega)$ into real and imaginary parts according to

$$\bar{g}(n\omega) = \bar{f}(c + in\omega) = A(n\omega) + iB(n\omega) \qquad (4.70)$$

From equation (4.63) we have

$$
\begin{aligned}
\bar{g}(n\omega) &= \int_0^\infty e^{-in\omega t} g(t)\,dt \\
&= \int_0^\infty [\cos(n\omega t) - i\sin(n\omega t)]\, g(t)\,dt \\
&= \int_0^\infty \cos(n\omega t)\, g(t)\,dt - i\int_0^\infty \sin(n\omega t)\, g(t)\,dt \\
&= A(n\omega) + iB(n\omega) \qquad (4.71)
\end{aligned}
$$

so that

$$
\begin{aligned}
\bar{g}(-n\omega) &= \int_0^\infty e^{in\omega t} g(t)\,dt \\
&= \int_0^\infty [\cos(n\omega t) + i\sin(n\omega t)]\, g(t)\,dt \\
&= \int_0^\infty \cos(n\omega t)\, g(t)\,dt + i\int_0^\infty \sin(n\omega t)\, g(t)\,dt \\
&= A(n\omega) - iB(n\omega) \qquad (4.72)
\end{aligned}
$$

We substitute equations (4.71) and (4.72) into equation (4.69) to obtain

$$g(t) = \frac{\omega}{2\pi}\left[A(0) + iB(0) + \sum_{n=1}^\infty \left([A(n\omega) + iB(n\omega)]\,e^{in\omega t} + [A(n\omega) - iB(n\omega)]\,e^{-in\omega t}\right)\right] \qquad (4.73)$$

From equation (4.72) it follows that $B(0) = 0$ and after simplifying, we can write equation (4.73) as

$$g(t) = \frac{\omega}{\pi}\left[\frac{A(0)}{2} + \sum_{n=1}^\infty A(n\omega)\cos(n\omega t) - \sum_{n=1}^\infty B(n\omega)\sin(n\omega t)\right] \qquad (4.74)$$

113

Then, from equation (4.59) we obtain the function $f(t)$ as

$$f(t) = \frac{e^{ct}\omega}{\pi}\left[\frac{A(0)}{2} + \sum_{n=1}^{\infty} A(n\omega)\cos\left(n\omega t\right) - \sum_{n=1}^{\infty} B(n\omega)\sin\left(n\omega t\right)\right] \qquad (4.75)$$

Equation (4.75) expresses the desired function $f(t)$ as a Fourier series, in terms of equidistant values of the transform $\bar{f}(p)$ along the straight line $\text{Re}[p] = c$. The value of c is chosen so that all of the singular points of $\bar{f}(p)$ lie to the left of the line $\text{Re}[p] = c$ in the complex plane. In practice, the summations in equation (4.75) cannot be carried out to infinity and instead we use the equation

$$f(t) = \frac{e^{ct}\omega}{\pi}\left[\frac{A(0)}{2} + \sum_{n=1}^{M} A(n\omega)\cos\left(n\omega t\right) - \sum_{n=1}^{M} B(n\omega)\sin\left(n\omega t\right)\right] \qquad (4.76)$$

where M is the maximum number of summations. According to equation (4.66) ω is the angular frequency of a wave with period T. Therefore, we chose M large enough so that we reproduce the highest frequencies that we expect to see in our result. For example, if we use the same discretization values as before

$$n_t = 32$$

$$\Delta t = 0.4\,[\mu s]$$

we have

$$T = n_t\Delta t = 12.8 \times 10^{-6}\,[s]$$

$$\nu = \frac{1}{T} = 78.125\,\text{KHz}$$

$$\omega = \frac{2\pi}{T} = 2\pi\nu = \frac{2\pi}{12.8 \times 10^{-6}\,[s]} = 4.908 \times 10^5 \frac{\text{Rad}}{s}$$

and if we chose $M = 100$ the maximum frequency component that we can reproduce is

$$m\omega = 4.908 \times 10^7 \frac{\text{Rad}}{s} = 7.8\,\text{MHz}$$

114

Equation (4.75) was used to numerically invert the Laplace transform in equation (4.38) and the three-dimensional Fourier transform was numerically inverted as in the previous section. The same discretization values and material parameters were used in both cases. The maximum number of summations in equation (4.76) was $m = 100$ and the value of c was set to $\omega/2$. The results are presented in Figures 4.14 through 4.19. Figures 4.14 and 4.15 correspond to Figures 4.11 and 4.12. We see that the numerically inverted Laplace transform agrees qualitatively and quantitatively with the analytically determined inverse transform until the next to last time step when a sharp spike develops at the center of the plot. Figures 4.16 shows the numerical and analytical results plotted as a function of y at the x-z point $(0,0)$ from 0.0 to 5.6 μs with each successive plots separated by 0.4 μs. The analytic solution is represented by the solid line while the numerical solution is drawn as a dashed line. We see that the two curves are indistinguishable at each time step. Figure 4.18 shows an enlargement at time step 6.0 μs. We see that the analytic and numeric solutions agree very well here. Figure 4.17 shows the same comparison as Figure 4.16 for the time steps 6.0 to 11.6 μs. We see that the agreement between the analytic and numerical solutions remains good during these later times except for the sharp spike that begins to develop at the center of the graphs. Figure 4.19 shows an enlargement of the time step 12.0 μs. Here, we clearly see that the analytic and numeric solutions are only significantly different at the location of the spike. This spike may be due to an accumulation of artifacts during the numerical inversions. We also note that the analytically Laplace inverted equations (4.39), (4.40), and (4.41) are singular at the point $(\xi, \eta, \zeta) = (0,0,0)$ and a small offset had to be introduced to numerically invert the Fourier transform at this point. It may be that the numerical inversion of equations (4.36), (4.37), and (4.38) did not take this singularity into account and the spike is a result. Figure 4.20 shows contour plots of the z-component displacement in the y-z plane computed from the analytical inversion. Here,

115
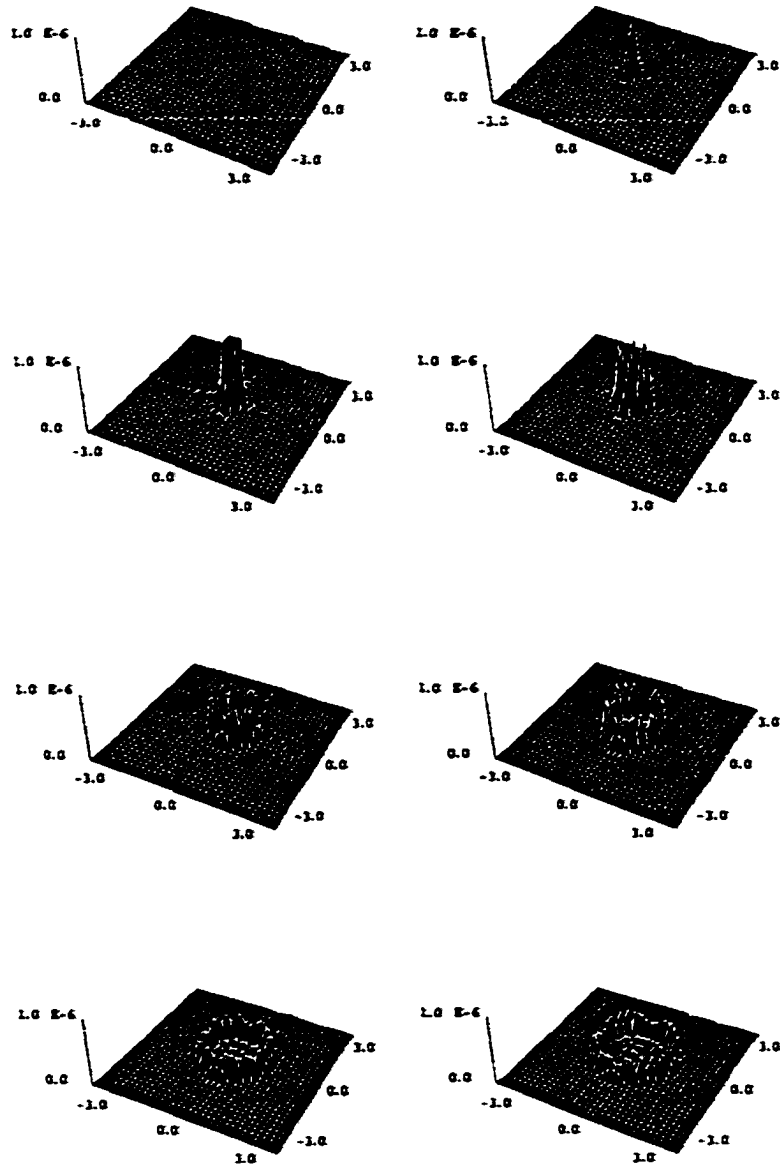
Figure 4.14: Surface plots of z-component displacement in isotropic aluminum numerically computed from numerical inverse Laplace transform. 0.0-2.8 μs in steps of 0.4 μs.

116
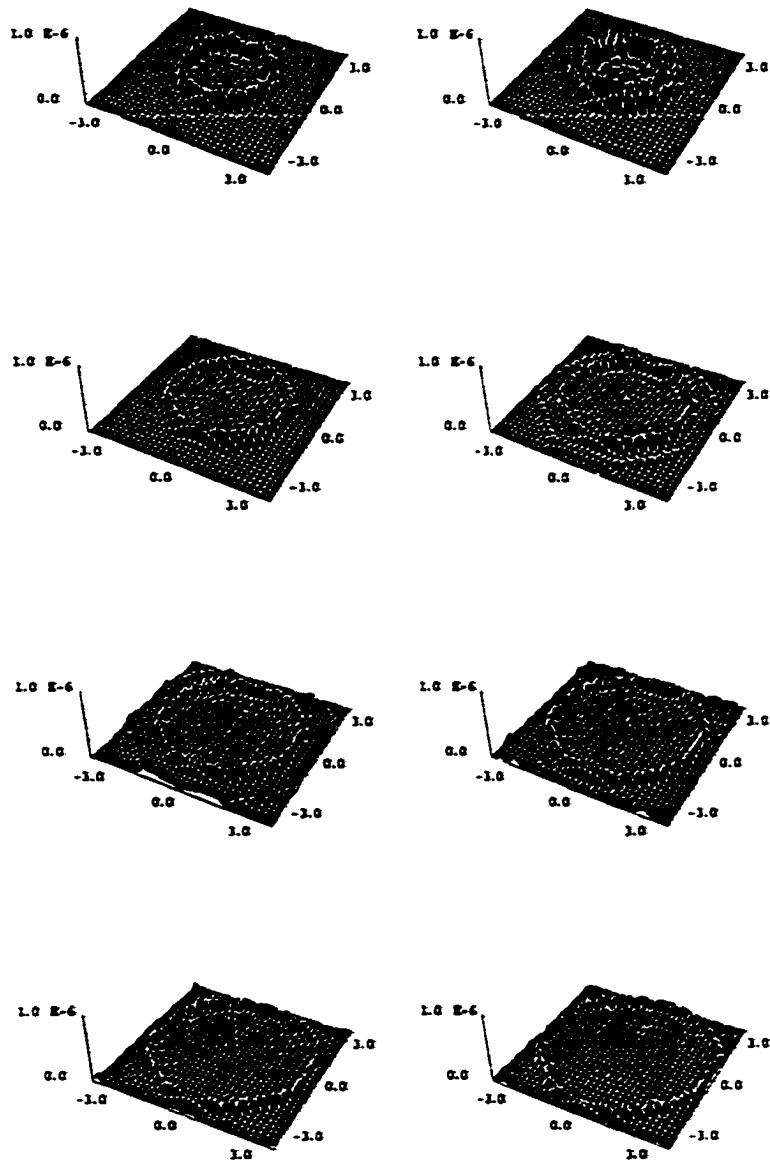
Figure 4.15: Surface plots of z-component displacement in isotropic aluminum numerically computed from numerical inverse Laplace transform. 3.2-6.0 μs in steps of 0.4 μs.

117
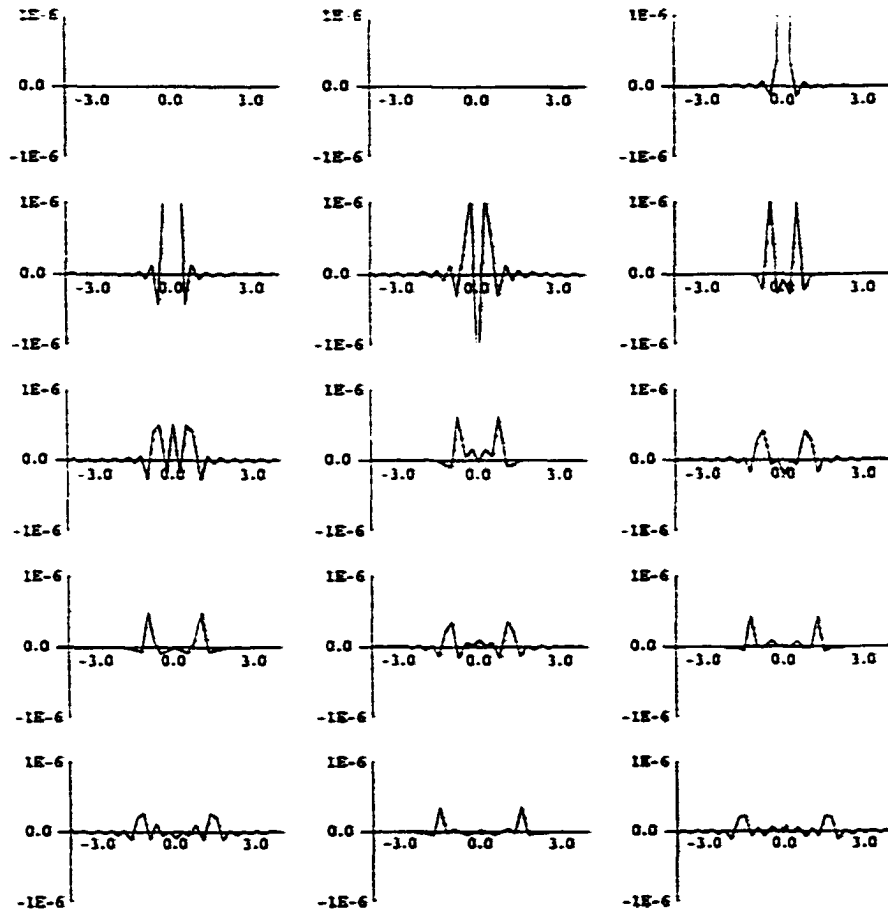
Figure 4.16: Comparison of solutions with exact inverse Laplace transform (solid) and numerical inverse Laplace transform (dashed). Time intervals of 0.4 μs.

118
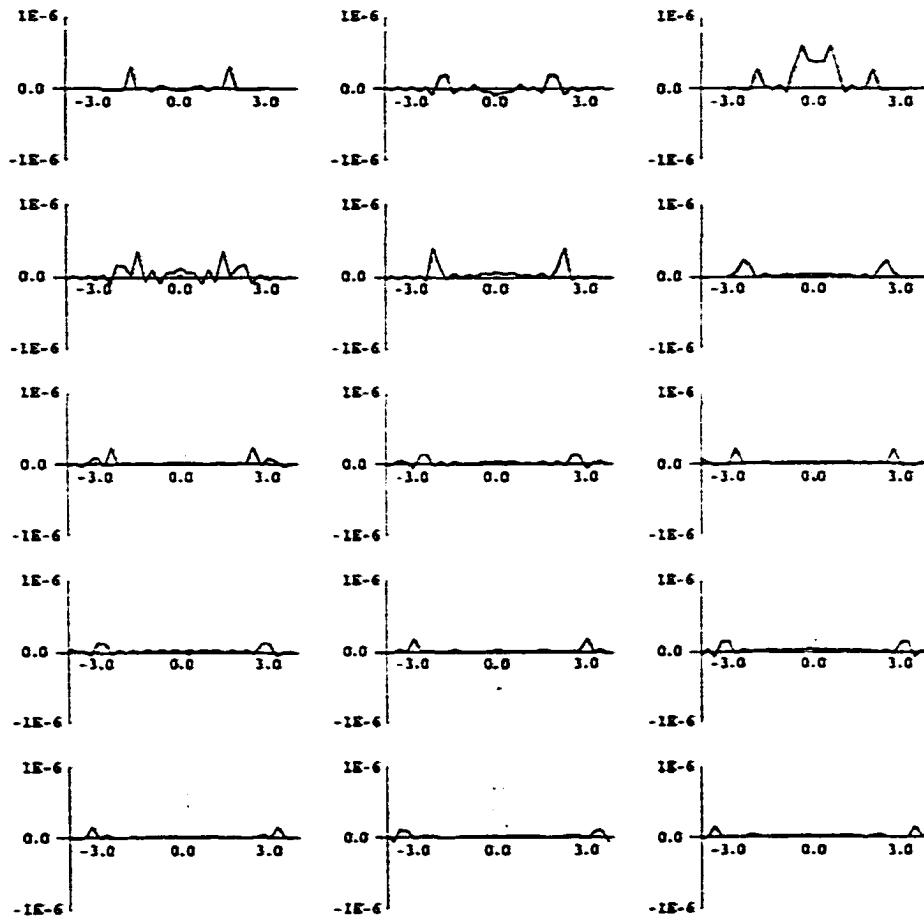
Figure 4.17: Comparison of solutions with exact inverse Laplace transform (solid) and numerical inverse Laplace transform (dashed). Time intervals of 0.4 μs.

119
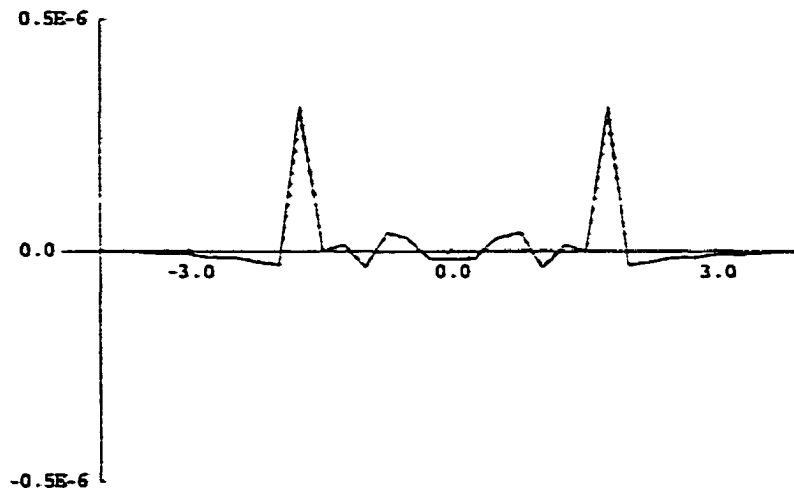
Figure 4.18: Comparison of solutions with exact inverse Laplace transform (solid) and numerical inverse Laplace transform (dashed) at 6.0 μs.
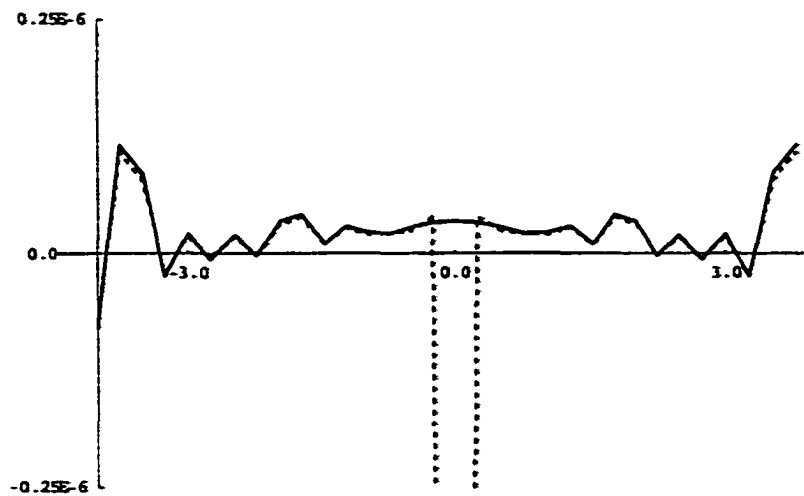
Figure 4.19: Comparison of solutions with exact inverse Laplace transform (solid) and numerical inverse Laplace transform (dashed) at 12.0 μs.

120
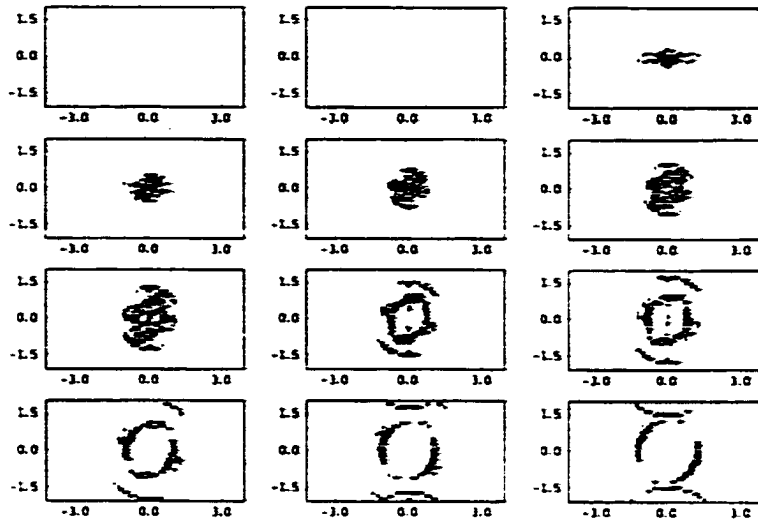
Figure 4.20: Contour plots of the z-component displacement in the y-z plane in aluminum. Computed from analytical inversion of the Laplace transform.

the time interval between plots is 0.4 μs. In this plane, the z-component displacement contributes to both the longitudinal and transverse waves so that the transverse wave is not the only visible wave and we can see the longitudinal wave. As expected, we see that the longitudinal wave travels approximately twice as fast as the shear wave. As a final example, we consider the y-component displacement in the x-z plane computed by numerically inverting equation (4.37). In this plane, the y-component displacement should correspond to the pure transverse wave mode and since the material is isotropic, we expect to see a single circular wave as in Figure 4.13. This is illustrated in Figure 4.21.

121
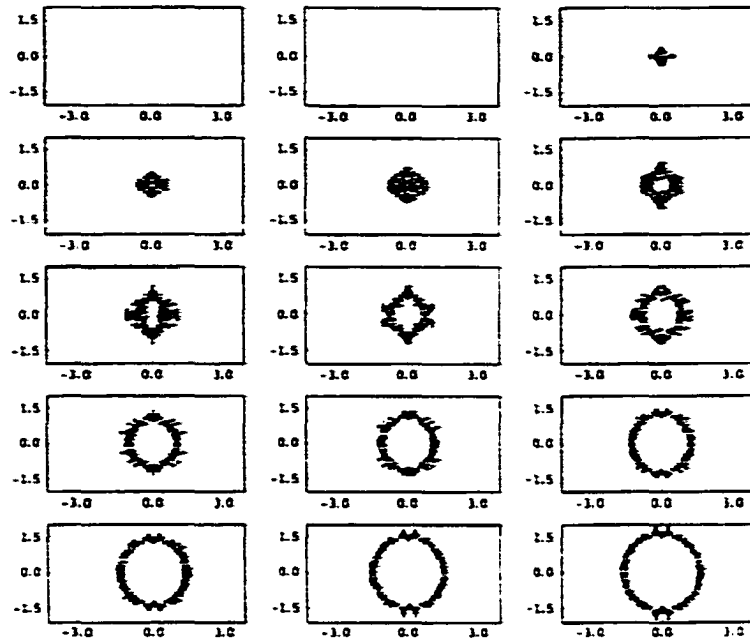
Figure 4.21: Contour plots of the y-component displacement in the x-z plane in isotropic aluminum. z-axis is vertical.

4.1.6 Anisotropic Solutions

In this section, we use the numerical techniques described above to solve equations (4.12)-(4.14) with an impulse forcing function for various anisotropic materials. We compare our results with slowness surfaces given by Auld [33] to verify our solutions. These slowness surfaces are reproduced for convenience.

Just as in the isotropic problem we, consider equations (4.12)-(4.14) with an impulse forcing function

$$\bar{f}(x,y,z,t) = \bar{Q}\,\delta\,(x_1)\,\delta(x_2)\delta\,(x_3)\,\delta(t) \tag{4.77}$$

After applying the Laplace transform in time and the three-dimensional Fourier transform

122

in space, we obtain an algebraic system of equations that we can write as

$$
\begin{pmatrix} K11 & K12 & K13 \\ K12 & K22 & K23 \\ K13 & K23 & K33 \end{pmatrix} \begin{pmatrix} \hat{u}_1 \\ \hat{u}_2 \\ \hat{u}_3 \end{pmatrix} = - \begin{pmatrix} Q_{x_1} \\ Q_{x_2} \\ Q_{x_3} \end{pmatrix}
\tag{4.78}
$$

with

$$
K11 = -C_{11}\xi^2 - C_{66}\eta^2 - C_{55}\varsigma^2 - 2C_{16}\xi\eta - 2C_{15}\xi\varsigma - 2C_{56}\eta\varsigma - \rho p^2
\tag{4.79}
$$

$$
K22 = -C_{66}\xi^2 - C_{22}\eta^2 - C_{44}\varsigma^2 - 2C_{26}\xi\eta - 2C_{46}\xi\varsigma - 2C_{24}\eta\varsigma - \rho p^2
\tag{4.80}
$$

$$
K33 = -C_{55}\xi^2 - C_{44}\eta^2 - C_{33}\varsigma^2 - 2C_{45}\xi\eta - 2C_{35}\xi\varsigma - 2C_{34}\eta\varsigma - \rho p^2
\tag{4.81}
$$

$$
\begin{aligned}
K12 = {} & -C_{16}\xi^2 - C_{26}\eta^2 - C_{45}\varsigma^2 - (C_{12} + C_{66})\,\xi\eta \\
& - (C_{14} + C_{56})\,\xi\varsigma - (C_{46} + C_{25})\,\eta\varsigma
\end{aligned}
\tag{4.82}
$$

$$
\begin{aligned}
K13 = {} & -C_{15}\xi^2 - C_{46}\eta^2 - C_{35}\varsigma^2 - (C_{14} + C_{56})\,\xi\eta \\
& - (C_{13} + C_{55})\,\xi\varsigma - (C_{36} + C_{45})\,\eta\varsigma
\end{aligned}
\tag{4.83}
$$

$$
\begin{aligned}
K23 = {} & -C_{56}\xi^2 - C_{24}\eta^2 - C_{34}\varsigma^2 - (C_{46} + C_{25})\,\xi\eta \\
& - (C_{36} + C_{45})\,\xi\varsigma - (C_{23} + C_{44})\,\eta\varsigma
\end{aligned}
\tag{4.84}
$$

We use *Mathematica* to solve this system for the transformed displacement components. These solutions are very long and we omit them here in the interest of space. These general solutions are too complicated to be analytically inverted and we must apply the numerical techniques described previously. We note that numerical results presented in the previous section for isotropic aluminum were obtained by numerically inverting these equations with appropriate material parameters.

123

	Stiffness $[10^{10}$ N/m$^2]$								
Material	C_{11}	C_{22}	C_{33}	C_{44}	C_{55}	C_{66}	C_{12}	C_{13}	$\rho \left[\frac{kg}{m^3}\right]$
BaNaNb	23.9	24.7	13.5	6.5	6.6	7.6	10.4	5.0	5300
CdS	9.07		9.38	1.504			5.81	5.1	4820
rutile	26.60		46.99	12.39		18.86	17.33	13.62	4260

Table 4.1: Material parameters used to compute the elastic Green's function.

We first consider displacement solutions in barium sodium niobate which is in the orthotropic $2mm$ crystal symmetry class. The stiffness coefficient matrix in this class has nine independent constants and has the form [33]

$$
\begin{pmatrix}
C_{11} & C_{12} & C_{13} & 0 & 0 & 0 \\
C_{12} & C_{22} & C_{23} & 0 & 0 & 0 \\
C_{13} & C_{23} & C_{33} & 0 & 0 & 0 \\
0 & 0 & 0 & C_{44} & 0 & 0 \\
0 & 0 & 0 & 0 & C_{55} & 0 \\
0 & 0 & 0 & 0 & 0 & C_{66}
\end{pmatrix}
\tag{4.85}
$$

The material parameters used for barium sodium niobate (BaNaNb) and the other materials considered here are from Auld [33] and are listed in Table 4.1. Figure 4.23 shows contour plots of the z-component displacement in the x-y plane with each plot separated by two time steps equal to 0.8 μs. In these plots, the darker contours represent larger amplitude. By solving the Christoffel equations, it can be shown that three wave modes are possible in this plane. There exists a pure shear wave polarized along the z-axis with inverse velocity

$$
\left(\frac{k}{\omega}\right)_I = \frac{\rho^{1/2}}{\sqrt{C_{44}\cos^2\phi + C_{55}\sin^2\phi}}
\tag{4.86}
$$

124

a quasishear wave with inverse velocity

$$\left(\frac{k}{\omega}\right)_2 = \frac{(2\rho)^{1/2}}{\sqrt{C_{66} + C_{11}\cos^2\phi + C_{22}\sin^2\phi - \left\{\left(C_{66} + C_{11}\cos^2\phi + C_{22}\sin^2\phi\right)^2 - 4C\right\}^{1/2}}}$$

(4.87)

and a quasilongitudinal wave with inverse velocity

$$\left(\frac{k}{\omega}\right)_3 = \frac{(2\rho)^{1/2}}{\sqrt{C_{66} + C_{11}\cos^2\phi + C_{22}\sin^2\phi + \left\{\left(C_{66} + C_{11}\cos^2\phi + C_{22}\sin^2\phi\right)^2 - 4C\right\}^{1/2}}}$$

(4.88)

with

$$C \equiv \left(C_{11}\cos^2\phi + C_{66}\sin^2\phi\right)\left(C_{66}\cos^2\phi + C_{22}\sin^2\phi\right) - \left(C_{12} + C_{66}\right)^2\cos^2\phi\sin^2\phi$$

and where ϕ is the polar angle [33]. The slowness surfaces defined by these equations are shown in Figure 4.22. In Figure 4.23, we see a wave which propagate outward from the origin. This wave reaches the edges of the computational space along the x-axis (horizontal) in approximately 29 time steps or 11.6 μs. The distance travelled is 4.0 cm so that the wave velocity is $3448.28\frac{m}{s}$. From the slowness surfaces presented in Figure 4.22, and equation (4.86) the theoretical wave speed of the pure transverse wave mode along the y-axis is given as [1]

$$c_T^A = \sqrt{\frac{C_{44}}{\rho}} = \sqrt{\frac{6.5 \times 10^{10}}{5300}} = 3502.0\frac{m}{s}$$

so that the percent error is

$$\frac{|3448.28 - 3502.0|}{3502.0} \times 100 = 1.56\%$$

Figure 4.24 shows surface plots of the first eight time steps of Figure 4.23. Figure 4.25 shows contour plots of the z-component displacement in the x-z plane. From Auld, the three possible wave modes in this plane are a quasishear wave, a quasilongitudinal wave,

[1]The superscript in the wave speed notation matches Auld's designations.

125
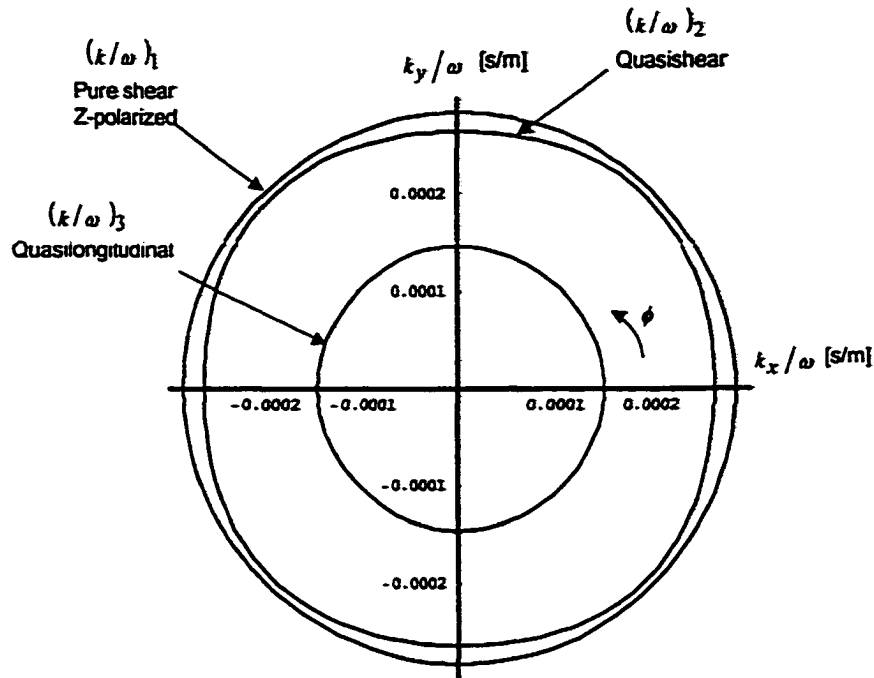
Figure 4.22: Slowness surfaces in Barium Sodium Niobate for the x-y plane.

and a pure shear wave polarized along the y-axis. The quasilongitudinal wave propagates with a wave speed of

$$c_{ql}^s = \sqrt{\frac{C_{33}}{\rho}} = \sqrt{\frac{13.5 \times 10^{10}}{5300}} = 5046.9 \frac{m}{s}$$

along the z-axis. In Figure 4.25 two wave fronts are visible. The faster wave reaches the the edge of the computational space along the z-direction in 20 time steps or 8 μs and therefore has a wave speed of 5000 $\frac{m}{s}$. This represents a percent error of

$$\frac{|5046.9 - 5000.0|}{5046.9} \times 100 = 0.93\%$$

126
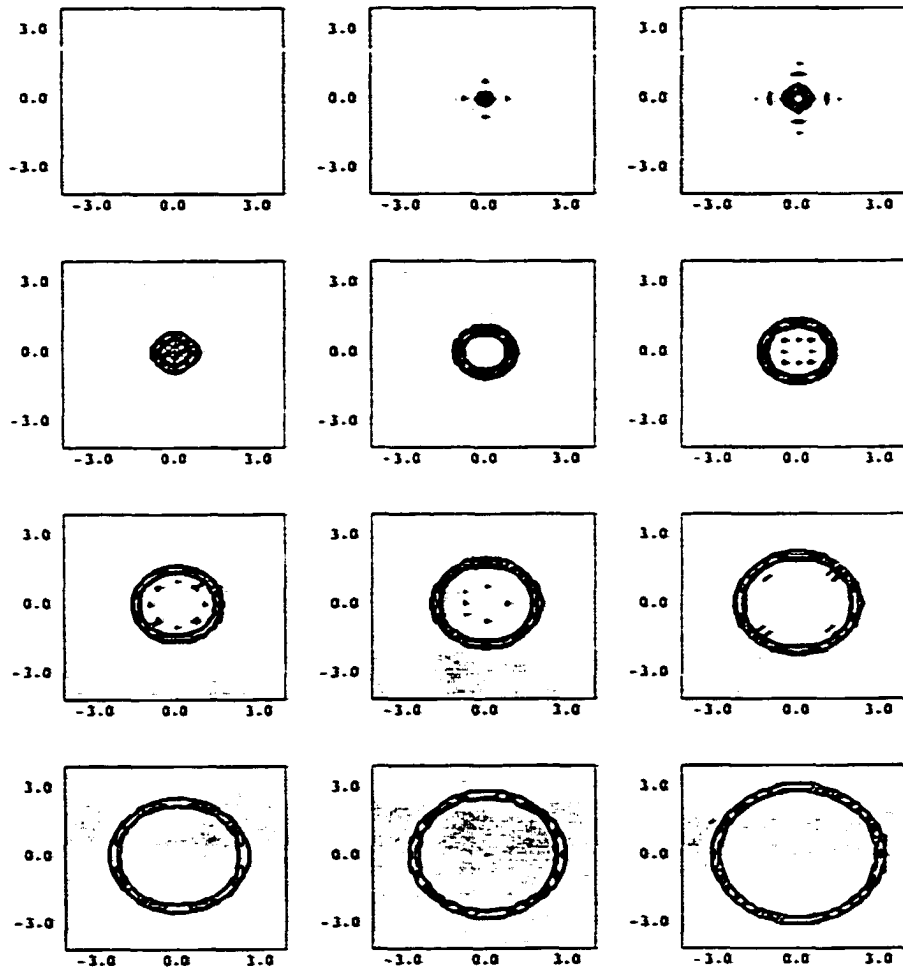
Figure 4.23: Contour plots of the z-component displacement in the x-y plane for BaNaNb at time intervals of 0.8 μs. y-axis is vertical.
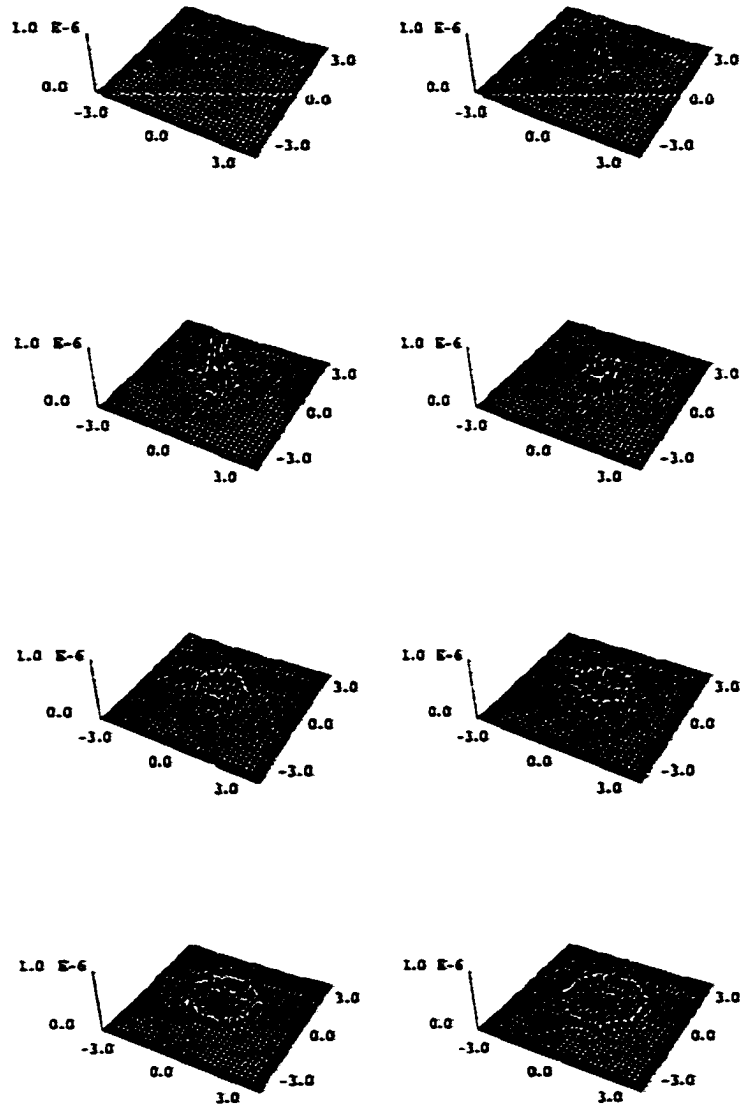
Figure 4.24: Surface plots of the z-component dispalcement in the x-y plane computed for BaNaNb at time intervals of 0.8 μs.

128

The pure shear wave propagates with a wave speed of

$$c_T^7 = \sqrt{\frac{C_{55}}{\rho}} = \sqrt{\frac{6.6 \times 10^{10}}{5300}} = 3528.9 \frac{m}{s}$$

along both the x- and z-axis. The quasishear wave propagates along the x-axis with speed

$$c_{qt}^3 = \sqrt{\frac{C_{66}}{\rho}} = \sqrt{\frac{7.6 \times 10^{10}}{5300}} = 3786.8 \frac{m}{s}$$

and along the z-axis with the same speed as the pure transverse wave

$$c_{qt}^9 = c_T^7$$

We calculate that the speed of the slower wave in our plots along the x-axis as

$$c = 3333.33 \frac{m}{s}$$

giving a percent errors of

$$\frac{|3333.33 - 3528.9|}{3528.9} \times 100 = 5.54\%$$

$$\frac{|3333.33 - 3786.8|}{3786.8} \times 100 = 11.98\%$$

relative to the pure shear wave and quasishear wave, respectively. From these values we suggest that the second wave in our plots corresponds to the pure transverse wave. Finally, Figure 4.27 shows contour plots of the y-component displacement in the x-z plane. In this plane, there exists a pure shear wave polarized along the y-axis with inverse velocity

$$\left(\frac{k}{\omega}\right)_2 = \frac{\rho^{1/2}}{\sqrt{C_{66} \sin^2 \theta + C_{44} \cos^2 \theta}} \tag{4.89}$$

a quasishear wave with inverse velocity

$$\left(\frac{k}{\omega}\right)_1 = \frac{(2\rho)^{1/2}}{\sqrt{C_{55} + C_{11} \sin^2 \theta + C_{33} \cos^2 \theta - \left\{ \left(C_{55} + C_{11} \sin^2 \theta + C_{33} \cos^2 \theta \right)^2 - 4\bar{C} \right\}^{1/2}}} \tag{4.90}$$

129
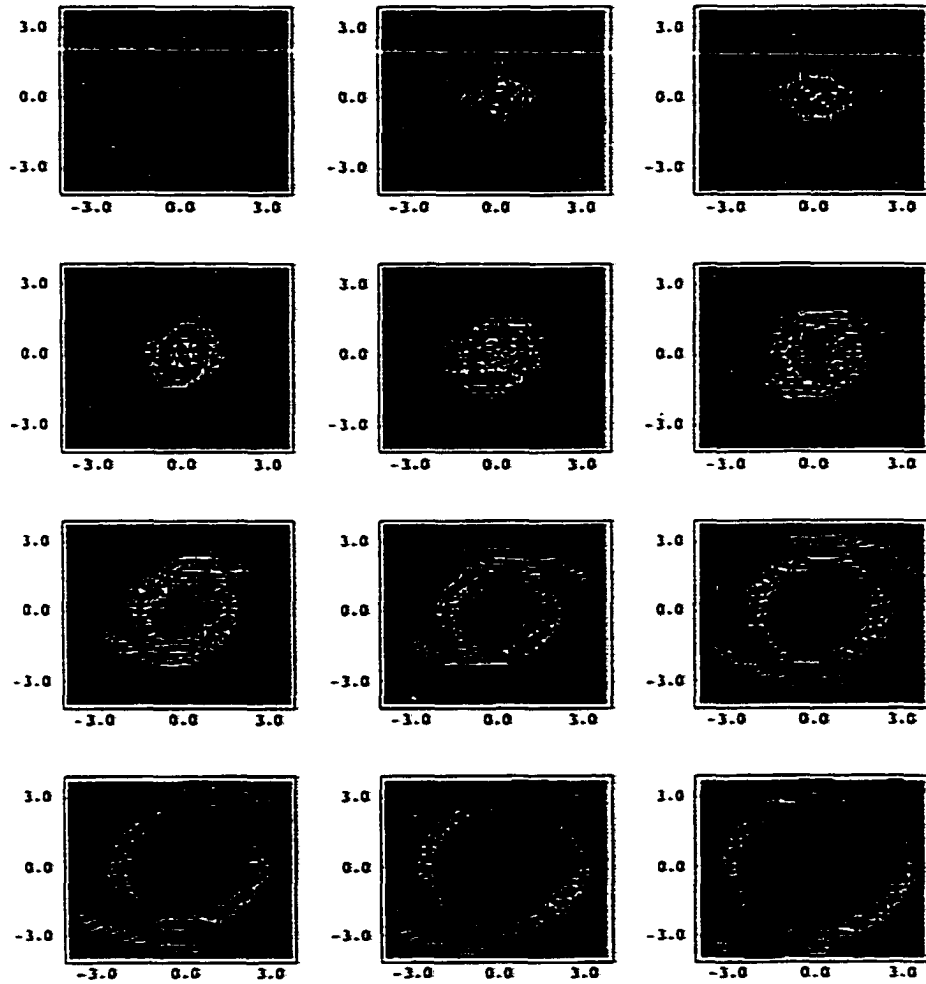
Figure 4.25: Contour plots of the z-component displacement in the x-z plane for BaNaNb at time intervals of 0.8 μs. z-axis is vertical.
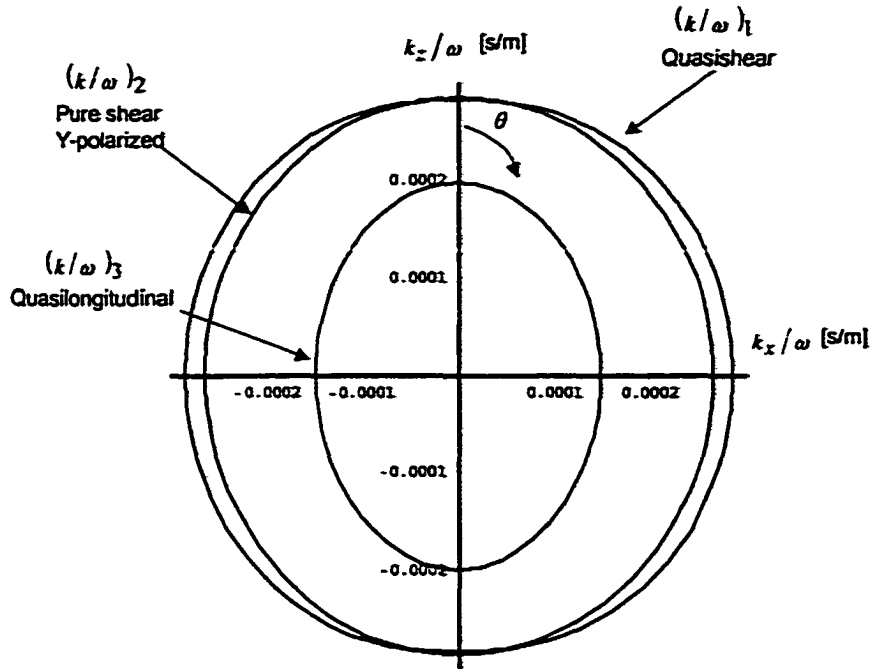
Figure 4.26: Slowness surfaces in Barium Sodium Niobate for the x-z plane.

and a quasilongitudinal wave with inverse velocity

$$\left(\frac{k}{\omega}\right)_3 = \frac{(2\rho)^{1/2}}{\sqrt{C_{55} + C_{11}\sin^2\theta + C_{33}\cos^2\theta + \left\{(C_{55} + C_{11}\sin^2\theta + C_{33}\cos^2\theta)^2 - 4\bar{C}\right\}^{1/2}}}$$

(4.91)

with

$$\bar{C} \equiv (C_{11}\sin^2\theta + C_{55}\cos^2\theta)(C_{55}\sin^2\theta + C_{33}\cos^2\theta) - (C_{13} + C_{55})^2\cos^2\theta\sin^2\theta$$

The slowness surfaces described by these equations are presented in Figure 4.26. Now, the pure transverse wave is the dominant wave since it is polarized along the y-direction and it is the only wave visible in our plots. From Figure 4.27, we calculate that the wave speed

131

of this wave along the x-axis is $3571.43\frac{m}{s}$ which gives a percent error of 1.98 percent with respect to the theoretical value for the pure shear wave.

Next, we consider wave propagation in the material cadmium sulfide (CdS) which belongs to the hexagonal $6mm$ crystal symmetry class. The stiffness coefficient matrix in this class has five independent constants and has the form

$$
\begin{pmatrix}
C_{11} & C_{12} & C_{13} & 0 & 0 & 0 \\
C_{12} & C_{11} & C_{13} & 0 & 0 & 0 \\
C_{13} & C_{13} & C_{33} & 0 & 0 & 0 \\
0 & 0 & 0 & C_{44} & 0 & 0 \\
0 & 0 & 0 & 0 & C_{44} & 0 \\
0 & 0 & 0 & 0 & 0 & C_{66}
\end{pmatrix}
\tag{4.92}
$$

with

$$
C_{66} = \frac{1}{2}\left(C_{11} - C_{12}\right)
\tag{4.93}
$$

Figure 4.29 shows contour plots of the z-component displacement in the x-y plane. From Auld, we expect a pure shear wave polarized parallel to the z-axis, a pure shear wave polarized perpendicular to the z-axis, and a pure longitudinal wave to propagate in this plane. The inverse velocity of these waves are simply

$$
\left(\frac{k}{\omega}\right)_1 = \left(\frac{\rho}{C_{44}}\right)^{1/2}
\tag{4.94}
$$

$$
\left(\frac{k}{\omega}\right)_2 = \left(\frac{\rho}{C_{66}}\right)^{1/2}
\tag{4.95}
$$

$$
\left(\frac{k}{\omega}\right)_2 = \left(\frac{\rho}{C_{11}}\right)^{1/2}
\tag{4.96}
$$

The inverse velocity surfaces for these waves are show in Figure 4.28. Since we are looking at the z-component displacement, we only see the pure shear wave polarized parallel to the

132
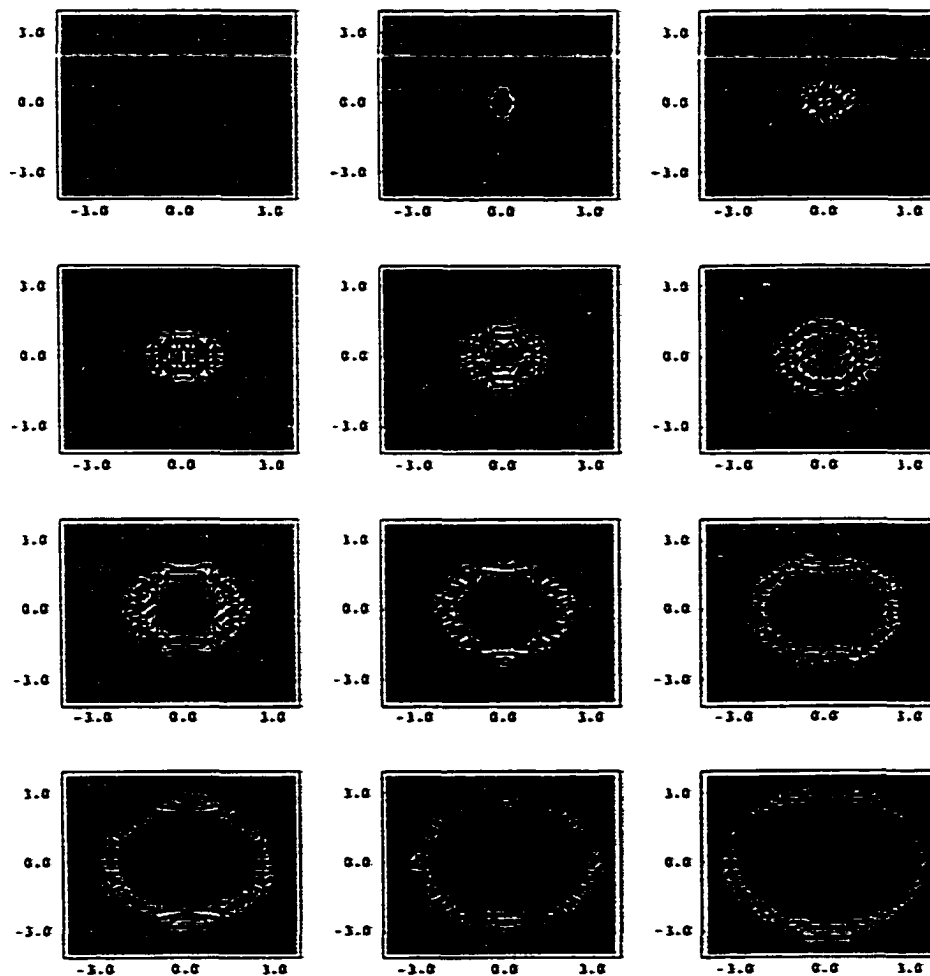
Figure 4.27: Contour plots of the y-component displacement in the x-z plane for BaNaNb at time intervals of 0.8 μs. z-axis is vertical.

133
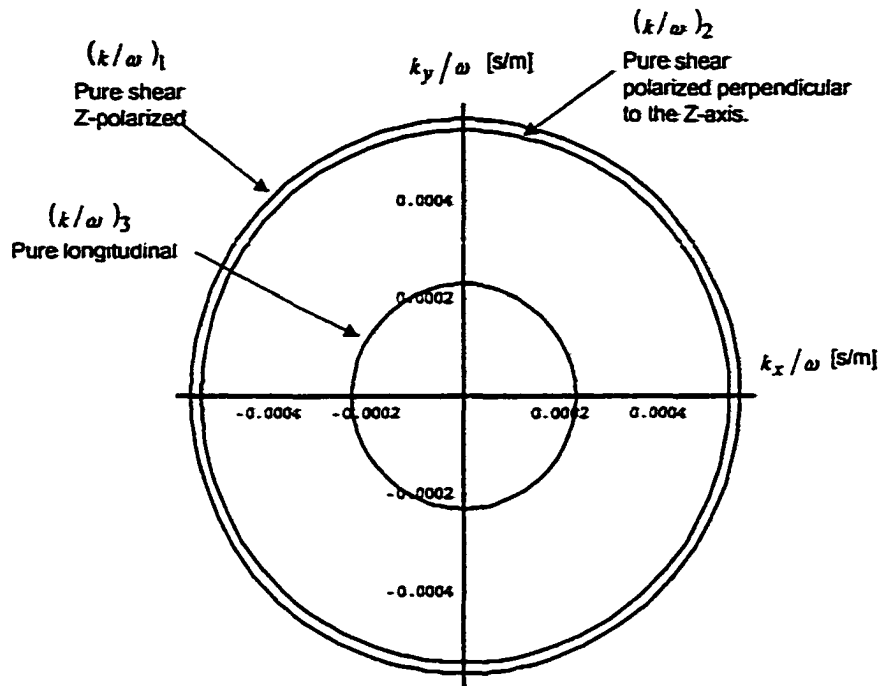
Figure 4.28: Slowness surfaces in CdS for the x-y plane.

z-axis in Figure 4.29. We calculate that the shear wave speed is $1757.81\frac{m}{s}$ which represents an error of 0.49 percent from the theoretical value

$$c_{T_{11}} = \sqrt{\frac{C_{44}}{\rho}} = \sqrt{\frac{1.504 \times 10^{10}}{4820}} = 1766.4\frac{m}{s}$$

As a final example, we consider wave propagation in rutile which belongs to the tetragonal $3/mmm$ crystal symmetry class. The stiffness matrix for this class has six independent

134
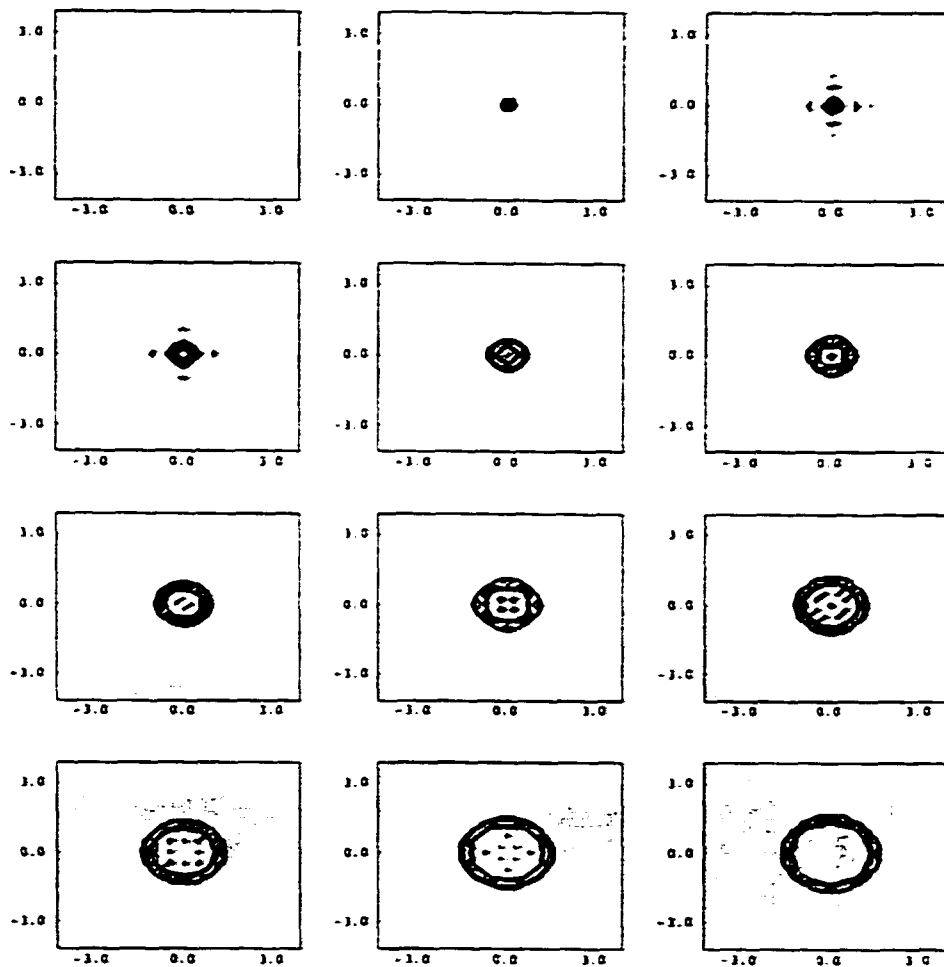
Figure 4.29: Contour plots of the z-component displacement in the x-y plane for CDS. at time intervals of 0.8 μs. y-axis is vertical.

135

constants and is of the form

$$
\begin{pmatrix}
C_{11} & C_{12} & C_{13} & 0 & 0 & 0 \\
C_{12} & C_{11} & C_{13} & 0 & 0 & 0 \\
C_{13} & C_{13} & C_{33} & 0 & 0 & 0 \\
0 & 0 & 0 & C_{44} & 0 & 0 \\
0 & 0 & 0 & 0 & C_{44} & 0 \\
0 & 0 & 0 & 0 & 0 & C_{66}
\end{pmatrix}
\tag{4.97}
$$

Figure 4.31 shows contour plots of the z-component displacement in the x-y plane. Again, darker regions represent larger positive amplitude. In this plane, solutions of the Christoffel equations permit a pure shear wave polarized along the z-axis, with inverse velocity

$$
\left(\frac{k}{\omega}\right)_1 = \left(\frac{\rho}{C_{44}}\right)^{1/2}
\tag{4.98}
$$

a quasishear wave with inverse velocity

$$
\left(\frac{k}{\omega}\right)_2 = \frac{(2\rho)^{1/2}}{\sqrt{C_{11} + C_{66} - \left\{(C_{11} - C_{66})^2 \cos^2 2\phi + (C_{12} + C_{66})^2 \sin^2 2\phi\right\}^{1/2}}}
\tag{4.99}
$$

and a quasilongitudinal wave with inverse velocity

$$
\left(\frac{k}{\omega}\right)_3 = \frac{(2\rho)^{1/2}}{\sqrt{C_{11} + C_{66} + \left\{(C_{11} - C_{66})^2 \cos^2 2\phi + (C_{12} + C_{66})^2 \sin^2 2\phi\right\}^{1/2}}}
\tag{4.100}
$$

where ϕ is the polar angle. The slowness surfaces are illustrated in Figure 4.30. Again, the shear wave polarized along the z-axis is the dominant wave in this representation since we are looking at the z-component of displacement. From Figure 4.31, we calculate that the wave speed of the transverse wave is $5263.16\frac{m}{s}$. The theoretical value is given as

$$
c_T = \sqrt{\frac{C_{44}}{\rho}} = \sqrt{\frac{12.39 \times 10^{10}}{4260}} = 5393.0\frac{m}{s}
$$

which gives a percent error of 2.4 percent. The quasilongitudinal wave is visible when we

136
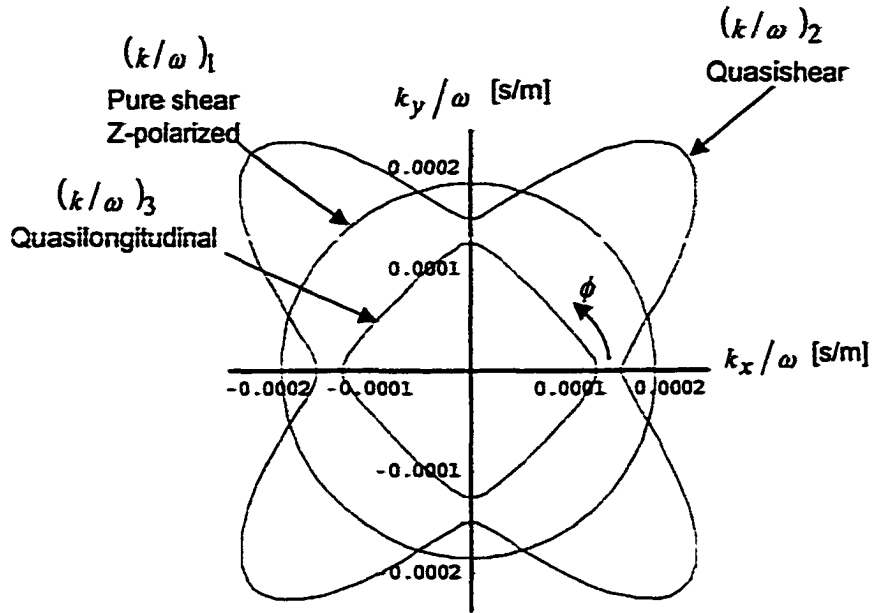
Figure 4.30: Slowness surfaces in rutile for the x-y plane.

look at the y-component displacement in the x-y plane which is shown as contour plots in Figure 4.32. Here, we can clearly see that the quasilongitudinal wave does not propagate in the circular shape of previous examples. From Auld, the quasilongitudinal wave propagates along the diagonal with a speed given by

$$c_{ql}^4 = \sqrt{\frac{C_{11} + 2C_{66} + C_{12}}{2\rho}} = 9789.45 \frac{m}{s}$$

From Figure 4.32 we calculate the quasilongitudinal wave speed along the diagonal bewtween the y and x-axes as $9428.09 \frac{m}{s}$ which represents a 3.7 percent error.

Figure 4.34 shows the y-component displacement in the x-z plane. A pure transverse wave polarized along the y-axis propagates in this plane with inverse velocity

$$\left(\frac{k}{\omega}\right)_2 = \frac{\rho^{1/2}}{\sqrt{C_{66} \sin^2 \theta + C_{44} \cos^2 \theta}} \tag{4.101}$$

137
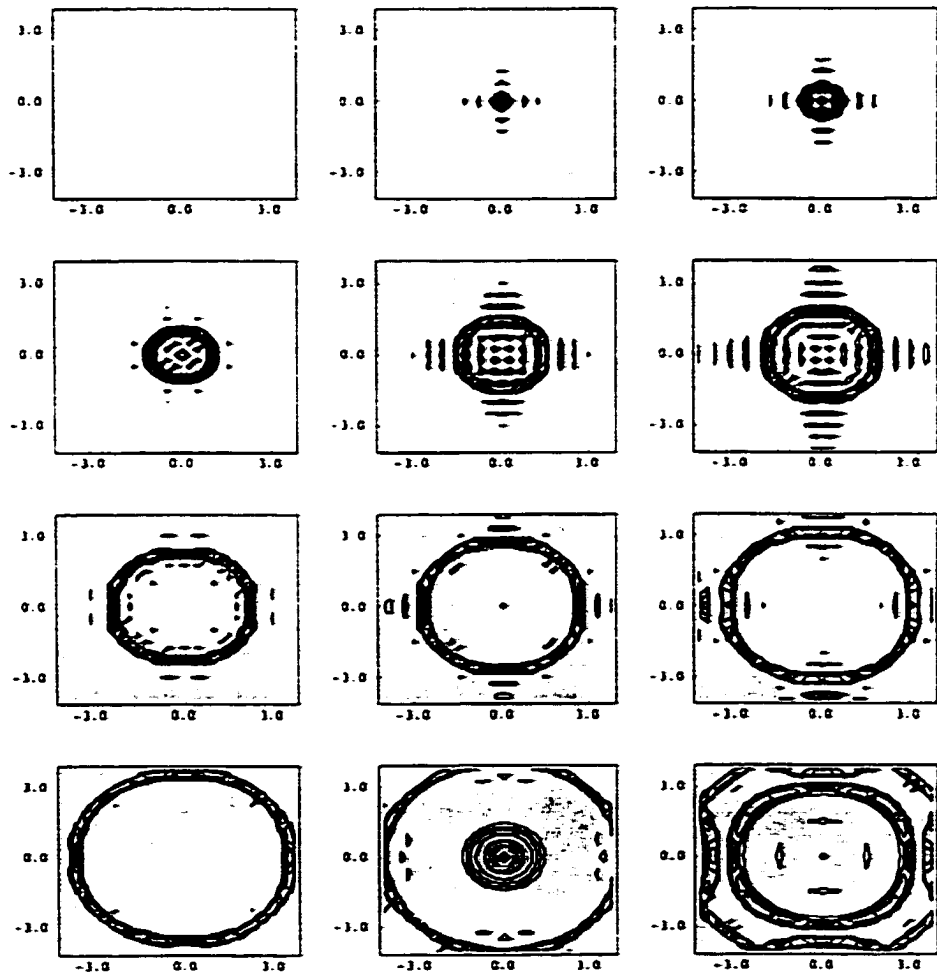
Figure 4.31: Contour plots of the z-component displacement in the x-y plane for rutile at time intervals of 0.8 μs. y-axis is vertical.

138
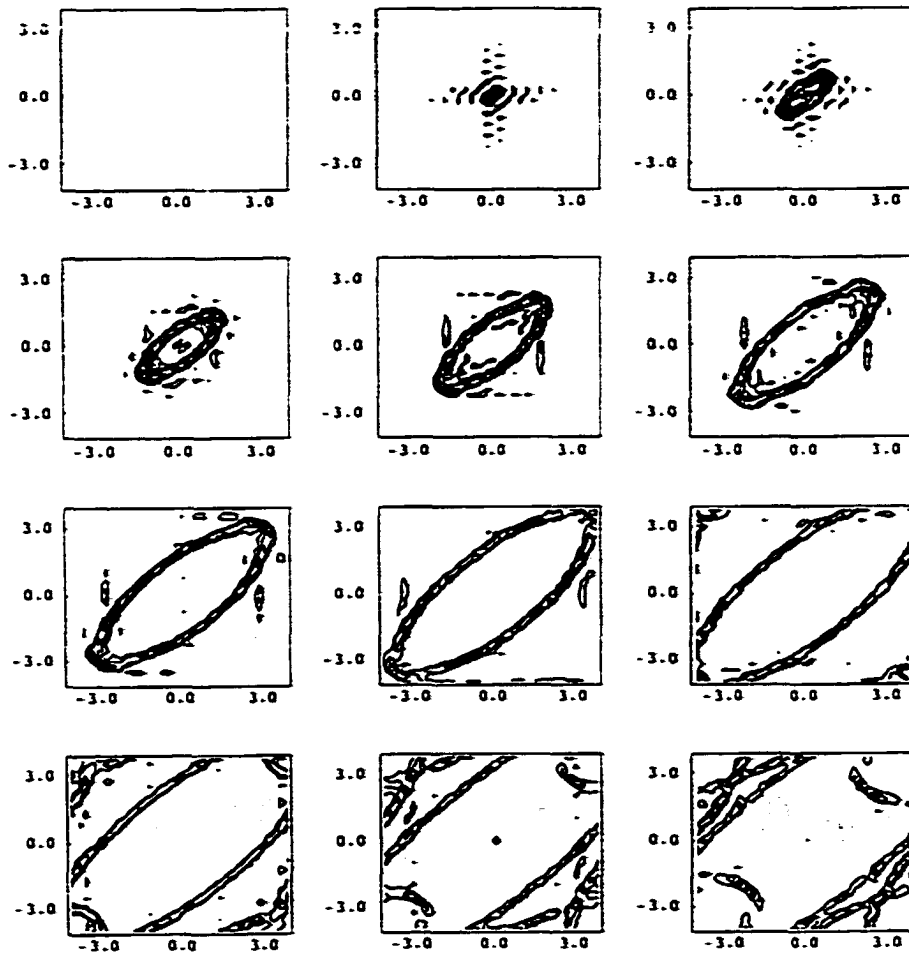
Figure 4.32: Contour plots of the y-component displacement in the x-y plane for rutile at time intervals of 0.8 μs. y-axis is vertical.

139

There is also a quasishear and quasilongitudinal wave described respectively by

$$\left(\frac{k}{\omega}\right)_1 = \frac{(2\rho)^{1/2}}{\sqrt{A - (B^2 + C)^{1/2}}} \tag{4.102}$$

and

$$\left(\frac{k}{\omega}\right)_3 = \frac{(2\rho)^{1/2}}{\sqrt{A + (B^2 + C)^{1/2}}} \tag{4.103}$$

with

$$A \equiv C_{11}\sin^2\theta + C_{33}\cos^2\theta + C_{44}$$

$$B \equiv (C_{11} - C_{44})\sin^2\theta + (C_{44} - C_{33})\cos^2\theta$$

$$C \equiv (C_{13} - C_{44})^2 \sin^2 2\theta$$

Figure 4.33 presents these slowness surfaces. Along the x-axis the pure shear wave velocity given by equation (4.101) is

$$c_T = \sqrt{\frac{C_{66}}{\rho}} = \sqrt{\frac{18.86 \times 10^{10}}{4260}} = 6653.7\frac{m}{s}$$

The speed computed from Figure 4.34 for the first wave arrival is $6666.67\frac{m}{s}$ or 0.19 percent error. The computed speed for the second wave arrival along the x-axis is $4545.45\frac{m}{s}$ which represents a 15 percent error realtive to the quasishear wave. We note that the two waves in our plots travel with the same velocity along the z-axis as expected from the slowness surface in Figure 4.33.

140
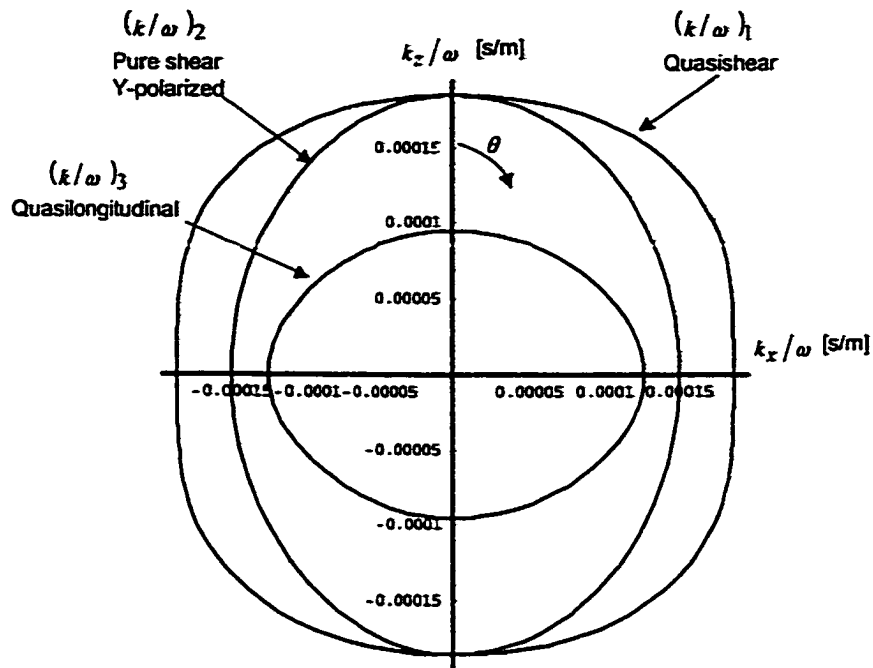
Figure 4.33: Slowness surfaces in rutile for the x-z plane.

4.2 Computing the Thermoelastic Strain Displacement

In this section, we describe how we model the thermoelastic displacement from the thermal fields computed in Chapter 3 and the elastic Green's function which were computed in the previous sections. Calculating the thermoelastic displacement is accompished in two steps. First, we determine the force generated by the thermal fields. Second, we convolve this force with the elastodynamic Green's function.

To calculate the force generated by the thermoelastic source, we consider equation (3.1). Ignoring body forces, equation (3.1) indicates that the thermal field is related to the

141
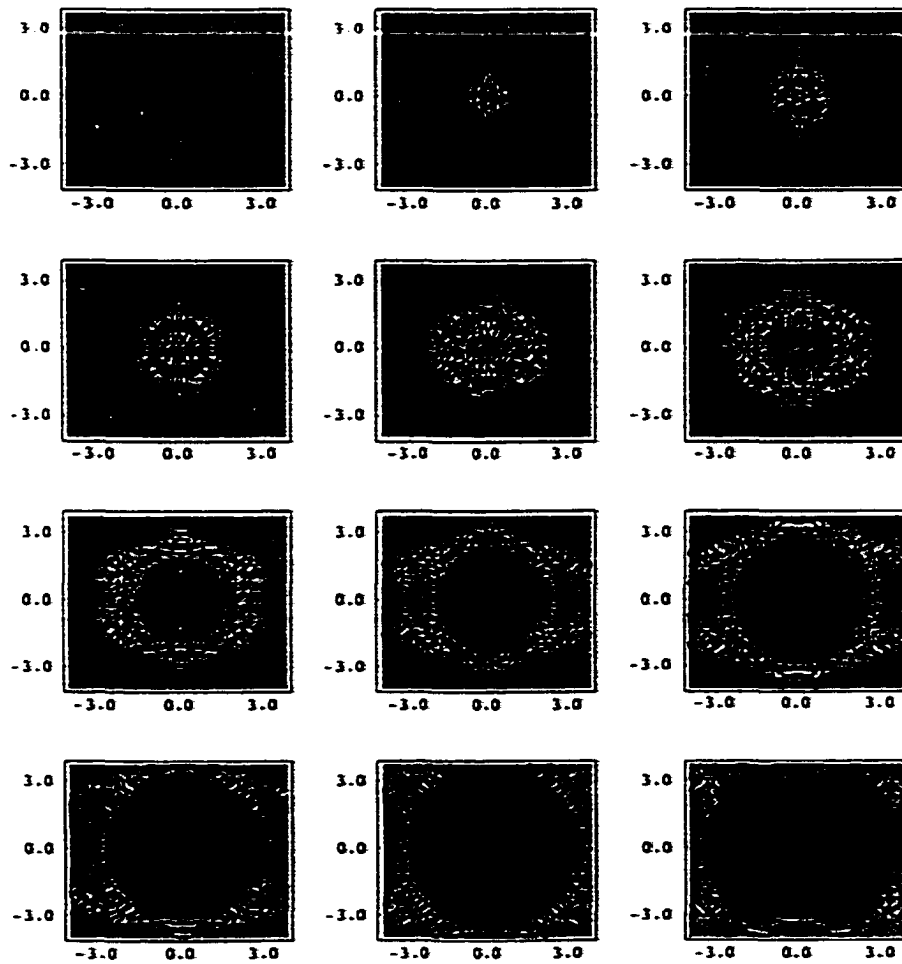
Figure 4.34: Contour plots of the y-component displacement in the x-z plane for rutile at time intervals of 0.8 μs. z-axis is vertical.

142

elastic displacement according to.

$$\rho\ddot{u}_i - C_{ijkl}\,u_{k,ij} = \beta_{ij}\theta_{,j} \tag{4.104}$$

The right hand side of equation (4.104) represents the thermal forcing function and is composed of the thermal moduli tensor, β_{ij} and the gradient of the thermal field, $\theta_{,j}$. Since we have assumed that our materials are thermally isotropic we may rewrite the thermal force as [91]

$$\frac{2\alpha\,(1+\nu)}{(1-2\nu)}\theta_{,j} \tag{4.105}$$

where α is the thermal linear expansion coefficient and ν is the Poission's ratio. We are most interested in the out of plane or z-component displacement since that is the quantity measured in our experiments. We see from the subscripts in equation (4.104) that the z-component displacement depends upon the derivative of the thermal field with respect to the z-direction. Accordingly, we compute the thermal force given by equation (4.105) as

$$\frac{2\alpha\,(1+\nu)}{(1-2\nu)}\frac{\partial\theta(x,y,z,t)}{\partial z} \tag{4.106}$$

In the previous chapter we described how we computed the thermal field $\theta(x,y,z,t)$. This field was computed along the grid points

$$x_i = (i - n_x - 1) \times \Delta x, \quad i = 1\ldots 2n_x$$

$$y_j = (j - n_y - 1) \times \Delta y, \quad j = 1\ldots 2n_y$$

$$z_k = k \times \Delta z, \quad k = 1\ldots n_z + 1$$

$$t_h = h \times \Delta t, \quad h = 1\ldots n_t$$

143

We then use a simple forward difference approximation

$$\frac{\partial \theta(x,y,z,t)}{\partial z} \approx \frac{\theta(x_i,y_j,z_{k+1},t_h) - \theta(x_i,y_j,z_k,t_h)}{\Delta z},\qquad \begin{cases} i = 1 \ldots 2n_x \\ j = 1 \ldots 2n_y \\ k = 1 \ldots n_z \\ h = 1 \ldots n_t \end{cases} \qquad (4.107)$$

to numerically compute the derivative of the thermal field at each point (x_i, y_j, z_j, t_h). Then, we can compute the force according to equation (4.106) with the appropriate values for the thermal expansion coefficient and the Poisson's ratio.

Once the force has been computed, we convolve the four-dimensional force matrix with the four-dimensional elastic Green's function matrix. We use *Mathematica* to perform this convolution. *Mathematica 4.0* has a routine called "ListConvolve" which performs the cyclic convolution of two lists. This routine works for nested lists with any number of dimensions. We tested the *Mathematica* routines with three-dimensional Gaussian functions as well as with other three-dimensional functions that exhibited no symmetry to ensure that the routines produced the expected results. To do this, we computed the numerical Fourier transforms of the functions and then used the convolution rule in equation (3.65) to obtain the convolution. We compared this convolution to the convolution generated by the *Mathematica* routines and found them to be identical.

144

Chapter 5

Experimental Results

In this chapter we describe our experiments to study laser and material parameter effects on the generation of ultrasound waves and present an analysis of the data. We used a modular laser system that allowed us to vary the pulse width and wavelength of the generation laser. Ultrasound was generated in four materials with each laser configuration and the ultrasonic waveforms were analyzed in both the time and frequency domain. From this analysis, we make conclusions about the relationship between the varied parameters and the generated ultrasound.

5.1 Experimental Setup

Figure 5.1 illustrates a schematic of our experimental setup. An SEO 1-2-3 laser was used as the generation laser. This laser can accommodate different laser crystals and Q-switching mechanisms so that both the wavelength and pulse width can be varied. The five different laser crystals used in our experiments were Alexandrite (0.720-0.790 μm), Nd:YAG (1.064 μm), Nd:YAG (1.32μm), CTH:YAG (Chromium, Thulium, Homium:YAG at 2.10 μm), and Er:YAG (2.94 μm). Three Q-switching mechanisms were available to vary

145

Wavelength	Q-Switch	Pulse Width [ns]
Alexandrite 0.720-0.790 μm	EO	80-120
	AO	100-150
	RM	150-250
Nd:YAG 1.064 μm	EO	20-60
	AO	70-150
	RM	50-250
Nd:YAG 1.320 μm	RM	150-250
CTH:YAG 2.1 μm	EO	100-150
	RM	150—250
Er:YAG 2.94 μm	RM	150-250

Table 5.1: Theoretical wavelengths and pulse widths available for experiments.

the pulse width. These included an electro-optic (EO) Q-switch, an acousto-optic (AO) Q-switch, and a rotary mirror (RM) Q-switch. Table 5.1 lists the different laser wavelength and pulse width configurations that were available for our experiments. This experimental phase space of pulse width versus wavelength is shown graphically in Figure 5.2.

The generation beam from the SEO was passed through a Coherent VARM attenuator and was normally incident on one of four different samples. The first sample was an aluminum plate approximately 7.5 cm by 7.5 cm and 1.255 cm thick (0.494 inches). The second sample was a 0.452 cm (0.178 inch) thick woven graphite/epoxy composite sample approximately 10 cm by 10 cm. The third sample was a 0.699 cm (0.275 inch) thick epoxy plate of Hercules 3501-6 Amine-cured epoxy approximately 15 cm by 15 cm. This epoxy was the binder materials used in the fourth sample which was a woven graphite/epoxy composite with translaminar Kevlar stitches. This fourth sample was 1.473 cm (0.58 inch) thick and consisted of ten stacks of [45/-45/0$_2$/90/0$_2$/-45/45] AS-4-3501-6 graphite epoxy material stitched together with Kevlar reinforcements in rows spaced 0.5 to 1.0 cm apart

146

Lecroy 9354

Fabry-Perot Interferometer

MR106 Receiver

To Dell 133 MHz PC

UltraOptec LISOR

Newport 875 PIN Photodiode Supply

Molectron MAX 5100
Power Meter

Nikon Lens

Newport Photodiode*

Laser Crystal

Alignment HeNe

Molectron PM10VI

Fiber Optics

Sample

Coherent VARM Attenuator

SEO 1-2-3

Generation Laser

Adlas 532 nm Detection Laser

Coherent BeamView

Frame Grabber

Electrophysics

CCD Camera

EO   AO   RM
Q-Switches

Figure 5.1: Schematic of experimental setup.

with stitch spacing approximately 0.254 cm. A piece of masking tape was used to mark the generation spot on the two graphite/epoxy samples so that the measurements were made at the same place in all experiments. These samples are shown in Figure 5.3 and the masking tape marker is visible on the woven graphite/epoxy sample. With the sample removed, the power of the laser was measured with a Molectron model Power MAX 5100 power meter and PV10VI energy detector. The laser beam profile was also measured with an Electrophysics model 7290 CCD camera and Coherent Beamview[TM] software.

The pulse width of the generation beam was measured by observing the backscattered light from the sample with a PIN diode photodetector. For the Alexandrite and first

147
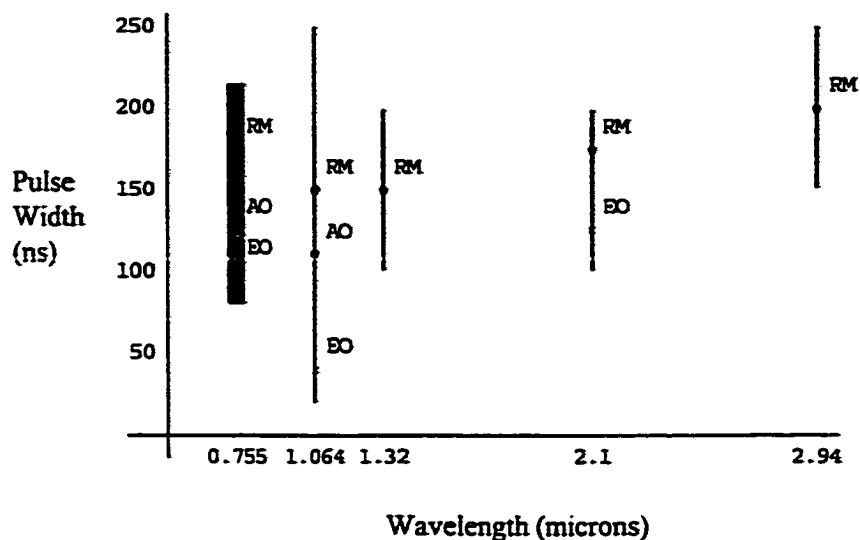
Figure 5.2: Theoretical experimental phase space of pulse width versus wavelength.

Nd:YAG wavelength (1.064 μm), a Newport Model 875 silicon PIN diode detector was used. For the second Nd:YAG line (1.32 μm) and the CTH:YAG line, a Thor model DET310 Germanium PIN detector had to be used. The Er:YAG line required a EG&G Judson J12 series INAS detector. The response time of this detector was not fast enough to resolve pulses less than 0.5 microseconds wide. In most cases, the photodetector response was used to trigger the data acquisition. In some cases, the response was too small and the laser lamp discharge was used as a trigger.

An UltraOptec LISOR Fabry-Perot interferometer was used to measure epicentral ultrasonic displacement on the opposite side of the sample. The inteferometer was operated in the "reflection" mode which is more sensitive to the frequencies of interest in our work. An Adlas 400 mW frequency doubled Nd:YAG (532 nm) laser was used as the detection laser. Light from the Adlas was delivered through fiber optics to a Nikon camera lens which

148
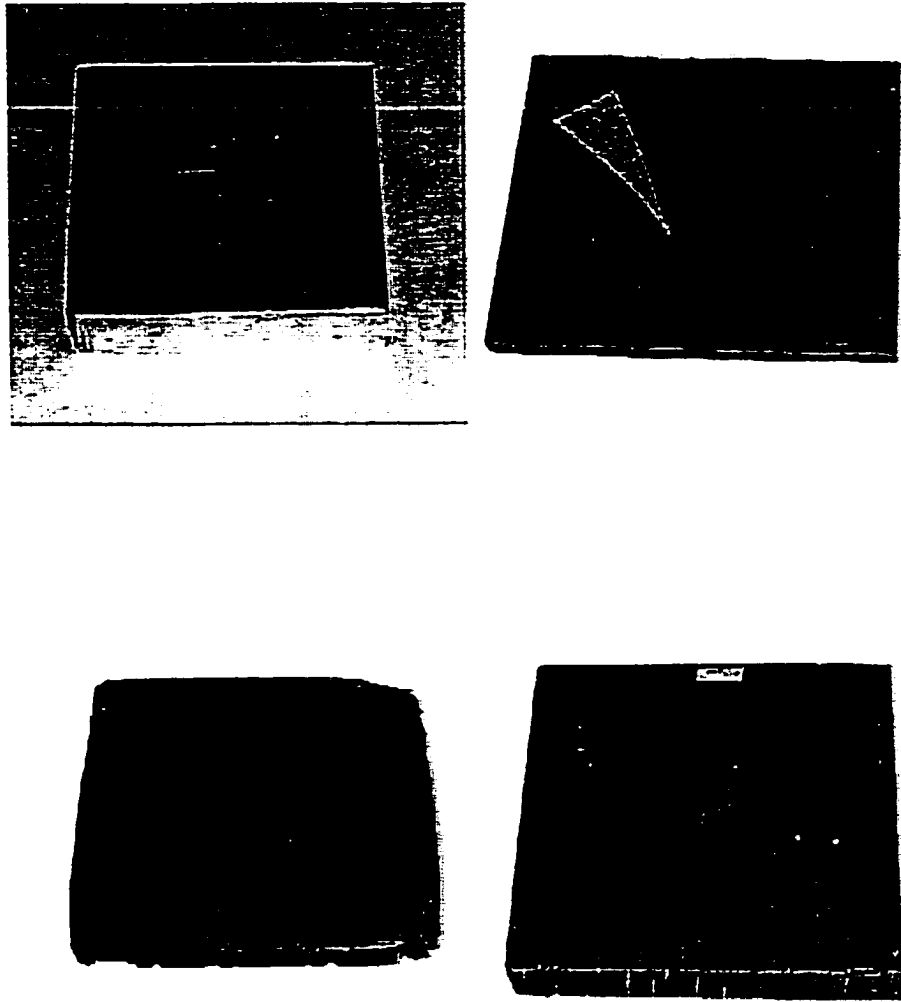
Figure 5.3: Samples used in the experiments: Clockwise from the upper left: Aluminum plate, woven GR/Epoxy composite, epoxy plate, Kevlar reinforced woven GR/Epoxy composite.

149

focused the light onto a one mm spot on the sample. This spot was made to coincide with the HeNe laser used to align the generation laser cavity. This ensured that the detection spot was directly opposite the generation spot. A matching Nikon lens collected the reflected light which was transferred by fiber optics to the interferometer. The output signal from the inteferometer was amplified by a Metrotek MR106 receiver and recorded by a Lecroy 9354 digital oscilloscope. Lecroy "Scope Explorer" software was used to store the recorded waveforms on a PC for further manipulation.

We had difficulties achieving the pulse widths listed in Table 5.2 at power levels that were adequate for thermoelastic (nondamaging) ultrasonic generation. We used the attenuator and adjustments to the laser power output to obtain power levels that would not damage the samples, typically around 10-15 mJ per pulse. However, we found that the pulse widths depended strongly upon the cavity alignment and the power settings of the laser. In most cases, the pulse widths tabulated in Table 5.2 could only be obtained with the laser running at near maximum power which ranged from 20 to 400 mJ per pulse. The lowest attenuation setting on the VARM transmitted ten percent of the light and the attenuator steps were coarse enough that it was not always possible to produce the pulse width listed in Table 5.2 at a nondamaging power level. Furthermore, since the pulse widths depended upon the wavelength of the laser, it was not possible to obtain consistent pulse widths between each laser wavelength even though the same Q-switching mechanism was used. Figure 5.4 shows the average values of the pulse widths that were obtained at each wavelength along with the theoretical values presented in Figure 5.2.

As noted above, the photodiode detector could not respond fast enough at the Er:YAG wavelength and the pulse width could not be accurately measured. To better estimate the pulse width, the Newport 875 photodetector was used to measure the light produced when this laser vaporized surface material on one of the samples.

150

400

300

200

100

0.755 1.064 1.32   2.1   2.94

RM
RM
EO
AO
RM
RM
AO
RM
EO
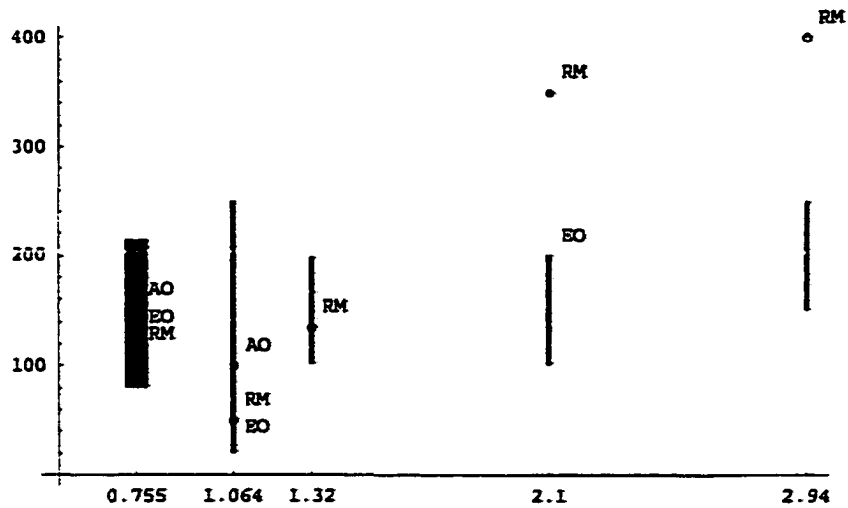
Figure 5.4: Actual experimental phase space of pulse width versus wavelength.

A final difficulty was the maintenance of the LISOR inteferometer and Adlas laser. The sensitivity of the interferometer was very dependent on the alignment of the Fabry-Perot cavity and the amount of light collected. Through the course of our experiments, we found that it was difficult to optimize the alignment of the cavity. Furthermore, the Adlas laser exhibited some variability in its power output. In addition, we discovered in later work that a lens on one of the photodetectors in the LISOR had become damaged and consequently the LISOR exhibited a significant loss in sensitivity.

5.2 Results

In this section, we present the ultrasonic waveforms recorded in each material with each laser configuration. In addition, a Panametrics 10 MHz piezoelectic transducer driven by a model MP101 pulser and coupled by a thin film of vacuum grease was used to generate

151

ultrasound in each sample. The ultrasound was detected with the inteferometer on the opposite side for comparison with the laser generated signals and to calibrate the interferometer. We note that the time origin in the presented ultrasonic signals has been adjusted so that the most interesting features of the signals can be seen. The frequency spectrum of each signal is computed and discussed.

5.2.1 Aluminum

Transducer

The first plot in Figure 5.5 shows an average of 200 samples of the transducer signal obtained with the aluminum sample. The first arrival represents the longitudinal wave after traversing the thickness of sample one time. The second arrival represents the round-trip journey of the wave. The time interval between these two wave arrivals is approximately four microseconds. The round-trip distance through the sample is 2.51 cm giving a longitudinal wave velocity of 6275 $\frac{m}{s}$, which agrees with the value presented in the last chapter. In this plot, we also see the characteristic ringing associated with contact transducers and a viscous physical couplant. The second plot in Figure 5.5 shows the frequency content of the first wave arrival normalized to unity. We see that most of the energy is present in a frequency range of 10 MHz centered about 5 MHz.

Alexandrite (720-790 μm)

Electro-Optic Q-Switch   The first plot in Figure 5.6 shows the photodiode response for the Alexandrite laser operated with the electro-optic Q-switch. The full-width-half maximum (FWHM) of the pulse was approximately 125 ns. The second plot shows the intensity profile of the laser beam spot measured with the CCD camera. The beam spot radius was about 1.5 mm. The curves on the left and bottom edges show the intensity
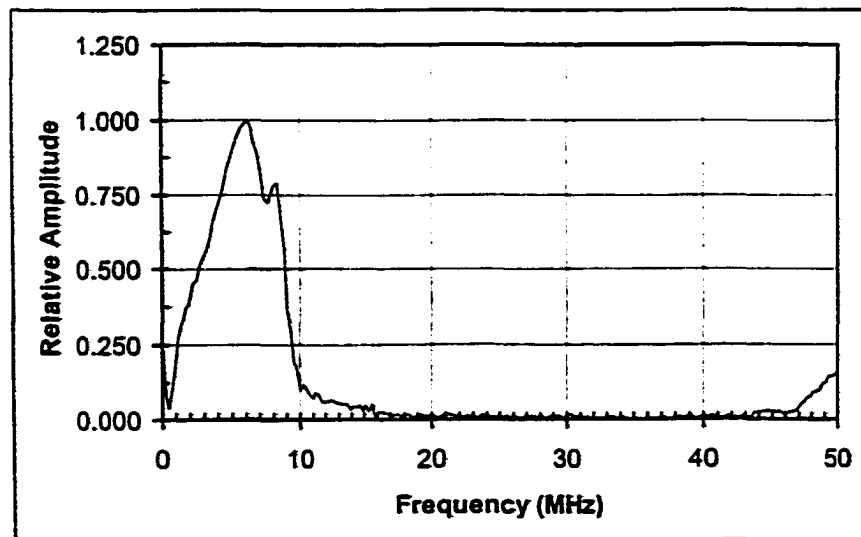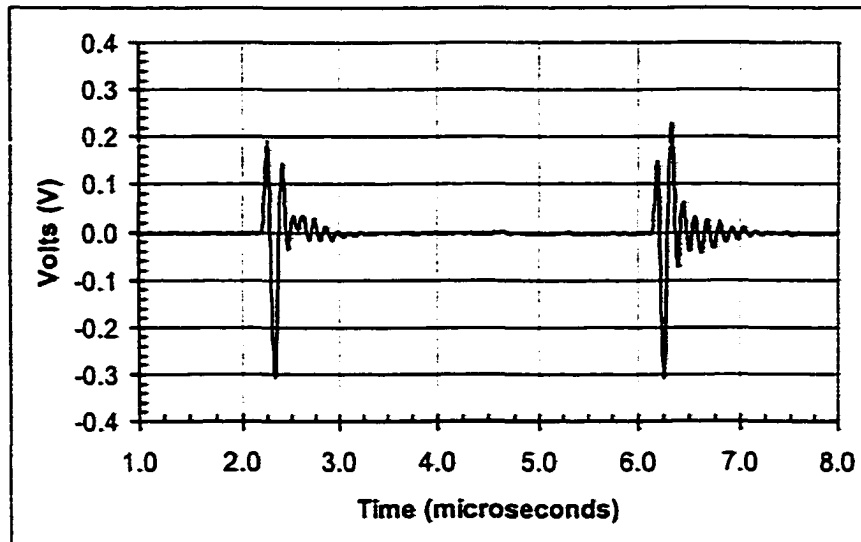
Figure 5.5: 10 MHz transducer response and frequency spectrum of the first wave arrival in the aluminum sample.

153

profile, and an ideal Gaussian function, at the point indicated by the cross-hair in the y and x-directions, respectively. We see that the beam was nearly a TEM_{00} mode. The first plot in Figure 5.7 shows an average of 200 samples of the ultrasonic waveform generated with 8 mJ per pulse reaching the aluminum sample. The negative spike near 2 μs represents the first arrival of the longitudinal wave. The second positive spike is the first arrival of the shear wave, which travels approximately twice as slowly. The round trip arrival of the longitudinal wave is barely visible just past 6 μs. The frequency spectrum of the signal is shown in the second plot. The thicker line represents the frequency content obtained by windowing 512 points centered about the first longitudinal wave arrival. The thinner line represents frequencies obtained from the same window centered around the first arrival of the shear wave. In both spectra, we see the strongest contributions from frequencies below 10 MHz. The longitudinal wave frequency is centered about 5 MHz and has a bandwidth of a few megahertz. The shear wave has a similar frequency bandwidth. Figure 5.9 shows a second average waveform and frequency spectrum obtained with the same settings except that a lens was used to expand the radius of the beam to approximately 2.5 mm. The intensity profile of this beam is shown in Figure 5.8. We see the same general features as in Figure 5.7 but the magnitude of the displacement has been reduced slightly because the energy density is smaller. Figure 5.10 shows another average waveform and frequency spectra of the longitudinal and shear wave arrivals. In this case, a thin film of vacuum grease was applied to the surface of the aluminum. The pulse width was also slightly longer at approximately 160 ns. We see that the longitudinal ultrasonic displacement is larger than in the previous examples. This is because the grease acts as a constraining layer and enhances the longitudinal wave mode. The shear wave has also been enhanced but its frequency content is similar to the previous examples. We also see some ringing in the longitudinal waves similar to the ringing found in the transducer signal. This is due

154

Figure 5.6: EO Q-swtiched Alexandrite (0.755 μm) laser. Top: Photodiode measurement of pulsewidth. Bottom: CCD measurement of beam profile.

155

Figure 5.7: Epicentral displacement in aluminum generated by the EO Q-switched Alexandrite laser.

156

Figure 5.8: Beam profile of EO Q-switched Alexandrite laser expanded with a lens.

to the ultrasound reflecting within the grease layer. This ringing produces slightly higher frequency components similar to the transducer frequency spectrum.

Acousto-Optic Q-Switch Figure 5.11 shows the pulse width and intensity profile obtained with the Alexandrite laser using the acousto-optic Q-switch. Here, the pulse width was approximately 150 ns and the beam radius was about 2.5 mm. Figure 5.12 shows the average ultrasonic signal and corresponding frequency spectrum generated in the aluminum sample. The power reaching the sample surface was approximately 10 mJ per pulse. The waveform is similar to the signal generated with the electro-optic Q-switch in Figure 5.7 except that the displacements are larger. In particular, the amplitude of the shear wave is slightly larger relative to the amplitude of the first longitudinal wave arrival. This may be

157
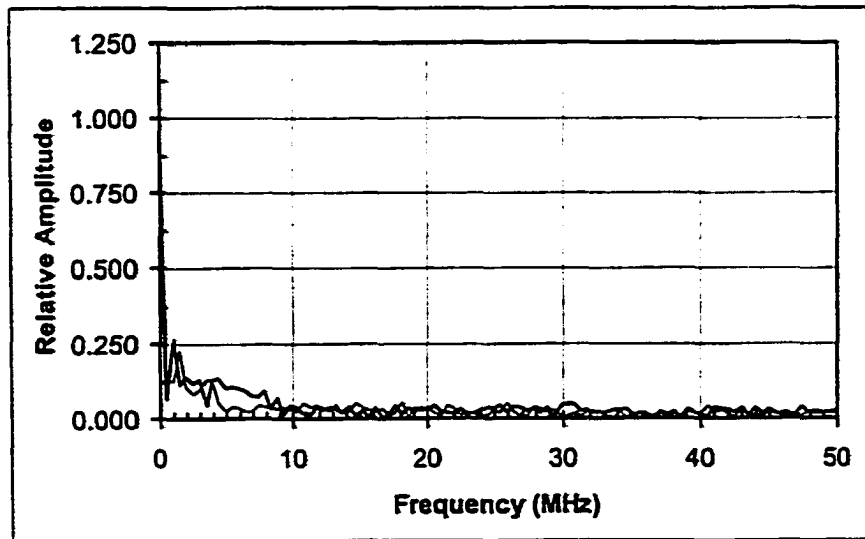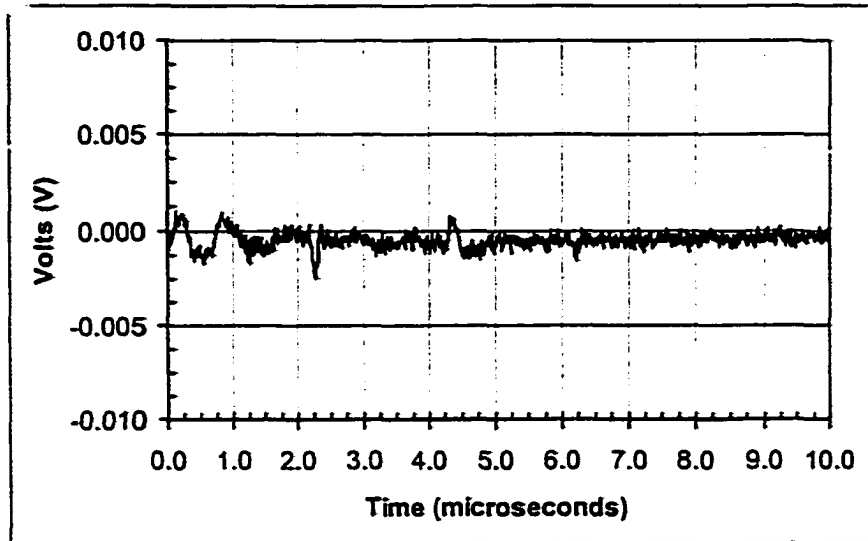
Figure 5.9: Epicentral displacement in aluminum generated by the EO Q-switched Alexandrite laser with expanded beam radius.

158
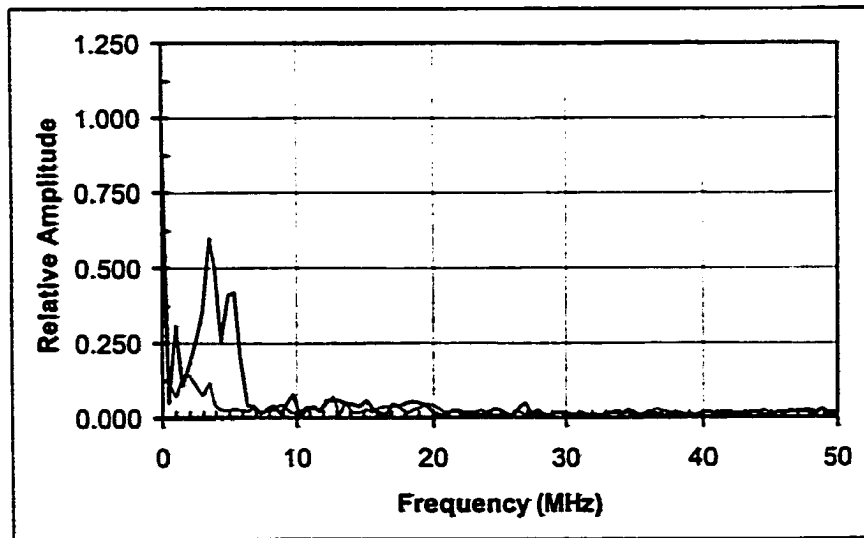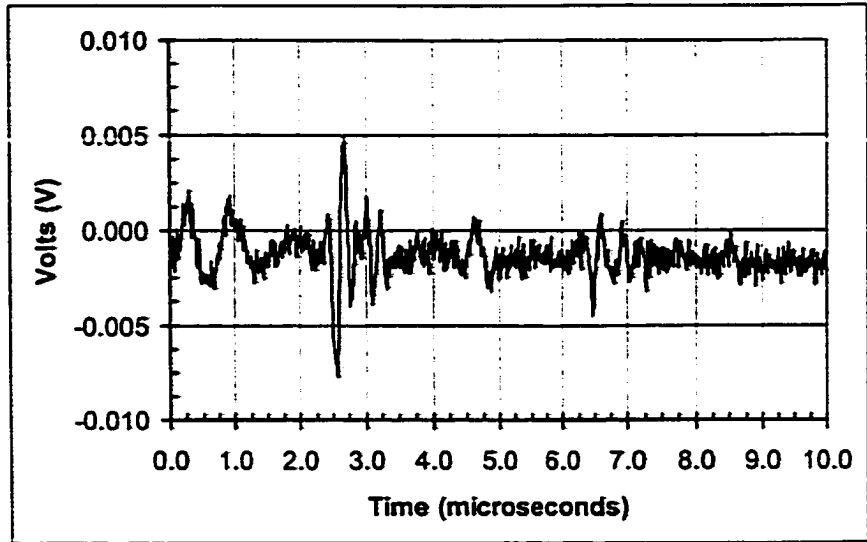
Figure 5.10: Epicentral displacement in aluminum generated by the EO Q-switched Alexandrite laser with a constraining layer of grease.

159

Figure 5.11: AO Q-swtiched Alexandrite (0.755 μm) laser. Top: Photodiode measurement of pulsewidth. Bottom: CCD measurement of beam profile.

160
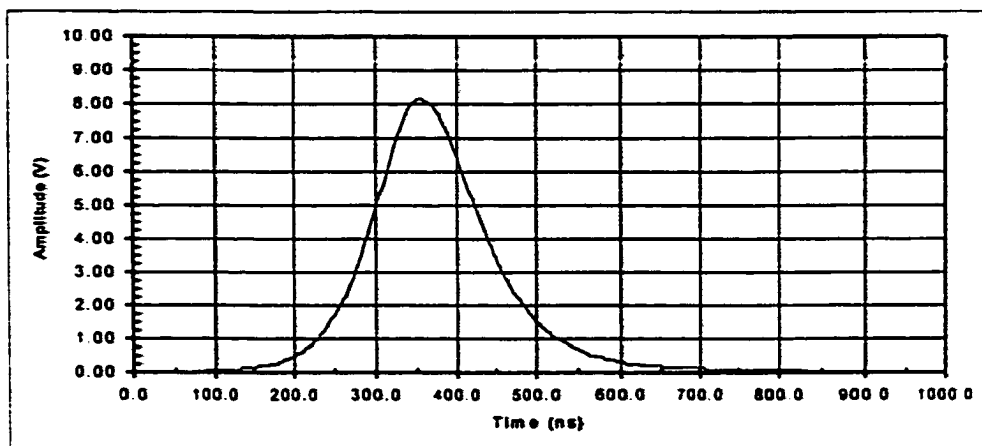
because the generation energy was slightly larger or because of the larger pulse width. The frequency spectrum does not show a clear component around 1 MHz but there is a broad range of contributions around 1 MHz. The shear wave has a sharper frequency content centered around 2 MHz.

Rotating Mirror Q-Switch Figure 5.13 shows the pulse width and intensity profile of the Alexandrite laser Q-switched with the rotary mirror. The pulse width was approximately 115 ns and the spot radius was about 2.0 mm with a lens used to expand the spot. Figure 5.14 shows the average ultrasonic signal and its frequency spectrum produced in aluminum. Approximately 7 mJ per pulse reached the aluminum surface and an extremely thin layer of grease approximately 200 microns thick had to be applied to get any signal at all. The ultrasonic signal is similar to previous examples where no grease was used except that the displacement amplitude is smaller. The lack of signal without grease may be because the energy level was lower. It is also possible that even though the sample surface had been cleaned with alcohol in the previous experiments, a very thin layer of grease or other contaminant was present. We see in the second plot that the frequency content of both the first longitudinal and shear wave arrival is almost obscured by noise but there is a contribution from a small band between 1 and 5 MHz. Figure 5.15 shows another averaged signal and frequency spectrum. The settings were the same as in the previous experiment except that the layer of grease was thicker. We see the longitudinal modes have been greatly enhanced and the shear wave mode is almost not visible. We also see the ringing of the ultrasound in the layer of grease. This ringing appears as a relatively sharp spike in the frequency spectrum around 2 MHz.
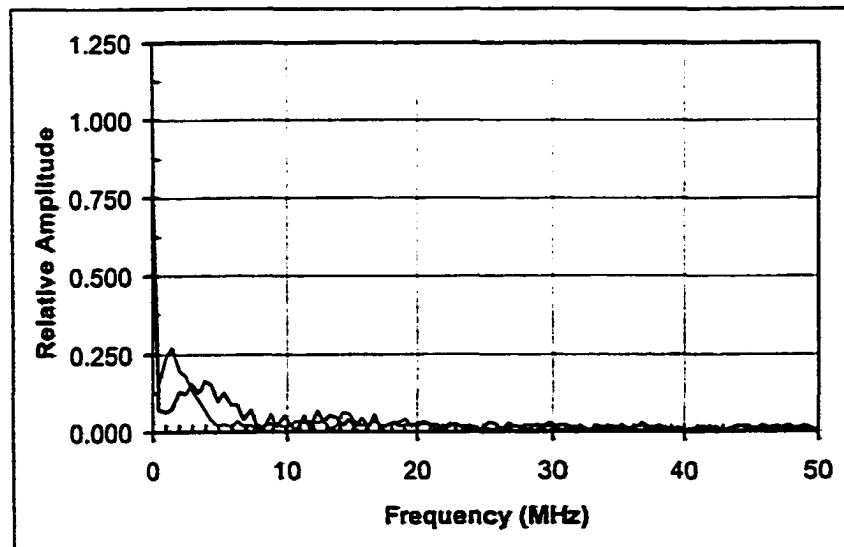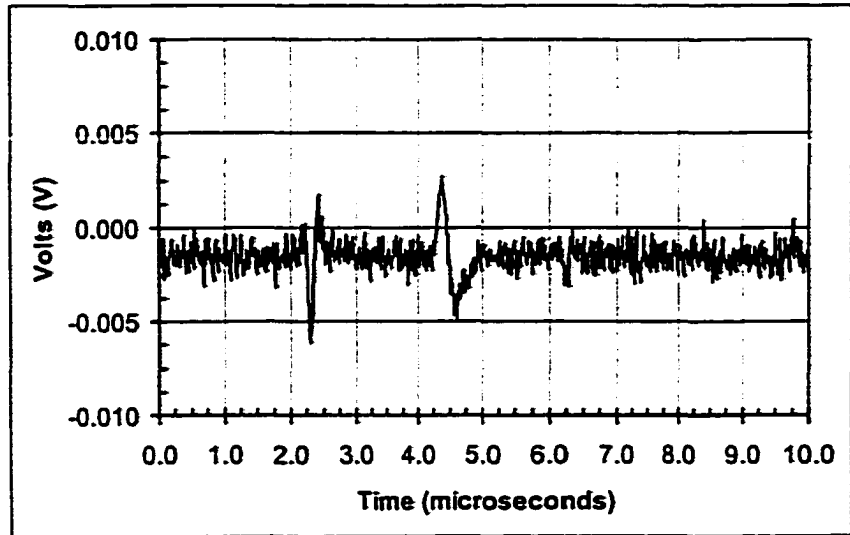
Figure 5.12: Epicentral displacement in aluminum generated by the AO Q-switched Alexandrite laser.
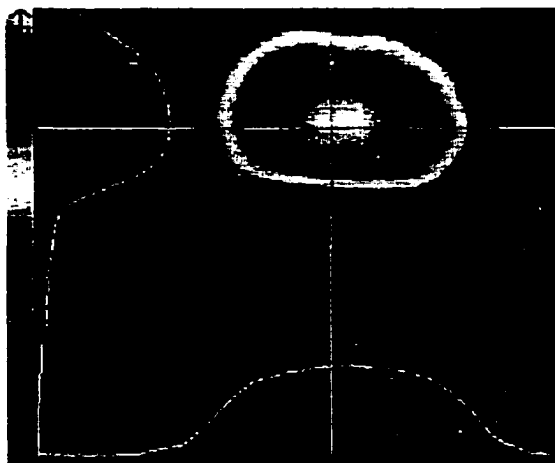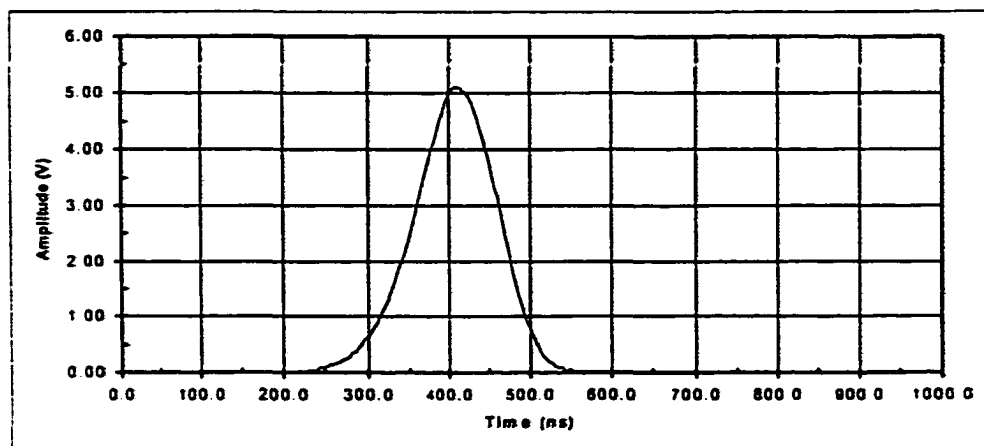
162

Figure 5.13: RM Q-swtiched Alexandrite (0.755 μm) laser. Top: Photodiode measurement of pulsewidth. Bottom: CCD measurement of beam profile.

163
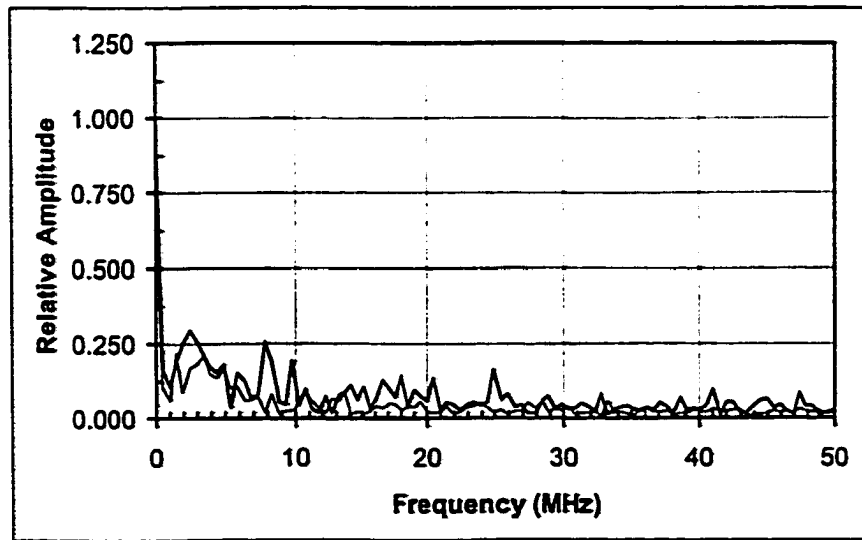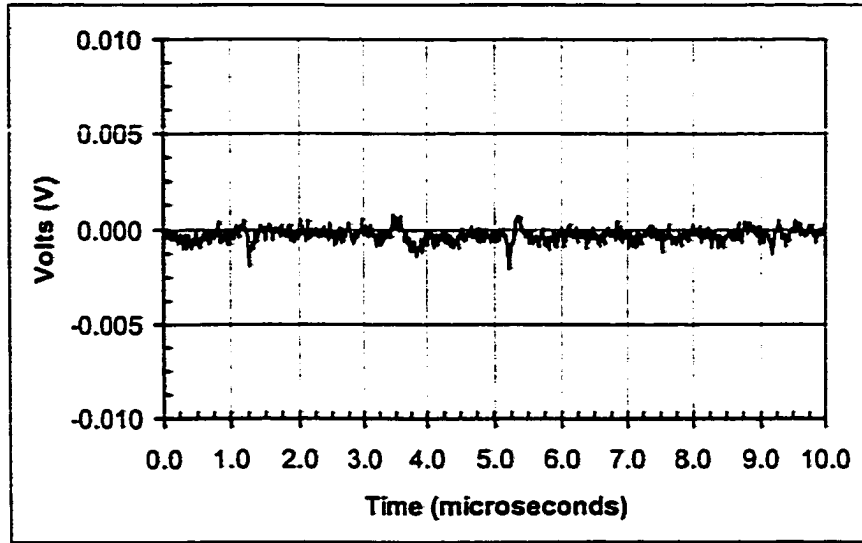
Figure 5.14: Epicentral displacement in aluminum generated by the RM Q-switched Alexandrite laser.

164
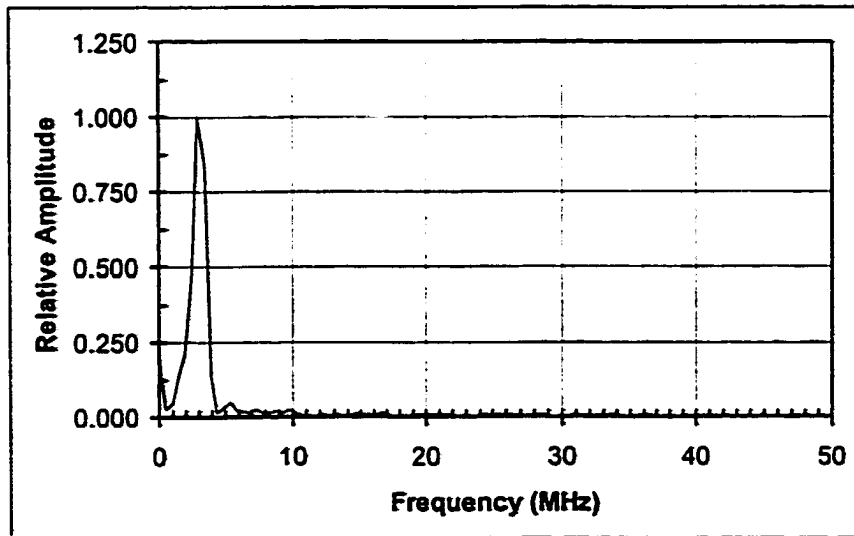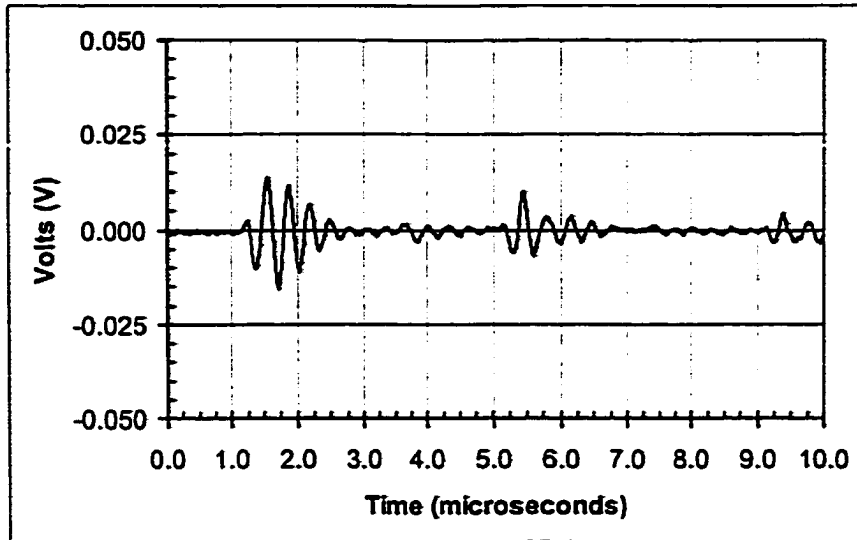
Figure 5.15: Epicentral displacement in aluminum generated by the RM Q-switched Alexandrite laser with a thicker layer of grease.

165

Nd:YAG (1.064 μm)

Electro-Optic Q-Switch The first plot in Figure 5.16 shows the pulse width of the Nd:YAG laser operated with the electro-optic Q-switch. We see that the FWHM of the pulse was approximately 25 ns. The intensity profile in the second plot indicates that the beam radius was approximately 2 mm. Figure 5.17 shows the average ultrasonic signal generated in the aluminum sample and the corresponding frequency spectrum. The energy delivered to the sample was approximately 8 mJ per pulse. We can compare this signal with the signal generated by the Alexandrite laser with the electro-optic Q-switch. The time scale has been expanded from the scale in Figure 5.7 but we see that the waveform has the similar features except that the amplitude is larger and the signal to noise ratio is much better. However, we also see that the longitudinal wave arrivals have a higher frequency than the waves due to the Alexandrite laser. This is because the pulse width of the Nd:YAG laser is so much smaller than the pulse width of the Alexandrite laser. We can explain the amplitude difference by considering the instantaneous power density in each pulse. Assuming that the laser power was absorbed at the surface, which is appropriate for the aluminum sample [1], the instantaneous power density of the Alexandrite pulse was approximately

$$\frac{8 \text{ mJ/Pulse} \times \left(125 \frac{\text{ns}}{\text{pulse}}\right)^{-1}}{\pi (1.5 \text{ mm})^2} = 9054.15 \frac{\text{MW}}{\text{m}^2}$$

and the power density of the Nd:YAG pulse was

$$\frac{8 \text{ mJ/Pulse} \times \left(25 \frac{\text{ns}}{\text{pulse}}\right)^{-1}}{\pi (2.0 \text{ mm})^2} = 25464.79 \frac{\text{MW}}{\text{m}^2}$$

The instantaneous power density of the Nd:YAG pulse was 2.81 times greater than the power density of the Alexandrite pulse. Figure 5.18 shows both waveforms on the same scale with the Alexandrite signal multiplied by this factor. We see that the shear waves
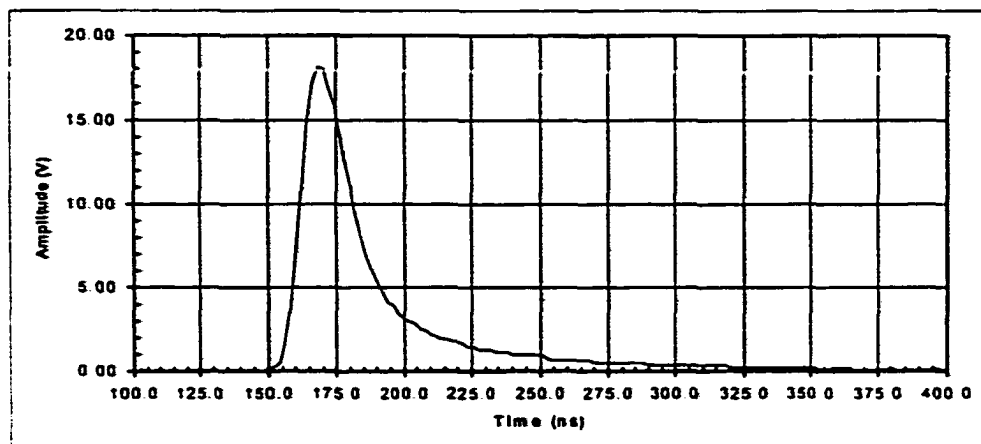
166

Figure 5.16: EO Q-swtiched Nd:YAG (1.064 μm) laser. Top: Photodiode measurement of pulsewidth. Bottom: CCD measurement of beam profile.

are nearly the same amplitude. The amplitudes of the longitudinal waves are close but the Alexandrite waveform does not have the initial positive spike. The frequency spectrum in Figure 5.17 shows a broad range of frequencies below 10 MHz. The higher frequency components caused by the noise in Figure 5.7 are less prominent. A thin layer of grease was applied to the aluminum sample and the same laser settings were used. The results are shown in Figure 5.19. As with the Alexandrite laser, we see a much larger signal compared to the signal generated without the layer of grease. We also see the ringing in the layer of grease which dominates the frequency spectrum.

Acousto-Optic Q-Switch   The pulse width and intensity profile of the acousto-optic Q-switched Nd:YAG laser are shown in Figure 5.20. The pulse width was approximately 125 ns, the energy output was 12 mJ per pulse, and the beam radius was about 2.5 mm. We see that the mode structure of this beam was not as close to the TEM_{00} mode as we had obtained in the previous examples. Figure 5.21 shows the averaged ultrasonic signal and associated frequency spectrum when the laser was applied to the aluminum sample with a layer of grease. A signal could not be obtained without the layer of grease even though the laser parameters were similar to previous examples where grease was not necessary. We attribute this to the poor stability of the AO Q-switching mechanism. As before, we see the ringing of the longitudinal wave in the layer of grease. The frequency spectrum looks similar to the spectrum produced by the 10 MHz transducer in Figure 5.5.

Rotating Mirror Q-Switch   The plots in Figure 5.22 show the pulse width and intensity profile produced with the rotating mirror Q-switch. The pulse width was about 40 ns and the beam radius was about 2.5 mm. Figure 5.23 shows the averaged ultrasonic signal and corresponding frequency spectrum with 8 mJ per pulse applied to the aluminum sample. We see the same features as in previous examples. This signal has a high level of noise

168
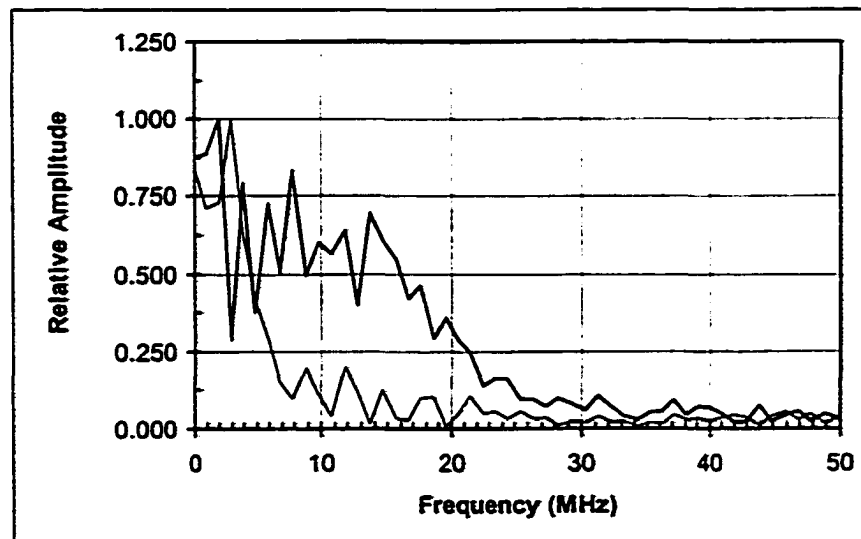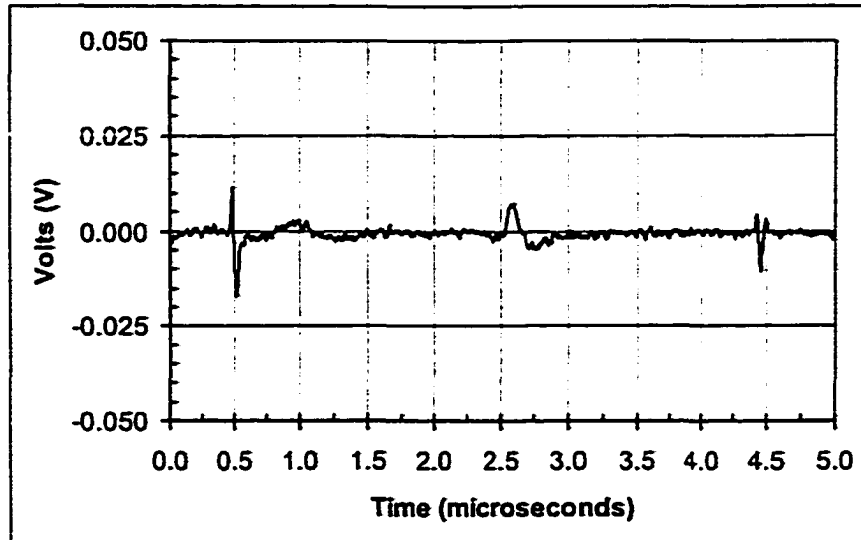
Figure 5.17: Epicentral displacement in aluminum generated by the EO Q-switched Nd:YAG (1.064 μm) laser.

169
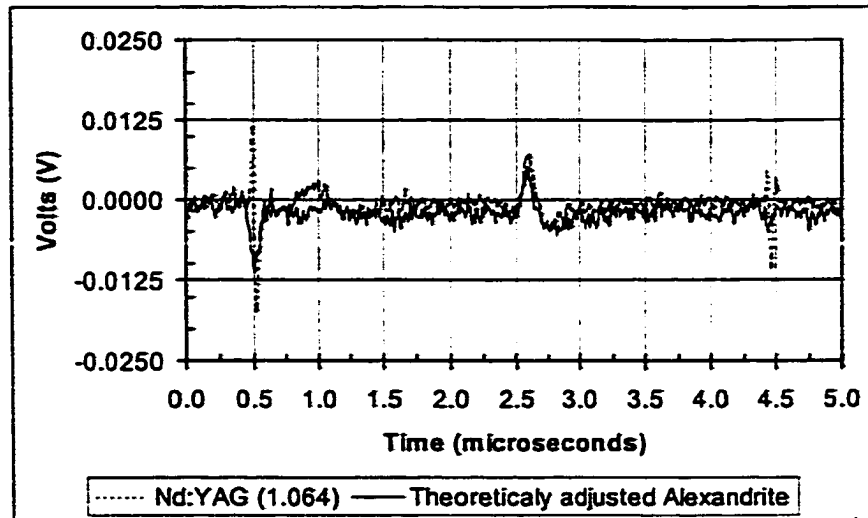
Figure 5.18: Comparison of the EO Q-switched Nd:YAG (1.064 μm) and theoretically modified Alexandrite and lasers.

and consequently the frequency spectrum is broader and has more contributions from the higher frequencies.

Nd:YAG (1.32 μm) Rotating Mirror Q-Switch

Figure 5.24 shows the pulse width and intensity profile of the second Nd:YAG wavelength, Q-switched with the rotating mirror mechanism. The pulse width was measured with a Thor model DET310 Germanium PIN photodiode and was approximately 125 ns. The beam spot radius was about 3 mm. The first plot in Figure 5.25 shows the average ultrasonic signal generated by 10 mJ per pulse and a thin layer of grease on the aluminum sample. A signal could not be obtained without the grease. The waveform resembles previous examples where no grease was used except that the longitudinal wave amplitudes are still slightly enhanced relative to the shear wave amplitude. The amplitude of the signal as

170

Figure 5.19: Epicentral displacement in aluminum generated by the EO Q-switched Nd:YAG (1.064 μm) laser with a constraining layer of vacuum grease.

171

Figure 5.20: AO Q-swtiched Nd:YAG (1.064 μm) laser. Top: Photodiode measurement of pulsewidth. Bottom: CCD measurement of beam profile.

172
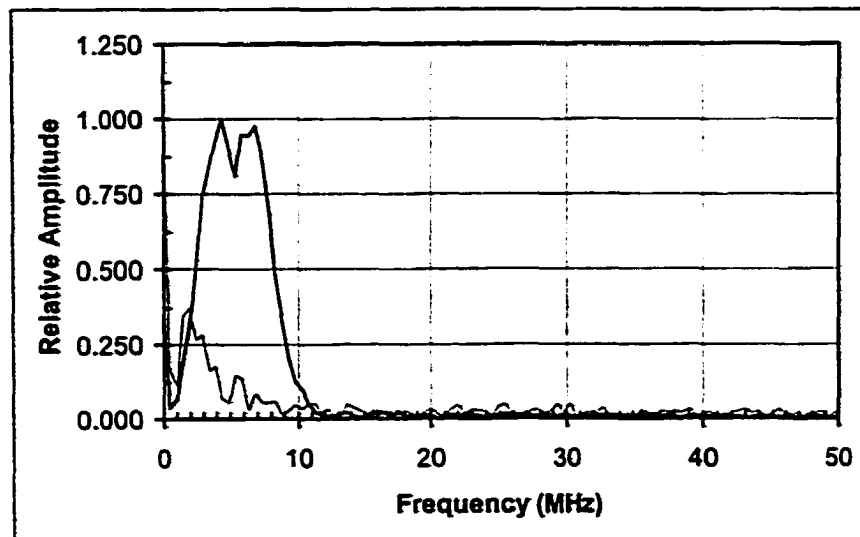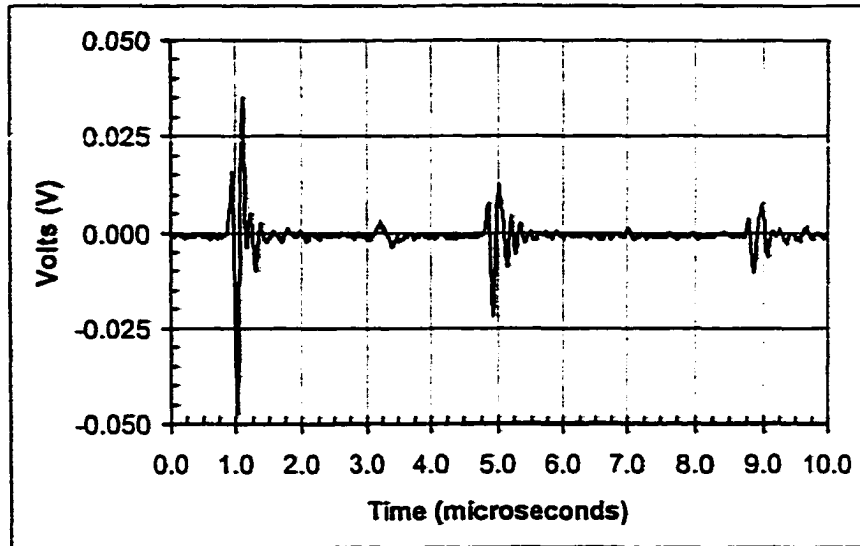
Figure 5.21: Epicentral displacement in aluminum generated by the AO Q-switched Nd:YAG (1.064 μm) laser with a constraining layer of vacuum grease.

173

Figure 5.22: RM Q-swtiched Nd:YAG (1.064 μm) laser. Top: Photodiode measurement of pulsewidth. Bottom: CCD measurement of beam profile.

174
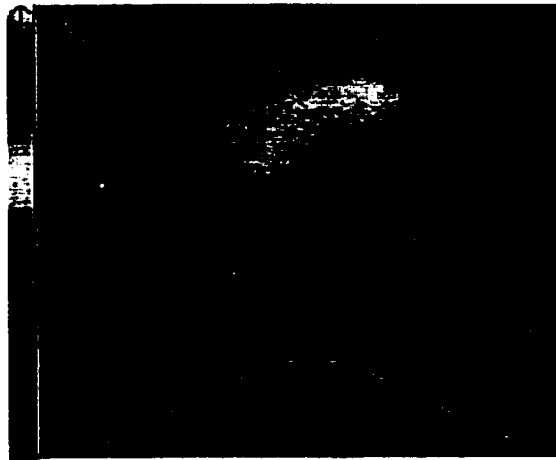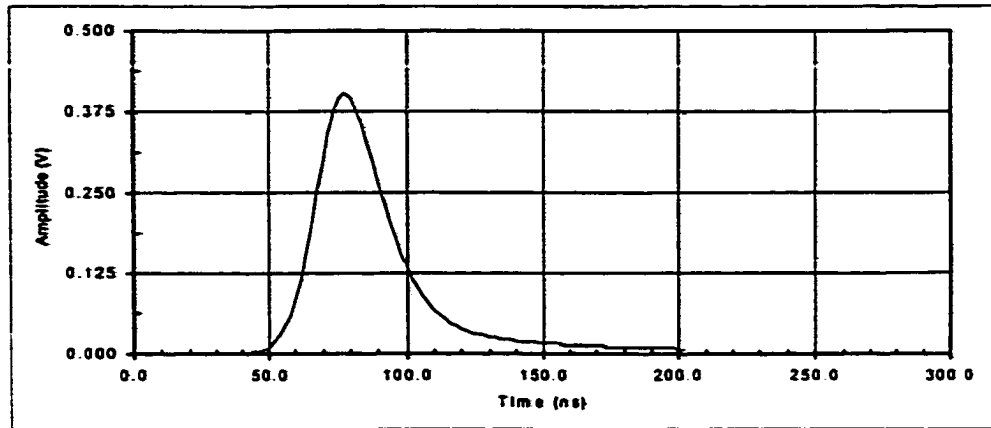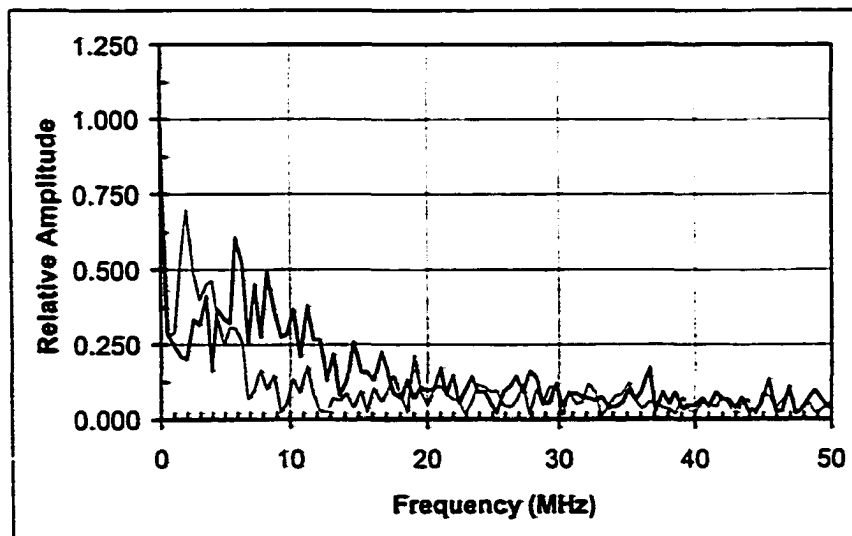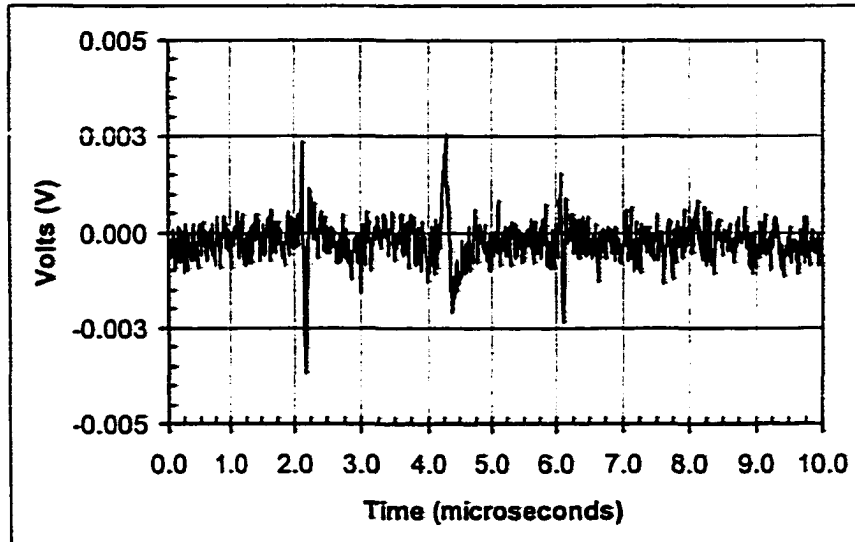
Figure 5.23: Epicentral displacement in aluminum generated by the RM Q-switched Nd:YAG (1.064 μm) laser.
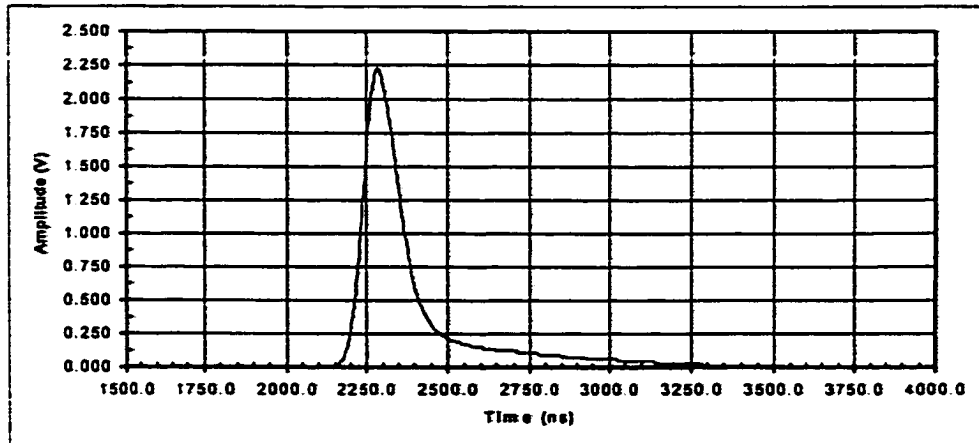
Figure 5.24: RM Q-swtiched Nd:YAG (1.32 μm) laser. Top: Photodiode measurement of pulsewidth. Bottom: CCD measurement of beam profile.

176

a whole is larger and the signal to noise ratio is better than in those previous examples. The second plot shows the frequency content of the waveform and this more closely resembles the frequency spectra of the examples where grease was used.

CTH:YAG (2.10 μm)

Electro-Optic Q-Switch Figure 5.26 shows the pulse width and intensity profile of the CTH:YAG line with the electro-optic Q-switch. The pulse width was measured with a Thor model DET310 Germanium PIN model detector and was about 100 ns. The beam spot radius was approximately 1.0 mm. Figure 5.27 shows the averaged ultrasonic signal and frequency spectrum with 8 mJ per pulse applied to the aluminum surface. Only the first longitudinal wave arrival is visible and the remainder of the signal is buried in noise. The frequency spectrum has a contribution around 2 MHz but there is significant contribution from the high frequency noise.

Rotating Mirror Q-Switch Figure 5.28 shows the pulse width and intensity profile of the CTH:YAG line Q-switched with the rotating mirror Q-switch. The pulse width was measured with a Thor model DET310 Germanium PIN model detector and was about 200 ns. The beam spot radius was approximately 2.0 mm. An ultrasonic signal could not be measured in the aluminum without a thin layer of grease applied to the surface. Figure 5.29 shows the average signal and the corresponding frequency spectrum with 12 mJ per pulse reaching the sample surface. As with the second Nd:YAG wavelength (1.32 μm), the signal is similar to previous examples where there was no layer of grease but the frequency spectrum is similar to examples where the constraining grease layer was applied.

Er:YAG (2.94 μm) Rotating Mirror Q-Switch Figure 5.30 illustrates the pulse width and intensity profile of the Er:YAG wavelength Q-switched with the rotating mirror Q-
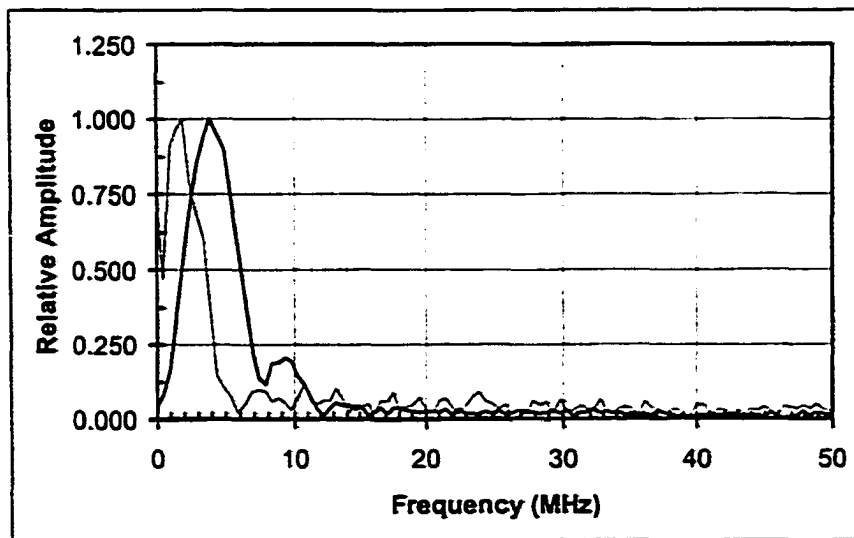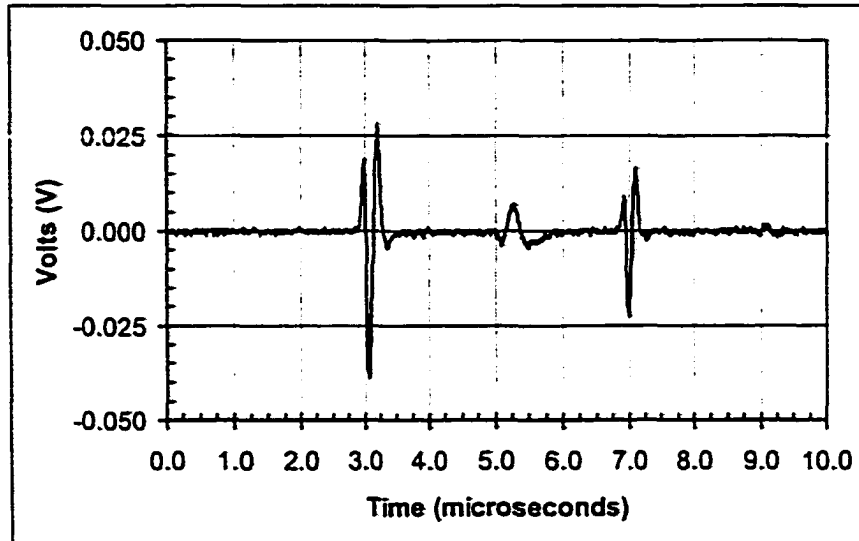
Figure 5.25: Epicentral displacement in aluminum generated by the RM Q-switched Nd:YAG (1.32 μm) laser.
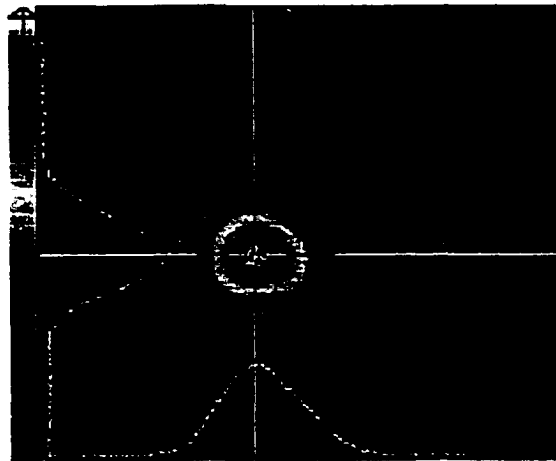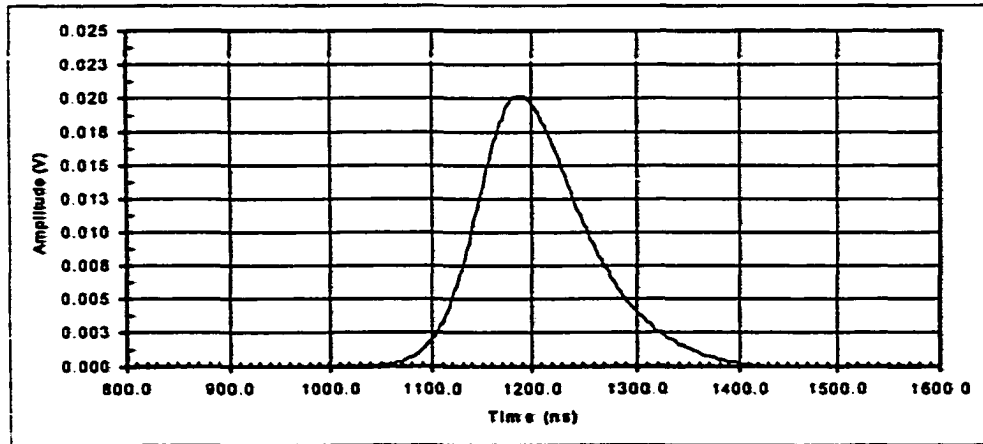
178

Figure 5.26: EO Q-swtiched CTH:YAG (2.10 μm) laser. Top: Photodiode measurement of pulsewidth. Bottom: CCD measurement of beam profile.

179
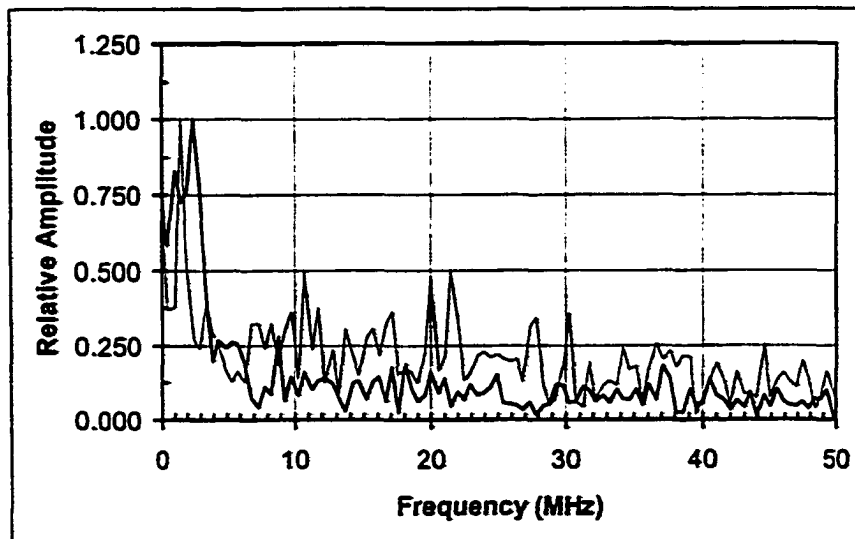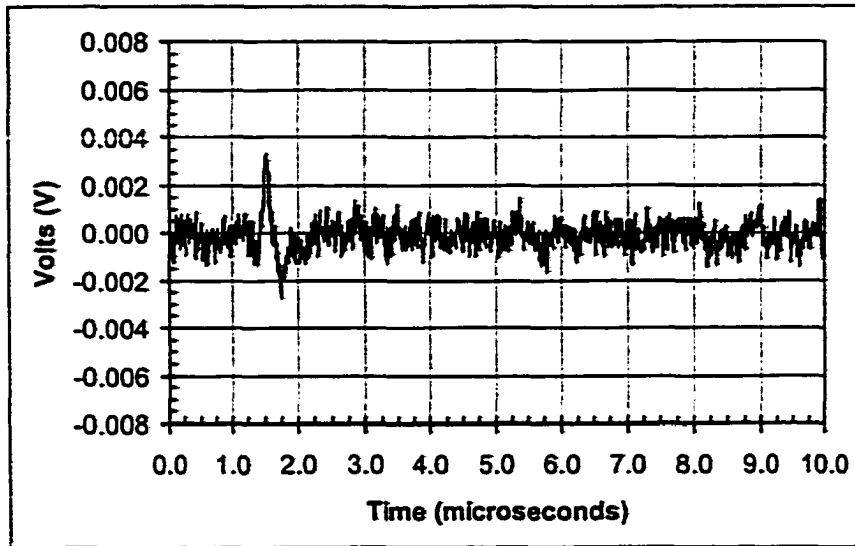
Figure 5.27: Epicentral displacement in aluminum generated by the EO Q-switched CTH:YAG (2.10 μm).
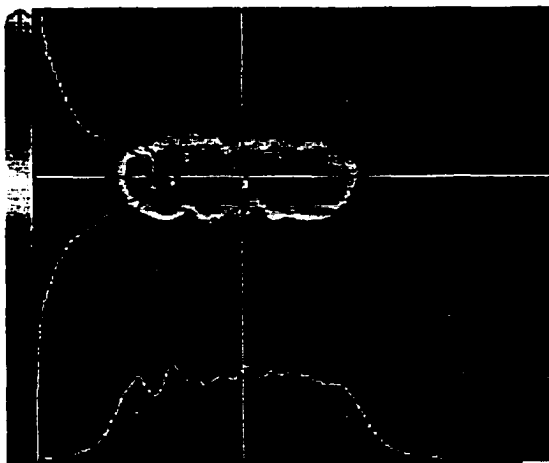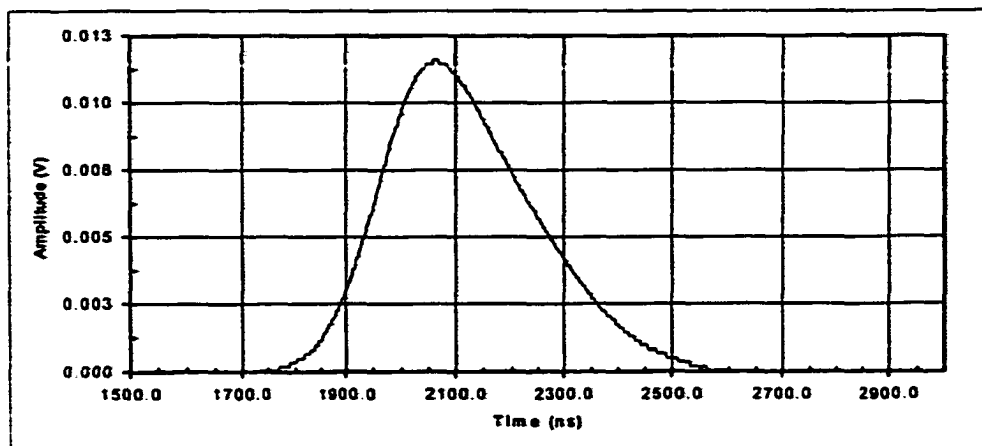
180

Figure 5.28: RM Q-swtiched CTH:YAG (2.10 μm) laser. Top: Photodiode measurement of pulsewidth. Bottom: CCD measurement of beam profile.

181
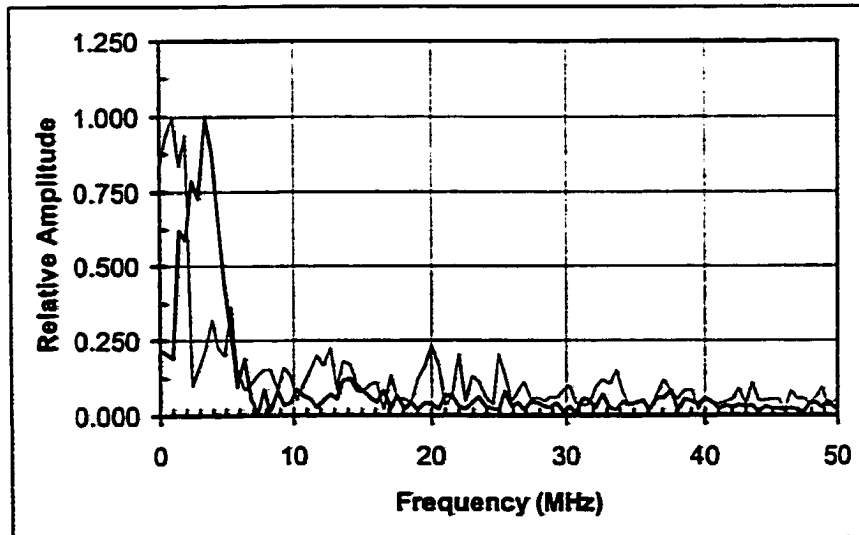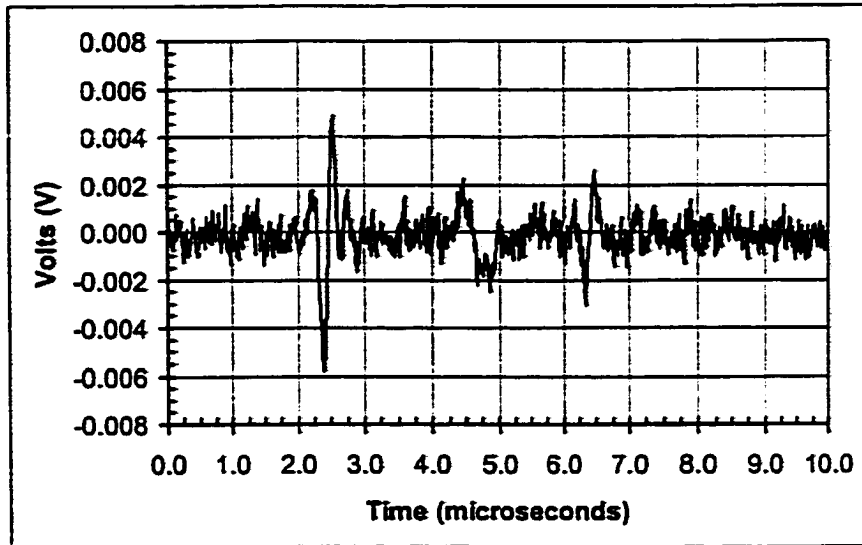
Figure 5.29: Epicentral displacement in aluminum generated by the RM Q-switched CTH:YAG (2.10 μm) laser with a constraining layer of vacuum grease.

182

switch. The generation power was 30 mJ per pulse. The attenuator could not be used with this wavelength and we had less control over the output power. The pulse width was measured with a EG&G Judson J12 series INAS model detector and was about 500 ns. By checking the frequency content of this photodetector to white noise, we determined that its response time was too slow to resolve pulses shorter than 500 ns. Consequently, this is probably not an accurate measure of the pulse width. To more accurately measure the pulse width, we used the model Newport model 875 PIN detector to observe the fluorescence caused by vaporizing surface material on the woven composite sample. The photodiode response is shown in Figure 5.32 and we get a more realistic estimate of 180 ns. The beam spot radius was approximately 2.5 mm. The first plot in Figure 5.31 shows the average ultrasonic signal with 30 mJ per pulse incident on the aluminum sample. The signal is similar to the waveforms generated in the previous examples. The second plot shows the corresponding frequency spectrum. We see a broad contribution around 2 MHz and another smaller component around 5 MHz.
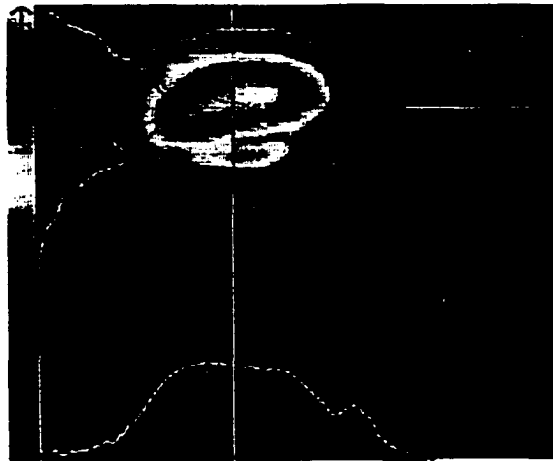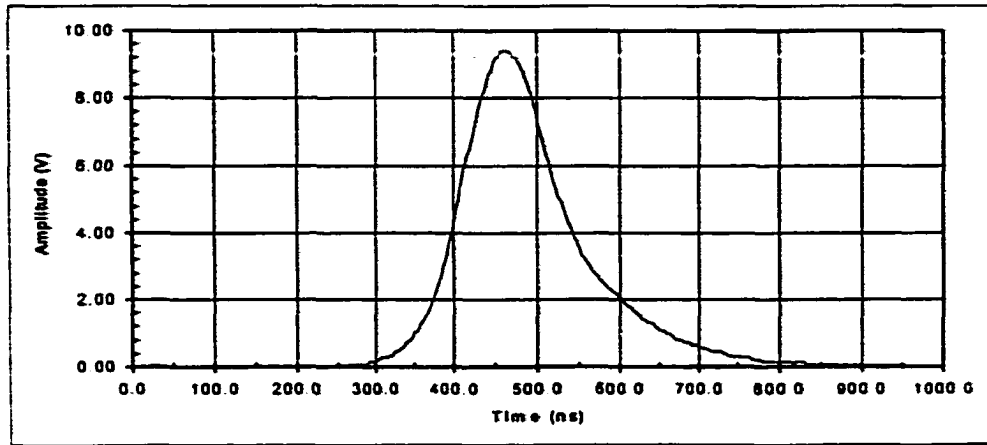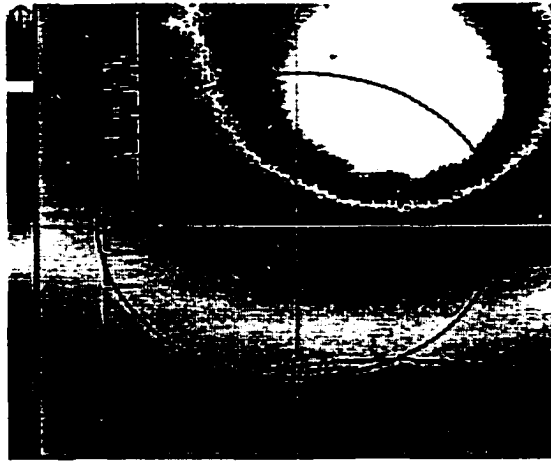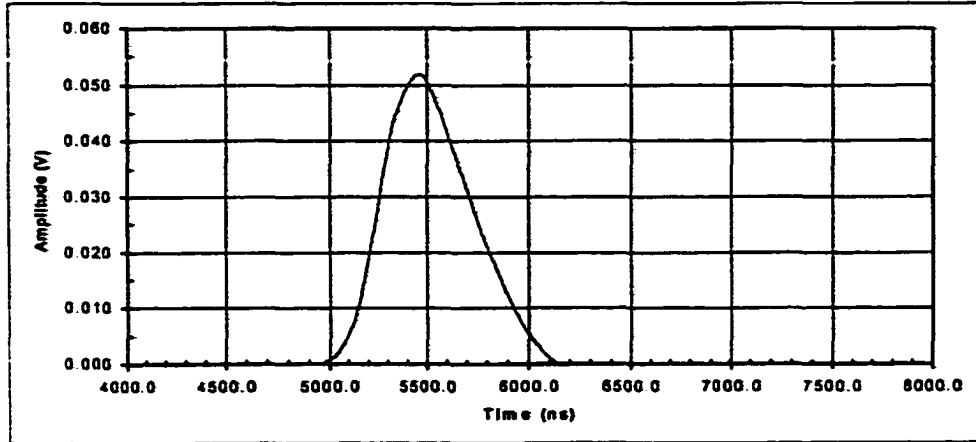
Figure 5.30: EO Q-swtiched Er:YAG (2.94 μm) laser. Top: Photodiode measurement of pulsewidth. Bottom: CCD measurement of beam profile.

184
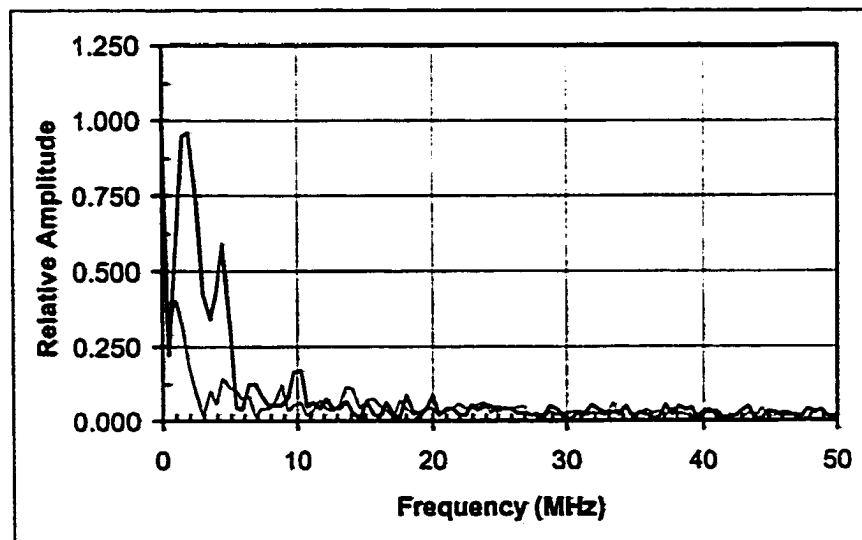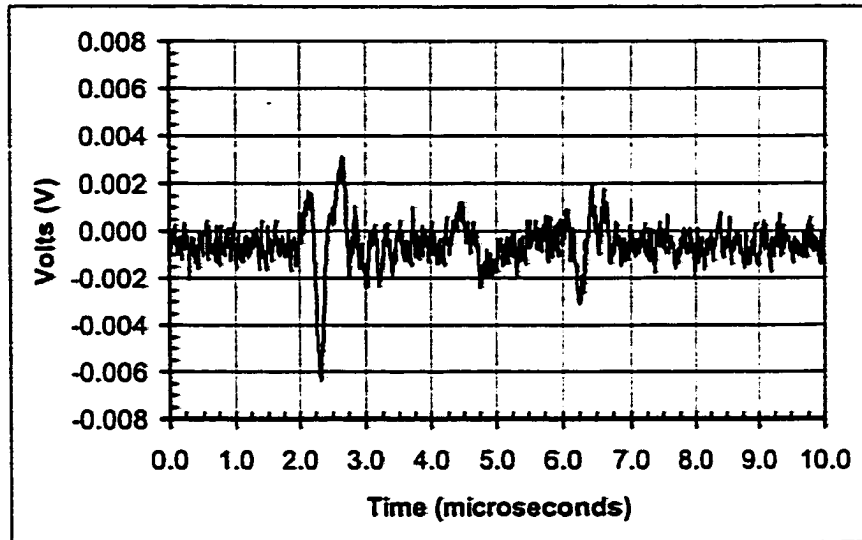
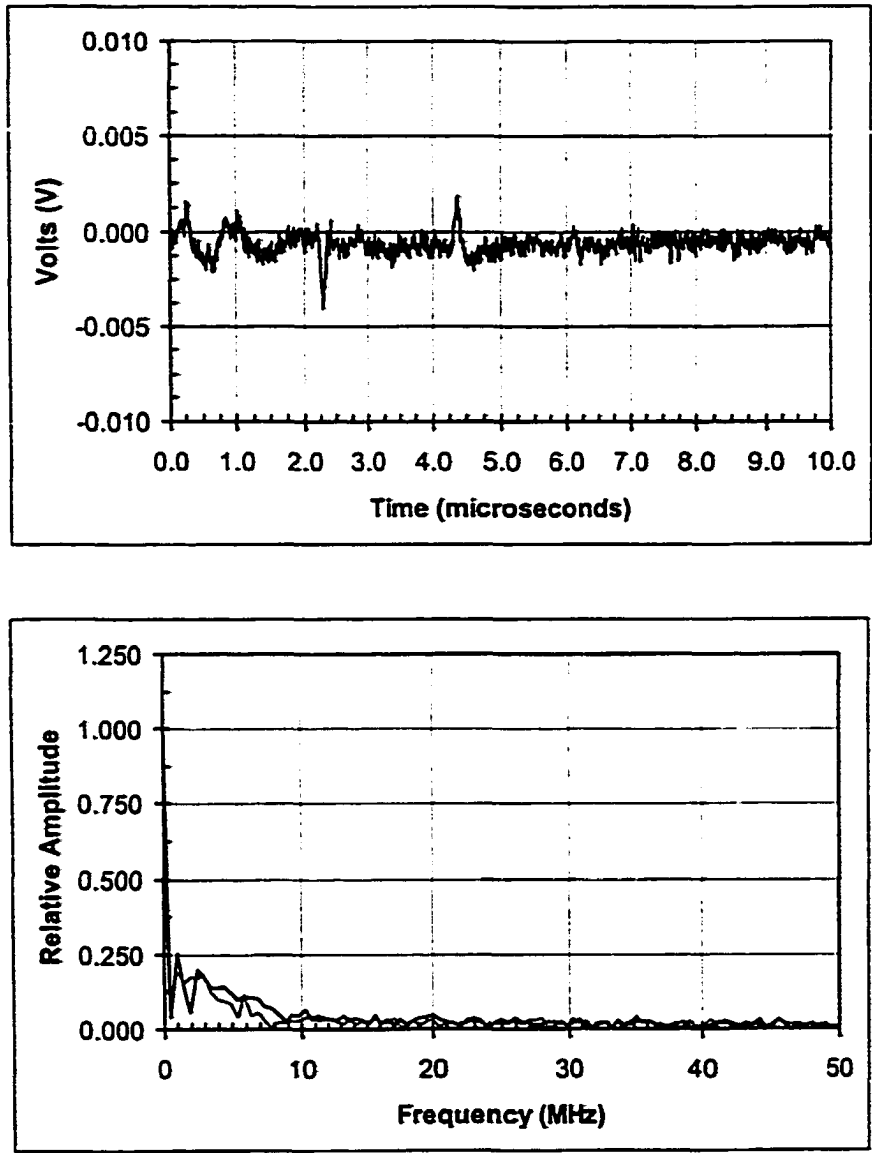Figure 5.31: Epicentral displacement in aluminum generated by the RM Q-switched Er:YAG (2.94 μm) laser.

185

Summary of Aluminum Data

In this section, we summarize experimental results with the aluminum sample. From Scruby [1] we can estimate the reflectivity of a clean metal surface as a function of wavelength. The skin depth of a metal, δ, is defined as the depth such that the amplitude of an incident electromagnetic wave falls to $1/e$ of its initial value. For longer wavelengths, (i.e. in the infrared) we can calculate the skin depth according to

$$\delta = (\pi\sigma\mu_r\mu_0\nu)^{-1/2} \tag{5.1}$$

where σ and μ_r are the conductivity and relative permeability of the metal respectively, $\mu_0 = 4\pi \times 10^{-7} \mathrm{H\ m^{-1}}$ is the permeability of free space, and ν is the frequency of radiation. The reflectivity of the surface can be expressed in terms of the skin depth by

$$R = \frac{2 - 2\xi + \xi^2}{2 + 2\xi + \xi^2} \tag{5.2}$$

where $\xi = \mu_0\sigma c\delta$ and c is the speed of light. For aluminum, we substitute $\sigma = 4.0 \times 10^7$ $(\Omega\ \mathrm{m})^{-1}$ and $\mu_r = 1$. Table 5.2 lists the skin depths and the corresponding reflectivities for the wavelengths used in our experiments. We use equation (5.1) to estimate the skin depth for the Alexandrite laser even though an accurate value requires a quantum mechanical treatment for this wavelength. Our computed value for the Alexandrite wavelength agrees with a value presented by Hecht [257]. The absorbed power densities are computed from the incident power densities by multiplying by the factor $(1 - R)$. Table 5.3 lists the pulse widths, energy levels, beam radius, and the instantaneous incident and absorbed power densities obtained for each laser configuration where no or very little vacuum grease was used. The maximum peak-to-peak displacement measurement for the first longitudinal and shear wave arrivals is also listed.

Figure 5.33 shows plots of the displacement magnitude versus absorbed power density for both the longitudinal and shear wave. It is difficult to see any trend in the top plot but

186
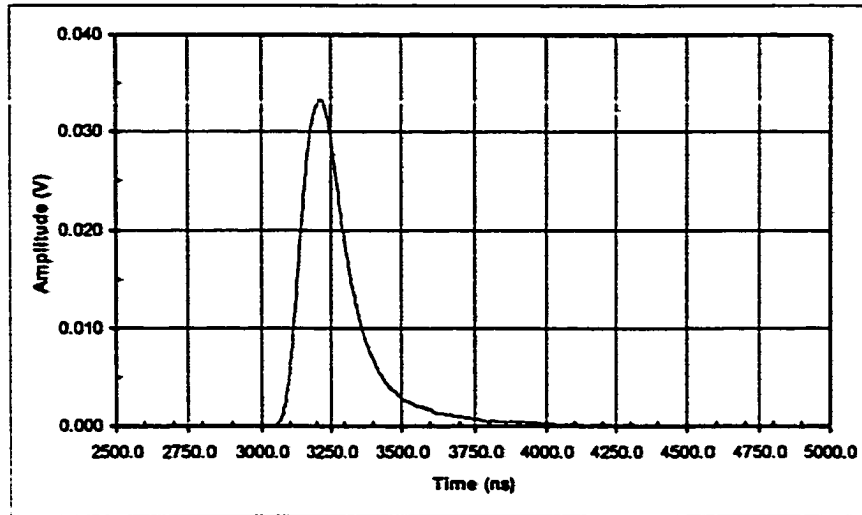
Figure 5.32: Approximate pulsewidth measurement of the RM Q-Switched Er:YAG laser obtained by observing flourescence during vaporization.

Wavelength [μm]	δ [nm]	R
0.755	3.99	0.936
1.064	4.74	0.946
1.320	5.28	0.951
2.10	6.66	0.961
2.940	7.88	0.967

Table 5.2: Computed skin depth and reflectivity for aluminum.

λ [μm]	Pulse Width [ns]	Energy [$\frac{mJ}{pulse}$]	Radius [mm]	Incident Power Density [$\frac{MW}{m^2}$]	Absorbed Power Density [$\frac{MW}{m^2}$]	P Wave [mV]	S Wave [mV]
0.755 EO (a)	125.0	8.0	1.5	9050.0	582.0	4.7	3.9
0.755 EO (b)	160.0	8.0	2.5	2550.0	164.0	2.8	2.3
0.755 AO	150.0	10.0	2.5	3400.0	218.0	7.9	7.6
0.755 RM	115.0	7.0	2.0	4840.0	311.0	2.4	2.8
1.064 EO	25.0	8.0	2.0	25500.0	1390.0	28.8	11.9
1.064 RM	40.0	8.0	2.5	10200.0	554.0	6.0	4.7
1.320 RM²	125.0	10.0	3.0	2830.0	139.0	66.9	11.9
2.100 EO	100.0	8.0	1.0	25500.0	995.0	6.1	3.1
2.100 RM	200.0	12.0	2.0	4770.0	186.0	10.7	4.7
2.940 RM	180.0	30.0	2.5	8490.0	281.0	9.5	3.6

Table 5.3: Summary of experiments with the aluminum sample.

188

when we remove the first data point as shown in the bottom plot, the general trend is that the displacement increases with absorbed power. The abnormally large displacement at the lower power density is probably due to a thicker layer of grease on the surface. Other factors that could have effected these measurement were the inconsistency of the interferometer and the detection laser power. As mentioned above, the interferometer was difficult to maintain at an optimal level. In addition, the output power of the detection laser varied slightly between tests and this affected the signal levels. Except for the one measurement made with the Nd:YAG laser at 1.32 μm where too much grease may have been present, the greatest displacement was obtained with the EO Q-switched Nd:YAG laser at 1.064 μm which had the shortest pulse width of 25 ns. The laser produced the greatest absorbed power density because of the wavlength and the short pulse width. Qualitatively, we observed the same general features in each ultrasonic waveform. A typical waveform is presented in Figure 5.34. As expected, we found that a constraining layer of grease enhanced the ultrasonic signal.

In general, the frequency content of the signals was dominated by contributions below 10 MHz with peaks around 2 and 5 MHz. the frequency content was relatively independent of the absorbed power density and pulse widths of the laser source.

189
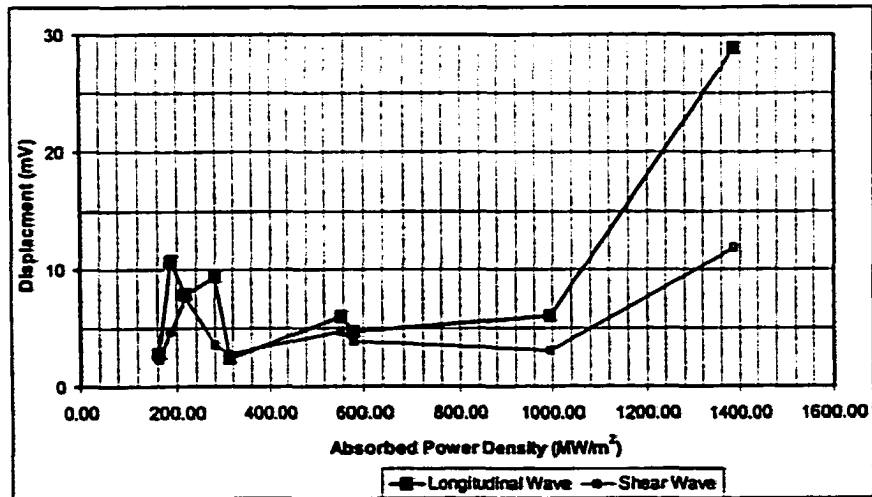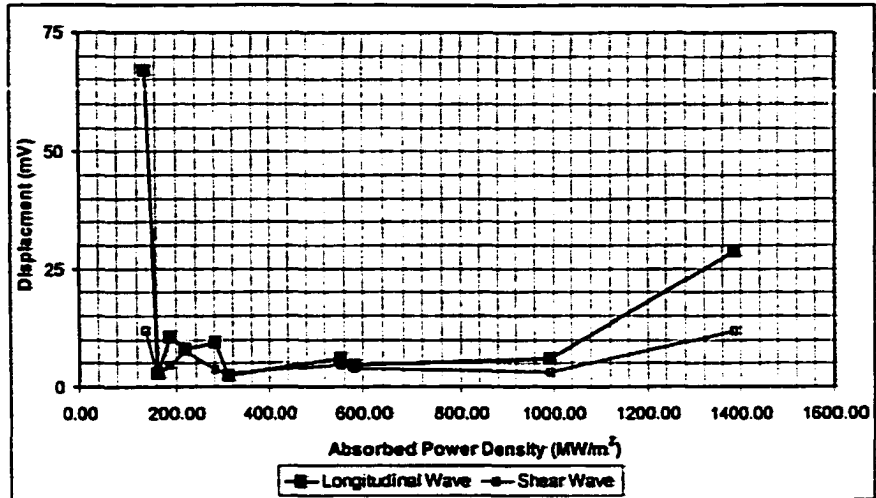
Figure 5.33: A plot of displacement magnitude versus absorbed power density for the aluminum sample. Bottom: First data point omitted.

190
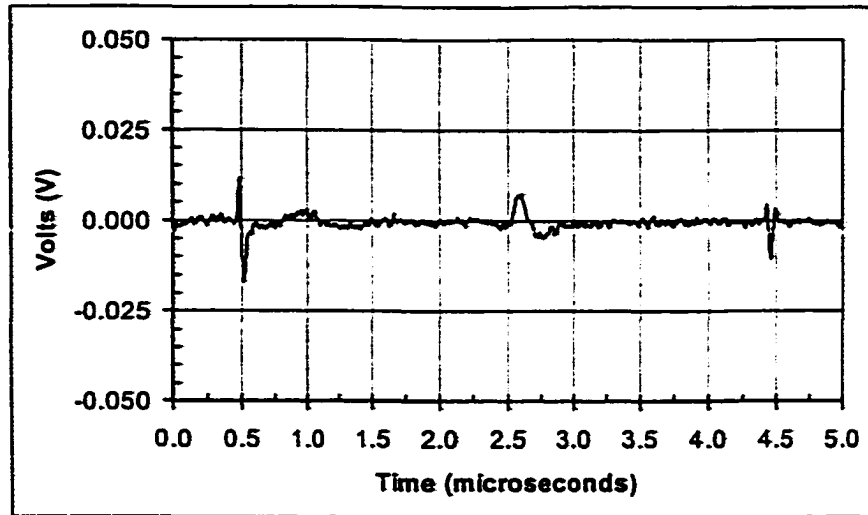
Figure 5.34: Typical laser generated ultrasound signal in aluminum without a constraining layer of grease.

5.2.2 Woven Graphite/Epoxy

Transducer

Figure 5.35 shows the average ultrasonic waveform and frequency spectrum of the transducer signal obtained with the woven graphite/epoxy composite sample. Here, we see three echoes in the ultrasonic signal because the plate was thin enough that the wave was still visible after two round trips. The time interval between the wave arrivals is approximately three microseconds and the round trip distance is 0.904 cm so that the wave speed is 3013 $\frac{m}{s}$. We again see that the frequency content of the signal has a range of 10 MHz and is centered about 5 MHz.

191
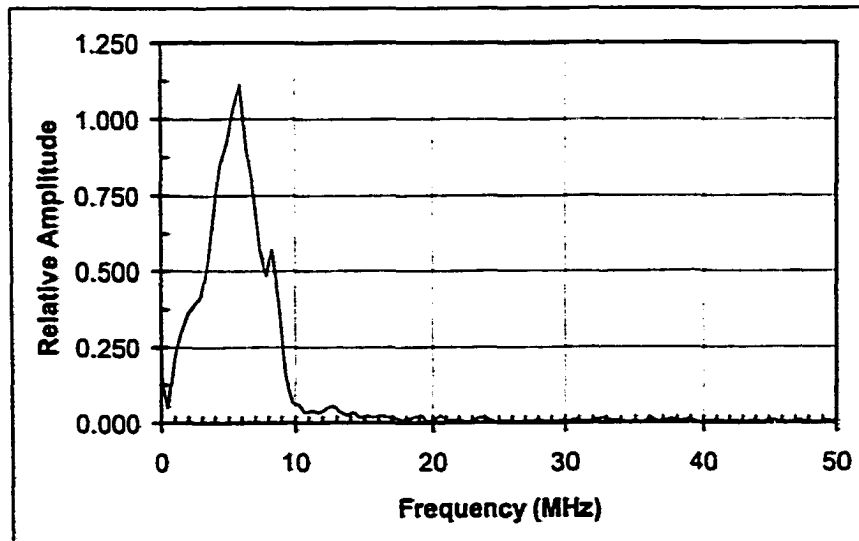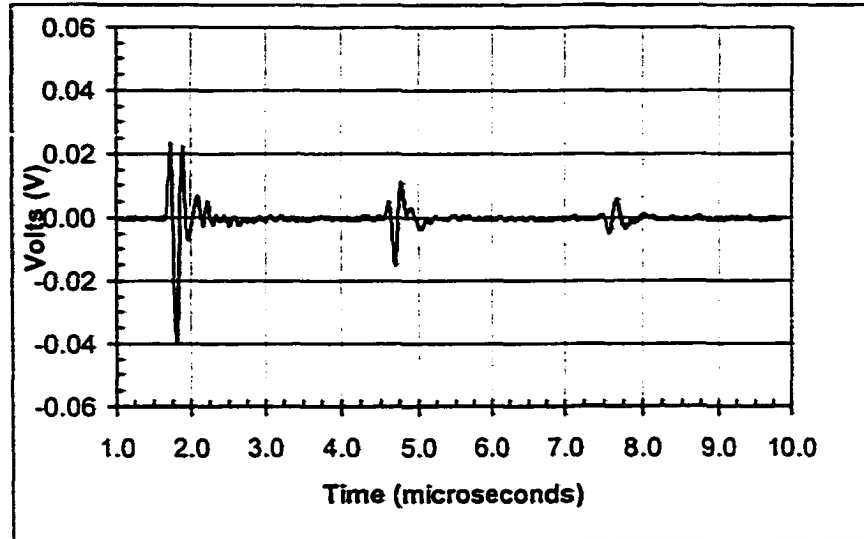
Figure 5.35: 10 MHz transducer response and frequency spectrum of the first wave arrival in the woven GR/Epoxy sample.

192

Alexandrite (0.720-0.790 μm)

Electro-Optic Q-Switch   Figure 5.36 shows the averaged ultrasonic signal and frequency spectrum produced in the woven composite sample by the EO Q-switched Alexandrite laser. Approximately 10 mJ per pulse was delivered to the sample surface and the pulse width and intensity profile were the same as in Figure 5.6. The generation spot was marked on the sample so that data could be taken at the same location in subsequent experiments. We see that the ultrasonic signal is very small but a round trip arrival is visible around 4.5 μs. The frequency spectrum was computed by windowing the first arrival at 1.5 μs. It is noisy because the signal-to-nose ratio in the waveform is low. However, there does appear to be some contribution around 1 and 3 MHz. Some slight surface damage was noted at this power level.

Acousto-Optic Q-Switch   The first plot in Figure 5.37 presents the average ultrasonic signal generated in the woven composite sample by a 10 mJ pulse from the acousto-optically Q-switched Alexandrite laser. The pulse width was approximately 160 ns and the intensity profile was similar to that shown in Figure 5.11. We see the first wave arrival around 1.75 μs and the can barely see the round trip arrival at approximately 4.75 μs. The second plot in Figure 5.37 shows the corresponding frequency spectrum. As in the previous example, the low SNR produces a noisy spectrum. However, we again see relatively large contributions around 1 and 5 MHz.

Rotating Mirror Q-Switch   Figure 5.38 shows the average ultrasonic signal and frequency spectrum generated using the rotating mirror Q-switch at 10 mJ per pulse. The pulse width was approximately 105 ns and a lens was used to expand the beam radius so that the intensity profile was similar to the profile given in Figure 5.13. A thin layer of
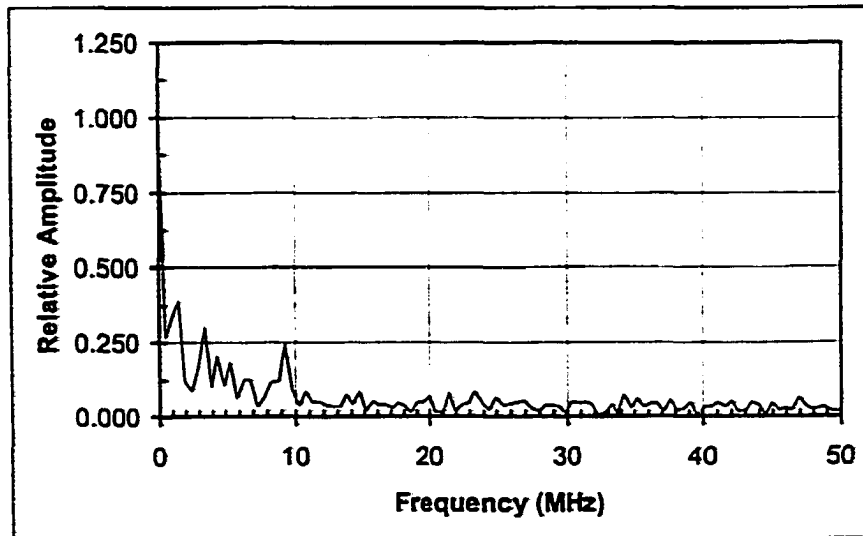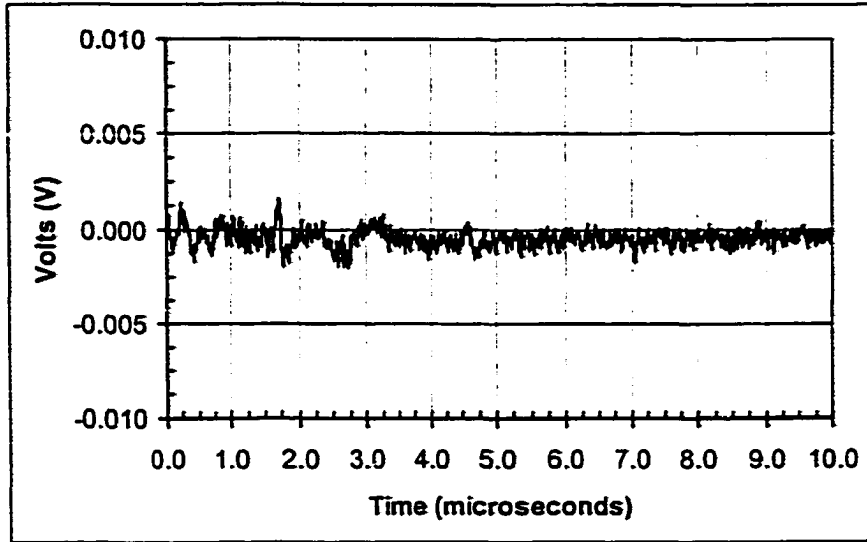
193

Figure 5.36: Epicentral displacement in woven GR/Epoxy generated by the EO Q-switched Alexandrite laser.

194
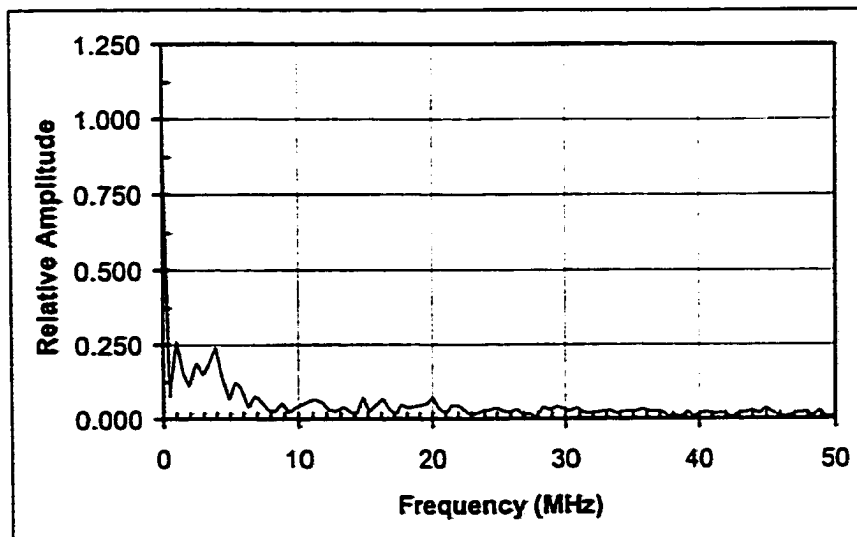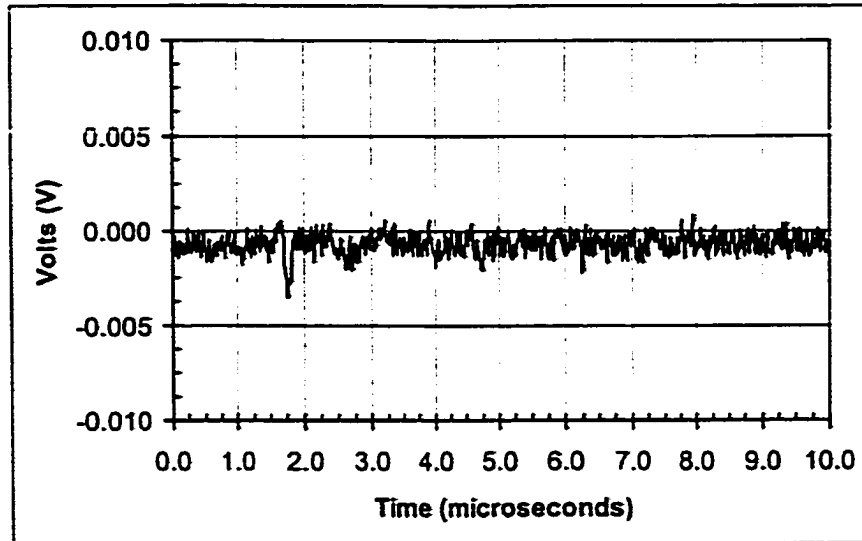
Figure 5.37: Epicentral displacement in woven GR/Epoxy generated by the AO Q-switched Alexandrite laser.

195

grease had to be applied to the surface to obtain any signal. We see three wave arrivals in the first plot of Figure 5.38. These three arrivals correlate well with the three arrivals generated in the transducer signal in Figure 5.38. The frequency spectrum was computed by windowing the first arrival at 1.75 μs (thick line) and by windowing the second arrival at 4.5 μs (thin line). We again see some relatively strong components around 3 and 4 MHz and we note that the frequency content of the two wave arrivals is similar. We also see some similarity to the frequency spectrum generated by the transducer.

Nd:YAG (1.064 μm)

Electro-Optic Q-Switch Figure 5.39 shows the average ultrasonic signal and corresponding frequency spectrum generated in the woven composite sample with 12 mJ per pulse from the EO Q-switched Nd:YAG laser. The pulse width is displayed in Figure 5.40 and we see that the FWHM is about 25 ns. The intensity profile was similar to the profile illustrated in Figure 5.16. In Figure 5.39, the three wave arrivals observed in the last example and in the signal generated by the transducer are clearly visible. The amplitude of the displacements are significantly larger than the amplitude of the displacements generated by the Alexandrite laser. The frequency spectrum was generated by windowing the second reverberation at 5.0 μs so that the transient noise appearing between 1.0 and 1.5 μs was not included. The frequency spectrum shows a broad response around 5 MHz extending to about 15 MHz.

Acousto-Optic Q-Switch Figure 5.41 gives the averaged ultrasonic signal and frequency spectrum generated in the woven composite with the AO Q-switched laser at 12 mJ per pulse. The pulse width was approximately 100 ns and the intensity profile similar to the profile in Figure 5.20. A thin layer of grease was applied to obtain a measurable signal.

196
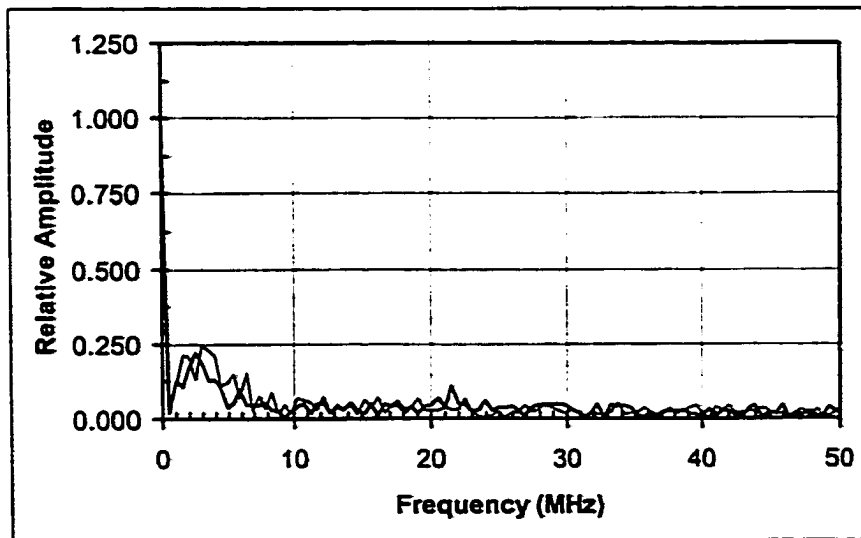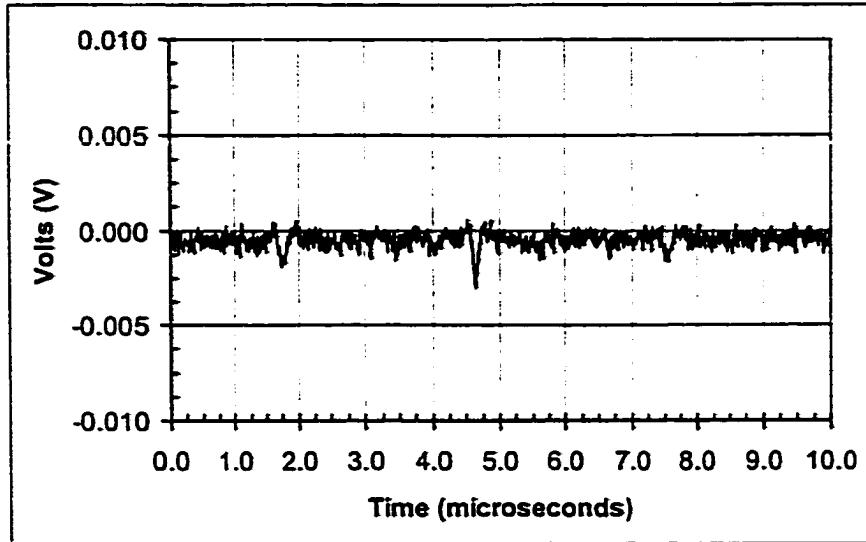
Figure 5.38: Epicentral displacement in woven GR/Epoxy generated by the RM Q-switched Alexandrite laser with a constraining layer of vacuum grease.

197
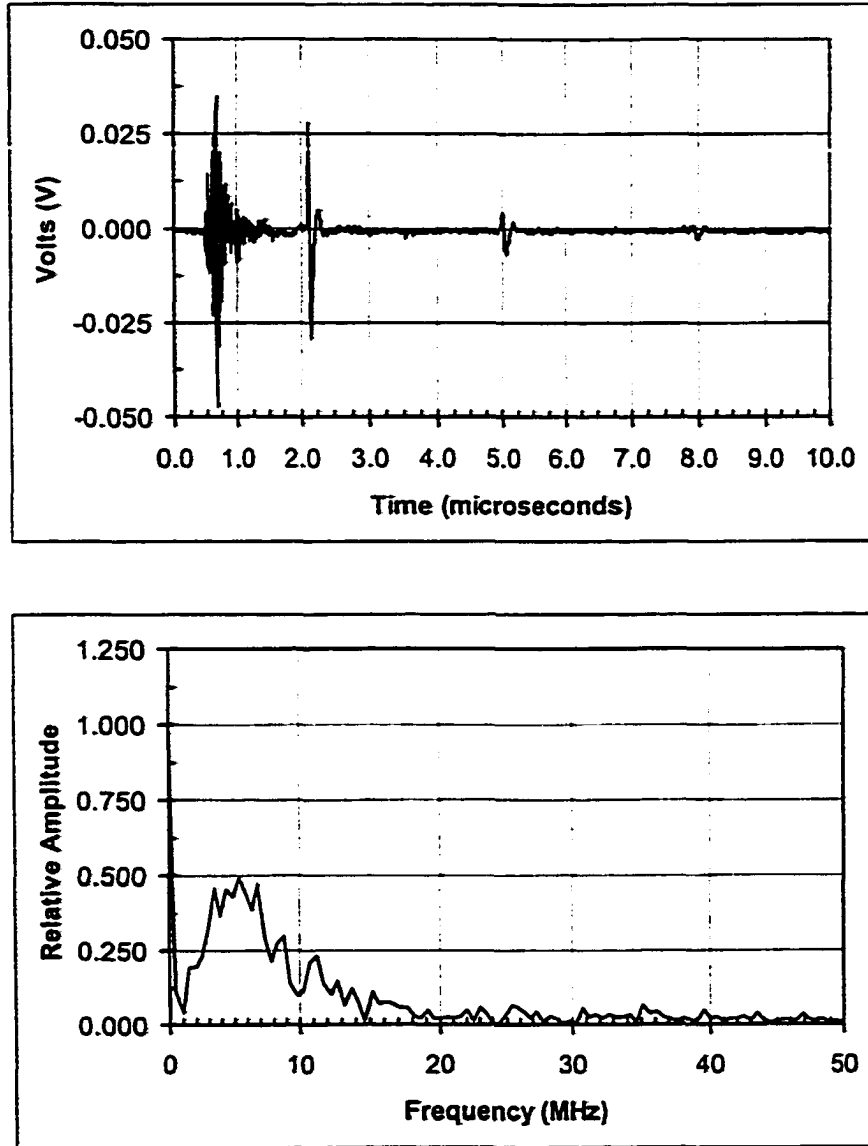
Figure 5.39: Epicentral displacement in woven GR/Epoxy generated by the EO Q-switched Nd:YAG (1.064 μm).

198
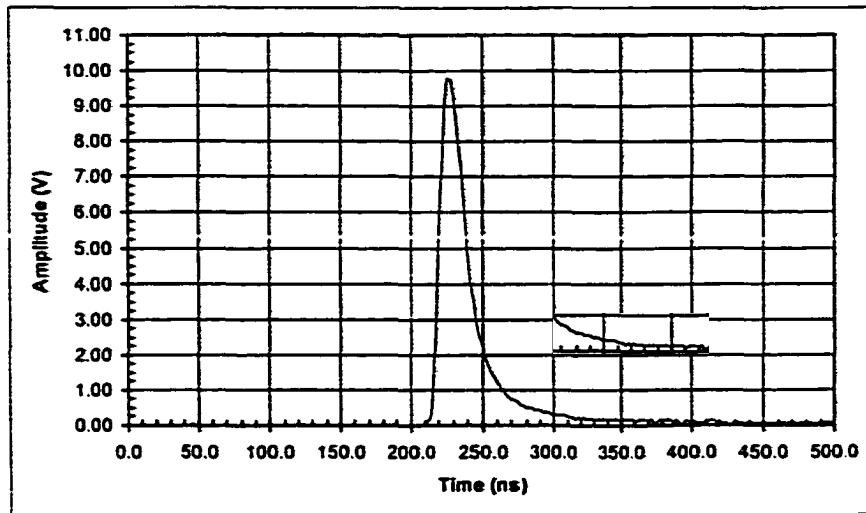
Figure 5.40: Photodiode measurement of EO Q-Switched Nd:YAG (1.064 μm) pulse width with woven GR/Epoxy sample.

The pulse width was approximately 100 ns and the intensity profile was similar to the profile presented in Figure 5.20. We again see three wave arrivals but their amplitude is much smaller than the amplitude of the waves generated by the EO Q-switched laser. The frequency response computed from the first wave arrival is more localized and indicates a strong contribution arround 3-5 MHz.

Rotating Mirror Q-Switch Figure 5.42 shows the average ultrasonic signal and frequency spectrum generated in the composite sample with 10 mJ per pulse from the Nd:YAG laser with the rotating mirror Q-switch. The pulse width was 50 ns and the intensity profile was similar to the profile given in Figure 5.22. The three wave arrivals present in the previous examples are visible at 1.5, 4.5 and 7.5 μs. The frequency spectrum has significant contributions around 5 MHz.
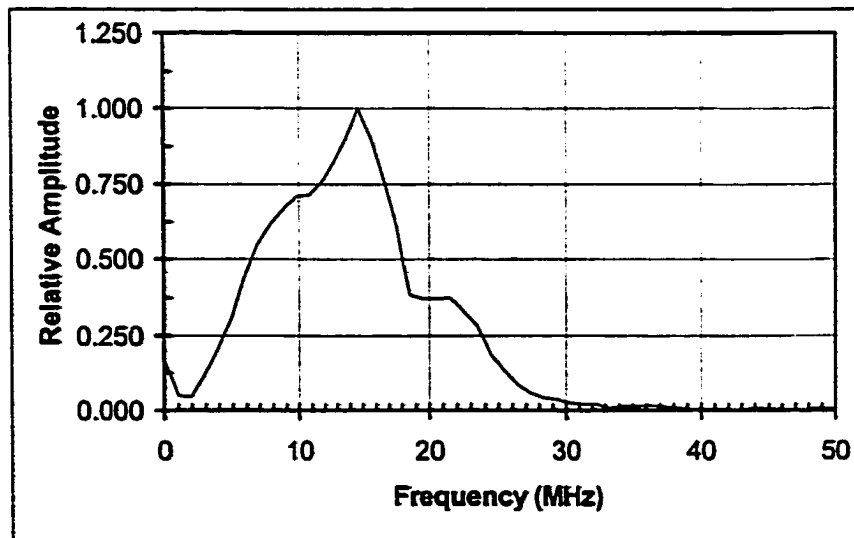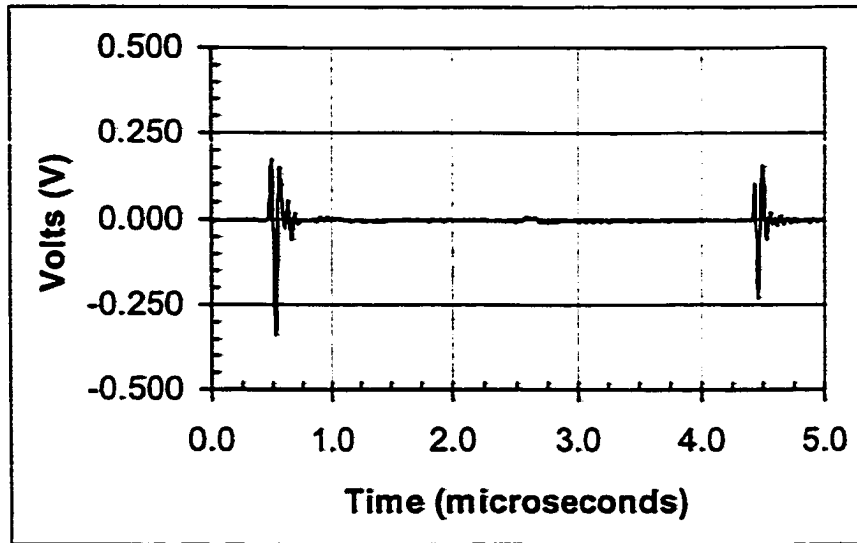
199
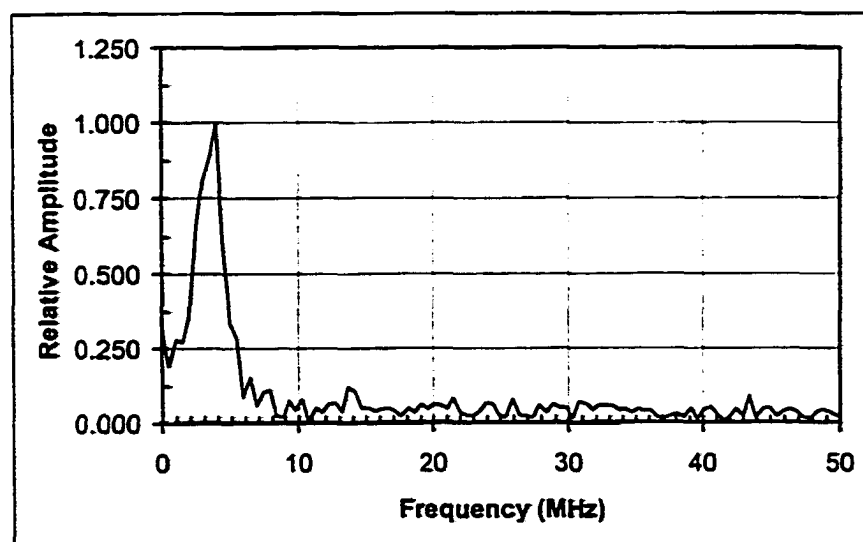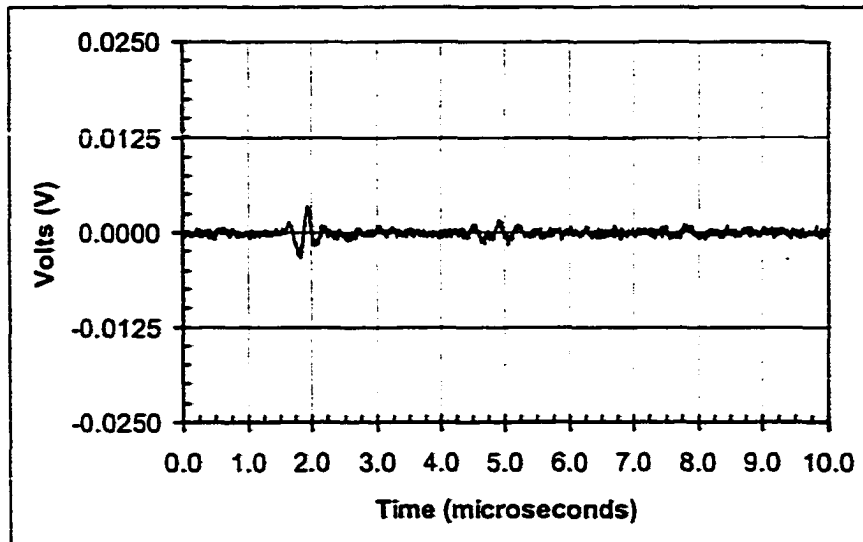
Figure 5.41: Epicentral displacement in woven GR/Epoxy generated by the AO Q-switched Nd:YAG (1.064 μm) with a constraining layer of vacuum grease.
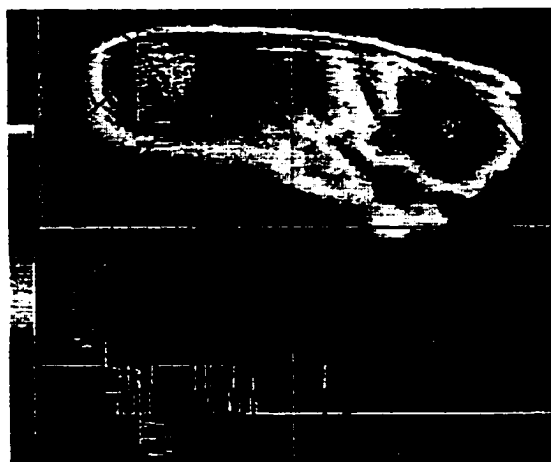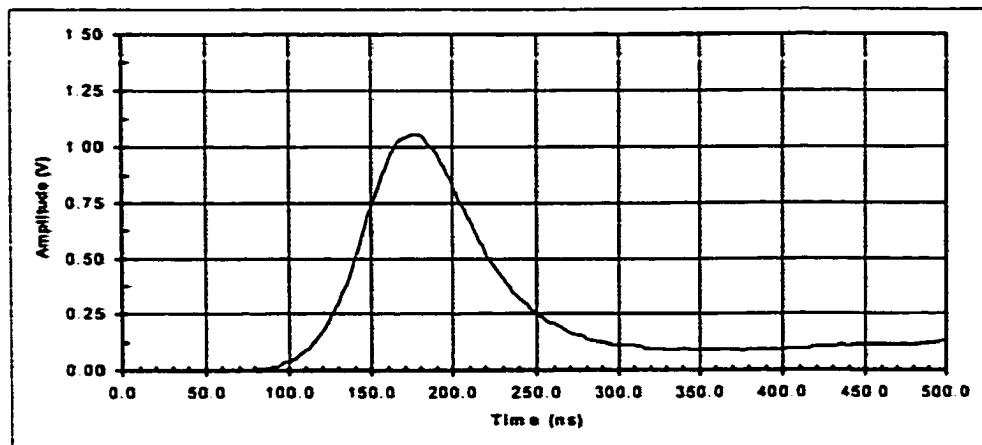
200
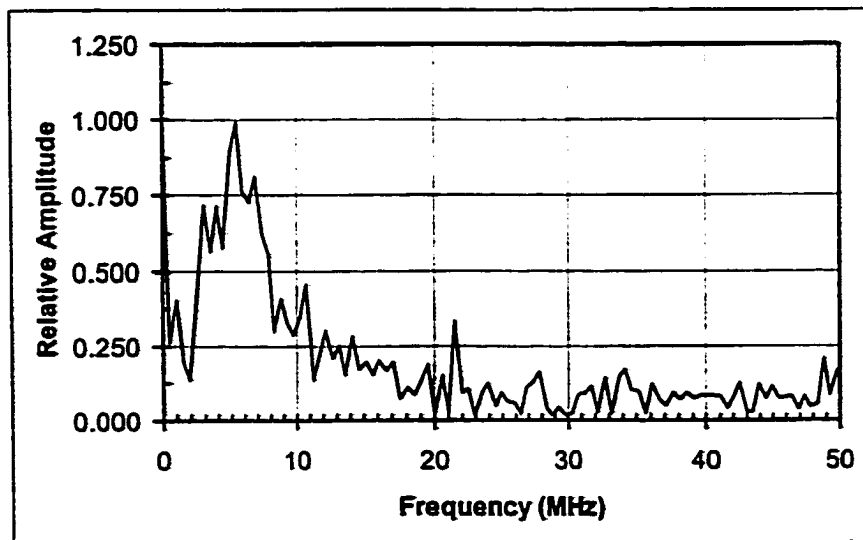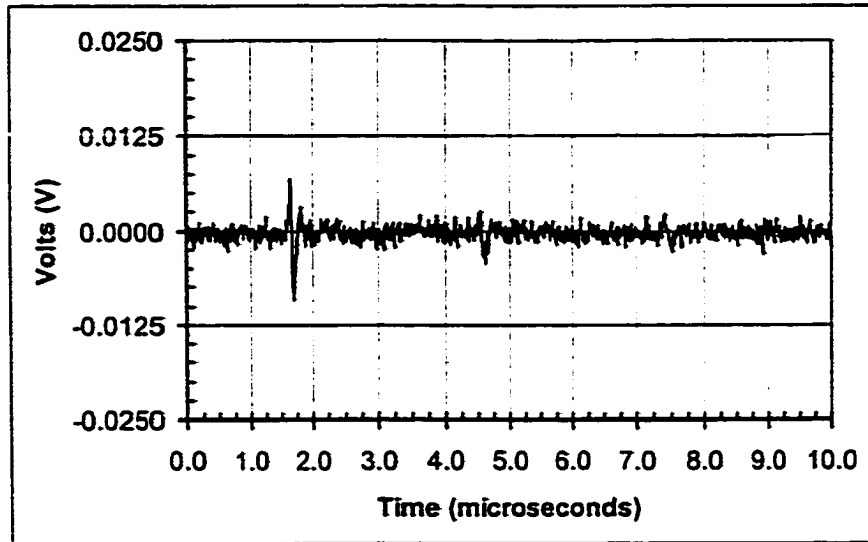
Figure 5.42: Epicentral displacement in woven GR/Epoxy generated by the RM Q-switched Nd:YAG (1.064 μm).

201

Nd:YAG (1.32 μm) Rotating Mirror Q-Switch

Figure 5.43 represents the averaged ultrasonic signal and corresponding frequency spectrum produced in the composite with 15 mJ per pulse from the Nd:YAG (1.32 μm) Q-switched with the rotating mirror. The pulse width was approximately 130 ns and the intensity profile was similar to the profile given in Figure 5.24. As with the first Nd:YAG wavelength, we see three wave arrivals but the amplitude is significantly smaller. Here, the frequency spectrum shows strong contributions around 1-3 MHz.

CTH:YAG (2.10 μm)

Electro-Optic Q-Switch Figure 5.44 shows the averaged ultrasonic displacement and frequency spectrum generated in the composite sample with 8 mJ per pulse from the EO Q-switched CTH:YAG laser. The pulse width was 200 ns and the intensity profile was similar to the profile in Figure 5.26. There may be a wave arrival just before 2 μs but the SNR is too poor to be certain.

Rotating Mirror Q-Switch Figure 5.45 shows the average ultrasonic signal and frequency spectrum generated with 12 mJ per pulse from the CTH:YAG laser Q-switched with the rotating mirror. The pulse width was approximately 250 ns and the intensity profile was similar to the profile given in Figure 5.28. We see that the displacement of the first wave arrival is barely visible. The frequency spectrum is dominated by the noise. Figure 5.46 shows the ultrasonic signal and frequency spectrum with the same laser and setting with the addition of a thin layer of grease on the sample surface. We see that the amplitude of the first wave arrival has been enhanced and the second wave arrival is barely visible at 4.5 μs. The frequency spectrum of this signal shows contributions from components around 2 MHz.

202
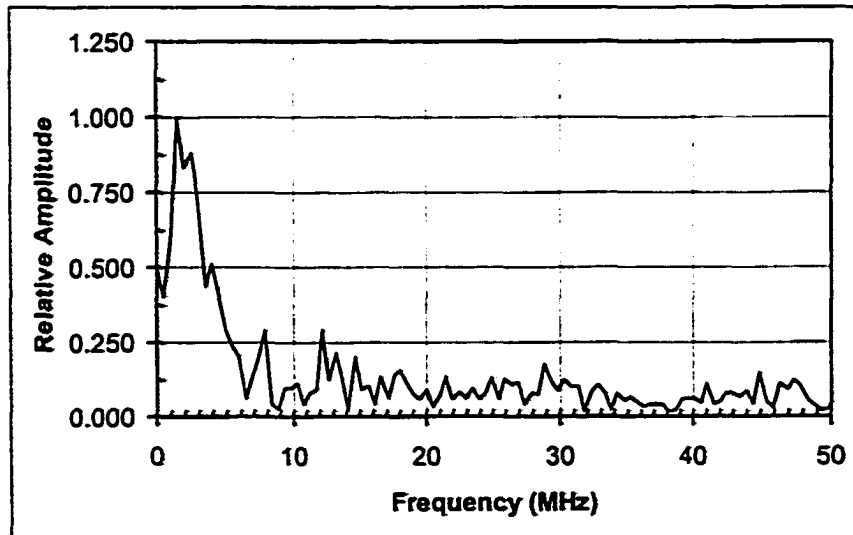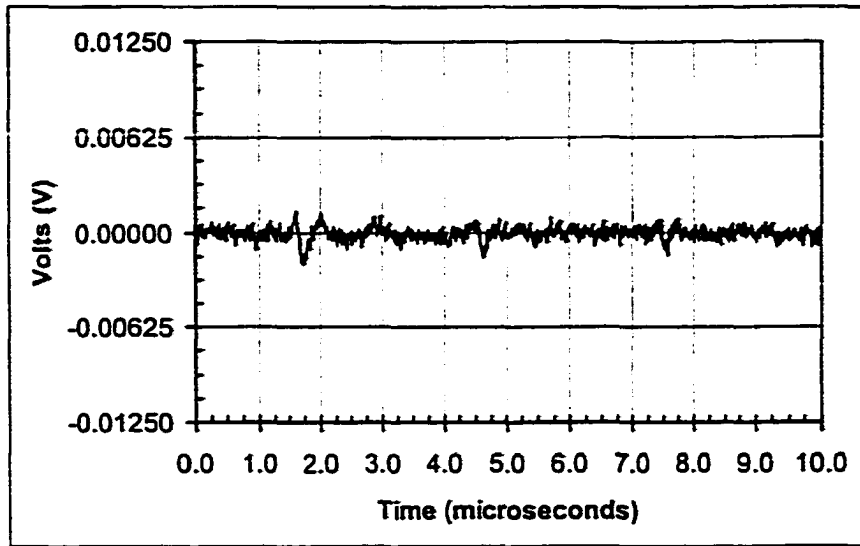
Figure 5.43: Epicentral displacement in woven GR/Epoxy generated by the RM Q-switched Nd:YAG (1.320 μm).
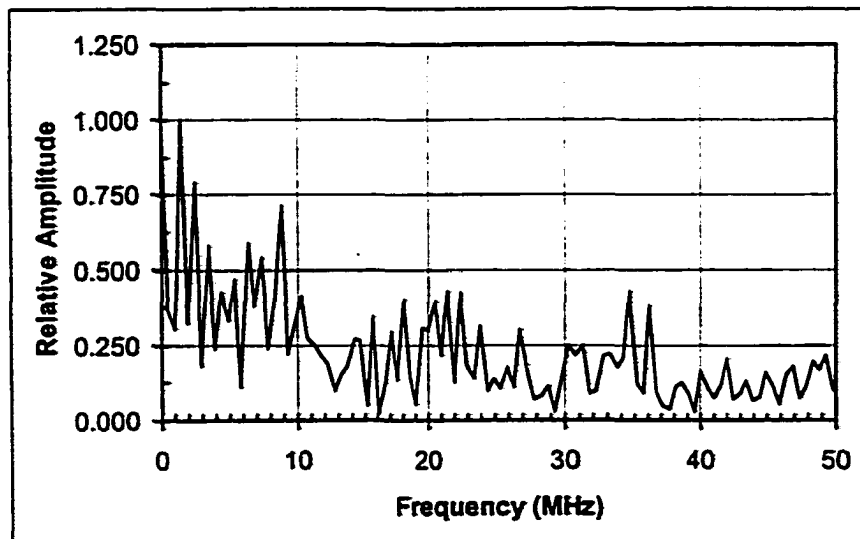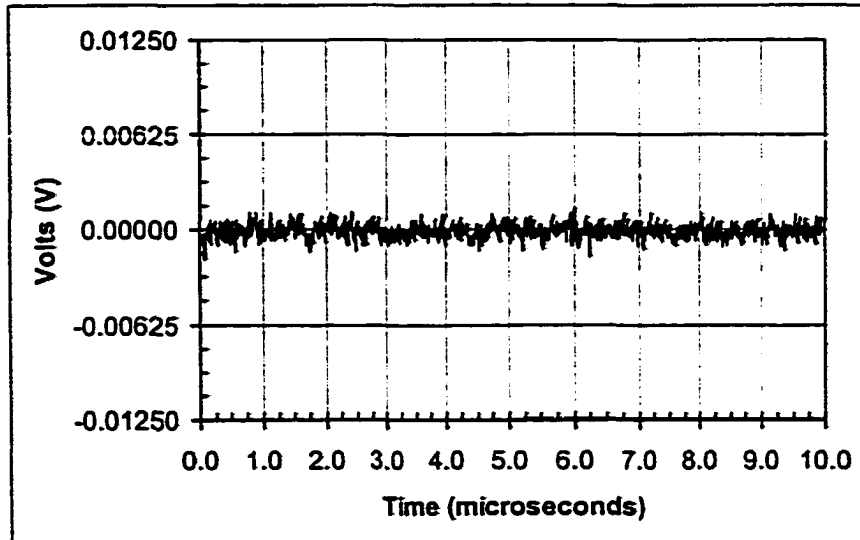
Figure 5.44: Epicentral displacement in GR/Epoxy generated by the EO Q-switched (2.10 μm).

204
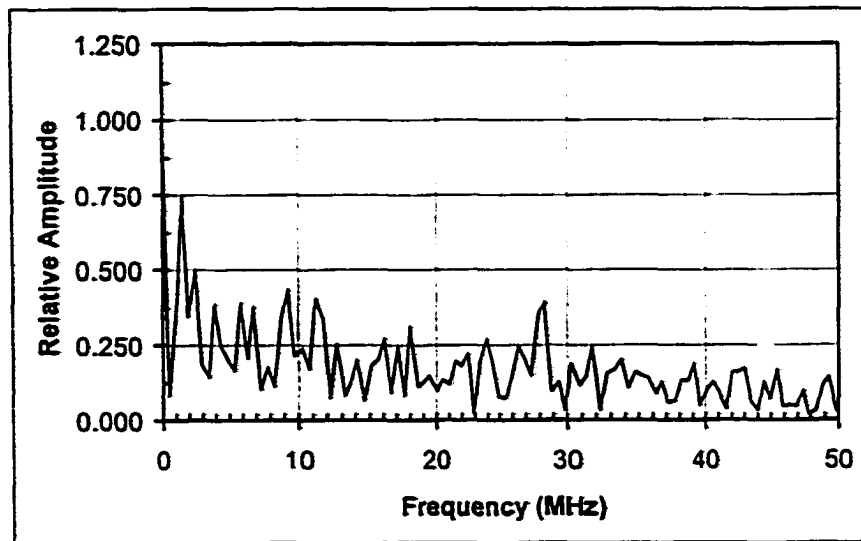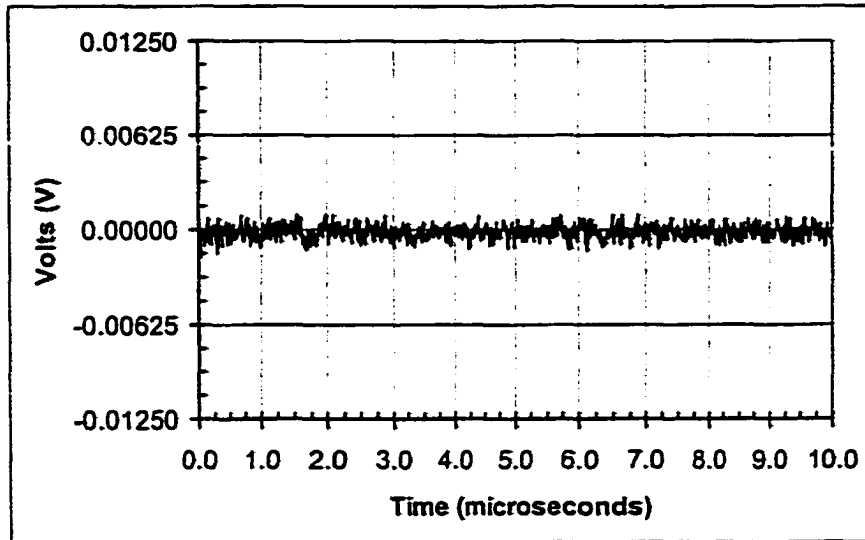
Figure 5.45: Epicentral displacement in woven GR/Epoxy generated by the RM Q-switched CTH:YAG (2.10 μm).

205
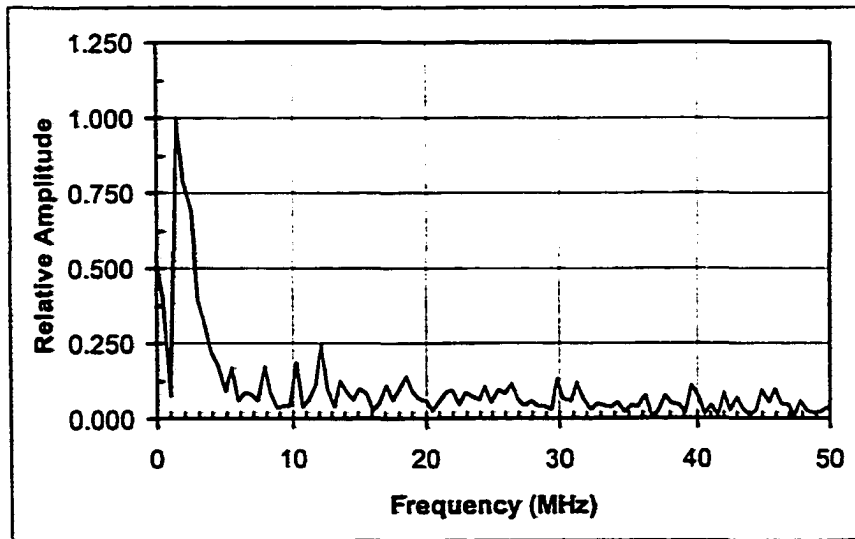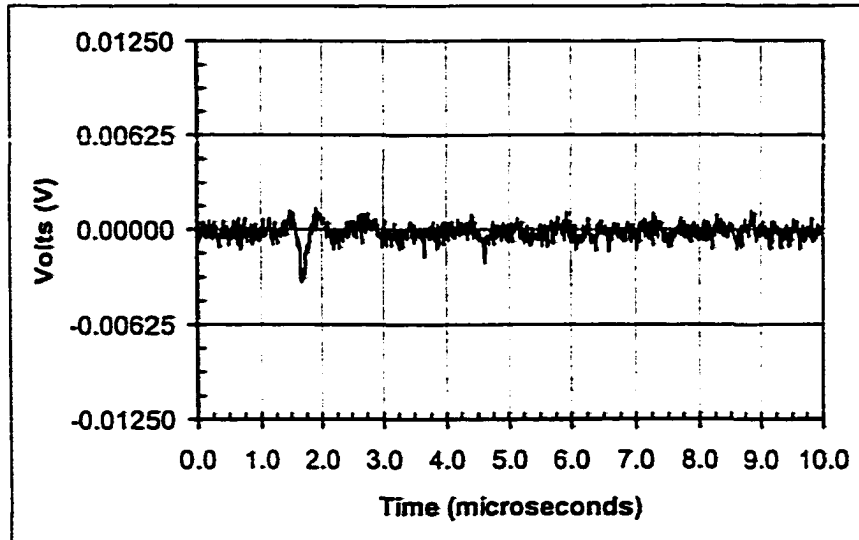
Figure 5.46: Epicentral displacement in woven Gr/Epoxy generated by the RM Q-switched CTH:YAG (2.10 μm) with constraining layer of vacuum grease.

206

Er:YAG (2.94 μm) Rotating Mirror Q-Switch

Figure 5.47 shows the averaged ultrasonic signal and corresponding frequency spectrum generated in the woven composite sample with 30 mJ per pulse from the Er:YAG laser Q-switched with the rotating mirror. The pulse width could not be measured but we assume that it was similar to the pulse width given in Figure 5.32 so that it was about 180 ns. The first wave arrival appears at 4.0 μs and a second arrival occurs at 7 μs. The third arrival is cut off at the 10 μs mark. We see that the displacement amplitude is larger than the displacement generated by the CTH:YAG. We also see that the frequency content copmuted from the first wave arrival is again dominated by frequencies around 2 MHz.
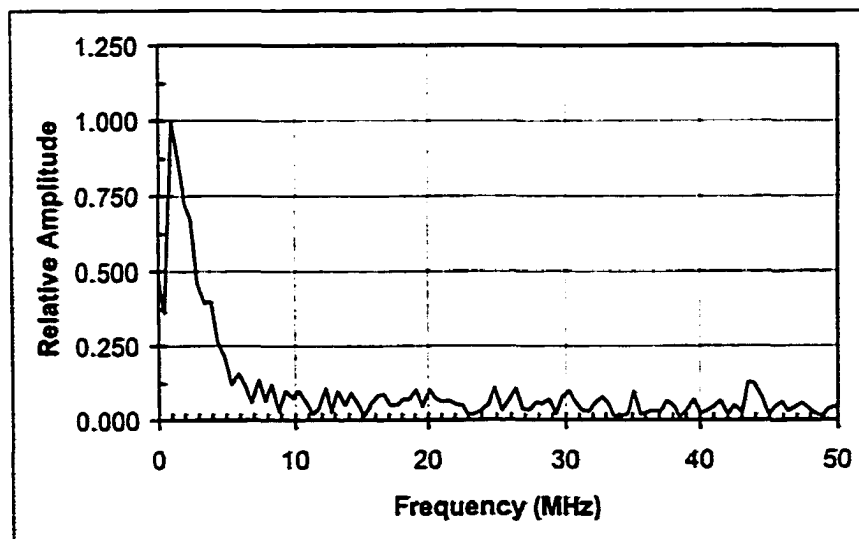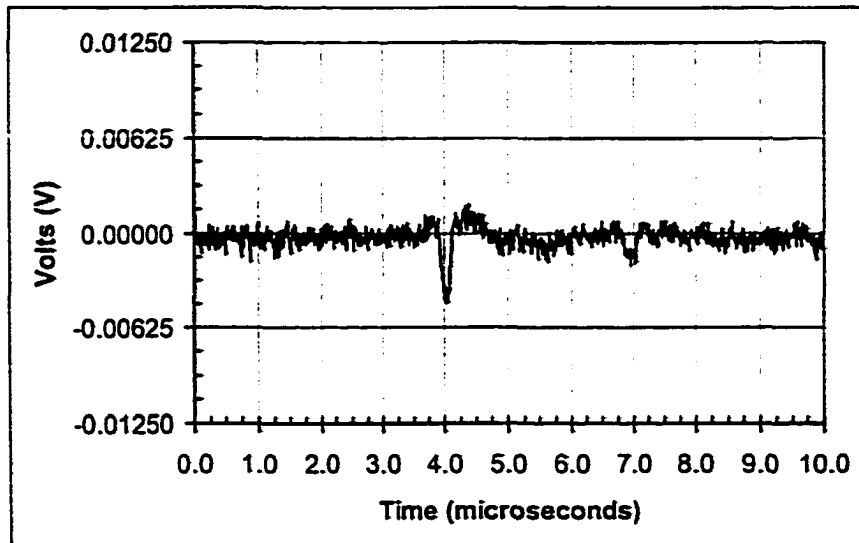
Figure 5.47: Epicentral displacement in woven GR/Epoxy generated by the RM Q-switched Er:YAG (2.94 μm)

208

Summary of Woven Graphite/Epoxy Data

To determine the absorbed instantaneous absorbed power density in the Graphite/Epoxy sample we make the approximation that the reflectivity of the sample is similar to the reflectivity of graphite. From the Fresnel equations we find that for normal incidence at the interface between two materials the reflection coefficient is given by [257]

$$r = \frac{n_2 - n_1}{n_2 + n_1} \tag{5.3}$$

where n_1 and n_2 are the indices of refraction of the first and second materials, respectively. Then, the reflectance is given by

$$R = rr^* \tag{5.4}$$

where the superscript star denotes complex conjugation. For air, $n_1 = 1$ so that we have

$$R = \left(\frac{n_2 - 1}{n_2 + 1}\right)\left(\frac{n_2 - 1}{n_2 + 1}\right)^* \tag{5.5}$$

Now, we write out n_2 in complex form as

$$n_2 = n_2 + ik_2 \tag{5.6}$$

so that

$$\begin{aligned}
R &= \left(\frac{n_2 - 1}{n_2 + 1}\right)\left(\frac{n_2 - 1}{n_2 + 1}\right)^* = \left(\frac{(n_2 - 1) + ik_2}{(n_2 + 1) + ik_2}\right)\left(\frac{(n_2 - 1) - ik_2}{(n_2 + 1) - ik_2}\right) \\
&= \left(\frac{(n_2 - 1)^2 + k_2^2}{(n_2 + 1)^2 + k_2^2}\right)
\end{aligned} \tag{5.7}$$

The values for n_2 and k_2 have been determined and tabulated for a wide range of wavelengths [265] and Table 5.4 lists these values extrapolated for the wavelengths used in our experiments along with the corresponding reflectance. The absorbed power densities are computed from the incident power densities by multiplying by the factor $(1 - R)$. Table 5.5 lists the pulse widths, energy levels, beam radius, and the instantaneous incident and

209

Wavelength [μm]	n_2	k_2	R
0.755	3.01	1.84	0.38
1.064	3.19	2.07	0.42
1.320	3.39	2.70	0.49
2.10	4.24	3.25	0.55
2.940	4.75	3.71	0.59

Table 5.4: Computed skin depth and reflectivity for graphite.

absorbed power densities obtained for each laser configuration where no or very little vacuum grease was used. The maximum peak to peak displacement measurement for the first longitudinal wave arrival is also listed.

Figure 5.48 shows plots of the displacement magnitude versus incident and absorbed power density for the first longitudinal arrival. Linear trend lines are also shown and in the first plot it appears that the displacement magnitude increases linearly with absorbed power. However, if we omit the displacement produced by the EO Q-switched Nd:YAG (1.064 μm) laser, we see in the second graph that this trend is less clear. The frequency content of the ultrasonic signals exhibited relatively strong contributions from around the 2-5 MHz range. As with the aluminum sample, the frequency content was independent of the laser parameters.

λ [μm]	Pulse Width [ns]	Energy [$\frac{mJ}{pulse}$]	Radius [mm]	Incident Power Density [$\frac{MW}{m^2}$]	Absorbed Power Density [$\frac{MW}{m^2}$]	P Wave [mV]
0.755 EO	125.0	10.0	1.5	11300.0	7000.0	3.688
0.755 AO	160.0	10.0	2.5	3180.0	1968.0	4.125
0.755 RM	105.0	10.0	2.0	7580.0	4688.0	2.438
1.064 EO	25.0	12.0	2.0	38200.0	22316.0	57.50
1.064 AO	100.0	12.0	2.5	6110.0	3571.0	6.875
1.064 RM	50.0	10.0	2.5	10200.0	5951.0	16.10
1.320 RM	130.0	15.0	3.0	4080.0	2083.0	3.375
2.100 EO	200.0	8.0	1.0	12700.0	5680.0	2.625
2.100 RM	250.0	12.0	2.0	3820.0	1704.0	2.313
2.940 RM	180.0	30.0	2.5	8490.0	3444.0	6.500

Table 5.5: Summary of experiments with the woven composite Gr/Epoxy sample.

211
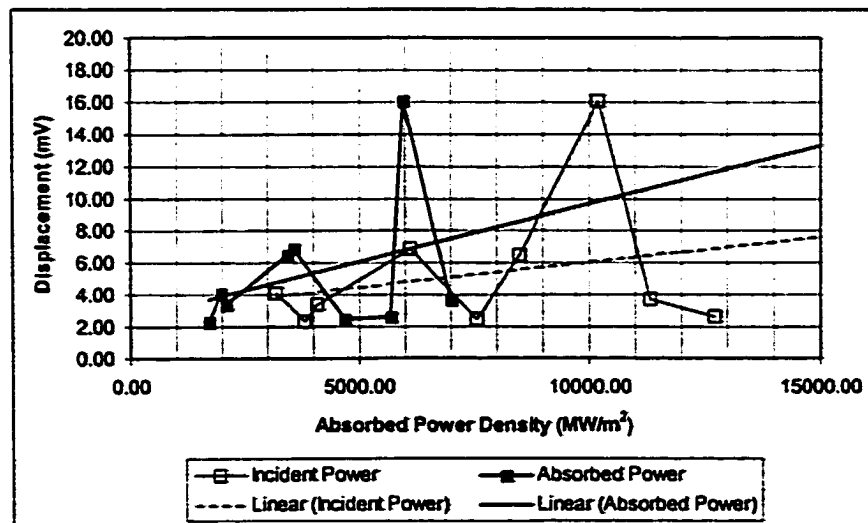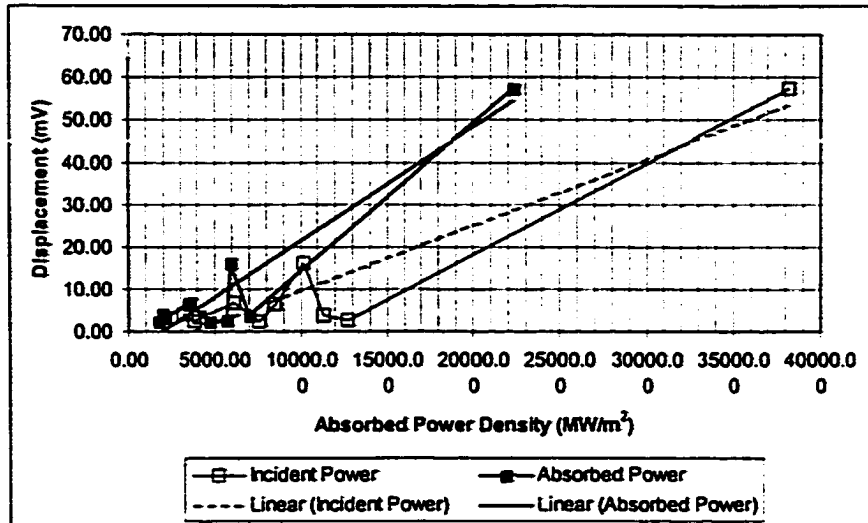
Figure 5.48: Displacement magnitude of the first arrival as a function of incident and absorbed power densities in the woven Gr/Epoxy composite sample. Bottom: Last data point omitted.

212

5.2.3 Epoxy

Transducer

Figure 5.49 illustrates the average ultrasonic waveform and frequency spectrum produced by the transducer in the epoxy sample. The time interval between the two wave arrivals in the first plot is about six microseconds. The round trip distance is 1.398 cm so that the wave speed is 2330 $\frac{m}{s}$. As before, the frequency content of the waveform has a range of 10 MHz centered about 5 MHz.

Alexandrite (0.720–0.790 μm)

Electro-Optic Q-Switch Figure 5.50 shows the average ultrasonic waveform and frequency spectrum generated in the epoxy sample with 10 mJ per pulse from the Alexandrite laser with the electro-optic Q-switch. Since this sample was translucent, the power transmitted through the sample was also measured. In this case, the transmitted power was 2.5 mJ per pulse. The pulse width was approximately 125 ns and the intensity profile was similar to the profile given in Figure 5.6. We see from in the first plot of Figure 5.50 that there are two wave arrivals corresponding to the two arrivals in the transducer generated signal in Figure 5.49. The first arrival occurs at 1 μs and the second around 8 μs. The frequency content has strong contributions around 0.5 and 1.5 MHz and all of the energy is contained in a frequency range below 5 MHz.

Acousto-Optic Q-Switch Figure 5.51 shows the averaged ultrasonic waveform and frequency spectrum produced in the epoxy sample with 12 mJ per pulse from the AO Q-switched Alexandrite laser. The pulse width was approximately 160 ns and the intensity profile was similar to the profile given in Figure 5.11. After the data was taken, the transmitted power through the sample was initially measured as 5 mJ per pulse. However, during

213
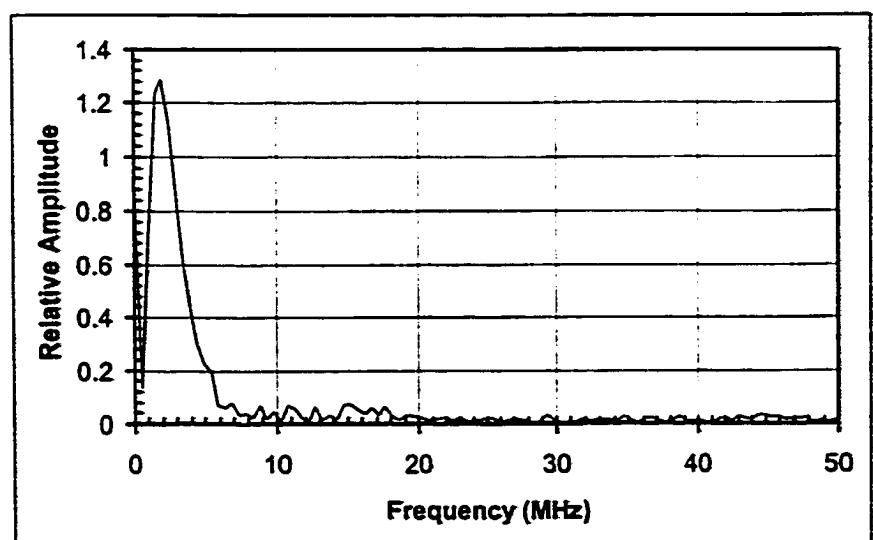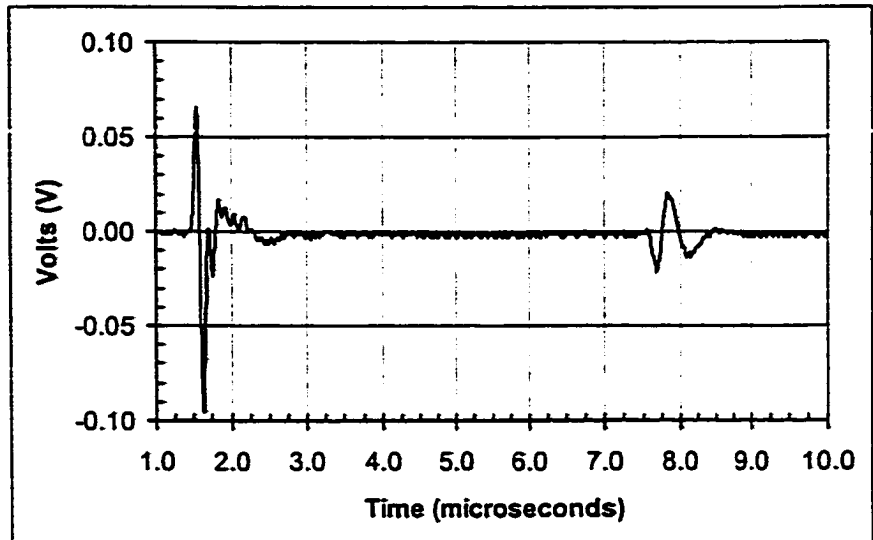
Figure 5.49: 10 MHz transducer response and frequency spectrum of the second wave arrival in the epoxy sample.

214
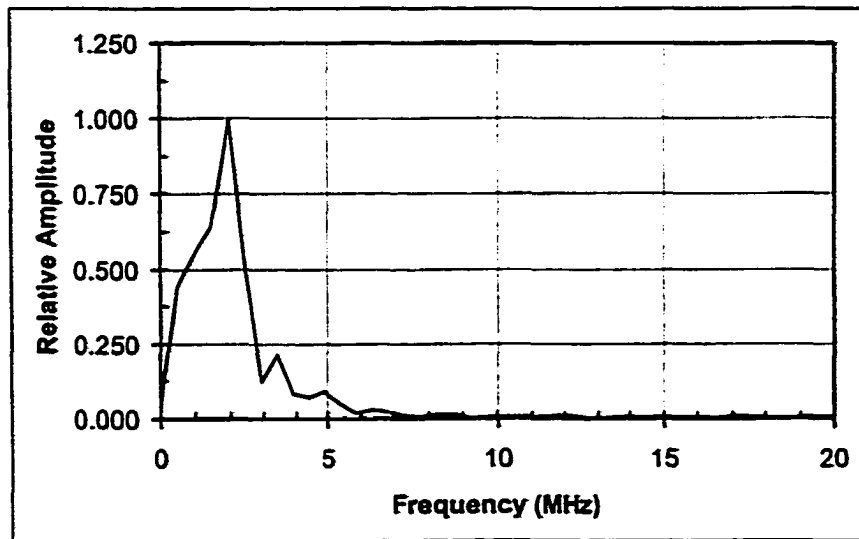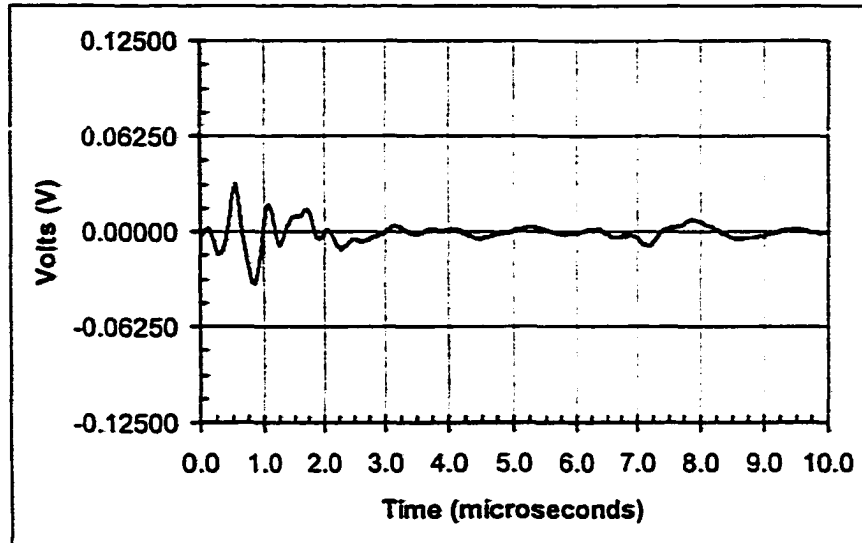
Figure 5.50: Epicentral displacement in epoxy generated by the EO Q-switched Alexandrite laser.

215

the data collection, the detection laser had damaged the sample. The damage appeared as a black spot near the surface (on the detection side) of the sample. The damage was severe enough that the amount of reflected detection light was reduced and the interferometer lost stability. The transmitted power was again measured in a new location where there was no damage from the detection laser. In this case, the measured transmitted power was 7 mJ per pulse. We see in Figure 5.51 that the signal amplitude is smaller than the signal due to the EO Q-switched laser and that the second wave arrival is not visible. The frequency spectrum, however, is similar to the spectrum produced by the EO Q-switched laser. There is a peak around 1.5 MHz and the energy is contained in a frequency range below 5 MHz.

Rotating Mirror Q-Switch Figure 5.52 shows the average ultrasonic signal and corresponding frequency spectrum generated in the epoxy sample with 10 mJ per pulse from the Alexandrite laser Q-switched with the rotating mirror. The pulse width was measured as 105 ns and a lens was used to expand the beam radius so that the intensity profile was similar to the profile shown in Figure 5.13. The transmitted power was measured as 5 mJ per pulse. In comparison to the previous waveforms generated with the Alexandrite laser, we see a significantly different waveform. Instead of one or two arrivals, three wave arrivals are visible at 0.5, 4.0, and 7.5 μs but the overall amplitude is much smaller than in the previous waveforms. The arrival at 4.0 μs may be a shear wave arrival or it may be due to a void, crack or other inclusion. Although we consider the epoxy sample isotropic, it was not homogeneous and had slightly different thicknesses and features at different locations. Since the detection laser damaged the sample during each test, the experiment could not be repeated at the same location for each different laser configuration. Consequently, these difference could be due to slightly different features at the different locations. The frequency spectrum is noiser than in the previous examples because of the lower SNR but there is still
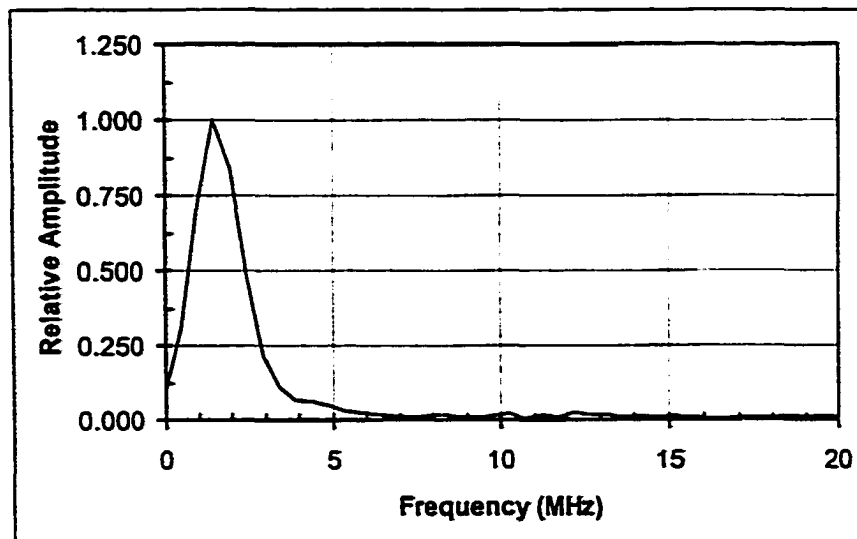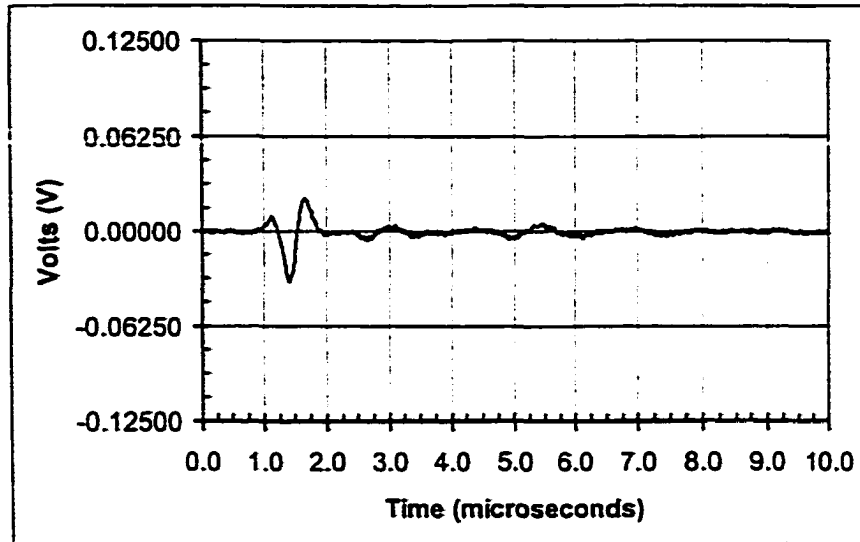
Figure 5.51: Epicentral displacement in epoxy generated by the AO Q-switched Alexandrite laser.

217

a strong contribution around 1.5 MHz and the energy dies out after 5 MHz.

Nd:YAG (1.064 μm)

Electro-Optic Q-Switch Figure 5.53 illustrates the averaged ultrasonic signal and frequency spectrum produced in the epoxy sample with 80 mJ per pulse from the EO Q-switched Nd:YAG laser. The pulse width was approximately 25 ns and the intensity profile was similar to the profile indicated in Figure 5.16. The transmitted power was initially 30 mJ per pulse but this dropped as the sample was damaged and scarred. No signal could be obtained without causing some damage probably because most of the light transmitted through the sample until some damage developed to stop the transmission. A higher power level was used in this experiment because the transmission was high and no signal was visible at lower powers. We see two wave arrivals separated by 6.0 μs in the first plot of Figure 5.53 corresponding to two arrivals in Figure 5.49 generated with the transducer at 1.5 and 7.5 μs. We also see a very high frequency ringing throughout the signal. This is most likely due to electrical interference but may be due to nonlinear effects as the epoxy was melted and damaged. It may also be due to damage caused by the detection laser. This high frequency ringing appears as a sharp spike in the frequency spectrum around 7 MHz. There are still contributions around 1 MHz as in the previous examples with the epoxy sample. Also, besides the high frequency spike, most of the energy is contained below 5 MHz. Figure 5.54 shows the results of using the same laser at 70 mJ per pulse with a thin layer of grease applied to the surface. We see that the waveform is similar except that the amplitude of the two wave arrivals has been significantly enhanced. The frequency spectrum still shows the peak due to the ringing at 7 MHz but now is dominated by the lower frequency signals around 1.0 MHz.
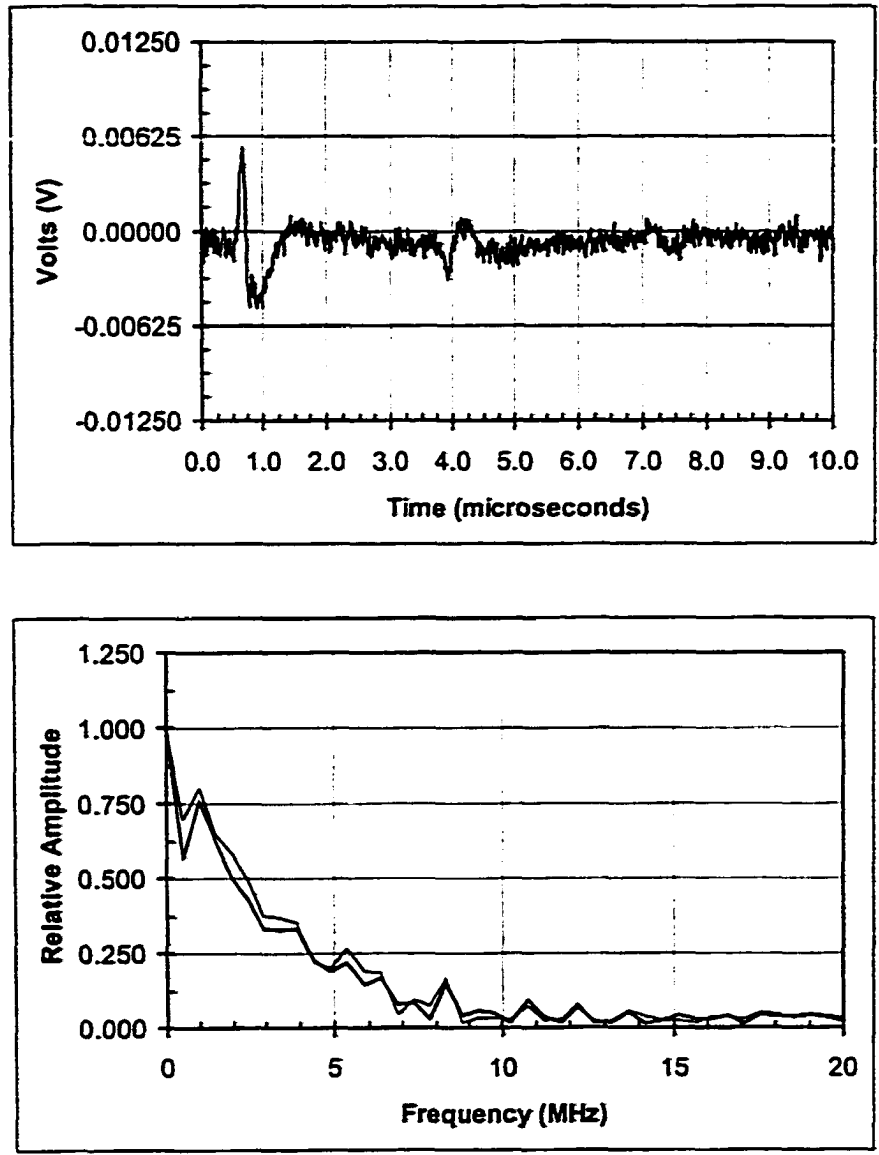
Figure 5.52: Epicentral displacement in epoxy generated by the RM Q-switched Alexandrite laser.

219
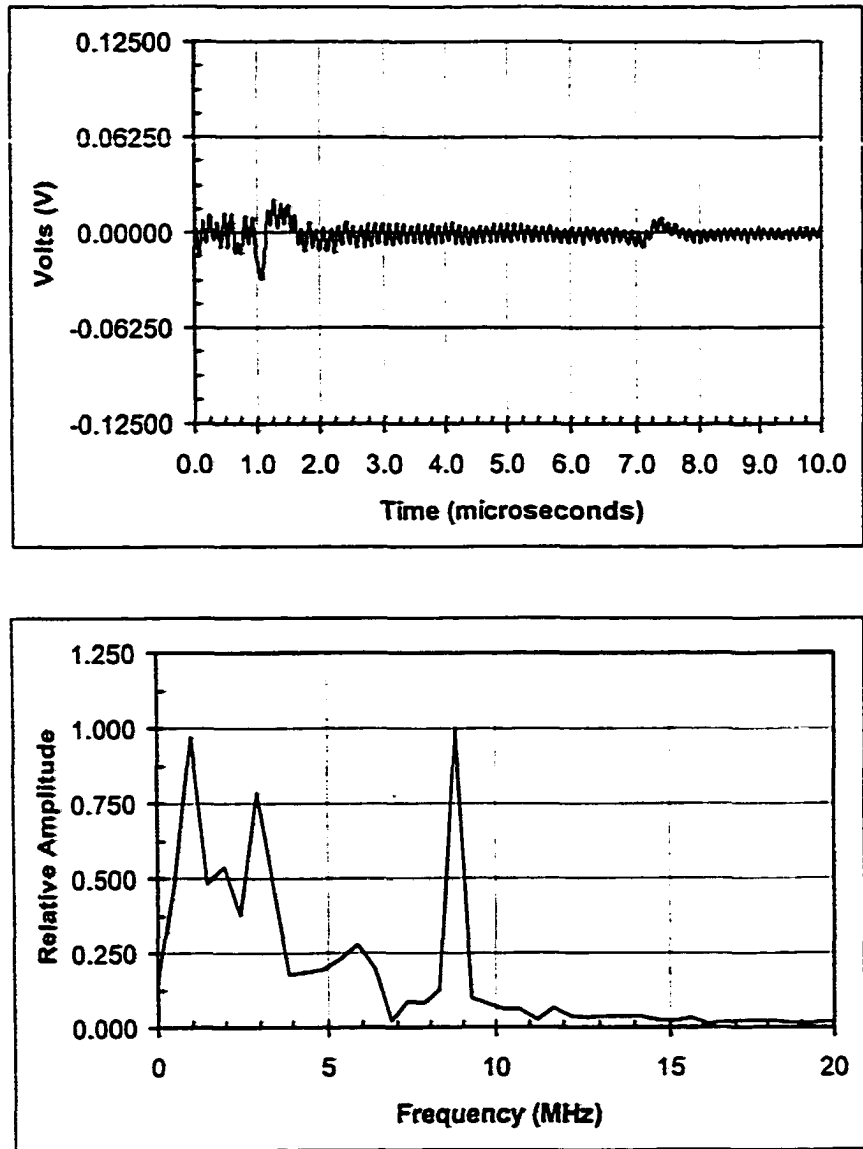
Figure 5.53: Epicentral displacement in epoxy generated by the EO Q-switched Nd:YAG (1.064 μm) laser.
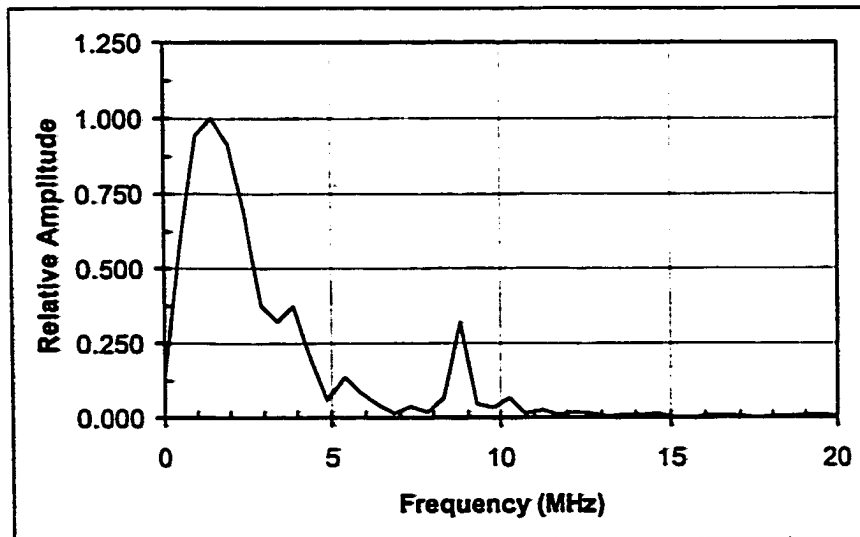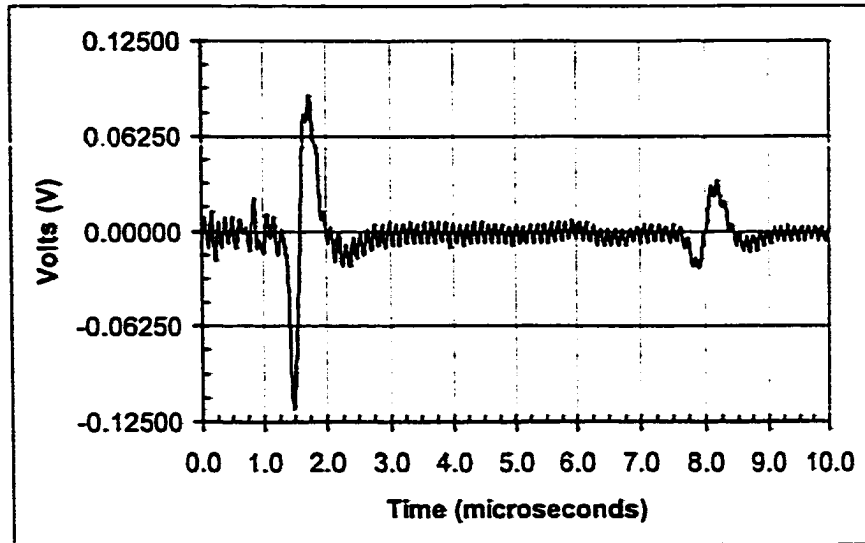
220

Figure 5.54: Epicentral displacement in epoxy generated by the EO Q-switched Nd:YAG (1.064 μm) laser with a constraining layer of vacuum grease.

221

Acousto–Optic Q-Switch Figure 5.55 shows the average ultrasonic signal and corresponding frequency spectrum generated in the epoxy sample by the AO Q-switched Nd:YAG laser with 12 mJ per pulse. The pulse width was approximately 90 ns and the intensity profile was similar to the profile given in Figure 5.20. The transmitted power was measured at 10 mJ per pulse. We see that the amplitude of the ultrasonic signal is significantly smaller than the previous signals with the EO Q-switch. The is expected because of the reduced power. We see also that the high frequency ringing is absent probably because the sample was not damaged at this low power level. The frequency spectrum is noisy because of the low SNR but there are still contributions around 1 MHz.

Rotating Mirror Q-Switch Figure 5.56 illustrates the average ultrasonic signal and corresponding frequency spectrum obtained with 8 mJ per pulse from the Nd:YAG laser Q-switched with the rotating mirror. The pulse width was approximately 40 ns and the intensity profile was similar to the profile in Figure 5.22. The transmitted power was not measured in this case. We see two prominent wave arrivals in the first plot of Figure 5.56 corresponding to the two arrivals generated by the transducer in Figure 5.49. The two waveforms are very similar except that the displacements generated by the transducer have a higher frequency than the displacements generated by the laser. This is clear in the frequency spectra of the two signals. We see in Figure 5.56 that the frequency content is dominated by components around 1 to 2 MHz in the laser generated signal whereas the transducer signal has components from 1 to 10 MHz.

Nd:YAG (1.32 μm) Rotating Mirror Q-Switch

Figure 5.57 shows the averaged ultrasonic signal and frequency spectrum generated in the epoxy sample by 15 mJ per pulse from the second Nd:YAG wavelength Q-switched

222
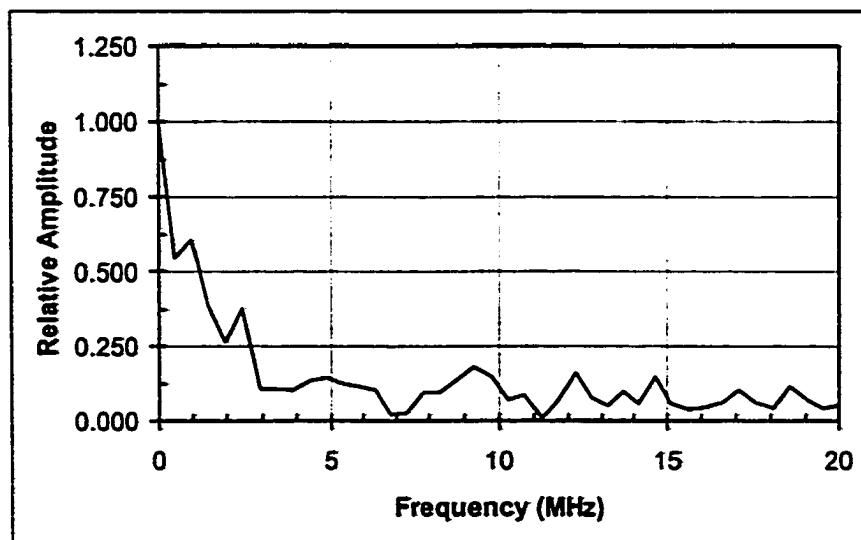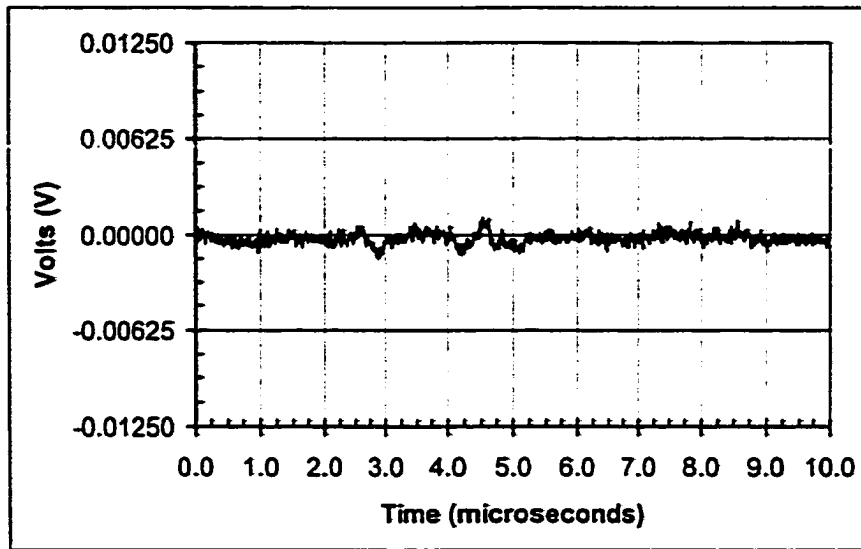
Figure 5.55: Epicentral displacement in epoxy generated by the AO Q-switched Nd:YAG (1.064 μm) laser.

223
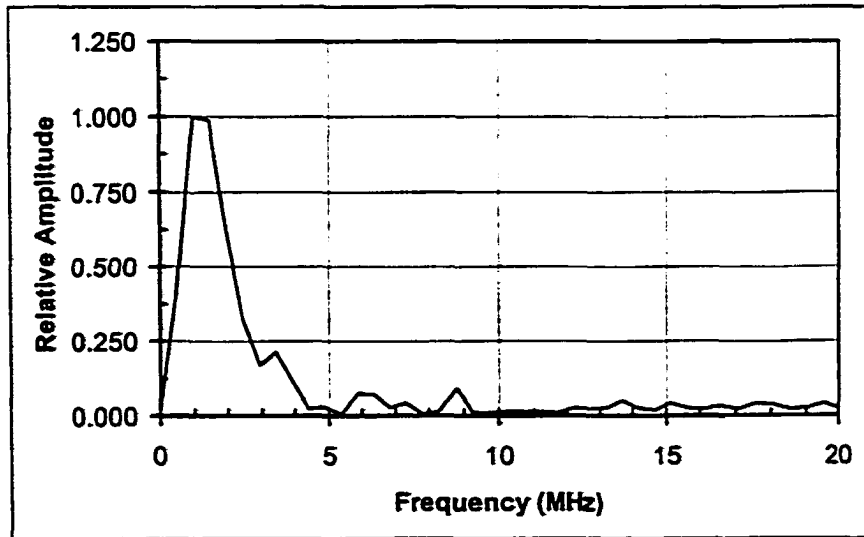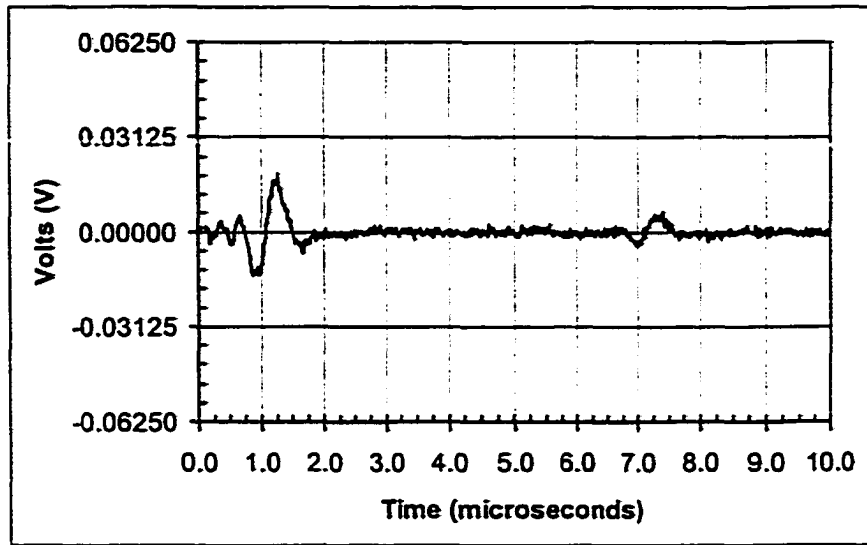
Figure 5.56: Epicentral displacement in epoxy generated by the RM Q-switched Nd:YAG (1.064 μm) laser.

224

with the rotating mirror. The pulse width was approximately 130 ns and the intensity profile was similar to the profile shown in Figure 5.24. The transmitted power was measured as 11 mJ per pulse and a thin layer of grease was applied to the sample surface. We see that no real ultrasonic signal is visible and that the frequency spectrum is dominated by noise.

CTH:YAG (2.10 μm)

Electro-Optic Q-Switch Figure 5.58 illustrates the average ultrasonic signal and corresponding frequency spectrum generated by 7 mJ per pulse from the EO Q-switched CTH:YAG laser. The pulse width was approximately 200 ns and the intensity profile was similar to the profile indicated in Figure 5.26. Here, all of the power was absorbed in the sample and no power was observed to transmit through the sample. We see that despite the relatively low power density, there are still two wave arrivals separated by 6.0 μs in Figure 5.58. This suggests that this wavelength is more efficient at generating ultrasound in this material. As in some of the previous examples, the frequency spectrum shows a strong contribution around 1 MHz.

Rotating Mirror Q-Switch Figure 5.59 shows the average ultrasonic signal and frequency spectrum produced in the epoxy sample with 12 mJ per pulse from the CTH:YAG laser Q-switched with the rotating mirror. The pulse width was approximately 250 ns and the intensity profile was similar to the profile shown in Figure 5.28. Once again, no power transmitted through the sample. We see two clear wave arrivals separated by 6.0 μs as in the signal generated by he transducer. Similar to previous examples, the frequency content shows strong contributions from frequency components around 1 MHz.

225
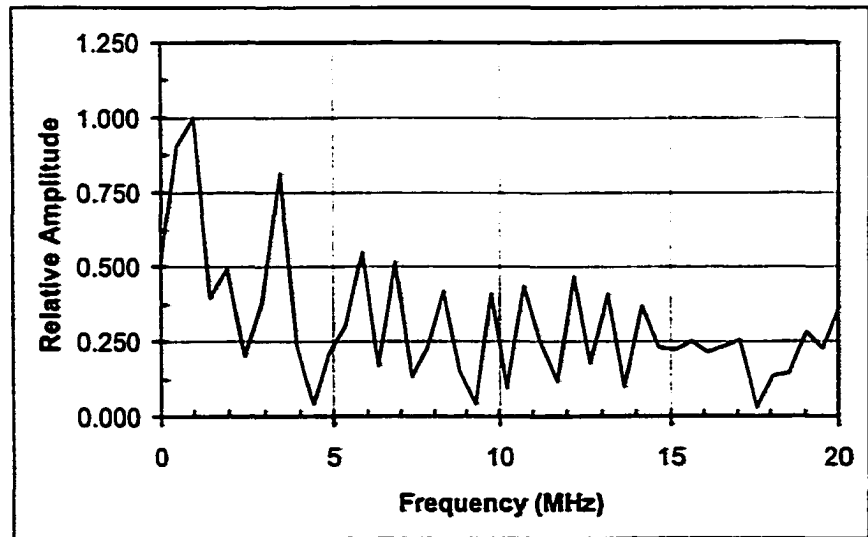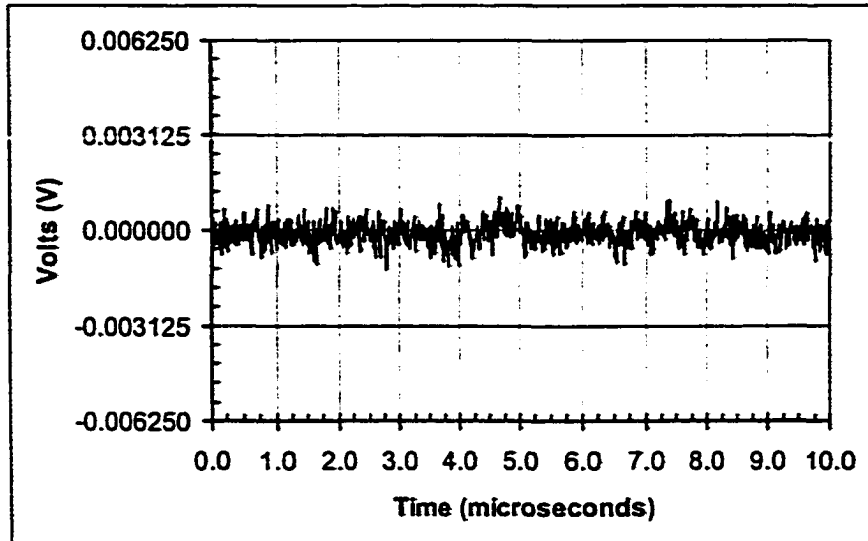
Figure 5.57: Epicentral displacement in epoxy generated by the RM Q-switched Nd:YAG (1.320 μm) laser.
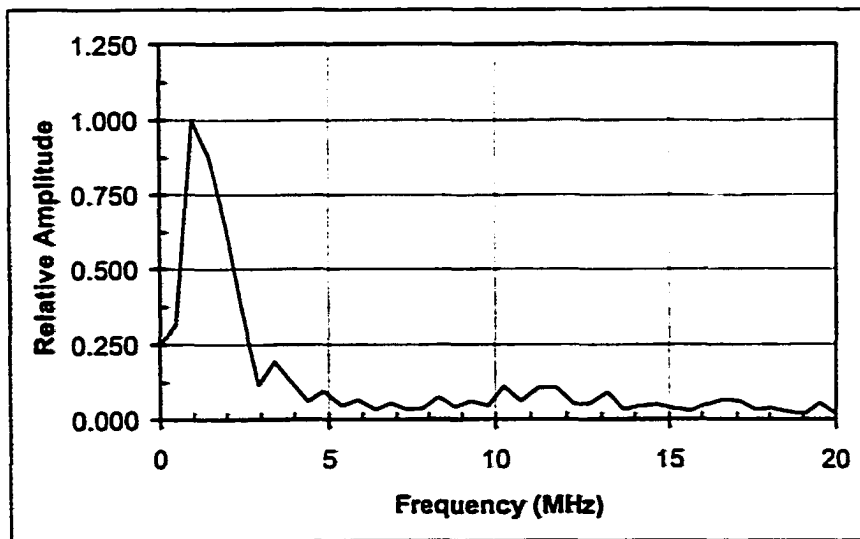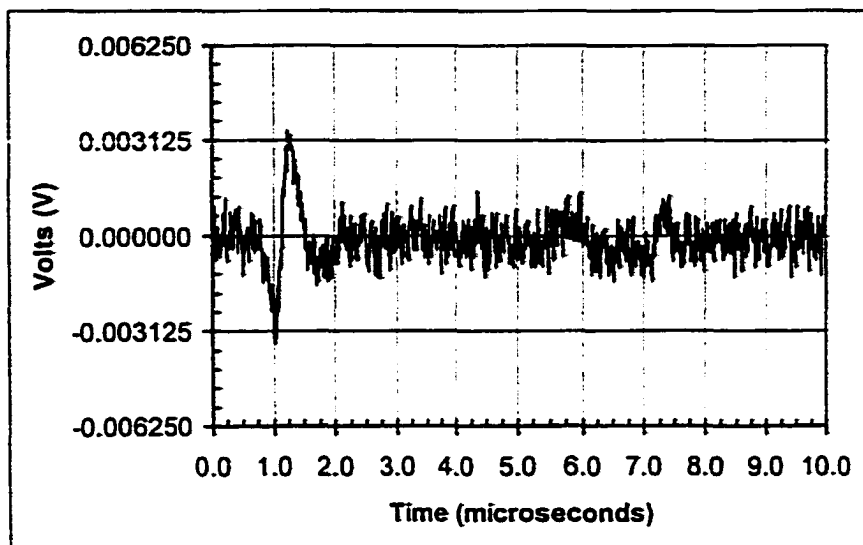
226

Figure 5.58: Epicentral displacement in epoxy generated by the EO Q-switched CTH:YAG (2.10 μm) laser.

227
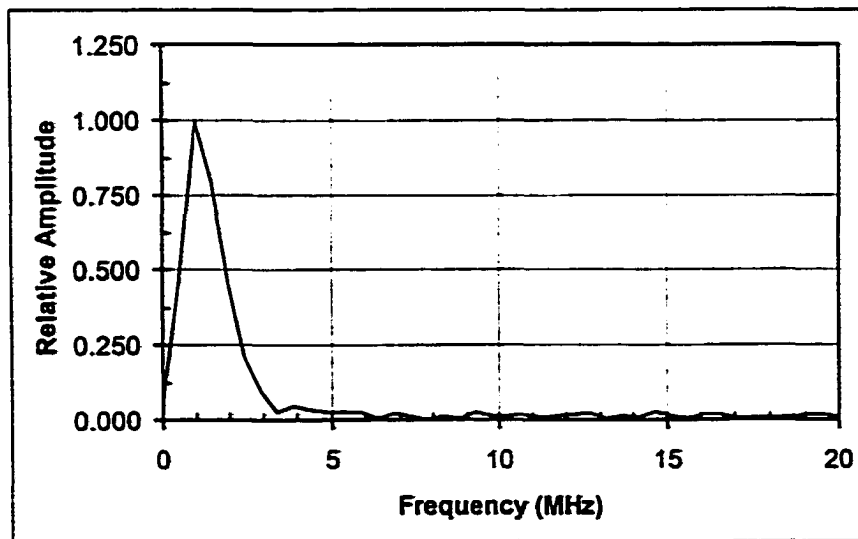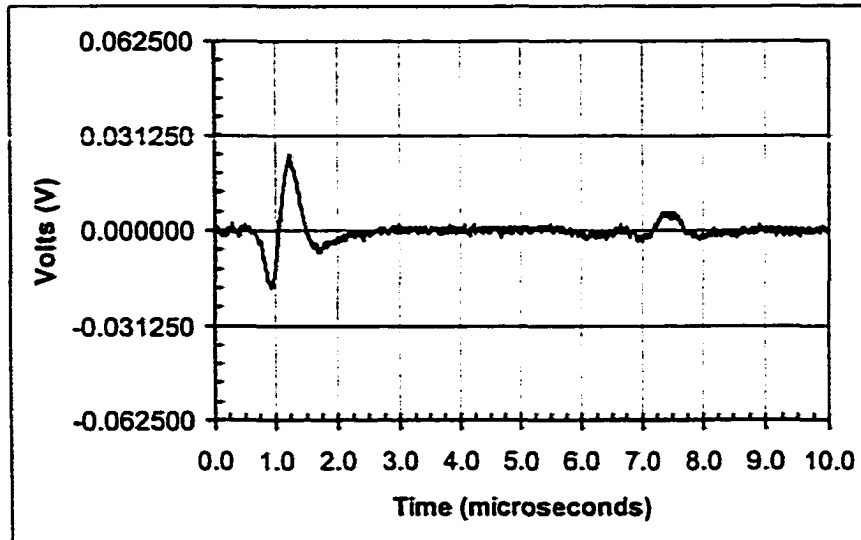
Figure 5.59: Epicentral displacement in epoxy generated by the RM Q-switched CTH:YAG (2.10 μm) laser.

228

Er:YAG (2.94 μm) Rotating Mirror Q-Switch

Figure 5.60 shows the averaged ultrasonic signal and corresponding frequency spectrum generated in the epoxy sample with 24 mJ per pulse from the Er:YAG laser Q-switched with the rotating mirror. The pulse width was estimated to be 180 ns. No power was measured transmitted through the sample As in the last example, we see two clear wave arrivals separated by 6.0 μs. The amplitude of these arrivals is larger than the amplitude of the waves produced by the CTH:YAG laser in Figure 5.59. However, the frequency spectra are similar and we once again see strong contribution around 1 MHz.
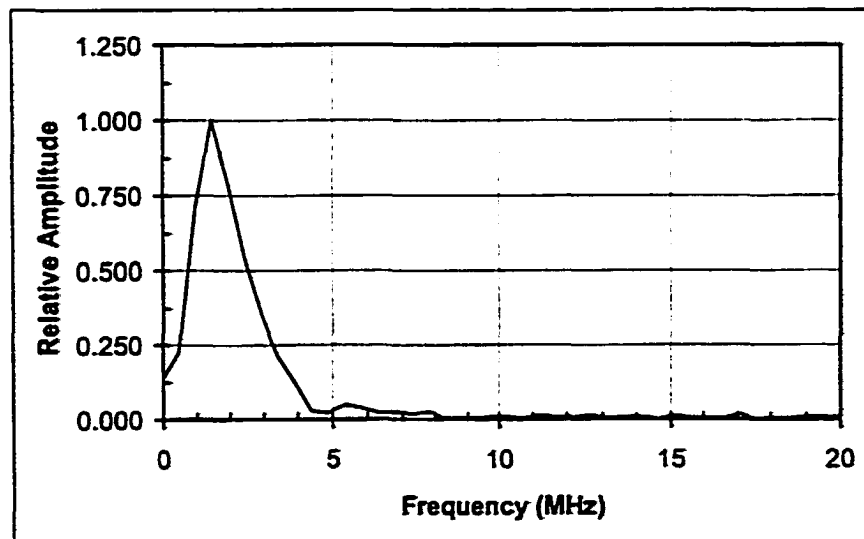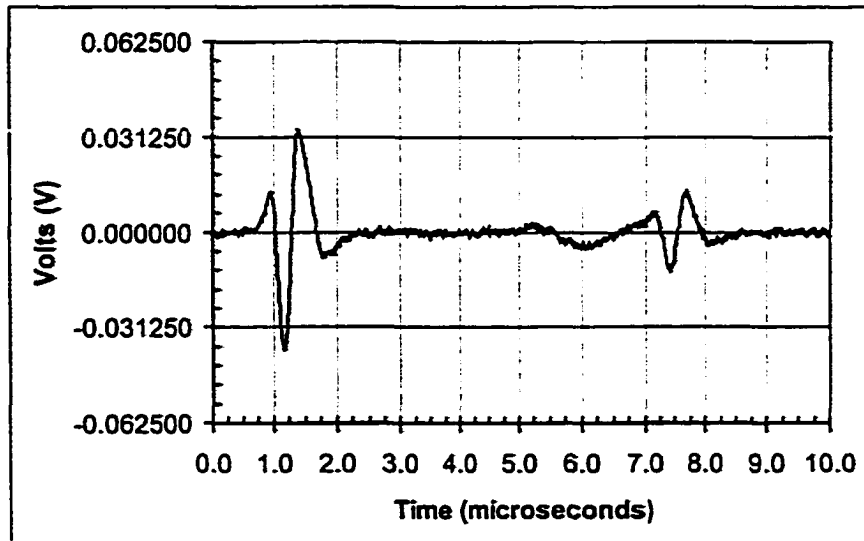
Figure 5.60: Epicentral displacement in epoxy generated by the RM Q-switched Er:YAG (2.94 μm) laser.

230

Summary of Epoxy Data

This sample is unique among the samples because it was translucent and a considerable amount of the laser energy transmitted through the sample. This transmitted energy was measured for each laser configuration. The reflected energy was also measured but was neglibly small for our wavelengths so that we can estimate the absorbed energy by subtracting the transmitted energy from the incident energy. Table 5.6 lists the pulse widths, energy levels, beam radius, measured transmitted energy, and the instantaneous incident and absorbed power densities obtained for each laser configuration where no or very little vacuum grease was used. The maximum peak-to-peak displacement measurement for the first longitudinal wave arrival is also listed. Figure 5.61 shows plots of the displacement magnitude versus incident power density for the first longitudinal arrival on two different scales. Figure 5.62 illustrates the displacement magnitude versus incident power density for the first longitudinal arrival. By comparing the second plot in Figure 5.61 with the values in Table 5.6 we see that the maximum displacement was generated by the Er:YAG laser at a relatively lower instantaneous incident power density. This is because the the Er:YAG wavelength was absorbed better so that the instantaneous absorbed power density was higher. The CTH:YAG wavelength was also absorbed more easily so that a higher absorbed power density was obtained. Consequently, a larger displacement was generated with this wavelength and the RM Q-switch. However, the EO Q-switched CTH:YAG, which had an even higher instantaneous absorbed power density, did not generate a large displacement. The Alexandrite laser was also able to generate larger amplitude displacements even though it was not absorbed as well and produced lower absorbed power densities. We note that the RM Q-switched Alexandrite laser generated almost the same absorbed density as the RM Q-switched CTH:YAG laser but generated a much smaller displacement. However, the EO Q-switched Alexandrite actually produced a relatively high abosrbed power density and a

231

λ [μm]	Pulse Width [ns]	Energy $[\frac{mJ}{pulse}]$	Radius [mm]	Measured Transmitted Energy $[\frac{mJ}{pulse}]$	Incident Power Density $[\frac{MW}{m^2}]$	Absorbed Power Density $[\frac{MW}{m^2}]$	P Wave [mV]
0.755 EO	125.0	10.0	1.5	2.5	11317.0	8488.0	66.3
0.755 AO	160.0	12.0	2.5	5.0-7.0	3820.0	1273.0	55.0
0.755 RM	105.0	10.0	2.0	5.0	7579.0	3789.0	10.6
1.064 EO	25.0	80.0	2.0	30.0	2540481.0	159155.0	52.8
1.064 AO	90.0	12.0	2.5	10.0	6791.0	1132.0	2.31
1.064 RM	40.0	8.0	2.5	6.7[1]	10186.0	1655.0	34.1
1.320 RM	130.0	15.0	3.0	11.0	4081.0	1088.0	1.94
2.100 EO	200.0	7.0	1.0	0.0	11141.0	11141.0	7.00
2.100 RM	250.0	12.0	2.0	0.0	3820.0	3820.0	43.8
2.940 RM	180.0	24.0	2.5	0.0	6791.0	6791.0	72.2

Table 5.6: Summary of experiments with the Epoxy sample.

232

correspondingly large displacement. We suggest that these inconsitencies can be attributed to experimental difficulties with this sample. Specifically, the detection laser would damage the sample during each test. This damage changed the transmission properties of the sample and therefore changed the absorbed power. The greatest incident power and absorbed was obtained with the EO Q-switched Nd:YAG (1.064 μm) laser and a large displacement was generated. However, the laser had to be operated at significantly higher power levels since a high percentage of the light was transmitted. Furthermore, the generated waveform exhibits a high frequency ringing probably due to nonlinear effects caused by damage to the sample. The frequency content of the ultrasonic signals generally shows strong contributions around 1-3 MHz and appears relatively insensitive to the laser parameters.
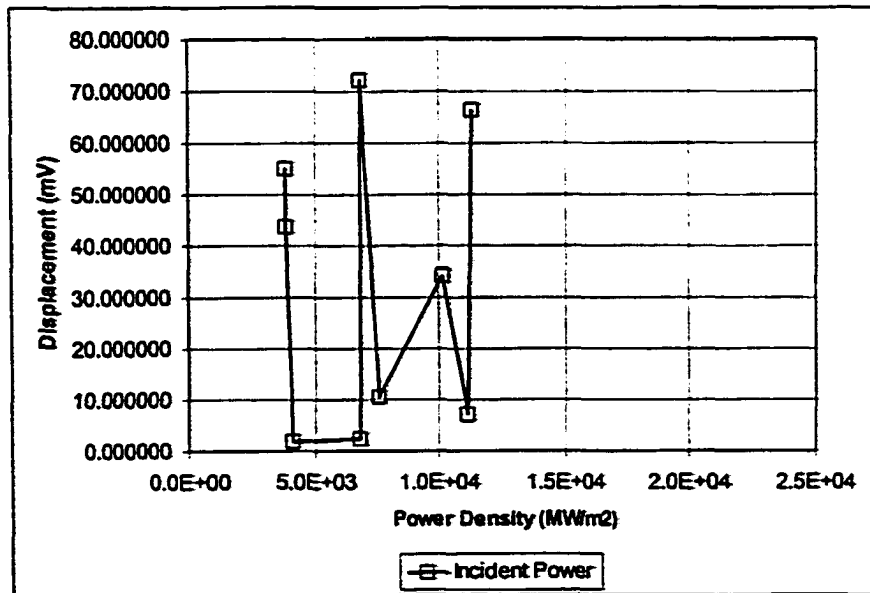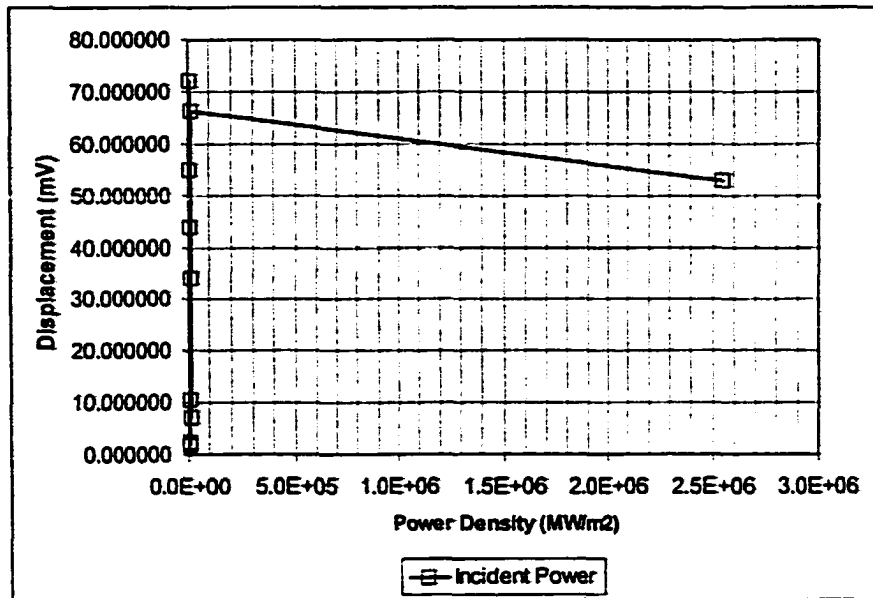
Figure 5.61: Displacment magnitude of the first arrival as a function of incident power densities in the epoxy sample. Bottom: Magnified scale for smaller densities.

234
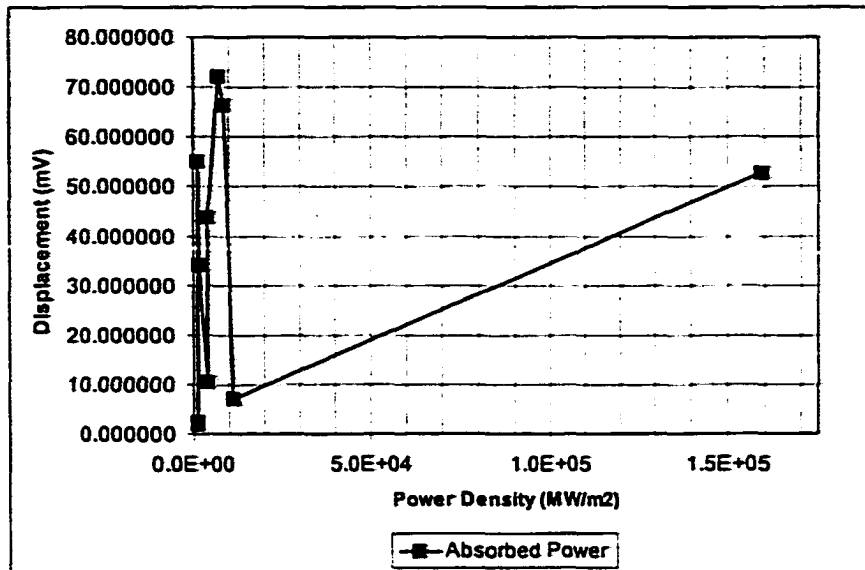
Figure 5.62: A plot of displacement magnitude versus absorbed power density for the epoxy sample.

5.2.4 Woven Graphite/Epoxy with Kevlar Stitches

Transducer

Figure 5.63 shows the average ultrasonic waveform and frequency spectrum generated by the transducer in the Kevlar stitched woven graphite/epoxy sample. This sample attenuates and scatters ultrasound so severely that it is difficult to image with conventional contact ultrasound techniques. We see that the sample was too thick to observe a round trip arrival and we cannot estimate the wave speed. We also see that the frequency content of the signal is dominated by lower frequency components around 1 and 2 MHz. This is expected because higher frequencies are attenuated faster so that only the lower frequency components arrive through the thickness of the sample.

235
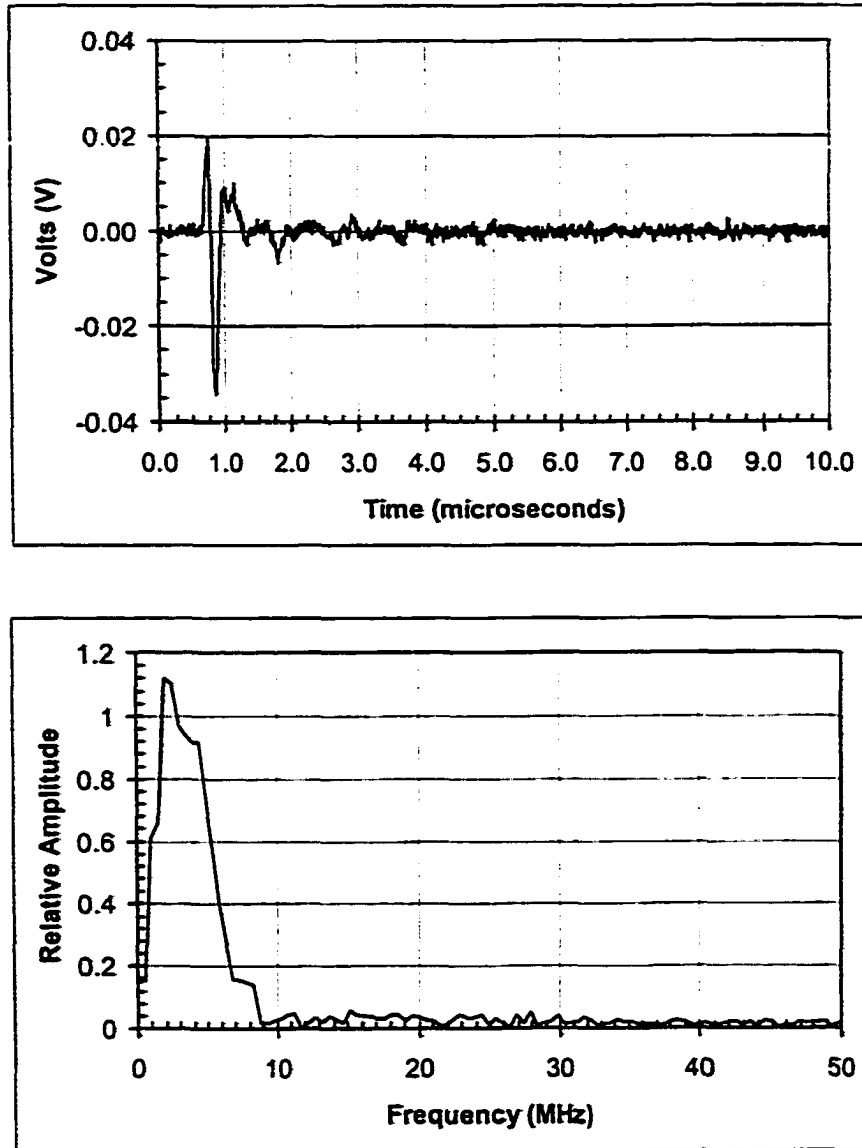
Figure 5.63: 10 MHz transducer response and frequency spectrum of the first wave arrival in the stitched woven GR/Epoxy sample.

236

Alexandrite   (0.720-0.790 μm)

Electro-Optic Q-Switch   Figure 5.64 shows the averaged ultrasonic signal and corresponding frequency spectrum generated in the stitched woven composite with 10 mJ per pulse from the EO Q-switched Alexandrite laser. The pulse width was approximately 125 ns and the intensity profile was similar to the profile given in Figure 5.6. The generation spot was chosen to lie between two rows of translaminar stitching, pictorially shown in Figure 5.65. As with the other composite sample, the generation spot was marked so that data could be taken at the same location in the subsequent experiments. We see in Figure 5.64, only the first wave arrival is clearly visible. Similar to the unstitched composite, the frequency spectrum shows significant contributions around 1-2 MHz. Figure 5.66 shows the data taken with the same laser settings except that the generation power was only 8 mJ per pulse and a lens was used to expand the beam so that the intensity profile was similar to the profile given in Figure 5.8. We see the same general features as in the previous figure, except that the amplitude of the wave arrival is larger.

Acousto-Optic Q-Switch   Figure 5.67 shows the average ultrasonic signal and corresponding frequency spectrum produced in the stitched composite sample with 10 mJ per pulse from the AO Q-switched Alexandrite laser. The pulse width was approximately 160 ns and the intensity profile was similar to the profile indicated in Figure 5.11. Just like with the EO Q-switch results, we see a single clear wave. The amplitude of this wave is slightly larger than the amplitude of the wave generated by the EO Q-switched laser. There may be a disturbance around 6.0 μs, but the noise is too high to be certain. The frequency spectrum is also similar to the spectrum of the EO Q-switched laser with strong contributions around 1 and 2 MHz.

237
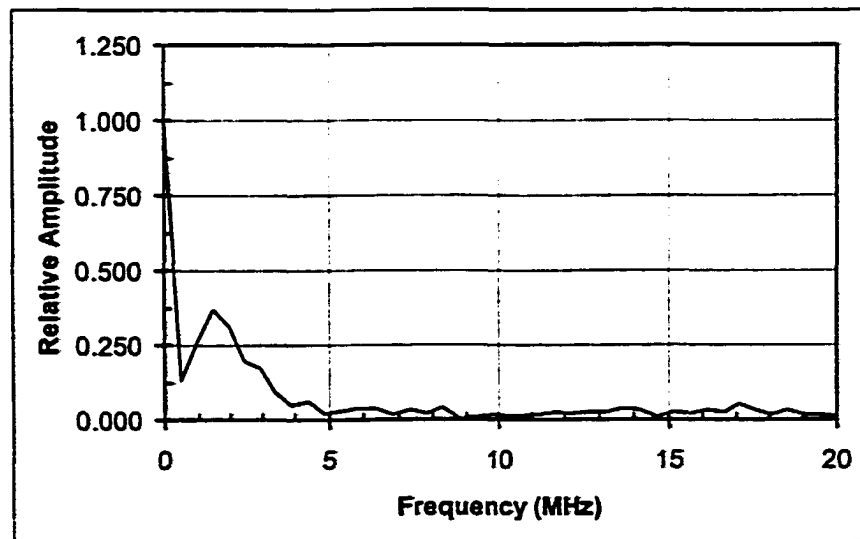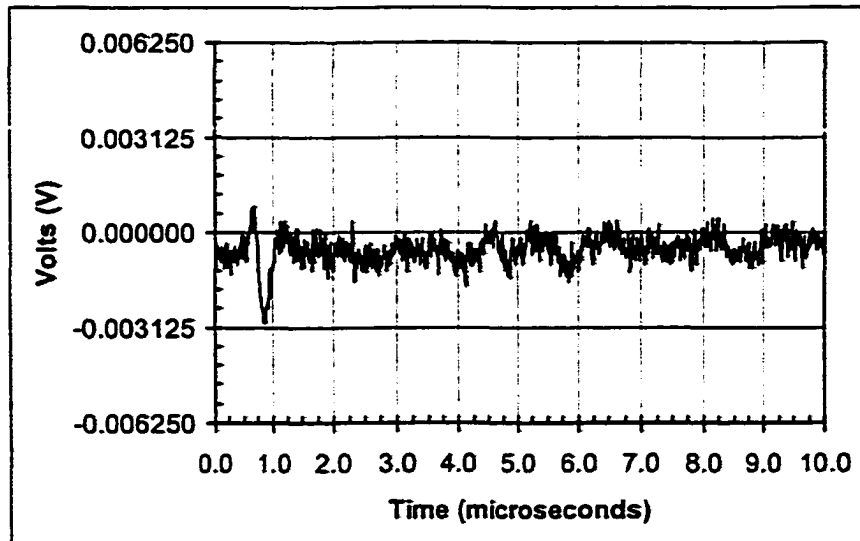
Figure 5.64: Epicentral displacement in stitched woven GR/Epoxy generated by the EO Q-switched Alexandrite laser.

238
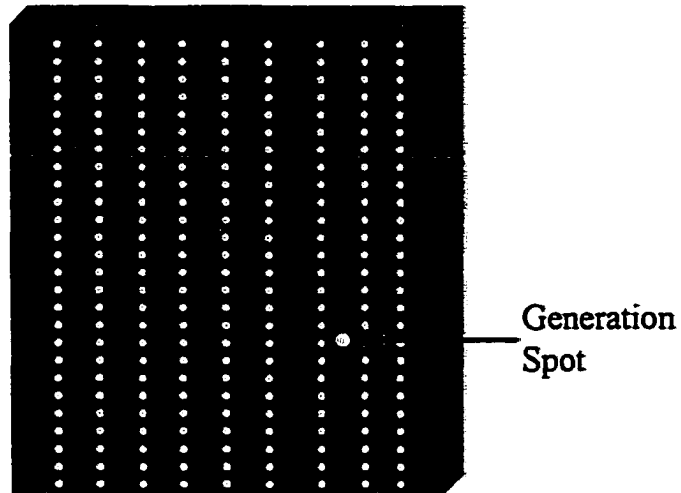
Figure 5.65: Schematic showing the generation spot with the stitched woven Gr/Epoxy sample.

Rotating Mirror Q-Switch   Figure 5.68 shows the averaged ultrasonic signal and corresponding frequency spectrum obtained in the stitched composite sample with 12 mJ per pulse from the Alexandrite laser Q-switched with the rotating mirror. The pulse width was 105 ns and the intensity profile was similar to the profile given in Figure 5.13. We see one clear wave arrival and its amplitude is larger than the wave amplitudes generated with the other Q-switches at this wavelength. The frequency spectrum once again shows strong contributions around 1 and 2 MHz.

239
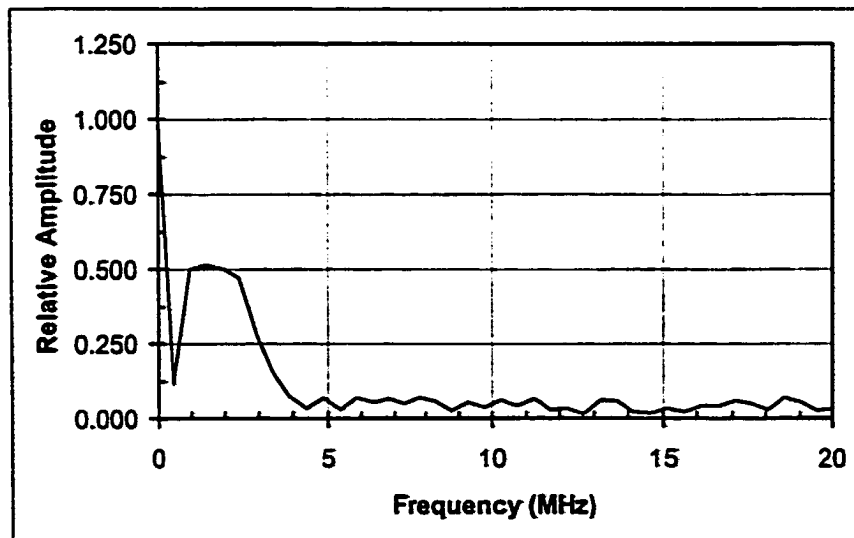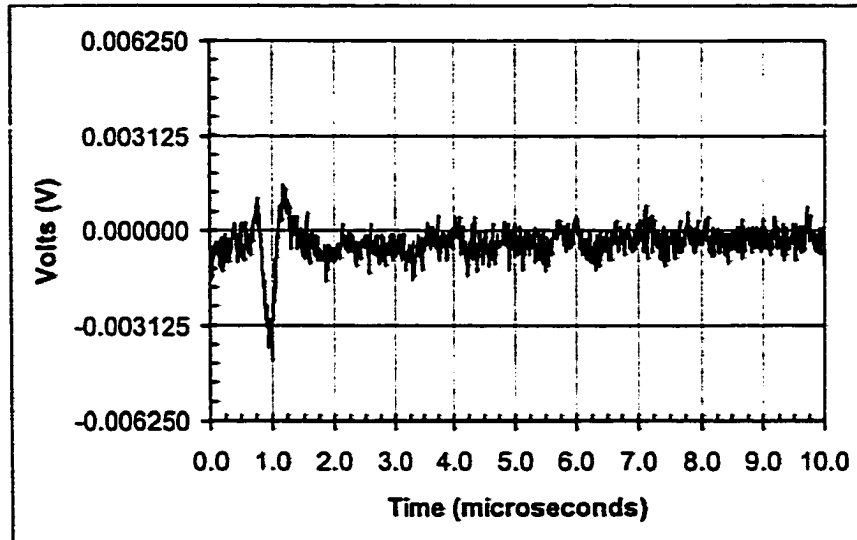
Figure 5.66: Epicentral displacement in stitched woven GR/Epoxy generated by the EO Q-switched Alexandrite laser with expanded beam radius.

240
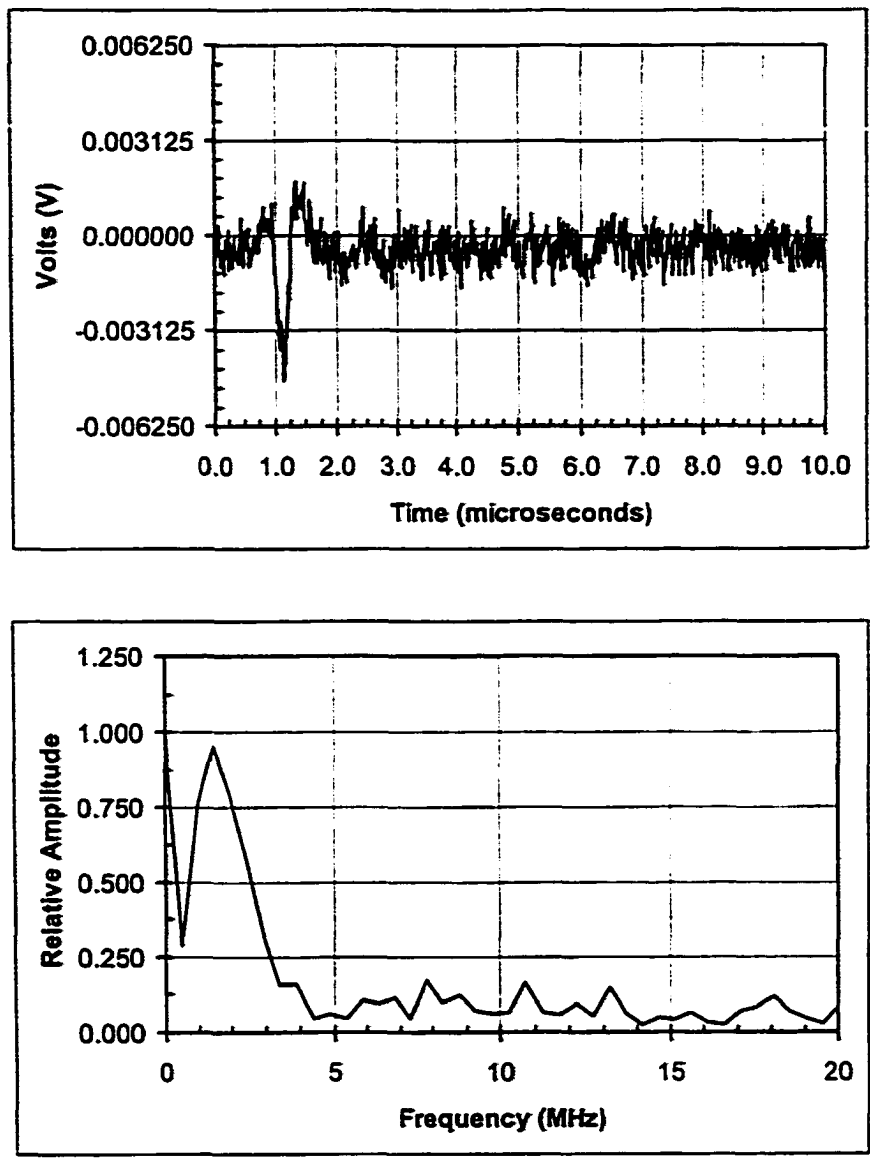
Figure 5.67: Epicentral displacement in stitched woven GR/Epoxy generated by the AO Q-switched Alexandrite laser.

Figure 5.68: Epicentral displacement in stitched woven GR/Epoxy generated by the RM Q-switched Alexandrite laser.

242
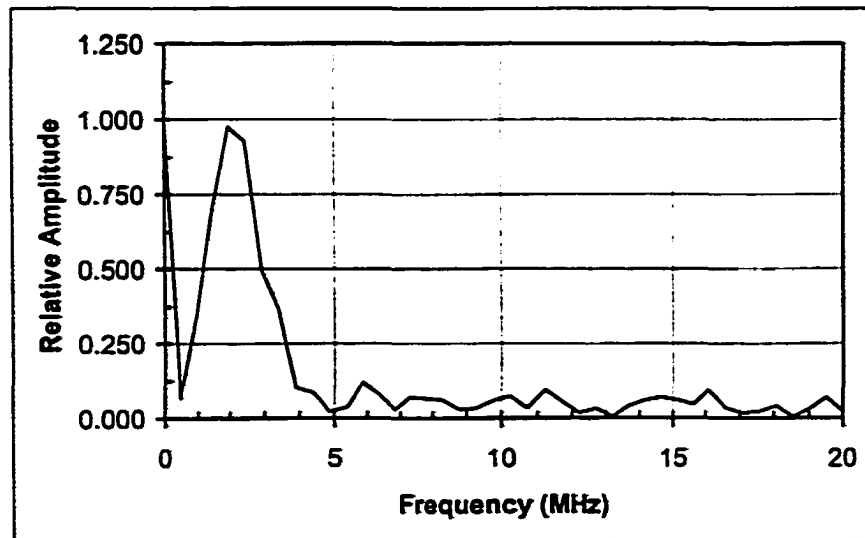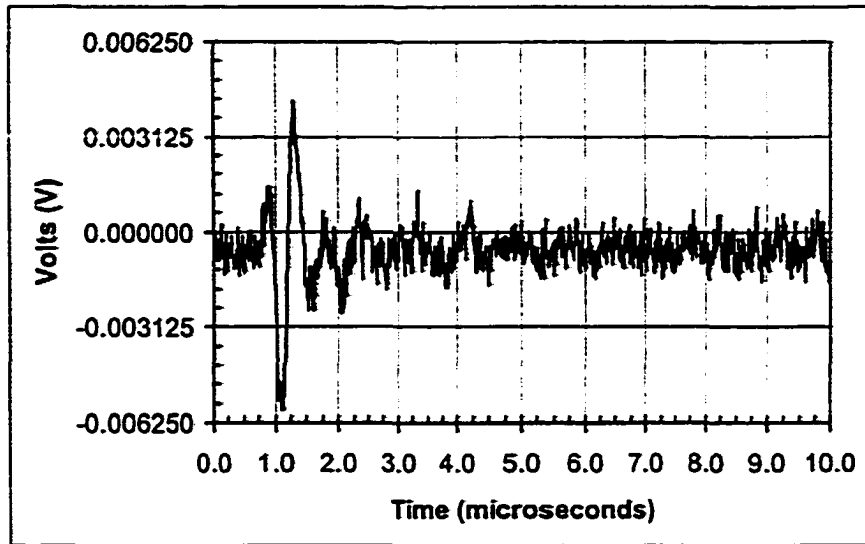
Nd:YAG (1.064 μm)

Electro-Optic Q-Switch   Figure 5.69 indicates the average ultrasonic signal and corresponding frequency spectrum generated in the stitched composite sample with 11 mJ per pulse from the EO Q-switched Nd:YAG laser. The pulse width was 25 ns and the intensity profile was similar to the profile show in Figure 5.16. We can still only see one wave arrival but it's amplitude is significantly larger than in previous examples. The frequency content is similar to the spectra in the previous examples is dominated by contributions around 1 and 2 MHz.

Acousto-Optic Q-Switch   Figure 5.70 illustrates the average ultrasonic signal and corresponding frequency spectrum generated in the stitched composite sample by 12 mJ per pulse from he AO Q-switched Nd:YAG laser. The pulse width was approximately 125 ns and the intensity profile was similar to the profile given in Figure 5.22. There is one wave arrival at 1.0 μs. The frequency content is similar to the previous examples with strong contributions around 1 and 2 MHz.

Rotating Mirror Q-Switch   Figure 5.71 shows the averaged ultrasonic signal and frequency spectrum generated in the stitched composite sample with 11 mJ per pulse from the Nd:YAG laser Q-switched with the rotating mirror. The pulse width was 35 ns and the intensity profile was similar to the profile given in Figure 5.22. Similar to the previous waveforms, one wave arrival is clearly visible and the frequency content is dominated by contributions around 1 and 2 MHz.

Nd:YAG (1.32 μm) Rotating Mirror Q-Switch

Figure 5.72 shows the averaged ultrasonic signal and corresponding frequency spectrum generated in the stitched composite sample with 15 mJ per pulse from the second

243
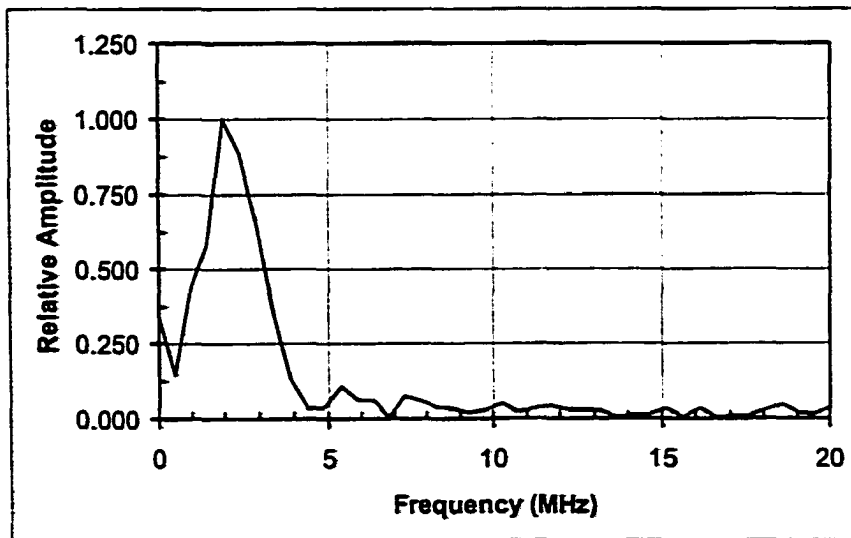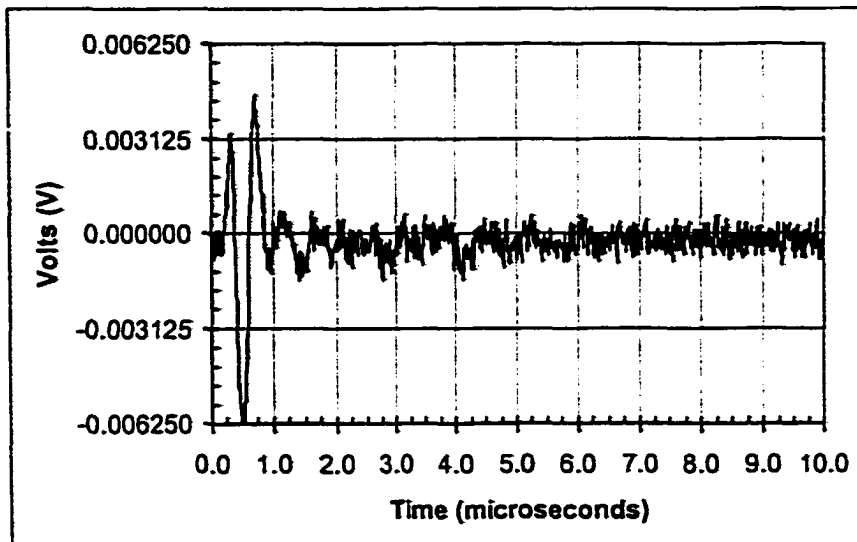
Figure 5.69: Epicentral displacement in stitched woven GR/Epoxy generated by the EO Q-switched Nd:YAG (1.064 μm).

244
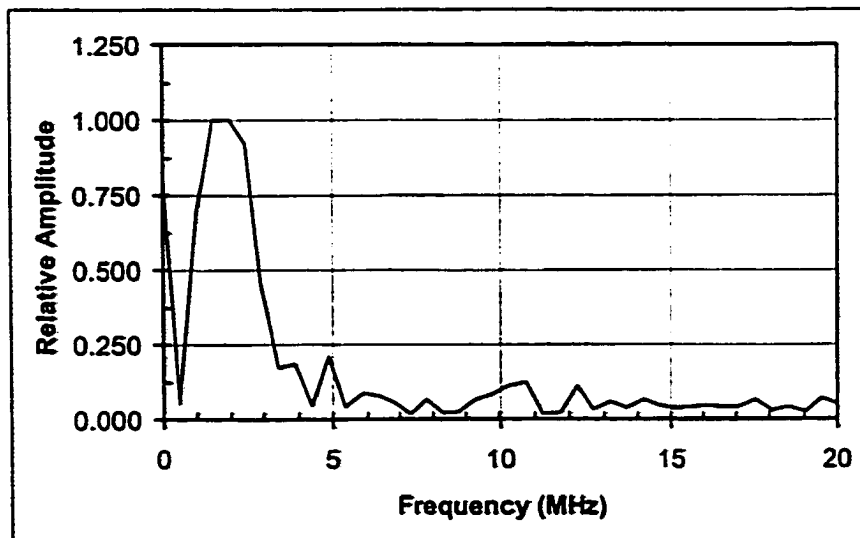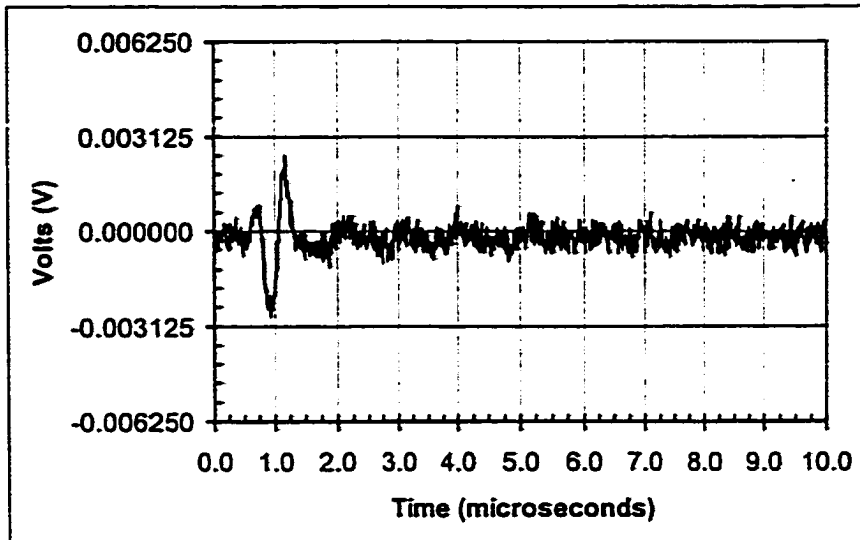
Figure 5.70: Epicentral displacement in stitched woven GR/Epoxy generated by the AO Q-switched Nd:YAG (1.064 μm).

245
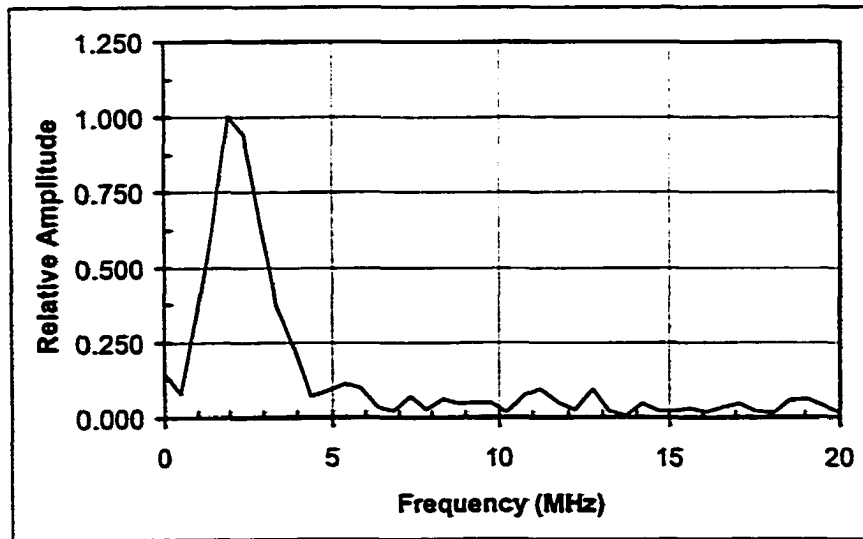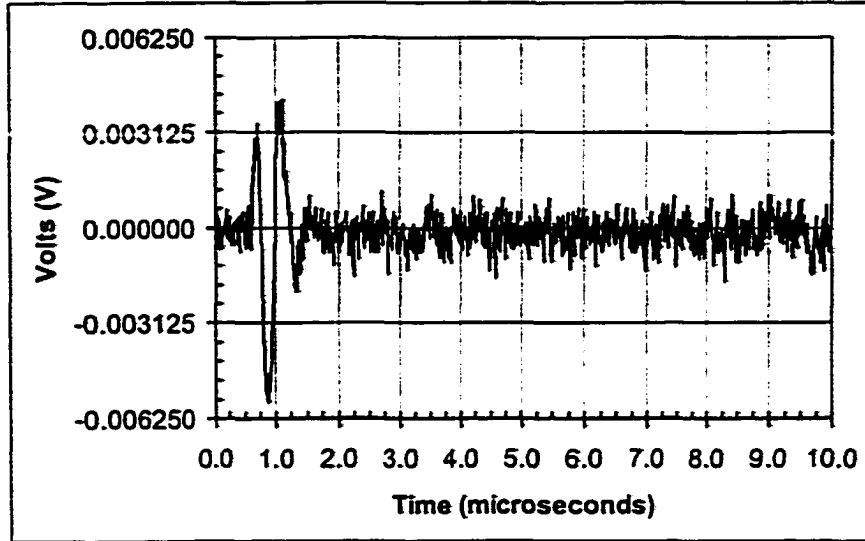
Figure 5.71: Epicentral displacement in stitched woven GR/Epoxy generated by the RM Q-switched Nd:YAG (1.064 μm).

246

wavelength (1.32 μm) of the Nd:YAG laser Q-switched with the rotating mirror. The pulse width was 130 ns and the intensity profile was similar to the profile depicted in Figure 5.24. The ultrasonic waveform is similar to the waveform generated in the previous examples. Once again only one wave arrival is clearly visible and the frequency content is dominated by contributions around 1 and 2 MHz. Figure 5.73 shows the signal generated with the same setting except that the generation spot was shifted slightly so that it was partially coincident with one of the stitches. We see that waveform is slightly different in that wave takes longer to decay. The frequency spectrum is also slightly shifted towards the lower frequencies so that the 1 MHz frequency component is more dominate than in the last example.

CTH:YAG (2.10 μm)

Electro-Optic Q-Switch   Figure 5.74 shows the averaged ultrasonic response and corresponding frequency spectrum generated in the stitched composite with 8 mJ per pulse from the EO Q-switched CTH:YAG laser. The pulse width was approximately 180 ns and the intensity profile was similar to the profile given in Figure 5.26. We see that the generated waveform is significantly different than the waveforms in the previous examples. The initial wave arrival at 2.0 μs is similar to the wave arrivals in the earlier experiments, but there is still a detectable signal beyond this time. There may also be a distinct arrival near 9.0 μs, but the noise is too high to be certain. The frequency content is also different than the frequencies obtained in the previous experiments. Here there is are strong contributions around 0.5 and 3 MHz. Furthermore, these two frequency components are more distinct and separated than the 1 and 2 MHz contributions in the other experiments.

247
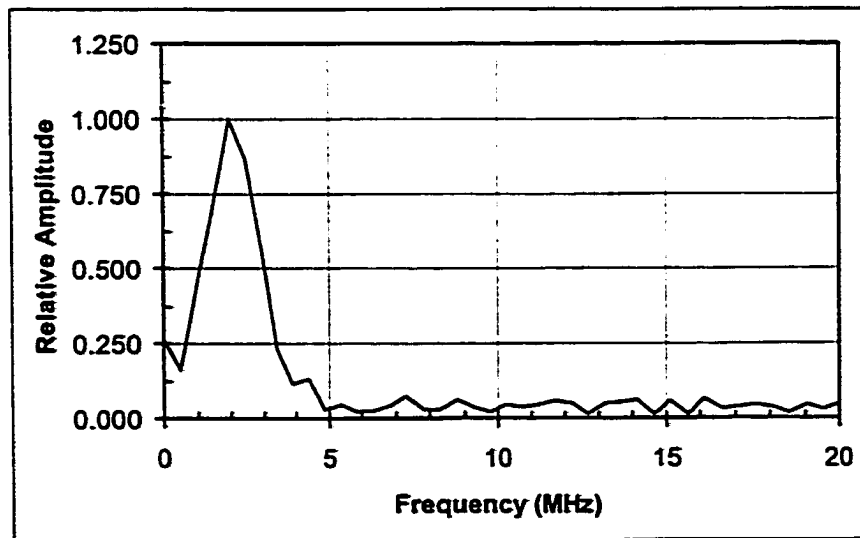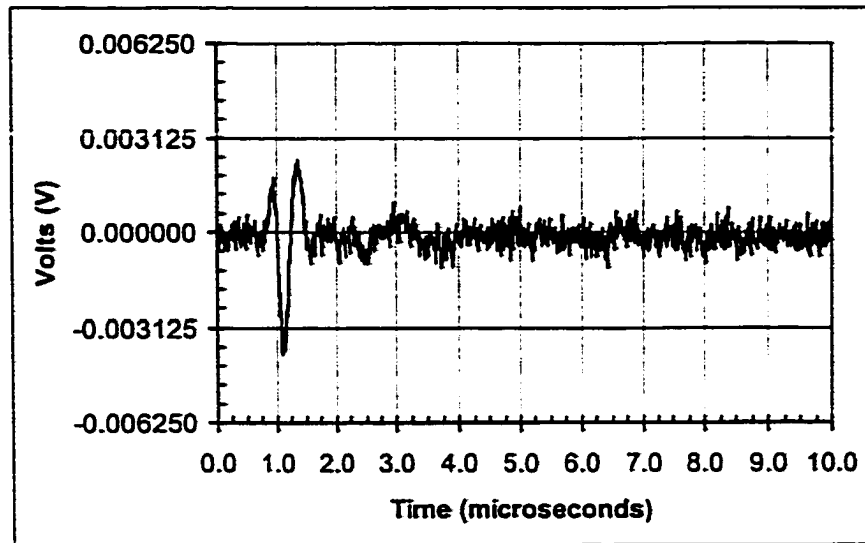
Figure 5.72: Epicentral displacement in stitched woven GR/Epoxy generated by the RM Q-switched Nd:YAG (1.320 μm).

248
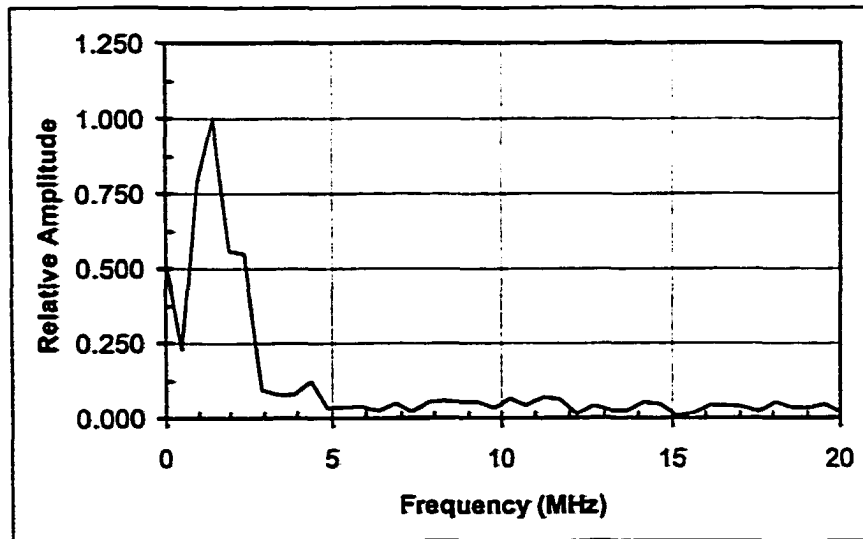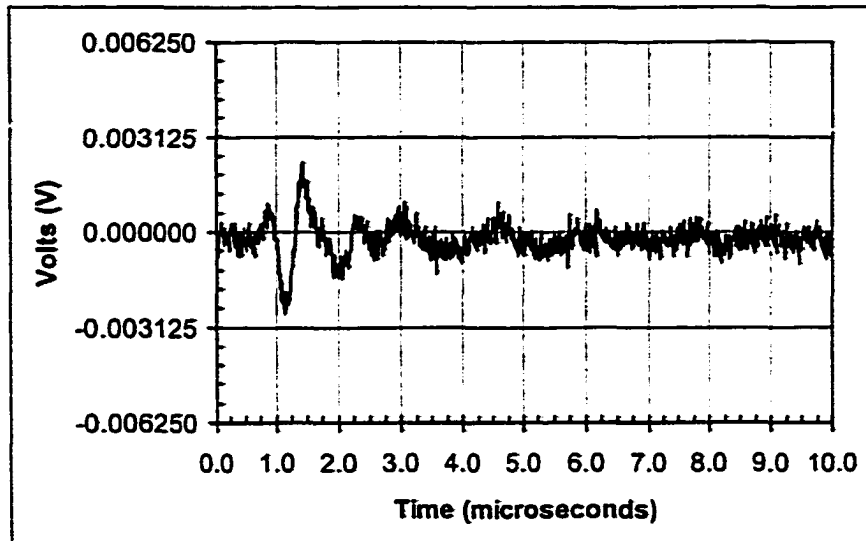
Figure 5.73: Epicentral displacement in stitched woven GR/Epoxy generated by the RM Q-switched Nd:YAG (1.320 μm) with generation spot partially coincident with a stitch.

249
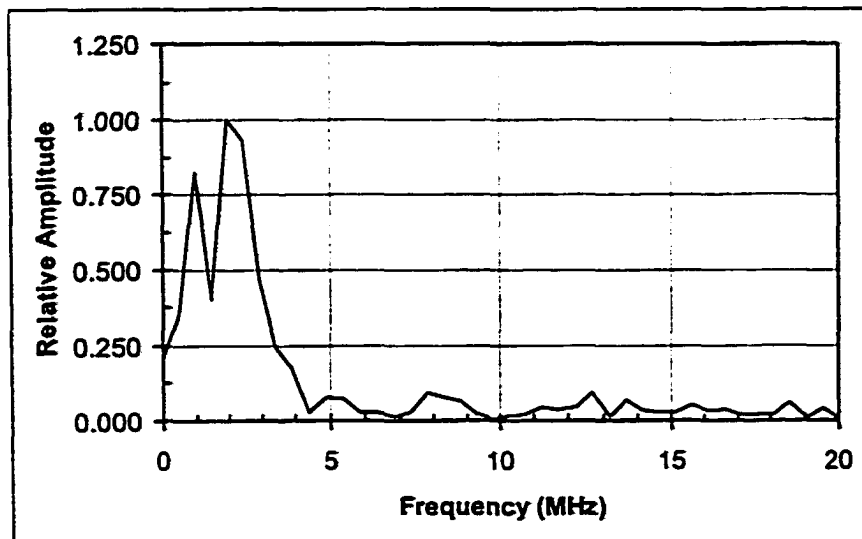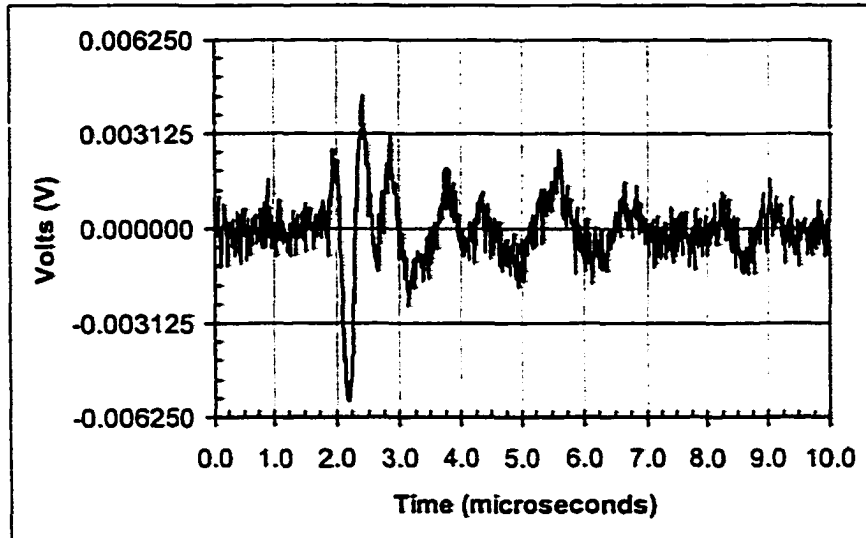
Figure 5.74: Epicentral displacement in stitched woven GR/Epoxy generated by the EO Q-switched CTH:YAG (2.10 μm).

250

Rotating Mirror Q-Switch Figure 5.75 shows the averaged ultrasonic response and corresponding frequency spectrum generated in the stitched composite with 12 mJ per pulse from the CTH:YAG laser Q-switched with the rotating mirror. The pulse width was approximately 250 ns and the intensity profile was similar to the profile shown in Figure 5.28. Like the signal generated by the electro-optic Q-switch, there is a relatively large initial displacement which does not decay immediately. The frequency content is also similar in that the dominate contributions at 1 and 2 MHz are relatively separate.

Er:YAG (2.94 μm) Rotating Mirror Q-Switch

Finally, Figure 5.76 shows the average ultrasonic signal and corresponding waveform generated in the stitched composite sample with 24 mJ per pulse from the Er:YAG laser Q-switched with the rotating mirror. The pulse width was estimated to be 180 ns and the intensity profile was similar to the profile presented in Figure 5.30. In Figure 5.76 we see only one clear wave arrival with a relatively small amplitude. The frequency spectrum is dominated by noise but there are visible contributions around 1 and 1.5 MHz.
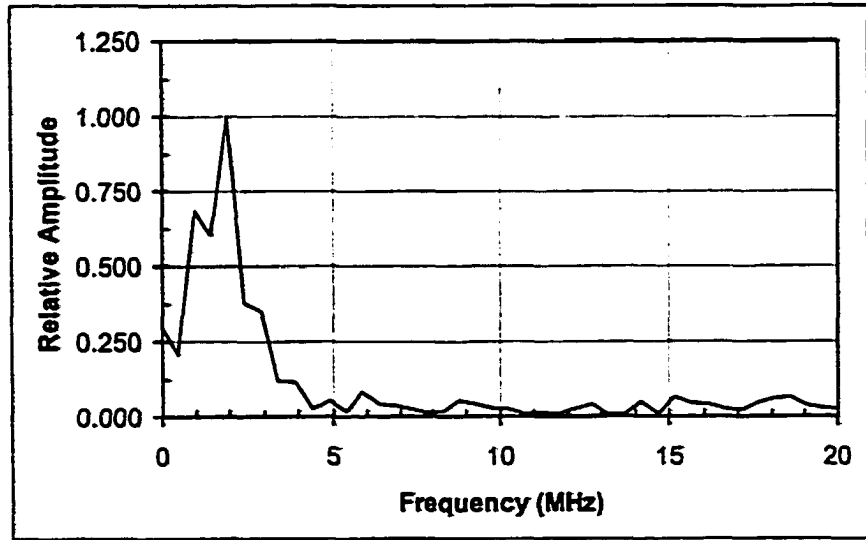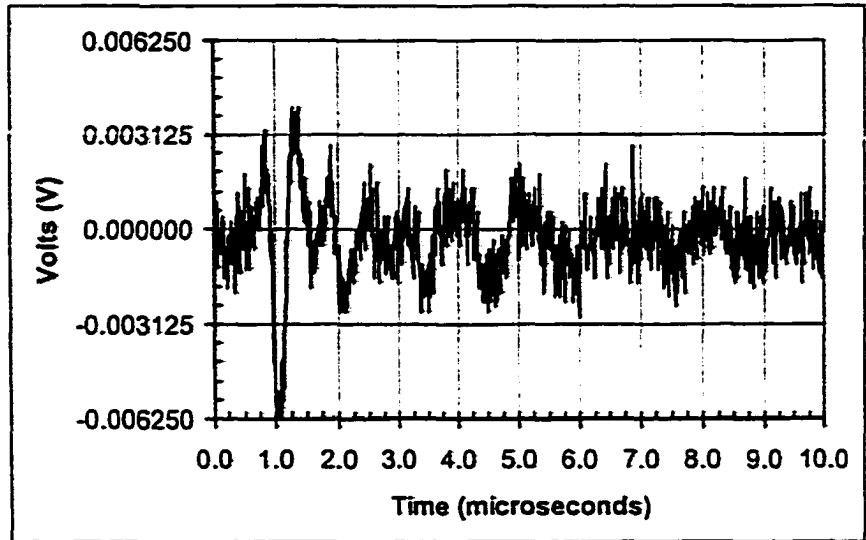
Figure 5.75: Epicentral displacement in stitched woven GR/Epoxy generated by the RM
Q-switched CTH:YAG (2.10 μm).

252
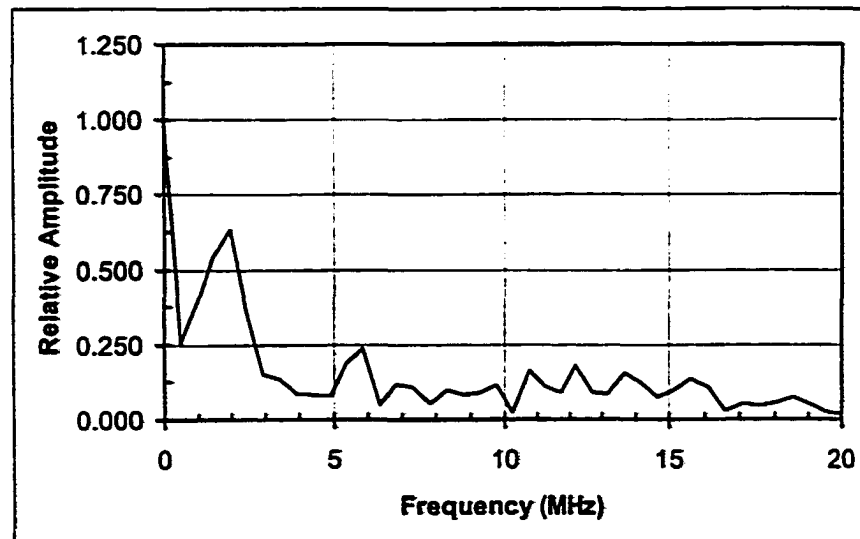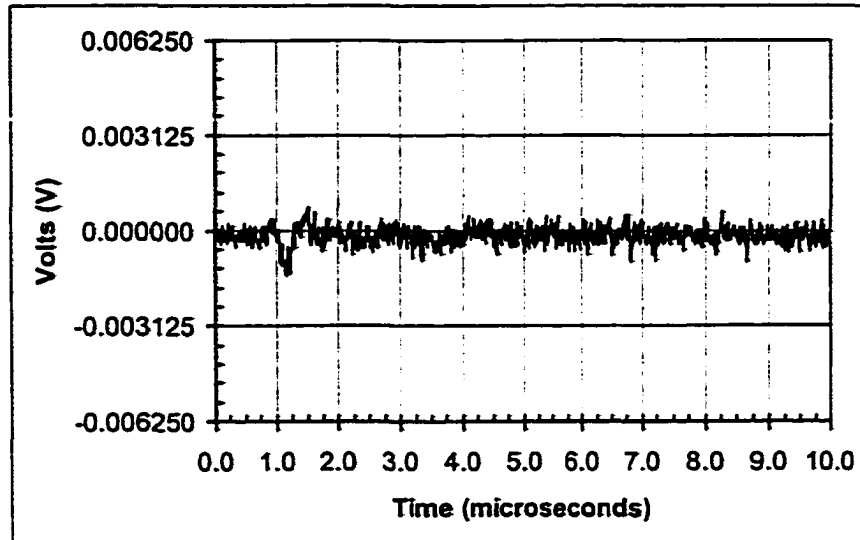
Figure 5.76: Epicentral displacement in stitched woven GR/Epoxy generated by the RM Q-switched Er:YAG (2.94 μm).

253

Summary of Stitched Woven Graphite/Epoxy Data

As with the other composite sample, we make the approximation that the reflectivity of this sample is similar to the reflectivity of graphite. We use the values listed in Table 5.4 for the reflectance at each wavlength. The absorbed power densities are computed from the incident power densities by multiplying by the factor $(1 - R)$. This is less accurate than with the other composite sample because of the layer of epoxy on the surface of the sample. From our experience with the epoxy sample, we expect that for most of our wavelengths, the laser light will penetrate through the epoxy layer and interact mostly with the first layer of graphite fibers. We expect that the longer wavelengths (i.e. 2.1 and 2.94 μm) will be mostly absorbed in the epoxy layer. Table 5.7 lists the pulse widths, energy levels, beam radius, and the instantaneous incident and absorbed power densities obtained for each laser configuration where no or very little vacuum grease was used. The maximum peak to peak displacement measurement for the first longitudinal wave arrival is also listed. Figure 5.77 shows a plot of the displacement magnitude versus incident and absorbed power density for the first longitudinal arrival. There does not seem to be a general trend in the results. The maximum displacement occurs at the lowest power density with the RM Q-switched CTH:YAG laser. Here, we expect that the laser light was absorbed in the epoxy layer. A displacement with similar magnitude was generated with the EO Q-switched Nd:YAG (1.064 μm) laser. In this case, we expect that the laser light would be mostly absorbed in the first layer of graphite fibers and the epoxy layer would have then behaved as a constraining layer. Therefore, we would expect a larger amplitude displacement.

The frequency content of the ultrasonic signals for the different laser configurations was more consistant than in the other samples. The frequency spectrum of every signal is similar with a 5 MHz bandwidth centered around 2-3 MHz. As with the other samples, the frequency content was independent of the laser parameters.

254

λ [μm]	Pulse Width [ns]	Energy [mJ/pulse]	Radius [mm]	Incident Power Density [MW/m²]	Absorbed Power Density [MW/m²]	P Wave [mV]
0.755 EO	125.0	10.0	1.5	11300.0	7000.0	3.9
0.755 AO	160.0	10.0	2.5	3180.0	1968.0	6.6
0.755 RM	105.0	12.0	2.0	9095.0	5625.0	10.1
1.064 EO	25.0	11.0	2.0	35014.0	20456.0	11.1
1.064 AO	90.0	12.0	2.5	6791.0	3967.0	5.3
1.064 RM	35.0	11.0	2.5	16007.0	9351.0	9.9
1.320 RM	130.0	15.0	3.0	4080.0	2083.0	5.0
2.100 EO	180.0	8.0	1.0	14147.0	6311.0	3.9
2.100 RM	250.0	12.0	2.0	3820.0	1704.0	11.4
2.940 RM	180.0	24.0	2.5	6791.0	2755.0	2.3

Table 5.7: Summary of experiments with the stitched woven composite Gr/Epoxy sample.

255
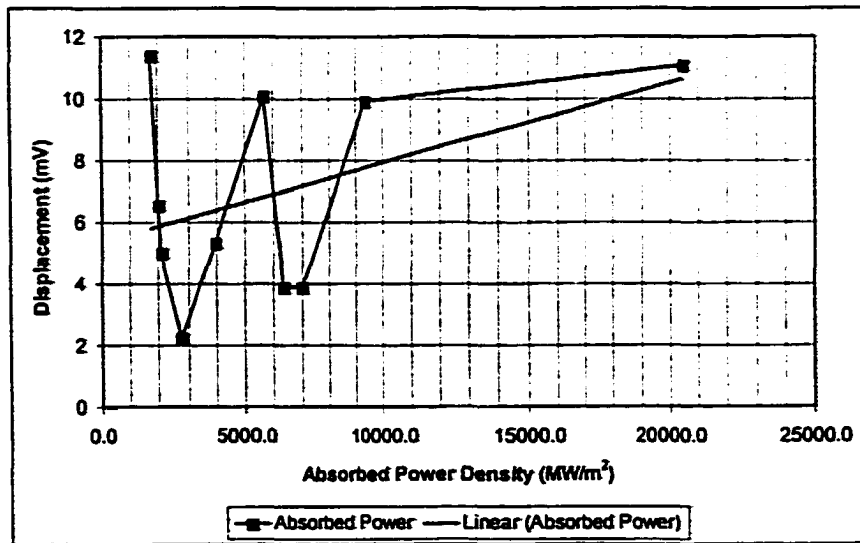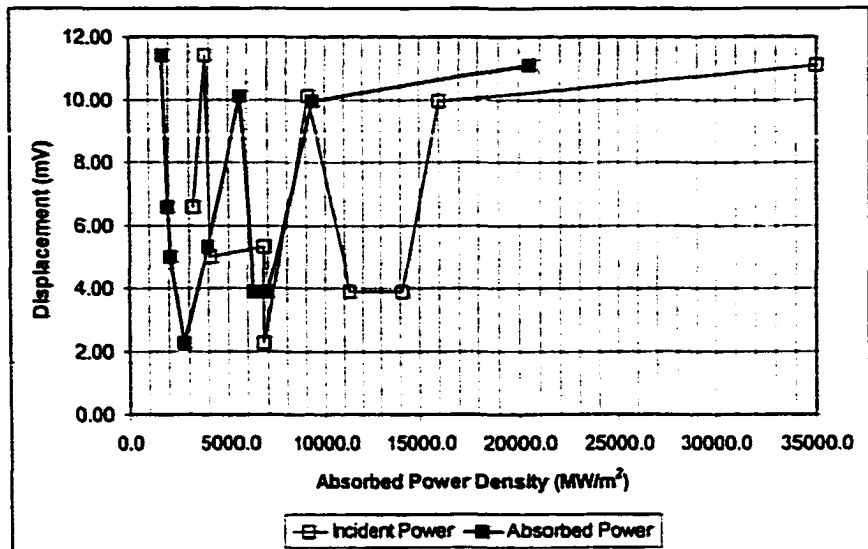
Figure 5.77: Displacment magnitude of the first arrival as a function of incident and absorbed power densities in the stitched woven Gr/Epoxy composite sample.

256

5.3 Summary

Here, we summarize the main features of the experimental data. In the aluminum sample, we found that each laser configuration generated an ultrasonic waveform with similar qualitative features. The reflectivity for a clean aluminum surface was calculated and the instantaneous absorbed power density was computed from the measured incident power density. We compared the ultrasonic displacement to the absorbed power and the results were summarized in Figure 5.33. The largest displacement was generated by the EO Q-switched Nd:YAG (1.064 μm) laser which had a pulse width of 25 ns at 8 mJ/pulse. This produced the highest instanteous power density because of the short pulse width and because the reflectivity of the aluminum was lower at this wavelength. A general trend in the data was not obvious but the displacement magnitude increased with the instantaneous absorbed power density. We found that the frequency content of the ultrasonic signals was insensitive to the laser parameters and had contributions from 2-5 MHz. As expected, a constraining layer of grease enhanced the ultrasonic signal.

For the woven graphite/epoxy composite, we used the Fresnel equations to estimate the reflectance from tabulated values of the index of refraction of graphite. We computed the instantaneous absorbed power density from the measured incident power density and compared both the incident and absorbed power densities to the displacement amplitude. An initial evaluation of the data in Figure 5.48 suggested that the displacement magnitude increased somewhat linearly with the instantaneous absorbed power. However, this trend was less clear when we omitted the last data point which corresponded to the largest absorbed power density. Once again, the frequency content of the ultrasonic signals was independent of the laser parameters and had strong components around 2-5 MHz.

In the epoxy sample, we measured the transmitted energy through the sample and subtracted this from the incident energy to compute the instantaneous absorbed power

density. We compared this absorbed power to the displacement amplitude. We found that the longer wavelength lasers (i.e. 2.10 μm and 2.94 μm) were absorbed better in the epoxy and produced greater instantaneous power densities. The Er:YAG laser at 2.94 μm produced the largest displacement. However, the results were not consistent. The CTH:YAG laser at 2.10 μm produced a relatively high power density with the EO Q-switch but did not generate a large signal. Conversely, the RM Q-switched CTH:YAG generated a large signal but not a large absorbed power density. Furthermore, we found that the Alexandrite laser with the shortest wavelength (0.720-0.790 μm) could generate large displacements even though the absorbed power density was smaller. We suggested that the difficulties were caused by the detection laser which damaged the sample during each test.

As with the first composite sample, we used the Fresnel equations to estimate the reflectance from tabulated values of the index of refraction of graphite. We computed instantaneous absorbed power density from the measured incident power density and compared both the incident and absorbed power densities to the displacement amplitude. There did not seem to be a general trend in the results. The maximum displacement occurred at the lowest power density with the RM Q-switched CTH:YAG laser at 2.10 μm. From our experience with the epoxy sample, we suggested that this wavelength was absorbed in the epoxy layer. A displacement with similar magnitude was generated with the EO Q-switched Nd:YAG (1.064 μm) laser. Since this wavelength easily transmitted though the epoxy sample, we suggested that the laser light was mostly absorbed in the first layer of graphite fibers and that the epoxy layer then behaved as a constraining layer and generated a larger amplitude displacement. The frequency content of the ultrasonic signals for the different laser configurations was more consistant than in the other samples. The frequency spectrum of every signal was similar with a 5 MHz bandwidth centered around 2-3 MHz. As with the other samples, the frequency content was independent of the laser parameters.

258

Chapter 6

Analysis

In this chapter we compare our mathematical model to the experimental data presented in the previous chapter. Specifically, we consider the ultrasonic generation in the aluminum sample and the woven graphite/epoxy sample. We present computed waveforms for some of the laser parameters used in our experiments and compare features in these waveforms to the corresponding features in experimentally obtained waveforms.

6.1   Aluminum Sample

6.1.1   Approximations for the Model

We had to make approximations to mathematically model the laser generated thermoelastic displacement in the aluminum sample due to limitations in the available computer resources. A 450 MHz Pentium XEON II with 512 megabytes of RAM was used in all of the mathematical modeling. The main problem encountered was that the time and spatial scales of the thermal and elastic problems are very different. For example, the thermal fields calculated in aluminum and presented in Chapter 3 were generated with the discretization

259

Parameter	Units	Value
n_x = number of steps in x-direction	-	16
n_y = number of steps in y-direction	-	16
n_z = number of steps in z-direction	-	20
n_t = number of time steps	-	128
Δx = x-increment	m	0.0025
Δy = y-increment	m	0.0025
Δz = z-increment	m	1.0×10^{-7}
Δt = t-increment	s	0.5×10^{-9}

Table 6.1: Aluminum discrtization values for the thermal problem

values listed in Table 6.1.

To adequately reproduce the thermal field we required a high resolution, Δz, in the z-direction which represented depth into the sample. Our aluminum sample was 1.255 cm thick so that we would require 125,500 steps with the Δz listed in Table 6.1 to model the full thickness of the sample. Similarly, we required a high resolution in time, Δt, to accurately reproduce the thermal fields. In our experimental waveforms, we observed two longitudinal reverberations. The first corresponded to the first arrival of the wave through the sample, and the second corresponded to a subsequent round trip wave arrival through the sample. Therefore, to compare our model with the experiments, we needed enough time for the ultrasonic wave to traverse the thickness of the sample three times. For a longitudinal wave velocity of 6301.0 $\frac{m}{s}$ and a distance of $3 \times 1.255 = 3.765$ cm, this corresponds to a total time of approximately 6.0 microseconds which would require 12,000 time steps with the Δt listed in Table 6.1.

It was not possible to create or convolve two four-dimensional arrays with these dimensions in depth and time. Instead, we made the approximation that the thermal forcing function was instantaneous and acted only at the surface of the sample. To implement this approximation, we used the following technique. First, we computed the thermal field with

260

the discretization values in depth and time required to accurately reproduce the thermal field. The discretization values for the x and y dimensions were determined by the elastic problem and the requirements for the convolution explained below. We took the numerical derivative of the thermal field with respect to the z-direction and computed the thermal force as described in Chapter 3. Then, at each spatial point, we extracted the maximum value of the force with respect to time and created an instantaneous force computed for the entire computational space. At each point (x,y) we then extracted the maximum value of this force with respect to the z-direction. This array of values is shown as a three-dimensional surface plot in Figure 6.1 except that the x and y dimensions of the array are different than those used in the actual convolutions. We note that the force is negative as expected because the thermoelastic expansion is towards the unconstrained surface, which is the negative z-direction in the thermal problem. We used these values as the approximate surface force and created a new four-dimensional array where the only nonzero values occurred at $z = 0$ and $t = 0$. The dimensions of this new array were determined by the elastic problem and the requirements of the convolution.

Memory requirements for the convolution also restricted the size of the arrays that we could use. We wanted maximum resolution in time and in the z-direction. Although the *Mathematica* convolution routines were very convenient, they were not memory efficient. Furthermore, to implement the *Mathematica* routines properly, we had to make the arrays symmetric so that we had to have "negative time" and "negative depth" even though this did not correspond to the physical problem. With 512 megabytes of RAM and 512 megabytes of swap space, we found that the largest arrays we could convolve had dimensions

$$n_x = 8, \ n_y = 8, \ n_z = 64, \ n_t = 128$$

261
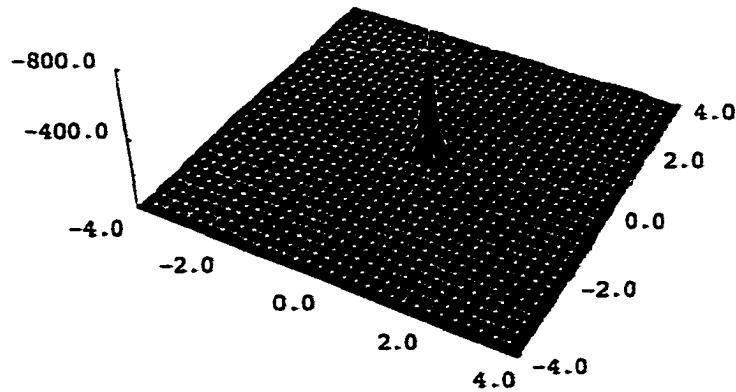
Figure 6.1: Approximate instantaneous surface force.

for a total array size of:

$$2n_x \times 2n_y \times 2n_z \times 2n_t = 8,388,608 \text{ cells}$$

We found that the optimal array dimensions and resolutions depended upon the specific problem that we were trying to model. If more memory resources were available, we suggest that an adequate array size would have had minimum dimensions of

$$n_x = 32, \; n_y = 32, \; n_z = 64, \; n_t = 128$$

or 16 times the available memory which was approximately one gigabyte. We also suggest that much more memory efficient convolution routines could be implemented to greatly increase the array dimensions

262

6.1.2 Results

In this section, we present the comparison of our mathematical model to the experimental results. We list the numerical parameters used in the model and compare the computed waveforms to the experimental waveforms. We compare results from the numerical solution of the exact inverse Laplace transform as well as from numerically inverting the transform. For aluminum, we used the values 2.31×10^{-5} K^{-1} and 0.345 for the thermal linear expansion coefficient α and the Poisson's ratio, ν, respectively in all of the mathematical models. Unless otherwise noted, we used the following discretization values in our thermal field calculations

$$n_x = 8 \quad \Delta x = 0.46875 \text{ cm}$$
$$n_y = 8 \quad \Delta y = 0.46875 \text{ cm}$$
$$n_z = 64 \quad \Delta z = 0.25 \times 10^{-7} \text{ m}$$
$$n_t = 128 \quad \Delta t = 0.25 \times 10^{-9} \text{ s}$$

We then created a surface force and an elastic Green's function with discretization values

$$n_x = 8 \quad \Delta x = 0.46875 \text{ cm}$$
$$n_y = 8 \quad \Delta y = 0.46875 \text{ cm}$$
$$n_z = 64 \quad \Delta z = 0.019609375 \text{ cm}$$
$$n_t = 128 \quad \Delta t = 0.75 \times 10^{-7} \text{ s}$$

Unless otherwise noted, the elastic Green's function was computed using the exact inverse Laplace transform.

The displacement measurements made by the interferometer were not absolutely calibrated so that we had to approximate the vertical scale when comparing the theoretical waveforms to the experimental waveforms. The procedure for this approximation is as follows. For each modeled laser, we found the maximum peak-to-peak displacement in the

263

computed waveforms, P_{Theory}. We then found the same maximum peak-to-peak displacement in the corresponding experimental data, P_{Data}. We then took the ratio of these two numbers, $R = \frac{P_{Theory}}{P_{Data}}$ and averaged these ratios from each modeled laser. We then used this as a multiplication factor, $R_{Avg} = 267.0$ by which we multiplied the experimental data. We used this same factor in each case so that the scale would be consistent between the different lasers modeled.

EO Q-switched Alexandrite (0.755 μm) Laser

We first consider the electro-optic Q-switched Alexandrite laser. From Table 5.3 we see that in our experiments, we had a pulse width of 125 ns, a 1.5 mm radius, and an absorbed power flux of 582 MW/m^2. We found that a pulse rise time of $\tau = 50$ ns approximated the laser pulse time dependence. We used these parameters in our thermal field calculations with the discretization values listed above. We convolved the surface force and elastic Green's function arrays together to compute the thermoelastic displacement. The first plot in Figure 6.2 shows the theoretically computed z-component epicentral displacement in the aluminum sample on the opposite side of the generation spot. We see the two longitudinal wave arrivals and their separation correspond to the correct wave velocity for the thickness of the sample. We see a slight displacement half-way between the two arrivals which may correspond to the mode conversion of the first shear wave arrival. The shear wave travels at approximately one-half the longitudinal wave speed so that this displacement occurs at the correct time for the shear wave arrival. The second plot shows the experimentally measured values on the same scale. In Figure 6.2 we see that the computed longitudinal wave arrivals, P_1 and P_2, coincide with the experimental wave arrivals and that the possible shear wave arrival, S_1 correlates with the experimental shear wave arrival. We see that the magnitudes of the displacement are the same order of magnitude. The

264

resolution of our computed waveforms was too low to compare the Fourier transforms of the modeled waveforms to the experimental data. However, we see in Figure 6.2 that the frequency of the computed longitudinal wave arrivals (P_1 and P_2) appear to have similar frequencies to the experimental data. The shear wave arrivals have different frequencies. We attribute this to the extremely low resolution of our model in the x-y plane so that the shear wave could not be adequately resolved.

EO Q-Switched Nd:YAG (1.064 μm) Laser

Here we consider the electro optic Q-switched Nd:YAG (1.064 μm) laser. From Table 5.3 we see that in our experiments, we had a pulse width of 25 ns, a 2.0 mm radius, and an absorbed power flux of 1390.0 MW/m^2. We found that a pulse rise time of $\tau = 10$ ns approximated the laser pulse time dependence. We used these parameters in our thermal field calculations with the discretization values listed above. We convolved the surface force and elastic Green's function arrays together to compute the thermoelastic displacement. The first plot in Figure 6.3 shows the theoretically computed z-component epicentral displacement in the aluminum sample. As with the previous example, we clearly see the two longitudinal wave arrivals and a possible shear wave arrival. The second plot in Figure 6.3 shows the experimental data on the same scale. Again, we see that the longitudinal wave arrivals in the two waveforms are coincident and the possible shear wave arrival in the computed waveform correlates with the experimental data. The magnitude of the computed displacements corresponds well to the magnitude of the experimental displacements. The frequency of the experimental longitudinal waves appears to be significantly higher than the frequency of the computed longitudinal waves. We attribute this to the relatively low resolution of our computational space.

To examine the effect of changing the resolution of the computational space, we

265
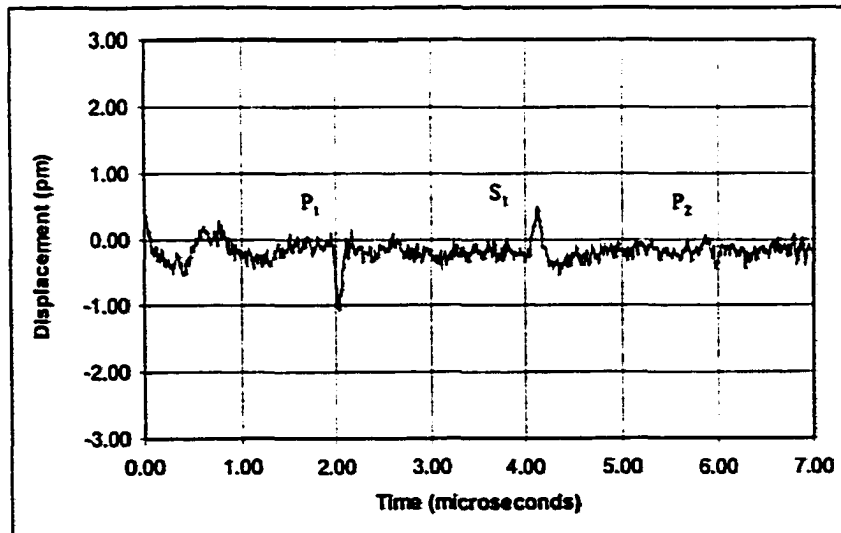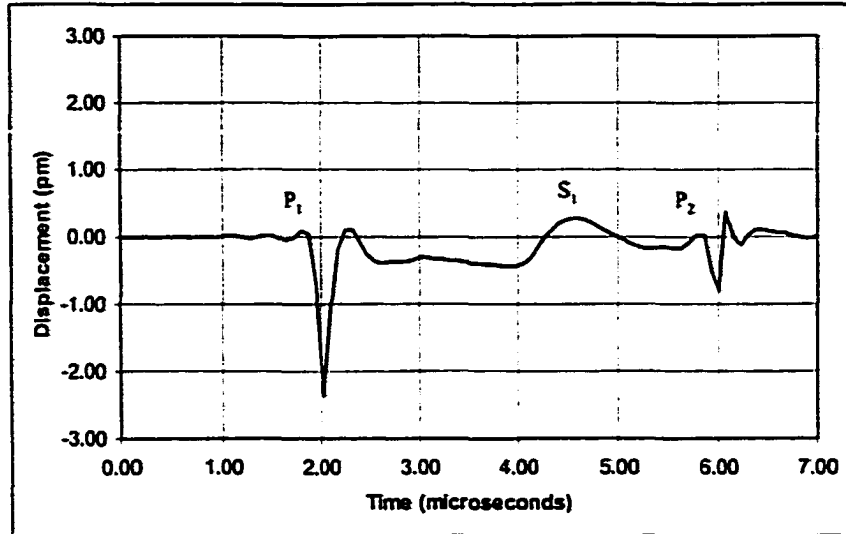
Figure 6.2: Computed epicentral displacement compared with experimental data for the EO Q-Switched Alexandrite laser on the aluminum sample.

266
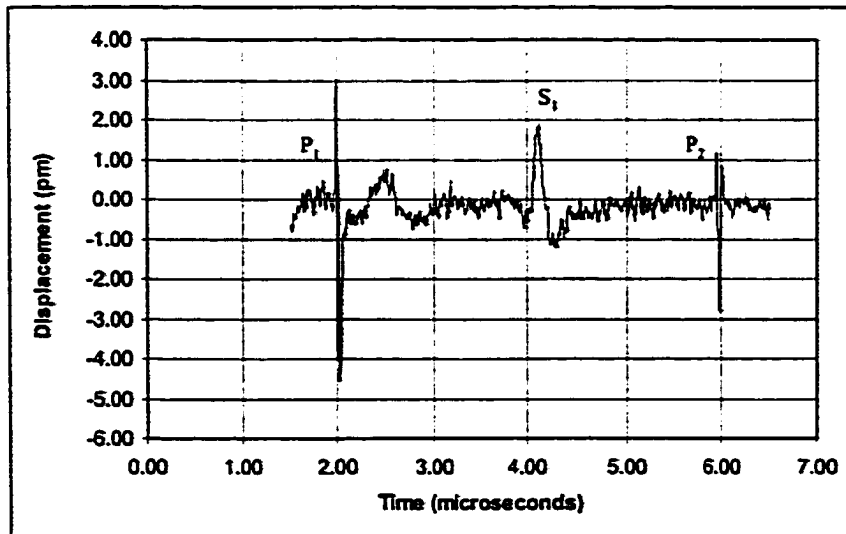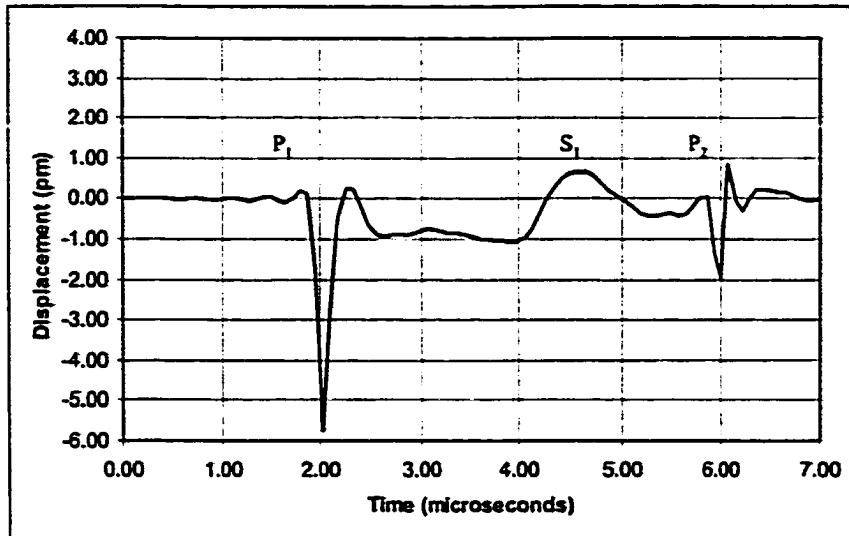
Figure 6.3: Computed epicentral displacement compared with experimental data for the EO Q-Switched Nd:YAG (1.064 μm) laser on the aluminum sample.

267

modeled this laser in two additional cases. We reduced the resolution in the z-direction (depth) and increased the resolution in the x- and y-dimensions and computed the epicentral displacement. The discretization values used were

$$n_x = 16 \quad \Delta x = 0.234375 \text{ cm}$$
$$n_y = 16 \quad \Delta y = 0.234375 \text{ cm}$$
$$n_z = 16 \quad \Delta z = 0.0784375 \text{ cm}$$
$$n_t = 128 \quad \Delta t = 0.75 \times 10^{-7} \text{ s}$$

so that the entire sample was modeled. The computed epicentral waveform is shown in the first plot of Figure 6.4. We see that the loss of resolution in the z-dimension has significantly altered the appearance of the longitudinal wave arrivals at 2.0 and 6.0 μs. The longitudinal wave corresponds to displacement in the z-dimension so that we expect the lower spatial resolution to degrade the longitudinal wave arrivals. We note also that there is a more distinct shear wave arrival at 4.0 μs than in the previous examples. The shear wave corresponds to displacement in the x-y plane so that we expect the increased resolution to clarify the shear wave arrival. Finally, we see that the magnitude and shape of the entire waveform is much different from the previous examples and does not fit the experimental data as well.

The second plot in Figure 6.4 shows the computed epicentral displacement with discretization values:

$$n_x = 8 \quad \Delta x = 0.25 \text{ cm}$$
$$n_y = 8 \quad \Delta y = 0.25 \text{ cm}$$
$$n_z = 64 \quad \Delta z = 0.019609375 \text{ cm}$$
$$n_t = 128 \quad \Delta t = 0.75 \times 10^{-7} \text{ s}$$

In this case, the resolution in the x- and y-dimensions is higher than in our first model (see Page 265) but the resolution in the z-dimension is unchanged. The entire aluminum

268

sample was not modeled with these values since the spatial extent in the x- and y-dimensions was only 4.0 cm. We see that the computed waveform again resembles the experimentally observed waveforms and the two longitudinal wave arrivals are clearly visible. However, the shear wave arrival is not more distinct than in our first model despite the increased resolution. This may be because the same number of grid points was used in both models.

RM Q-Switched Er:YAG (2.940 μm) Laser

Here we consider the Er:YAG laser Q-switched with the rotating mirror. From Table 5.3 we see that in our experiments, we had a pulse width of 180 ns, a 2.5 mm radius, and an absorbed power flux of 281.0 MW/m^2. We found that a pulse rise time of $\tau = 75$ ns approximated the laser pulse time dependence. We used these parameters in our thermal field calculations with the discretization values listed above. We convolved the surface force and elastic Green's function arrays together to compute the thermoelastic displacement. The first plot in Figure 6.5 shows the theoretically computed z-component epicentral displacement in the aluminum sample. As with the previous examples, we clearly see the two longitudinal wave arrivals and a possible shear wave arrival. The second plot in Figure 6.5 shows the experimental data on the same scale. Again, we see that the longitudinal wave arrivals in the two waveforms are coincident and the possible shear wave arrival in the computed waveform correlates with the experimental data. The displacement magnitudes of the two waveforms have the same order of magnitude but do not correlate as well as with the previous examples. However, the frequency content of the two waveforms appears very similar.

269
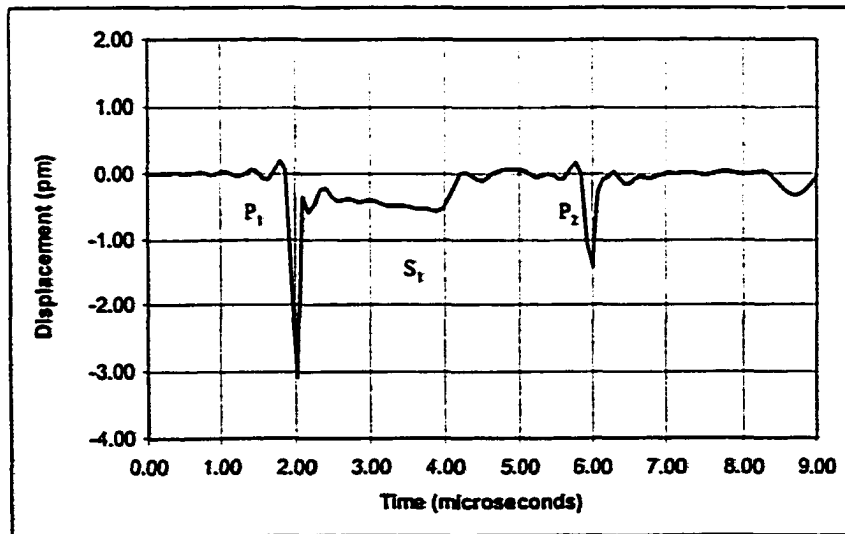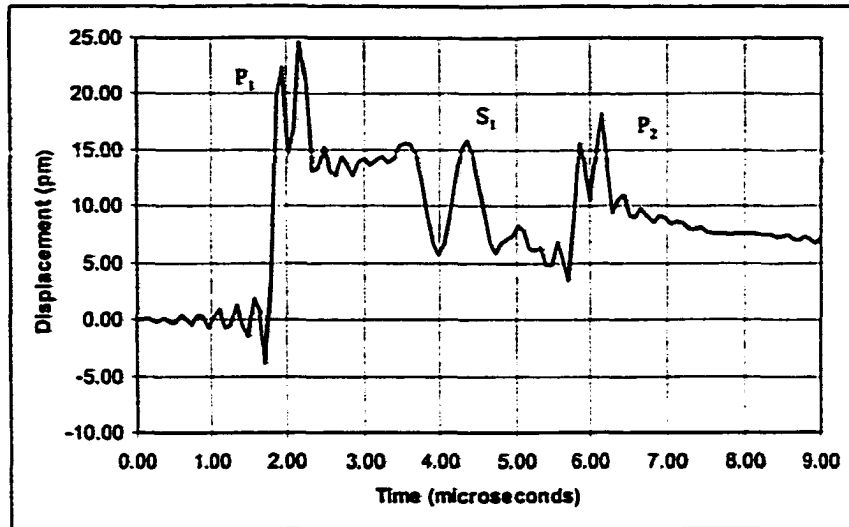
Figure 6.4: The effects of the computational space resolution on the epicentral displacements computed for the EO Q-switched Nd:YAG (1.064 μm) laser. Top: Increased resolution in the x-y plane. Decreased Resolution in the z-direction. Bottom: Increase resolution in the x-y plane without changing z-direction resolution.

270
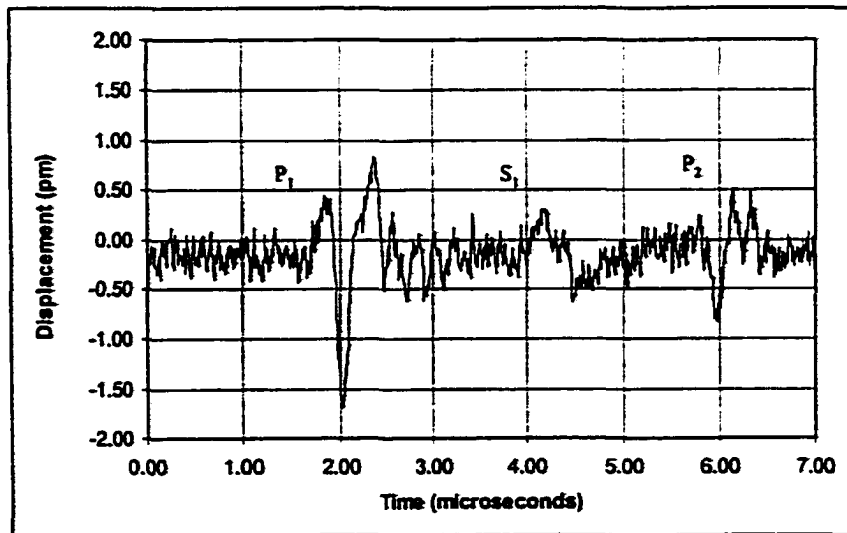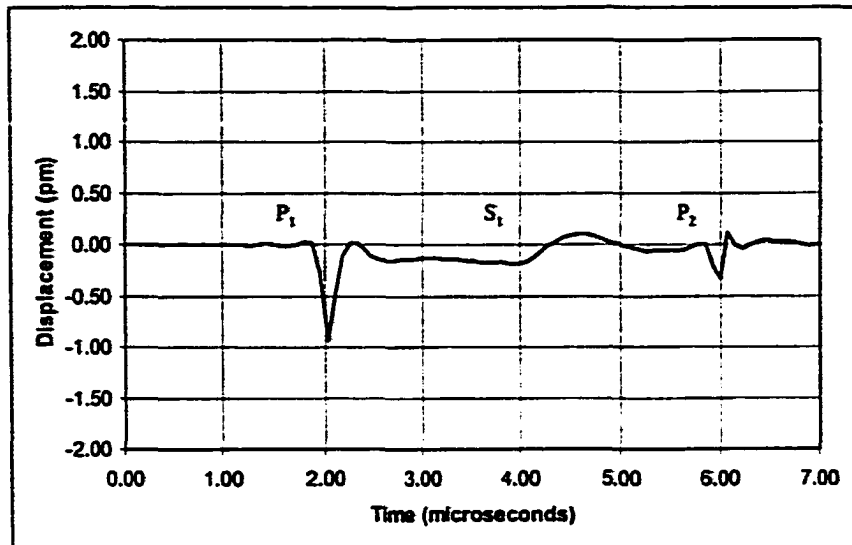
Figure 6.5: Computed epicentral displacement compared with experimental data for the RM Q-Switched Er:YAG laser on the aluminum sample.

271

Numerical Inversion of Laplace Transform for the EO Q-Switched Nd:YAG (1.064 μm) Laser

In this section we discuss results of modeling the electro optic Q-switched Nd:YAG (1.064μm) laser with the numerically computed inverse Laplace transform. The first plot in Figure 6.6 shows the computed waveform with $M = 100$ in equation (4.76). The second plot in Figure 6.6 shows the computed waveform with $M = 500$ in equation (4.76). We see that although both waveforms agree well with the exact inversion depicted in Figure 6.3, the greater number of summations makes a significant difference in the accuracy of the inversion at later times.

6.1.3 Summary of the Aluminum Model

Here we summarize the results of modeling the thermoelastic response in the aluminum sample. In general, we found that regardless of the laser parameters, the same general features were observed. Specifically, we saw two clear longitudinal wave arrivals and a possible shear wave arrival. This was consistent with the experimental data where we observed similar features with all of the laser configurations.

Our mathematical model generated waveforms that were qualitatively and quantitatively similar to the experimental waveforms. Qualitatively, the shapes of the computed waveforms were similar to the experimental data. Quantitatively, the separation of the longitudinal wave arrivals was extremely consistent with the experimentally measured data. The magnitude of the computed waveforms was also consistent with the experimental data. Except for the Nd:YAG laser, the frequency content of the computed waveforms appeared similar to the frequency content of the experimental waveforms. We attribute the differences in the waveforms to the relatively low resolution of our computational space, specifically in the x-y dimensions. We found that changing the resolution of the computational space

272
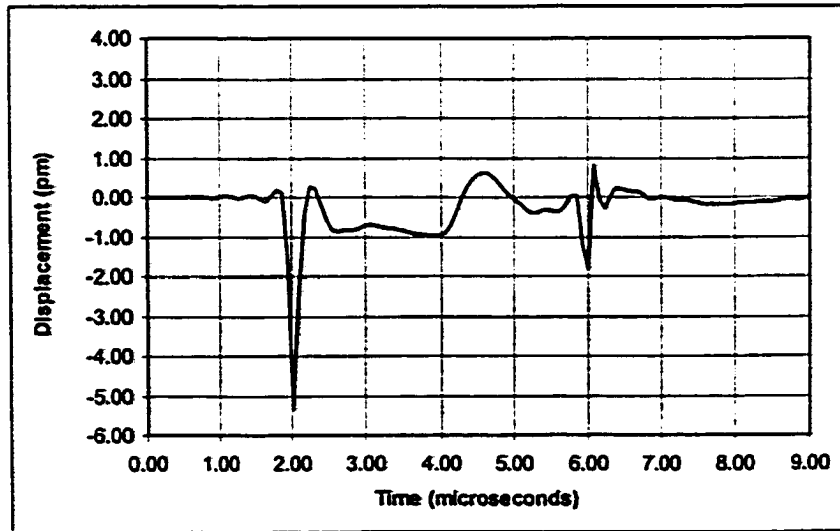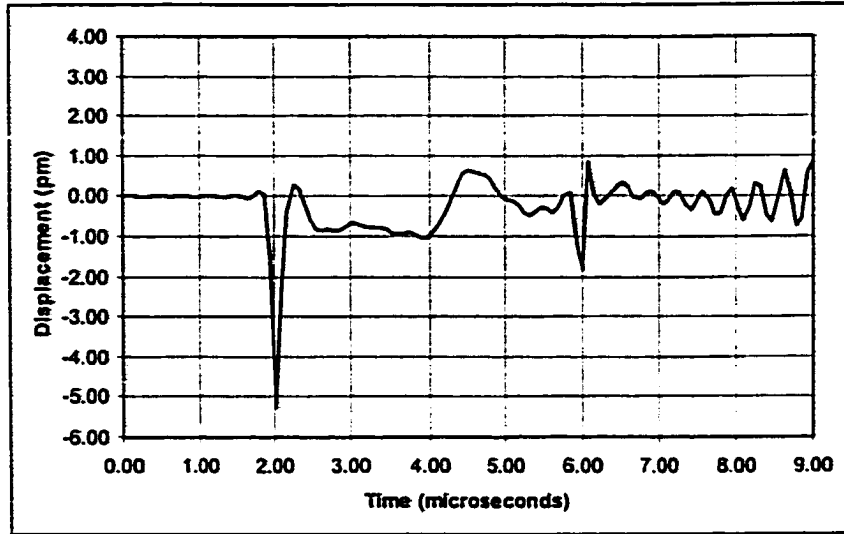
Figure 6.6: Comparison of waveforms computed for the EO Q-Switched Nd:YAG (1.064 μm) laser with the numerical inverse Laplace transform. Top: $M = 100$ summations. Bottom: $M = 500$ summations.

273

significantly affected the computed waveforms.

Our numerical Laplace inversion technique produced waveforms that agreed with the exact solutions even with the low resolution of the computational space. We did find, however, that more summations in the numerical inversion were required to accurately reproduce the waveforms at longer times.

6.2 Woven Graphite/Epoxy Sample

6.2.1 Approximations for the Model

As with the aluminum sample, we had to approximate the thermoelastic force. For insulating materials like the Graphite/Epoxy, we initially expected to use the buried thermal source described by equation (3.59) and compute the thermal fields on the same scale as the Green's function. However, we found that on this scale, the depth resolution was insufficient to accurately model the thermal field. According to Scruby[1], we can neglect thermal diffusion into the material if the optical penetration depth is greater than 0.1 μm. With that in mind, we created a "pseudoburied" source in the following manner: we used sufficient depth resolution and solved equation (3.59) to compute the temperature fields due to a buried thermal source in the composite. We then used the procedure described above for aluminum to create an instantaneous force acting only within the first surface layer. For comparison, we also generated an instantaneous surface force using the surface thermal source described by equation (3.58).

6.2.2 Results

Here, we present the comparison of our mathematical model to the experimental results. We list the numerical parameters used in the model and compare the computed

274

waveforms to the experimental waveforms. For the Graphite/Epoxy sample, we obtained the Poisson's ratio, ν, for AS4/3501-6 Carbon/Epoxy as 0.27 from the ASM Engineered Materials Handbook on Composites. We obtained the coefficient of thermal expansion, α, the thermal conductivity, the density, and the specific heat of graphite as 3.6×10^{-6} K^{-1}, 5.7 $\left[\frac{W}{m\,k}\right]$, 2560.0 kg/m^3, and 837 $\left[\frac{J}{kg\,K}\right]$, respectively. We used these values to calculate a thermal diffusivity of 2.66×10^{-6} m^2s^{-1}. We used Nayfeh's values for the stiffness coefficient matrix of a 65% Graphite, 35% epoxy material which is given in units of $\times 10^{10}$ $dynes/cm^2$ as [45]:

$$C_{IJ} = \begin{pmatrix} 155.43 & 3.72 & 3.72 & 0 & 0 & 0 \\ 3.72 & 16.34 & 4.96 & 0 & 0 & 0 \\ 3.72 & 4.96 & 16.34 & 0 & 0 & 0 \\ 0 & 0 & 0 & 3.37 & 0 & 0 \\ 0 & 0 & 0 & 0 & 7.48 & 0 \\ 0 & 0 & 0 & 0 & 0 & 7.48 \end{pmatrix}$$

We also used the listed value for the density, $\rho = 1.6$ g/cm^3. For the pseudoburied source, we set the optical absorption coefficient to 0.9×10^{-6} m^{-1}. For the surface source, we set the optical absorption coefficient to 1.0×10^{-8} m^{-1}. These material parameters are summarized in Table 6.2.

Unless otherwise noted, we used the following discretization values in our thermal field calculations for the pseudoburied and surface forces, respectively

$$\left. \begin{array}{ll} n_x = 8 & \Delta x = 0.113 \text{ cm} \\ n_y = 8 & \Delta y = 0.113 \text{ cm} \\ n_z = 64 & \Delta z = 1.0 \times 10^{-6} \text{ m} \\ n_t = 128 & \Delta t = 6.0 \times 10^{-8} \text{ s} \end{array} \right\} \text{ Pseudoburied Thermal Source}$$

Parameter	Value
Poisson Ratio for AS4/3501-6 Carbon/Epoxy, ν	0.27
Thermal expansion coefficient, α for graphite	$3.6 \times 10^{-6} \text{ K}^{-1}$
Thermal conductivity of graphite	$5.7 \left[\frac{W}{m \cdot k}\right]$
Density of graphite	2560.0 kg/m^3
Specific heat of graphite	$837 \left[\frac{J}{kg \cdot K}\right]$
Density of 65%-35% Graphite/Epoxy, ρ	1.6 g/cm^3
C_{IJ}	As listed, $\times 10^{10}$ dynes/cm^2
Optical absorption coefficient	$0.9 \times 10^{-6} \text{ m}^{-1}, 1 \times 10^{-8} \text{ m}^{-1}$

Table 6.2: Material paramters for Graphite/Epoxy.

$$
\left.\begin{array}{ll}
n_x = 8 & \Delta x = 0.113 \text{ cm} \\[6pt]
n_y = 8 & \Delta y = 0.113 \text{ cm} \\[6pt]
n_z = 64 & \Delta z = 1.0 \times 10^{-7} \text{ m} \\[6pt]
n_t = 128 & \Delta t = 0.5 \times 10^{-9} \text{ s}
\end{array}\right\} \quad \text{Surface Thermal Source}
$$

The discretization values for the Green's function and thermoelastic forces (either pseudoburied or surface) were

$$
\begin{array}{ll}
n_x = 8 & \Delta x = 0.113 \text{ cm} \\[6pt]
n_y = 8 & \Delta y = 0.113 \text{ cm} \\[6pt]
n_z = 64 & \Delta z = 7.0625 \times 10^{-3} \text{ m} \\[6pt]
n_t = 128 & \Delta t = 6.0 \times 10^{-8} \text{ s}
\end{array}
$$

The maximum number of summations used in the numerical inverse Laplace algorithm was $M = 500$ which required approximately nine hours to run on the available computer.

EO Q-Switched Nd:YAG (1.064 μm) Laser

Here we consider the electro optic Q-switched Nd:YAG (1.064 μm) laser. From Table 5.5 we see that in our experiments, we had a pulse width of 25 ns, a 2.0 mm radius, and an absorbed power flux of 22,316.0 MW/m². We used these parameters and a pulse rise time of $\tau = 10$ ns and in our thermal field calculations with the discretization values listed above for both a pseudoburied and surface thermal source. We convolved the thermal force and elastic Green's function arrays together to compute the thermoelastic displacement. The first plot in Figure 6.7 shows the theoretically computed z-component epicentral displacement in the graphite/epoxy composite sample with the pseudoburied thermal source. We clearly see three longitudinal wave arrivals. The second plot in Figure 6.7 shows the experimental data on the same scale. As with the computed waveform, we see three longitudinal wave arrivals. From Figure 6.7 we see that the wave arrivals in the waveforms are nearly coincident indicating a slight difference between the computed and measured longitudinal wave speed. This is because the values used for the stiffness matrix are not specific to our sample. We also see that the magnitude of the last two arrivals of the computed displacements corresponds well to the magnitude of the experimental displacements. The magnitude of the first wave arrivals are significantly different but are still within the same order of magnitude of each other. The frequency of the experimental longitudinal waves appears to be significantly higher than the frequency of the computed longitudinal waves. We attribute this to the relatively low resolution of our computational space. We observed with the aluminum sample that the resolution of the convolution significantly affected the results. We expect that these effect are more serious here with the anisotropic material. Figure 6.8 shows the same representation except that the surface thermal source was used to calculate the thermoelastic forcing function. Once again we see the three longitudinal wave arrivals that correlate well to the three arrivals observed experimentally. However, the magnitude of the

277
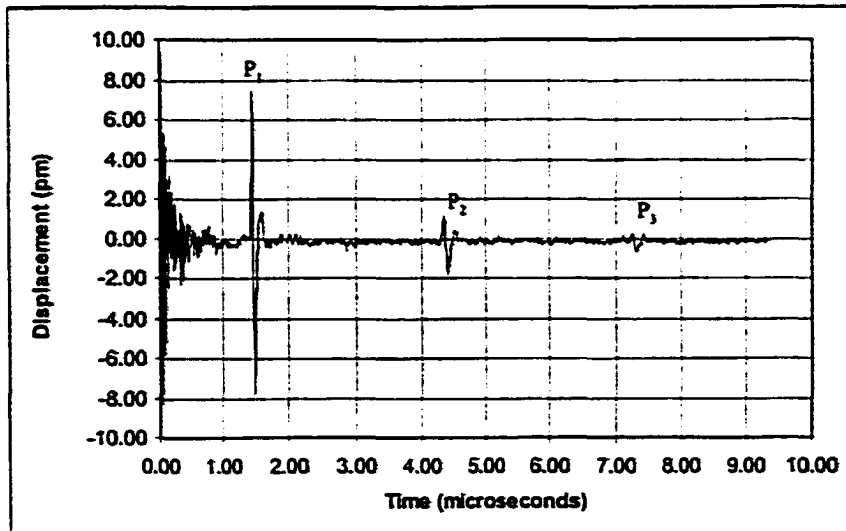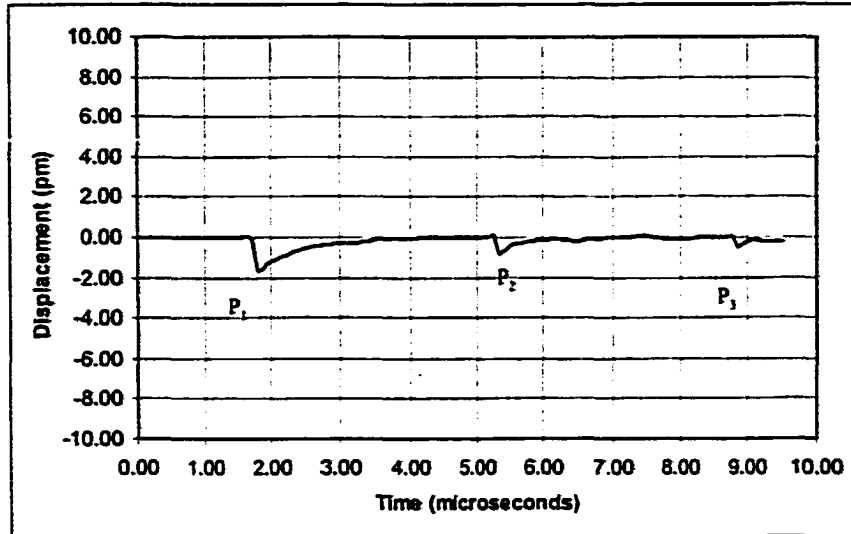
Figure 6.7: Computed epicentral displacement using the pseudoburied thermal source compared with experimental data for the EO Q-Switched Nd:YAG (1.064 μm) laser on the woven GR/Epoxy sample.

278

computed waveform is approximately two orders of magnitude larger than the experimental data.

RM Q-Switched Nd:YAG (1.320 μm) Laser

Here we consider the Nd:YAG laser (1.320 μm) Q-switched with the rotating mirror. From Table 5.5 we see that in our experiments, we had a pulse width of 130 ns, a 3.0 mm radius, and an absorbed power flux of 2083.0 MW/m^2. We found that a pulse rise time of $\tau = 65$ ns approximated the laser pulse time dependence. We used these parameters in our thermal field calculations with the discretization values listed above. We convolved the thermal force and elastic Green's function arrays together to compute the thermoelastic displacement. The first plot in Figure 6.9 shows the theoretically computed z-component epicentral displacement in the graphite/epoxy sample with the pseudoburied thermal source. As with the previous examples, we clearly see the three longitudinal wave arrivals. The second plot in Figure 6.9 shows the experimental data on the same scale. Again, we see that the longitudinal wave arrivals in the two waveforms are nearly coincident. The displacement magnitudes of the two waveforms in Figure 6.9 do not correlate as well as the waveforms for the EO Q-switched Nd:YAG (1.064 μm) presented in Figure 6.7.

Figure 6.10 shows the same representation except that the surface thermal source was used to calculate the thermoelastic forcing function. Once again we see the three longitudinal wave arrivals that correlate well to the three arrivals observed experimentally. In this case, the magnitude of the computed waveform is approximately one order of magnitude larger than the experimental data.

279
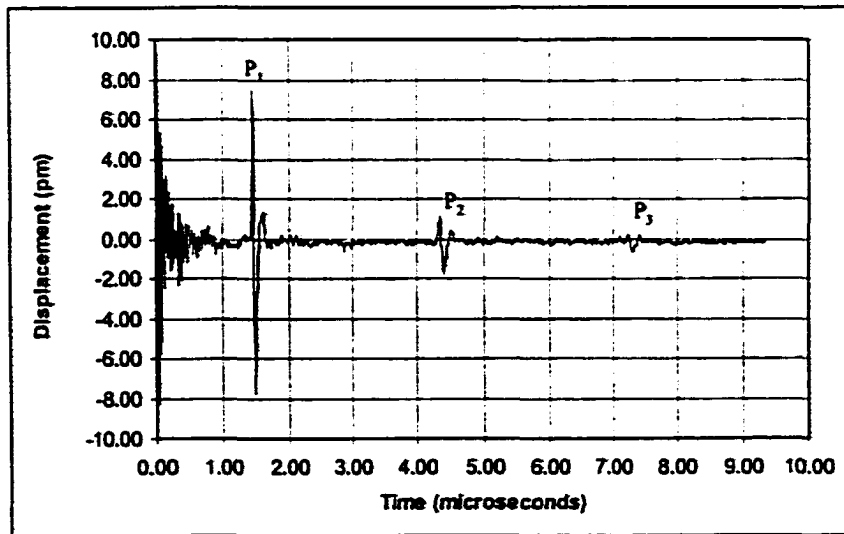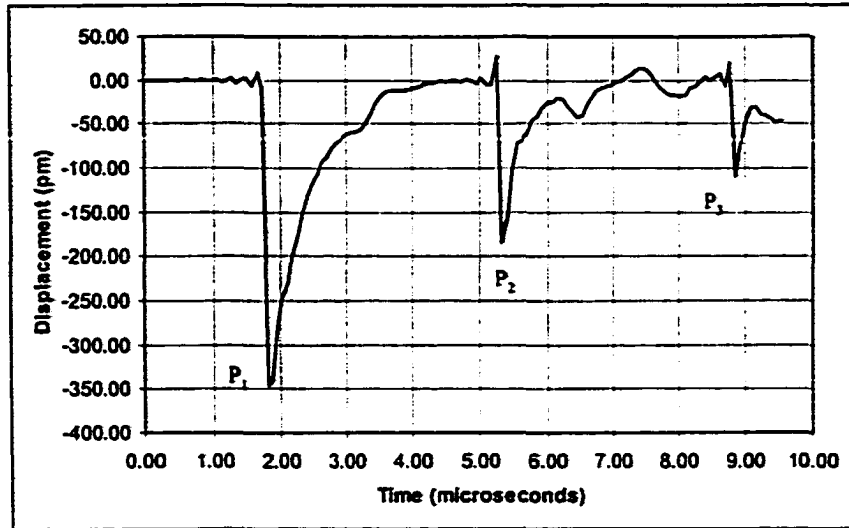
Figure 6.8: Computed epicentral displacement using the surface thermal source compared with experimental data for the EO Q-Switched Nd:YAG (1.064 μm) laser on the woven GR/Epoxy sample.

280
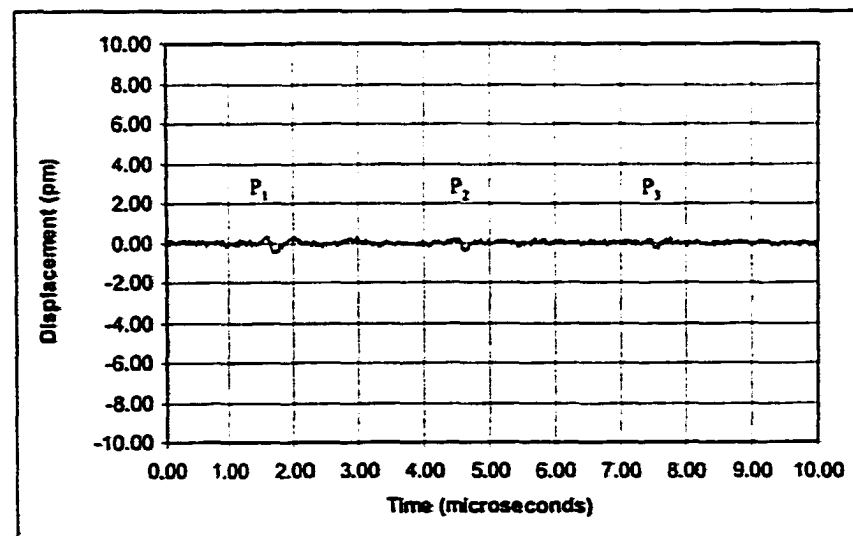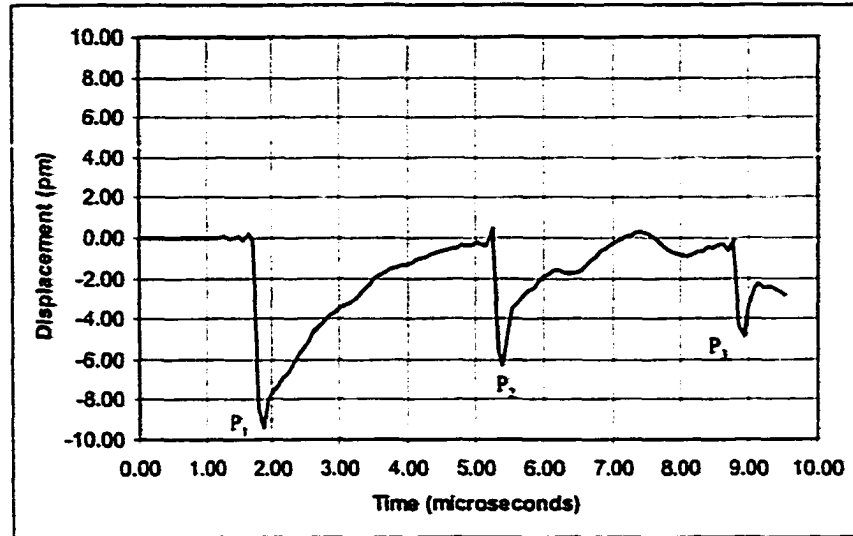
Figure 6.9: Computed epicentral displacement using the pseudoburied thermal source compared with experimental data for the RM Q-Switched Nd:YAG (1.32 μm) laser on the woven GR/Epoxy sample.

281
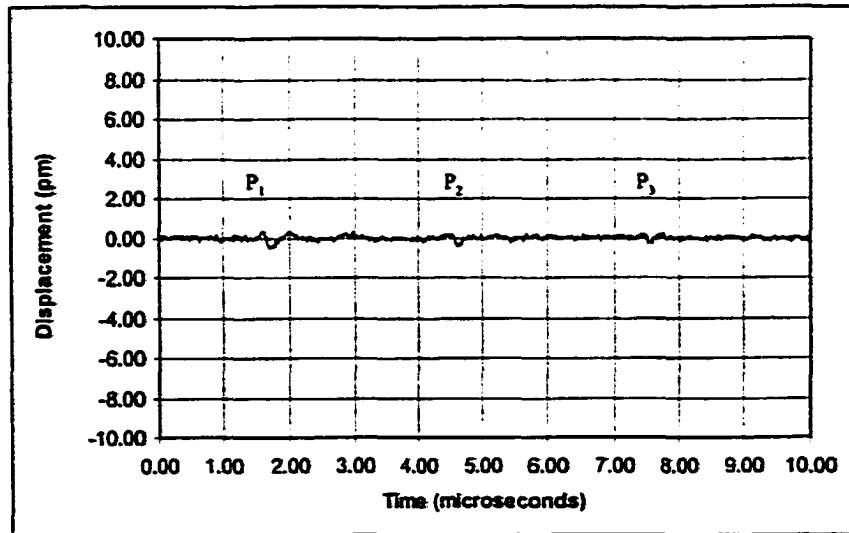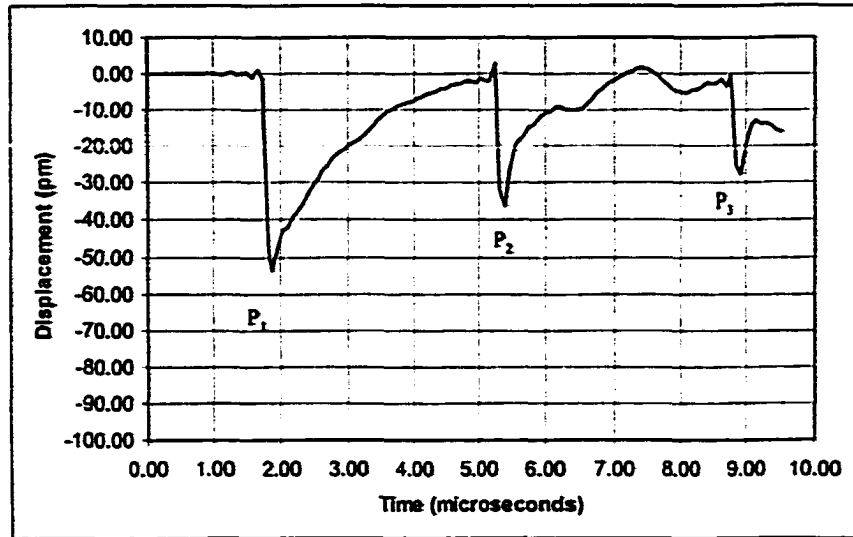
Figure 6.10: Computed epicentral displacement using the surface thermal source compared with experimental data for the RM Q-Switched Nd:YAG (1.32 μm) laser on the woven GR/Epoxy sample.

282

Green's Function

Here we consider the unconvolved Green's function for the graphite/epoxy composite sample. The first plot in Figure 6.11 shows the epicentral displacement due to the unconvolved Green's function. The second plot shows the experimental data obtained with the EO-Q-switched Nd:YAG (1.064 μm) laser. We see that the waveform generated by the pure Green's function qualitatively matches the experimental data better than the convolution solutions presented earlier. The magnitude is several orders of magnitude larger, but the general shape of the waveform more closely matches the data. We suggest that this is due to the relatively poor time resolution of our convolution model. Our "instantaneous" thermoelastic sources were essentially one time unit (Δt) in duration, or 6.0×10^{-8} s. In reality, the thermal source should be modeled on the time scale of the laser pulse which is much smaller than this. We suggest that the broadening of the wave arrivals in the convolution solutions is a result.

6.2.3 Summary of the Woven Graphite/Epoxy model

Here we summarize the results of modeling the thermoelastic response in the woven Graphite/Epoxy sample. We generated epicentral displacement waveforms with both a pseudoburied and surface thermoelastic source for two different laser configurations. In general, we found that regardless of the laser parameters, the same general features were observed. Specifically, we saw three clear longitudinal wave arrivals with amplitudes and arrival times that correlated with the wave arrivals in the experimental data. We suggested that the slight discrepancy between the computed and measured wave speed was due to our choice of material parameters for the stiffness coefficient matrix.

Our mathematical model generated waveforms that were qualitatively and quantitatively similar to the experimental waveforms. Qualitatively, the shapes of the computed

283
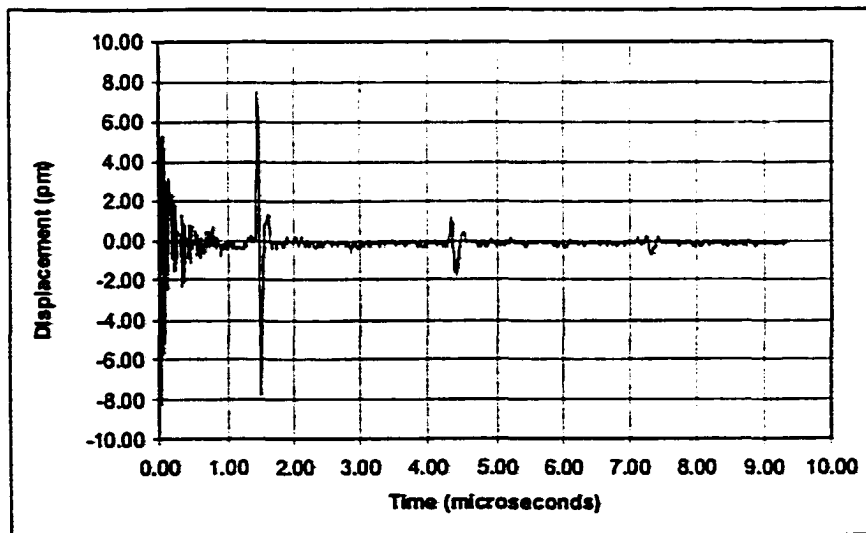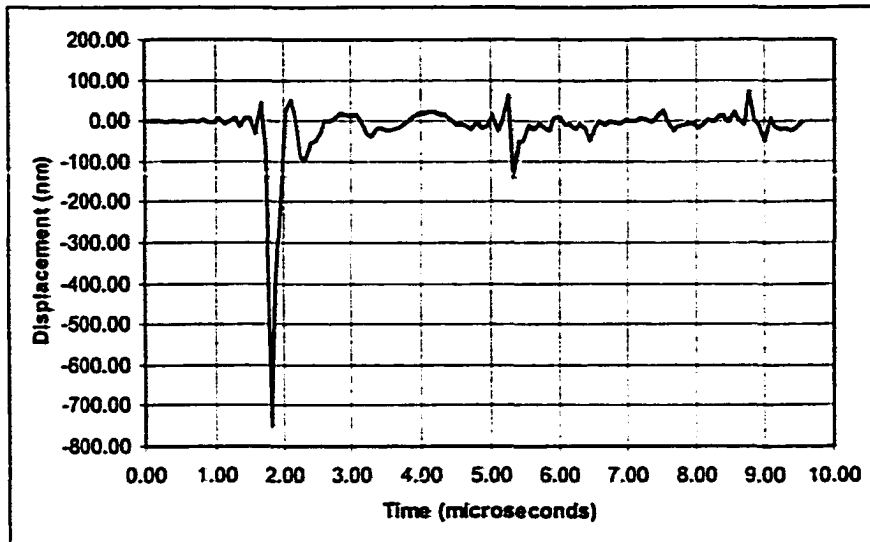
Figure 6.11: Computed epicentral displacement in the graphite/epoxy sample due to the unconvolved Green's function compared with experimental data for the EO Q-Switched Nd:YAG (1.064 μm) laser on the woven GR/Epoxy sample.

284

waveforms were somewhat similar to the experimental data. However, we found that the shape of the Green's function was more similar to the data than the convolution solutions. We suggested that the poor time resolution caused the broadening of the wave arrivals in the convolution solutions. Quantitatively, the magnitude of the computed waveforms was consistent with the experimental data when we used the pseudoburied thermal source.

285

Chapter 7

Conclusions

In this chapter we review the motivation for this research and discuss our theoretical model in relation to our experimental data. Finally, we suggest directions for future work.

7.1 Motivation

Nondestructive evaluation (NDE) to investigate material integrity and for process control has become increasingly important. There is a strong incentive to develop techniques that allow rapid and accurate inspection of materials without interfering with the function or operation of the product. Laser based ultrasonic NDE is a technique that has many attractive characteristics for NDE and process control.

Laser based ultrasonic NDE offers significant advantages over conventional ultrasonic NDE methods because it is a completely *non-contact* technique and does not require close proximity to the sample. Laser based ultrasound can remotely measure samples in environments that are inaccessible to contact techniques because physical couplants are undesirable or impossible. Furthermore, laser based ultrasound can be used to remotely examine structures in hostile environments that are hazardous to human operators and

286

equipment. Laser based ultrasound can be used during experiments where other methods might interfere with the experiment. Samples with complex geometries or confined spaces can be inspected more easily with laser based ultrasound. Similarly, delicate samples can be investigated since no physical contact is required. Laser ultrasound can inspect samples with sensitive surfaces or surfaces that must be kept clean and free of scratches. Laser ultrasound can also be used for area inspections at speeds that cannot be obtained by mechanical techniques. Furthermore, any type of ultrasonic wave can be generated with a laser source. Finally, laser based ultrasound solves difficulties encountered by other non-contact ultrasound techniques.

However, contact techniques currently have some advantages over laser based ultrasound. Contact techniques are considerably less expensive than laser based ultrasonics. Also, special safety precautions like eye protection which are not required for contact techniques, are required to use laser based ultrasonics. Most significantly, contact ultrasound techniques currently provide a superior signal-to-noise ratio than laser based ultrasound.

To be competitive with contact techniques and to fully realize its potential, laser based ultrasonics must be better understood. Work has been done to improve the sensitivity of laser detection of ultrasound but less attention has been devoted to optimizing the laser ultrasound source. This research has been an effort to more fully understand generation mechanisms so that ultrasonic generation can be optimized for a given laser/sample system.

Finally, in our efforts to implement laser ultrasound in the COLTS structures laboratory, we found that practical considerations further reduce the efficiency of the technique. In general, there will always be design constraints when trying to implement laser based ultrasound outside of a laser laboratory. Furthermore, the nature of the advanced composite materials of interest makes laser ultrasonic inspection difficult. Our research is an attempt to mitigate these obstacles.

287

7.2 Mathematical Model and Experimental Data

7.2.1 Mathematical Model

In Chapter 3, we derived analytical equations describing the thermal fields produced by a surface and buried laser source in a thermally isotropic material. We described how we numerically evaluated these equations and computed thermal fields for a surface source in aluminum and a buried source in Pyrex. We showed that the buried source equation analytically and numerically reduced to the surface source equation when the appropriate parameters were used.

In Chapter 4, we computed the Green's function for the elastodynamic equations of motion for a general anisotropic half-space. We first Laplace transformed the equations of motion in time and subsequently Fourier transformed the equations of motion in space. We solved the resulting algebraic system of equations for the displacement amplitudes in the transform domain. For isotropic materials, we were able to analytically invert the Laplace transform and numerically invert the Fourier transform to compute the Green's function. For general anisotropic materials, we described a technique to numerically invert the Laplace transform. We showed that the numerical method produced results that were almost identical to the analytic Laplace inversion for isotropic materials.

Also in Chapter 4, we numerically computed Green's functions for three different anisotropic materials with three different crystal symmetry classes. Specifically, we examined barium sodium niobate (BSN) in the orthotropic $2mm$ symmetry class, cadmium sulfide (CdS) in the hexagonal $6mm$ symmetry class, and rutile in the tetragonal $3/mmm$ crystal symmetry class. We compared our numerical solutions for wave propagation in these materials to the slowness surfaces presented by Auld and obtained good agreement. Finally, we described how we computed the thermoelastic force and how we convolved this force

288

with the Green's function to determine the thermoelastic displacements.

7.2.2 Experimental Data

In Chapter 5, we presented experimental data to investigate how material and laser parameters affected laser generated ultrasound. We considered four different materials including an isotropic piece of aluminum, a quasi-isotropic woven Graphite/Epoxy plate, an isotropic plate of epoxy, and a woven Graphite/Epoxy plate with translaminar Kevlar stitching. We generated ultrasound in each material with five different laser wavelengths: 0.755 μm, 1.064 μm, 1.320 μm, 2.10 μm, and 2.940 μm. For each laser wavelength, we had up to three different Q-switching mechanisms that allowed us to vary the pulse width of each laser wavelength..

In the aluminum sample, we found that each laser configuration generated an ultrasonic waveform with similar qualitative features. We compared the ultrasonic displacement to the absorbed power. The largest displacement was generated by the EO Q-switched Nd:YAG (1.064 μm) laser which had a pulse width of 25 ns at 8 mJ/pulse. This produced the highest instantaneous power density because of the short pulse width and because the reflectivity of the aluminum was lower at this wavelength. A general trend in the data was not obvious, but it does appear that the displacement magnitude increases with the instantaneous absorbed power density. We found that the frequency content of the ultrasonic signals was relatively insensitive to the laser parameters and generally had contributions from 2-5 MHz. As expected, a constraining layer of grease greatly enhanced the ultrasonic signal.

For the woven graphite/epoxy composite, we used the Fresnel equations to estimate the reflectance from tabulated values of the index of refraction of graphite. We computed instantaneous absorbed power density from the measured incident power density and com-

289

pared both the incident and absorbed power densities to the displacement amplitude. An initial evaluation of the data suggested that the displacement magnitude increased somewhat linearly with the instantaneous absorbed power. However, this trend was less clear when the last data point was omitted. Once again, the frequency content of the ultrasonic signals appeared to be independent of the laser parameters and had strong components around 2-5 MHz.

In the resin sample, we measured the transmitted energy through the sample and subtracted this from the incident energy to compute the instantaneous absorbed power density. We compared this absorbed power to the displacement amplitude. We found that the longer wavelength lasers (i.e. 2.1 μm and 2.94 μm) were absorbed better in the resin and produced greater instantaneous power densities. However, the results were not consistent. Furthermore, we found that the Alexandrite laser with the shortest wavelength (0.720-0.790 μm) could generate large displacements even though the absorbed power density was smaller. We suggested that this difficulty was caused by the detection laser which damaged the sample during each test.

As with the first composite sample, we used the Fresnel equations to estimate the reflectance from tabulated values of the index of refraction of graphite. We computed instantaneous absorbed power density from the measured incident power density and compared both the incident and absorbed power densities to the displacement amplitude. There did not seem to be a general trend in the results. The maximum displacement occurred at the lowest power density with the RM Q-switched CTH:YAG laser at 2.1 μm. A displacement with similar magnitude was generated with the EO Q-switched Nd:YAG (1.064 μm) laser. Since this wavelength easily transmitted though the resin sample, we suggested that the laser light was mostly absorbed in the first layer of graphite fibers and that the resin layer then behaved as a constraining layer and generated a larger amplitude displacement. The

frequency content of the ultrasonic signals for the different laser configurations was more consistent than in the other samples. The frequency spectrum of every signal was similar with a 5 MHz bandwidth centered around 2-3 MHz. As with the other samples, the frequency content was independent of the laser parameters.

7.2.3 Comparison of the Mathematical Model and Data

In Chapter 6, we compared the mathematical model to the experimental data. We presented computed waveforms for the z-component magnitude of the epicentral displacement in the aluminum sample, and the woven graphite/epoxy sample. We compared these waveforms to the experimentally obtained waveforms presented in Chapter 5.

In the aluminum sample, we found good qualitative and quantitative agreement between the computed waveforms and the experimental waveforms. The computed waveforms clearly reproduced the first two longitudinal wave arrivals. The magnitude of these waves had the same order of magnitude as the experimental data and had the same general shape. In general the frequency content of these wave arrivals was consistent with the frequency content of the data.

A possible first shear wave arrival was also visible in the computed waveforms. This wave did not match the experimental data as accurately as the longitudinal wave arrivals had. We attributed this to the poor resolution of our mathematical model in the x-y plane.

In the woven graphite/epoxy sample we obtained some qualitative and quantitative agreement between the computed waveforms and the experimentally measured data. The computed waveforms showed three longitudinal wave arrivals that correlated with the three wave arrivals visible in the data. The slight discrepancy between the computed wave speed and the measured wave speed was due to the choice of values for the stiffness coefficient matrix.

291

The computed wave arrivals were much broader than the experimental data. In contrast, the unconvolved Green's function more closely resembled the shape of the experimental data. We attributed this to the poor time resolution in the convolution.

The magnitude of the convolution solutions was of the same order of magnitude as the experimental data when we used a pseudoburied thermal source. We compared these results to displacements computed for a surface thermal source and found that the magnitude of the surface source was too large.

7.3 Directions for Future Work

7.3.1 Experimental

Here, we suggest some possible future experiments to improve upon the experiments presented in this work. Although our laser source had a variable wavelength and pulsewidth, the laser was extremely difficult to work with and it was not possible to reproduce consistent laser parameters for our comparison. As technology improves and laser sources become less expensive, it would be fruitful to reproduce our experiments with more exact control over the laser parameters. Also, because the process of changing the laser parameters involved replacing laser cavity elements and realigning the cavity each time, the process was very time consuming. Consequently, only one or possibly two data sets were taken for any given laser/material system. It would be better if the process could be shortened so that more data sets could be taken for a more representative data set.

7.3.2 Theoretical

There are several directions for future work on the mathematical model both theoretically and computationally. Theoretically, analytical and/or numerical solutions could be

292

obtained for the thermal fields in anisotropic materials. This would allow a more accurate reproduction of the thermoelastic source. Also, different Green's functions could be derived to more accurately represent the physical system. We derived a point source infinite space Green's function for an arbitrary anisotropic material in Cartesian coordinates. Green's functions for plates or half-spaces could be considered. Also, line source Green's functions could be used in some cases.

Numerically, more work could be done to optimize the computer algorithms for speed and memory conservation. Some of the computer algorithms could be parallelized for greatly enhanced performance. By improving the memory management, larger and consequently, arrays with better resolution could be computed so that the model could be more accurate. Most significantly, a four-dimensional convolution routine could be written to replace the *Mathematica* routines used in our work. This was the biggest limitation in speed and memory and prevented us from considering larger, better resolved arrays.

Appendix A

Computer Code

A.1 Thermal Calculations:

```
PROGRAM thermal

C    4/9/00

C    CACULATES THE THERMAL FIELD AND RESULTING FORCE

C    2nx BY 2ny BY nz IN SPACE=TOTAL COMPUTATIONAL SPACE, READ FROM FILE.

C    SPATIAL STEPS OF dx, dy and, dz, READ FROM FILE.
C    nt TIME STEPS OF dt SECONDS, READ FROM FILE


C    READS FILE thermal.in WHICH HAS PARAMETERS FOR A GIVEN MATERIAL:
C    CONDUCTIVITY, DIFFUSIVITY, ABSORPTION,
C    EXPANSION, GAUSS, TAU, POWER, nx,ny,nz,nt


C    MAXIMUM NUMBER OF SPATIAL GRID POINTS IN EACH DIMENSION.
C    MAXIMUNN NUMBER OF TIME STEPS.

     PARAMETER(nxmax=17,nzmax=257,ntmax=257)

     Integer nx,ny,nz,nt,i,j,h,t,k,itemp,m,n

     REAL*8 dx,dy,dz,dt,time,PI
```

294

```
      REAL*8 dt2

      REAL*8 C11, C12, C13, C14, C15, C16, C21, C22, C23,
     +      C24, C25, C26, C31, C32, C33, C34, C35, C36,
     +      C41, C42, C43, C44, C45, C46, C51, C52, C53,
     +      C54, C55, C56, C61, C62, C63, C64, C65, C66, density

      COMPLEX theta(nxmax,nxmax,nzmax,ntmax)

      COMPLEX pulse(ntmax)

      REAL*8 force(nxmax,nxmax,nzmax,ntmax)
      REAL*8 surfaceforce(nxmax,nxmax,nzmax,ntmax)
      REAL*8 conductivity,diffusivity,absorption,gauss,power,tau
      REAL*8 expansion,poisson,period,dw,dw2


      OPEN(UNIT=17,FILE='thermal_diagnostics.out')
      OPEN(UNIT=18,FILE='thermal.in',STATUS='OLD')

      OPEN(UNIT=20,FILE='surfaceforce.out')
      OPEN(UNIT=21,FILE='temperature.out')
      OPEN(UNIT=22,FILE='force.out')
CCCCCCCCCCCCCCCCCCCCCCCCCCCCCCCCCCCCCCCCCCCCCCCCCCCCCCCCCCCCCCCCC

C     MAIN PROGRAM


      PI=3.14159265358979


      WRITE(6,*)'BEGINNING'
      WRITE(17,*)'BEGINNING'

      WRITE(6,*)'READING IN MATERIAL CONSTANTS AND PARAMETERS'
      WRITE(17,*)'READING IN MATERIAL CONSTANTS AND PARAMETERS'

C     READ IN MATERIAL CONSTANTS AND PARAMETERS FROM constants.in
C     nx,ny,nz, and nt CAN HAVE A MAXIMUM VALUE OF (nxmax-1)/2,
C     (nzmax-1)/2  (ntmax-1)/2

      CALL READCONST(conductivity,diffusivity,absorption,expansion,
     +poisson,gauss,tau,power,
     +nx,dx,ny,dy,nz,dz,nt,dt)
```

295

```
CCCCCCCCCCCCCCCCCCCCCCCCCCCCCCCCCCCCCCCCCCCCCCCCCCCCCCCCCCCCCCCCCCCCCCC

C     CALCULATING THERMAL RESPONSE

CCCCCCCCCCCCCCCCCCCCCCCCCCCCCCCCCCCCCCCCCCCCCCCCCCCCCCCCCCCCCCCCCCCCCCC

        WRITE(6,*)'BEGINNING CALCULATION OF THERMAL RESPONSE'
        WRITE(17,*)'BEGINNING CALCULATION OF THERMAL RESPONSE'

        WRITE(6,*)'INITIALIZING ARRAY: nx,ny,nz,nt',nx,ny,nz,nt
        WRITE(17,*)'INITIALIZING ARRAY:nx,ny,nz,nt',nx,ny,nz,nt

        CALL INITIALIZE(theta,nx,ny,nz,nt)

C     DISPLAY VALUES AND OUTPUTS TO diagnostics.out


        CALL DISPLAY(conductivity,diffusivity,absorption,expansion,
       +poisson,gauss,tau,power,
       +nx,dx,ny,dy,nz,dz,nt,dt)

        period=REAL(nt)*dt


        WRITE(6,*)'period=',period
        WRITE(17,*)'period=',period


        n=INT(2*INT(period/dt))

        dw=1/(REAL(n*dt))

        WRITE(6,*)'n=',n
        WRITE(17,*)'n=',n

        WRITE(6,*)'dw=',dw
        WRITE(17,*)'dw=',dw



        WRITE(6,*)'CALCULATING IMPULSE THERMAL RESPONSE'
        WRITE(17,*)'CALCULATING IMPULSE THERMAL RESPONSE'

C     NOTE THAT n IS PASSED INSTEAD OF nt. n=2nt.

        CALL IMPULSE_TEMP(theta,nx,ny,nz,n,conductivity,
       +      diffusivity,absorption,gauss,tau,dx,dy,dz,
       +      dt,power,PI)
```

296

```fortran
C      BEGINNING CONVOLUTION OF IMPULSE THERMAL FIELD AND PULSE SHAPE

       CALL TIME_CONVOLUTION(theta,pulse,tau,PI,nx,ny,nz,n,dt,dw)


C      OUTPUTTING THERMAL FIELD TO temperature.out

       CALL DATAOUT1(theta,nx,ny,nz,n)


C      CALCULATING FORCE

       CALL THERMALFORCE(theta,nx,ny,nz,n,expansion,poisson,dz,
     +      force,surfaceforce)

C      OUTPUTTING FORCE

       CALL DATAOUT2(force,nx,ny,nz,n)
       CALL DATAOUT3(surfaceforce,nx,ny,nz,n)

       CLOSE(17)
       CLOSE(18)

       CLOSE(20)
       CLOSE(21)
       CLOSE(22)

       END
CCCCCCCCCCCCCCCCCCCCCCCCCCCCCCCCCCCCCCCCCCCCCCCCCCCCCCCCCCCCCCCCCC

       SUBROUTINE READCONST(conductivity,diffusivity,absorption,
     +expansion,poisson,
     +gauss,tau,power,
     +nx,dx,ny,dy,nz,dz,nt,dt)



       REAL*8  conductivity,diffusivity,absorption,expansion,
     +poisson,gauss,tau,power,dx,dy,dz,dt,PI

       INTEGER nx,ny,nz,nt


       READ(18,*,END=10) conductivity,diffusivity,absorption,expansion,
     +poisson,gauss,tau,power,
```

```
      +nx,dx,ny,dy,nz,dz,nt,dt

10    CONTINUE


      RETURN

      END

CCCCCCCCCCCCCCCCCCCCCCCCCCCCCCCCCCCCCCCCCCCCCCCCCCCCCCCCCCCCCCCCCCCCC

      SUBROUTINE DISPLAY(conductivity,diffusivity,absorption,expansion,
     +poisson,gauss,tau,power,
     +nx,dx,ny,dy,nz,dz,nt,dt)

C     DISPLAY PARAMETERS USED AND WRITES TO diagnostics.out


      REAL*8  conductivity,diffusivity,absorption,expansion,
     +poisson,gauss,tau,power,dx,dy,dz,dt

      INTEGER nx,ny,nz,nt


      WRITE(6,*)'THERMAL CONDUCTIVITY, k=',conductivity
      WRITE(17,*)'THERMAL CONDUCTIVITY, k=',conductivity

      WRITE(6,*)'THERMAL DIFFUSIVITY, K=',diffusivity
      WRITE(17,*)'THERMAL DIFFUSIVITY, K=',diffusivity

      WRITE(6,*)'ABSORPTION, alpha=',absorption
      WRITE(17,*)'ABSORPTION, alpha=',absorption

      WRITE(6,*)'COEFFICIENT OF EXPANSION=',expansion
      WRITE(17,*)'COEFFICIENT OF EXPANSION=',expansion

      WRITE(6,*)'POSSION=',expansion
      WRITE(17,*)'POISSON=',expansion

      WRITE(6,*)'ARRAY DIMENSIONS'
      WRITE(17,*)'ARRAY DIMENSIONS'

      WRITE(6,*)'nx=',nx
      WRITE(6,*)'ny=',ny
      WRITE(6,*)'nz=',nz
      WRITE(6,*)'nt=',nt
```

298

```
WRITE(17,*)'nx=',nx
WRITE(17,*)'ny=',ny
WRITE(17,*)'nz=',nz
WRITE(17,*)'nt=',nt

WRITE(6,*)'ARRAY SPACING'
WRITE(17,*)'ARRAY SPACING'


WRITE(6,*)'dx=',dx
WRITE(6,*)'dy=',dy
WRITE(6,*)'dz=',dz
WRITE(6,*)'dt=',dt

WRITE(17,*)'dx=',dx
WRITE(17,*)'dy=',dy
WRITE(17,*)'dz=',dz
WRITE(17,*)'dt=',dt


WRITE(17,*)'GAUSSIAN RADIUS OF SPOT=',gauss
WRITE(17,*)'LASER PULSE RISE TIME=',tau
WRITE(17,*)'LASER PULSE POWER (W)=',power

RETURN

END


CCCCCCCCCCCCCCCCCCCCCCCCCCCCCCCCCCCCCCCCCCCCCCCCCCCCCCCCCCCCCCCCCCCCCCCCC

      SUBROUTINE IMPULSE_TEMP(theta,nx,ny,nz,n,conductivity,
     +      diffusivity,absorption,gauss,tau,dx,dy,dz,
     +      dt,power,PI)

C     NOTE THAT n=2nt

      PARAMETER(nxmax=17,nzmax=257,ntmax=257)
      EXTERNAL derfc
      COMPLEX theta(nxmax,nxmax,nzmax,ntmax)

      REAL*8 conductivity,diffusivity,absorption,gauss
      REAL*8 tau,epsilon,time,x,y,z,dx,dy,dz,dt,power,PI

      REAL*8 test,temp,temp2,temp3

      INTEGER nx,ny,nz,n,i,j,h,t,two_nx,two_ny,two_nz
```

299

```
      two_nx=2*nx
      two_ny=2*ny

      epsilon=1.D-20

      WRITE(6,*)'IN IMPULSE_TEMP. nx,ny,nz,n',nx,ny,nz,n
      WRITE(17,*)'IN IMPULSE_TEMP. nx,ny,nz,n',nx,ny,nz,n

C     SETTING TEMPERATURE TO ZERO FOR THE FIRST HALF OF THE TOTAL TIME.
C     NOTE THAT WE OVERSHOOT ONE BIN IN THE Z-DIMENSION SO THAT WE CAN
C     TAKE THE FORWARD DIFFERENCE DERIVATIVE LATER.

      DO t=1,n/2-1
        DO i=1,two_nx
          DO j=1,two_ny
            DO h=1,nz+1
              theta(i,j,h,t)=CMPLX(0.0,0.0)
            ENDDO
          ENDDO
        ENDDO
      ENDDO

C     DECIDING WHETHER TO USE SURFACE SOURCE OR BURIED SOURCE EQUATIONS

      IF (absorption.GE.1.D6) THEN

C     SURFACE SOURCE

      WRITE(6,*)'USING SURFACE SOURCE EQUATION'
      WRITE(17,*)'USING SURFACE SOURCE EQUATION'

C     CALCULATING SURFACE SOURCE TEMPERATURE FOR THE ENTIRE SPACE
C     2nx X 2ny X nz+1 AND THE SECOND HALF OF THE TOTAL TIME.

      DO t=n/2,n
        DO i=1,two_nx
          DO j=1,two_ny
            DO h=1,nz+1

              time=(t-n/2+epsilon)*dt
              x=(i-(nx+1))*dx
              y=(j-(ny+1))*dy
              z=h*dz


              theta(i,j,h,t)=(DEXP
     -               (-((x**2 + y**2)/
     -               (gauss**2 +
```

300

```
     -         4*diffusivity*
     -         time)) -
     -         z**2/
     -         (4.*diffusivity*
     -         time))*gauss**2*
     -         DSQRT(diffusivity/PI)*
     -         power)/
     -         (conductivity*
     -         DSQRT(time)*
     -         (gauss**2 +
     -         4*diffusivity*time))


           ENDDO
         ENDDO
       ENDDO
     ENDDO

     ELSE

C    BURRIED SOURCE

     WRITE(6,*)'USING BURRIED SOURCE EQUATION'
     WRITE(17,*)'USING BURRIED SOURCE EQUATION'

C    CALCULATING BURRIED SOURCE TEMPERATURE FOR THE ENTIRE SPACE
C    2nx X 2ny X nz+1 FOR THE SECOND HALF OF THE TOTAL TIME.

     DO t=n/2,n
       DO i=1,two_nx
         DO j=1,two_ny
           DO h=1,nz+1

             time=(t-n/2+epsilon)*dt
             x=(i-(nx+1))*dx
             y=(j-(ny+1))*dy
             z=(h-1+epsilon)*dz

             theta(i,j,h,t)= (absorption*diffusivity*
     -           DEXP
     -           (absorption**2*
     -           diffusivity*time -
     -           (x**2 + y**2)/
     -           (gauss**2 +
     -           4*diffusivity*time)
     -           - absorption*z)*
     -           gauss**2*power*
     -           DERFC(absorption*
```

301

```
-               DSQRT(diffusivity*time)
-               - z/
-               (2.*
-               DSQRT(diffusivity*time)
-               )))/
-               (conductivity*
-               (gauss**2 +
-               4*diffusivity*time))

            ENDDO
          ENDDO
        ENDDO
      ENDDO
    ENDIF

    RETURN

    END


ccccccccccccccccccccccccccccccccccccccccccccccccccccccccccccc

      SUBROUTINE TIME_CONVOLUTION(theta,pulse,tau,PI,
     +nx,ny,nz,n,dt,dw)

C     CONVOLVES THE THERMAL IMPULSE WITH THE LASER PULSE TIME
C     DEPENDENCE.

C     NOTE THAT n=2nt

      PARAMETER(nxmax=17,nzmax=257,ntmax=257)

      COMPLEX pulse(ntmax),theta(nxmax,nxmax,nzmax,ntmax)

      REAL*8 r_theta(ntmax),c_theta(ntmax),dt,dt2,period

      REAL*8 r_pulse(ntmax),c_pulse(ntmax),dw,dw2,PI,tau

      INTEGER nx,ny,nz,i,j,h,t,m,n,two_nx,two_ny


      two_nx=2*nx
      two_ny=2*ny

C     FOURIER TRANSFORM THERMAL FIELD

      WRITE(6,*)'IN TIME_CONVOLUTION: nx,ny,nz,n',nx,ny,nz,n
      WRITE(17,*)'IN TIME_CONVOLUTION: nx,ny,nz,n',nx,ny,nz,n
```

302

```fortran
      WRITE(6,*)'FOURIER TRANSFORMING THERMAL FIELD IN TIME'
      WRITE(17,*)'FOURIER TRANSFORMING THERMAL FIELD IN TIME'


      m=INT(LOG(REAL(n))/LOG(2.))

      DO h=1,nz+1

        DO i=1,two_nx

          DO j=1,two_ny


            CALL SEPERATE_T(theta,i,j,h,n,r_theta,c_theta)

C     USING 'INVERSE TRANFORM' SFFTEU BECAUSE SFFTEU HAS OPPOSITE
C     SIGN CONVENTION THAN MATHEMATICA


            CALL sffteu(r_theta, c_theta, n, m, -1)


            CALL TOGETHER_t(i,j,h,n,dt,r_theta,c_theta,theta,0)


          ENDDO
        ENDDO
      ENDDO


      WRITE(6,*)'CALCULATING LASER PULSE SHAPE FOR CONVOLUTION'
      WRITE(17,*)'CALCULATING LASER PULSE SHAPE FOR CONVOLUTION'

      CALL PULSESHAPE(n,tau,dt,pulse)


C     FOURIER TRANSFORM PULSE SHAPE

      WRITE(6,*)'FOURIER TRANSFORMING PULSE IN TIME'
      WRITE(17,*)'FOURIER TRANFORMING PULSE IN TIME'


      DO t=1,n
        r_pulse(t)=pulse(t)
        c_pulse(t)=0.0

      ENDDO
```

```
C      USING 'INVERSE TRANFORM' SFFTEU BECAUSE SFFTEU HAS OPPOSITE
C      SIGN CONVENTION THAN MATHEMATICA
C      SQRT(n)*(SQRT(n))*dt*FOURIER

       CALL sffteu(r_pulse, c_pulse, n, m, -1)



       DO t=1,n

          pulse(t)=n*dt*CMPLX(r_pulse(t),c_pulse(t))

       ENDDO



C      USE CONVOLUTION RULE: MULTIPLY TERM BY TERM

       WRITE(6,*)'MULTIPLYING TERM BY TERM'
       WRITE(17,*)'MULTIPLYING TERM BY TERM'


       DO i=1,two_nx
          DO j=1,two_ny
             DO h=1,nz+1

       CALL MULTIPLY_t(theta,pulse,i,j,h,n)

             ENDDO
          ENDDO
       ENDDO



C      INVERSE FOURIER TO GET RESULT

       WRITE(6,*)'INVERSE FOURIER IN TIME TO GET RESULT'
       WRITE(17,*)'INVERSE FOURIER IN TIME TO GET RESULT'

       dw2=2*Pi*dw
       dt2=1/(REAL(n)*dw2)

       WRITE(6,*)'dw2=',dw2
       WRITE(17,*)'dw2=',dw2
```

304

```
      WRITE(6,*)'dt2=',dt2
      WRITE(17,*)'dt2=',dt2

      DO i=1,two_nx
        DO j=1,two_ny
          DO h=1,nz+1

            CALL SEPERATE_T(theta,i,j,h,n,r_theta,c_theta)

C     USING 'FORWARD TRANSFORM' SFFTEU TO MATCH SIGN CONVENTION
C     OF MATHEMATICA

C     1/SQRT(n)*SQRT(n)*dt*INVERSEFOURIER                        .

            CALL sffteu(r_theta, c_theta, n, m, 1)
            CALL TOGETHER_t(i,j,h,n,dw,r_theta,c_theta,
     +theta,1)

          ENDDO
        ENDDO
      ENDDO


      RETURN

      END


CCCCCCCCCCCCCCCCCCCCCCCCCCCCCCCCCCCCCCCCCCCCCCCCCCCCCCCCCCCCCCCC

      SUBROUTINE MULTIPLY_t(f,g,i,j,h,n)

C     MULTIPLIES TERM BY TERM IN TIME

      PARAMETER(nxmax=17,nzmax=257,ntmax=257)

      COMPLEX f(nxmax,nxmax,nzmax,ntmax),g(ntmax)

      REAL*8 d

      INTEGER n,i,j,h,t


      DO t=1,n

        f(i,j,h,t)=f(i,j,h,t)*g(t)

      ENDDO
```

305

```fortran
      RETURN

      END
ccccccccccccccccccccccccccccccccccccccccccccccccccccccccccccccccccccccc

      SUBROUTINE PULSESHAPE(n,tau,dt,pulse)

C     CALCULATES LASER PULSE TIME DEPENDENCE

      PARAMETER(nxmax=17,nzmax=257, ntmax=257)

      COMPLEX pulse(ntmax)

      REAL*8 tau,dt

      INTEGER n,t

      WRITE(17,*)'tau,dt',tau,dt

      DO t=1,n/2-1

         pulse(t)=0.0

      ENDDO


      DO t=n/2,n

         time=(t-n/2)*dt

         pulse(t)= (time/tau)*DEXP(1.-time/tau)

      ENDDO

      RETURN

      END



ccccccccccccccccccccccccccccccccccccccccccccccccccccccccccccccccccccc

      SUBROUTINE INITIALIZE(array,nx,ny,nz,n)

C     INITIALIZES ARRAY

      PARAMETER(nxmax=17,nzmax=257,ntmax=257)
```

306

```
      COMPLEX array(nxmax,nxmax,nzmax,ntmax)
      INTEGER nx,ny,nz,n,i,j,h,t,two_nx,two_ny

      two_nx=2*nx
      two_ny=2*ny


      WRITE(6,*)'INITIALIZING ARRAY'
      WRITE(17,*)'INITIALIZING ARRAY'

       DO t=1,n
          DO i=1,two_nx
             DO j=1,two_ny
                DO h=1,nz+1

                   array(i,j,h,t)=0.0

                ENDDO
             ENDDO
          ENDDO
       ENDDO

       RETURN

       END


CCCCCCCCCCCCCCCCCCCCCCCCCCCCCCCCCCCCCCCCCCCCCCCCCCCCCCCCCCCCCCCCCCCCCC

      SUBROUTINE SEPERATE_T(array,i,j,h,n,realt,imagt)

      PARAMETER(nxmax=17,nzmax=257,ntmax=257)

      INTEGER i,j,h,t,n

      COMPLEX array(nxmax,nxmax,nzmax,ntmax)
      REAL*8  realt(ntmax), imagt(ntmax)


      DO t=1,n

         realt(t)=REAL(array(i,j,h,t))
         imagt(t)=AIMAG(array(i,j,h,t))

      ENDDO

      RETURN
```

307

```
      END


cccccccccccccccccccccccccccccccccccccccccccccccccccccccccccccccc

      SUBROUTINE TOGETHER_t(i,j,h,n,dt,realt,imaginaryt,array,sign)

C     SETUP SO THAT WHEN YOU CALL THE INVERSE SFFTEU YOU GET THE
C     FORWARD TRANSFORM

C     SQRT(n)*(SQRT(n))*dt*FOURIER

      PARAMETER(nxmax=17,nzmax=257,ntmax=257)

      INTEGER i,j,h,t,n,sign

      COMPLEX array(nxmax,nxmax,nzmax,ntmax)
      REAL*8  realt(ntmax), imaginaryt(ntmax), temp, dt,coeff

      IF (sign.EQ.0) THEN

      DO t=1,n

         array(i,j,h,t)=n*dt*CMPLX(realt(t),
     +        imaginaryt(t))

      ENDDO

      ELSE

         DO t=1,n

            array(i,j,h,t)=dt*CMPLX(realt(t),
     +           imaginaryt(t))

         ENDDO

      ENDIF

      RETURN

      END


cccccccccccccccccccccccccccccccccccccccccccccccccccccccccccccccc

      SUBROUTINE THERMALFORCE(array1,nx,ny,nz,nt,expansion,
```

308

```
    +       poisson,dz,array2,array4)


C       NOTE THAT n HAS BEEN PASSED IN AS nt SO THAT nt IS TWICE THE
C       VALUE INITIALLY ENTERED.

        PARAMETER(nxmax=17,nzmax=257,ntmax=257)

        INTEGER h,j,i,t,k,nx,ny,nz,nt,two_nx,two_ny,two_nz

        COMPLEX array1(nxmax,nxmax,nzmax,ntmax)

        REAL*8 array2(nxmax,nxmax,nzmax,ntmax),
    +       array3(nxmax,nxmax,nzmax,ntmax),
    +       array4(nxmax,nxmax,nzmax,ntmax),
    +       deriv_z(nxmax,nxmax,nzmax,ntmax),dz,coeff,
    +       poisson,expansion,maxforce,temp,sgn


        two_nx=2*nx
        two_ny=2*ny
        two_nz=2*nz

        WRITE(6,*)'IN THERMALFORCE: nx,ny,nz,nt',nx,ny,nz,nt
        WRITE(17,*)'IN THERMALFORCE: nx,ny,nz,nt',nx,ny,nz,nt

        WRITE(6,*)'CALCUALTING DERIVATIVE OF TEMPERATURE FIELD'
        WRITE(17,*)'CALCUALTING DERIVATIVE OF TEMPERATURE FIELD'

        WRITE(6,*)'2nx,2ny,2nz,nt',two_nx,two_ny,two_nz,nt
        WRITE(17,*)'2nx,2ny,2nz,nt',two_nx,two_ny,two_nz,nt

C       FOR THE FIRST HALF OF THE TIME AND THE FIRST HALF OF THE
C       Z-DIMENSION, WE COMPUTE THE DERIVATIVE OF THE TEMPERATURE
C       IN THE Z-DIRECTION.  AT THE SAME TIME, WE SET THE VALUE
C       OF ARRAY3(x,y,z,t)=0.0 FOR THIS PORTION OF THE COMPUTATIONAL
C       SPACE

        DO i=1,two_nx
          DO j=1,two_ny
            DO t=1,nt/2
              DO h=1,nz

                deriv_z(i,j,h,t)=
    +               (array1(i,j,h+1,t)-array1(i,j,h,t))/dz

                array3(i,j,h,t)=0.0
```

309

```
                EMDDO
             EMDDO
          ENDDO
       ENDDO


C     HERE, WE MULTIPLY THE DERIVIATIVE OF THE TEMPERATURE
C     FIELD BY THE THERMAL EXPANSION COEFFICIENT TO GET A FORCE
C     THIS IS THE FORCE FOR ALL SPACE AND TIME BUT IT DOES NOT INCLUDE
C     THE 'NEFGATIVE' TIME WHEN THERE IS NO FORCE. ARRAY2 IS PASSED OUT
C     AS THE FORCE.


      WRITE(6,*)'MULTIPLYING BY THERMAL EXPANSION'
      WRITE(17,*)'MULTIPLYING BY THEMAL EXPANSION'


      coeff = 2 * expansion*(1+poisson)/(1-2*poisson)


      WRITE(6,*)'coeff=',coeff
      WRITE(17,*)'coeff=',coeff


      WRITE(6,*)'dz=',dz
      WRITE(17,*)'dz=',dz


      DO i=1,two_nx
         DO j=1,two_ny
            DO h=1,nz
               DO t=1,nt/2
                  array2(i,j,h,t)=coeff*deriv_z(i,j,h,t)
               ENDDO
            ENDDO
         ENDDO
      ENDDO


C     HERE, WE CREATE AN INSTANTANEOUS SOURCE
C     APPROPRIATE FOR ALUMINUM. AT EACH POINT (X,Y,Z)
C     WE PICK OUT THE MAXIMUM VALUE OF THE
C     FORCE IN TIME COMPUTED ABOVE AND SET ARRAY3(X,Y,Z,1)=MAXFORCE.
C     FROM BEFORE, ARRAY3=0 FOR ALL OTHER TIMES SO THIS IS AN
C     INSTANTANEOUS FORCE COMPUTED FOR THE ENTIRE SPATIAL DOMAIN
C     BUT DOES NOT INCLUDE THE 'NEGATIVE' TIME.


      WRITE(6,*)'CREATING INSTANTANEOUS SURFACE SOURCE'
      WRITE(17,*)'CREATING INSTANTANEOUS SURFACE SOURCE'


      maxforce = 0.0
      sgn=1


      DO i=1,two_nx
         DO j=1,two_ny
```

310

```
      DO h=1,nz
         DO t=1,nt/2

            temp=DABS(array2(i,j,h,t))

            IF (temp.GE.maxforce) THEN

               maxforce=temp
               sgn=SIGN(1.,array2(i,j,h,t))

C              WRITE(6,*)'maxforce,sgn',maxforce,sgn

            ELSE

               CONTINUE

            ENDIF

         ENDDO

         maxforce=sgn*maxforce
         array3(i,j,h,1)=maxforce

      ENDDO
   ENDDO
ENDDO

maxforce = 0.0
sgn=1

C    NOW AT EACH X,Y POINT WE PICK OUT THE MAXIMUM
C    FORCE IN THE Z-DIRECTION AND SET ARRAY3(X,Y,1,1)=MAXFORCE.
C    NOW, WE HAVE AN INSTANTANEOUS FORCE WITH THE MAXIMUM VALUE
C    IN THE Z-DIRECTION MOVED TO THE SURFACE.

DO i=1,two_nx
   DO j=1,two_ny
      DO h=1,nz

         temp=DABS(array3(i,j,h,1))

         IF (temp.GE.maxforce) THEN

            maxforce=temp
            sgn=SIGN(1.,array3(i,j,h,1))

C           WRITE(6,*)'maxforce,sgn',maxforce,sgn
```

311

```
            ELSE

                CONTINUE

            ENDIF

         ENDDO

         maxforce=sgn*maxforce
         array3(i,j,1,1)=maxforce

      ENDDO
   ENDDO

C     HERE, WE SET THE FORCE EQUAL TO ZERO FOR ALL POINTS BELOW THE SURFACE

      DO i=1,two_nx
        DO j=1,two_ny
          DO h=2,nz
            DO t=1,nt/2

                array3(i,j,h,t)=0.0

            ENDDO
          ENDDO
        ENDDO
      ENDDO

C     HERE, WE SET ARRAY4(X,Y,Z,T)=0 FOR THE FIRST HALF OF THE TIME
C     AND FOR THE FIRST HALF OF THE Z-DIRECTION. OTHERWISE, ARRAY4
C     IS EQUAL TO THE VALUES OF ARRAY3. NOTE: ARRAY4 HAS TWICE THE
C     LENGTH IN THE TIME DOMAIN COMPARED TO ARRAY3. THIS IS THE PERIOD
C     OF ZERO FORCE NEEDED FOR THE CONVOLUTION.

      DO i=1,two_nx
        DO j=1,two_ny
          DO h=1,two_nz          .
            DO t=1,nt

              IF ((t.LE.nt/2).OR.(h.LE.nz)) THEN

                 array4(i,j,h,t)=0.0

              ELSE
                 array4(i,j,h,t)=array3(i,j,h-nz,t-nt/2)

              ENDIF
```

312

```
              ENDDO
            ENDDO
          ENDDO
        ENDDO

        RETURN

        END
CCCCCCCCCCCCCCCCCCCCCCCCCCCCCCCCCCCCCCCCCCCCCCCCCCCCCCCCCCCCCCCCCCCCC

        SUBROUTINE DATAOUT1(array,nx,ny,nz,nt)

C       OUTPUTS RESULTS TO FILE temperature.out

        PARAMETER(nxmax=17,nzmax=257,ntmax=257)

        INTEGER h,j,i,t,k,nx,ny,nz,nt,nz2,two_nx,two_ny

        COMPLEX array(nxmax,nxmax,nzmax,ntmax)


        two_nx=2*nx
        two_ny=2*ny

C       CHANGE COMMENT STATUS WHEN CALCULATING TEMPERATURE FIELDS
C       CURRENTLY SET FOR FORCE CALCUALTIONS

        WRITE(6,*)'OUTPUTTING TEMPERATURE FIELD TO'
        WRITE(6,*)'temperature.out: nt',nt
C       WRITE(6,*)'ENTER NUMBER OF Z LAYERS TO OUTPUT FOR THERMAL'
C       WRITE(6,*)'FIELD nz=',nz


        WRITE(17,*)'OUTPUTTING TEMPERATURE FIELD TO'
        WRITE(17,*)'temperature.out: nt',nt
C       WRITE(17,*)'ENTER NUMBER OF Z LAYERS TO OUTPUT FOR THERMAL'
C       WRITE(17,*)'FIELD nz=',nz

C       READ(5,*)nz2

        nz2=nz

        WRITE(6,*)'nz2=',nz2
        WRITE(17,*)'nz2=',nz2

        DO i = 1,two_nx
           DO j = 1,two_ny
```

313

```
            DO h = 1,nz2

         WRITE(21,130) (
    +      REAL(array(i,j,h,t)),
    +      t = 1,nt/2)

130      FORMAT(E20.8)


            ENDDO
          ENDDO
        ENDDO

        RETURN

        END


ccccccccccccccccccccccccccccccccccccccccccccccccccccccccccccccccc

        SUBROUTINE DATAOUT2(array,nx,ny,nz,nt)

C    OUTPUTS FORCE TO FILE force.out

        PARAMETER(nxmax=17,nzmax=257,ntmax=257)

        INTEGER h,j,i,t,k,nx,y,nz,nt,two_nx,two_ny,two_nz

        REAL*8 array(nxmax,nxmax,nzmax,ntmax)
        REAL*8 temp(nxmax,nxmax,nzmax,ntmax)

        two_nx=2*nx
        two_ny=2*ny
        two_nz=2*nz

        DO t = 1,nt/2
           DO h = 1,two_nz
              DO i = 1,two_nx
                 DO j = 1,two_ny

                    temp(i,j,h,t)=0.0

                 ENDDO
              ENDDO
           ENDDO
        ENDDO

        DO t = nt/2+1,nt
```

314

```fortran
          DO h = 1,nz
            DO i = 1,two_nx
              DO j = 1,two_ny

                  temp(i,j,h+nz,t)=array(i,j,h,t-nt/2)

              ENDDO
            ENDDO
          ENDDO
        ENDDO

        WRITE(6,*)'OUTPUTTING FORCE TO force.out'
        WRITE(17,*)'OUTPUTTING FORCE TO force.out'


        DO t = 1,nt
          DO h = 1,two_nz
            DO i = 1,two_nx
              DO j=1,two_ny

                  WRITE(22,150) REAL(temp(i,j,h,t))

150               FORMAT(E10.4)

              ENDDO
            ENDDO
          ENDDO
        ENDDO

        RETURN

        END


CCCCCCCCCCCCCCCCCCCCCCCCCCCCCCCCCCCCCCCCCCCCCCCCCCCCCCCCCCCCCCCCCCCCCC

        SUBROUTINE DATAOUT3(array,nx,ny,nz,nt)

C       OUTPUTS FORCE TO FILE surfaceforce.out

        PARAMETER(nxmax=17,nzmax=257,ntmax=257)

        INTEGER h,j,i,t,k,nx,y,nz,nt,two_nx,two_ny,two_nz

        REAL*8 array(nxmax,nxmax,nzmax,ntmax)


        WRITE(6,*)'OUTPUTTING FORCE TO surfaceforce.out'
```

315

```
       WRITE(17,*)'OUTPUTTING FORCE TO surfaceforce.out'


       two_nx=2*nx
       two_ny=2*ny
       two_nz=2*nz

       DO t = 1, nt
          DO h = 1,two_nz
             DO i = 1,two_nx

          WRITE(20,250) (
     +    REAL(array(i,j,h,t)),
     +    j = 1,two_ny)

250       FORMAT(E10.4)



             ENDDO
          ENDDO
       ENDDO

       RETURN

       END


ccccccccccccccccccccccccccccccccccccccccccccccccccccccccccccccccccccccc
c--------------------------------------------------------------------c
c                                                                    c
c  Subroutine sffteu( x, y, n, m, itype )                            c
c                                                                    c
c  This routine is a slight modification of a COMPLEX split          c
c  radix FFT routine presented by C.S. Burrus.  The original         c
c  program header is shown below.                                    c
c                                                                    c
c  Arguments:                                                        c
c     x - real array containing real parts of transform             c
c             sequence (in/out)                                      c
c     y - real array containing imag parts of transform             c
c             sequence (in/out)                                      c
c     n - integer length of transform (in)                          c
c     m - integer such that n = 2**m  (in)                          c
c     itype - integer job specifier (in)                            c
c             itype .ne. -1 --> foward transform                     c
c             itype .eq. -1 --> backward transform                   c
c                                                                    c
c  The forward transform computes                                   c
c     X(k) = sum_{j=0}^{N-1} x(j)*exp(-2ijk*pi/N)                    c
```

316

```
c                                                c
c   The backward transform computes              c
c       x(j) = (1/N) * sum_{k=0}^{N-1} X(k)*exp(2ijk*pi/N)    c
c                                                c
c                                                c
c   Requires standard FORTRAN functions - sin, cos    c
c                                                c
c   Steve Kifowit, 9 July 1997                   c
c                                                c
C-------------------------------------------------C
C   A Duhamel-Hollman Split-Radix DIF FFT         C
C   Reference: Electronics Letters, January 5, 1984    C
C   COMPLEX input and output in data arrays X and Y    C
C   Length is N = 2**M                            C
C                                                C
C   C.S. Burrus          Rice University       Dec 1984     C
C-------------------------------------------------C
c

      SUBROUTINE SFFTEU( X, Y, N, M, ITYPE )

      PARAMETER(ntmax=257)

      INTEGER N, M, ITYPE

      REAL*8  X(ntmax), Y(ntmax)
      INTEGER I, J, K, N1, N2, N4, IS, ID, I0, I1, I2, I3
      REAL*8  TWOPI, E, A, A3, CC1, SS1, CC3, SS3
      REAL*8  R1, R2, S1, S2, S3, XT
      INTRINSIC SIN, COS
      PARAMETER ( TWOPI = 6.2831853071795864769 )
c
      IF ( N .EQ. 1 ) RETURN
c
      IF ( ITYPE .EQ. -1 ) THEN
         DO 1, I = 1, N
            Y(I) = - Y(I)
 1       CONTINUE
      ENDIF
c
      N2 = 2 * N
      DO 10, K = 1, M-1
         N2 = N2 / 2
         N4 = N2 / 4
         E = TWOPI / N2
         A = 0.0
         DO 20, J = 1, N4
            A3 = 3 * A
            CC1 = COS( A )
```

```fortran
              SS1 = SIN( A )
              CC3 = COS( A3 )
              SS3 = SIN( A3 )
              A = J * E
              IS = J
              ID = 2 * N2
40            DO 30, IO = IS, N-1, ID
                I1 = IO + N4
                I2 = I1 + N4
                I3 = I2 + N4
                R1 = X(IO) - X(I2)
                X(IO) = X(IO) + X(I2)
                R2 = X(I1) - X(I3)
                X(I1) = X(I1) + X(I3)
                S1 = Y(IO) - Y(I2)
                Y(IO) = Y(IO) + Y(I2)
                S2 = Y(I1) - Y(I3)
                Y(I1) = Y(I1) + Y(I3)
                S3 = R1 - S2
                R1 = R1 + S2
                S2 = R2 - S1
                R2 = R2 + S1
                X(I2) = R1 * CC1 - S2 * SS1
                Y(I2) = - S2 * CC1 - R1 * SS1
                X(I3) = S3 * CC3 + R2 * SS3
                Y(I3) = R2 * CC3 - S3 * SS3
30            CONTINUE
              IS = 2 * ID - N2 + J
              ID = 4 * ID
              IF ( IS .LT. N ) GOTO 40
20        CONTINUE
10    CONTINUE
C
C--------LAST STAGE, LENGTH-2 BUTTERFLY -----------------C
C
      IS = 1
      ID = 4
50    DO 60, IO = IS, N, ID
        I1 = IO + 1
        R1 = X(IO)
        X(IO) = R1 + X(I1)
        X(I1) = R1 - X(I1)
        R1 = Y(IO)
        Y(IO) = R1 + Y(I1)
        Y(I1) = R1 - Y(I1)
60    CONTINUE
      IS = 2 * ID - 1
      ID = 4 * ID
```

```
          IF ( IS .LT. N ) GOTO 50
c
C--------BIT REVERSE COUNTER--------------------------------C
c
 100  J = 1
      N1 = N - 1
      DO 104, I = 1, N1
          IF ( I .GE. J ) GOTO 101
          XT = X(J)
          X(J) = X(I)
          X(I) = XT
          XT = Y(J)
          Y(J) = Y(I)
          Y(I) = XT
 101      K = N / 2
 102      IF ( K .GE. J ) GOTO 103
          J = J - K
          K = K / 2
          GOTO 102
 103      J = J + K
 104  CONTINUE
c
      IF ( ITYPE .EQ. -1 ) THEN
          DO 2, I = 1, N
              X(I) = X(I) / N
              Y(I) = - Y(I) / N
  2       CONTINUE
      ENDIF
c
      RETURN
c
c ... End of subroutine SFFTEU ...
c
      END


ccccccccccccccccccccccccccccccccccccccccccccccccccccccccccccccccccc
      SUBROUTINE CALERF(ARG,RESULT,JINT)
C-------------------------------------------------------------------
C
C This packet evaluates  erf(x),  erfc(x),  and  exp(x*x)*erfc(x)
C    for a real argument  x.  It contains three FUNCTION type
C    subprograms: ERF, ERFC, and ERFCX (or DERF, DERFC, and DERFCX),
C    and one SUBROUTINE type subprogram, CALERF. The calling
C    statements for the primary entries are:
C
C                  Y=ERF(X)      (or   Y=DERF(X)),
C
```

319

```
C                    Y=ERFC(X)    (or   Y=DERFC(X)),
C    and
C                    Y=ERFCX(X)   (or   Y=DERFCX(X)).
C
C    The routine  CALERF  is intended for internal packet use only,
C    all computations within the packet being concentrated in this
C    routine. The function subprograms invoke  CALERF  with the
C    statement
C
C           CALL CALERF(ARG,RESULT,JINT)
C
C    where the parameter usage is as follows
C
C       Function                    Parameters for CALERF
C        call           ARG                 Result          JINT
C
C     ERF(ARG)      ANY REAL ARGUMENT        ERF(ARG)          0
C     ERFC(ARG)     ABS(ARG) .LT. XBIG       ERFC(ARG)         1
C     ERFCX(ARG)    XNEG .LT. ARG .LT. XMAX  ERFCX(ARG)        2
C
C    The main computation evaluates near-minimax approximations
C    from "Rational Chebyshev approximations for the error function"
C    by W. J. Cody, Math. Comp., 1969, PP. 631-638. This
C    transportable program uses rational functions that theoretically
C    approximate  erf(x)  and  erfc(x)  to at least 18 significant
C    decimal digits. The accuracy achieved depends on the arithmetic
C    system, the compiler, the intrinsic functions, and proper
C    selection of the machine-dependent constants.
C
C********************************************************************
C********************************************************************
C
C Explanation of machine-dependent constants
C
C    XMIN   = the smallest positive floating-point number.
C    XINF   = the largest positive finite floating-point number.
C    XNEG   = the largest negative argument acceptable to ERFCX;
C             the negative of the solution to the equation
C             2*exp(x*x) = XINF.
C    XSMALL = argument below which erf(x) may be represented by
C             2*x/sqrt(pi) and above which x*x will not underflow.
C             A conservative value is the largest machine number X
C             such that   1.0 + X = 1.0   to machine precision.
C    XBIG   = largest argument acceptable to ERFC; solution to
C             the equation: W(x) * (1-0.5/x**2) = XMIN, where
C             W(x) = exp(-x*x)/[x*sqrt(pi)].
C    XHUGE  = argument above which  1.0 - 1/(2*x*x) = 1.0  to
C             machine precision. A conservative value is
```

320

```
C            1/[2*sqrt(XSMALL)]
C   XMAX   = largest acceptable argument to ERFCX; the minimum
C            of XINF and 1/[sqrt(pi)*XMIN].
C
C   Approximate values for some important machines are:
C
C                         XMIN      XINF      XNEG     XSMALL
C
C   CDC 7600   (S.P.)  3.13E-294  1.26E+322  -27.220  7.11E-15
C   CRAY-1     (S.P.)  4.58E-2467 5.45E+2465 -75.345  7.11E-15
C   IEEE (IBM/XT,
C     SUN, etc.) (S.P.) 1.18E-38   3.40E+38   -9.382   5.96E-8
C   IEEE (IBM/XT,
C     SUN, etc.) (D.P.) 2.23D-308  1.79D+308  -26.628  1.11D-16
C   IBM 195    (D.P.)  5.40D-79   7.23E+75   -13.190  1.39D-17
C   UNIVAC 1108 (D.P.) 2.78D-309  8.98D+307  -26.615  1.73D-18
C   VAX D-Format (D.P.) 2.94D-39  1.70D+38   -9.345   1.39D-17
C   VAX G-Format (D.P.) 5.56D-309 8.98D+307  -26.615  1.11D-16
C
C
C                         XBIG      XHUGE      XMAX
C
C   CDC 7600   (S.P.)  25.922    8.39E+6    1.80X+293
C   CRAY-1     (S.P.)  75.326    8.39E+6    5.45E+2465
C   IEEE (IBM/XT,
C     SUN, etc.) (S.P.)  9.194    2.90E+3    4.79E+37
C   IEEE (IBM/XT,
C     SUN, etc.) (D.P.) 26.543    6.71D+7    2.53D+307
C   IBM 195    (D.P.)  13.306    1.90D+8    7.23E+75
C   UNIVAC 1108 (D.P.) 26.582    5.37D+8    8.98D+307
C   VAX D-Format (D.P.)  9.269    1.90D+8    1.70D+38
C   VAX G-Format (D.P.) 26.569    6.71D+7    8.98D+307
C
C    INITIAL VALUES
C
C     DATA XINF,XNEG,XSMALL/1.79D308,-26.628D0,1.11D-16/.
C   1    XBIG,XHUGE,XMAX/26.543D0,6.71D7,2.53D307/
C
C
C**********************************************************************
C**********************************************************************
C
C Error returns
C
C  The program returns  ERFC = 0      for  ARG .GE. XBIG;
C
C                        ERFCX = XINF  for  ARG .LT. XNEG;
C        and
```

```
C                      ERFCX = 0    for  ARG .GE. XMAX.
C
C
C Intrinsic functions required are:
C
C     ABS, AINT, EXP
C
C
C Author: W. J. Cody
C         Mathematics and Computer Science Division
C         Argonne National Laboratory
C         Argonne, IL 60439
C
C Latest modification: March 19, 1990
C
C----------------------------------------------------------------
      INTEGER I,JINT

      DOUBLE PRECISION
     1     A,ARG,B,C,D,DEL,FOUR,HALF,P,ONE,Q,RESULT,SIXTEN,SQRPI,
     2     TWO,THRESH,X,XBIG,XDEN,XHUGE,XINF,XMAX,XNEG,XNUM,XSMALL,
     3     Y,YSQ,ZERO
      DIMENSION A(5),B(4),C(9),D(8),P(6),Q(5)
C----------------------------------------------------------------
C Mathematical constants
C----------------------------------------------------------------
      DATA FOUR,ONE,HALF,TWO,ZERO/4.0D0,1.0D0,0.5D0,2.0D0,0.0D0/,
     1     SQRPI/5.6418958354775628695D-1/,THRESH/0.46875D0/,
     2     SIXTEN/16.0D0/
C----------------------------------------------------------------
C Machine-dependent constants
C----------------------------------------------------------------
      DATA XINF,XNEG,XSMALL/1.79D308,-26.628D0,1.11D-16/,
     1     XBIG,XHUGE,XMAX/26.543D0,6.71D7,2.53D307/
C----------------------------------------------------------------
C Coefficients for approximation to  erf  in first interval
C----------------------------------------------------------------
      DATA A/3.16112374387056560D00,1.13864154151050156D02,
     1       3.77485237685302021D02,3.20937758913846947D03,
     2       1.85777706184603153D-1/
      DATA B/2.36012909523441209D01,2.44024637934444173D02,
     1       1.28261652607737228D03,2.84423683343917062D03/
C----------------------------------------------------------------
C Coefficients for approximation to  erfc  in second interval
C----------------------------------------------------------------
```

322

```fortran
      DATA C/5.64188496988670089D-1,8.88314979438837594D0,
     1     6.61191906371416295D01,2.98635138197400131D02,
     2     8.81952221241769090D02,1.71204761263407058D03,
     3     2.05107837782607147D03,1.23033935479799725D03,
     4     2.153115354744038446D-8/
      DATA D/1.57449261107098347D01,1.17693950891312499D02,
     1     5.37181101862009858D02,1.62138957456669019D03,
     2     3.29079923573345963D03,4.36261909014324716D03,
     3     3.43936767414372164D03,1.23033935480374942D03/
C----------------------------------------------------------------------
C Coefficients for approximation to  erfc  in third interval
C----------------------------------------------------------------------

      DATA P/3.05326634961232344D-1,3.60344899949804439D-1,
     1     1.25781726111229246D-1,1.60837851487422766D-2,
     2     6.58749161529837803D-4,1.63153871373020978D-2/
      DATA Q/2.56852019228982242D00,1.87295284992346047D00,
     1     5.27905102951428412D-1,6.05183413124413191D-2,
     2     2.33520497626869185D-3/
C----------------------------------------------------------------------
      X = ARG
      Y = ABS(X)
      IF (Y .LE. THRESH) THEN
C----------------------------------------------------------------------
C Evaluate  erf  for  |X| <= 0.46875
C----------------------------------------------------------------------
         YSQ = ZERO
         IF (Y .GT. XSMALL) YSQ = Y * Y
         XNUM = A(5)*YSQ
         XDEN = YSQ
         DO 20 I = 1, 3
            XNUM = (XNUM + A(I)) * YSQ
            XDEN = (XDEN + B(I)) * YSQ
   20    CONTINUE
         RESULT = X * (XNUM + A(4)) / (XDEN + B(4))
         IF (JINT .NE. 0) RESULT = ONE - RESULT
         IF (JINT .EQ. 2) RESULT = EXP(YSQ) * RESULT
         GO TO 800
C----------------------------------------------------------------------
C Evaluate  erfc  for 0.46875 <= |X| <= 4.0
C----------------------------------------------------------------------
      ELSE IF (Y .LE. FOUR) THEN
         XNUM = C(9)*Y
         XDEN = Y
         DO 120 I = 1, 7
            XNUM = (XNUM + C(I)) * Y
            XDEN = (XDEN + D(I)) * Y
```

323

```
120     CONTINUE
        RESULT = (XNUM + C(8)) / (XDEN + D(8))
        IF (JINT .NE. 2) THEN
            YSQ = AINT(Y*SIXTEN)/SIXTEN
            DEL = (Y-YSQ)*(Y+YSQ)
            RESULT = EXP(-YSQ*YSQ) * EXP(-DEL) * RESULT
        END IF
C------------------------------------------------------------
C Evaluate erfc for !X! > 4.0
C------------------------------------------------------------
        ELSE
            RESULT = ZERO
            IF (Y .GE. XBIG) THEN
                IF ((JINT .NE. 2) .OR. (Y .GE. XMAX)) GO TO 300
                IF (Y .GE. XHUGE) THEN
                    RESULT = SQRPI / Y
                    GO TO 300
                END IF
            END IF
            YSQ = ONE / (Y * Y)
            XNUM = P(6)*YSQ
            XDEN = YSQ
            DO 240 I = 1, 4
                XNUM = (XNUM + P(I)) * YSQ
                XDEN = (XDEN + Q(I)) * YSQ
240         CONTINUE
            RESULT = YSQ *(XNUM + P(5)) / (XDEN + Q(5))
            RESULT = (SQRPI - RESULT) / Y
            IF (JINT .NE. 2) THEN
                YSQ = AINT(Y*SIXTEN)/SIXTEN
                DEL = (Y-YSQ)*(Y+YSQ)
                RESULT = EXP(-YSQ*YSQ) * EXP(-DEL) * RESULT
            END IF
        END IF
C------------------------------------------------------------
C Fix up for negative argument, erf, etc.
C------------------------------------------------------------
300 IF (JINT .EQ. 0) THEN
            RESULT = (HALF - RESULT) + HALF
            IF (X .LT. ZERO) RESULT = -RESULT
        ELSE IF (JINT .EQ. 1) THEN
            IF (X .LT. ZERO) RESULT = TWO - RESULT
        ELSE
            IF (X .LT. ZERO) THEN
                IF (X .LT. XNEG) THEN
                    RESULT = XINF
                ELSE
                    YSQ = AINT(X*SIXTEN)/SIXTEN
```

324

```
                    DEL = (X-YSQ)*(X+YSQ)
                    Y = EXP(YSQ*YSQ) * EXP(DEL)
                    RESULT = (Y+Y) - RESULT
              END IF
           END IF
        END IF
  800 RETURN
C---------- Last card of CALERF ----------
        END


        DOUBLE PRECISION FUNCTION DERFC(X)
C-----------------------------------------------------------------
C
C This subprogram computes approximate values for erfc(x).
C   (see comments heading CALERF).
C
C   Author/date: W. J. Cody, January 8, 1985
C
C-----------------------------------------------------------------
        INTEGER JINT

        DOUBLE PRECISION X, RESULT
C-----------------------------------------------------------------
        JINT = 1
        CALL CALERF(X,RESULT,JINT)

        DERFC = RESULT
        RETURN
C---------- Last card of DERFC ----------
        END
```

A.2   Elastic Calculations

```
        PROGRAM elastic

C     4/17/00
C     INVERSE LAPLACE TRANSFORM OF THE Z-DISPLACEMENT COMPONENT
C     GIVING THE FOURIER TRANSFORMED VALUES IN 3 DIMENSIONS FOR
C     A GENERAL ANISOTROPIC MATERIAL.

C     INVERSE FOURIER TRANSFORM IN ALL THREE SPATIAL DIMENSIONS

C     2nx X 2ny X 2nz IN SPACE=TOTAL COMPUTATIONAL SPACE. READ FROM FILE.

C     SPATIAL STEPS OF dx, dy and, dz, READ FROM FILE.
```

325

```
C     nt TIME STEPS OF dt SECONDS, READ FROM FILE

C     kmax STEPS IN INVERSE LAPLACE SUMMATION, READ FROM FILE.

C     OMEGA =2*PI/(total_time)

C     INVERSE LAPLACE FROM U3ffl.txt GENERATED FROM MATHEMATICA NOTEBOOK
C     ALLOWS ARBITRAY IMPULSE VECTOR. ENTERED.

C     READS FILE constants.in WHICH HAS all PARAMETERS FOR A GIVEN MATERIAL:
C     STIFFNESS, DENSITY, nx, ny, nz, nt


C     MAXIMUM NUMBER OF SPATIAL GRID POINTS IN EACH DIMENSION.
C     MAXIMUNN NUMBER OF TIME STEPS.

      PARAMETER(nxmax=17,nzmax=257,ntmax=257)

      INTEGER nx,ny,nz,nt,n,ns,nn,na,choice,component

      COMPLEX array(nxmax,nxmax,nzmax,ntmax)

      REAL*8 dx,dy,dz,dt,time,A3,B3,A3_0,B3_0,PI
      REAL*8 ds,dn,da,c,w,Q1,Q2,Q3,total_time
      REAL*8 dx2,dy2,dz2,dt2,dw

      REAL*8 C11, C12, C13, C14, C15, C16, C21, C22, C23,
     +       C24, C25, C26, C31, C32, C33, C34, C35, C36,
     +       C41, C42, C43, C44, C45, C46, C51, C52, C53,
     +       C54, C55, C56, C61, C62, C63, C64, C65, C66, density

C     REAL PART OF DISPLACEMENT COMPONENTS

      OPEN(UNIT=14,FILE='u1.out')
      OPEN(UNIT=15,FILE='u2.out')
      OPEN(UNIT=16,FILE='u3.out')

C     DIAGNOSTICS

      OPEN(UNIT=17,FILE='diagnostics.out')

C     INPUT

      OPEN(UNIT=18,FILE='constants.in',STATUS='OLD')

C     IMAGINARY PART OF DISPLACEMENT COMPONENTS

      OPEN(UNIT=51,FILE='uI_c.out')
```

326

```
        OPEN(UNIT=52,FILE='u2_c.out')
        OPEN(UNIT=53,FILE='u3_c.out')

C       REAL PART OF FOURIER TRANSFORMED DISPLACEMENT COMPONENTS

c          OPEN(UNIT=54,FILE='fftu1_r.out')
c          OPEN(UNIT=55,FILE='fftu2_r.out')
c          OPEN(UNIT=56,FILE='fftu1_r.out')

C       IMAGINARY PART OF FOURIER TRANSFORMED DISPLACEMENT COMPONENTS

c          OPEN(UNIT=57,FILE='fftu1_c.out')
c          OPEN(UNIT=58,FILE='fftu2_c.out')
c          OPEN(UNIT=59,FILE='fftu1_c.out')


CCCCCCCCCCCCCCCCCCCCCCCCCCCCCCCCCCCCCCCCCCCCCCCCCCCCCCCCCCCCCCCCCCCC

C       MAIN PROGRAM

        PI=3.14159265358979

        WRITE(6,*)'BEGINNING'
        WRITE(17,*)'BEGINNING'

        WRITE(6,*)'READING IN MATERIAL CONSTANTS AND PARAMETERS'
        WRITE(17,*)'READING IN MATERIAL CONSTANTS AND PARAMETERS'

C       READ IN MATERIAL CONSTANTS AND PARAMETERS FROM constants.in

         CALL READCONST(C11,C12,C13,C14,C15,C16,C22,C23,
        +C24,C25,C26,C33,C34,C35,C36,C44,C45,C46,C55,C56,C66,density,
        +nx,dx,ny,dy,nz,dz,nt,dt,total_time,kmax,PI,v,c,
        +Q1,Q2,Q3,C21,C31,C32,C41,C42,C43,C51,C52,C53,C54,C61,C62,
        +C63,C64,C65)


C        DISPLAY VALUES AND OUTPUTS TO diagnostics.out

         CALL DISPLAY(C11,C12,C13,C14,C15,C16,C22,C23,
        +C24,C25,C26,C33,C34,C35,C36,C44,C45,C46,C55,C56,C66,density,
        +nx,dx,ny,dy,nz,dz,nt,dt,total_time,kmax,PI,v,c,
        +Q1,Q2,Q3,C21,C31,C32,C41,C42,C43,C51,C52,C53,C54,C61,C62,
        +C63,C64,C65)


C        CALCULATING ELASTIC GREEN'S FUNCTION

           n=nt
```

327

```
C    CALCULATE SAMPLING FREQUENCY

     WRITE(6,*)'CALCULATING SAMPLING FREQUENCY'

     WRITE(17,*)'CALCULATING SAMPLING FREQUENCY'

     CALL SAMPLE(nx,ny,nz,n,dx,dy,dz,dt,ds,dn,da,
   + dx2,dy2,dz2,PI,ns,nn,na)


C    INITIALIZE ARRAY

     CALL INITIALIZE(array,ns,nn,na,n)

C    CHOICE OF SOLVING EXACT INVERSE LAPLACE OR NUMERICAL INVERSE

     WRITE(6,*)'SOLVE EXACT EQUATIONS(1) OR NUMERICALLY INVERT(2)'
     WRITE(6,*)'OR INVERSE FOURIER GAUSSIAN(3)?'

C     READ(5,*)choice

     choice=2

     IF (choice.eq.2) THEN

        WRITE(6,*)'NUMERIC'
        WRITE(17,*)'NUMERIC'


        WRITE(6,*)'WHICH COMPONENT'
C       READ(5,*)component

        component=3

        WRITE(6,*)'COMPONENT=',component
        WRITE(17,*)'COMPONENT=',component

C    CALCULATE INVERSE LAPLACE TRANSFORM

        CALL INVERSE_LAPLACE(ns,nn,na,n,dt,w,c,kmax,Q1,
   +         Q2,Q3,PI,ds,dn,da,component,
   +         C11,C12,C13,C14,C15,C16,C21,C22,C23,
   +         C24, C25, C26, C31, C32, C33, C34, C35, C36,
   +         C41, C42, C43, C44, C45, C46, C51, C52, C53,
   +         C54, C55, C56, C61, C62, C63, C64, C65, C66,
   +         density,array)
```

328

```
      ELSEIF (choice.eq.1) THEN

          WRITE(6,*)'SOLVING EXACT FOR Z-COMPONENT'
          WRITE(17,*)'SOLVING EXACT FOR Z-COMPONENT'

          CALL EXACT(ns,nn,na,n,dt,ds,dn,da,Q1,Q2,Q3,
     +        C11,C44,C12,density,array)

      ELSE

C     TEST FUNCTION

          component=1

          n=1

          WRITE(6,*)'GAUSSIAN TEST FUNCTION. component=1'
          WRITE(17,*)'GAUSSIAN TEST FUNCTION. component=1'

          CALL GAUSSIAN(ns,nn,na,n,dt,ds,dn,da,PI,
     +        nx,ny,nz,dx,dy,dz,array)

      ENDIF

C     CALCULATE INVERSE FOURIER TRANSFORM

C     CHANGE COMMENT STATUS FOR CHOICE OF WINDOWING
CCCCCCCCCCCCCCCCCCCCCCCCCCCCCCCCCCCCCCCCCCCCCCCCCCCCCCCCCCCCCCC

C     CHANGE COMMENT IF YOU WANT THE CHOICE TO MULTIPLY BY A SUPERGAUSSIAN
C     WINDOW

C         WRITE(6,*)'MULTIPLY BY SUPERGAUSS(1) OR DO NOT WINDOW(2)'

C         READ(5,*)choice


          choice=2
CCCCCCCCCCCCCCCCCCCCCCCCCCCCCCCCCCCCCCCCCCCCCCCCCCCCCCCCCCCCCCC

      IF (choice.eq.1) THEN

          WRITE(6,*)'SUPERGAUSS WINDOW'
          WRITE(17,*)'SUPERGAUSS WINDOW'

          CALL SUPERGAUSS(ns,nn,na,n,dx,dy,dz,array)
```

329

```fortran
      CALL INVERSE_FOURIER_x_y_z(array,ns,nn,na,n,ds,dn,da,PI)

      ELSEIF (choice.eq.2) THEN

         WRITE(6,*)'NO WINDOW'
         WRITE(17,*)'NO WINDOW'

         CALL INVERSE_FOURIER_x_y_z(array,ns,nn,na,n,ds,dn,da,PI)

      ENDIF


C     WRITE OUT ELASTIC GREEN'S FUNCTION TO FILE

      CALL DATAOUT(array,component,ns,nn,na,n)

      CLOSE(14)
      CLOSE(15)
      CLOSE(16)
      CLOSE(17)
      CLOSE(18)

      CLOSE(51)
      CLOSE(52)
      CLOSE(53)
c        CLOSE(54)
c        CLOSE(55)
c        CLOSE(56)
c        CLOSE(57)
c        CLOSE(58)
c        CLOSE(59)

      END
cccccccccccccccccccccccccccccccccccccccccccccccccccccccccccccccc

      SUBROUTINE READCONST(C11,C12,C13,C14,C15,C16,C22,C23,
     +C24,C25,C26,C33,C34,C35,C36,C44,C45,C46,C55,C56,C66,density,
     +nx,dx,ny,dy,nz,dz,nt,dt,total_time,kmax,PI,w,c,
     +Q1,Q2,Q3,C21,C31,C32,C41,C42,C43,C51,C52,C53,C54,C61,C62,
     +C63,C64,C65)


      REAL*8 C11, C12, C13, C14, C15, C16, C21, C22, C23,
     +         C24, C25, C26, C31, C32, C33, C34, C35, C36,
     +         C41, C42, C43, C44, C45, C46, C51, C52, C53,
     +         C54, C55, C56, C61, C62, C63, C64, C65, C66, density

      REAL*8 dx,dy,dz,dt,total_time,PI,w,c,Q1,Q2,Q3
```

330

```fortran
      INTEGER nx,ny,nz,nt,kmax


      READ(18,*,END=10) C11, C12, C13, C14, C15, C16, C22, C23,
     +                  C24, C25, C26, C33, C34, C35, C36, C44, C45,
     +                  C46, C55, C56, C66, density,
     +nx,dx,ny,dy,nz,dz,nt,dt,kmax,
     +Q1,Q2,Q3


10    CONTINUE


      C21=C12
      C31=C13
      C32=C23
      C41=C14
      C42=C24
      C43=C34
      C51=C15
      C52=C25
      C53=C35
      C54=C45
      C61=C16
      C62=C26
      C63=C36
      C64=C46
      C65=C56


      WRITE(6,*)'DEFINING OMEGA AND C'
      WRITE(17,*)'DEFINING OMEGA AND C'


      total_time=dt*nt


      w=2.*PI/(total_time)



      c=w



      RETURN


      END


cccccccccccccccccccccccccccccccccccccccccccccccccccccccccccccccccccc

      SUBROUTINE DISPLAY(C11,C12,C13,C14,C15,C16,C22,C23,
     +C24,C25,C26,C33,C34,C35,C36,C44,C45,C46,C55,C56,C66,density,
     +nx,dx,ny,dy,nz,dz,nt,dt,total_time,kmax,PI,w,c,
```

331

```
+Q1,Q2,Q3,C21,C31,C32,C41,C42,C43,C51,C52,C53,C54,C61,C62,
+C63,C64,C65)


C      DISPLAY PARAMETERS USED AND WRITES TO diagnostics.out

       REAL*8 C11, C12, C13, C14, C15, C16, C21, C22, C23,
       +         C24, C25, C26, C31, C32, C33, C34, C35, C36,
       -         C41, C42, C43, C44, C45, C46, C51, C52, C53,
       +         C54, C55, C56, C61, C62, C63, C64, C65, C66, density


       REAL*8 dx,dy,dz,dt,total_time,PI,v,c,Q1,Q2,Q3


       INTEGER nx,ny,nz,nt,kmax

C      WRITE OUT  MATERIAL CONSTANTS

       WRITE(6,*)'MATERIAL CONSTANTS'

       WRITE(6,*) C11, C12, C13, C14, C15, C16
       WRITE(6,*) C21, C22, C23, C24, C25, C26
       WRITE(6,*) C31, C32, C33, C34, C35, C36
       WRITE(6,*) C41, C42, C43, C44, C45, C46
       WRITE(6,*) C51, C52, C53, C54, C55, C56
       WRITE(6,*) C61, C62, C63, C64, C65, C66
       WRITE(6,*) density

       WRITE(17,*)'MATERIAL CONSTANTS'


       WRITE(17,*) C11, C12, C13, C14, C15, C16
       WRITE(17,*) C21, C22, C23, C24, C25, C26
       WRITE(17,*) C31, C32, C33, C34, C35, C36
       WRITE(17,*) C41, C42, C43, C44, C45, C46
       WRITE(17,*) C51, C52, C53, C54, C55, C56
       WRITE(17,*) C61, C62, C63, C64, C65, C66
       WRITE(17,*) density


        WRITE(6,*)'ARRAY DIMENSIONS'
        WRITE(17,*)'ARRAY DIMENSIONS'

        WRITE(6,*)'nx=',nx
        WRITE(6,*)'ny=',ny
        WRITE(6,*)'nz=',nz
        WRITE(6,*)'nt=',nt

        WRITE(17,*)'nx=',nx
```

332

```
WRITE(17,*)'ny=',ny
WRITE(17,*)'nz=',nz
WRITE(17,*)'nt=',nt

WRITE(6,*)'ARRAY SPACING'
WRITE(17,*)'ARRAY SPACING'


WRITE(6,*)'dx=',dx
WRITE(6,*)'dy=',dy
WRITE(6,*)'dz=',dz
WRITE(6,*)'dt=',dt

WRITE(17,*)'dx=',dx
WRITE(17,*)'dy=',dy
WRITE(17,*)'dz=',dz
WRITE(17,*)'dt=',dt

WRITE(6,*)'total_time=',total_time
WRITE(6,*)'w=',w
WRITE(6,*)'c=',c

WRITE(17,*)'total_time=',total_time
WRITE(17,*)'w=',w
WRITE(17,*)'c=',c


WRITE(6,*)'SUMMATIONS (k) IN INVERSE LAPLACE'
WRITE(17,*)'SUMMATIONS (k) IN INVERSE LAPLACE'

WRITE(6,*)'k=',kmax
WRITE(17,*)'k=',kmax


WRITE(6,*)'IMPULSE VECTOR'

WRITE(6,*) Q1, Q2, Q3

WRITE(17,*)'IMPULSE VECTOR'

WRITE(17,*) Q1, Q2, Q3


RETURN

END
```

cccccccccccccccccccccccccccccccccccccccccccccccccccccccccccccccccccc

```fortran
      SUBROUTINE SAMPLE(nx,ny,nz,nt,dx,dy,dz,dt,ds,dn,da,
     +dx2,dy2,dz2,PI,ns,nn,na)

C     COMPUTES THE SAMPLING FREQUENCY.

      INTEGER nx,ny,nz,ns,nn,na

      REAL*8 ds,dn,da,dt,S_length,N_length,A_length,A_s,A_n,A_a
      REAL*8 dx,dy,dz,dx2,dy2,dz2,PI


C     SAMPLE FREQUENCIES

      ds=2.*PI/(DBLE(2*nx)*dx)
      dn=2.*PI/(DBLE(2*ny)*dy)
      da=2.*PI/(DBLE(2*nz)*dz)

      ns=nx
      nn=ny
      na=nz

      dx2=1/(DBLE(ns)*ds)
      dy2=1/(DBLE(nn)*dn)
      dz2=1/(DBLE(na)*da)

      WRITE(6,*)'ds=',ds
      WRITE(6,*)'dn=',dn
      WRITE(6,*)'da=',da

      WRITE(6,*)'ns=',ns
      WRITE(6,*)'nn=',nn
      WRITE(6,*)'na=',na

      WRITE(6,*)'dx2=',dx2
      WRITE(6,*)'dy2=',dy2
      WRITE(6,*)'dz2=',dz2
      WRITE(6,*)'dt2=',dt2

      WRITE(17,*)'ds=',ds
      WRITE(17,*)'dn=',dn
      WRITE(17,*)'da=',da

      WRITE(17,*)'dx2=',dx2
      WRITE(17,*)'dy2=',dy2
```

334

```
      WRITE(17,*)'dz2=',dz2

      WRITE(17,*)'ns=',ns
      WRITE(17,*)'nn=',nn
      WRITE(17,*)'na=',na


      RETURN

      END


CCCCCCCCCCCCCCCCCCCCCCCCCCCCCCCCCCCCCCCCCCCCCCCCCCCCCCCCCCCCCCCCCCCC

      SUBROUTINE INITIALIZE(array,ns,nn,na,n)

C     INITIALIZES ARRAY

      PARAMETER(nxmax=17,nzmax=257,ntmax=257)

      COMPLEX array(nxmax,nxmax,nzmax,ntmax)
      INTEGER ns,nn,na,n,i,j,h,t

      WRITE(6,*)'INITIALIZING ARRAY,n,ns,nn,na',n,ns,nn,na
      WRITE(17,*)'INITIALIZING ARRAY'

      DO t=1,2*n
         DO i=1,2*ns
            DO j=1,2*nn
               DO h=1,2*na

                  array(i,j,h,t)=0.0

               ENDDO
            ENDDO
         ENDDO
      ENDDO

      WRITE(6,*)'DONE INITIALIZING'

      RETURN

      END

CCCCCCCCCCCCCCCCCCCCCCCCCCCCCCCCCCCCCCCCCCCCCCCCCCCCCCCCCCCCCCCCCCCC

      SUBROUTINE INVERSE_LAPLACE(ns,nn,na,n,dt,w,c,kmax,Q1,
     + Q2,Q3,PI,ds,dn,da,component,
```

335

```
     +              C11,C12,C13,C14,C15,C16,C21,C22,C23,
     +              C24, C25, C26, C31, C32, C33, C34, C35, C36,
     +              C41, C42, C43, C44, C45, C46, C51, C52, C53,
     +              C54, C55, C56, C61, C62, C63, C64, C65, C66,
     +              density,array)

     PARAMETER(nxmax=17,nzmax=257,ntmax=257)


     COMPLEX array(nxmax,nxmax,nzmax,ntmax),temp,sum


     REAL*8 dt,w,c,Q1,Q2,Q3,PI,ds,dn,da,time,
     +              C11,C12,C13,C14,C15,C16,C21,C22,C23,
     +              C24, C25, C26, C31, C32, C33, C34, C35, C36,
     +              C41, C42, C43, C44, C45, C46, C51, C52, C53,
     +              C54, C55, C56, C61, C62, C63, C64, C65, C66,
     +              density,A3,A3_0,B3,B3_0,rval,cval


     INTEGER i,j,h,t,ns,nn,na,n,kmax,component,two_nn,two_ns,two_na,
     +     two_n

     two_ns=2*ns
     two_nn=2*nn
     two_na=2*na
     two_n=2*n

     WRITE(6,*)'BEGIN INVERSE LAPLACE'
     WRITE(17,*)'BEGIN INVERSE LAPLACE'


     IF (component.eq.1) THEN

        WRITE(6,*)'COMPONENT=1'
        WRITE(17,*)'COMPONENT=1'


C    FOR TIME LESS THAN ZERO, THE ARRAY IS SET TO ZERO

        DO t=1,two_n

           time=(t-n-1)*dt

           IF (time.LE.0.) THEN

              DO i=1,two_ns
                 DO j=1,two_nn
                    DO h=1,two_na

                       array(i,j,h,t)=0.0
```

336

```
                    ENDDO
                ENDDO
            ENDDO

        ELSE

            WRITE(6,*)'time=',time

            DO i= 1,two_ns
                DO j= 1,two_nn
                    DO h= 1,two_na


                    CALL CALC1(C11,C12,C13,C14,C15,C16,C21,C22,C23,
        +                   C24, C25, C26, C31, C32, C33, C34, C35, C36,
        +                   C41, C42, C43, C44, C45, C46, C51, C52, C53,
        +                   C54, C55, C56, C61, C62, C63, C64, C65, C66,
        +                   density,ds,dn,da,ns,nn,na,Q1,Q2,Q3,c,w,i,j,h,0,
        +                   A3_0,B3_0)

                    temp=0.

                    sum=0.

                    DO k=1,kmax

                    CALL CALC1(C11,C12,C13,C14,C15,C16,C21,C22,C23,
        +                   C24, C25, C26, C31, C32, C33, C34, C35, C36,
        +                   C41, C42, C43, C44, C45, C46, C51, C52, C53,
        +                   C54, C55, C56, C61, C62, C63, C64, C65, C66,
        +                   density,ds,dn,da,ns,nn,na,Q1,Q2,Q3,c,w,i,j,h,
        +                   k,A3,B3)


                    temp =(A3 * COS(k*w*time)) -
        +                   (B3 * SIN(k*w*time))

                    sum=temp+sum

                    ENDDO

                    array(i,j,h,t) =
        +               DSQRT(DBLE(2.0))*w*DEXP(c*time)/
        +               DSQRT(PI)*(A3_0/2+sum)

                    rval=REAL(array(i,j,h,t))
                    cval=AIMAG(array(i,j,h,t))
```

337

```
                    WRITE(54,*)rval
                    WRITE(57,*)cval


                ENDDO
            ENDDO
        ENDDO


        ENDIF


    ENDDO


    ELSEIF (component.eq.2) THEN


        WRITE(6,*)'COMPONENT=2'
        WRITE(17,*)'COMPONENT=2'


        DO t=1,two_n

            time=(t-n-1)*dt

C    FOR TIME LESS THAN ZERO, THE ARRAY IS SET TO ZERO

            IF (time.LE.0.) THEN

                DO i=1,two_ns
                    DO j=1,two_nn
                        DO h=1,two_na

                            array(i,j,h,t)=0.0

                        ENDDO
                    ENDDO
                ENDDO

            ELSE

                WRITE(6,*)'time=',time

                DO i=1,two_ns
                    DO j=1,two_nn
                        DO h=1,two_na


                CALL CALC2(C11,C12,C13,C14,C15,C16,C21,C22,C23,
    +               C24, C25, C26, C31, C32, C33, C34, C35, C36,
```

338

```fortran
     +          C41, C42, C43, C44, C45, C46, C51, C52, C53,
     +          C54, C55, C56, C61, C62, C63, C64, C65, C66,
     +          density,ds,dn,da,ns,nn,na,Q1,Q2,Q3,c,w,i,j,h,0,
     +          A3_0,B3_0)

          temp=0.

          sum=0.

          DO k=1,kmax

          CALL CALC2(C11,C12,C13,C14,C15,C16,C21,C22,C23,
     +          C24, C25, C26, C31, C32, C33, C34, C35, C36,
     +          C41, C42, C43, C44, C45, C46, C51, C52, C53,
     +          C54, C55, C56, C61, C62, C63, C64, C65, C66,
     +          density,ds,dn,da,ns,nn,na,Q1,Q2,Q3,c,w,i,j,h,
     +          k,A3,B3)


          temp =(A3 * COS(k*w*time)) -
     +          (B3 * SIN(k*w*time))

          sum=temp+sum

      ENDDO

          array(i,j,h,t) =
     +          DSQRT(DBLE(2.0))*w*DEXP(c*time)/
     +          DSQRT(PI)*(A3_0/2+sum)

          rval=REAL(array(i,j,h,t))
          cval=AIMAG(array(i,j,h,t))

          WRITE(55,*)rval
          WRITE(58,*)cval

        ENDDO
       ENDDO
      ENDDO

     ENDIF

    ENDDO

   ELSE

      WRITE(6,*)'COMPONENT=3'
      WRITE(17,*)'COMPONENT=3'
```

339

```
        DO t=1,two_n

            time=(t-n-1)*dt

C    FOR TIME LESS THAN ZERO, THE ARRAY IS SET TO ZERO

            IF (time.LE.0.) THEN

                DO i=1,two_ns
                    DO j=1,two_nn
                        DO h=1,two_na

                            array(i,j,h,t)=0.0

                        ENDDO
                    ENDDO
                ENDDO

            ELSE

                WRITE(6,*)'time=',time

                DO i=1,two_ns
                    DO j=1,two_nn
                        DO h=1,two_na


                    CALL CALC3(C11,C12,C13,C14,C15,C16,C21,C22,C23,
     +                  C24, C25, C26, C31, C32, C33, C34, C35, C36,
     +                  C41, C42, C43, C44, C45, C46, C51, C52, C53,
     +                  C54, C55, C56, C61, C62, C63, C64, C65, C66,
     +                  density,ds,dn,da,ns,nn,na,Q1,Q2,Q3,c,w,i,j,h,0,
     +                  A3_0,B3_0)

                    temp=0.

                    sum=0.

                    DO k=1,kmax

                    CALL CALC3(C11,C12,C13,C14,C15,C16,C21,C22,C23,
     +                  C24, C25, C26, C31, C32, C33, C34, C35, C36,
     +                  C41, C42, C43, C44, C45, C46, C51, C52, C53,
     +                  C54, C55, C56, C61, C62, C63, C64, C65, C66,
     +                  density,ds,dn,da,ns,nn,na,Q1,Q2,Q3,c,w,i,j,h,
     +                  k,A3,B3)
```

340

```
                        temp =(A3 * COS(k*w*time)) -
        +                       (B3 * SIN(k*w*time))


                        sum=temp+sum

                    ENDDO


                    array(i,j,h,t) =
        +               DSQRT(DBLE(2.0))*w*DEXP(c*time)/
        +                    DSQRT(PI)*(A3_0/2+sum)


                    rval=REAL(array(i,j,h,t))
                    cval=AIMAG(array(i,j,h,t))

c                       WRITE(56,*)rval
c                       WRITE(59,*)cval


                ENDDO
              ENDDO
            ENDDO
          ENDIF
        ENDDO
      ENDIF


      WRITE(6,*)'DONE COMPUTING NUMERICAL INVERSE LAPLACE'
      WRITE(17,*)'DONE COMPUTING NUMERICAL INVERSE LAPLACE'
      WRITE(17,*)'c, w, PI',c,w,PI

      RETURN

      END
ccccccccccccccccccccccccccccccccccccccccccccccccccccccccccccccccccc

      SUBROUTINE EXACT(ns,nn,na,nt,dt,ds,dn,da,Q1,Q2,Q3,
        +                C11,C44,C12,density,array)

C     USES EXACT INVERSE LAPLACE TRANSFORM AND COMPUTES THE
C     Z-COMPONENT DISPLACEMENT

      PARAMETER(nxmax=17,nzmax=257,ntmax=257)

      COMPLEX array(nxmax,nxmax,nzmax,ntmax)

      REAL*8 dt,w,c,Q1,Q2,Q3,ds,dn,da,time,
        +                C11,C12, C44,
```

341

```
     +                    density,epsilonx,
     +        epsilony,epsilonz,R,Ct,s,n,a

     INTEGER i,j,h,t,ns,nn,na,nt,two_ns,two_nn,two_na,two_nt

     WRITE(6,*)'BEGIN EXACT'
     WRITE(17,*)'BEGIN EXACT'

     two_ns=2*ns
     two_nn=2*nn
     two_na=2*na
     two_nt=2*nt

     epsilonx = 0.00001
     epsilony = 0.00001
     epsilonz = 0.00001

     Cl=DSQRT(C11/density)
     Ct=DSQRT(C44/density)
     R=Cl/Ct

     WRITE(6,*)'cl,ct',Cl,Ct
     WRITE(17,*)'cl,ct',Cl,Ct

     DO t=1,two_nt

        time=(t-nt-1)*dt

C    FOR TIME LESS THAN ZERO, THE ARRAY IS SET TO ZERO

        IF (time.LE.0.) THEN

           DO i=1,two_ns
              DO j=1,two_nn
                 DO h=1,two_na

                    array(i,j,h,t)=0.0

                 ENDDO
              ENDDO
           ENDDO

        ELSE

           WRITE(6,*)'TIME',time

           DO i=1,two_ns
              DO j=1,two_nn
```

342

```fortran
                 DO h=1,two_na

                 s=DBLE((i-ns-1+epsilonx))*ds
                 n=DBLE((j-nn-1+epsilony))*dn
                 a=DBLE((h-na-1+epsilonz))*da

                 array(i,j,h,t)=  (-(R*(a*(n*Q2 + Q1*s)
     +                  - Q3*(n**2 + s**2))*
     +                  DSIN(Ct*DSQRT(a**2 + n**2 + s**2)*time)) +
     +                  a*(n*Q2 + a*Q3 + Q1*s)*
     +                  DSIN(Ct*R*DSQRT(a**2 + n**2 + s**2)*time))/
     +                  (Ct*R*(a**2 + n**2 + s**2)**1.5)


             ENDDO
           ENDDO
         ENDDO
       ENDIF
     ENDDO



       WRITE(6,*)'DONE COMPUTING INVERSE LAPLACE'

       RETURN

       END

c cccccccccccccccccccccccccccccccccccccccccccccccccccccccccccccccccccccccc

       SUBROUTINE GAUSSIAN(ns,nn,na,n,dt,ds,dn,da,PI,
     +     nx,ny,nz,dx,dy,dz,array)

c    SUBROUTINE TO TEST INVERSE FOURIER.  COMPUTES VALUES FOR
c    1/8*EXP[-(u^2+v^2+w^2)/(16 PI)] WHICH IS THE INVERSE TRANSFORM
c    OF EXP[-PI(x^2/a^2+y^2/b^2+z^2/c^2)] WITH a=b=c=1/2

       PARAMETER(nxmax=17,nzmax=257,ntmax=257)

       COMPLEX array(nxmax,nxmax,nzmax,ntmax)

       REAL*8 PI,ds,dn,da,time,dt,x,y,z,arg,temp,dx,dy,dz

       INTEGER i,j,h,t,ns,nn,na,nx,ny,nz,two_ns,two_nn,two_na

       dx=.2
       dy=.2
```

343

```
dz=.2

ds=PI/(nx*dx)
dn=PI/(ny*dy)
da=PI/(nz*dz)

two_ns=2*ns
two_nn=2*nn
two_na=2*na

WRITE(6,*)'BEGIN GAUSSIAN'
WRITE(6,*)'nx,ny,nz,dx,dy,dz,ds'
WRITE(6,*)nx,ny,nz,dx,dy,dz,ds
WRITE(6,*)'dn,da,ns,nn,na,n'
WRITE(6,*)dn,da,ns,nn,na,n

WRITE(17,*)'BEGIN GAUSSIAN'
WRITE(17,*)'nx,ny,nz,dx,dy,dz,ds'
WRITE(17,*)nx,ny,nz,dx,dy,dz,ds
WRITE(17,*)'dn,da,ns,nn,na,n'
WRITE(17,*)dn,da,ns,nn,na,n


DO t=1,n

    time=(t-1)*dt

    DO i=1,two_ns
        DO j=1,two_nn
            DO h=1,two_na

                x=(i-ns-1)*ds
                y=(j-nn-1)*dn
                z=(h-na-1)*da

                arg=-(x**(2)/(16*PI)+
+                            y**(2)/(16*PI)+z**(2)/(16*PI))
                array(i,j,h,t)=1/8.*EXP(arg)

            ENDDO
        ENDDO
    ENDDO
ENDDO



WRITE(6,*)'DONE COMPUTING GAUSSIAN'
WRITE(17,*)'DONE COMPUTING GAUSSIAN'
```

344

```
          RETURN

          END

CCCCCCCCCCCCCCCCCCCCCCCCCCCCCCCCCCCCCCCCCCCCCCCCCCCCCCCCCCCCCCCCCC

          SUBROUTINE SUPERGAUSS(ns,nn,na,n,dx,dy,dz,array)

C     MULTIPLIES ARRAY IN BY SUPERGAUSSIAN WINDOW EXP(-ABS(t/A)^N) IN
C     THREE DIMENSIONS WITH REDUCTION OF 1000 DESCRIBED IN WEAVER P.287

          PARAMETER(nxmax=17,nzmax=257,ntmax=257)

          COMPLEX array(nxmax,nxmax,nzmax,ntmax)

          REAL*8 TT,AA,exponent,dx,dy,dz,x,y,z,arg1,arg2,arg3

          INTEGER bins,i,j,h,t,ns,nn,na,two_ns,two_nn,two_na

          two_ns=2*ns
          two_nn=2*nn
          two_na=2*na

          WRITE(6,*)'dx,dy,dz',dx,dy,dz
          WRITE(6,*)'ns,nn,na,t',ns,nn,na,n

          WRITE(6,*)'ENTER NUMBER OF BINS FROM EDGE TO CUT OFF'
          READ(5,*)bins

          WRITE(6,*)'ENTER EXPONENT, N'
          READ(5,*)exponent

          TT=(ns-bins)*dx

          AA=TT*(0.1448**(1/exponent))

          WRITE(6,*)'T, N, A',TT,exponent,AA
          WRITE(17,*)'T, N, A',TT,exponent,AA

          DO t=1,n
             DO i=1,two_ns
                DO j=1,two_nn
                   DO h=1,two_na

                      x=(i-ns-1)*dx
                      y=(j-nn-1)*dy
                      z=(h-na-1)*dz
```

345

```
                    arg1=-ABS(x/AA)**exponent
                    arg2=-ABS(y/AA)**exponent
                    arg3=-ABS(z/AA)**exponent


                array(i,j,h,t)=array(i,j,h,t)*
    +               EXP(arg1)*EXP(arg2)*EXP(arg3)


            ENDDO
          ENDDO
        ENDDO
      ENDDO


      WRITE(6,*)'DONE MULTIPLYING BY SUPER GAUSSIAN'
      WRITE(17,*)'DONE MULTIPLPYING BY SUPER GAUSSIAN'

      RETURN

      END


cccccccccccccccccccccccccccccccccccccccccccccccccccccccccccccccc

      SUBROUTINE CALC1(C11,C12,C13,C14,C15,C16,C21,C22,C23,
    +     C24,C25,C26,C31,C32,C33,C34,C35,C36,
    +     C41,C42,C43,C44,C45,C46,C51,C52,C53,
    +     C54,C55,C56,C61,C62,C63,C64,C65,C66,
    +     density,ds,dn,da,ns,nn,na,Q1,Q2,Q3,c,v,i,j,
    +     h,k,A3,B3)

C     COMPUTES THE REAL AND IMAGINARY VALUE OF X-COMPONENT

      INTEGER i,j,h,k,ns,nn,na
      COMPLEX temp
      REAL*8 A3,B3,ds,dn,da,s,n,a,Q1,Q2,Q3,c,v

      REAL*8  C11, C12, C13, C14, C15, C16, C21, C22, C23,
    +     C24, C25, C26, C31, C32, C33, C34, C35, C36,
    +     C41, C42, C43, C44, C45, C46, C51, C52, C53,
    +     C54, C55, C56, C61, C62, C63, C64, C65, C66, density


      s=(i-ns-1)*ds
      n=(j-nn-1)*dn
      a=(h-na-1)*da

      temp=(0.,0.)
```

346

```
temp= -(Q1/
-        (-(a**2*C55) - 2*a*C56*n - C66*n**2 -
-        2*a*C15*s - 2*C16*n*s - C11*s**2 -
-        density*(c + (0.1)*k*w)**2)) -
- ((-(a**2*C35) - a*(C36 + C45)*n - C46*n**2 -
-        a*(C13 + C55)*s - (C14 + C56)*n*s -
-        C15*s**2)*
-        (-((Q1*(-(a**2*C45) - a*(C25 + C46)*n -
-                C26*n**2 - a*(C14 + C56)*s -
-                (C12 + C66)*n*s - C16*s**2) -
-                Q2*(-(a**2*C55) - 2*a*C56*n -
-                C66*n**2 - 2*a*C15*s -
-                2*C16*n*s - C11*s**2 -
-                density*(c + (0.1)*k*w)**2)
-        )*(-((-(a**2*C35) -
-                a*(C36 + C45)*n - C46*n**2 -
-                a*(C13 + C55)*s -
-                (C14 + C56)*n*s - C15*s**2)*
-                (-(a**2*C45) - a*(C25 + C46)*n -
-                C26*n**2 - a*(C14 + C56)*s -
-                (C12 + C66)*n*s - C16*s**2)) +
-        (-(a**2*C34) - a*(C23 + C44)*n -
-                C24*n**2 - a*(C36 + C45)*s -
-                (C25 + C46)*n*s - C56*s**2)*
-                (-(a**2*C55) - 2*a*C56*n -
-                C66*n**2 - 2*a*C15*s -
-                2*C16*n*s - C11*s**2 -
-                density*(c + (0.1)*k*w)**2)
-        )) +
-        (Q1*(-(a**2*C35) - a*(C36 + C45)*n -
-                C46*n**2 - a*(C13 + C55)*s -
-                (C14 + C56)*n*s - C15*s**2) -
-                Q3*(-(a**2*C55) - 2*a*C56*n -
-                C66*n**2 - 2*a*C15*s - 2*C16*n*s -
-                C11*s**2 -
-                density*(c + (0.1)*k*w)**2))*
-        (-(-(a**2*C45) - a*(C25 + C46)*n -
-                C26*n**2 - a*(C14 + C56)*s -
-                (C12 + C66)*n*s - C16*s**2)**2 +
-        (-(a**2*C55) - 2*a*C56*n - C66*n**2 -
-                2*a*C15*s - 2*C16*n*s - C11*s**2 -
-                density*(c + (0.1)*k*w)**2)*
-        (-(a**2*C44) - 2*a*C24*n -
-                C22*n**2 - 2*a*C46*s - 2*C26*n*s -
-                C66*s**2 -
-                density*(c + (0.1)*k*w)**2)))
```

347

```
-     )/
-     ((-(a**2*C55) - 2*a*C56*n - C66*n**2 -
-         2*a*C15*s - 2*C16*n*s - C11*s**2 -
-         density*(c + (0,1)*k*w)**2)*
-       (-(-((-(a**2*C35) - a*(C36 + C45)*n -
-               C46*n**2 - a*(C13 + C55)*s -
-               (C14 + C56)*n*s - C15*s**2)*
-             (-(a**2*C45) - a*(C25 + C46)*n -
-               C26*n**2 - a*(C14 + C56)*s -
-               (C12 + C66)*n*s - C16*s**2)) +
-           (-(a**2*C34) - a*(C23 + C44)*n -
-             C24*n**2 - a*(C36 + C45)*s -
-             (C25 + C46)*n*s - C56*s**2)*
-           (-(a**2*C55) - 2*a*C56*n -
-             C66*n**2 - 2*a*C15*s -
-             2*C16*n*s - C11*s**2 -
-             density*(c + (0,1)*k*w)**2))
-         **2 +
-       (-(-(a**2*C35) - a*(C36 + C45)*n -
-             C46*n**2 - a*(C13 + C55)*s -
-             (C14 + C56)*n*s - C15*s**2)**2 +
-         (-(a**2*C55) - 2*a*C56*n - C66*n**2 -
-           2*a*C15*s - 2*C16*n*s - C11*s**2 -
-           density*(c + (0,1)*k*w)**2)*
-         (-(a**2*C33) - 2*a*C34*n -
-           C44*n**2 - 2*a*C35*s - 2*C45*n*s -
-           C55*s**2 -
-           density*(c + (0,1)*k*w)**2))*
-       (-(-(a**2*C45) - a*(C25 + C46)*n -
-             C26*n**2 - a*(C14 + C56)*s -
-             (C12 + C66)*n*s - C16*s**2)**2 +
-         (-(a**2*C55) - 2*a*C56*n - C66*n**2 -
-           2*a*C15*s - 2*C16*n*s - C11*s**2 -
-           density*(c + (0,1)*k*w)**2)*
-         (-(a**2*C44) - 2*a*C24*n -
-           C22*n**2 - 2*a*C46*s - 2*C26*n*s -
-           C66*s**2 -
-           density*(c + (0,1)*k*w)**2)))
-     ) - ((-(a**2*C45) - a*(C25 + C46)*n -
-       C26*n**2 - a*(C14 + C56)*s -
-       (C12 + C66)*n*s - C16*s**2)*
-     ((Q1*(-(a**2*C45) - a*(C25 + C46)*n -
-             C26*n**2 - a*(C14 + C56)*s -
-             (C12 + C66)*n*s - C16*s**2) -
-         Q2*(-(a**2*C55) - 2*a*C56*n -
-             C66*n**2 - 2*a*C15*s - 2*C16*n*s -
-             C11*s**2 -
-             density*(c + (0,1)*k*w)**2))/
```

348

```
-        (-(-(a**2*C45) - a*(C25 + C46)*n -
-           C26*n**2 - a*(C14 + C56)*s -
-           (C12 + C66)*n*s - C16*s**2)**2 +
-        (-(a**2*C55) - 2*a*C56*n - C66*n**2 -
-           2*a*C15*s - 2*C16*n*s - C11*s**2 -
-           density*(c + (0,1)*k*w)**2)*
-        (-(a**2*C44) - 2*a*C24*n -
-           C22*n**2 - 2*a*C46*s - 2*C26*n*s -
-           C66*s**2 -
-           density*(c + (0,1)*k*w)**2))
-        - ((-((-(a**2*C35) - a*(C36 + C45)*n -
-              C46*n**2 - a*(C13 + C55)*s -
-              (C14 + C56)*n*s - C15*s**2)*
-           (-(a**2*C45) - a*(C25 + C46)*n -
-              C26*n**2 - a*(C14 + C56)*s -
-              (C12 + C66)*n*s - C16*s**2)) +
-        (-(a**2*C34) - a*(C23 + C44)*n -
-           C24*n**2 - a*(C36 + C45)*s -
-           (C25 + C46)*n*s - C56*s**2)*
-        (-(a**2*C55) - 2*a*C56*n -
-           C66*n**2 - 2*a*C15*s -
-           2*C16*n*s - C11*s**2 -
-           density*(c + (0,1)*k*w)**2)
-        )*(-((Q1*
-              (-(a**2*C45) -
-               a*(C25 + C46)*n - C26*n**2 -
-               a*(C14 + C56)*s -
-               (C12 + C66)*n*s - C16*s**2)
-               - Q2*
-              (-(a**2*C55) - 2*a*C56*n -
-               C66*n**2 - 2*a*C15*s -
-               2*C16*n*s - C11*s**2 -
-               density*
-               (c + (0,1)*k*w)**2))*
-        (-((-(a**2*C35) -
-               a*(C36 + C45)*n - C46*n**2 -
-               a*(C13 + C55)*s -
-               (C14 + C56)*n*s - C15*s**2)*
-            (-(a**2*C45) -
-               a*(C25 + C46)*n - C26*n**2 -
-               a*(C14 + C56)*s -
-               (C12 + C66)*n*s - C16*s**2))
-            + (-(a**2*C34) -
-               a*(C23 + C44)*n - C24*n**2 -
-               a*(C36 + C45)*s -
-               (C25 + C46)*n*s - C56*s**2)*
-            (-(a**2*C55) - 2*a*C56*n -
-               C66*n**2 - 2*a*C15*s -
```

```
-           2*C16*n*s - C11*s**2 -
-           density*
-           (c + (0,1)*k*w)**2)))
-       + (Q1*
-         (-(a**2*C35) -
-           a*(C36 + C45)*n - C46*n**2 -
-           a*(C13 + C55)*s -
-           (C14 + C56)*n*s - C15*s**2) -
-         Q3*
-         (-(a**2*C55) - 2*a*C56*n -
-           C66*n**2 - 2*a*C15*s -
-           2*C16*n*s - C11*s**2 -
-           density*
-           (c + (0,1)*k*w)**2))*
-       (-(-(a**2*C45) - a*(C25 + C46)*n -
-           C26*n**2 - a*(C14 + C56)*s -
-           (C12 + C66)*n*s - C16*s**2)**
-         2 +
-         (-(a**2*C55) - 2*a*C56*n -
-           C66*n**2 - 2*a*C15*s -
-           2*C16*n*s - C11*s**2 -
-           density*
-           (c + (0,1)*k*w)**2)*
-         (-(a**2*C44) - 2*a*C24*n -
-           C22*n**2 - 2*a*C46*s -
-           2*C26*n*s - C66*s**2 -
-           density*
-           (c + (0,1)*k*w)**2)))}
-     /((-(-(a**2*C45) - a*(C25 + C46)*n -
-           C26*n**2 - a*(C14 + C56)*s -
-           (C12 + C66)*n*s - C16*s**2)**2
-       + (-(a**2*C55) - 2*a*C56*n -
-           C66*n**2 - 2*a*C15*s -
-           2*C16*n*s - C11*s**2 -
-           density*(c + (0,1)*k*w)**2)
-         *(-(a**2*C44) - 2*a*C24*n -
-           C22*n**2 - 2*a*C46*s -
-           2*C26*n*s - C66*s**2 -
-           density*(c + (0,1)*k*w)**2)
-       )*(-(-((-(a**2*C35) -
-               a*(C36 + C45)*n - C46*n**2 -
-               a*(C13 + C55)*s -
-               (C14 + C56)*n*s - C15*s**2)*
-             (-(a**2*C45) -
-               a*(C25 + C46)*n - C26*n**2 -
-               a*(C14 + C56)*s -
-               (C12 + C66)*n*s - C16*s**2))
-           + (-(a**2*C34) -
```

350

```
-            a*(C23 + C44)*n - C24*n**2 -
-            a*(C36 + C45)*s -
-            (C25 + C46)*n*s - C56*s**2)*
-            (-(a**2*C55) - 2*a*C56*n -
-            C66*n**2 - 2*a*C15*s -
-            2*C16*n*s - C11*s**2 -
-            density*
-            (c + (0,1)*k*w)**2))**
-        2 +
-        (-(-(a**2*C35) - a*(C36 + C45)*n -
-            C46*n**2 - a*(C13 + C55)*s -
-            (C14 + C56)*n*s - C15*s**2)**
-            2 +
-            (-(a**2*C55) - 2*a*C56*n -
-            C66*n**2 - 2*a*C15*s -
-            2*C16*n*s - C11*s**2 -
-            density*
-            (c + (0,1)*k*w)**2)*
-            (-(a**2*C33) - 2*a*C34*n -
-            C44*n**2 - 2*a*C35*s -
-            2*C45*n*s - C55*s**2 -
-            density*
-            (c + (0,1)*k*w)**2))*
-        (-(-(a**2*C45) - a*(C25 + C46)*n -
-            C26*n**2 - a*(C14 + C56)*s -
-            (C12 + C66)*n*s - C16*s**2)**
-            2 +
-            (-(a**2*C55) - 2*a*C56*n -
-            C66*n**2 - 2*a*C15*s -
-            2*C16*n*s - C11*s**2 -
-            density*
-            (c + (0,1)*k*w)**2)*
-            (-(a**2*C44) - 2*a*C24*n -
-            C22*n**2 - 2*a*C46*s -
-            2*C26*n*s - C66*s**2 -
-            density*
-            (c + (0,1)*k*w)**2))))
-        ))/
-    (-(a**2*C55) - 2*a*C56*n - C66*n**2 -
-        2*a*C15*s - 2*C16*n*s - C11*s**2 -
-        density*(c + (0,1)*k*w)**2)

        A3=REAL(temp)
        B3=AIMAG(temp)


        RETURN
```

351

```
                END
CCCCCCCCCCCCCCCCCCCCCCCCCCCCCCCCCCCCCCCCCCCCCCCCCCCCCCCCCCCCCCCCCCCC


        SUBROUTINE CALC2(C11,C12,C13,C14,C15,C16,C21,C22,C23,
     +      C24,C25,C26,C31,C32,C33,C34,C35,C36,
     +      C41,C42,C43,C44,C45,C46,C51,C52,C53,
     +      C54,C55,C56,C61,C62,C63,C64,C65,C66,
     +      density,ds,dn,da,ns,nn,na,Q1,Q2,Q3,c,v,i,j,
     +      h,k,A3,B3)


C    COMPUTES THE REAL AND IMAGINARY VALUE OF Y-COMPONENT


        INTEGER i,j,h,k,ns,nn,na
        COMPLEX temp
        REAL*8 A3,B3,ds,dn,da,s,n,a,Q1,Q2,Q3,c,v


        REAL*8  C11, C12, C13, C14, C15, C16, C21, C22, C23,
     +      C24, C25, C26, C31, C32, C33, C34, C35, C36,
     +      C41, C42, C43, C44, C45, C46, C51, C52, C53,
     +      C54, C55, C56, C61, C62, C63, C64, C65, C66, density



        s=(i-ns-1)*ds
        n=(j-nn-1)*dn
        a=(h-na-1)*da


        temp=(0.,0.)



        temp=(Q1*(-(a**2*C45) - a*(C25 + C46)*n -
     -          C26*n**2 - a*(C14 + C56)*s -
     -          (C12 + C66)*n*s - C16*s**2) -
     -          Q2*(-(a**2*C55) - 2*a*C56*n - C66*n**2 -
     -          2*a*C15*s - 2*C16*n*s - C11*s**2 -
     -          density*(c + (0,1)*k*v)**2))/
     -      (-(-(a**2*C45) - a*(C25 + C46)*n -
     -          C26*n**2 - a*(C14 + C56)*s -
     -          (C12 + C66)*n*s - C16*s**2)**2 +
     -      (-(a**2*C55) - 2*a*C56*n - C66*n**2 -
     -          2*a*C15*s - 2*C16*n*s - C11*s**2 -
     -          density*(c + (0,1)*k*v)**2)*
     -      (-(a**2*C44) - 2*a*C24*n - C22*n**2 -
     -          2*a*C46*s - 2*C26*n*s - C66*s**2 -
     -          density*(c + (0,1)*k*v)**2)) -
     -      ((-((-(a**2*C35) - a*(C36 + C45)*n -
     -              C46*n**2 - a*(C13 + C55)*s -
     -              (C14 + C56)*n*s - C15*s**2)*
     -              (-(a**2*C45) - a*(C25 + C46)*n -
```

                                                    352
```

```
-          C26•n••2 - a•(C14 + C56)•s -
-          (C12 + C66)•n•s - C16•s••2)) +
-       (-(a••2•C34) - a•(C23 + C44)•n -
-          C24•n••2 - a•(C36 + C45)•s -
-          (C25 + C46)•n•s - C56•s••2)•
-       (-(a••2•C55) - 2•a•C56•n - C66•n••2 -
-          2•a•C15•s - 2•C16•n•s - C11•s••2 -
-          density•(c + (0,1)•k•u)••2))•
-    (-((Q1•(-(a••2•C45) - a•(C25 + C46)•n -
-             C26•n••2 - a•(C14 + C56)•s -
-             (C12 + C66)•n•s - C16•s••2) -
-          Q2•(-(a••2•C55) - 2•a•C56•n -
-             C66•n••2 - 2•a•C15•s -
-             2•C16•n•s - C11•s••2 -
-             density•(c + (0,1)•k•u)••2)
-          )•(-((-(a••2•C35) -
-                a•(C36 + C45)•n - C46•n••2 -
-                a•(C13 + C55)•s -
-                (C14 + C56)•n•s - C15•s••2)•
-             (-(a••2•C45) - a•(C25 + C46)•n -
-                C26•n••2 - a•(C14 + C56)•s -
-                (C12 + C66)•n•s - C16•s••2)) +
-             (-(a••2•C34) - a•(C23 + C44)•n -
-                C24•n••2 - a•(C36 + C45)•s -
-                (C25 + C46)•n•s - C56•s••2)•
-             (-(a••2•C55) - 2•a•C56•n -
-                C66•n••2 - 2•a•C15•s -
-                2•C16•n•s - C11•s••2 -
-                density•(c + (0,1)•k•u)••2)
-          )) +
-       (Q1•(-(a••2•C35) - a•(C36 + C45)•n -
-             C46•n••2 - a•(C13 + C55)•s -
-             (C14 + C56)•n•s - C15•s••2) -
-          Q3•(-(a••2•C55) - 2•a•C56•n -
-             C66•n••2 - 2•a•C15•s - 2•C16•n•s -
-             C11•s••2 -
-             density•(c + (0,1)•k•u)••2)•
-          (-(-(a••2•C45) - a•(C25 + C46)•n -
-             C26•n••2 - a•(C14 + C56)•s -
-             (C12 + C66)•n•s - C16•s••2)••2 +
-          (-(a••2•C55) - 2•a•C56•n - C66•n••2 -
-             2•a•C15•s - 2•C16•n•s - C11•s••2 -
-             density•(c + (0,1)•k•u)••2)•
-          (-(a••2•C44) - 2•a•C24•n -
-             C22•n••2 - 2•a•C46•s - 2•C26•n•s -
-             C66•s••2 -
-             density•(c + (0,1)•k•u)••2)))
-    )/
```

353

```
-       ((-(-(a**2*C45) - a*(C25 + C46)*n -
-               C26*n**2 - a*(C14 + C56)*s -
-               (C12 + C66)*n*s - C16*s**2)**2 +
-           (-(a**2*C55) - 2*a*C56*n - C66*n**2 -
-               2*a*C15*s - 2*C16*n*s - C11*s**2 -
-               density*(c + (0,1)*k*w)**2)*
-           (-(a**2*C44) - 2*a*C24*n - C22*n**2 -
-               2*a*C46*s - 2*C26*n*s - C66*s**2 -
-               density*(c + (0,1)*k*w)**2))*
-       (-(-((-(a**2*C35) - a*(C36 + C45)*n -
-               C46*n**2 - a*(C13 + C55)*s -
-               (C14 + C56)*n*s - C15*s**2)*
-           (-(a**2*C45) - a*(C25 + C46)*n -
-               C26*n**2 - a*(C14 + C56)*s -
-               (C12 + C66)*n*s - C16*s**2)) +
-           (-(a**2*C34) - a*(C23 + C44)*n -
-               C24*n**2 - a*(C36 + C45)*s -
-               (C25 + C46)*n*s - C56*s**2)*
-           (-(a**2*C55) - 2*a*C56*n -
-               C66*n**2 - 2*a*C15*s -
-               2*C16*n*s - C11*s**2 -
-               density*(c + (0,1)*k*w)**2))
-       **2 +
-       (-(-(a**2*C35) - a*(C36 + C45)*n -
-               C46*n**2 - a*(C13 + C55)*s -
-               (C14 + C56)*n*s - C15*s**2)**2 +
-           (-(a**2*C55) - 2*a*C56*n - C66*n**2 -
-               2*a*C15*s - 2*C16*n*s - C11*s**2 -
-               density*(c + (0,1)*k*w)**2)*
-           (-(a**2*C33) - 2*a*C34*n -
-               C44*n**2 - 2*a*C35*s - 2*C45*n*s -
-               C55*s**2 -
-               density*(c + (0,1)*k*w)**2))*
-       (-(-(a**2*C45) - a*(C25 + C46)*n -
-               C26*n**2 - a*(C14 + C56)*s -
-               (C12 + C66)*n*s - C16*s**2)**2 +
-           (-(a**2*C55) - 2*a*C56*n - C66*n**2 -
-               2*a*C15*s - 2*C16*n*s - C11*s**2 -
-               density*(c + (0,1)*k*w)**2)*
-           (-(a**2*C44) - 2*a*C24*n -
-               C22*n**2 - 2*a*C46*s - 2*C26*n*s -
-               C66*s**2 -
-               density*(c + (0,1)*k*w)**2)))
-       )
     A3=REAL(temp)
     B3=AIMAG(temp)
```

354

```
        RETURN

        END
CCCCCCCCCCCCCCCCCCCCCCCCCCCCCCCCCCCCCCCCCCCCCCCCCCCCCCCCCCCCCCCCCCCC

        SUBROUTINE CALC3(C11,C12,C13,C14,C15,C16,C21,C22,C23,
   +        C24,C25,C26,C31,C32,C33,C34,C35,C36,
   +        C41,C42,C43,C44,C45,C46,C51,C52,C53,
   +        C54,C55,C56,C61,C62,C63,C64,C65,C66,
   +        density,ds,dn,da,ns,nn,na,Q1,Q2,Q3,c,w,i,j,
   +        h,k,A3,B3)

C   COMPUTES THE REAL AND IMAGINARY VALUE OF Z-COMPONENT

        INTEGER i,j,h,k,ns,nn,na
        COMPLEX temp
        REAL*8 A3,B3,ds,dn,da,s,n,a,Q1,Q2,Q3,c,w

        REAL*8 C11, C12, C13, C14, C15, C16, C21, C22, C23,
   +        C24, C25, C26, C31, C32, C33, C34, C35, C36,
   +        C41, C42, C43, C44, C45, C46, C51, C52, C53,
   +        C54, C55, C56, C61, C62, C63, C64, C65, C66, density


        s=(i-ns-1)*ds
        n=(j-nn-1)*dn
        a=(h-na-1)*da

        temp=(0.,0.)


        temp= (-((Q1*(-(a**2*C45) - a*(C25 + C46)*n -
   -            C26*n**2 - a*(C14 + C56)*s -
   -            (C12 + C66)*n*s - C16*s**2) -
   -            Q2*(-(a**2*C55) - 2*a*C56*n -
   -            C66*n**2 - 2*a*C15*s - 2*C16*n*s -
   -            C11*s**2 -
   -            density*(c + (0,1)*k*w)**2))*
   -            (-((-(a**2*C35) - a*(C36 + C45)*n -
   -            C46*n**2 - a*(C13 + C55)*s -
   -            (C14 + C56)*n*s - C15*s**2)*
   -            (-(a**2*C45) - a*(C25 + C46)*n -
   -            C26*n**2 - a*(C14 + C56)*s -
   -            (C12 + C66)*n*s - C16*s**2)) +
   -            (-(a**2*C34) - a*(C23 + C44)*n -
   -            C24*n**2 - a*(C36 + C45)*s -
   -            (C25 + C46)*n*s - C56*s**2)*
   -            (-(a**2*C55) - 2*a*C56*n - C66*n**2 -
```

355

```
-          2*a*C15*s - 2*C16*n*s - C11*s**2 -
-          density*(c + (0,1)*k*u)**2)))
-     + (Q1*(-(a**2*C35) - a*(C36 + C45)*n -
-          C46*n**2 - a*(C13 + C55)*s -
-          (C14 + C56)*n*s - C15*s**2) -
-       Q3*(-(a**2*C55) - 2*a*C56*n - C66*n**2 -
-          2*a*C15*s - 2*C16*n*s - C11*s**2 -
-          density*(c + (0,1)*k*u)**2))*
-       (-(-(a**2*C45) - a*(C25 + C46)*n -
-          C26*n**2 - a*(C14 + C56)*s -
-          (C12 + C66)*n*s - C16*s**2)**2 +
-       (-(a**2*C55) - 2*a*C56*n - C66*n**2 -
-          2*a*C15*s - 2*C16*n*s - C11*s**2 -
-          density*(c + (0,1)*k*u)**2)*
-       (-(a**2*C44) - 2*a*C24*n - C22*n**2 -
-          2*a*C46*s - 2*C26*n*s - C66*s**2 -
-          density*(c + (0,1)*k*u)**2)))/
-  (-(-(((-(a**2*C35) - a*(C36 + C45)*n -
-            C46*n**2 - a*(C13 + C55)*s -
-            (C14 + C56)*n*s - C15*s**2)*
-          (-(a**2*C45) - a*(C25 + C46)*n -
-            C26*n**2 - a*(C14 + C56)*s -
-            (C12 + C66)*n*s - C16*s**2)) +
-        (-(a**2*C34) - a*(C23 + C44)*n -
-            C24*n**2 - a*(C36 + C45)*s -
-            (C25 + C46)*n*s - C56*s**2)*
-          (-(a**2*C55) - 2*a*C56*n - C66*n**2 -
-            2*a*C15*s - 2*C16*n*s - C11*s**2 -
-            density*(c + (0,1)*k*u)**2))**2
-     + (-(-(a**2*C35) - a*(C36 + C45)*n -
-            C46*n**2 - a*(C13 + C55)*s -
-            (C14 + C56)*n*s - C15*s**2)**2 +
-        (-(a**2*C55) - 2*a*C56*n - C66*n**2 -
-            2*a*C15*s - 2*C16*n*s - C11*s**2 -
-            density*(c + (0,1)*k*u)**2)*
-        (-(a**2*C33) - 2*a*C34*n - C44*n**2 -
-            2*a*C35*s - 2*C45*n*s - C55*s**2 -
-            density*(c + (0,1)*k*u)**2))*
-     (-(-(a**2*C45) - a*(C25 + C46)*n -
-            C26*n**2 - a*(C14 + C56)*s -
-            (C12 + C66)*n*s - C16*s**2)**2 +
-        (-(a**2*C55) - 2*a*C56*n - C66*n**2 -
-            2*a*C15*s - 2*C16*n*s - C11*s**2 -
-            density*(c + (0,1)*k*u)**2)*
-        (-(a**2*C44) - 2*a*C24*n - C22*n**2 -
-            2*a*C46*s - 2*C26*n*s - C66*s**2 -
-            density*(c + (0,1)*k*u)**2)))
   A3=REAL(temp)
```

356

```
        B3=AIMAG(temp)


        RETURN

        END

ccccccccccccccccccccccccccccccccccccccccccccccccccccccccccccccccc

        SUBROUTINE INVERSE_FOURIER_x_y_z(array,ns,nn,na,n,ds,dn,da,PI)

        PARAMETER(nxmax=17,nzmax=257,ntmax=257)

        COMPLEX array(nxmax,nxmax,nzmax,ntmax)

        REAL*8  x(nzmax), y(nzmax),ds,dn,da,PI

        INTEGER ns,nn,na,n,i,j,h,t,m,srot,nrot,arot,two_ns,
       +two_nn,two_na,two_n

        two_ns=2*ns
        two_nn=2*nn
        two_na=2*na
        two_n=2*n

C       PERFORMS INVERSE FOURIER ROUTINES TO CALCULATE THE
C       ELASTIC IMPULSE RESPONSE.

C       ROTATE LEFT nz BINS IN THE Z-DIRECTION

        WRITE(6,*)'ROTATING LEFT nz IN Z-DIRECTION'
        WRITE(17,*)'ROTATING LEFT nz IN Z-DIRECTION'

        CALL ROTATE_Z(array,two_ns,two_nn,two_na,n,na)

C       INVERSE FOURIER IN THE Z-DIRECTION

        WRITE(6,*)'INVERSE FOURIER IN Z-DIRECTION'
        WRITE(17,*)'INVERSE FOURIER IN Z-DIRECTION'


        m=INT(LOG(REAL(two_na))/LOG(2.))

        DO t=1,two_n
          DO i=1,two_ns
            DO j=1,two_nn

              CALL SEPERATE_Z(array,i,j,t,two_na,x,y)
```

357

```
C       USING 'FORWARD TRANSFORM' SFFTEU TO MATCH SIGN CONVENTION
C       OF MATHEMATICA

             CALL sffteu(x, y, two_na, m,1)
             CALL TOGETHER_Z(i,j,t,da,two_na,x,y,array,t,PI)

          ENDDO
        ENDDO
      ENDDO



      WRITE(6,*)'ROTATING LEFT nz IN Z-DIRECTION'
      WRITE(17,*)'ROTATING LEFT nz IN Z-DIRECTION'

      CALL ROTATE_Z(array,two_ns,two_nn,two_na,two_n,na)

      WRITE(6,*)'REVERSING IN Z-DIRECTION'
      WRITE(17,*)'REVERSING IN Z-DIRECTION'

      DO t=1,two_n
        DO i=1,two_ns
          DO j=1,two_nn
            CALL REVERSE_Z(array,i,j,t,na)
          ENDDO
        ENDDO
      ENDDO

C       ROTATE LEFT ny BINS IN THE Y-DIRECTION

      WRITE(6,*)'ROTATING LEFT ny IN Y-DIRECTION'
      WRITE(17,*)'ROTATING LEFT ny IN Y-DIRECTION'

      CALL ROTATE_Y(array,two_ns,two_nn,two_na,two_n,nn)



C       INVERSE FOURIER IN THE Y-DIRECTION

      WRITE(6,*)'INVERSE FOURIER IN Y-DIRECTION'
      WRITE(17,*)'INVERSE FOURIER IN Y-DIRECTION'


      m=INT(LOG(REAL(two_nn))/LOG(2.))

      DO t=1,two_n
        DO i=1,two_ns
```

358

```
                DO h=1,two_na


                   CALL SEPERATE_Y(array,i,h,t,two_nn,x,y)

C       USING 'FORWARD TRANSFORM' SFFTEU TO MATCH SIGN CONVENTION
C       OF MATHEMATICA

                   CALL sffteu( x, y, two_nn, a, 1 )
                   CALL TOGETHER_Y(i,h,t,dn,two_nn,x,y,array,1,PI)


                ENDDO
             ENDDO
          ENDDO



          WRITE(6,*)'ROTATING LEFT ny IN Y-DIRECTION'
          WRITE(17,*)'ROTATING LEFT ny IN Y-DIRECTION'


          CALL ROTATE_Y(array,two_ns,two_nn,two_na,two_n,nn)


          WRITE(6,*)'REVERSING IN Y-DIRECTION'
          WRITE(17,*)'REVERSING IN Y-DIRECTION'


          DO t=1,two_n
             DO i=1,two_ns
                DO h=1,two_na
                   CALL REVERSE_Y(array,i,h,t,nn)
                ENDDO
             ENDDO
          ENDDO


C       ROTATE LEFT nx BINS IN THE X-DIRECTION

          WRITE(6,*)'ROTATING LEFT nx IN X-DIRECTION'
          WRITE(17,*)'ROTATING LEFT nx IN X-DIRECTION'      .


          CALL ROTATE_X(array,two_ns,two_nn,two_na,two_n,ns)



C       INVERSE FOURIER IN THE x-DIRECTION

          WRITE(6,*)'INVERSE FOURIER IN x-DIRECTION'
          WRITE(17,*)'INVERSE FOURIER IN x-DIRECTION'



          m=INT(LOG(REAL(two_ns))/LOG(2.))
```

359

```
      DO t=1,two_n
         DO j=1,two_nn
            DO h=1,two_na

               CALL SEPERATE_X(array,j,h,t,two_ns,x,y)

C     USING 'FORWARD TRANSFORM' SFFTEU TO MATCH SIGN CONVENTION
C     OF MATHEMATICA

               CALL sffteu( x, y, two_ns, m, 1 )
               CALL TOGETHER_X(j,h,t,ds,two_ns,x,y,array,1,PI)

            ENDDO
         ENDDO
      ENDDO

      WRITE(6,*)'ROTATING LEFT nx IN X-DIRECTION'
      WRITE(17,*)'ROTATING LEFT nx IN X-DIRECTION'

      CALL ROTATE_X(array,two_ns,two_nn,two_na,two_n,ns)

      WRITE(6,*)'REVERSING IN X-DIRECTION'
      WRITE(17,*)'REVERSING IN X-DIRECTION'

      DO t=1,two_n
         DO j=1,two_nn
            DO h=1,two_na
               CALL REVERSE_X(array,j,h,t,ns)
            ENDDO
         ENDDO
      ENDDO

      RETURN

      END



CCCCCCCCCCCCCCCCCCCCCCCCCCCCCCCCCCCCCCCCCCCCCCCCCCCCCCCCCCCCCCCCCCC

      SUBROUTINE REVERSE_Z(array,i,j,t,n3)

      PARAMETER(nxmax=17,nzmax=257,ntmax=257)

      INTEGER i,j,h,t,n3,two_n3            -

      COMPLEX  array(nxmax,nxmax,nzmax,ntmax), temp(nzmax)
```

360

```fortran
      two_n3=2*n3

      DO h=1,two_n3

         temp(h)=array(i,j,h,t)

      ENDDO

      DO h=two_n3,1,-1

         array(i,j,h,t)=temp(h)

      ENDDO

      RETURN

      END

ccccccccccccccccccccccccccccccccccccccccccccccccccccccccccccccccccc

      SUBROUTINE REVERSE_Y(array,i,h,t,n2)

      PARAMETER(nxmax=17,nzmax=257,ntmax=257)

      INTEGER i,j,h,t,n2,two_n2

      COMPLEX  array(nxmax,nxmax,nzmax,ntmax),temp(nzmax)


      two_n2=2*n2

      DO j=1,two_n2

         temp(j)=array(i,j,h,t)

      ENDDO

      DO j=two_n2,1,-1

         array(i,j,h,t)=temp(j)

      ENDDO

      RETURN

      END
```

361

CCCCCCCCCCCCCCCCCCCCCCCCCCCCCCCCCCCCCCCCCCCCCCCCCCCCCCCCCCCCCCCCC

```fortran
      SUBROUTINE REVERSE_X(array,j,h,t,nl)

      PARAMETER(nxmax=17,nzmax=257,ntmax=257)

      INTEGER i,j,h,t,nl,two_nl

      COMPLEX array(nxmax,nxmax,nzmax,ntmax),temp(nzmax)


      two_nl=2*nl

      DO i=1,two_nl

         temp(i)=array(i,j,h,t)

      ENDDO

      DO i=two_nl,1,-1

         array(i,j,h,t)=temp(i)

      ENDDO

      RETURN

      END
```


CCCCCCCCCCCCCCCCCCCCCCCCCCCCCCCCCCCCCCCCCCCCCCCCCCCCCCCCCCCCCCCCC

```fortran
      SUBROUTINE SEPERATE_Z(array,i,j,t,n,x,y)

      PARAMETER(nxmax=17,nzmax=257,ntmax=257)

      INTEGER i,j,h,t,n

      COMPLEX array(nxmax,nxmax,nzmax,ntmax)
      REAL*8    x(nzmax), y(nzmax)

      DO h=1,n

         x(h)=REAL(array(i,j,h,t))
         y(h)=AIMAG(array(i,j,h,t))
```

362

```
      ENDDO

      RETURN

      END
cccccccccccccccccccccccccccccccccccccccccccccccccccccccccccccccccccc

      SUBROUTINE TOGETHER_Z(i,j,t,da,n,x,y,array,sign,PI)

C     SETUP SO THAT WHEN YOU CALL THE INVERSE SFFTEU YOU GET THE
C     FORWARD TRANSFORM AND VISE VERSA

C     SIGN=0->SQRT(n)*(SQRT(n))*da*FOURIER
C     SIGN=1->SQRT(n)*(1/SQRT(n))*da*INVERSEFOURIER

      PARAMETER(nxmax=17,nzmax=257,ntmax=257)

      INTEGER i,j,h,t,n,sign

      COMPLEX  array(nxmax,nxmax,nzmax,ntmax)
      REAL*8   x(nzmax), y(nzmax), da,PI


      IF (sign.EQ.0) THEN

      DO h=1,n

        array(i,j,h,t)=1/(2*PI)*n*da*CMPLX(x(h),
     +        y(h))


      ENDDO

      ELSE

        DO h=1,n

          array(i,j,h,t)=1/(2*PI)*da*CMPLX(x(h),
     +          y(h))

        ENDDO

      ENDIF

      RETURN

      END
```

363

```
ccccccccccccccccccccccccccccccccccccccccccccccccccccccccccccccccc

      SUBROUTINE SEPERATE_Y(array,i,h,t,n,x,y)

      PARAMETER(nxmax=17,nzmax=257,ntmax=257)

      INTEGER i,j,h,t,n

      COMPLEX  array(nxmax,nxmax,nzmax,ntmax)
      REAL*8   x(nzmax), y(nzmax)

      DO j=1,n

         x(j)=REAL(array(i,j,h,t))
         y(j)=AIMAG(array(i,j,h,t))

      ENDDO

      RETURN

      END


ccccccccccccccccccccccccccccccccccccccccccccccccccccccccccccccccc

      SUBROUTINE TOGETHER_Y(i,h,t,dn,n,x,y,array,sign,PI)


C     SETUP SO THAT WHEN YOU CALL THE INVERSE SFFTEU YOU GET THE
C     FORWARD TRANSFORM AND VISE VERSA

C     SIGN=0->SQRT(n)*(SQRT(n))*da*FOURIER
C     SIGN=1->SQRT(n)*(1/SQRT(n))*da*INVERSEFOURIER


      PARAMETER(nxmax=17,nzmax=257,ntmax=257)

      INTEGER i,j,h,t,n,sign

      COMPLEX  array(nxmax,nxmax,nzmax,ntmax)
      REAL*8   x(nzmax), y(nzmax),dn,PI


      IF (sign.EQ.0) THEN

      DO j=1,n
```

364

```
        array(i,j,h,t)=1/(2*PI)*n*dn*CMPLX(x(j),
     +       y(j))

     ENDDO

     ELSE

        DO j=1,n

           array(i,j,h,t)=1/(2*PI)*dn*CMPLX(x(j),
     +          y(j))

        ENDDO

     ENDIF

     RETURN

     END



ccccccccccccccccccccccccccccccccccccccccccccccccccccccccccccccccc

     SUBROUTINE SEPERATE_X(array,j,h,t,n,x,y)

     PARAMETER(nxmax=17,nzmax=257,ntmax=257)

     INTEGER i,j,h,t,n

     COMPLEX array(nxmax,nxmax,nzmax,ntmax)
     REAL*8  x(nzmax), y(nzmax)

     DO i=1,n

        x(i)=REAL(array(i,j,h,t))
        y(i)=AIMAG(array(i,j,h,t))

     ENDDO

     RETURN

     END


ccccccccccccccccccccccccccccccccccccccccccccccccccccccccccccccccc
```

365

```
      SUBROUTINE TOGETHER_X(j,h,t,ds,n,x,y,array,sign,PI)

C     SETUP SO THAT WHEN YOU CALL THE INVERSE SFFTEU YOU GET THE
C     FORWARD TRANSFORM AND VISE VERSA

C     SIGN=0->SQRT(n)*(SQRT(n))*da*FOURIER
C     SIGN=1->SQRT(n)*(1/SQRT(n))*da*INVERSEFOURIER


      PARAMETER(nxmax=17,nzmax=257,ntmax=257)

      INTEGER i,j,h,t,n,sign

      COMPLEX  array(nxmax,nxmax,nzmax,ntmax)
      REAL*8   x(nzmax), y(nzmax),ds,PI


      IF (sign.EQ.0) THEN

      DO i=1,n

         array(i,j,h,t)=1/(2*PI)*n*ds*CMPLX(x(i),
     +        y(i))

      ENDDO

      ELSE

         DO i=1,n

            array(i,j,h,t)=1/(2*PI)*ds*CMPLX(x(i),
     +           y(i))

         ENDDO

      ENDIF

      RETURN

      END



CCCCCCCCCCCCCCCCCCCCCCCCCCCCCCCCCCCCCCCCCCCCCCCCCCCCCCCCCCCCCCCCCCCCCC

      SUBROUTINE ROTATE_Z(array,n1,n2,n3,n4,n3rot)

      PARAMETER(nxmax=17,nzmax=257,ntmax=257)
```

```
COMPLEX array(nxmax,nxmax,nzmax,ntmax)
COMPLEX temp(nxmax,nxmax,nzmax,ntmax)


INTEGER i,j,h,t,n1,n2,n3,n4,n3rot
INTEGER itemp,temp2

DO t=1,n4

   DO i=1,n1
      DO j=1,n2
         DO h=1,n3

            temp(i,j,h,t)=array(i,j,h,t)

         ENDDO

      ENDDO

   ENDDO

ENDDO

temp2=n3-n3rot

WRITE(17,*)'n3rot,temp2',n3rot,temp2

DO t=1,n4

   DO i=1,n1

      DO j=1,n2

         itemp=0

         DO h=1,n3

            IF ((h-n3rot).le.0) THEN

               itemp=itemp+1

               array(i,j,h,t)=temp(i,j,temp2+itemp,t)


            ELSE

               array(i,j,h,t)=temp(i,j,h-n3rot,t)
```

367

```fortran
            ENDIF

         ENDDO

      ENDDO

   ENDDO

ENDDO

RETURN

END
```

CCCCCCCCCCCCCCCCCCCCCCCCCCCCCCCCCCCCCCCCCCCCCCCCCCCCCCCCCCCCCCC

```fortran
      SUBROUTINE ROTATE_X(array,n1,n2,n3,n4,n1rot)

      PARAMETER(nxmax=17,nzmax=257,ntmax=257)

      COMPLEX array(nxmax,nxmax,nzmax,ntmax)
      COMPLEX temp(nxmax,nxmax,nzmax,ntmax)


      INTEGER i,j,h,t,n1,n2,n3,n4,n1rot
      INTEGER itemp

      DO t=1,n4

         DO i=1,n1
            DO j=1,n2
               DO h=1,n3

                  temp(i,j,h,t)=array(i,j,h,t)

               ENDDO

            ENDDO

         ENDDO

      ENDDO

      temp2=n1-n1rot

      DO t=1,n4
```

```fortran
      DO h=1,n3

        DO j=1,n2

          itemp=0

          DO i=1,n1

            IF ((i-n1rot).le.0) THEN

              itemp=itemp+1

              array(i,j,h,t)=temp(temp2+itemp,j,h,t)

              ELSE

              array(i,j,h,t)=temp(i-n1rot,j,h,t)

            ENDIF

          ENDDO

        ENDDO

      ENDDO

      ENDDO

      RETURN

      END

ccccccccccccccccccccccccccccccccccccccccccccccccccccccccccccccc

      SUBROUTINE ROTATE_Y(array,n1,n2,n3,n4,n2rot)

      PARAMETER(nxmax=17,nzmax=257,ntmax=257)

      COMPLEX array(nxmax,nxmax,nzmax,ntmax)
      COMPLEX temp(nxmax,nxmax,nzmax,ntmax)


      INTEGER i,j,h,t,n1,n2,n3,n4,n2rot
      INTEGER itemp,temp2

      DO t=1,n4
```

```
DO i=1,n1
    DO j=1,n2
        DO h=1,n3

            temp(i,j,h,t)=array(i,j,h,t)

        ENDDO

    ENDDO

  ENDDO

ENDDO

temp2=n2-n2rot

DO t=1,n4

  DO i=1,n1
    DO h=1,n3

        itemp=0

      DO j=1,n2

          IF ((j-n2rot).le.0) THEN

              itemp=itemp +1

              array(i,j,h,t)=temp(i,temp2+itemp,h,t)

              ELSE

                  array(i,j,h,t)=temp(i,j-n2rot,h,t)

          ENDIF

        ENDDO

      ENDDO

    ENDDO

  ENDDO

RETURN

END
```

```
cccccccccccccccccccccccccccccccccccccccccccccccccccccccccccccccccc

      SUBROUTINE DATAOUT(array,component,nx,ny,nz,n)

C     OUTPUTS RESULTS TO FILE

      PARAMETER(nxmax=17,nzmax=257,ntmax=257)

      INTEGER h,j,i,t,k,nx,y,nz,n,component,two_nx,two_ny,two_nz
      INTEGER two_n

      COMPLEX array(nxmax,nxmax,nzmax,ntmax)

      two_nx=2*nx
      two_ny=2*ny
      two_nz=2*nz
      two_n=2*n

      IF (component.eq.1) THEN

         WRITE(6,*)'OUTPUTTING TO u1.out and u1_c.out'
         WRITE(17,*)'OUTPUTTING TO u1.out and u1_c.out'

         DO t = 1,two_n
            DO h = 1,two_nz
               DO i = 1,two_nx
                  DO j = 1,two_ny

                     WRITE(14,100) REAL(array(i,j,h,t))

100                  FORMAT((E20.8))

C     WRITE(51,101) AIMAG(array(i,j,h,t))

C     101              FORMAT((E20.8))

                  ENDDO
               ENDDO
            ENDDO
         ENDDO

      ELSEIF(component.eq.2) THEN

         WRITE(6,*)'OUTPUTTING TO u2.out and u2_c.out'
         WRITE(17,*)'OUTPUTTING TO u2.out and u2_c.out'
```

371

```
            DO t = 1,two_n
              DO h = 1,two_nz
                DO i = 1,two_nx
                  DO j = 1,two_ny

                    WRITE(15,110) REAL(array(i,j,h,t))

110                   FORMAT((E20.8))

C     WRITE(52,111) AIMAG(array(i,j,h,t))

C 111                   FORMAT((E20.8))

                  ENDDO
                ENDDO
              ENDDO
            ENDDO

          ELSE

            WRITE(6,*)'OUTPUTTING TO u3.out and u3_c.out'
            WRITE(17,*)'OUTPUTTING TO u3.out and u3_c.out'
            WRITE(6,*)'nx,ny,nz,n',nx,ny,nz,n
            WRITE(17,*)'nx,ny,nz,n',nx,ny,nz,n

            DO t = 1,two_n
              DO h = 1,two_nz
                DO i = 1,two_nx
                  DO j = 1,two_ny

                    WRITE(16,120) REAL(array(i,j,h,t))

120                   FORMAT((E10.4))


C     WRITE(53,121) AIMAG(array(i,j,h,t))

C     121               FORMAT((E20.8))

                  ENDDO
                ENDDO
              ENDDO
            ENDDO

          ENDIF
```

```
            RETURN

            END




cccccccccccccccccccccccccccccccccccccccccccccccccccccccccccccccc
c--------------------------------------------------------------c
c                                                              c
c  Subroutine sffteu( x, y, n, m, itype )                      c
c                                                              c
c  This routine is a slight modification of a COMPLEX split    c
c  radix FFT routine presented by C.S. Burrus.  The original   c
c  program header is shown below.                              c
c                                                              c
c  Arguments:                                                  c
c     x - real array containing real parts of transform        c
c              sequence (in/out)                               c
c     y - real array containing imag parts of transform        c
c              sequence (in/out)                               c
c     n - integer length of transform (in)                     c
c     m - integer such that n = 2**m  (in)                     c
c     itype - integer job specifier (in)                       c
c              itype .ne. -1 --> foward transform              c
c              itype .eq. -1 --> backward transform            c
c                                                              c
c  The forward transform computes                              c
c     X(k) = sum_{j=0}^{N-1} x(j)*exp(-2ijk*pi/N)              c
c                                                              c
c  The backward transform computes                             c
c     x(j) = (1/N) * sum_{k=0}^{N-1} X(k)*exp(2ijk*pi/N)       c
c                                                              c
c                                                              c
c  Requires standard FORTRAN functions - sin, cos              c
c                                                              c
c  Steve Kifowit, 9 July 1997                                  c
c                                                              c
C--------------------------------------------------------------C
C  A Duhamel-Hollman Split-Radix DIF FFT                       C
C  Reference:  Electronics Letters, January 5, 1984            C
C  COMPLEX input and output in data arrays X and Y             C
C  Length is N = 2**M                                          C
C                                                              C
C  C.S. Burrus          Rice University          Dec 1984      C
C--------------------------------------------------------------C
c
            SUBROUTINE SFFTEU( X, Y, N, M, ITYPE )
```

```fortran
      PARAMETER(ntmax=257)
      INTEGER  N, M, ITYPE

      REAL*8   X(ntmax), Y(ntmax)
      INTEGER  I, J, K, N1, N2, N4, IS, ID, IO, I1, I2, I3
      REAL*8   TWOPI, E, A, A3, CC1, SS1, CC3, SS3
      REAL*8   R1, R2, S1, S2, S3, XT
      INTRINSIC SIN, COS
      PARAMETER ( TWOPI = 6.2831853071795864769 )
c
      IF ( N .EQ. 1 ) RETURN
c
      IF ( ITYPE .EQ. -1 ) THEN
          DO 1, I = 1, N
             Y(I) = - Y(I)
1         CONTINUE
      ENDIF
c
      N2 = 2 * N
      DO 10, K = 1, M-1
          N2 = N2 / 2
          N4 = N2 / 4
          E = TWOPI / N2
          A = 0.0
          DO 20, J = 1, N4
             A3 = 3 * A
             CC1 = COS( A )
             SS1 = SIN( A )
             CC3 = COS( A3 )
             SS3 = SIN( A3 )
             A = J * E
             IS = J
             ID = 2 * N2
40           DO 30, IO = IS, N-1, ID
                I1 = IO + N4
                I2 = I1 + N4
                I3 = I2 + N4
                R1 = X(IO) - X(I2)
                X(IO) = X(IO) + X(I2)
                R2 = X(I1) - X(I3)
                X(I1) = X(I1) + X(I3)
                S1 = Y(IO) - Y(I2)
                Y(IO) = Y(IO) + Y(I2)
                S2 = Y(I1) - Y(I3)
                Y(I1) = Y(I1) + Y(I3)
                S3 = R1 - S2
                R1 = R1 + S2
```

374

```
                    S2 = R2 - S1
                    R2 = R2 + S1
                    X(I2) = R1 * CC1 - S2 * SS1
                    Y(I2) = - S2 * CC1 - R1 * SS1
                    X(I3) = S3 * CC3 + R2 * SS3
                    Y(I3) = R2 * CC3 - S3 * SS3
30          CONTINUE
            IS = 2 * ID - N2 + J
            ID = 4 * ID
            IF ( IS .LT. N ) GOTO 40
20      CONTINUE
10  CONTINUE
c
C--------LAST STAGE, LENGTH-2 BUTTERFLY --------------------C
c
        IS = 1
        ID = 4
50  DO 60, I0 = IS, N, ID
            I1 = I0 + 1
            R1 = X(I0)
            X(I0) = R1 + X(I1)
            X(I1) = R1 - X(I1)
            R1 = Y(I0)
            Y(I0) = R1 + Y(I1)
            Y(I1) = R1 - Y(I1)
60  CONTINUE
        IS = 2 * ID - 1
        ID = 4 * ID
        IF ( IS .LT. N ) GOTO 50
c
C--------BIT REVERSE COUNTER-------------------------------C
c
100 J = 1
        N1 = N - 1
        DO 104, I = 1, N1
            IF ( I .GE. J ) GOTO 101
            XT = X(J)
            X(J) = X(I)
            X(I) = XT
            XT = Y(J)
            Y(J) = Y(I)
            Y(I) = XT
101         K = N / 2
102         IF ( K .GE. J ) GOTO 103
            J = J - K
            K = K / 2
            GOTO 102
103         J = J + K
```

```
 104 CONTINUE
c
      IF ( ITYPE .EQ. -1 ) THEN
         DO 2, I = 1, N
            X(I) = X(I) / N
            Y(I) = - Y(I) / N
 2       CONTINUE
      ENDIF
c
      RETURN
c
c ... End of subroutine SFFTEU ...
c
      END
```

A.3 Example Mathematica Convolution:

```
<< Utilities'MemoryConserve'
nx = 8
ny = 8
nz = 64
nt = 128
Directory[]
SetDirectory["/data/convolution/quasi/april23/1064eo"]
force = Table[0, {t, 2nt}, {z, 2nz}, {x, 2nx}, {y, 2ny}];
forcefunction = OpenRead["surfaceforce.out"]
For[t = 1, t < 2nt + 1, t++,
    For[z = 1, z < 2 nz + 1, z++,
      For[x = 1, x < 2nx + 1, x++,
        For[y = 1, y < 2ny + 1, y++,
            force[[t, z, x, y]] = Read[forcefunction, Number]]]]];
Close[forcefunction]
SetDirectory["/data/convolution/quasi/green1"]
green = Table[0, {t, 2nt}, {z, 2nz}, {x, 2nx}, {y, 2ny}];
zout = OpenRead["u3.out"]
For[t = 1, t < 2nt + 1, t++,
    For[z = 1, z < 2nz + 1, z++,
      For[x = 1, x < 2 nx + 1, x++,
        For[y = 1, y < 2ny + 1, y++,
            green[[t, z, x, y]] = Read[zout, Number]]]]];
Close[zout]
Off[MemoryConserve]
SetDirectory["/data/convolution/quasi/april23/1064eo"]
dx = .113
dy = .113
dz = 7.0625*10^-3
```

376

```
dt = 6.*10^-8
result1 = dx dy dz dt ListConvolve[ force, green, {-1}];
result2 =
    Table[RotateLeft[result1[[t, z, x]], ny + 1], {t, 2nt}, {z, 2nz}, {x,
        2nx}];
result1 =
    Table[result2[[t, z, x, y]], {t, 2nt}, {z, 2nz}, {y, 2ny}, {x, 2nx}];
result2 =
    Table[RotateLeft[result1[[t, z, y]], nx + 1], {t, 2nt}, {z, 2nz}, {y,
        2ny}];
result1 =
    Table[result2[[t, z, y, x]], {t, 2nt}, {x, 2nx}, {y, 2ny}, {z, 2nz}];
result2 =
    Table[RotateLeft[result1[[t, x, y]], nz + 1], {t, 2nt}, {x, 2nx}, {y,
        2ny}];
result1 =
    Table[result2[[t, x, y, z]], {x, 2nx}, {y, 2ny}, {z, 2nz}, {t, 2nt}];
result2 =
    Table[RotateLeft[result1[[x, y, z]], nt + 1], {x, 2nx}, {y, 2ny}, {z,
        2nz}];
result1 =
    Table[result2[[x, y, z, t]], {t, 2nt}, {z, 2nz}, {x, 2nx}, {y, 2ny}];
timeseries4 = Table[0, {t, nt}];
Do[timeseries4[[t]] = result1[[t + nt, 2nz, nx + 1, ny + 1]], {t, nt}];
Export["sql064eo.out", timeseries4, "List"]
a = Min[result1]
b = Max[result1]
a1 = Min[green]
b1 = Max[green]
timeseries1 = Table[0, {t, nt}];
Do[timeseries1[[t]] = result1[[t + nt, nz + 1, nx + 1, ny + 1]], {t, nt}];
ListPlot[timeseries1, PlotJoined -> True, PlotRange -> {a, b}];
timeseries2 = Table[0, {t, nt}];
Do[timeseries2[[t]] = green[[t + nt, nz + 1, nx + 1, ny + 1]], {t, nt}];
ListPlot[timeseries2, PlotJoined -> True, PlotRange -> All];
timeseries3 = Table[0, {t, nt}];
Do[timeseries3[[t]] = green[[t + nt, 2nz, nx + 1, ny + 1]], {t, nt}];
ListPlot[timeseries3, PlotJoined -> True, PlotRange -> All];
ListPlot[-timeseries4, PlotJoined -> True, PlotRange -> All];
```

Appendix B

Laser Based Ultrasound NDE for

COLTS

The laser based ultrasound system is schematically illustrated in Figure B.1. A Q-switched Nd:YAG operating at 1064 nm with a variable pulse energy up to 200 mJ per pulse and a 12 ns pulse width is used to generate the ultrasound. A 400 mW continuous wave Nd:YAG laser operating at 532 nm is used to detect the ultrasonic signals. Both lasers are delivered to an enclosed scanning head through fiber optics for eye safety. The scanning head consists of optics to focus the laser light onto the sample surface and collect the reflected detection light. The detection light is delivered through an optical fiber to a 1/2 meter cavity confocal Fabry-Perot interferometer. A translation stage is used to move the scanning head assembly across the sample surface. The user defined scanning area can have a maximum width of 24 inches and length of 36 inches with a spatial resolution of 0.05 inches to 1.00 inch. The translation stage can also be shrouded for eye safety. RF waveforms from the Fabry-Perot interferometer are digitized by an eight bit resolution A/D board with a maximum sampling rate of 100 MHz and stored on a PC computer. Both

FIBER OPTICS

SCANNING HEAD

DETECTION LASER: Nd:YAG 532nm

GENERATION LASER: Nd:YAG 1064nm

TRANSLATION STAGE

ULTRASONIC DETECTION:
FABRY-PEROT INTERFEROMETER

AXIS ENCODER BOARD

RF SIGNAL

A/D BOARD

TRANSLATION STAGE
CONTROLLER

PC COMPUTER
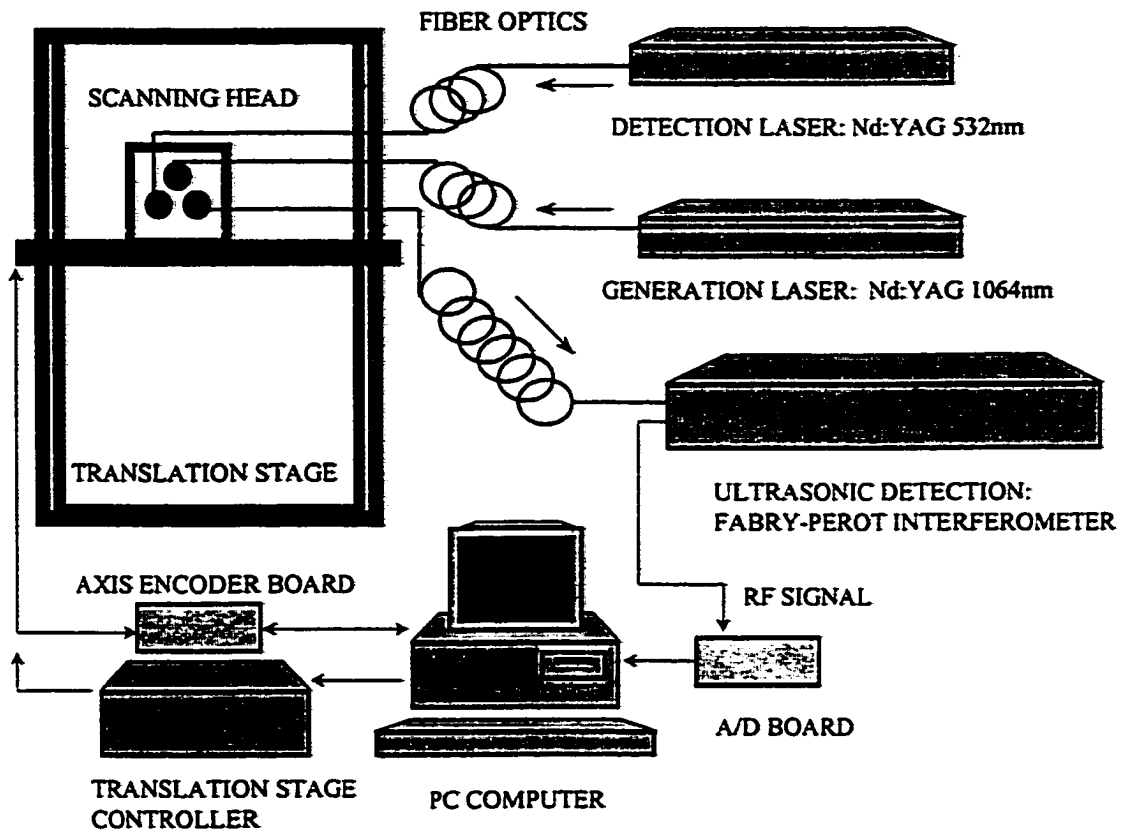
Figure B.1: Schematic of laser based ultrasound system for the COLTS facility.

the translation stage and data acquisition system are controlled by a PC-based virtual instrument controller.

Two complex composite samples were obtained from a composite wing stub box that had been structurally tested to failure. The first sample is a flat plate from a section of the wing box skin. A drop weight test machine was used to impact damage this specimen and create internal delaminations. A one inch diameter impact head weighing 25.25 lb. was dropped from a height of 3 ft 11.5 inches to generate an impact energy of 100 ft-lb. This

379

produced a dent approximately 1 mm deep on the front surface and small localized cracks on the back surface. The second sample has bi-directional T-stiffeners that are attached to the skin with through-the-thickness stitches. These stiffeners are constructed from the same material as the skin. This sample had interlaminar failure along the stiffener/skin interface that is not visible from the top skin surface. The wing box skin consists of ten stacks of [45/-45/0$_2$/90/0$_2$/-45/45] AS-4-3501-6 graphite epoxy material stitched together for a total thickness of 0.58 inches. Through-the-thickness Kevlar stitches are in rows spaced 0.2 to 0.5 inches apart with a stitch spacing of approximately 0.1 inches.

These samples were scanned with the laser ultrasound system in the laboratory. The samples were positioned approximately 8-10 inches away from the scanning head optics. The generation beam spot size was approximately 5 mm with an average pulse energy about 50 mJ/pulse. The detection beam spot size was 2 mm at approximately 235 mW. The scan area of the impact damaged plate was 2.5 inches by 2.5 inches with a 0.05 inch step size. The scan area of the stiffened plate was 6.0 inches by 6.0 inches with a 0.10 inch step size. Ultrasonic signals were recorded and processed to produce C-scan images. In all experiments, the entire A-scan waveform was recorded at each point and stored for post processing. C-scans were generated by plotting the maximum amplitude of the individual A-scan in a gated section of the waveform. Since the entire A-scan waveforms were recorded, this gate could be repositioned to produce C-scans at any depth into the sample.

Figure B.2 illustrates peak detected back wall C-Scan images of the impact damaged plate obtained with a laser based inspection (top) and an immersion tank inspection (bottom). The extended area of subsurface delamination is apparent in both plots as a dark circular region approximately 5.7 cm (2.25 inches) in diameter. The circular shape of the damage region is characteristic of impact damage in stitched composites. The rows of stitching are also visible in both C-scan representations as light horizontal bands. These

380

bands occur because the ultrasonic velocity in the stitches is greater than in the surrounding material. Consequently, there is a phase-distorted wavefront at the stitch surface which is observed as a reduced signal. Some light spots appear in the damaged region in the laser ultrasonic scan but not in the immersion tank scan. These spots may be due to stitches in the damaged region that did not break and acted as an ultrasonic waveguide, transmitting the ultrasound to the back wall. This illustrates the advantage of the point source detection in the laser ultrasound system. The results from the laser and immersion tank ultrasonic inspections of the bi-directionally T-stiffened plate are also similar. In both scans, the thickness variation due to the T-stiffeners is visible and the rows of stitching are evident.

A time-of-flight C-scan contour plot of the T-stiffened plate represented in Figure B.3 reveals more detailed information about internal structure. Two dark bands are apparent in the vertical direction corresponding to the increased thickness of the vertical T-stiffener. The light vertical band in the middle of these dark bands corresponds to the extreme thickness of the T-stiffener where the back wall signal could not be detected. Similar features are present in the horizontal direction. However, the circled region shows a region along the horizontal T-stiffener/intercostal-clip where the thickness is equal to the skin thickness. This indicates a delamination along the stiffener/skin interface in this region. This delamination was visible from the edge of the sample. The C-scan reveals that this damage extends across most of the interface.

Laser based ultrasonic NDE has promising possibilities for many applications. Specifically, it is desired to use laser based ultrasound to monitor samples during loading in a structures laboratory. We have found that it is difficult to implement laser ultrasound outside of a laser laboratory, especially on complex composite materials. However, we have constructed a prototype field deployable laser based NDE system for use in the COLTS facility and have imaged thick stitched composite samples with it. To maximize the usefullness

381
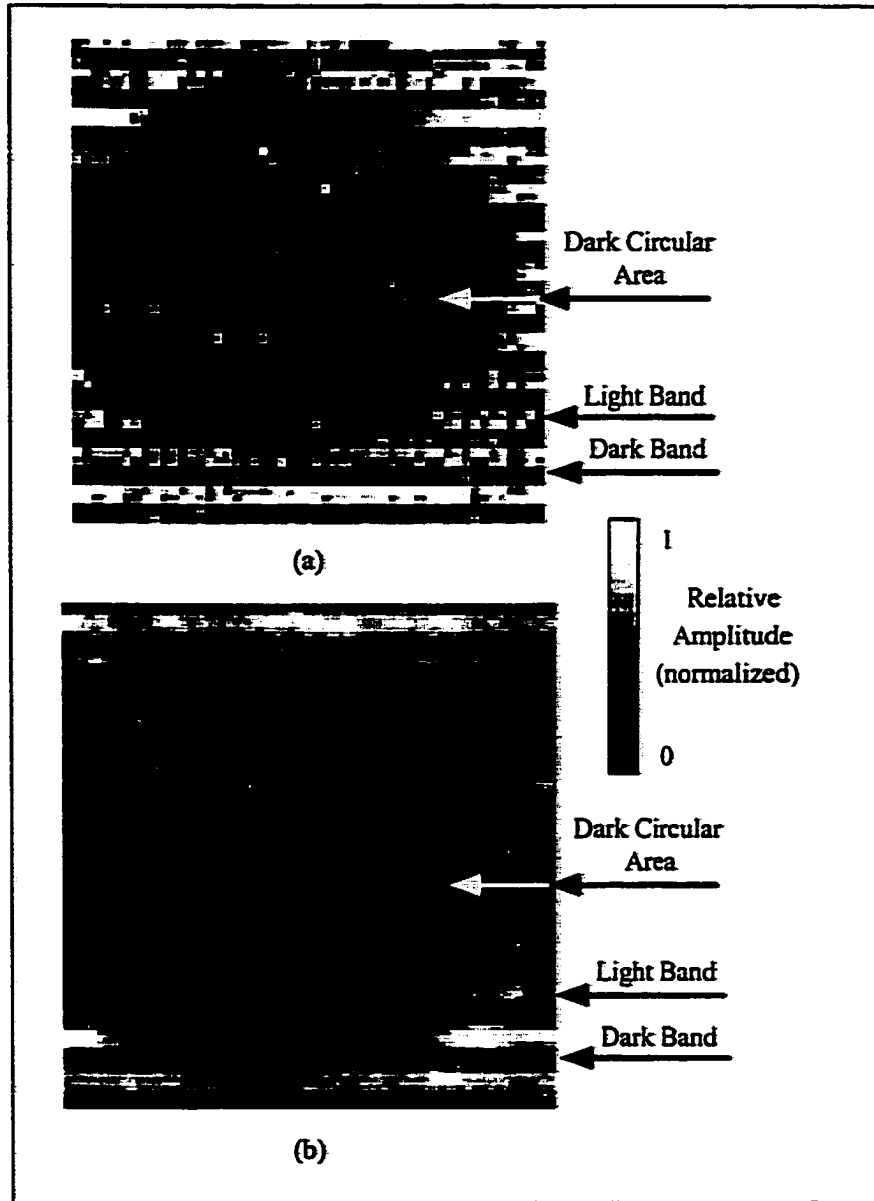
Figure B.2: Ultrasonic C-scans of impact damaged sample. Top: Laser based scan. Bottom: Immersion tank scan.
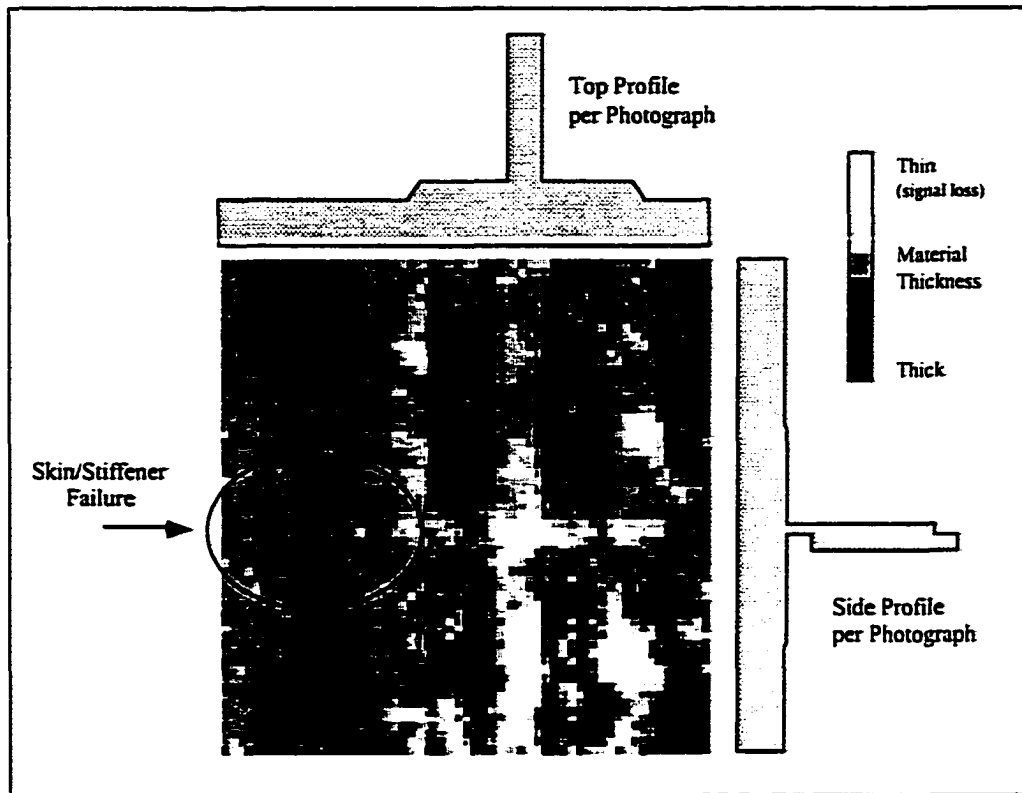
Figure B.3: A time-of-flight C-scan contour plot of the T-stiffened plate revealing interlaminar failure.

of this technique, its signal-to-noise ratio must be improved.

Bibliography

[1] C B Scruby and L E Drain. *Laser Ultrasonics Techniques and Applications*. Adam Hilger, 1990.

[2] A D W McKiew and R C Addison Jr. Practical considerations for the rapid inspection of composite materials using laser-based ultrasound. *Ultrasonics*, 32(5):333–345, 1994.

[3] C B Scruby, R J Dewhurst, D A Hutchins, and S B Palmer. Quantitative studies of thermally generated elastic waves in laser-irradiated metals. *Journal of Applied Physics*, 51:6210–6216, 1980.

[4] L R F Rose. Point-source representation for laser-generated ultrasound. *J. Acoust. Soc. Am.*, 7(3):723, March 1984.

[5] P A Doyle. On epicentral waveforms for laser-generated ultrasound. *J. Phys. D: Appl. Phys.*, 19:1613–1623, 1986.

[6] K L Telschow and R J Conant. Optical and thermal parameter effects on laser-generated ultrasound. *J. Acoust. Soc. Am.*, 88(3):1494–1502, September 1990.

[7] J B Spicer. *Laser Ultrasonics in Finite Structures: Comprehensive Modelling with Supporting Experiment*. PhD thesis, Johns Hopkins University, 1991.

[8] H Lamb. On the propagation of tremors over the surface of an elastic solid. *Phil. Trans. Roy. Soc.*, A203:1, 1904.

[9] W M Ewing, W S Jardetzky, and F Press. *Elastic waves in layered media.* McGraw-Hill, New York, 1957.

[10] J Miklowitz. *Elastic wave propagation.* Applied mechanics surveys. Spartan Books, Washington D. C., 1966.

[11] K F Graff. *Wave Motion in Elastic Solids.* Oxford: Clarendon, 1975.

[12] J D Achenbach. *Wave Propagation in Elastic Solids.* Amsterdam: North-Holland, 1973.

[13] C L Pekeris and H Lifson. Motion of the surface of a uniform elastic half-space produced by a buried pulse. *J. Acoust. Soc. Am.*, 29(11):1233–1238, November 1957.

[14] E A Kraut. Advances in the theory of anisotropic half-space. *Rev. Geophys.*, 1:401–448, 1963.

[15] L Cagniard. *Reflection and refraction of progressive seismic waves.* New York: McGraw-Hill, 1962.

[16] W J Pardee. Acoustic emission and the plate green's function. *J. Math. Phys.*, 18:676–686, 1977.

[17] Y-H Pao, R R Gajewshi, and A N Ceranoglu. Acoustic emission and transient waves in an elastic plate. *J. Acoust. Soc. Am.*, 65(1):96–105, January 1979.

[18] Y-H Pao and R R Gajewski. *The generalized ray theory and transient response of layered elastic solids*, volume 13 of *Physical Acoustics*, chapter 6. Academic, New York, 1977.

[19] J E Sinclair. Epicentre solutions for point multipole sources in an elastic half-space. *J. Phys. D*, 12:1309–1315, 1979.

[20] J R Willis. *Phil. Trans. R. Soc.*, A 274:435–491, 1973.

[21] L R Johnson. Green's function for lamb's problem. *Geophys. J. R. Astron. Soc.*, 37:99–131, 1974.

[22] R Burridge and L Knopoff. Body force equivalents for seismic dislocations. *Bull. Seismol. Soc. Am.*, 54:1875–1888, 1964.

[23] C B Scruby, H N G Wadley, and J Hill. Dynamic elastic displacements at the surface of an elastic half-space due to defect sources. *J. Phys. D: Appl. Phys.* 16:1069–1083. 1983.

[24] F R Yeatts. Elastic radiation from a point force in an anisotropic medium. *Phys. Rev. B*, 29:1674–1684, 1984.

[25] C Chang and W Sachse. Analysis of elastic wave signals from an extended source in a plate. *J. Acoust. Soc. Am.*, 77:1335–1341. 1985.

[26] A N Ceranoglu and Y-H Pao. Propagation of elastic pulses and acoustic emission in a plate. *Trans. ASME*, 48:125–147. 1981.

[27] A Tverdokhlebov and J L Rose. On green's function for elastic waves in anistropic media. *J. Acoust. Soc. Am.*, 83:118–121. 1988.

[28] A Tverdokhlebov and J L Rose. On the application domain of the green's function approximation for mild anisotropic media. *J. Acoust. Soc. Am.*, 86:1606–1607. 1989.

[29] K Wu, P B Nagy, and L Adler. Far field radiation of a point source on the frees urface of semi-infinite anisotropic solids. In D O Thompson and D E Chimenti, editors,

Review of Progress in Quantitative NDE, volume 9 A, pages 149–156. Plenum New York, 1990.

[30] L Y Gutin. *Sov. Phys. Acoust.*, 9, 1964.

[31] A E Lord Jr. *J. Acoust. Soc. Am.*, 39:650, 1966.

[32] V K Tewary and C M Fortunko. A computationally efficient representation for propagation of elastic waves in anisotropic solids. *J. Acoust. Soc. Am.*, 91(4):1888–1894, April 1992.

[33] B A Auld. *Acoustic fields and waves in solids*. Robert E Krierger Publ. Co., 1990.

[34] J Miklowitz. *The theory of elastic waves and waveguides*. North-Holland, Amsterdam, 1978.

[35] A G Every and Kim K Y. Time domain dynamic response functions of elastically anistropic solids. *J. Acoust. Soc. Am.*, 95(5):2505–2516, May 1994.

[36] M Spies. Elastic wavs in homogeneous and layered transversely isotropic media: plane waves and gaussian wave packets. a general approach. *J. Acoust. Soc. Am.*, 95(4):1748–1760, April 1994.

[37] M Spies. Elastic wave propagation in general transversely isotropic media i. green's functions and elastodynamic holography. *J. Acoust. Soc. Am.*, 96(2):1144–1157, August 1994.

[38] M Spies. Elastic wave propagation in transversely isotropic media ii. the generalized rayleigh function and an integral representaion for the transducer field. theory. *J. Acoust. Soc. Am.*, 97(1):1–13, January 1995.

[39] A Mourad and M Deschamps. Lamb's problem for an anisotropic half-space studied by the cagniard de hoop method. *J. Acoust. Soc. Am.*, 97(5):3194–3197, May 1995.

[40] G P Eatwell, J A Simmons, and G R Willis. A new representation for the dynamic green's tensor of an elastic half-space or layered medium. *Wave motion*, 4:53–73, 1982.

[41] C Y Wang and J D Achenbach. A new method to obtain 3-d green's functions for anisotropic solids. *Wave motion*, 18:273–289, 1993.

[42] M Dubois, F Enguehard, and L Bertrand. Modelling of laser thermoelastic generation in an orthotropic medium. *Appl. Phys. Lett.*, 64(5):554–556, 1994.

[43] A Mourad. *Etude du ptrobleme de Lamb en milieux anisotropes pour leur caracterisation ultrasonore par impact laser.* PhD thesis, University of Bordeaux, 1995.

[44] K Y Kim and W Sachse. Some novel applications of point source and point detector for ultrasonic waves. 1992.

[45] A H Nayfeh. *Wave propagation in layered anisotropic media.* Elsevier Science B.V., 1995.

[46] M Spies and M Kroning. Green's fuction for lamb's problem and rayleigh wave propagation in general transversely isotropic materials. In D O Thompson and D E Chimenti, editors, *Review of Progress in Quantitative Nondestructive Evaluation*, volume 15, pages 161–168. Plenum Press, New York, 1996.

[47] M Spies. Green's tensor for lamb's problem: The general anisotropic case. *J. Acoust. Soc. Am.*, 102(4):2438–2441, October 1997.

[48] C Bescond and M Deschamps. Dynamical surface response of a semi-infinite anisotropic elastic medium to an impulsive force. *J. Acoust. Soc. Am.*, 103(1):114–124, January 1998.

[49] J H M T Van Der Hijden. *Propagation of transient elastic waves in stratified anisotropic media.* North-Holland, Amsterdam, 1987.

388

[50] J W Weight. A model for the propagation of short pulses of ultrasound in a solid. *J. Acoust. Soc. Am.*, 81:815–825, 1987.

[51] J L Synge. Elastic waves in anisotropic media. *J. Math. Phys.*, 35:323–335, 1957.

[52] M J P Musgrave. On the propagation of elastic waves in aeolotropic media i. general principles. *Proc. R. Soc. London, Ser.*, A 226:339–355, 1954.

[53] M J P Musgrave. On the propagation of elastic waves in aeolotropic meida ii. media of hexagonal symmetry. *Proc. R. Soc. London, Ser.*, A 226:356–366. 1954.

[54] C L Pekeris. The seismic surfce pulse. *Proc. Natl. Acad. Sci.*, 41:469–480, 1955.

[55] C L Pekeris. The seismic burried pulse. *Proc. Natl. Acad. Sci.*, 41:629–638. 1955.

[56] C L Pekeris. *Proc. Natl. Acad. Sci.*, 42:439, 1956.

[57] G Eason, J Fulton, and I N Sneddon. *Philos. Trans. ROy. Soc. London.* A248:575–680. 1956.

[58] C B Scruby, J C Collingwood, and H N G Wadley. *J. Phys. D: Appl. Phys.*, 11:2359–2369, 1978.

[59] F R Breckenridge, C E Tschiegg, and M Greenspan. Acoustic emission: Some applications of lamb's problem. *J. Acoust. Soc. Am.*, 57:626–631, 1975.

[60] A G Mencher. Epicentral displacements caused by elastic waves in an infinite slab. *J. Appl. Phys.*, 24:1240, 1953.

[61] L Knopoff. Surface motions of a thick plate. *J. Appl. Phys.*, 29:661–670, 1958.

[62] N Davids. Transient analysis of stress-wave penetration in plates. *J. Appl. MEch.*, 26:651–660, 1959.

[63] C L Pekeris, Z Alterman, F Abramovici, and H Jarosch. Propagation of a compressional pulse in a layered solid. *Rev. Geophys.*, 3:25–47, 1965.

389

[64] M Shmuley. Stress wave propagation in plates subjected to a transient line source. *Int. J. Solids Struct.*, 11:670–691, 1975.

[65] J H H Wu and F R Norwood. Transient analysis of a three-dimensional plate by ray grouping technique. *Int. J. Solids Struct.*, 11:679–691, 1975.

[66] Y H Pao and R K Kaul. Waves and vibrations in isotropic and anisotropic plates. In George Herrman, editor, *R. D. Mindlin and Applied Mechanics*. Pergamon, New York, 1974.

[67] I Tolystoy and E Usdin. Wave propagation in elastic plates: low and high mode dispersion. *J. Acoust. Soc. Am.*, 29:37–42, 1977.

[68] V T Buchwald. Elastic waves in anisotropic media. *Proc. R. Soc. London Ser.*, A 253:563–580, 1959 1960?

[69] Y H Pao. Theory of acoustic emission. In Y H Pao, editor, *Elastic Waves and Nondestructive Testing of Materials*, volume AMD-29, pages 107–128. ASME. New York, 1978.

[70] R L Weaver and Y H Pao. Axisymmetric elastic waves excited by a point source in a plate. *J. Appl. Mech.*, 49:821–836, 1982.

[71] T M Proctor, F R Breckenridge, and Y H Pao. Transient waves in an elastic plate. *J. Acoust. Soc. Am.*, 74:1905–1906, 1983.

[72] K Aki and P G Richards. *Quantitative Seismology*. San Francisco: Freeman, 1980.

[73] G F D Duff. *Philos. Trans. R. Soc. London*, 252:249, 1960.

[74] G F Miller and H Pursey. *Proc. R. Soc.*, A 223:521, 1954.

[75] A N Norris. A theory of pulse propagation in elastica anisotropic solids. *Wave motion*, 9:509–532, 1987.

[76] N Cameron and G Eason. *Q. J. Mech. Appl. Math.*, 20:23, 1967.

[77] R G Payton. Epicenter and epicentral-axis motions of a transversely isotropic elstic half-space. *SIAM J. Appl. Math.*, 40(373):373, 1981.

[78] R G Payton. *Elastic waves in transversely isotropic media.* The Hague, 1983.

[79] C Y Wang and J D Achenbach. Lamb's problem for solids of general anisotropy. *Wave motion*, 24:227–242, 1996.

[80] R Burridge, P Chadwick, and A N Norris. *Proc. R. Soc. London. Ser.*, A 440:655, 1993.

[81] R G Payton. *Q. J. Mech. Appl. Math.*, 45:183, 1992.

[82] S L Suh, W Goldsmith, J L Sackman. and R L Taylor. Impact on the transversely anisotropic half-space. *Int. J. Rock. Mech. Min. Sci.*, 11:413–421, 1974.

[83] L R Weaver, W Sachse, and K Y Kim. Transient elastic waves in a transversely isotropic plate. *J. Appl. Mech.*, 1994.

[84] M Spies. Green's function for lamb's problem in anisotropic materials.

[85] M Spies. Theory of transducer radiation in transversely isotropic media introducing the generailzed rayleigh function. In D O Thompson and D E Chimenti. editors, *Reviw of Progress in Quantitative Nondestructive Evaluation.* volume 14B. pages 1005–1012. Plenum Press, New York, 1995.

[86] R L Ryan. Pulse propagation in a transversely isotropic half-space. *J. Sound Vib.*, 14:511–524, 1971.

[87] A G Every, K Y Kim. and A A Maznev. The elastodynamic response of a semi-infinte anistropic solid to sudden surface loading. *J. Acoust. Soc. Am.*, To be published.

[88] R M White. Elastic wave generation by electron bombardment or electromagnetic wave absorption. *J. Appl. Phys.*, 34:2123–2124, 1963.

[89] R M White. Generation of elastic waves by surface heating. *J. Appl. Phys.*, 34:3559–3567, 1963.

[90] H S Carslaw and J C Jaeger. *Conduction of Heat in Solids.* Oxford:clarendon, 1959.

[91] J L Nowinski. *Theory of Thermoelasticity with Applications.* Sijthoff and Noordhoff International Publihers, The Netherlands, 1978.

[92] R J Dewhurst, D A Hutchins, S B Palmer, and C B Scruby. Quantitative measurements of laser-generated acoustic waveforms. *J. Appl. Phys.*, 53(6):4064–4071, June 1982.

[93] G C Wetsel Jr. Ultrasonic-wave generation by harmonic heating in composite structures. *Appl. Phys. Lett.*, 41(6):511–513, 1982.

[94] A T De Hoop. A modification of cagniard's method for solving seismic pulse problems. *Appl. Sci. Res.. Sect. B,* 8:349–356, 1960.

[95] G Bachus and M Mulcahy. *Geophys. J. R. Astron. Soc.,* 46(46):341. 1976.

[96] J F Ready. *Effects of High Power Laser Radiation.* New York: Academic, 1971.

[97] L F Bresse and D A Hutchins. Transient acoustic radiation fields in solids from wide sources. In D O Thompson and D E Chimenti, editors, *Review of Progresss in Quantitative Nondestrutive Evaluation,* volume 7A, page 629. Plenum Press. New York, 1988.

[98] L F Bresse and D A Hutchins. Transient generation by a wide thermoelastic source at a solid surface. *J. Appl. Phys.,* 65(4):1441–1446, February 1989.

392

[99] L F Bresse and D A Hutchins. Transient generation of elastic waves in solids by a disk shaped normal force source. *J. Acoust. Soc. Am.*, 86(2):810–817, August 1989.

[100] U Schliechert and K J Langenberg. A quantitative theory of laser-generated ultrasound. In D O Thompson and D E Chimenti, editors, *Review of Progress in Quantitative Nondestructive Evaluation*, volume 8A, pages 489–496. Plenum Press, New York, 1989.

[101] F A McDonald. Practical quantitative theory of photoacoustic pulse generation. *Appl. Phys. Lett.*, 54(16):1504–1506, April 1989.

[102] A E Green and K A Lindsay. Thermoelasticity. *J. Elasticity*, 2:1–7, 1972.

[103] T Sanderson, C Ume, and J Jarzynski. Hyperbolic heat equations in laser generated ultrasound models. *Ultrasonics*, 33(6):415–421, 1995.

[104] H W Lord and Y A Schulman. A generalized dynamical theory of thermoelasticity. *J. Mech. Phys. Solids*, 15:299–309, 1967.

[105] F A McDonald and G C Wetsel. Generalized theory of the photoacoustic effect. *J. Appl. Phys.*, 49(4):2313–2322, April 1978.

[106] D A Hutchins, R J Dewhurst, S B Palmer, and C B Scruby. Laser generation as a standard acoustic source in metals. *Appl. Phys. Lett.*, 38(9):677–679, May 1981.

[107] D A Hutchins, R J Dewhurst, and S B Palmer. Directivity patterns of lasder-generated ultrasound in aluminum. *J. Acoust. Soc. Am.*, 70(5):1362–1369, 1981b.

[108] H N G Wadley, C K Stockton, J A Simmons, M Rosen, S D Ridder, and R Mehrabian. Quantitative acoustic emission studies for materials processing. In D O Thomspon and D E Chimenti, editors, *Review of Progress in Quantitative Nondestructive Evaluation*, volume 1, pages 421–431. Plenum Press, New York, 1982.

[109] M Kasai, S Fukushima, Y Gohski, T Sawada, M Ishika, and M Kaihara. A basic analysis of pulsed photoacoustic signals using the finite elements method. *J. Apl. Phys.*, 64(3):972–976, August 1988.

[110] A F McDonald. On the precursor in laser-generated ultrasound. *Appl. Phys. Lett.*, 56:230–232, 1990.

[111] R J Conant and K L Telschow. Longitudinal wave prescursor signal from an optically penetrating thermoelastic laser source. In D O Thompson and D E Chimenti, editors, *Review of Progress in Nondestructive Evaluation*, volume 8A, pages 497–504. Plenum Press, New York, 1989.

[112] J B Spicer, J B Deaton, and J W Wagner. Effects of laser source parameters on the generation of narrow band and directed laser ultrasound. In D O Thompson and D E Chimenti, editors, *Review of Progress in Quantitative Nondestructive Evaluation*, volume 11, pages 617–624. Plenum Press, New York. 1992.

[113] J-C Cheng, L Wu, and S-Y Zhang. Characteristic elastic waveform excited by pulse laser in a plate. In D O Thompson and D E Chimenti, editors, *Review of Progress in Quantitat*, volume 13A, pages 493–499. Plenum Press, New York. 1994.

[114] R J Von Gutfeld and R L Melcher. 20-mhz acoustic waves from pulsed thermoelastic expansions of constrained surfaces. *Appl. Phys. Lett.*, 30(6):257–259, March 1977.

[115] H K Wickramasinghe, R C Bray, V Jipson, C F Quate, and J R Salcedo. Photoacoustics on a microscopic scale. *Appl. Phys. lett.*, 33(11):923–925. December 1978.

[116] G M Sessler, J E West, and R Gerhard. Measurement of charge distribution in polymer electrodes by a new pressure pulse method. *Polym. Bull.*, 9:109–111, 1981.

[117] G M Sessler, J E West, R Gerhard-Multhaupt, and H Von Seggern. Non-destructive

laser method for measuring charge profiles in irradiated polymer fibres. *IEEE Trans. Nucl. Sci.*, NS-29:1644–1649, 1982.

[118] A C Tam. Pulsed laser generation of ultrashort acoustic pulses: Application for thin-film ultrasonic measurements. *Applied physics letters*, 45:510–512, 1984.

[119] J A Cooper, R A Crosbie, R J Dewhurst, and S B Palmer. The application of laser-generated ultrasound to the remote testing of laminar defects. pages 207–212. Buttersworths, London, UK, 1985.

[120] J A Cooper. R J Dewhurst, and S B Palmer. Characterization of surface breaking defects in metals sing laser-generated ultrasound. *Phil. Trans. Roy. Soc. London.* 320A:319–328, 1986.

[121] J A Cooper, R A Crosbie, R J Dewhurst, A D W McKie, and S B Palmer. Surface acoustic wave interaction with cacks and solids: A non-contacting study using lasers. *IEEE Trans. in UFFC.* UFFC-33:462–470, 1986.

[122] H Sontag and A C Tam. Optical monitoring of photacoustic pulse propagation in silicon wafers. *Appl. Phys. Lett.*, 46:725, 1985.

[123] J P Monchalin and R Heon. Laser ultrasonic generation and optical detection with a confocal fabry-perot interferometer. *Materials Evaluation*, 44:1231–1237. September 1986.

[124] C B Scruby, R L Smith, and B C Moss. Microstructural monitoring by laser-ultrasonic attenuation and forward scattering. *NDT Int*, 19:307–313, 1986.

[125] R J Dewhurst, C Edwards, A D W Mckie, and S B Palmer. Estimation of the thickness of thin metal sheet usin laser generated ultrasound. *Appl. Phys. Lett.* 51(14):1066–1068, October 1987.

[126] H I Ringermacher and C A Kittredge. Photoacoustic microscopy of ceramics using

laser heterodyne detection. In D O Thompson and D E Chimenti, editors, *Review of Progress in Quantitat,* volume 6B, page 1231. Plenum Press, New York, 1987.

[127] R D Greenough, R J Dewhurst, and C Edwards. Magnetomechanical sensing of laser-generated ultrasound to assess structural changes in metallic amorphous ribbons. *J. Appl. Phys.,* 62:4728-4731, 1987.

[128] R J Dewhurst, C Edwards, A D W McKie, and S B Palmer. A remote laser system for material characterization at high temperatures. pages 1615-1622. Plenum Press, New York, 1988.

[129] L F Bresse, D A Hutchins, and K Lundgren. Elastic constant determination using generation by pulse lasers. *J. Acoust. Soc. Am.,* 84(5):1751-1757, November 1988.

[130] L F Bresse, D A Hutchins, and K Lundgren. Elastic determination using generation by pulsed laser. In D O Thompson and D E Chimenti, editors, *Review of Progress in Quantitative Nondestructive Evaluation,* volume 7B, pages 1219-1226. Plenum Press, New York, 1988.

[131] K Telschow. Microstructural characterization with a pulsed laser ultrasonic source. In D O Thompson and D E Chimenti, editors, *Review of Progress in Quantitative Nondestructive Evaluation,* volume 7B, pages 1211-1218. Plenum Press. New York, 1988.

[132] D A Hutchins and K L Lundgren. Quantitative studies of lamb waves in thin materials using laser techniques. In D O Thompson and D E Chimenti, editors, *Review of Progress in Quantitat,* volume 7A, pages 79-84. Plenum Press, New York, 1988.

[133] D A Hutchins, K Lundgren, and S Palmer. A laser study of transient lamb waves in thin materials. *J. Acoust. Soc. Am.,* 85(4):1441-1448, April 1989.

[134] J-D Aussel and J-P Monchalin. Study of surface acoustic wave dispersion using laser-

ultrasonics and application to thickness measurement. In D O Thompson and D E Chimenti, editors, *Review of Progressin Quantitative Nondestructive Evaluation*, volume 8A, pages 535–542. Plenum Press, New York, 1989.

[135] L F Bresse, D A Hutchins, and F Hauser. Ultrasonic nde of layered composites using pulsed laser. In D O Thompson and D E Chimenti, editors, *Review of Progress in Quantitat*, volume 8A, pages 527–534. Plenum Press, New York, 1989.

[136] B R Tittmann, R S Linebarger, and R C Addison. Laser-based ultrasonics on gr/epoxy composite: A systems analysis. In D O Thompson and D E Chimenti, editors, *Review of Progress in Quantitative Nondestructive Evaluation*, volume 8A, pages 513–520. Plenum Press, New York, 1989.

[137] B Tittmann, R Linenbarger, and R Addison. Laser-based ultrasonics on gr epoxy. *J of Nondestructive Eval*, 9, 1990.

[138] B R Tittmann, R S Linebarger, and R C Addison. Laser-based ultrasonics on gr/epoxy compsite:interferometric detection. In D O Thompson and D E Chimenti, editors. *Review of Progress in Quantitat*, volume 9A, pages 479–486. Plenum Press, New York, 1990.

[139] H I Ringermacher, B N Cassenti, J R Strife, and J L Swindal. Laser thermomechanical evaluation of bonding integrity. In D O Thompson and D E Chimenti, editors. *Review of Progress in Quantitat*, volume 9A, pages 471–478. Plenum Press, New York, 1990.

[140] A G Every and W Sachse. Determination of the elastic constants of anisotropic solids from acoustic-wave group-velocity measurements. *Phys. Rev. B*, 42:8196–8205. 1990.

[141] P A Doyle and C M Scala. Ultrasonic measurement of elastic constants for composite

397

overlays. In D O Thompson and D E Chimenti, editors, *Review of Progress in Quantitat*, volume 10B, pages 1453–1459. Plenum Press, New York, 1991.

[142] R C Addison, H A Ryden, and A D W McKie. Laser-based ultrasonics for the inspection of large area gr/epoxy composites. In D O Thompson and D E Chimenti, editors, *Review of Progress in Quantitat*, volume 10A, pages 485–492. Plenum Press, New York, 1991.

[143] S J Davies and Palmer S B. Investigation of the phase characteristics of laser-generated ultrasound interactions with various sized bulk defects as an aid to characterization. In D O Thompson and D E Chimenti, editors, *Review of Progress in Quantitat*, volume 10A, pages 499–506. Plenum Press, New York, 1991.

[144] R J Dewhurst and Q Shan. Through-transmission ultrasonic imaging of sub-surface defects using non-contact laser ultrasonics. *Optics and lasers in engineering*, 16(2-3):163–178, 1992.

[145] G Tas. Noninvasive picosecond ultrasonic detection of ultrathin interfacial layers:cfx a the ai/si interface. *Appl. Phys. Lett.*, 61:1787–1789, 1992.

[146] C M Scala and P A Doyle. Elastic constants for unidirectional boron-epoxy composites. In D O Thompson and D E Chimenti, editors, *Review of Progress in Quantitat*, volume 11A, pages 585–592. Plenum Press, New York, 1992.

[147] D A Hutchins. Pulsed lasers for quantitative ultrasonic nde. In D O Thompson and D E Chimenti, editors, *Review of Progress in Quantitat*, volume 11A, pages 561–568. Plenum Press, New York, 1992.

[148] A C Bushell, C Edwards, and C Palmer. A description of an improved homodyne laser interferometer. In D O Thompson and D E Chimenti, editors, *RPNDE*, volume 11A, pages 569–576. Plenum Press, New York, 1992.

398

[149] J Huang and J D Achenbach. Measurements of local surface waves speeds by a dual porbe laser interferometer. In D O Thompson and D E Chimenti, editors, *Review of Progress in Quantitat*, volume 11A, pages 593–600. Plenum Press, New York, 1992.

[150] J O Kim and J D Achenbach. Elastic constants of single-crystal transition-metal nitride films measured by line-focus acoustic microscopy. *J. Appl. Phys.*, 72:2830–2834, 1992.

[151] A D W McKie and R C Addison. Inspection of components having copmlex geometries using laser-based ultrasound. In D O Thompson and D E Chimenti, editors, *Review of Progress in Quantitat*, volume 11A, pages 577–584. Plenum Press, New York, 1992.

[152] A D W McKie and R C Addison. Rapid inspection of components using laser-based ultrasound. In D O Thompson and D E Chimenti, editors, *Review of Progress in Quantitative Nondestructive Evaluation*, volume 12A, pages 507–516. Plenum Press, New York, 1993.

[153] P B Nagy, G Blaho, and A Laszlo. Improved laser interferometry for ultrasonic nde. In D O Thompson and D E Chimenti, editors, *Review of Progress in Quantitat*, volume 12A, pages 527–538. Plenum Press, New York, 1993.

[154] C Edwards, A Al-Kassim, and S B Palmer. Laser ultrasound for the study of thin sheets. In D O Thompson and D E Chimenti, editors, *Review of Progress in Quantitat*, volume 12A, pages 539–548. Plenum Press, New York, 1993.

[155] H I Ringermacher, F A Reed, and J R Strife. Laser ultrasonics for coating thickness evaluation at 1200 c. In D O Thompson and D E Chimenti, editors, *Review of Progress in Quantitat*, volume 12A, pages 549–558. Plenum Press, New York, 1993.

399

[156] M Oksanen, R Lehtiniemi, and J Wu. Thermoelastic sounds source: waveforms in a sensing application. In D O Thompson and D E Chimenti, editors, *Review of Progress in Quantitat*, volume 12A, pages 559–569. Plenum Press, New York, 1993.

[157] M-C Wu, F R Parker, and W P Winfree. Laser ultrasonic and photoacoustic characterization of subsurface structures. In D O Thompson and D E Chimenti, editors, *Review of Progress in Quantitat*, volume 12A, pages 563–569. Plenum Press, New York, 1993.

[158] L P Scudder, D A Hutchins, and G Hayward. Reception of laser generated ultrasound from a cfrp plate by an air matched peizoelectric composite transducer. In D O Thompson and D E Chimenti, editors, *Review of Progress in Quantitat*, volume 12A, pages 571–578. Plenum Press. New York, 193.

[159] R D Costley and Y H Berthelot. Laser generation of rayleigh and lamb waves for ultrasonic nondestructive testing. In D O Thompson and D E Chimenti, editors, *Review of Progress in Quantitat*, volume 12A, pages 579–586. Plenum Press. New York, 1993.

[160] S G Pierce, R E Corbett, and R J Dewhurst. An actively-stabilized fiber-optic interferometer for laser-ultrasonic flaw detection. In D O Thompson and D E Chimenti, editors, *Review of Progress in Quantitat*, volume 12A, pages 587–593. Plenum Press, New York, 1993.

[161] D R Billson and D A Hutchins. Visualization of laser generated ultrasound in a solid, a liquid and in air. In D O Thompson and D E Chimenti, editors, *Review of Progress in Quantitat*, volume 12A, pages 595–601. Plenum Press, New York, 1993.

[162] F H et al. Chang. Laser ultrasonic ispection of honeycomb aircraft structures. In D O

400

Thompson and D E Chimenti, editors, *Review of Progress in Quantitat*, volume 12A, pages 611–616. Plenum Press, New York, 1993.

[163] J P Monchalin. Progress towards application of laser-ultrasonics in industry. In D. O. Thompson and D. E. Chimenti, editors, *Review of Progress in Quantitive Nondestructive Evaluation*, volume 12, pages 495–506. Plenum Press, New Yok, 1993.

[164] K Y Kime, W Sachse, and A G Evergy. On the determination of sound speeds in cubic crystals and isotropic media using a broad band ultrasonic point-source/point recevier method. *J. Acoust. Soc. Am.*, 93:1393–1406. 1993.

[165] A Idris, C Edwards, and S B Palmer. Acoustic wave measurements at elevated temperature using a pulsed laser generator and an electromagnetic acoustic transducer detector. *Nondest. Test. Eval.*, 11:195–213, 1994.

[166] S Ashley. Nondestructive evaluation with laser ultrasound. *Mechanical Engineering*, 116(10):63–66, October 1994.

[167] J-F Chai and T-T Wu. Determination of anistropic elastic constants using laser generated surface waves. *J. Acoust. Soc. Am.*, 95:3232–3241, 1994.

[168] D W Schindel, D A Hutchins, S T Smith, and B Farahbakhsh. High-temperature pulsed photoacoustic studies of surface waves on solids. *J. Acoust. Soc. Am.*, 95(5):2517–2524, May 1994.

[169] J Huang, S Krishnaswamy, and J D Achenbach. A fiber-optic heterodyne dual-probe interferometer for laser-ultrasonic crack detection. In D O Thompson and D E Chimenti, editors, *Review of Progress in Quantitat*, volume 13A, pages 485–492. Plenum Press, New York, 1994.

[170] Y Lu, M V Moore, D T Queheillalt, and N G Haydn. A lamb wave temperature sensor

401

for semiconductor wafer processing. In D O Thompson and D E Chimenti, editors, *Review of Progress in Quantitat*, volume 13A, pages 509–516. Plenum Press, New York, 1994.

[171] A D W McKie and R C Addison. A laser-based ultrasound system incorporating a long-pulse probe laser for increased sensitivity. In D O Thompson and D E Chimenti, editors, *Review of Progress in Quantitative Nondestructive Evaluation*, volume 13A, pages 517–523. Plenum Press, New York, 1994.

[172] Z Zhang, G Changming, and D Fei. Application of laser ultrasonics in characterization pmma. In D O Thompson and D E Chimenti, editors, *Review of Progress in Quantitat*, volume 13A, pages 525–532. Plenum Press, New York, 1994.

[173] H Endoh, Y Hiwatashi, and T Hoshimiya. Nde of a variable-depth crach by photoacoustic imaging. *IEEE Ultrasonics symposium*, pages 825–827, 1995.

[174] R Weiss and M W Sigrist. Broadband fiber-optic interferometer as ultrasonic transducer suitable for coating adhesion measurements. *Rev. Sci. Instrum.*, 66(8):4114–4123, August 1995.

[175] D M Pepper, G J Mitchell, G J Dunning, S W McCahon, M B Klein, and T R O'Meara. Double-pumped conjugate and photo-induced emf sensors: Two novel, high-bandwidth, auto-compensating, laser-based ultrasound detectors. 7th International Symposium on Nondestructive Characterization of Materials (Prague), 1995.

[176] A A Karabutov and N B Podymova. Nondestructive evaluation of fatigue-induced changes in he structure of copmistes by and ultrasonic method using a laser. *Mechanics of composite materials*, 31(3):301–304, 1995.

[177] D A Oursler and J W Wagner. Narrow-band hybrid pulsed laser/emat system for

402

noncontact ultrasonic inspection using angled shear waves. *Materials Evaluation*, pages 593–597, May 1995.

[178] G J Dunning, P V Michell, T R O'Meara, M B Klein, and D M Pepper. Remote ultrasonic inspection system for in-process, high volume industrial applications. ANSI, 1995.

[179] C Chenu, D Royer, and F Mathias. Defecet detection by surface acoustic waves generated by a multiple beam laser. IEEE Ultrasonics Symposium. 1995.

[180] X R Zhang, D Fei, C M Gan, and S Y Zhang. Ultrasonic velocities of c/al composites determined by laser ultrasonic method. In D O Thompson and D E Chimenti, editors, *Review of Proegress in Quantitative Nondestructive Evaluation*, volume 15. Plenum Press, New York. 1996.

[181] A Abbate, S C Schroeder, B E Knight, F Yee, and J Frankel. Characterization of surface and coatings using laser-generated ultrasonic surface waves. In D O Thompson and D E Chimenti. editors, *Review of Progress in Quantitat*, volume 15A, pages 585–592. Plenum Press, New York, 1996.

[182] J B Walter and K L Telschow. Laser ultrasonic detection of the solidification front during casting. In D O Thompson and D E Chimenti, editors, *Review of Progress in Quantitative Nondestructive Evaluation*, volume 15. Plenum Press, New York, 1996.

[183] D M Pepper, G J Dunning, P V Mitchell, S W McCahon, M B Klein, and T R O'Meara. Materials inspection and process control using compensated laser ultrasound evaluation (clue): Demonstration of a low-cost laser-ultrasonics sensor. SPIE Proceedings, 1996.

[184] G J Dunning, P V Mitchell, M B Klein, D M Pepper, T R O'Meara, and Y Owecko.

403

Remote laser-based ultrasonic inspection of weld joints for high volume industrial applications. In Thompson D O and Chimenti D E, editors, *Review of Progress in Quantitative Nondestructive Evaluation*, volume 15, pages 2257–2264. Plenum Press, New York, 1996.

[185] P Delaye, A Blouin, D Drolet, and J P Monchalin. Heterodyne detection of ultrasound from rough surfaces using a double phase conjugate mirror. In D O Thompson and D E Chimenti, editors, *Review of Progress in Quantitative Nondestructive Evaluation*, volume 15. Plenum Press, New York, 1996.

[186] J A Smith and C P Burger. Injection locked laser sensor for ultrasonic sensing. In D O Thompson and D E Chimenti, editors. *Review of Progress in Quantitative Nondestructive Evaluation*, volume 15. Plenum Press, New York, 1996.

[187] B Audoin, C Bescond, and M Deschamps. Measurements of stiffness coefficients of anisotropic materials from point-like generation and detection of acousitc waves. *J. Appl. Phys.*, 80:3760–3771, 1996.

[188] D Drolet, A Blouin, C Neorn, and J P Monchalin. Specifications of an ultrasonic receiver based on two-wave mixing in photorefractive gallium arsenide implemented in a laser-ultrasonic system. In D O Thompson and D E Chimenti, editors. *Review of Progress in Quantitaive Nondestructive Evaluation*, volume 15. Plenum Press, New York, 1996.

[189] P Fomitchov, S Krishnaswamy, and J D Achenbach. Fiberized sagnac interferometer for ultrasound measurement. In D O Thompson and D E Chimenti, editors, *Review of Progress in Quantitative Nondestructive Evaluation*, volume 15. Plenum Press, New York, 1996.

[190] P V Mitchell, G J Dunning, S W McCahon, M B Klein, T R O'Meara, and D M

Pepper. Compensated high-bandwidth laser ultrasonic detector based on photo-induced emf in gaas. In D O Thompson and D E Chimenti, editors, *Review of Progress in Quantitative Nondestructive Evaluation*, volume 15. Plenum Press, New York, 1996.

[191] L J Jacobs and W Whitcomb. Laser generation and detection of ultrasound in concrete. *Journal of Nondestructive Evaluation*, 16(2):57-65, 1997.

[192] J-S Yang, T Sanderson, C Ume, and J Jarzynski. Laser phased array generated ultrasound for nondestructive evaluation of ceramic materials. *Journal of nondestructive evaluation*, 16(1):1-9, 1997.

[193] S G Pierce, B Culshaw, W R Philp, F Lecuyer, and R Farlow. Broadband lamb wave measurements in aluminum and carbon/glass fibre reinforced composite materials using non-contact laser generation and detection. *Ultrasonics*, 35:105-114, 1997.

[194] C J Morath, G J Collins, R G Wolf, and R J Stoner. Ultrasonic multilayer metal film metrology. *Solid state technology*, pages 85-92, June 1997.

[195] B Audoin and C Bescond. Measurements by laser-generated ultrasound of four stiffness coefficients of an anisotropic material at elevated temperatures. *J. Nondestr. Eval.*, pages 91-100, 1997.

[196] R Coulette, E Lafond, C Nadal, M-H Andd Gondard, F Lepoutre, and O Petillon. Laser-generated ulrasound applied to two-layered materials chaacterization: semi-analytical model and experimental validation. *Ultrasonics*, 36:239-243, 1998.

[197] R F Anastasi, A D Friedman, M K Hinders, and E I Madaras. Application of laser based ultrasound for nde of damage in thick stitched composites. pages 3-7, 1997.

[198] R F Anastasi, A D Friedman, Hinders M K, and E I Madaras. Nondestructive evalu-

ation of damage in stitched composites using laser based ultrasound. pages 66–78, 1997.

[199] R F Anastasi, A D Friedman, M K Hinders, and E I Madaras. Nde of damage in thick stitched composites using laser based ultrasound with optical fibers for remote generation and detection. *Materials Evaluation*, 56(12):1402–1406, 1998.

[200] A D Friedman, M K Hinders, E I Madaras, and R F Anastasi. Study of generation mechanisms for laser ultrasonics. volume 18, page 293, 1999.

[201] A D Friedman, M K Hinders, R F Madaras, and E I Madaras. Generation mechanisms for laser ultrasonics. In G Gasklini, C Lebositz, and E Boltz, editors, *Nondestructive Evaluation of Aging Materials and Composites*, pages 248–259. SPIE, 1999.

[202] J Huang and J D Achenbach. Measurements of surface waves speed and attenuation by a dual-probe laser interferometer. In D O Thomspon and D E Chimenti, editors, *Review of Progress in Quantitat*, volume 10A, pages 523–530. Plenum Press, New York, 1991.

[203] E F Carome, N A Clark, and C E Moeller. Generation of acoustic signals in liquids by ruby laser-induced thermal stress transients. *Applied Physics Letters*, 4(6):95–97, 1964.

[204] E F Carome, C E Moeller, and N A Clark. Intense ruby-laser-induced acoustic impulses in liquids. *J. Acoust. Soc. Am.*, 40(6):1462–1466, 1966.

[205] J F Ready. Effects dues to absorption of laser radiation. *Journal of Applied Physics*, 36(2):462–468, February 1965.

[206] L S Gournay. *J. Acoust. Soc. Am.*, 40:1322, 1966.

[207] S S Penner and O P Sharma. Interaction of laser radiation with an absorbing semi-infinite solid bar. *Journal of Applied Physics*, 37(6):2304–2308, May 1966.

[208] M J Brienza and A J Demaria. Laser-induced microwave sound by surface heating. *Applied Physics Letters*, 11(2):44–46, 15 July 1967.

[209] R E Lee and R M White. Excitation of surface waves by transient surface heating. *Applied Physics Letters*, 12(1):12–14, 1 January 1968.

[210] G Cachier. Laser excitation of microwave sound in solids. *J. Acoust. Soc. Am.*, 49(3):974–978, 1971.

[211] Y Kohanzadeh, J R Whinnery, and M M Carroll. Thermoelastic waves generated by laser beams of low power. *J. Acoust. Soc. Am.*, 57(1):67–70, 1975.

[212] H M Ledbetter and J C Moulder. Laser-induced rayleigh waves in aluminum. *J. Acoust. Soc. Am.*, 65(3):840–842, 1979.

[213] A M Aindow, R J Dewhurst, D A Hutchins, and S B Palmer. Laser-generated ultrasonic pulses at free metal surface. *J. Acoust. Soc. Am.*, 62(2):449–455. 1981.

[214] A M Aindow, R J Dewhurst, and S B Palemer. Laser-generation of directional surface acoustic wave pulses in metals. *Optics Comm.*, 42(2):116–120. 1982.

[215] H M Lai and K Young. Theory of the pulsed optoacoustic technique. *J. Acoust. Soc. Am.*, 72(6):2000–2007, December 1982.

[216] T Berthelot and I Busch-Vishniac. Laser-induced thermoacoustic radiation. *J. Acoust. Soc. Am.*, 78:2074–2082, 1985.

[217] R J Von Gutfeld, F A McDonald, and R W Dreyfus. Surface deformation measurements following excimer laser irradiation of insulators. *Appl. Phys. Lett.*, 49(17):1059–1061, October 1986.

[218] F A McDonald. Photoacoustic, photothermal, and related techniques: a review. *Can. J. Phys.*, 64:1023–1029. 1986.

407

[219] A C Tam. Applications of photoacoustic sensing techniques. *Rev. Mod. Phys.*, 58(2):381–431, April 1986.

[220] D A Hutchins. Mechanisms of pulsed photoacoustic generation. *Can. J. Phys.*, 64:1247–1264, 1986.

[221] R W Dreyfus, F A McDonald, and R J Von Gutfeld. Laser energy deposition at sapphire surfaces studied by pulse photothermal deformation. *Appl. Phys. Lett.*, 50(21):=14931491, May 1987.

[222] J A Vogel, A J A Bruinsma, and A J Berkhout. Beamsteering of laser generated ultrasound. In *Ultrasonics International Conference Proceedings*. pages 141–152, UK, 1987.

[223] R C Addison, L J Graham, R S Linebarger. and B R Tittmann. Laser-based ultrasonics for the inspection of solids. In D O Thompson and D E Chimenti, editors, *Review of Progress in Quantitative Nondestructive Evaluation*. volume 7A. pages 585–594. Plenum Press, New York, 1988.

[224] J Wagner, J Deaton, and J Spicer. Generation of ultrasound by repetitively q-switching a pulsed nd:yag laser. *Appl. Opt.*, 27:4696–4700. 1988.

[225] J W Wagner and J B Deaton. Laser generation of narrow band ultrasound. In D O Thompson and D E Chimenti, editors, *Review of Progress in Quantitat.* volume 8A. pages 505–512. Plenum Press, New York, 1989.

[226] B A Barna, D M Tow, and R T Allemeier. Laser detection of acoustic displacements by destabilizing a frequency stabilized helium neon laser. In D O Thompson and D E Chimenti, editors, *Review of Progress in Quantitat.* volume 8A, pages 543–549. Plenum Press, New York, 1989.

[227] C Edwards, G S Taylor, and S B Palmer. *J. Phys. D: Appl. Phys.*, 22:1266. 1989.

408

[228] R J Dewhurst and W S A R Al'Rubai. Generation of short acoustic pulses from an energetic picosecond laser. *Ultrasonics*, 27:262–269, 1989.

[229] J Jarzynski and Y Bertherlot. The use of optical fibers to enhance the laser generation of ultrasonic waves. *J. Acoust. Soc. Am.*, 85(1):158–162, 1989.

[230] J Wagner, A Mckie, J Spicer, and J Deaton. Modulated laser array sources for generation of narrowband and directed ultrasound. *J Nondestrucitve Evaluation*, 9:263–270, 1990.

[231] J W Wagner, A D W McKie, J B Spicer, and J B Deaton. Laser generation of "directed" ultrasound in solids using spatial and temporal beam modulation. In D O Thompson and D E Chimenti. editors, *Review of Progress in Quantitat*, volume 9A, pages 487–494. Plenum Press. New York, 1990.

[232] Y H Bertherlot and J Jarzynski. Directional laser generation and detection of ultrasound with arrays of optical fibers. In D O Thompson and D E Chimenti, editors, *Review of Progress in Quantitat*, volume 9A, pages 463–494. Plenum Press. New York, 1990.

[233] J Deaton, A McKie, J Spicer, and J Wagner. Generation of narrow-band ultrasound with a long cavity mode-locked nd:yag laser. *Appl. Phys. Lett.*, 56:2390–2392. 1990.

[234] J B Deaton, A D W McKie, and J B Spicer. Mode-locked laser generation of narrowband ultrasound. In D O Thompson and D E Chimenti, editors, *Review of Progress in Quantitat*, volume 10A, pages 493–497. Plenum Press, New York, 1991.

[235] R O Claus and D O Thompson. Optical fiber-based ultrasonic wave generation and detction in materials. In D O Thompson and D E Chimenti. editors, *Review of Progress in Quantitat*, volume 10A, pages 515–521. Plenum Press, New York, 1991.

409

[236] N M Carlson and J A Johnson. Ultrasound generation through a fiber optic delivery system using pulsed laser energy. In D O Thompson and D E Chimenti, editors, *Review of Progress in Quantitat*, volume 10A, pages 507–514. Plenum Press, New York, 1991.

[237] J Huang, S Krishnaswami, and J D Achenbach. Laser generation of narrow-band surface waves. *J. Acoust. Soc. Am.*, 92(5):2527–2531, November 1992.

[238] J B Deaton, J B Spicer, and Wagner J W. Long cavity laser excitation and digital filtering of narrowband ultrasound for enhanced signal-to-noise ratio. In D O Thompson and D E Chimenti, editors, *Review of Progress in Quantitat*, volume 11A, pages 601–608. Plenum Press. New York, 1992.

[239] L S Koo and K L Telschow. Analysis of laser ultrasonic measurements of surface waves on elastic spheres. In D O Thompson and D E Chimenti, editors, *Review of Progress in Quantitat*, volume 11A, pages 609–615. Plenum Press. New York, 1992.

[240] M-H Noroy, D Royer, and M Fink. The laser-generated ultrasonic phased array: Analysis and experiments. *J. Acoust. Soc. Am.*, 94(4):1934–1943, October 1993.

[241] S J Davies, C Edwards, G C Taylor. and S B Palmer. Laser-generated ultrasound: its properties, mechanisms and mulitfarious applications. *J. Phys. D.: Appl. Phys.*, 26:329–348, 1993.

[242] J W Wagner. Source efficiency and sensor detectablility factors in alser ultrasonnics. In D O Thompson and D E Chimenti, editors, *Review of Progress in Quantitat*, volume 12A, pages 517–525. Plenum Press, New York, 1993.

[243] T W Murray and J W Wagner. Progress in pulsed laser array techniques ofr generation

of acoustic waves. In D O Thompson and D E Chimenti, editors, *Review of Progress in Quantitat*, volume 13A, pages 533–539. Plenum Press, New York, 1994.

[244] W M D Wright, D W Schindel, and D A Hutchins. Studies of laser-generated ultrasound using a micromachined silicon electrostatic transuducer in air. *J. Acoust. Soc. Am.*, 95(5):2567–2575, May 1994.

[245] J H Lee and C P BUrger. Finite element modeling of laser-generated lamb waves. *Computers and Structures*, 54(3):499–514, 1995.

[246] R Pierce, C Ume, and J Jarzynski. Temporal modulation of a laser source for the generation of ultrasonic waves. *Ultrasonics*, 33(2):133–137, 1995.

[247] J S Steckenrider, T W Murray, J B Deaton, and J W Wagner. Sensitivity enhancement in laser ultrasonics using a versatile laser array system. *J. Acoust. Soc. Am.*, 97(1):273–279, January 1995.

[248] A R Dougal and C P Yakymyshyn. Optical detection of ultrasound using a microchip laser. *Rev. Sci. Instrum.*, 66(8):4102–4113, August 1995.

[249] C E Duffer and C P Burger. Narrow band ultrasonic nde. In D O Thompson and D E Chimenti, editors, *Review of Progress in Quantitative Nondestructive Evaluation*, volume 15. Plenum Press, New York, 1996.

[250] J N Caron, J B Mehl, and K V Steiner. Laser ultrasonic thermoelastic/ablation generation with laser interferometric detection in graphite/polymer composites. In D O Thompson and D E Chimenti, editors, *Review of Progress in Quantitative Nondestructive Evaluation*, volume 15. Plenum Press, New York, 1996.

[251] L G Hector Jr. and R B Hetnarski. Thermal stresses due to a laser pulse: Elastic solution. *Transactions of the ASME*, 63:38–46, March 1996.

[252] M I Khan and G J Diebold. The photoacoustic effect by laser irradiation of an isotropic solid cylinder. *Ultrasonics*, 34:19–24, 1995.

[253] T W Murray, J B Deaton, and J W Wagner. Experimental evaluation of enhanced generation of ultrasonic waves using an array of laser sources. *Ultrasonics*, 34:69–77, 1996.

[254] T Sanderson, U Ume, and J Jarzynski. Laser generated ultrasound: a thermoelastic analysis of the source. *Ultrasonics*, 35:115–124, 1997.

[255] D A Hutchins. *Ultrasonic Generation by Pulsed Lasers*, volume XVIII, pages 21–123. Academic Press, 1988.

[256] M R Spiegel. *Mathematical Handbook*. McGraw-Hill, Inc., 1992.

[257] E Hecht. *Optics*. Addison-Wesley Publishing Company, 1990.

[258] Boas M L. *Mathematical Methods in the Physical Sciences*. John Wiley & Sons, 1983.

[259] R N Bracewell. *The Fourier Trasnform and Its Applications*. McGraw-Hill, Inc., 2nd, revised edition, 1986.

[260] J H Weaver. *Theory of Discete and Continuous Fourier Analysis*. John Wiley and Sons, 1989.

[261] R A Kline. *Nondestructive Characterization of Composite Media*. Technomic Publishing Co., Inc., 1992.

[262] A D Poularikas, editor. *The transforms and applications handbook*. CRC press, 1996.

[263] A H Nayfeh. The general problem of elastic wave propagation in anisotropic medi. *J. Acoust. Soc. Am.*, 89:1521–1531, 1991.

[264] V I Krylov and N S Skoblya. *Handbook of Numerical Inversion of Laplace Transforms*. Israel Program for Scientific Translations, 1969.

[265] E D Palik, editor. *Handbook of Opticla Constants of SOlids II*, volume II. Academic

Press, 1998.

.

413

Vita

Adam Friedman was born on February 17, 1972 in Denver, Colorado. He received his Bachelor of Science degree from the Department of Physics with High Honors at the College of William and Mary in 1994. He received his Masters of Science degree from the Department of Applied Science at the College of William and Mary in 1995.